JOURNAL OF THE ELECTROCHEMICAL SOCIETY

ELECTROCHEMICAL SCIENCE AND TECHNOLOGY

SOLID-STATE SCIENCE AND TECHNOLOGY

REVIEWS AND NEWS



VOL. 126, NO. 3 MARCH 1979

Boston, Massachusetts Meeting Program

JESOAN 126 (3) 349-506, 77C-174C

FUTURE MEETINGS

BOSTON, MASSACHUSETTS—MAY 6, 7, 8, 9, 10, & 11, 1979

Headquarters at the Sheraton Boston Hotel

Final program published in the March 1979 issue of **This Journal.** If you would like a copy of the advance program booklet and other information pertaining to this meeting, please write: Boston Meeting, The Electrochemical Society, Inc., P.O. Box 2071, Princeton, N.J. 08540.

LOS ANGELES, CALIFORNIA—OCTOBER 14, 15, 16, 17, 18, & 19, 1979

Headquarters at the Los Angeles Bonaventure

The detailed Call for Papers published in 1978 December-1979 May issues of **This Journal.** Final program published in 1979 August issue of **This Journal.**

Planned symposia for the Los Angeles Meeting include the following Divisions, Group, Subcommittee, and subjects:

Battery—Ambient Temperature Lithium Batteries, Lead Acid-New Developments, Power Sources for Biomedical Implantable Applications, General Session; **Battery/Electrothermics & Metallurgy/Physical Electrochemistry/Energy Technology**—Electrochemical Processes in High Temperature Batteries and Fuel Cells; **Battery/Energy Technology**—Electrochemical and Thermal Modeling of Batteries; **Battery/Energy Technology/Physical Electrochemistry**—Catalyst Structure and Catalyst Support Interactions in Energy Conversion and Storage Devices; **Corrosion**—Electrochemistry of Hot Corrosion, General Session; **Corrosion/Electronics**—Contact Metallurgy and Contact Resistance; **Corrosion/Electrothermics & Metallurgy/New Technology/The Metallurgical Society of AIME**—Amorphous Metals and Films; **Corrosion/Energy Technology**—Geothermal Energy Systems; **Dielectrics & Insulation**—General Session; **Dielectrics & Insulation/Electronics**—Applications of Glasses in Device Technology, Degradation Mechanisms in Electronic Devices, Second Symposium on Display Technology, Heteroepitaxial Silicon on Sapphire and Competing Technologies, Thin Film Interfaces and Interactions; **Dielectrics & Insulation/Electronics/Electrothermics & Metallurgy**—Seventh International Conference on Chemical Vapor Deposition; **Electrodeposition**—General Session; **Electrodeposition/Electronics**—Metal Patterning by Selective Deposition; **Electronics**—Business Trends in the Electronics Industry, International Symposium on Gettering in Semiconductors, Laser and Electron Beam Processing of Electronic Materials, Magneto-Optical Materials, Semiconductors and Other Electronic Materials General Session; **Electronics/Energy Technology**—Photoelectrochemistry at Semiconductor Electrodes; **Energy Technology**—General Session; and **New Technology**—Ion-Selective Electrodes.

ST. LOUIS, MISSOURI—MAY 11, 12, 13, 14, 15, & 16, 1980

Headquarters at the Chase Park Plaza

The detailed Call for Papers published in 1979 July-December issues of **This Journal.** Final program published in 1980 March issue of **This Journal.**

Planned symposia for the St. Louis Meeting include the following Divisions, Group, Subcommittee, and subjects:

Battery/Energy Technology—Load Leveling and Regenerative Breaking for Transportation; **Corrosion/Electrothermics & Metallurgy/Energy Technology/Industrial Electrolytic/Physical Electrochemistry**—New Electrode Materials in Molten Salt Processes; **Corrosion/Physical Electrochemistry**—Substrate Morphology Effects in Electrode Processes; **Dielectrics & Insulation**—Electronic Devices for Chemical Analysis, Switching Phenomena, and Filamentary Conduction in Dielectrics, General Session; **Dielectrics & Insulation/Electronics**—Bubble Memory Technology, Plasma Etching and Deposition, Conducting Polymers; **Electronics**—Diffusion Processes in Semiconducting Materials, Processing of Optical Imaging Devices, Semiconductors and Other Electronic Materials General Session, Semiconductors Recent News Papers, Phosphor Depreciation and Surface Properties, U.V. Emitting Phosphors and Lamps, Luminescence General Session; **Electronics/Electrothermics & Metallurgy**—Ninth International Conference on Electron and Ion Beams in Science and Technology; **Electronics/Electrothermics & Metallurgy/Energy Technology**—Low Cost Silicon Crystal Growth, Electronic and Optical Properties of Polycrystalline and Impure Silicon; **Electronics/Energy Technology**—Current Voltage Characteristics of Photovoltaic Devices; **Electrothermics & Metallurgy/Energy Technology**—Thermochemical Energy Storage; **Energy Technology**—General Session; **Industrial Electrolytic**—Electrochemical Methods of Waste Water Purification, Engineering Analysis of Electrochemical Systems, General Session; **Physical Electrochemistry**—General Session; **New Technology**—Electrochemical Aspects of Weather and Space Phenomena, Supercritical Fluids, Zero Gravity Phenomena; and **New Technology/Corrosion**—Enhanced Oil Recovery.

THE ELECTROCHEMICAL SOCIETY BOOKS IN PRINT

Monograph Series

The following hardbound volumes are sponsored by The Electrochemical Society, Inc. and published by John Wiley & Sons, Inc., 605 Third Avenue, New York, N.Y. 10016. Members of the Society can receive a 33% discount by ordering from Society Headquarters. Books and invoice are mailed by publisher. Nonmembers (including subscribers) must order direct from the publisher. All prices subject to change without notice.

Corrosion Handbook, edited by Herbert H. Uhlig (1948). 1188 pages, **$42.95.**

Arcs in Inert Atmospheres and Vacuum, *edited by* W. E. Kuhn. A 1956 Spring Symposium (1956). 188 pages, **$13.95.**

The Stress Corrosion of Metals, by Hugh I. Logan (1966). 306 pages, **$27.95.**

The Corrosion of Light Metals, by H. P. Godard, W. B. Jepson, M. R. Bothwell, and R. L. Kane (1967). 360 pages, **$24.95.**

High-Temperature Materials and Technology, edited by I. E. Campbell and E. M. Sherwood (1967). 1022 pages, **$48.75.**

Alkaline Storage Batteries, by S. Uno Falk and Alvin J. Salkind (1969). 656 pages, **$49.50.**

The Primary Battery, Volume I, edited by George W. Heise and N. Corey Cahoon (1971). 500 pages, **$42.95.**

Zinc-Silver Oxide Batteries, edited by Arthur Fleischer and John J. Lander (1971). 544 pages, **$43.95.**

Handbook on Corrosion Testing and Evaluation, edited by W. H. Ailor (1971). 873 pages, **$58.25.**

Modern Electroplating, edited by Frederick A. Lowenheim. Third Edition (1974). 801 pages, **$37.95.**

Marine Corrosion, *by Francis L. LaQue (1975). 332 pages,* **$27.50.**

The Primary Battery, Volume II, edited by George W. Heise and N. Corey Cahoon (1975). 528 pages, **$42.95.**

Lead-Acid Batteries, by Hans Bode (1977). 387 pages, **$31.00.**

Thin Films—Interdiffusion and Reactions, edited by J. M. Poate, K. N. Tu, and J. W. Mayer (1978). 576 pages, **$35.00.**

Society Symposium Series

The following softbound symposium volumes are sponsored and published by The Electrochemical Society, Inc., P.O. Box 2071, Princeton, N.J. 08540. Orders filled at the list price given, subject to availability. Enclose payment with order.

High-Temperature Metallic Corrosion of Sulfur and Its Compounds. Z. A. Foroulis, Editor. A 1969 symposium. 276 pages, **$4.50.**

Electron and Ion Beam Science and Technology, Fourth International Conference. R. Bakish, Editor. A 1970 symposium. 680 pages, **$7.50.**

Fundamentals of Electrochemical Machining. C. L. Faust, Editor. A 1970 symposium. 365 pages, **$4.50.**

Electron and Ion Beam Science and Technology, Fifth International Conference. R. Bakish, Editor. A 1972 symposium. 420 pages, **$5.50.**

Electrochemical Contributions to Environmental Protection. T. R. Beck, O. B. Cecil, C. G. Enke, J. McCallum, and S. T. Wlodek, Editors. A 1972 symposium. 173 pages, **$4.00.**

Oxide-Electrolyte Interfaces. R. S. Alwitt, Editor. A 1972 symposium. 312 pages, **$9.00.**

Marine Electrochemistry. J. B. Berkowitz, M. Banus, M. J. Pryor, R. Horne, P. L. Howard, G. C. Whitnack, and H. V. Weiss, Editors. A 1972 symposium. 416 pages, **$15.00.**

Semiconductor Silicon 1973. H. R. Huff and R. R. Burgess, Editors. A 1973 symposium. 936 pages, **$15.00.**

Electrochemical Bioscience and Bioengineering. H. T. Silverman, I. F. Miller, and A. J. Salkind, Editors. A 1973 symposium. 268 pages, **$8.00.**

Chlorine Bicentennial Symposium. T. C. Jeffery, P. A. Danna, and H. S. Holden, Editors. A 1974 symposium. 404 pages, **$11.00.**

Electrocatalysis. M. W. Breiter, Editor. A 1974 symposium. 378 pages, **$12.00.**

Electron and Ion Beam Science and Technology, Sixth International Conference. R. Bakish, Editor. A 1974 symposium. 594 pages, **$16.00.**

Properties of Electrodeposits—Their Measurement and Significance. R. Sard, H. Leidheiser, Jr., and F. Ogburn, Editors. A 1974 symposium. 430 pages, **$13.00.**

Metal-Slag-Gas Reactions and Processes. Z. A. Foroulis and W. W. Smeltzer, Editors. A 1975 symposium. 1032 pages, **$20.00.**

Chemistry and Physics of Aqueous Gas Solutions. W. A. Adams, G. Greer, J. E. Desnoyers, G. Atkinson, G. S. Kell, K. B. Oldham, and J. Walkley, Editors. A 1975 symposium. 522 pages, **$11.00.**

Chemical Vapor Deposition, Fifth International Conference. J. M. Blocher, Jr., H. E. Hintermann, and L. H. Hall, Editors. A 1975 symposium. 848 pages, **$18.00.**

Thermal and Photostimulated Currents in Insulators. D. M. Smyth, Editor. A 1975 symposium. 215 pages, **$7.00.**

Energy Storage. H. P. Silverman and J. B. Berkowitz, Editors. A 1975 symposium. 258 pages, **$8.00.**

Etching. H. G. Hughes and M. J. Rand, Editors. A 1976 symposium. 203 pages, **$7.00.**

Electron and Ion Beam Science and Technology, Seventh International Conference. R. Bakish, Editor. A 1976 symposium. 632 pages, **$18.00.**

International Symposium on Solar Energy. J. B. Berkowitz and I. A. Lesk, Editors. A 1976 symposium. 372 pages, **$10.00.**

International Symposium on Molten Salts. J. P. Pemsler, J. Braunstein, K. Nobe, D. R. Morris, and N. E. Richards, Editors. A 1976 symposium. 632 pages, **$16.00.**

Properties of High Temperature Alloys. Z. A. Foroulis and F. S. Pettit, Editors. 851 pages, **$12.00.**

Semiconductor Silicon 1977. H. R. Huff and E. Sirtl, Editors. A 1977 symposium. 1100 pages, **$15.00.**

A History of The Electrochemical Society. R. M. Burns with E. G. Enck. 160 pages, **$5.00.**

Semiconductor-Liquid Junction Solar Cells. A. Heller, Editor. A 1977 symposium. 340 pages, **$7.00.**

Load-Leveling. N. P. Yao and J. R. Selman, Editors. A 1977 symposium. 412 pages, **$13.00.**

Chemical Vapor Deposition, Sixth International Conference. L. F. Donaghey, P. Rai-Choudhury, and R. N. Tauber, Editors. A 1977 symposium. 596 pages, **$14.00.**

Electrode Materials and Processes for Energy Conversion and Storage. J. D. E. McIntyre, S. Srinivasan, and F. G. Will, Editors. A 1977 symposium. 1048 pages, **$20.00.**

High Temperature Metal Halide Chemistry. *D. L. Hildenbrand and D. D. Cubicciotti, Editors. A 1977 symposium.* 678 pages, **$17.00.**

Thin Film Phenomena—Interfaces and Interactions. J. E. E. Baglin and J. M. Poate, Editors. A 1977 symposium. 525 pages, **$14.00.**

Semiconductor Characterization Techniques. P. A. Barnes and G. A. Rozgonyi, Editors. A 1978 symposium. 532 pages. **$16.00.**

Industrial Water Electrolysis. S. Srinivasan, F. J. Salzano, and A. R. Landgrebe, Editors. A 1978 symposium. 297 pages, **$12.00.**

Electron and Ion Beam Science and Technology, Eighth International Conference. Robert Bakish, Editor. A 1978 symposium. 684 pages, **$20.00.**

Selected Topics in the History of Electrochemistry. George Dubpernell and J. H. Westbrook, Editors. A 1977 symposium. 523 pages; $11.00.

3/79

ห้องสมุด กรมวิทยาศาสตร์บริการ
23 พ.ค. 2528

EDITOR
Norman Hackerman
Dorothy Cox, **Assistant to the Editor**

DIVISIONAL EDITORS

Battery
R. J. Brodd — Boone B. Owens
Elton J. Cairns — J. L. Weininger
G. F. Nordblom

CORROSION
J. W. Faust, Jr. — Ken Nobe
R. P. Frankenthal — Earl S. Snavely, Jr.
Jerome Kruger — Ellis D. Verink
Florian Mansfeld — J. Bruce Wagner

DIELECTRICS AND INSULATION
Robert S. Alwitt — George L. Schnable
Dennis Hess — Lawrence Young
T. W. Hickmott

ELECTRODEPOSITION
Ugo Bertocci — Nathan Feldstein
Huk Y. Cheh — Y. Okinaka

ELECTRONICS
Ephraim Banks — Simon Larach
D. M. Brown — Ernest Paskell
George R. Cronin — Bertram Schwartz
Glenn W. Cullen — Frederic N. Schwettmann
John A. DeLuca — A. K. Sinha
Murray Gershenzon — P. Wang
James S. Harris — J. M. Woodall

ELECTROTHERMICS AND METALLURGY
William A. Adams — Gene F. Wakefield
Joan B. Berkowitz — Jack H. Westbrook
W. E. Kuhn

High Temperature Science and Technology
Leo Brewer — E. D. Cater
Daniel Cubicciotti

INDUSTRIAL ELECTROLYTIC
Richard C. Alkire — Scott Lynn

ORGANIC AND BIOLOGICAL ELECTROCHEMISTRY
Martin Blank — Stanley Wawzonek
Arthur A. Pilla

PHYSICAL ELECTROCHEMISTRY
A. J. de Bethune — Keith B. Oldham
M. J. Dignam — Robert A. Osteryoung
Larry R. Faulkner — David K. Roe
George J. Janz — C. W. Tobias
Barry Miller — F. G. Will

News Editor—Jack H. Westbrook

Book Review Editor—Julius Kleror

JOURNAL OF THE ELECTROCHEMICAL SOCIETY
(USPS 284-140)

The JOURNAL OF THE ELECTROCHEMICAL SOCIETY (USPS 284-140) is published monthly by The Electrochemical Society, Inc. at 215 Canal St., Manchester, N.H. 03108. The address for the Executive Offices, Editorial and Advertising Office, and Circulation Department of The Electrochemical Society, Inc. is P.O. Box 2071, Princeton, N.J. 08540. Subscription to members as part of membership service; subscription to nonmembers $60.00 plus $5.00 for postage outside U.S. and Canada. Single copies $3.25 to members, $5.00 to nonmembers. © Copyright 1979 by The Electrochemical Society, Inc. Second Class Postage paid at Princeton, New Jersey and at additional mailing offices.

POSTMASTER: Send address changes to THE ELECTROCHEMICAL SOCIETY, INC., P.O. Box 2071, Princeton, N.J. 08540.

March 1979

ELECTROCHEMICAL SCIENCE AND TECHNOLOGY

TECHNICAL PAPERS

D. W. Murphy, J. N. Carides ... 349 — Low Voltage Behavior of Lithium/Metal Dichalcogenide Topochemical Cells

C. P. Wales ... 351 — Cupric Oxalate Cathodes for Seawater Cells

R. F. Savinell, C. C. Liu, R. T. Galasco, S. H. Chiang, J. F. Coetzee ... 357 — Discharge Characteristics of a Soluble Iron-Titanium Battery System

K. R. Bullock ... 360 — The Effect of Phosphoric Acid on the Positive Electrode in the Lead-Acid Battery II. Constant Potential Corrosion Studies

B. K. Mahato ... 365 — The Cyclic Corrosion of the Lead-Acid Battery Positive

T. M. Devine ... 374 — Mechanism of Intergranular Corrosion and Pitting Corrosion of Austenitic and Duplex 308 Stainless Steel

E. McCafferty ... 385 — Inhibition of the Crevice Corrosion of Iron in Chloride Solutions by Chromate

H. Leidheiser, Jr., A. Vértes, M. L. Varsányi, I. Czakó-Nagy ... 391 — The Chemical State of Cobalt in Cobalt-Hardened Gold Electrodeposits

B. K. W. Baylis, C-C. Huang, M. Schlesinger ... 394 — A Study of the Products of Ultraviolet Irradiation of Palladium-Containing Catalysts for Electroless Metal Deposition

K. Viswanathan, H. Y. Cheh ... 398 — Mass Transfer Aspect of Electrolysis by Periodic Currents

S. Wawzonek, J. M. Shradel ... 401 — Electrochemical Reduction of Benzal Chloride in the Presence of Carbon Dioxide

R. C. Hallcher, D. A. White, M. M. Baizer ... 404 — Electrochemical and Secular Syntheses of Derivatives of O-Carboxymethyltartronic Acid (1)

D. R. Rolison, K. Kuo, M. Umana, D. Brundage, R. W. Murray ... 407 — Properties of RuO_x Working Electrodes in Nonaqueous Solvents

ELECTROCHEMICAL SOCIETY

Vol. 126 • No. 3

J. D. Luttmer, A. J. Bard ... 414 — Electrogenerated Chemiluminescence 34. Photo-Induced Electrogenerated Chemiluminescence and Up-Conversion at Semiconductor Electrodes

S. M. Wilhelm, K. S. Yun, L. W. Ballenger, N. Hackerman ... 419 — Semiconductor Properties of Iron Oxide Electrodes

S. H. Glarum, J. H. Marshall ... 424 — An A-C Admittance Study of the Platinum/Sulfuric Acid Interface

K. Tokuda, S. Bruckenstein ... 431 — Sinusoidal Hydrodynamic Voltammetry at the Rotating Disk Electrode I. Theory of Electron Transfer Kinetics

Y. Kanzaki, S. Bruckenstein ... 437 — Sinusoidal Hydrodynamic Voltammetry at the Rotating Disk Electrode II. Experimental Test of the Electron Transfer Theory

TECHNICAL NOTE

M. Cohen, D. Mitchell, K. Hashimoto ... 442 — The Composition of Anodically Formed Iron Oxide Films

SOLID-STATE SCIENCE AND TECHNOLOGY

TECHNICAL PAPERS

J. H. Thomas III, S. P. Sharma ... 445 — High Temperature Film Formation on Cobalt-Hardened Gold

J. B. Theeten, F. Hottier ... 450 — In Situ Surface Analysis of the Vapor Phase Epitaxy of GaAs

R. A. Porter, W. R. Harshbarger ... 460 — Gas Rotational Temperature in an RF Plasma

G. C. Schwartz, L. B. Rothman, T. J. Schopen ... 464 — Competitive Mechanisms in Reactive Ion Etching in a CF_4 Plasma

M. Zamin, M. B. Ives ... 470 — The Anodic Oxidation of Nickel in 1N H_2SO_4 Solution

D. Laser, S. Gottesfeld ... 475 — Photocurrents Induced by Subbandgap Illumination in a Ti-Oxide Film Electrode

DIVISION OFFICERS

Battery Division
Albert Himy, Chairman
John Pierson, Vice-Chairman
Gene Gagnon, Secretary-Treasurer
General Motors Corp.
Research Laboratories, Dept. 37
12 Mile and Mound Rds.
Warren, Mich. 48090

Corrosion Division
Ken Nobe, Chairman
Robert P. Frankenthal, Vice-Chairman
Florian Mansfeld, Secretary-Treasurer
Rockwell International
Science Center
P.O. Box 1085
Thousands Oaks, Calif. 91360

Dielectrics and Insulation Division
Rudolf G. Frieser, Chairman
Richard Tauber, Vice-Chairman
James A. Amick, Treasurer
Alexis T. Bell, Secretary
Dept. of Chemical Engineering
University of California
Berkeley, Calif. 94720

Electrodeposition Division
Nathan Feldstein, Chairman
Richard Sard, Vice-Chairman
Thomas C. Franklin, Secretary-Treasurer
Dept. of Chemistry
Baylor University
Waco, Texas 76703

Electronics Division
Glenn Cullen, Chairman
Arnold Reisman, Vice-Chairman (Semiconductors)
George Gillooly, Vice-Chairman (Luminescence)
Thomas Sedgwick, Vice-Chairman (General Materials and Processes)
Gerard Blom, Treasurer
Pat Castro, Secretary
Hewlett-Packard Associates
Palo Alto, Calif. 94304

Electrothermics and Metallurgy Division
John M. Blocher, Chairman
H. Stephen Spacil, Vice-Chairman
J. Bruce Wagner, Jr., Junior Vice-Chairman
William A. Adams, Secretary-Treasurer
DREO
Dept. of National Defence
Ottawa, Ont., Canada K1A 0Z4

Energy Technology Group
S. Srinivasan, Chairman
Henry Brandhorst, Vice-Chairman
A. J. Nozik, Treasurer
James McBreen, Secretary
Brookhaven National Laboratory
Upton, N.Y. 11973

Industrial Electrolytic Division
Richard C. Alkire, Chairman
Leonard Nanis, Vice-Chairman
M. P. Grotheer, Secretary-Treasurer
Hooker Chemical Corp.
P.O. Box 344
Niagara Falls, N.Y. 14302

Organic and Biological Electrochemistry Division
Arthur A. Pilla, Chairman
Larry Miller, Vice-Chairman
John Wagenknecht, Secretary-Treasurer
Monsanto Co.
800 N. Lindbergh Blvd.
St. Louis, Mo. 63166

Physical Electrochemistry Division
Stanley Bruckenstein, Chairman
Fritz G. Will, Vice-Chairman
Elton J. Cairns, Secretary-Treasurer
General Motors Corp.
Research Laboratories
12 Mile and Mound Rds.
Warren, Mich. 48090

SOCIETY OFFICERS AND STAFF

Dennis R. Turner, President
Bell Laboratories
Room 7F-506
Murray Hill, N.J. 07974

Joan B. Berkowitz, Vice-President
Arthur D. Little, Inc.
15 Acorn Park
Cambridge, Mass. 02140

Erik M. Pell, Vice-President
Xerox Corp.
Xerox Square—W105
Rochester, N.Y. 14644

Ralph J. Brodd, Vice-President
ESB Technology Inc.
19 W. College Ave.
Yardley, Pa. 19067

Paul C. Milner, Secretary
Bell Laboratories
Room 1D-259
Murray Hill, N.J. 07974

John L. Griffin, Treasurer
Research Laboratories
General Motors Corporation
General Motors Technical Center
Warren, Mich. 48090

V. H. Branneky, Executive Secretary
The Electrochemical Society, Inc.
P.O. Box 2071
Princeton, N.J. 08540

Donna Kimberlin, Administrative Assistant
The Electrochemical Society, Inc.
P.O. Box 2071
Princeton, N.J. 08540

PUBLICATION STAFF

Sarah A. Kilfoyle, **Publication Editor**
Suzanne C. Neilson, **Assistant Publication Editor**

PUBLICATION COMMITTEE

Newton Schwartz, **Chairman**
Richard C. Alkire
Judith Ambrus
Robert T. Foley
Norman Hackerman
Paul C. Milner
John Pringle
Lawrence Young

Manuscripts submitted to the JOURNAL should be sent in triplicate to the Editorial Office at P.O. Box 2071, Princeton, N.J. 08540. They should conform to the revised "Instructions to Authors" available from Society Headquarters. Manuscripts so submitted, as well as papers presented before a Society technical meeting, become the property of the Society and may not be published elsewhere in whole or in part without written permission of the Society. Address such requests to the Editor.

The Electrochemical Society does not maintain a supply of reprints of papers appearing in its JOURNAL. A photoprint copy of any particular paper may be obtained from University Microfilms, Inc., 300 N. Zeeb St., Ann Arbor, Mich. 48106.

Inquiries regarding positive microfilm copies of issues should be addressed to University Microfilms, Inc., 300 N. Zeeb St., Ann Arbor, Mich. 48106.

Walter J. Johnson, Inc., 355 Chestnut St., Norwood, N.J. 07648, have reprint rights to out-of-print volumes of the JOURNAL, and also have available for sale back volumes and single issues with the exception of the last two calendar years.

The JOURNAL OF THE ELECTROCHEMICAL SOCIETY combines the JOURNAL and TRANSACTIONS OF THE ELECTROCHEMICAL SOCIETY. Statements and opinions given in articles and papers in the JOURNAL OF THE ELECTROCHEMICAL SOCIETY are those of the contributors, and The Electrochemical Society, Inc. assumes no responsibility for them.

Claims for a missing issue should be reported within 60 days of normal delivery date to the Circulation Dept., The Electrochemical Society, Inc., P.O. Box 2071, Princeton, N.J. 08540.

Notice of a change in address should be sent to the Circulation Dept., The Electrochemical Society, Inc., P.O. Box 2071, Princeton, N.J. 08540. Include the mailing label or the number from the mailing label from your previous issue of the JOURNAL to ensure proper identification.

SOLID-STATE SCIENCE (Cont.)

D. G. Schimmel ... 479 — Defect Etch for <100> Silicon Evaluation

M. Komuro, **N. Atoda**, **H. Kawakatsu** ... 483 — Ion Beam Exposure of Resist Materials

K. H. Lau, **D. Cubicciotti**, **D. L. Hildenbrand** ... 490 — Effusion Studies of the Vaporization/Decomposition of Potassium Sulfate

TECHNICAL NOTE

J. L. Stakebake ... 495 — Temperature Dependence of the Reaction of Hydrogen with Highly Reactive Uranium Powders

ACCELERATED BRIEF COMMUNICATIONS

D. W. Murphy, **P. A. Christian**, **F. J. DiSalvo**, **J. N. Carides** ... 497 — Vanadium Oxide Cathode Materials for Secondary Lithium Cells

T. Matsue, **M. Fujihira**, **T. Osa** ... 500 — Selective Chlorination with a Cyclodextrin-Modified Electrode

A. G. Revesz ... 502 — On the Initial Oxidation Rate of Silicon

H. Ono, **H. Tango** ... 504 — A New Technology for Tapered Windows in Insulating Films

REVIEWS AND NEWS

D. A. Vermilyea ... 81C — Edward Goodrich Acheson Medal Award Address—Social Change and Future Economic Growth

PROGRAM

... 92C

NEWS

... 159C

JOURNAL OF THE ELECTROCHEMICAL SOCIETY

ELECTROCHEMICAL SCIENCE AND TECHNOLOGY

MARCH 1979

Low Voltage Behavior of Lithium/Metal Dichalcogenide Topochemical Cells

D. W. Murphy* and J. N. Carides

Bell Laboratories, Murray Hill, New Jersey 07974

ABSTRACT

The formation of Li_2VX_2 (X = S, Se) in Li/Li^+, propylene carbonate (PC)/$LiVX_2$ cells occurs near 1.0V. The selenide, Li_2VSe_2, has been previously described. Magnetic susceptibility and x-ray powder diffraction data are presented for Li_2VS_2. The $LiVX_2/Li_2VX_2$ couples are reversible and two phase between the limiting compositions. The selenide is reversible over the range VSe_2 to Li_2VSe_2, but the sulfide deteriorates if not confined to the $LiVS_2/Li_2VS_2$ couple. TiS_2 has a similar voltage profile near 0.5V assigned to the $LiTiS_2/Li_2TiS_2$ couple, which appears to be reversible, but is accompanied by either side reaction with the electrolyte or slow decomposition of Li_2TiS_2.

Nonaqueous batteries based on lithium intercalation in layered dichalcogenides (1-3) of group IVB and VB metals are well known with the cathodic reaction of Eq. [1]

$$Li^+ + MX_2 + e^- = LiMX_2 \qquad [1]$$

The voltage range for this process is generally 2.5-1.5V *vs.* Li/Li^+. The cathodic discharge products can be prepared chemically by treatment of the MX_2 with n-BuLi (4, 5). Among group IVB and VB MX_2 compounds, only VSe_2 consumed more than one equivalent of Li by this method, and Murphy *et al.* (5) characterized a compound formulated as Li_2VSe_2. Whittingham (2) has reported some reversible electrochemical addition of Li to $LiCrS_2$.[1]

In this report we present electrochemical data on Li_2VSe_2 as well as electrochemical preparation and cycling of Li_2VS_2, and evidence for Li_2TiS_2.

Experimental

The MX_2 and $LiMX_2$ compounds used were prepared by standard methods [see Ref. (5)] and gave good x-ray powder patterns. Reagent grade propylene carbonate (PC) (Aldrich) was vacuum distilled from Li metal and $LiClO_4$ (Alfa) was vacuum dried at 150°C. The electrolyte used was 1.0*M* $LiClO_4$ in PC.

Cells were constructed as previously described (6), and were cycled at constant current between preset voltage limits. The cathodes contained only the pure MX_2 or $LiMX_2$ without any binders or conductive additives.

X-ray powder patterns of air-sensitive compounds were taken on a Phillips diffractometer, with the sample mounted in an evacuated holder, through a Be window.

Results

VSe_2.—Electrochemical cycle data for a $Li/LiClO_4$, PC/VSe_2 cell is shown in Fig. 1. The upper voltage plateau agrees with previous data (2). Cycling just the first plateau (not illustrated) under similar conditions gave 81% of theoretical capacity (based on one Li per V) on the first cycle, decaying to 75% on the 6th cycle. A second reversible plateau occurs near 1.1V *vs.* Li/Li^+ with a capacity nearly equal to that of the first. The fully discharged product was found to be identical (by x-ray powder diffraction) to Li_2VSe_2 prepared by the n-BuLi method (5). That the structure of Li_2VSe_2 is closely related to VSe_2 was confirmed by the formation of VSe_2 on treatment with iodine (7).

The constant emf's of both plateaus suggest two phase regions between VSe_2-$LiVSe_2$ and $LiVeS_2$-Li_2VSe_2. This was verified by x-ray powder data for each plateau. A sample of composition $Li_{0.5}VSe_2$ prepared by the n-BuLi and iodine methods showed equal amounts of VSe_2 and $LiVSe_2$. Cathodes partially discharged on the lower plateau showed $LiVSe_2$ and Li_2VSe_2 by x-ray powder diffraction.

VS_2.—A $Li/LiClO_4$, $PC/LiVS_2$ cell gave additional discharge capacity (Fig. 2) of 0.95 equivalents per V near 1.0V which decayed to 0.70 equivalents after 15 deep cycles and 0.60 equivalents after 30 cycles.

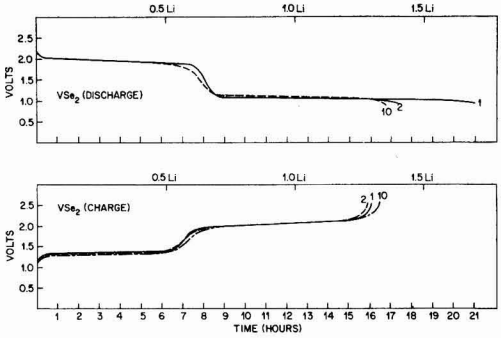


Fig. 1. Voltage of a $Li/LiClO_4$, PC/VSe_2 cell constructed as in Ref. (6) containing 19.3 mg VSe_2 cycled at 0.20 mA. One equivalent of Li/V is 12.4 hr. Cycle numbers are indicated

* Electrochemical Society Active Member.

[1] Note added in proof: Since the submission of this work, electrochemical studies of Li_2VSe_2 have been reported by Whittingham (10).

Key words: secondary battery, intercalation, diffraction.

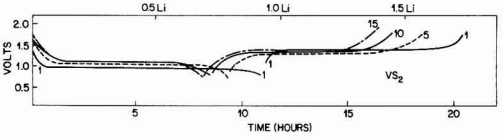


Fig. 2. Voltage of a $Li/LiClO_4$, $PC/LiVS_2$ cell containing 10.7 mg $LiVS_2$ cycled at 0.20 mA. One equivalent of Li/V is 11.75 hr.

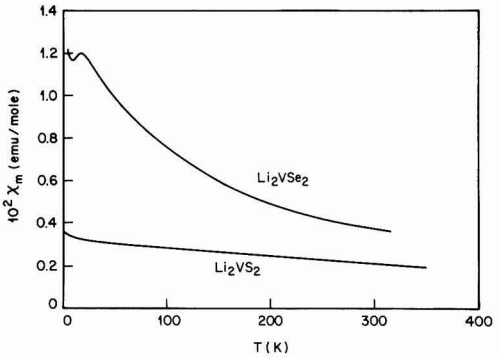


Fig. 3. The magnetic susceptibility of Li_2VS_2 compared to Li_2VSe_2 (5).

The cathode of a cell containing 300 mg $LiVS_2$ was discharged to 95% of the theoretical amount for a second equivalent of lithium, removed, washed in PC, and dried. X-ray powder diffraction data (Table I) show a highly expanded a axis (3.381Å in $LiVS_2$ to 3.830Å in Li_2VS_2). Treatment with I_2 in acetonitrile yields VS_2. The magnetic susceptibility of Li_2VS_2 (Fig. 3) exhibits only a small temperature dependence from 360 to 4.2°K in comparison to, for example, Li_2VSe_2 (5). The susceptibility is about an order of magnitude higher than that of either VS_2 or $LiVS_2$ (at 360°K $\chi_M = 2.3 \times 10^{-4}$ and 4.6×10^{-4} emu/mole, respectively), suggesting that the V^{2+} d^3 configuration is nearly, if not entirely, localized in a S = 3/2 nonmetallic configuration. The weak temperature dependence suggests a large exchange interaction on the order of 300°-400°K, which is larger than that found in Li_2VSe_2 by a factor of about four, but consistent with the smaller V-V distance in the sulfide.

Although the $Li_2VS_2/LiVS_2$ couple is readily reversible, further charging toward VS_2 rapidly leads to deterioration over the entire voltage range. The substitution of Fe for V which gave enhanced reversibility for $V_{1-x}Fe_xS_2/LiV_{1-x}Fe_xS_2$ couples (6) causes the lower voltage process to be irreversible. Differences in structure most likely account for the report by Chianelli (8) that amorphous VS_2 consumes 1.5 equivalents of n-BuLi.

TiS_2.—The titanium chalcogenides exhibit a low voltage plateau near 0.5V *vs.* Li/Li^+. For TiS_2 this plateau (Fig. 4) has a capacity near 1 equiv. Electrochemical cycling was poor when both plateaus were included, but improved reversibility was observed when cycling was restricted to the lower plateau. We have been unsuccessful to date in attempts to prepare good-quality Li_2TiS_2 for a study of physical properties.

Table I. X-ray data for Li_2VS_2

Hexagonal a = 3.830A, c = 6.215Å

d obs	d calc	hkl	I/I_o
6.215	6.215	001	100
2.926	2.926	101	100
2.259	2.268	102	60
1.914	1.915	110	30
1.827	1.830	111	10
1.743	1.757	103	20
1.642	1.658	200	5
	1.630	112	
1.542	1.554	004	10
1.457	1.463	202	10

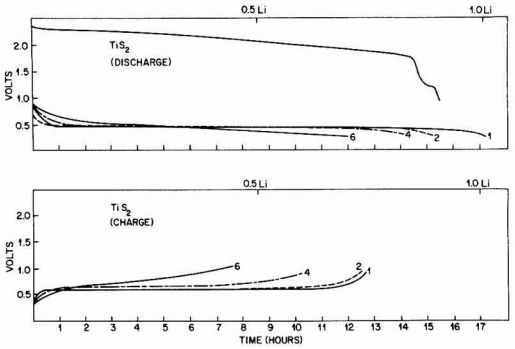


Fig. 4. Voltage of a $Li/LiClO_4$, PC/TiS_2 cell containing 14.3 mg TiS_2 cycled at 0.20 mA. One equivalent of Li/Ti is 17.1 hr.

$LiCrS_2$.—Starting with $LiCrS_2$, further reduction occurred at 0.7V *vs.* $Li//Li^+$, but was irreversible. This is in contrast to prevous results (2), indicating reversible addition of ~0.3 Li/Cr near 2V.

$NbSe_2$.—A lower voltage plateau was observed in $NbSe_2$ at 0.25V which was totally irreversible.

Discussion

Magnetic susceptibility data confirms that the electrochemical formation of Li_2VX_2 involves a reduction to V^{2+}. These compounds are isoelectronic with VCl_2 which also has a CdI_2-type layer structure. The lattice sites occupied by the Li ions are undetermined, but at least one (or both) must occupy a tetrahedral site.

The similarity of the voltage profile of TiS_2 to that of VS_2, and the existence of the layered $TiCl_2$ suggest that Li_2TiS_2 is the discharge product associated with the low voltage plateaus in TiS_2. Formation of Li_2TiS_2 is clearly kinetically controlled compared to decomposition to a number of lower Ti sulfides ($Ti_{1-x}S$), illustrated in Eq. [2] for TiS

$$2Li + TiS_2 = TiS + Li_2S \qquad [2]$$

with a theoretical emf of 1.87V. The consistently larger capacity on discharge *vs.* charge (~15%) for $LiTiS_2/Li_2TiS_2$ indicates some concomitant side reaction with the electrolyte or a slow decomposition of Li_2TiS_2. The difference in voltage between the Ti and V $LiMX_2/Li_2MX_2$ couples reflects the reduction potentials of M^{3+}/M^{2+}.

Although reduction of PC to carbonate and propene at a graphite electrode has been observed at 0.6V *vs.* Li/Li^+ (9), we do not believe that such a reduction is responsible for the TiS_2 results because the electrolyte was nonreactive to 0.25V with $NbSe_2$, and because with graphite (or $NbSe_2$) reduction is completely irreversible. Thus we suggest that intercalation of lithium into $LiTiS_2$ is the primary electrochemical process. A kinetically slow reaction with the electrolyte may subsequently occur.

The formation of Li_2VSe_2, but not Li_2VS_2, with n-BuLi places the reduction potential of n-BuLi in such systems at very near 1.0V *vs.* Li/Li^+.

The addition of a second Li to VX_2 could add nearly 50% to the energy density of an Li/MX_2 cell, but VS_2 has poor reversibility of addition of the first Li, and $Fe_xV_{1-s}S_2$, which has good reversibility for addition of the first Li, has poor reversibility of the second.

The low potential of the $LiTiS_2/Li_2TiS_2$ couple *vs.* Li/Li^+ might make it an attractive anode in cells of the type $Li_2TiS_2/Li^+/TiS_2$, yielding ~1.5-1.9V and circumventing Li plating inefficiency if the decomposition can be controlled.

Acknowledgments

The authors are indebted to F. J. Di Salvo and J. V. Waszczak for the magnetic susceptibility data of Li_2VS_2.

Manuscript submitted Aug. 9, 1978; revised manuscript received Sept. 25, 1978.

Any discussion of this paper will appear in a Discussion Section to be published in the December 1979 JOURNAL. All discussions for the December 1979 Discussion Section should be submitted by Aug. 1, 1979.

Publication costs of this article were assisted by Bell Laboratories.

REFERENCES

1. D. W. Murphy and F. A. Trumbore, *J. Crystal Growth*, **39**, 185 (1977).
2. M. S. Whittingham, *Prog. Solid State Chem.*, **12**, 1 (1978).
3. G. L. Holleck and J. R. Driscoll, *Electrochim. Acta*, **22**, 647 (1977).
4. M. B. Dines, *Mater. Res. Bull.*, **10**, 287 (1975).
5. D. W. Murphy, F. J. DiSalvo, G. W. Hull, Jr., and J. V. Waszczak, *Inorg. Chem.*, **15**, 17 (1976).
6. D. W. Murphy, J. N. Carides, F. J. DiSalvo, C. Cros, and J. V. Waszczak, *Mater. Res. Bull.*, **12**, 825 (1977).
7. D. W. Murphy, C. Cros, F. J. DiSalvo, and J. V. Waszczak, *Inorg. Chem.*, **16**, 3027 (1977).
8. R. R. Chianelli and M. B. Dines, *Ger. Offen.*, **2**, 556, 472 (1975) and *Inorg. Chem.*, **17**, 2758 (1978).
9. A. N. Dey and B. P. Sullivan, *This Journal*, **117**, 222 (1970).
10. M. S. Whittingham, *Mater. Res. Bull.*, **13**, 959 (1978).

Cupric Oxalate Cathodes for Seawater Cells

Charles P. Wales*

Naval Research Laboratory, Washington, D.C. 20375

ABSTRACT

As part of a study on seawater batteries, cells with cupric oxalate cathodes and aluminum alloy A6 anodes were discharged at room temperature. The cupric oxalate cathodes gave their highest capacity, about 94-96% of theoretical capacity, when discharges lasted 4-8 days. Metallic copper was the predominant discharge product. Adding sulfur to the cupric oxalate increased the average discharge potential by about 0.17V, increased the total ampere-hour efficiency by 2-3%, and lowered the rate of self-discharge. Cells using a sulfur-cupric oxalate mixture delivered most of their capacity at about 1.45V when discharged at the 11-day rate, and at an average of 1.1V when discharged at the one-day rate. When sulfur was present, the predominant discharge product was CuS instead of Cu. If cupric oxalate remained after all sulfur had reacted to CuS, then the cupric oxalate and CuS were reduced simultaneously with the final product being $Cu_{1.97}S$.

The results of using aluminum-zinc alloys as anodes (1) and MnO_2 as cathode active material (2) have already been reported as part of a study on improving seawater batteries. This work has been extended to include cupric oxalate as the cathode active material. Aoki and Hiroi reported that cupric oxalate was an effective cathode material in a seawater battery (3, 4). They also reported that adding sulfur increased cell potential by about 0.2V, increased utilization of cupric oxalate, and gave CuS as the discharge product. Optimum composition was given as 50% cupric oxalate, 10% sulfur, 30% graphite (for conductivity), and 10% ammonium chloride. This composition is equivalent to 1 mole of sulfur per mole of cupric oxalate. The active material was pasted onto copper gauze. Their anode was magnesium.

There has apparently been no commercial development of cells using cupric oxalate. The present work was undertaken to study in more detail the behavior of cupric oxalate in seawater and to determine if cupric oxalate is a practical cathode material.

Experimental

It was necessary to add conductive material to the cupric oxalate. UCET acetylene black (Union Carbide Corporation) gave good results. Sulfur was also added to many of the cathodes. In order to determine the effect of varying the amount of sulfur, the weight ratios of sulfur:cupric oxalate ranged from 0.02:1 to 0.40:1. This gave mole ratios of 0.095:1 to 1.90:1 for sulfur:cupric oxalate. The binder was Neoprene AD-20 (du Pont) dissolved in toluene to give a 10% solution, using a modification of the polymer bonding method given by Weininger and Secor (5). Most cathodes contained weight ratios of 6:1:0.40 for active material:acetylene black:neoprene (dry weight), where the active material was considered to be the cupric oxalate plus any sulfur. Sometimes 6:0.2:0.26 ratios were used. These proportions were not critical over this range.

The active material mix was pressed onto conductive grids at 1.5 kg mm^{-2} and allowed to air dry for at least one week before use in a cell. The grids were 36 × 36 mm with a 10 mm wide lead extending 44 mm up from one corner. The grid material was either a woven carbon fiber made by Fiberite using Thornel 300 or size 3/0 expanded copper (Exmet Company). Copper grids had the lower half of their lead coated with an inert material such as silicone rubber for corrosion protection of the exposed copper. The total weight of cupric oxalate plus sulfur was about 5g in a cathode. Cathodes using the 6:1:0.40 ratio mix pressed on carbon fiber grids averaged 4.5 mm thick. Cathodes using the same mix on copper grids were about 3.8 mm thick and were 2.7 mm thick when using the 6:0.2:0.26 ratio.

The cupric oxalate was a product of BDH Chemicals Limited, England. The cupric oxalate came from two different lots, both labeled as being $(COO)_2Cu \cdot \frac{1}{2} H_2O$ with 160.57 formula weight. Copper was analyzed by electroplating and also by atomic absorption. Carbon and hydrogen were analyzed by heating in oxygen and absorbing evolved CO_2 and H_2O. The results indi-

* Electrochemical Society Active Member.
Key words: electrolyte, electrode, potential, additive.

cated that the cupric oxalate did not contain ½ H_2O but was nearly anhydrous. The analytical results gave an uncertainty range for hydrogen that was quite large, since the weight of hydrogen was very small compared to the total weight. The composition of the first lot was $(COO)_2Cu \cdot 0.05\ H_2O$ with an uncertainty of $\pm$ 0.03 H_2O, formula weight about 152.46. The second lot was $(COO)_2Cu \cdot 0.07\ H_2O \pm 0.02\ H_2O$, formula weight about 152.80. These formula weights were used in computing electrode efficiencies.

The anodes were cut from 0.18 mm thick aluminum alloy A6, an alloy of Al-Sn-Mg-Ga (Conalco Incorporated). The anodes were 36 × 36 mm with a lead 11 mm wide. The top 1-2 mm of the anodes and the lower part of the leads were given a protective coating as described earlier (1, 2). A cell contained one cupric oxalate cathode in a loosely covered beaker, two anodes of aluminum alloy placed about 30 mm apart with one on each side of the cathode, a porous inert separator between each electrode, and a reference electrode of Ag/AgCl. Potentials were recorded using a strip chart recorder. Recording circuit impedance was 50 × $10^3\Omega$ for cell potential and 40 × $10^6\Omega$ to the reference electrode.

A cell was activated by adding 150 ml simulated seawater (Sea-Salt of Lake Products Company with *p*H adjusted to 8). Cells were acclimated in seawater for 1 hr before the discharges were begun. Cells were discharged at room temperature (19°-24°C) using constant current. Discharges were limited by capacity of the cupric oxalate cathode. The anodes were replaced if the original anodes corroded away before completion of the discharge.

Results and Discussion

Some typical discharges of cupric oxalate cells are shown in Fig. 1. Changes in cell potential can be taken to represent changes in cathode potential, with the exception of the first 5% of a discharge where the anodes had a potential 0.05-0.07V more negative than they showed for the rest of a discharge. The change in anode potential took place as a corrosion film formed on the surface of the aluminum. Most discharges showed a decrease in potential when the cupric oxalate was 40-60% discharged. The two potential steps could indicate two discharge reactions.

Various proportions of acetylene black were used in the cathodes to determine the importance of a conductive material. A wide range of values gave good results, but some conductive material must be present.

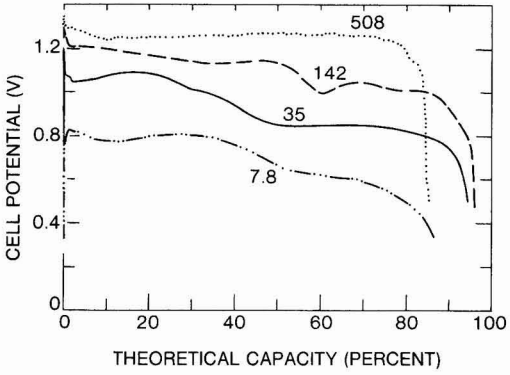


Fig. 1. Constant current discharges of seawater cells containing cupric oxalate cathodes and aluminum alloy A6 anodes. The cathodes contained weight ratios of 6:0.2:0.26 for cupric oxalate: acetylene black:Neoprene AD-20. This mix was pressed on expanded copper grids. Numbers on curves give total discharge lengths in hours. Discharge currents (from top curve to bottom) were 3, 12, 48, and 192 mA.

A cathode without any conductive material added had such a high resistance that potential fell to zero when a discharge at the 35-hr rate was attempted. A cupric oxalate:acetylene black ratio of 6:0.1 gave a relatively flat discharge with potential about 0.15V lower than is shown in Fig. 1 during the first 20% of a discharge at the 35-hr rate. Ratios of 6:0.5 and 6:1 gave potentials 0.10V higher than are shown in Fig. 1 for the first 20% of the discharge at the 35-hr rate. This higher potential may have been caused by oxygen adsorbed on the acetylene black. After the discharges were about 20% complete, these cathode mixes containing from 6:0.1 to 6:1 ratios all tended to give potentials close to each other. Metallic copper particles were visible in cathodes at the end of a discharge. Formation of the copper should improve conductivity as a discharge progresses. Most of the cathodes were made with a 6:1 ratio of active material:acetylene black to ensure that results would not be affected by low conductivity.

The discharge efficiency of cupric oxalate is given in Fig. 2. Efficiency was calculated using a discharge endpoint 0.35V below the potential obtained when the cell was 50% discharged, since large voltage drops such as some shown in Fig. 1 would not be tolerated for many applications of a seawater cell. Self-discharge of the cupric oxalate caused efficiency to decrease as the discharge length exceeded one week. To see the effect of long stands, two cupric oxalate cathodes were discharged at the 135-hr rate with a stand of 600 hr when half-discharged. One cathode had a copper grid and the other had a carbon fiber grid. These cathodes gave 73.6 and 72.7% of theoretical capacity, respectively, instead of the normal 94.6% average for a discharge at the 135-hr rate (Fig. 2). Self-discharge became a major problem when the cupric oxalate was in seawater for longer than about two weeks. Capacity of the 508-hr discharge shown in Fig. 1 was lowered by self-discharge that occurred during the long time in seawater.

Cathodes containing cupric oxalate and sulfur.—The cathodes gave a higher potential when sulfur was added to the cupric oxalate. The cathodes in Fig. 3 were made with 6:1:0.4 ratios for combined weight of cupric oxalate plus sulfur:acetylene black:neoprene. Discharge currents (from top curve of Fig. 3 to bottom) were 3, 12, 48, and 196 mA. Compare with Fig. 1 to see the effect of added sulfur. Since the cathodes used in Fig. 3 had much more acetylene black than those in Fig. 1, the potentials were somewhat increased by this acetylene black in the first 20% of the discharge as mentioned above, in addition to the larger increase resulting from the presence of sulfur. Cathodes containing sulfur usually gave 0.13-0.22V higher potential than those without sulfur, with 0.17V the average increase.

Another effect of sulfur was to increase efficiency 2-3% over the values shown in Fig. 2 for discharge lengths of 8-140 hr. Self-discharge was lower when

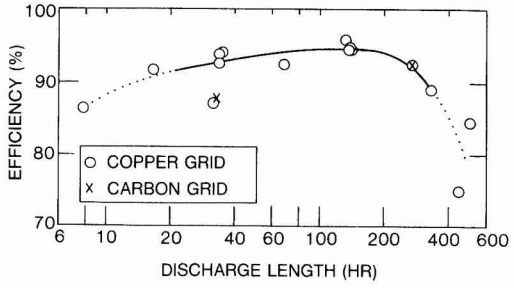


Fig. 2. Ampere-hour efficiency for constant current discharges of cupric oxalate electrodes in seawater.

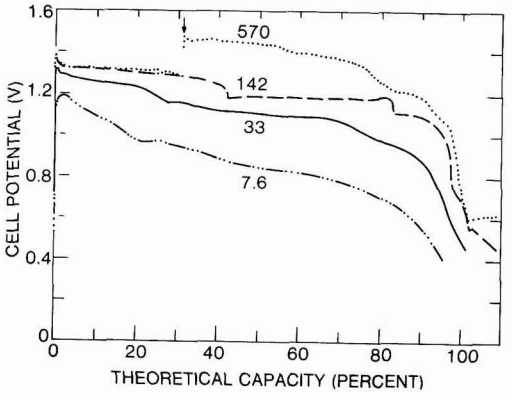


Fig. 3. Discharges of seawater cells containing cathodes with expanded copper grids and a weight ratio of 1:0.12 (mole ratio 1:0.57) for cupric oxalate:sulfur. Anodes were aluminum alloy A6. Numbers on curves give total discharge lengths in hours. Arrow indicates point in longest discharge where copper lead broke and was replaced by wrapping platinum wire around the cathode.

sulfur was present. The discharge lasting 570 hr shown in Fig. 3 gave 94% of theoretical capacity to 1.1V. This efficiency is considerably higher than was obtained from cupric oxalate alone (Fig. 2). Theoretical capacity was based on the weight of cupric oxalate in the cathode and was calculated assuming a valence change of two. The main discharge reaction was sulfur reacting with cupric oxalate to form CuS. When sulfur was present, the capacity of deep discharges often exceeded 100% of what could be obtained if the reaction only involved S going to S^{2-}. Some of the CuS produced in the main discharge reaction was reduced in a secondary reaction to give this added capacity.

A red-brown deposit of copper formed on the aluminum anodes when the cupric oxalate cathodes contained little or no sulfur. This copper deposit usually did not occur when sulfur content was over 10% of the cupric oxalate weight. This difference is another indication that sulfur changed the discharge reaction so that a less soluble form of copper was produced. Copper sulfides are known to be quite insoluble.

Most of a discharge took place at relatively high potentials when a large proportion of sulfur was present (Fig. 4). Cathodes with copper grids gave capacities whose average value tended to be 1-2% above the line shown for 1.0V in Fig. 4, and 1-2% less than is shown to 1.2V. For simplicity, these values are not included in Fig. 4. The curves in Fig. 4 can be considered to be pairs of straight lines meeting at about 0.9

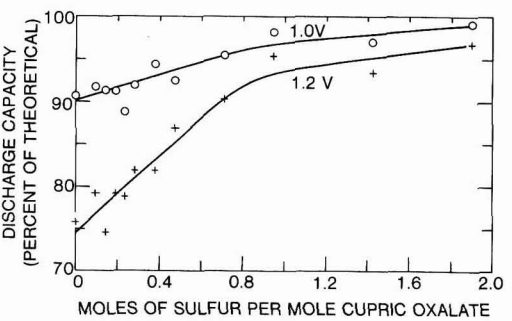


Fig. 4. Relationship between sulfur content and discharge capacity measured to final cell potentials of 1.2 and 1.0V. Cells were discharged at the 11-day rate in seawater. Cathodes contained carbon fiber grids.

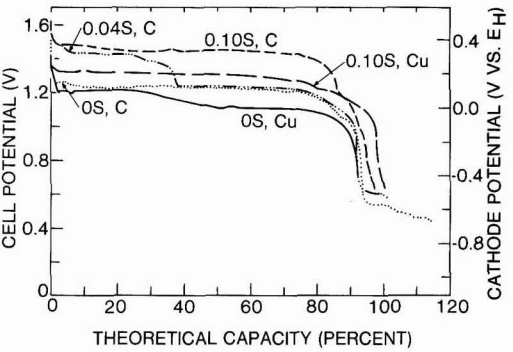


Fig. 5. Cell potentials and approximate cathode potentials for discharges of cupric oxalate with and without added sulfur. The cathodes were discharged at the 11-day rate in cells containing seawater and anodes of aluminum alloy A6. Parts by weight of sulfur per part cupric oxalate are given for the cathodes, and whether the grid was carbon fiber (C) or copper (Cu).

mole sulfur per mole cupric oxalate. Above this value, additional sulfur had less effect.

Carbon fiber grids resulted in higher potentials than copper grids (Fig. 5). The presence of sulfur resulted in copper grids becoming quite thin by the end of a discharge. Since potentials were higher when using carbon grids, and about the same amount higher when the electrical contact was a platinum wire wrapped around the cathode (top discharge, Fig. 3), obviously the potential of the bulk of the active material was not obtained when using copper grids. Attack of the copper grids was smaller when cathodes did not contain sulfur.

The cathodes containing sulfur gave several potential plateaus during discharge (Fig. 3 and 5). As the proportion of sulfur increased, the length of the upper plateau increased. This can be seen in Fig. 5 by comparing discharges of cathodes containing sulfur:cupric oxalate weight ratios of 0.0:1, 0.04:1, and 0.10:1 on carbon grids. The last part of a discharge gave potentials similar to what was obtained when no sulfur was present. The change in plateau length as the proportion of sulfur changed proved that sulfur was consumed during discharge.

The relationship between the proportion of sulfur present and the length of discharge taking place at the higher potential plateau was not exactly linear (Fig. 6). The curves in Fig. 6 are parabolas that were fitted by the method of least squares. A sulfur:cupric oxalate weight ratio of 0.1:1 equals a mole ratio of 0.475:1. Extrapolation of these curves suggested that 100% of the discharge would take place at the upper plateau if the sulfur:cupric oxalate mole ratio was 0.56:1 with carbon fiber grids and 0.65:1 with copper grids. The value with copper grids involved a much longer extrapolation and should be considered less reliable. More sulfur was always required when using copper grids than when using carbon grids to obtain a particular length of discharge at the upper plateau. This is another indication that part of the sulfur was reacting with the copper grid.

The proportion of discharge taking place at the higher potential decreased as current density increased (Fig. 3). When cathodes were discharged at four times the current density used in Fig. 6, an electrode containing a copper grid and 0.285 mole sulfur per mole cupric oxalate gave the higher potential for 25% of the discharge instead of the 53% shown in Fig. 6. Thus at low current densities a mole ratio of sulfur to cupric oxalate of about 0.5-0.6 was sufficient to maintain high potentials until the cupric oxalate was consumed, but at high currents a mole ratio of about 1 was necessary.

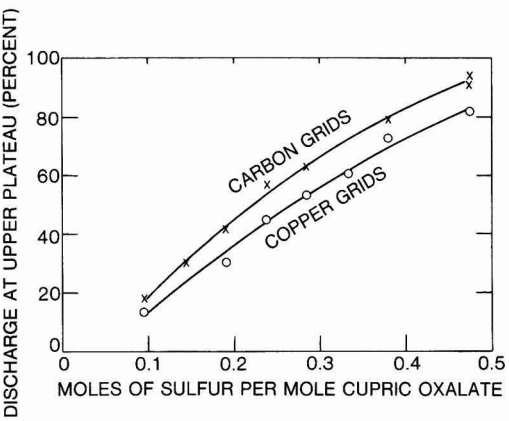


Fig. 6. Effect of sulfur on the percent of a discharge that took place at the higher potential plateaus. Electrodes were discharged in seawater at the 11-day rate.

This occurred because simultaneous reduction of CuC_2O_4 and CuS could support a low current and deliver a high potential. At higher currents, potentials dropped to a lower level after sulfur was all converted to CuS. In order for potentials to remain high when using higher currents, sufficient sulfur had to be present that reduction of sulfur could continue as the predominant reaction of the entire discharge.

X-ray diffraction.—The results of x-ray diffraction of a cathode containing no sulfur verified the visual observation that the cupric oxalate had largely been reduced to metallic copper at the end of a discharge. The diffraction pattern also indicated the presence of some Cu_2O and small amounts of CuCl.

Samples were also taken from a cathode made with 0.5 mole sulfur per mole cupric oxalate. The cathode contained 6 parts by weight of this mixture per 0.2 part acetylene black and 0.26 part neoprene. A carbon fiber grid was used. The x-ray diffraction pattern before beginning a discharge showed only cupric oxalate and sulfur. A sample was removed when a discharge at the 11-day rate had delivered 50% of theoretical capacity based on cupric oxalate content. The x-ray diffraction patterns at this point indicated that cupric oxalate and CuS were present, but did not reveal any sulfur. At the end of the discharge to a final cell potential of 0.616V, the strongest lines in the diffraction patterns were those of $Cu_{1.97}S$. Some cupric oxalate and a small amount of copper metal were also present. CuS was no longer present.

Equilibrium potentials.—A number of equilibrium relationships involving possible reactions at cupric oxalate electrodes were determined using Gibbs free energies (6). Apparently the discharge begins with divalent copper being reduced to monovalent copper. One possible product is cuprous oxalate, but its existence is not well established and no thermodynamic data is available for it. Two likely monovalent products are a cuprous ion and Cu_2O. Cuprous copper exists predominantly as $CuCl_2^-$ in a chloride solution

$$CuC_2O_4 + 2Cl^- + e^- = CuCl_2^- + C_2O_4^{2-} \quad [1]$$

$$E = -0.106 + 0.0592 \log [Cl^-]^2/[CuCl_2^-][C_2O_4^{2-}]$$

$$2CuC_2O_4 + H_2O + 2e^- = Cu_2O + 2C_2O_4^{2-} + 2H^+ \quad [2]$$

$$E = -0.347 + 0.0592\,pH - 0.0592 \log [C_2O_4^{2-}]$$

The monovalent copper produced in reaction [1] or [2] would be reduced to metallic copper, the final discharge product when sulfur was not present

$$CuCl_2^- + e^- = Cu + 2Cl^- \quad [3]$$

$$E = 0.232 + 0.0592 \log [CuCl_2^-]/[Cl^-]^2$$

$$Cu_2O + 2H^+ + 2e^- = 2Cu + H_2O \quad [4]$$

$$E = 0.472 - 0.0592\,pH$$

Calculations indicate that CuCl can form if the activity of $CuCl^{2-}$ in seawater reaches $4.6 \times 10^{-3}M$. This CuCl can be reduced according to Eq. [5]

$$CuCl + e^- = Cu + Cl^- \quad [5]$$

$$E = 0.118 - 0.0592 \log [Cl^-]$$

If the discharge goes in one step from divalent copper to metallic copper, the reaction is given by Eq. [6]

$$CuC_2O_4 + 2e^- = Cu + C_2O_4^{2-} \quad [6]$$

$$E = 0.063 - 0.0296 \log [C_2O_4^{2-}]$$

Hydrogen will be produced if the discharge is continued to a low cathode potential

$$2H^+ + 2e^- = H_2 \quad [7]$$

$$E = -0.0592\,pH$$

When sulfur was present, the major discharge product was CuS, probably according to Eq. [8]

$$CuC_2O_4 + S + 2e^- = CuS + C_2O_4^{2-} \quad [8]$$

$$E = 0.340 - 0.0296 \log [C_2O_4^{2-}]$$

Sulfur can also be reduced as given in Eq. [9]

$$S + H^+ + 2e^- = HS^- \quad [9]$$

$$E = -0.062 - 0.0296\,pH - 0.0296 \log [HS^-]$$

When an electrode contained less than one mole of sulfur per mole CuC_2O_4, first the S was converted to CuS and then additional discharge of the cathode gave $Cu_{1.97}S$. This $Cu_{1.97}S$ may have been produced when a cuprous copper ion formed according to Eq. [1] and then reacted with CuS according to Eq. [10]

$$1.03CuS + CuCl_2^- + e^- = 1.03Cu_{1.97}S + 2Cl^- \quad [10]$$

$$E = 0.572 + 0.0592 \log [CuCl_2^-]/[Cl^-]^2$$

Copper and sulfur are known to form stoichiometric compounds intermediate between CuS and Cu_2S. In order to estimate the free energy of $Cu_{1.97}S$, first the free energy of $Cu_{1.95}S$ was calculated to be −20.2 kcal/mole based on changes in free energy given in (7, 8) and using −20.6 kcal/mole as the free energy of Cu_2S (6). The free energy of $Cu_{1.97}S$ should be between the values for $Cu_{1.95}S$ and CuS, or approximately −20.4 kcal/mole.

Equation [11] gives another possible reaction

$$CuC_2O_4 + 1.03CuS + 2e^- = 1.03Cu_{1.97}S + C_2O_4^{2-} \quad [11]$$

$$E = 0.233 - 0.0296 \log [C_2O_4^{2-}]$$

Equation [11] is less likely than Eq. [10] to take place since it requires CuC_2O_4 to be in contact with CuS, while the ions produced by [1] can migrate to the CuS. A third possibility is that CuC_2O_4 was reduced to Cu in the usual way and then the Cu reacted according to Eq. [12]

$$CuS + 0.97Cu = Cu_{1.97}S \quad [12]$$

It is unlikely that Eq. [12] would take place at a fast enough rate to account for all CuS in a cathode being reduced to $Cu_{1.97}S$ and almost all Cu disappearing, as was observed at the end of a discharge when the starting cathode contained 0.5 mole S per mole CuC_2O_4. Equation [12] could account for attack on copper grids being greater when cathodes contained sulfur.

Copper sulfides can also be reduced if a discharge is continued to a low cathodic potential

$$2CuS + H^+ + 2e^- = Cu_2S + HS^- \quad [13]$$

$$E = -0.171 - 0.0296\,pH - 0.0296 \log [HS^-]$$

The above potential becomes 0.001V more positive if CuS is reduced to $Cu_{1.97}S$ instead of Cu_2S. The Cu_2S or $Cu_{1.97}S$ can be reduced to Cu

$$Cu_2S + H^+ + 2e^- = 2Cu + HS^- \quad [14]$$

$$E = -0.509 - 0.0296\,pH - 0.0296 \log [HS^-]$$

This potential is 0.004V more positive if the sulfide is $Cu_{1.97}S$ instead of Cu_2S. Equations [13] and [14] also represent limits for the potential range in which Eq. [12] can take place.

Evaluation of the potentials is complicated because of uncertainty as to ion concentrations in the cells. When seawater is first added, the concentration of $C_2O_4^{2-}$ is low because of the low solubility of CuC_2O_4. Aoki and Hiroi (4) reported the solubility of CuC_2O_4 in seawater to be 0.031 g/liter which is about 2×10^{-4}M. The predominant form of dissolved cupric copper is $Cu(C_2O_4)_2^{2-}$ (9, 10). Formation of this ion lowers the concentration of $C_2O_4^{2-}$. Additional $C_2O_4^{2-}$ enters the solution as a discharge proceeds. If all oxalate in a cathode entered the solution, the final concentration could have reached 0.22 molal in the cells. The actual concentration was much less, since relatively insoluble oxalates would be formed by any copper or aluminum ions present.

Equilibrium potentials were evaluated by taking the activity of Cl^- to be 0.38*M*, and by arbitrarily taking the other ion activities to be $10^{-5}M$. The results are given in Table I. The values were calculated to three decimal places since a change in ion activity will change potentials by the same number of millivolts for most of the listed reactions that involve this ion.

Potential plateaus from cupric oxalate cathodes.— Many other cupric oxalate cathodes were discharged in addition to those shown in Fig. 1, 3, and 5. There was little reproducibility in the course potential took as it changed from one potential plateau to the next one. But cathodes were fairly reproducible in that the same composition usually gave potential plateaus within a few hundredths of a volt of each other. This degree of reproducibility indicated that the potential plateaus during discharge might give a measure of the equilibrium potential for the reaction taking place, after corrections were made for the potential drop caused by current flow. As one simplification, the only results used were from cathodes that contained either no sulfur, or 0.5 or more mole of sulfur per mole cupric oxalate. As an additional simplification, the results were limited to cathodes discharged at the 11-day rate.

In order to obtain another measure of equilibrium potentials, one cathode without sulfur and another with 0.5 mole sulfur per mole cupric oxalate were discharged at what was normally the 11-day rate but discharges were stopped for 5 hr each day. Potentials at the end of these open-circuit periods were assumed to be close to the equilibrium potentials.

Table II gives a summary of potential plateaus obtained under various conditions. Approximate cathode potentials *vs.* the standard hydrogen electrode are given on the right side of Fig. 5 to aid in relating cathode potentials with cell potentials. This scale gives values usually within 0.02V of the cathode potentials measured on open circuit.

Many of the values in Table II are close to each other, indicating the likelihood that they represent the same reaction. The highest potentials were obtained with carbon fiber electrodes. These high potentials were probably affected by substances adsorbed on the acetylene black and carbon fibers, with oxygen undoubtedly present. Cathodes with copper grids showed an open-circuit potential before beginning a discharge that was reasonably close to the 0.211V given in Table I for equilibrium between cupric oxalate and copper. Some cupric oxalate that did not contain acetylene black added for conductivity was pressed onto platinum screen, in order to determine the potential when no carbon or metallic copper was present. This cupric oxalate electrode gave a maximum potential 0.66V 1 min after adding seawater. Potential dropped to 0.49V in 1 hr and reached a minimum of 0.41V after one day. Then potential rose slowly, reaching 0.42V in 5 days and 0.47V in 25 days. These potentials, as well as the open-circuit potentials before discharge when using carbon grids, were probably caused by reaction [1]. Potential from this reaction would decrease as CuC_2O_4 dissolved. Cathodes using carbon grids continued to show these high potentials when on open circuit in the first third of a discharge (Table II), indicating Eq. [1] or perhaps [2].

The major potential plateau obtained during discharge was at 0.14-0.09V for cathodes not containing sulfur (Table II). This could represent Eq [3] or [5]. Equation [3] gives a potential of 0.143V when activity of $CuCl_2^-$ is at $4.6 \times 10^{-3}M$, the highest activity possible when Cl^- has an activity of 0.38*M*. When $CuCl_2^-$ is at 4.6×10^{-3}, it is in equilibrium with solid CuCl, so the same potential of 0.143V is also obtained from Eq. [5]. Apparently the reduction of cupric oxalate took place near the potential of cuprous species/metallic copper instead of the cupric/cuprous potential. This resembles what occurs in a CuO electrode, which is well

Table I. Calculated equilibrium potentials in seawater at 25°C

Potential (V *vs.* SHE)	Reaction	Conditions*
0.488	8	A
0.436	1	A, B, C
0.423	2	A
0.381	11	A
0.326	10	B, C
0.211	6	A
0.143	5	C
−0.002	4	D
−0.014	3	B, C
−0.151	9	D, E
−0.260	13	D, E
−0.473	7	D
−0.598	14	D, E

* A, $[C_2O_4^{2-}] = 10^{-5}M$; B, $[CuCl_2^-] = 10^{-5}M$; C, $[Cl^-] = 0.38M$; D, pH = 8; E, $[HS^-] = 10^{-5}M$.

Table II. Potential plateaus obtained from cupric oxalate cathodes in seawater

Potential range (V *vs.* SHE)	Grid	Conditions*
	A. No sulfur present	
0.43 to 0.36	C	oc when 0-30% d
0.20 to 0.16	Cu	oc before d
0.14 to 0.10	C	0-75% d and oc when 45-80% d
0.13 to 0.09	Cu	0-30% d and oc when 10-70% d
0.02 to 0.00	C	85-95% d and oc when 85-100% d
0.03 to −0.02	Cu	60-90% d and oc when 80-110% d
−0.3 to −0.6	C	>105% d
−0.5 to −0.8	Cu	>105% d and oc when >130% d
	B. Sulfur added to cupric oxalate	
0.43 to 0.38	C	oc before d
0.37 to 0.31	C	0-70% d and oc when 5-70% d
0.25 to 0.22	Cu	oc before d
0.23 to 0.18	C	oc when 75-85% d
0.21 to 0.16	Cu	0-80% d and oc when 1-85% d
0.14 to 0.10	C	75-85% d
0.08 to 0.03	Cu	Sometimes when 85-95% d and oc when 90-100% d
−0.36 to −0.50	Cu	105-110% d and oc when 105-120% d
−0.43 to −0.48	C	oc when 105-120% d
−0.72 to −0.79	Cu, C	>130% d and oc when >135% d

* oc = open circuit, d = discharge or discharged.

known to discharge at the Cu_2O/Cu potential instead of the CuO/Cu_2O potential. The potentials from 0.03 to −0.02V that were observed near the end of discharges may represent Eq. [3] or [4], or a mixed potential. Some Cu_2O was detected in the x-ray diffraction pattern of a discharged cathode, although this Cu_2O may have formed as the sample oxidized while drying. Deep discharges gave slowly decreasing potentials as hydrogen evolved, Eq. [7].

When the cupric oxalate contained sulfur, the open-circuit potentials were the same as those obtained when sulfur was absent. This suggested that again Eq. [1] took place, although the potentials obtained from Eq. [8] were sufficiently close that this reaction could have been involved instead of, or in addition to, Eq. [1]. The main potential plateau at 0.37-0.31V for cathodes with carbon grids (Table II) could be due to Eq. [8] or a mixed potential. Since potentials measured from a copper grid were lower than the potential of the active material when measured by contact with carbon or platinum, it is believed that the copper of the grid caused potential to be determined by the CuC_2O_4/Cu couple (Eq. [6]), even though CuS was being produced in the active material.

When the electrode mix contained less than one mole sulfur per mole CuC_2O_4, at low current densities the potential was maintained by Eq. [10] or perhaps [11] after the elemental sulfur was consumed. At higher currents, the potential dropped and was probably determined by Eq. [3]. The electrode having a sulfur mole ratio of 0.5 gave an open-circuit plateau of 0.23-0.18V near the end of a discharge, perhaps indicating the metallic copper that formed near the end of a discharge under these conditions.

Deep discharges of electrodes containing sulfur gave two plateaus (Table II). The first was in the vicinity of the equilibrium value for hydrogen evolution, Eq. [7], but the odor of H_2S indicated that a reaction such as [9] or [13] was taking place simultaneously. On continued deep discharge, the cathodes gave a plateau at −0.72 to −0.79V, potentials low enough to allow Eq. [14].

Two cathodes were made using CuS (Mallinckrodt) as the active material in order to see if CuS was responsible for the low potential plateaus observed. The discharges of the CuS cathodes in seawater gave transient potentials initially, perhaps due to small amounts of $CuSO_4$ in the CuS (11). Then the cathodes gave declining potentials that began at −0.35V *vs.* SHE for one electrode and −0.41V for the other. These potentials include approximate corrections for current flow. The potentials slowly decreased almost 0.2V from these values until about one-third of the theoretical capacity had been consumed. Potentials then dropped sharply to a level at about −0.8V. These two potential plateaus are close to those given in Table II for deep discharges of cupric oxalate cathodes that contained sulfur. This indicates that reactions [13] and [14] took place during the deep discharges. Reduction of the sulfides allowed the cathodes to deliver more capacity than could be obtained from CuC_2O_4 if the valence change was only two. The added capacity was obtained at low potentials, however (Fig. 3 and 5).

Conclusions

Some advantages and disadvantages of cupric oxalate cathodes are evident when the results with cupric oxalate are compared to earlier work with MnO_2 in seawater (2). Cupric oxalate gave a higher discharge efficiency than MnO_2. For example, at the 10-hr discharge rate, the efficiency was about 65% with MnO_2 while cupric oxalate gave between 85 and 90%. Efficiency was 2-3% higher when sulfur was added to the cupric oxalate. Cupric oxalate gives 40-75% more capacity than an equal weight of MnO_2, but this advantage decreases as sulfur is added. At low current densities, the beneficial results of sulfur lasted for the entire discharge when 0.5 mole sulfur was present per mole cupric oxalate, but 1 mole was necessary at higher currents. The combination of cupric oxalate with sulfur gave a potential about 0.2V higher than cupric oxalate alone.

One disadvantage of cupric oxalate cathodes is that they showed a larger potential drop as current increased than did MnO_2 cathodes. Cathodes with cupric oxalate and sulfur gave 0.15V lower potential than MnO_2 cathodes when each was discharged at the one-day rate, while at the three-week rate cupric oxalate plus sulfur gave 0.1V higher potential than MnO_2. Other disadvantages of cupric oxalate are that it requires 20-35% larger volume than MnO_2, has a higher rate of self-discharge, and has a higher cost.

Acknowledgments

I wish to thank Dr. S. M. Caulder for performing the x-ray diffraction analysis, Mr. J. M. Hall for the elemental analyses, and Mr. J. F. Murray for the atomic absorption analysis. Dr. J. L. Weininger provided information concerning neoprene as a binder in electrodes. Thanks are also due to E. I. du Pont de Nemours & Company for a sample of Neoprene AD-20, to Conalco, Incorporated, for providing some A6 aluminum alloy, and to Union Carbide Corporation and Dr. R. J. Brodd for the acetylene black.

Manuscript submitted June 12, 1978; revised manuscript received Sept. 18, 1978.

Any discussion of this paper will appear in a Discussion Section to be published in the December 1979 JOURNAL. All discussions for the December 1979 Discussion Section should be submitted by Aug. 1, 1979.

Publication costs of this article were assisted by the Naval Research Laboratory.

REFERENCES

1. C. P. Wales, A. C. Simon, and S. Schuldiner, *Electrochim. Acta*, **20**, 895 (1975).
2. C. P. Wales, *This Journal*, **124**, 809 (1977).
3. Y. Aoki and M. Hiroi, *J. Electrochem. Soc. Jpn.*, **35**, 158 (1967).
4. Y. Aoki and M. Hiroi, *Electrochim. Acta*, **13**, 1563 (1968).
5. J. L. Weininger and F. W. Secor, *This Journal*, **121**, 1541 (1974).
6. D. D. Wagman, W. H. Evans, V. B. Parker, I. Halow, S. M. Bailey, and R. H. Schumm, Nat. Bur. Stand. Tech. Note 270-3 (Jan. 1968) and 270-4 (May 1969).
7. H. J. Mathieu and H. Rickert, *Z. Phys. Chem. (Frankfurt)*, **79**, 315 (1972).
8. D. F. A. Koch and R. J. McIntyre, *J. Electroanal. Chem.*, **71**, 285 (1976).
9. L. Meites, *J. Am. Chem. Soc.*, **72**, 184 (1950).
10. A. McAuley and G. H. Nancollas, *Trans. Faraday Soc.*, **56**, 1165 (1960).
11. Y. Aoki and M. Hiroi, *J. Electrochem. Soc. Jpn.*, **35**, 70 (1967).

Discharge Characteristics of a Soluble Iron-Titanium Battery System

R. F. Savinell,[1] C. C. Liu, R. T. Galasco, and S. H. Chiang

Department of Chemical and Petroleum Engineering, University of Pittsburgh, Pittsburgh, Pennsylvania 15261

and J. F. Coetzee

Department of Chemistry, University of Pittsburgh, Pittsburgh, Pennsylvania 15261

ABSTRACT

Constant-load and constant-current discharge data are presented for a soluble iron-titanium electrochemical system. Output performance is limited mainly by activation polarization in the anodic reaction, Ti(III) $- e^- \rightarrow$ Ti(IV). The influence of different electrode materials, including platinum, graphite foil, and titanium-base electrodes, and of temperature was investigated.

Electrochemical energy systems in which reactants as well as products are present entirely in solution offer certain potentially attractive features which have been the subject of several discussions. Thus, Singman and Bond (1, 2) demonstrated the feasibility of employing a soluble bromine-titanium(III) system for the generation of electrochemical energy. Recently, Thaller (3) discussed the possibility of using a soluble iron(III/II)-titanium(III/IV) system in the mode of a secondary battery, while Warshay and Wright (4) made size and cost estimates for bulk energy storage based on the preliminary results of Thaller. In principle, such soluble battery systems may offer particular advantages for large-scale "peak-shaving" operations of power plants because the deterioration encountered when solid anode and cathode materials are repeatedly discharged and charged would be avoided.

We have now investigated some of the essential discharge characteristics of the soluble iron-titanium system in a stationary cell under constant load as well as under constant current conditions. We have also studied the influence of temperature and evaluated the performance of different electrode materials, including platinum and various forms of graphite. Finally, the operation of soluble electrochemical systems is particularly sensitive to the efficiency of the cell separator. We had studied before (5) the characteristics of several types of anion-permeable membranes suited to this purpose.

The results obtained in this study indicated what energy levels can be obtained from the soluble iron-titanium battery and identify the factors limiting the performance of the system.

Principles

In the iron-titanium soluble electrochemical system investigated in this study, the cathodic reaction during discharge is Fe(III) $+ e^- \rightarrow$ Fe(II), while the anodic reaction is Ti(III) $- e^- \rightarrow$ Ti(IV). During charging, both reactions are reversed. The catholyte and anolyte solutions are separated by an anion-exchange membrane which allows passage of anions (chloride ions) necessary to preserve electroneutrality of both solutions. Ideally, the electrodes undergo no electrochemical or chemical reactions during either the charging or discharging cycles, and serve only as reaction sites and electron collectors.

The current density obtainable under constant-load discharge is given by Eq. [1] for the case when the cell performance per unit electrode area is limited by simple diffusion and migration is eliminated (6)

$$i = n\mathbf{F}C_0(D/\pi t)^{1/2} \qquad [1]$$

Here, n is the number of electrons exchanged, $\mathbf{F}$ is the Faraday constant, C_0 is the bulk concentration of the electroactive species, D is its diffusion coefficient, and t is the time of discharge. Hence, if the current density is limited only by diffusion, it should vary linearly with $t^{-1/2}$.

Discharge of a stationary cell under constant-current conditions results in decay of the cell potential with time. Considering the combined effects of diffusion and activation polarization, this decay is given by Eq. [2] for the case of a single-step cathodic process occurring after charging of the electric double layer and with negligible contribution of the back reaction (7, 8)

$$E(t) = E_e + \{RT/\alpha_a n\mathbf{F}\}\{\ln[i_o/i] + \ln[1 - (t/\tau)^{1/2}]\} \qquad [2]$$

Here, E_e is the equilibrium potential, α_a is the transfer coenicient, i_o is the exchange current density, and τ is the transition time.

The potential of a galvanic cell during constant-current discharge can also be described (9) by Eq. [3]

$$E = E_e - |\eta_{conc}| - |\eta_{act}| - IR_i \qquad [3]$$

where η_{conc} and η_{act} are the total concentration and activation overpotentials, I is the total current delivered, and R_i is the internal cell resistance. It will be shown that for the iron-titanium system, the activation overpotential of the titanium couple imposes a particularly significant limitation on the performance of the system.

Experimental

The prototype electrochemical cell used (Fig. 1) consisted of two half-cells made of lucite. The inside chamber of each half-cell was 5.0 cm diam and 1.0 cm in depth. The electrodes were placed on the back wall of each half-cell compartment. A portion of the electrode was extended through the port on top of each compartment. This permitted a direct connection of the electrode with the lead wires in the external circuitry. An O-ring seal was used to hold the membrane separator in place between the two half-cell compartments. A calomel reference electrode was placed in each half-cell. The cell was immersed in a water bath to maintain operation at constant temperature.

The supporting electrolyte of the catholyte (1M $FeCl_3$) was 3M HCl while 3.5M HCl was used for the anolyte (1M $TiCl_3$). The high concentration of supporting electrolyte was intended to minimize migration effects and also to increase reactant stability. Other concentrations of supporting electrolyte have also been used, but the comparison of the results is

[1] Present address: Diamond Shamrock Corporation, Research Center, Cleveland, Ohio.

Key words: battery, energy storage, membrane.

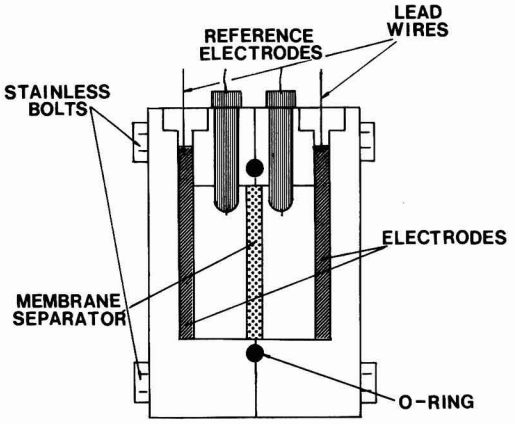


Fig. 1. The electrochemical cell

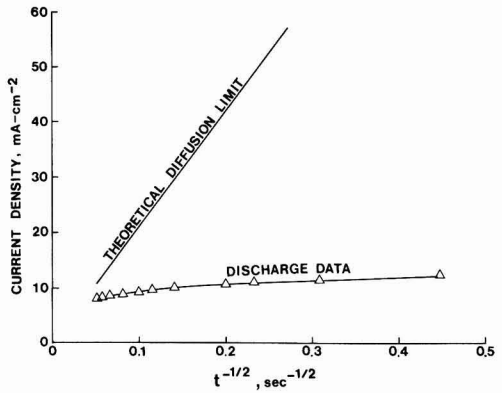


Fig. 2. Typical constant-load discharge data compared with theoretical output limited by diffusion only.

presented here. The 1M titanium(III) chloride solution was prepared by diluting a commercial 20% stock solution (Fisher Scientific Company, Pittsburgh, Pennsylvania). The 1M iron(III) chloride solution was prepared by dissolving the salt in 3M hydrochloric acid solution. All solutions, concentrated hydrochloric acid, distilled water, and reactant solutions, were deoxygenated by bubbling with nitrogen for approximately 15 min before the experimental runs.

The principal electrode material used was graphite foil (GTA, Union Carbide, Chicago, Illinois). It was pretreated by heating to 350°C for 20 min. This pretreatment enhanced the wettability of the electrode. For comparison purposes, other electrode materials were also employed, namely platinized platinum foil and a titanium-base chlorine anode (DSA®, Electrode Corporation, Cleveland, Ohio).

The separator preferred on the basis of our previous studies (5) was the anion-permeable membrane Ionac MA-3745. Several methods of pretreatment were investigated; that recommended by the manufacturer was finally chosen.

The assembled cell was discharged both under constant load and under constant current conditions. During discharge, the cell potential was recorded as a function of time. The half-cell potentials between the working electrodes and the reference electrodes were measured using high impedance digital voltmeters equipped with recording devices. The over-all cell potential was recorded directly by an X-Y recorder. For constant-load discharge, a calibrated resistor, 1.06Ω, was used as external load. For constant-current discharge, a constant-current power supply (Hewlett-Packard Model 6177C), the cell, and a 1000Ω ballast resistor were placed in series to induce a desired current from the cell. Most discharges were for 400 sec at which time a steady state was usually reached.

Results and Discussion

The iron-titanium cell was discharged under a constant load of 1.06Ω at room temperature. In Fig. 2, the relation between the current density and $t^{-1/2}$ is compared with the theoretical response calculated from Eq. [1], using a value of D of 1.5×10^{-5} cm^2 sec^{-1}, which was measured in our laboratory for titanium(III) at infinite dilution in 3.5M hydrochloric acid (10). It is clear that the performance of the cell was not limited by diffusion only. Consequently, the performance was evaluated in terms of total overpotentials of both half cells. Results are shown in Fig. 3. The electrolyte and membrane potential drops were calculated using resistivity data. The area resistivity of the membrane (6 Ω-cm^2) was measured in a conductivity cell built for that purpose. The internal self-

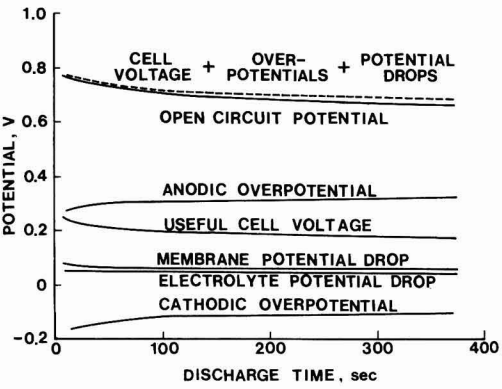


Fig. 3. Dissection of constant-load discharge data

consistency of the dissection is illustrated by the good agreement between the sum of all components (dashed line) and the open-circuit voltage. The most important result is that anodic activation polarization is the main cause of the decreased useful cell voltage. Recently, this has been shown to be the case by Reid *et al.* (11), but for a different cell configuration.

A comparison of our data was made with data presented by Reid *et al.* At nearly equivalent current densities, the anodic polarization and cell voltage of our cell was found to be comparable to the cell used by Reid. The difference between cells being the latter is a flow cell packed with graphite cloth and using graphite foil as a current collector. From this comparison, it appears that under these conditions the graphite cloth electrode has limited effectiveness.

Overpotentials encountered during constant-current discharge are shown in Fig. 4. The time-dependent overpotentials were linearized according to Eq. [2], with results such as those shown in Fig. 5. Since overpotentials of the titanium half-cell were much greater than those of the iron half-cell, analysis of the former data would be more instructive. Results are shown in Table I. The transfer coefficient was calculated from the slope of the linear section of the curve in Fig. 5, and the exchange current density was calculated from the intercept.

The range of values of the exchange current density obtained is consistent with data from NASA (12). It is clear, therefore, that the output performance of the cell is limited mainly by the anodic reaction. Also reported in Table I are values of the forward rate con-

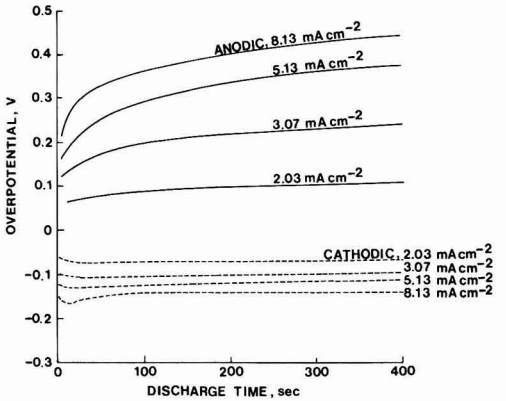


Fig. 4. Overpotentials at constant-current discharge

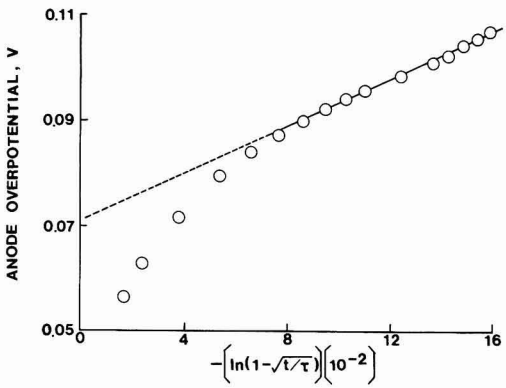


Fig. 5. Typical plot of constant-current discharge data

stant which would apply if a simple electron-transfer reaction were taking place, in which case $k_o = i_o/FC_o$. However, values of the transfer coefficient are small and inconsistent with simple electron transfer. It is likely that the mechanism is complex, but it is not yet clear which factors contribute to the complexity. Under our experimental conditions, both titanium (III) and titanium(IV) may be present as a series of chloro-complexes. Furthermore, it is conceivable that adsorption or desorption steps may be present. Consequently, we have also studied other electrode materials, namely, platinized platinum and DSA®. The results presented in Fig. 6 show that the cell performance is strongly dependent on the electrode material. The influence of temperature was also investigated. Results are shown in Fig. 7; there is some improvement at higher temperatures, but considerable activation polarization remains.

Table I. Kinetic parameters for the anodic reaction Ti(III)-e$^-$ → Ti(IV) during constant-current discharge of an Fe-Ti cell

Discharge current density (mA cm^{-2})	Exchange current density (mA cm^{-2})	$10^5\ k_o$ (cm sec^{-1})	Transfer coefficient
2.03	1.5	1.5	0.11
3.07	1.6	1.6	0.10
5.10	2.5	2.6	0.11
5.13	1.9	2.0	0.10
8.13	1.1	1.1	0.15
8.16	1.4	1.4	0.17

* Provided electron transfer were a simple process; however, see text.

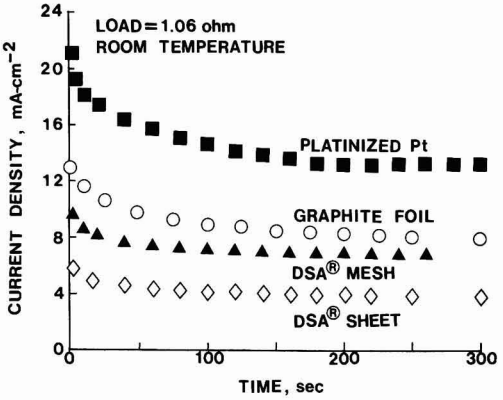


Fig. 6. Constant-load discharge at different electrode materials

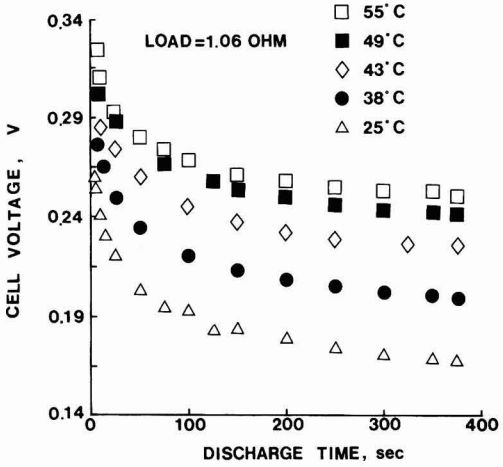


Fig. 7. Constant-load discharge at diffusion temperatures

Singman and Bond (1) have studied the kinetics of the Ti^{III}/Ti^{IV} couple on electrodes of platinum and impregnated carbon at 60° and 30°C. Although their experimental conditions were different from ours and direct comparison is not possible, they did find that the degree of reaction irreversibility was strongly dependent on the electrode material.

We conclude that the performance of the iron-titanium soluble battery system tested is seriously compromised by activation polarization, particularly in the titanium half-cell. In attempts to minimize polarization, we are now studying the influence of changes in the chemical nature and physical configuration of the electrode materials and in the nature of the supporting electrolyte and solvent.

Acknowledgment

We acknowledge the initial work done on this project by Edward J. Lahoda, the technical assistance of Carol Williams, and partial financial support by Alcoa Foundation.

Manuscript submitted April 10, 1978; revised manuscript received Sept. 28, 1978.

Any discussion of this paper will appear in a Discussion Section to be published in the December 1979 JOURNAL. All discussions for the December 1979 Discussion Section should be submitted by Aug. 1, 1979.

Publication costs of this article were assisted by the University of Pittsburgh.

REFERENCES

1. A. Bond and D. Singman, "Electrode Kinetics of Oxidation-Reduction Couples," Diamond Ordinance Fuze Labs, PB-146,398, April 15, 1960.
2. D. Singman and A. Bond, "Flow-Through Porous Electrodes for Redox Couples," U. S. Army Command, AD-426,952, Oct. 4, 1963.
3. L. Thaller, in "Proc. 9th Intersociety of Energy Conversion Engineering Conference," San Francisco, Aug. 26-30, 1974, American Soc. of Mech. Eng., New York, 1974.
4. M. Warshay and L. Wright, *This Journal*, **124**, 173 (1977).
5. E. J. Lahoda, Ph.D. Dissertation, University of Pittsburgh, Pittsburgh, Pa. (1974).
6. R. N. Adams, "Electrochemistry at Solid Electrodes," p. 50, Marcel Dekker, New York (1969).
7. P. Delahay and T. Berzins, *J. Am. Chem. Soc.*, **75**, 2486 (1953).
8. J. Kuta and E. Yeager, in "Techniques of Electrochemistry," Vol. 1, E. Yeager and A. Salkind, Editors, p. 226, Wiley-Interscience, New York (1972).
9. J. O'M. Bockris and A. K. N. Reddy, "Modern Electrochemistry," Vol. 2, pp. 1132, 1363, Plenum Publishing Corp., New York (1970).
10. R. F. Savinell, Ph.D. Dissertation, University of Pittsburgh, Pittsburgh, Pa. (1977).
11. M. A. Reid and R. F. Gahn, "Factors Affecting the Open-Circuit Voltage and Electrode Kinetics of Some Iron/Titanium Redox Flow Cells," NASA-TM-X-73669 (1977).
12. L. H. Thaller, Abstract 85, p. 229, The Electrochemical Society Extended Abstracts, Fall Meeting, Atlanta, Georgia, Oct. 9-14, 1977.

The Effect of Phosphoric Acid on the Positive Electrode in the Lead-Acid Battery

II. Constant Potential Corrosion Studies

Kathryn R. Bullock*

Globe-Union, Incorporated, Milwaukee, Wisconsin 53201

ABSTRACT

The effect of H_3PO_4 on the constant potential corrosion of the positive grid in the lead-acid battery has been studied. The metallurgical and chemical properties of the corrosion products have been examined and correlated with their electrochemical behavior during self-discharge and voltammetric cycling. Low concentrations of H_3PO_4 in the electrolyte modify the crystal growth of PbO_2 on the lead grid, producing a structure which is not readily discharged to $PbSO_4$.

In a previous paper (1), the effect of phosphoric acid on the PbO_2 electrode was examined by cyclic voltammetry. It was proposed that one effect of phosphoric acid is to modify the crystal growth of PbO_2 on the lead grid during charge, producing a structure which is less easily reduced to lead sulfate. In this paper, that conclusion is substantiated by further studies of lead grids corroded at constant potential in electrolyte containing small quantities of phosphoric acid.

The literature on the use of phosphoric acid in lead-acid batteries was reviewed in an earlier paper (1) and is not repeated here. Since that paper was written, two studies of the effect of phosphoric acid on the cyclic voltammograms of PbO_2 electrodes have been published (2, 3). Some of the details of the cyclic voltammograms differ from one study to another, depending on the pretreatment of the electrode and the experimental conditions used. This is not surprising since it is well known that a variety of lead oxides and sulfates are formed on lead electrodes when they are cycled (4). The exact nature of the corrosion layer formed is dependent on the voltage range, temperature, scan rate, acid activity, and electrode history. Nevertheless, the authors who have published these voltammetric studies (1-3) agree that adding small quantities of H_3PO_4 to approximately 5M H_2SO_4 modifies the kinetics of the $PbO_2/PbSO_4$ couple. This is evidenced by a shift in the oxidation wave to a more positive potential and a decrease in the height of the reduction wave.

Although cyclic voltammetry is very sensitive to changes in the kinetics of electrode reactions, it has the disadvantage of covering a large voltage range. A variety of products can be formed, making it difficult to isolate the reactions of interest. We have attempted to overcome this difficulty and to further clarify the effect of H_3PO_4 on the $PbO_2/PbSO_4$ couple by corroding lead electrodes at constant potentials between 0.8 and 1.425V in electrolyte containing 0-1.15% H_3PO_4. The metallurgical and chemical properties of the corrosion products have been examined and correlated with their electrochemical behavior during self-discharge and voltammetric cycling.

Experimental

Cast lead grids were corroded at 49°C at constant potentials from 0.800 to 1.425V *vs.* an $Hg/Hg_2SO_4/4.5M$ H_2SO_4 reference electrode. Two lead grids, placed on either side of the working electrode, served as the counterelectrode. The electrolyte, which was 4.5M H_2SO_4 containing 0-1.15 weight percent (w/o) H_3PO_4, was made from reagent grade acids and distilled, deionized water. During the corrosion test, the current was monitored as a function of time.

After the grid had corroded for 2-4 days, the portion around the tab was cut out and allowed to self-discharge in the same solution at the same temperature. The open-circuit voltage of this grid sample was monitored as a function of time by a high impedance digital voltmeter.

The remaining portion of the grid was prepared for further analysis by rinsing it in distilled, deionized water and drying it at room temperature. The oxidized lead on the grid was stripped off with a solution containing sodium hydroxide, mannitol, and hydrazine dihydrochloride and analyzed by atomic absorption.

The morphology of the corroded surface was examined using a JEOL U3 scanning electron microscope. Grid wires were vapor coated with a gold-palladium alloy for this purpose.

* Electrochemical Society Active Member.
Key words: additive, battery, corrosion, discharge.

Select samples from pure lead grids were analyzed for phosphorus and sulfur content using an ARL electron microprobe analyzer. A portion of the grid frame was carbon coated for this analysis, since it was the flattest part of the grid. The phosphorus standard was a National Bureau of Standards glass containing P_2O_5 with a phosphorus content of 34.6%. Lead sulfate crystals grown in the laboratory were used as a sulfur standard. A 50 × 50μ area was scanned.

Cyclic voltammograms of lead electrodes corroded under similar conditions were also obtained. Pure lead was corroded for 6 hr at 49°C in 5*M* H_2SO_4 containing 0 and 0.2% H_3PO_4 at potentials from 1.150 to 1.425V *vs.* an $Hg/Hg_2SO_4/5M$ H_2SO_4 reference electrode. A Wenking potentiostat held the potential constant during the corrosion test and a stepping motor was then used to decrease the potential to 0.975V in 1 mV increments at a rate of 3 mV/min. The electrodes corroded at 1.425V were further cycled between 0.975 and 1.425V.

Results and Discussions

Scanning electron micrographs of the surfaces of pure lead cast grids corroded at 1.230V in H_2SO_4 containing 0 and 0.2 w/o H_3PO_4 are shown in Fig. 1. The grid corroded in pure electrolyte is covered with small prismatic crystals normal to the lead surface. In contrast, the grid corroded in the phosphated electrolyte is covered with coalesced spherical particles. Some of these spherical particles are growing spirally out from the surface, forming the large, flowerlike structures seen in the photograph. The surface area appears to be reduced in the presence of H_3PO_4.

Similar results can be seen at higher potentials. Figures 2, 3, and 4 compare the surfaces with and without H_3PO_4 at corrosion potentials of 1.275, 1.315, and 1.425V, respectively. Although the surface morphology varies with potential in the pure electrolyte, the coalesced spherical particles are found at all four corrosion potentials in the phosphated electrolyte. Phosphate apparently reduces the surface area of the corrosion film throughout the potential range where PbO_2 is formed. At the lower potentials of 0.800, 1.000, and 1.100V, however, H_3PO_4 has no observable effect on the morphology of the corrosion layer.

The P and S contents of these surfaces, determined to a depth of about 1μ by electron microprobe analysis, are shown in Table I. At potentials from 0.800 to 1.100V, the S content showed the surface to be primarily $PbSO_4$. No P was detected in any of these samples. At potentials from 1.230 to 1.425V, P was detected in all of the grids corroded in phosphated electrolyte and was not detected in any of the grids corroded in pure electrolyte. The amount of P detected did not vary significantly with either the corrosion potential or the H_3PO_4 concentration. Less S was found in the samples corroded at 1.230-1.315V and none in the samples corroded at 1.425V. Presumably, at the highest potential, $PbSO_4$ is completely oxidized to PbO_2. These results show that H_3PO_4 interacts specifically with the PbO_2 film, modifying its structure.

It was also found that the PbO_2 film formed in the presence of H_3PO_4 requires longer to self-discharge to $PbSO_4$ than the PbO_2 film formed in pure electrolyte. Figure 5 shows the voltage decay curves for pure Pb grids which were corroded at 1.425V at 49°C in 4.5*M* H_2SO_4 for 2 days and then left on open circuit in the

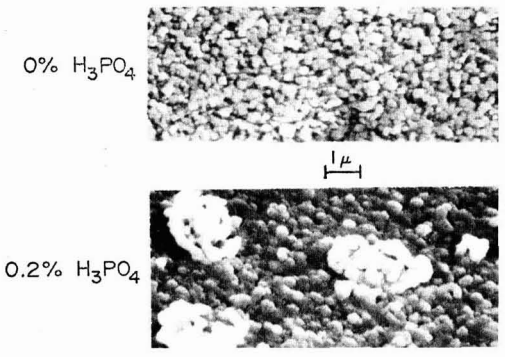


Fig. 1. Pure lead cast grids corroded at 1.230V for 50 hr in 4.5M H_2SO_4 at 49°C.

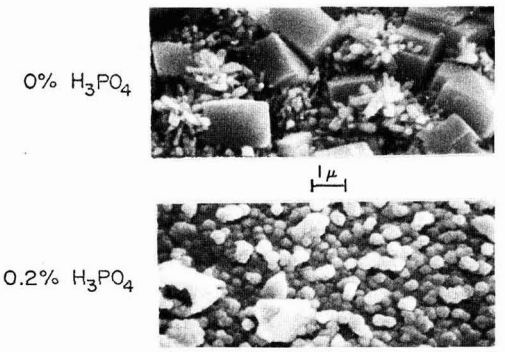


Fig. 2. Pure lead cast grids corroded at 1.275V for 48 hr in 4.5M H_2SO_4 at 49°C.

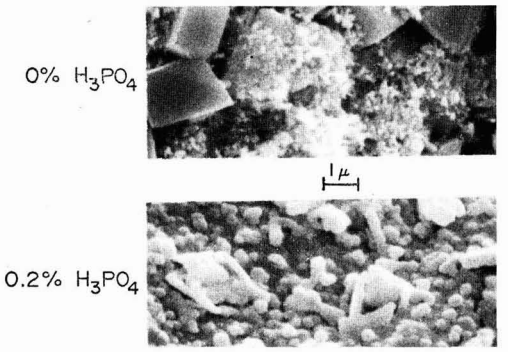


Fig. 3. Pure lead cast grids corroded at 1.315V for 50 hr in 4.5M H_2SO_4 at 49°C.

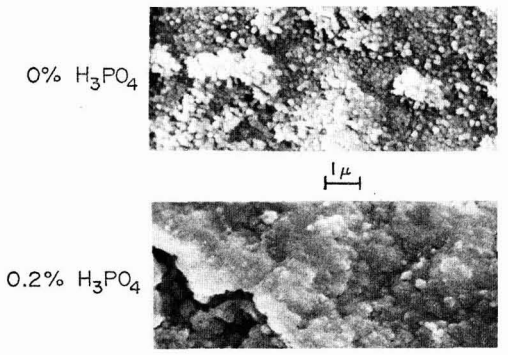


Fig. 4. Pure lead cast grids corroded at 1.425V for 48 hr in 4.5M H_2SO_4 at 49°C.

Table I. Electron microprobe analysis of corroded grids

Corrosion potential	Percent H_3PO_4	Percent S	Percent P
0.800	0	8.7	nil
	0.19	8.0	nil
1.000	0	9.1	nil
	0.19	8.6	nil
1.100	0	7.6	nil
	0.19	8.8	nil
1.230	0	1.0	nil
	0.19	1.7	0.32
1.275	0	3.2	nil
	0.19	0.7	0.39
1.315	0	5.1	nil
	0.19	0.8	0.32
1.425	0	<0.1	nil
	0.23	<0.1	0.28
	1.15	<0.1	0.31

Table II. Weight of oxidized lead in grid corroded at 1.425V at 49°C in 4.5M H_2SO_4 for 48.29 + 0.11 hr

Percent H_3PO_4	mg Pb/12g sample
0	260
0	240
0.23	233
0.46	270
0.69	250
0.92	310
1.15	251

same solution at the same temperature. The length of the plateau at about 1.1V is a measure of the time it takes the PbO_2 in the corrosion layer to reduce to $PbSO_4$ (5). Additions of H_3PO_4 to the electrolyte significantly increase the length of the plateau.

In order to determine whether this increase in sulfation time is due to a reduced rate of sulfation or to an increased amount of corrosion to PbO_2, 12g samples of the same grids were analyzed for the oxidized lead in the corrosion layer. Table II shows the results obtained for grids corroded at 1.425V in electrolyte containing 0-1.15% H_3PO_4. No significant trend in the amount of grid corrosion is observed.

When the weight of lead in the corrosion layer is divided by the sulfation time, a "rate" for the sulfation is obtained. This "rate" is plotted in Fig. 6 as a function of H_3PO_4 concentration. Although this number is not a true rate constant, it is a useful means of comparing the effect of varying H_3PO_4 concentrations. It is apparent that the greatest effect is in going from 0 to 0.2% H_3PO_4. Further increases in H_3PO_4 concentration decrease the "rate" only slightly.

The magnitude of the effect is also dependent on the corrosion potential. Figure 7 shows the "rate" of sulfation as a function of potential for 0 and 0.2% H_3PO_4. It is relatively constant in the phosphated electrolyte but reaches a peak at 1.275V in the pure electrolyte. Thus, the largest effect of H_3PO_4 is seen for grids corroded at 1.275V.

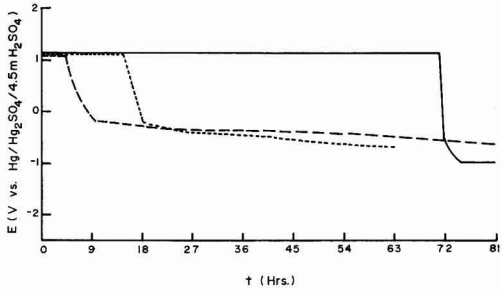


Fig. 5. Voltage decay curves at 49°C in 4.5M H_2SO_4 for grids corroded at 1.425V. ———— 0% H_3PO_4; - - - - - 0.23% H_3PO_4; ———— 1.15% H_3PO_4.

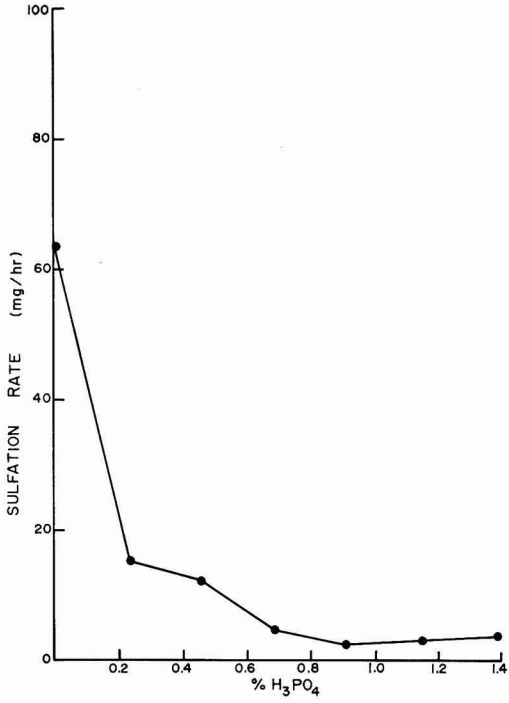


Fig. 6. Effect of H_3PO_4 concentration on sulfation of grids corroded at 1.425V.

One possible interpretation of these results is that the sulfation time increases in the presence of phosphoric acid because a higher percentage of the PbO_2 in the corrosion film self-discharges. A second method of measuring sulfation "rates" was used to exclude this possibility. Pure lead grids were corroded at 1.275V for 2.5 days at 49°C in 4.5*M* H_2SO_4 containing 0 and 0.2% H_3PO_4. The grids were then allowed to self-discharge under the same conditions in 4.5*M* H_2SO_4 saturated with $PbSO_4$. At the end of the PbO_2 potential plateau, the grids were removed from solution, rinsed in distilled, deionized water, and analyzed for the weight of sulfate in the corrosion layer.

The amount of PbO_2 which had self-discharged was calculated from the weight of sulfate in the corrosion film. This quantity was then divided by the sulfation time to obtain a "rate" of 176 mg/hr for the grid corroded in pure electrolyte and 29 mg/hr for the grid corroded in phosphated electrolyte.

The question remains whether H_3PO_4 influences the reduction as well as the oxidation process. In an experiment designed to answer this question, pure lead grids were corroded in 4.5*M* H_2SO_4 containing 0 and 0.2% H_3PO_4 at 1.275V for 2 days at 49°C. At the end of the anodization, they were removed from the acid, cut into smaller grids as before, and washed with distilled, deionized water. The grid which had been corroded in the phosphated electrolyte was then allowed to self-discharge in the pure electrolyte and vice versa. The results were compared with those obtained for grids corroded under the same conditions which self-discharged in the same acid in which they were corroded. The grids corroded in phosphated electrolyte sulfated at a much slower rate than those corroded in pure electrolyte, regardless of the presence or absence of H_3PO_4 during self-discharge. Scanning electron micrographs of the discharged surfaces looked the same under all conditions. It is clear from these results that H_3PO_4 in the electrolyte will reduce the rate of

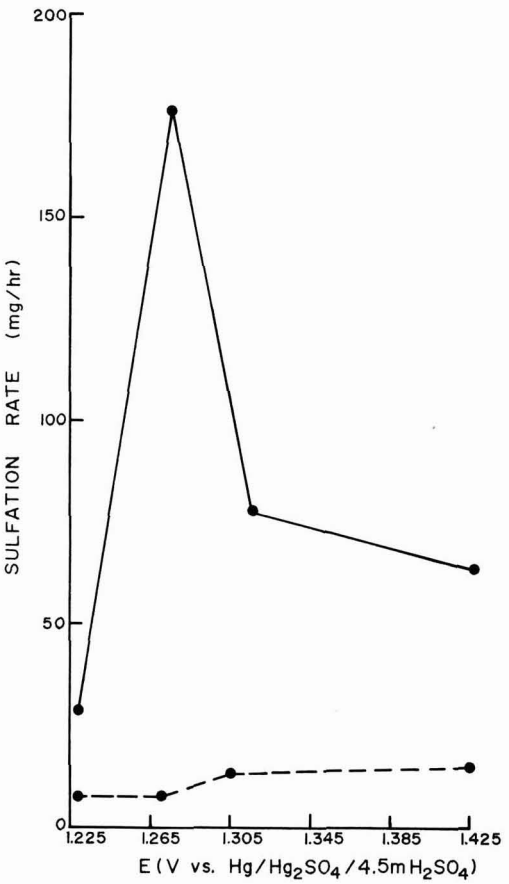


Fig. 7. Effect of corrosion potential on sulfation rate. ——— 0% H_3PO_4; — — — — — 0.2% H_3PO_4.

sulfation of PbO_2 only if it is present during the formation of the corrosion film.

Similar results are observed on both antimonial and nonantimonial lead alloys. For example, the sulfation "rates" for a typical lead-calcium alloy corroded at 49° and 60°C in 4.5*M* H_2SO_4 containing 0 and 0.2% H_3PO_4 are shown in Table III. Figure 8 shows the scanning electron micrographs of the calcium grids corroded at 60°C. The micrographs of typical antimonial grids corroded at 49°C at 1.275V in 4.5*M* H_2SO_4 containing 0 and 0.2% H_3PO_4 are shown in Fig. 9. The sulfation "rates" could not be obtained for the antimonial grids because the voltage decay curves did not have plateaus at 1.1V. Nevertheless, it is apparent from the micrographs that H_3PO_4 affects a drastic alteration of the morphology of the corrosion film.

Observations of the effect of H_3PO_4 on battery performance are in agreement with these results. Tudor, Weisstuch, and Davang (6-8) have observed by an

Table III. Rate of sulfation of lead calcium grids

Percent H_3PO_4	Temperature	Corrosion time (hr)	Plateau time (hr)	Oxidized Pb (mg)	Sulfation rate (mg/hr)
0	49	64	0.3	27.2	91
0.2	49	64	2.6	25.2	10
0	60	47	0.5	34.6	69
0.2	60	47	2.8	33.8	12

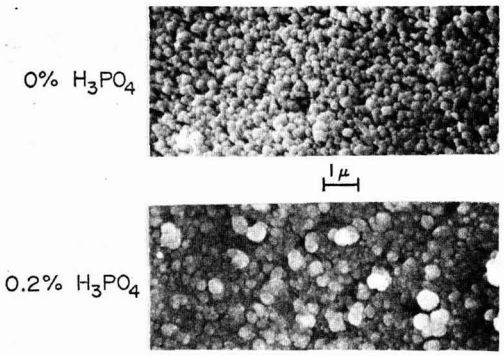


Fig. 8. Cast lead grids containing 0.09% Ca corroded at 1.275V for 47 hr in 4.5M H_2SO_4 at 60°C.

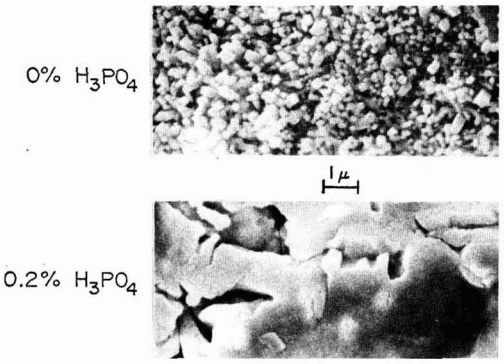


Fig. 9. Cast lead grids containing 4.1% Sb corroded at 1.275V for 64 hr in 4.5M H_2SO_4 at 49°C.

autoradiographic technique that the insulating layer of $PbSO_4$ which forms between the positive grid and the active material during deep cycling is not present in cells containing phosphoric acid. Bullock and McClelland (9) have shown that H_3PO_4 decreases the rate of the self-discharge reaction

$$PbO_2 + H_2SO_4 \rightarrow PbSO_4 + H_2O + \tfrac{1}{2} O_2$$

in sealed lead-acid cells with pure lead grids.

Previous results obtained by cyclic voltammetry (1-3) have shown a decrease in the peak height of the wave corresponding to the reduction of PbO_2 to $PbSO_4$ when H_3PO_4 is added to the electrolyte. This result would also suggest that H_3PO_4 decreases the rate of sulfation.

In order to correlate the constant potential corrosion results with the results of cyclic voltammetry, the potential of pure lead rods was held constant in the range where PbO_2 is formed for 6-24 hr and was then reduced to 0.975V at a rate of 3 mV/min. Figure 10 shows the cyclic voltammetry of pure lead corroded at 1.425V for 6 hr in 5*M* H_2SO_4 at 49°C. On the first cathodic scan, represented by the solid line, the reduction of PbO_2 to $PbSO_4$ at 1.11V (peak a) was followed by an anodic peak (peak b), which probably resulted from a subsurface corrosion reaction. On subsequent cycling between 0.975 and 1.425V, peak b disappeared and no further evidence of subsurface corrosion was seen. Peak c, which corresponds to the oxidation of $PbSO_4$ to PbO_2, shifted to a lower potential as the electrode cycled. The voltammograms no longer changed after the third cycle. In the steady state, the potential of peak c was 1.23V.

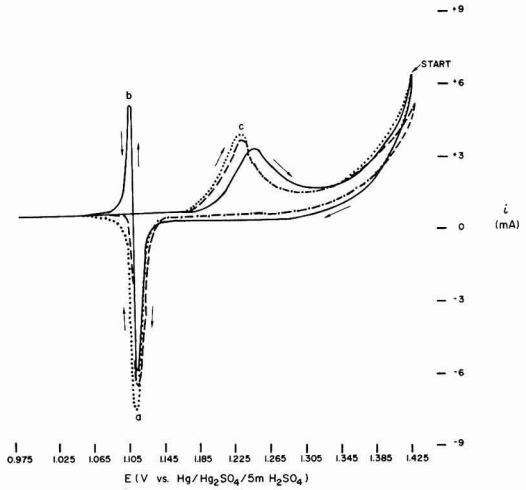


Fig. 10. Cyclic voltammograms of pure lead corroded at 1.425V for 6 hr in 5M H_2SO_4 at 49°C. Scan rate = 3 mV/min. ——— cycle 1; — — — — — cycle 2; . . . . . cycles 3 and 4.

The secondary peaks noted previously (1) on the negative side of the reduction wave do not appear when the electrode is pretreated by corroding it at constant potentials in the PbO_2 potential range. However, if the electrode potential is held at 0.975V for several hours, these secondary peaks will appear. They probably result from reduction of suboxide corrosion films beneath the PbO_2 layer.

Figure 11 shows the cyclic voltammetry of a lead rod corroded under the same conditions in electrolyte containing 0.2% H_3PO_4. On the first cycle, peak a is broader and shorter than in the pure electrolyte. On subsequent cycles, the potential of peak a shifts to 1.135V in agreement with previous observations (1). At potentials from 1.195 to 1.315V, this positive shift in the reduction wave is observed on the first scan. It may be that the absence of lead sulfate crystals on the surface corroded at 1.425V (see Table I) leads to a nucleation overpotential on the first scan. A positive shift in peak c to 1.265V is also observed in the presence of H_3PO_4, in agreement with previous results (1-3).

Peak b is nearly identical in the two solutions at 1.425V; however, at the lower voltages, a much broader subsurface corrosion wave is observed in the presence of H_3PO_4. Results obtained on the first cathodic scan of electrodes corroded at 1.235V are shown in Fig. 12, for example. The potential shift and broadening of the reduction wave are also apparent in this figure.

These results suggest that the observations of changes in the electrochemistry of the $PbO_2/PbSO_4$ couple in the presence of H_3PO_4 which have been made by cyclic voltammetry and by constant potential corrosion studies have the same source—the modification of the morphology of the PbO_2 in the corrosion film.

Conclusions

The following conclusions may be drawn:

1. Phosphate is incorporated into the PbO_2 structure during corrosion.
2. Phosphate modifies the morphology of PbO_2 formed by grid corrosion.
3. The PbO_2 formed in the presence of H_3PO_4 discharges to $PbSO_4$ at a slower rate than the PbO_2 formed in pure electrolyte.
4. These effects occur with as little as 0.2 w/o H_3PO_4 in the electrolyte.
5. These effects occur on pure lead, and on antimonial and nonantimonial lead alloys.
6. Results from constant potential corrosion and cyclic voltammetric experiments agree.

Acknowledgments

The author is grateful to Globe-Union, Incorporated, for the support of this research, and to the following people for their contributions: M. Mueller, who carried out the corrosion and self-discharge experiments; A. Ortiguera, who did the electron probe analyses and scanning electron microscopy; and E. Sensabaugh, who analyzed the lead content of the corrosion layer. The

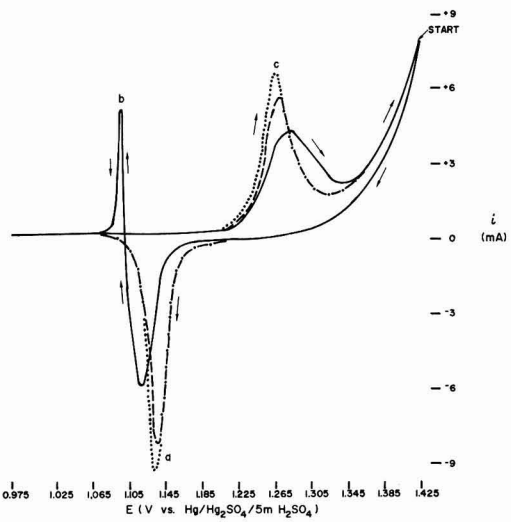


Fig. 11. Cyclic voltammograms of pure lead corroded at 1.425V for 6 hr in 5M H_2SO_4 containing 0.2% H_3PO_4 at 49°C. Scan rate = 3 mV/min. ——— cycle 1; — — — — — cycle 2; . . . . . cycles 3 and 4.

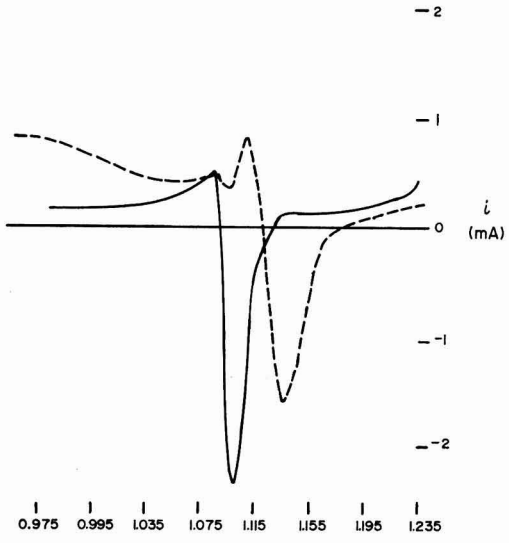


Fig. 12. Cathodic scans of pure lead corroded at 1.235V for 6 hr in 5M H_2SO_4 at 49°C. Scan rate = 3 mV/min. ——— 0% H_3PO_4; — — — — — 0.2% H_3PO_4 in electrolyte.

interest and helpful discussions of W. Tiedemann, B. Mahato, and R. Rizzo are also appreciated.

Manuscript submitted July 11, 1978; revised manuscript received Oct. 5, 1978. This was Paper 56 presented at the Pittsburgh, Pennsylvania, Meeting of the Society, Oct. 15-20, 1978.

Any discussion of this paper will appear in a Discussion Section to be published in the December 1979 JOURNAL. All discussions for the December 1979 Discussion Section should be submitted by Aug. 1, 1979.

Publication costs of this article were assisted by Globe-Union, Incorporated.

REFERENCES

1. K. R. Bullock and D. H. McClelland, *This Journal*, **124**, 1478 (1977).
2. W. Visscher, *J. Power Sources*, **1**, 257 (1977).
3. H. Tamura, H. Yoneyama, C. Iwakura, and O. Ikeda, International Lead Zinc Research Organization Report on Project LE-254, March 10, 1977.
4. J. Burbank, A. C. Simon, and E. Willihnganz, in "Advances in Electrochemistry and Electrochemical Engineering," Vol. 8, P. Delahay and C. W. Tobias, Editors, p. 208, Wiley-Interscience, New York (1971).
5. J. Burbank, *This Journal*, **103**, 87 (1956).
6. S. Tudor, A. Weisstuch, and S. H. Davang, *Electrochem. Technol.*, **3**, 90 (1965).
7. S. Tudor, A. Weisstuch, and S. H. Davang, *ibid.*, **4**, 406 (1966).
8. S. Tudor, A. Weisstuch, and S. H. Davang, *ibid.*, **5**, 21 (1967).
9. K. R. Bullock and D. H. McClelland, *This Journal*, **123**, 327 (1976).

The Cyclic Corrosion of the Lead-Acid Battery Positive

B. K. Mahato*

Globe-Union Incorporated, Corporate Applied Research Group, Milwaukee, Wisconsin 53201

ABSTRACT

Simulated deep discharge cycling of a lead-acid battery positive, using a linear potential sweep technique, was performed on pure and antimonial lead electrodes in sulfuric acid electrolyte with and without phosphoric acid additive. Discharge capacity, depth of corrosion, corrosion product morphology, adhesion between the substrate and corrosion product, and distribution of antimony, phosphorus, and sulfur in the corrosion product layer were monitored. Results indicated that the cyclic corrosion process occurring at the lead/lead dioxide electrode interface was controlled by the corrosion product layer consisting of an inner layer dominated by α-PbO_2 and an overlapping outer layer dominated by β-PbO_2. Presence of antimony in the alloy was noted to improve the adhesion between the grid substrate and the inner layer, integrity of the inner layer, and interparticle bonding of lead dioxide particles. Phosphoric acid additive in electrolyte was noted to alter the structure of corrosion product layer resulting in improved adhesion between the grid and the inner layer and between the inner and outer layer.

The corrosion of lead alloys under constant potential and current conditions has been studied extensively (1-10). This has resulted in a significant understanding of the over-all corrosion process such as the dependence of the corrosion product on potential and pH (1-4); the existence of a minimum corrosion rate close to the $PbO_2/PbSO_4$ equilibrium potential (5, 6); the permselective behavior of the discharged lead sulfate product layer causing a gradient of pH within the product layer (7, 8); the tendency of the corrosion layer to disintegrate under internal stress (9); and the influence of mechanical flaws in the corrosion layer caused by similar flaws in the substrate such as grain boundaries, dislocations, and varying crystal orientations (10). In continuous cyclic operation the grid corrosion of the positive plate is complicated by its continuous exposure to varied potential or current, acidity, and to some extent temperature. The complexity of this corrosion process, during early cycling, is to a limited extent depicted by current-potential diagrams (11-16). In practice the cyclically corroded positive grid experiences a potential high enough to generate free oxygen at the end of charge and a potential low enough to form tet-PbO or basic lead sulfates at the lead-lead dioxide interface at the end of discharge. The over-all grid corrosion process resembles closely the formation of a planté-type positive in sulfuric acid solution. Upon continuous cycling a multiphase corrosion product film with a β-PbO_2-rich exterior facing the electrolyte and the tet-PbO and/or α-PbO_2-rich interior develops. The exterior layer resembles β-PbO_2 active mass. The inner layer, mostly consists of PbO_x, x varies from 1 in tet-PbO to 2 in α-PbO_2, has a dense structure, and restricts the corrosive attack of the grid during cycling. However, as corrosion of the substrate continues, an internal stress develops and stress cracking of the protective inner layer may occur. Presence of antimony in the alloy to some extent restricts the intensity of stress cracking. Antimony leached out provides space for expansion created by the change from lead to lead dioxide. The less stress within the dense corrosion product layer in turn allows it to be thicker and more protective for an antimonial grid (9). Better cycling ability of antimonial lead compared to a pure lead or a lead-calcium alloy positive may be related to the physical nature of this inner corrosion product layer. Improvement in cycling ability of the pure lead or Pb-Ca alloy in the presence of phosphoric acid additive might result from the modifying influence of phosphoric acid on this inner layer. The objective of this study is to determine the effect of antimony in the grid alloy and phosphoric acid additive in the electrolyte on the cyclic corrosion process of the lead-acid battery positive grid.

In order to better define the cyclic corrosion process and to avoid corrosion unrelated to the cyclic operation (such as chemical corrosion occurring at the grid during plate preparation), a planté-type electrode as studied by Weininger (17) is used here. Such a study for understanding the corrosion process is relevant since as in most circumstances the thickness of the

* Electrochemical Society Active Member.

Key words: voltammetry, lead dioxide, antimony, phosphoric acid additive.

active material layer on the positive grid has little effect on the thickness of the corrosion product formed on the grid (18). Over and above a rotating disk electrode voltammetry is used to elucidate the corrosion kinetics of lead alloys at the onset of the cyclic operation.

Experimental

Lead alloy master ingots were prepared from 99.999% lead and antimony metal. Portions of the ingots were used for casting ¼ and ⅛ in. diam lead alloy rods. The ¼ in. diam rod was used for preparation of rotating disk electrodes (RDE) after Albery and Bruckenstein (19). The ⅛ in. diam rods were used to prepare 2 mm diam test electrodes by swaging carried out at Northwestern University (Illinois) facility.

The RDE cyclic voltammetric experiments were carried out at ambient temperature conditions with a PAR™ Model 371 potentiostat/galvanostat equipped with a PAR™ Model 175 universal programmer and a Hewlett Packard/Moseley Autograph Model 7000 AM X-Y recorder. A two-compartment Pyrex glass cell separated by a fritted glass disk was used as a test cell. The top compartment had a side connection for the reference electrode and was used for housing the working disk electrode. The counterelectrode, a gold foil of ~10 cm^2 area, was placed in the bottom compartment. A Hg/Hg_2SO_4/1.250 sp gr H_2SO_4 was used as the reference electrode. The tip of the reference electrode was always within 2 mm from the edge of the disk electrode. A rotor made by Pine Instrument Company and held at 600 rpm was used for this series of experiments. The surface preparation of the disk electrode was carried out to 600 μm surface finish.

Potentiostatically controlled linear potential sweep cycling of the test electrode was carried out with a 10A Wenking potentiostat equipped with a PAR™ Model 175 universal programmer, a Keithley 616 digital electrometer, and a Hewlett Packard Model 17501A two-channel recorder. An oversized circular lead foil was used as the counterelectrode. The test electrode of required length, usually 5 cm, was isolated by coating the remainder with hot wax followed by two layers of heat shrinkable Teflon tubing. The electrode was degreased with tissue paper soaked with acetone until it achieved a shiny appearance. At the start the elecrode was held at 1425 mV *vs.* Hg/Hg_2SO_4/1.250 sp gr H_2SO_4 reference for 5 min. This was followed by linear potential sweep cycling between 1425 and 975 mV (*vs.* reference). The cathodic and anodic scan at 10 and 2.5 mV/sec, respectively, were selected to assure complete conversion of lead sulfate to lead dioxide at the end of charge or anodic scan. All experiments were carried out in a thermostated bath in which temperature was controlled within ±0.5°C.

The information gathered during linear sweep cycling was (*i*) cathodic capacity buildup characteristics, (*ii*) differential corrosion depth ($d_{initial}$-d_{final}), (*iii*) thickness of corrosion product layer, (*iv*) thickness of inner layer, *i.e.*, the dense phase of the corrosion product layer, (*v*) surface morphology of the corrosion product, (*vi*) concentration of antimony and phosphorus when applicable in the corrosion layer, and (*vii*) adhesion characteristics of the substrate and inner layer as well as the inner and outer corrosion product layer. The cathodic discharge capacity was obtained from the integration of discharge curves. Thickness of the corrosion layer was obtained from the optically examined polished cross section, averaging 8 to 16 readings over the circumference. The surface morphology of the corrosion product was examined by JEOL U3 scanning electron microscope. The gross concentration of antimony in the corrosion product was carried out by atomic absorption spectrometry from the chemically stripped corrosion product. The concentration profile of Sb, S, and P in the corrosion product layer was carried out by electron microprobe analysis of the corroded electrode cross section. The adhesion behavior between the substrate and inner layer and outer layer was optically examined from microtomed and polished cross sections of the corroded specimens.

In several cases the progress of cyclic corrosion was monitored by sectioning a portion of the electrode cycled up to 5000 cycles.

Results and Discussion

Rotating disk electrode voltammetry.—The effect of antimony content in the alloy on the cyclic voltammogram is shown in Fig. 1 between hydrogen and oxygen evolution at 5 mV/sec scan rate, in 1.050 sp gr H_2SO_4 solution. These are similar in several respects to the study reported by Tamura *et al.* (20), Visscher (21), Brennan *et al.* (22), Panesar (11), Chang *et al.* (12), and Sharpe (13). Thus, in the positive sweep from hydrogen evolution (−1600 mV) through oxygen evolution (+1600 mV), the anodic peaks to be seen are oxidation of lead at ~ −900 mV and antimony around ~ −380 mV; no distinct anodic peak for PbO_2 formation is noted; apparently it coincided with the oxygen evolution (17, 21, 22). Reversing the direction of potential sweep, a complex mixture of anodic and cathodic activities between 600 to 1000 mV and noticeable cathodic peaks at −800 and −1000 mV are observed. The antimonial electrode has an additional cathodic peak at −670 mV. The explanation of these voltammetric peaks is detailed by Chang *et al.* (12) and the complexity of peaks around $PbO_2/PbSO_4$ potential by Sharpe (13). The latter has hypothesized that the complexity of voltammetric peaks are caused by simultaneous cathodic and anodic reactions of leady ions that occur in 600-1000 mV (*vs.* Hg/Hg_2SO_4) potential range. The formation of nonstoichiometric oxide close to $PbO_2/PbSO_4$ equilibrium potential has also

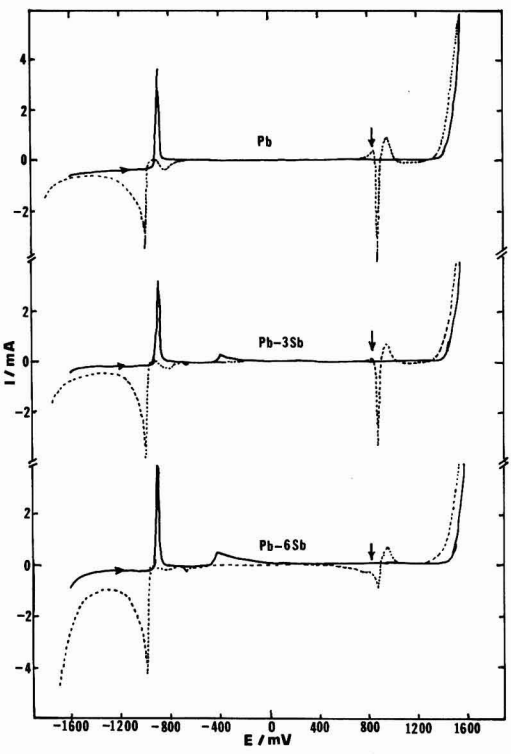


Fig. 1. The effect of antimony content in the lead alloy on the RDE voltammograms in 1.050 sp gr H_2SO_4 at 24°C, 600 rpm, and 5 mV/sec scan rate. The arrow indicates the subsurface oxidation under the reduced lead dioxide film.

been noted (14, 15). The pertinent observations here are the oxidation peaks (see arrow) that follow the cathodic discharge of the lead dioxide and the dependency of the peak intensity as a function of antimony content in the alloy. Thus the presence of antimony appears to suppress the anodic reaction that follows the cathodic reduction of the lead dioxide film (or corrosion under lead sulfate discharge product layer). This is further substantiated by the cathodic peak at −800 mV (*vs.* Hg/Hg_2SO_4) representing the reduction of sublayer corrosion product (basic oxides of lead) to metallic lead (8). The manner in which the presence of antimony suppresses this anodic reaction below the $PbO_2/PbSO_4$ potential is not clear. Sharpe (13) also noted the reduced intensity of this peak in the antimonial alloy. This is also, in some respects, in agreement with the work carried out by Weininger (17), Ritchie (23), and Burbank (24). Weininger noted the average anodic current of potentiostatically controlled cycled electrodes to be less for Pb-5.7 Sb than either Pb or Pb-0.07Ca-0.7Sn or Pb-0.54Ca-0.7Sn (17). Ritchie noticed that the Sb_2O_3 inhibits the oxidation of free metallic lead in battery paste (23). Burbank observed the enhancement of α-PbO_2 in the corroding interface in the presence of antimony in the alloy (24).

Figure 2 shows the effect of acid concentration on the RDE voltammogram. The apparent shift of the $PbO_2/PbSO_4$ potential is associated with the acid concentration. Oxygen overpotential is increased with increasing acid concentration. All voltammetric peaks with the exception of cathodic peaks at −800 mV are decreased with increasing acid concentration. These have resulted from the ease of lead passivation and slower kinetics of $PbSO_4 \rightarrow PbO_2$ conversion with increasing acid concentration. Under linear potential sweep cycling of the lead electrode between 800 to 1500 mV potential range, Tamura *et al.* (20) have also observed a significant decrease in cathodic discharge capacity with increasing acid concentration. The increased cathodic peak at −800 mV in 1.250 sp gr compared to 1.050 sp gr H_2SO_4 is the reflection of greater anodic oxidation of the lead substrate as a basic leady compound underneath the lead sulfate reduction product film. The nonpermeability of SO_4^{2-} and HSO_4^- ions in the lead sulfate film is apparently increased with increasing acid concentration, resulting in a greater amount of basic leady compound as the anodic product in 1.250 sp gr than in 1.050 sp gr H_2SO_4. Figure 2 also indicates that between 975 to 1425 mV *vs.* Hg/Hg_2SO_4 reference the cycling behavior of the lead dioxide electrode involves deep discharge and charge without excessive oxygen gas evolution. This is in agreement with Weininger (17) and is selected for the study of cyclic corrosion of the lead dioxide electrode.

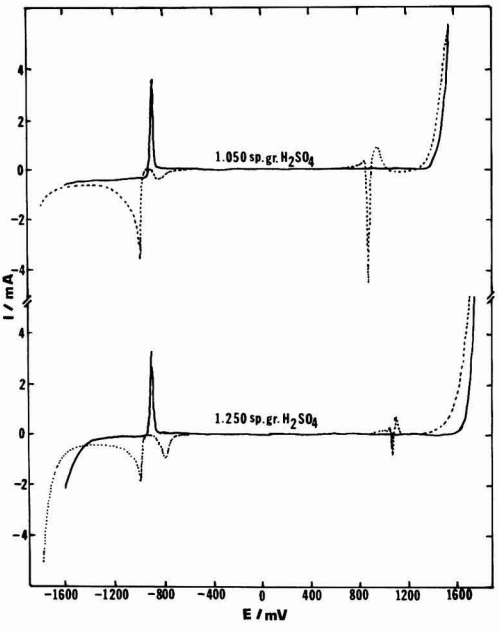


Fig. 2. The effect of acid concentration on the RDE voltammograms of the lead electrodes at 24°C, 600 rpm, and 5 mV/sec scan rate.

Cyclic corrosion of lead-alloy grids.—Capacity buildup characteristics.—The results of the effect of antimony on the potentiostatically controlled linear sweep cyclic corrosion of lead alloys are summarized in Fig. 3 as cathodic discharge capacity *vs.* cycle number. It indicates that the initial capacity buildup is almost independent of antimony concentration in the alloy, at least the concentration range tested here, but the steady-state capacity increased with increasing antimony concentration. This is in agreement with the recent study carried out by Weininger (17). He used 5 mV/sec linear potential sweep cycling of the lead electrode between 975 to 1425 mV *vs.* Hg/Hg_2SO_4 reference and noted higher discharge capacity of Pb-5.7Sb than either pure lead or Pb-Ca-Sn alloys. The increased steady-state capacity in the presence of antimony in the alloy could be due to higher corrosion, or amount of PbO_2 on the electrode, or to the improved discharge efficiency of PbO_2 in the presence of antimony (25), or to decreased polarization resistance during discharge (22, 26), or a combination of effects.

Figure 4 shows the effect of temperature on the capacity buildup characteristics during linear potential sweep cycling described earlier. As expected the capacity increased with increased temperature.

The discharge capacity was used as a measure of lead/lead dioxide electrode corrosion caused by constant current oxidation (27) and linear potential sweep cycling between 975 to 1425 mV (*vs.* Hg/Hg_2SO_4) in sulfuric acid solution (17). A reasonable correlation between the discharge capacity and the gross amount of corrosion is difficult as the discharge process is limited to only two components of the multicomponent corrosion products, *i.e.*, α-PbO_2 and β-PbO_2 and their mass utilization coefficients. In cyclic corrosion, the

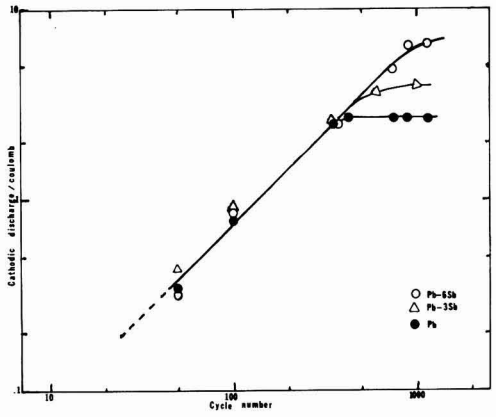


Fig. 3. Influence of antimony concentration in the alloy on the cathodic discharge capacity during linear potential sweep cycling between 975 to 1425 mV (*vs.* Hg/Hg_2SO_4/1.250 sp gr H_2SO_4) in 1.250 sp gr H_2SO_4 at 20°C. The cathodic and anodic sweep rates are 10 and 2.5 mV/sec, respectively.

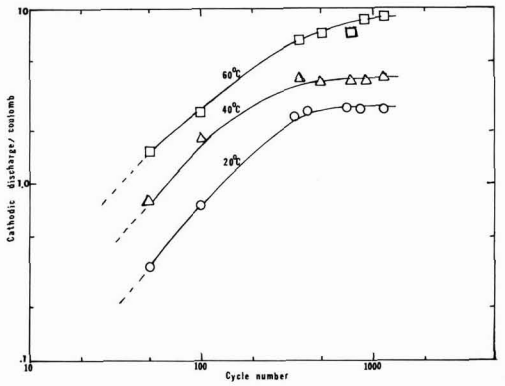


Fig. 4. The effect of temperature on the cathodic discharge capacity during linear potential sweep cycling of lead electrodes between 975 to 1425 mV (vs. Hg/Hg_2SO_4/1.250 sp gr H_2SO_4) in 1.250 sp gr H_2SO_4. The cathodic and anodic sweep rates are 10 and 2.5 mV/sec, respectively.

discharge capacity may represent a small fraction of the total corrosion product. For example: a lead electrode which was cycled for 1150 times in the mode stated earlier (Fig. 3) gave 145.2 mg Pb as total corrosion in terms of Pb and 0.211C as capacity at 1150th cycle indicating the presence of ~10% dischargeable lead dioxide in the corrosion product. The cumulative anodic activity defined as the net excess anodic charge (Q_a-Q_c) as used by Weininger (17) may also be imprecise as it does not involve correction for oxygen evolution and the charge state of the anodic product. Thus it has been apparent that the corrosive attack of the lead dioxide grid would remain incomplete unless the role of corrosion product and its morphology on the continued anodic activity is fully realized. A detailed examination of the corrosion product layer is followed as a means of monitoring anodic activity during cycling.

Corrosion product morphology.—Development of inner layer and effect of antimony.—Figures 5a through f are cross-sectional views of cyclically corroded Pb, 3% antimonial lead (Pb-3Sb), and 6% antimonial lead (Pb-6Sb) at the 250 cycle point under charge and discharge conditions. These micrographs indicate that the corrosion product layer (or lead dioxide developed during cycling) broadly consists of an inner layer, close to the substrate, and an outer layer, overlapping the inner layer close to the electrolyte phase. The inner layer is dense and compact whereas the outer layer is highly porous and less dense. When microscopically viewed under cross polarized light, the inner layer was dark brown, typical of the α-PbO_2-rich phase (28) and the outer layer a light brown, fairly typical of the β-PbO_2-rich phase (28). These micrographs (comparison of Fig. 5a, 5c, and 5e with 5b, 5d, and 5f) also revealed that the discharge of the electrode was heavy at the β-PbO_2-rich phase and was terminated at the outskirt of the dense phase. The role of the inner layer in protecting the grid during the deep discharge process is apparent from these micrographs.

The effect of antimony in the grid alloy on the development of the inner layer is qualitatively noted from the comparison of micrographs in Fig. 5a and 5b with those of Fig. 5c to 5f. The inner layer is highly nonuniform for pure lead electrode (Fig. 5a and 5b) compared to very uniform for antimonial lead (Fig. 5c to 5f). The discontinuity of the inner layer for pure lead could result from nonuniform corrosion of the substrate and/or stress cracking of the inner layer to accommodate the growth of the product at the corroding

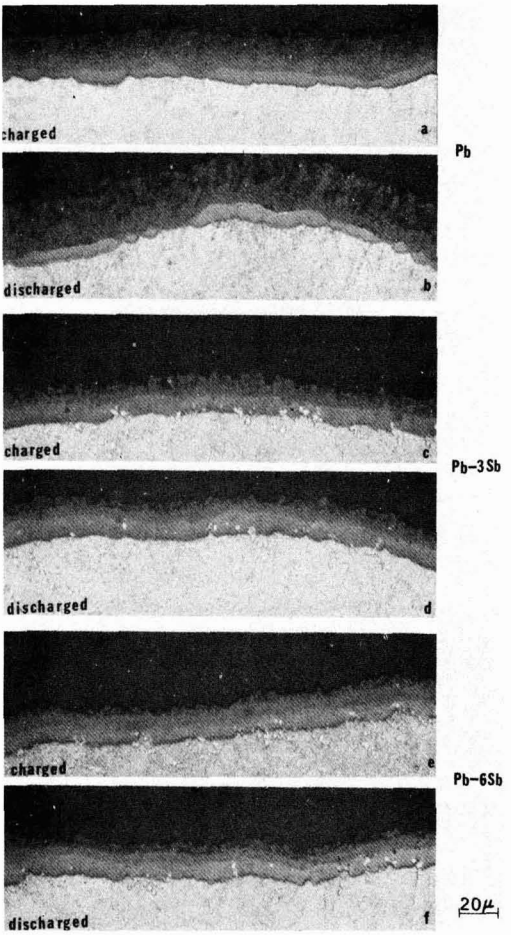
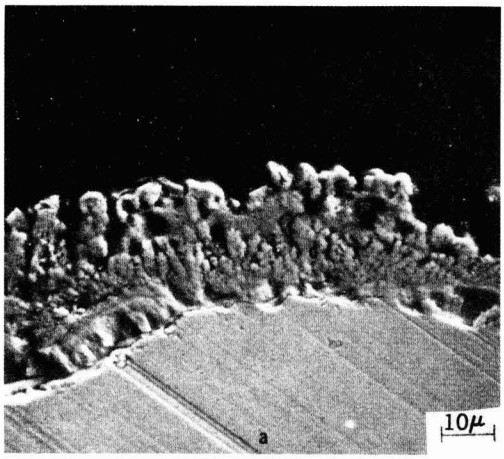


Fig. 5. Charged and discharged cross section of linear potential sweep cycled lead dioxide electrode formed on Pb, Pb-3Sb, and Pb-6Sb in 1.250 sp gr H_2SO_4 at 60°C after 250 cycles.

interface. The cracks in the inner layer could allow acid penetration and the formation of the sulfate barrier layer at the corroding interface. The presence of the sulfate barrier layer in the cycled nonantimonial positive is well recognized (26). The uniformity of the inner layer for corroded antimonial electrode, on the other hand, could be caused by the uniform corrosion of the substrate and/or by the ease of releasing stress in the expanding corroding layer. It is plausible that as antimony migrates out of the corrosion product layer, it allows the needed growth of the oxide layer in compact form (both inner and outer layer), controls the stress on the inner layer, and maintains the integrity of the inner layer.

Figure 6 is a microtomed cross section of Pb and Pb-6Sb taken at the end of discharge at the 250 cycle point. This indicates a very strong bond between the substrate and the inner layer for Pb-6Sb (no visible separation) but a clear separation for the lead electrode. The separation observed here is not associated with the microtoming or the difference in hardness of the corrosion product and the substrate. We have examined multiple samples of artificially fractured surfaces of heavily cycled electrodes and noted the presence of the fine structure of the β-PbO_2 layer (apparently converted from lead sulfate) underneath the



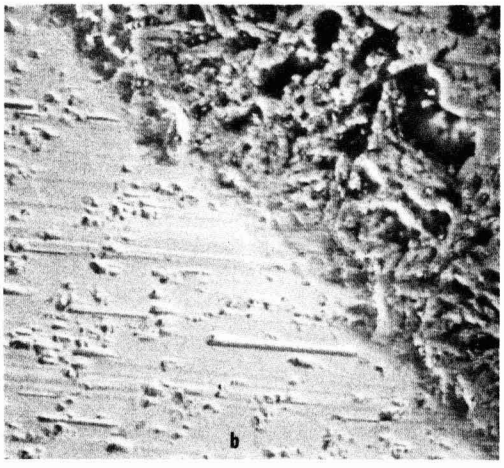


Fig. 6. Microtomed cross section of discharged lead dioxide electrode formed on (a) Pb and (b) Pb-6Sb by linear potential sweep cycling between 975 to 1425 mV (vs. Hg/Hg_2SO_4/1.250 sp gr H_2SO_4) in 1.250 sp gr H_2SO_4 at 60°C after 250 cycles.

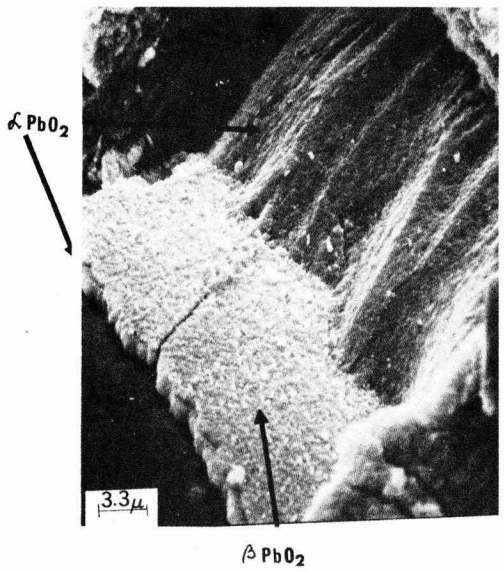


Fig. 7. Artificially fractured inner layer of the lead dioxide electrode formed on Pb by linear potential sweep cycling in 1.250 sp gr H_2SO_4 at 60°C after 5000 cycles shows the presence of β-PbO_2 structures in between the dense α-PbO_2 layers.

dense α-PbO_2 layer (Fig. 7) only for pure lead and not in antimonial lead electrodes The permeation of acid electrolyte in the ruptured inner layer and weakly bonded interface between the substrate and inner layer (Fig. 6) appears to cause lead sulfate formation at the interface and to be responsible for the existence of the β-PbO_2 underneath the α-PbO_2 dense phase. This explains the mechanism of formation of the sulfate barrier layer in nonantimonial positive under cycling service.

Effect of antimony on surface texture and particle morphology.—Figure 8 shows the surface texture of cyclically corroded Pb and Pb-1Sb specimens at 1000 cycle point at the end of charge. A large number of interconnected fissures are noted at the corroded lead electrode compared to very limited numbers in the Pb-1Sb electrode. No noticeable difference in surface texture of Pb-1Sb, Pb-3Sb, and Pb-6Sb was noted. The physical structures of the charged active mass formed on Pb, Pb-3Sb, and Pb-6Sb electrodes after 1000 cycles are shown in Fig. 9. These micrographs indicate that the particle morphology of PbO_2 formed on pure Pb is different from those formed on antimonial lead. The structure of the PbO_2 active mass, which is evenly distributed, interconnected, and porous, is very regular in the presence of antimony in the grid alloy. This closely resembles the coralloid structure of PbO_2 observed by Simon *et al.* (29) in the cycled lead-acid battery positive electrode. The active mass on pure lead (Fig. 9) is characterized by large voids, lack of interparticle cohesion, and the presence of unconverted sulfate particles.

The corrosion product analyses of three antimonial alloys at the 1000 cycle point are given in Table I. The percentage antimony was calculated from the lead content in the corosion product and in the alloy. These data suggest that the cyclic corrosion product of Pb-1Sb, Pb-3Sb, and Pb-6Sb could retain 89, 55, and 35% antimony present in the alloy, respectively. The concentration gradient of antimony within the lead dioxide matrix of the Pb-6Sb electrode is noted in Table II. The presence of antimony in the lead dioxide matrix suggests a strong possibility of its direct participation in altering the electrochemical behavior (oxygen overvoltage and suppression of sublayer corrosion, Fig. 1), lead dioxide morphology (Fig. 8 and 9), the adhesion between the inner layer and the substrate (Fig. 6), and the interparticle cohesion (Fig. 8 and 9). The retention of antimony in the lead dioxide active mass is reported to be due to surface adsorption of Sb^{3+} and Sb^{5+} species (30). The increased oxygen overpotential of the lead dioxide in the presence of

Table I. Analysis of corrosion product

(Formed on antimonial lead in 1.250 sp gr H_2SO_4 at 60°C by linear potential sweep cycling after 1000 cycles; stripping solution used was 1:2:10:87 = $Cl_2H_6N_2$:$C_6H_{14}O_6$:NaOH:H_2O)

Electrode type	Ratio of Pb:Sb in stripping solution/mg	Antimony retained in the corrosion product (%)
Pb-1Sb	89:0.8	89
Pb-3Sb	88:1.5	55
Pb-6Sb	84:1.9	35

ห้องสมุด กรมวิทยาศาสตรบริการ

Table II. Antimony in the corroded cross section of Pb-6Sb electrode by electron microprobe

(Corrosion carried out in 1.250 sp gr H_2SO_4 at 60°C by linear potential sweep cycling to 1000 cycles; total thickness of corrosion layer = 50.0 ± 3.2 μm; thickness of inner layer = 11.4 ± 1.7 μm)

Distance from the substrate surface (μm)	Elemental Sb (%)
5	3.98
15	2.00
25	2.05
45	1.90

antimony may be responsible for the improved $PbSO_4 \rightarrow PbO_2$ electroconversion process (Fig. 1). The maintenance of the reactivity of the lead dioxide active mass and interparticle cohesion (Fig. 8 and 9) may be related to the role of adsorbed antimony species in restructuring either a PbO_2 crystal lattice and/or enhancing the formation of α-PbO_2 in the active matrix as suggested by Burbank (24).

Effect of antimony on the growth of inner layer.—Figures 10 and 11 are micrographs depicting the growth of inner layer during potentiostatically controlled linear sweep cycling of Pb and Pb-1Sb electrodes in the positive electrode potential range up to 5000 cycles.

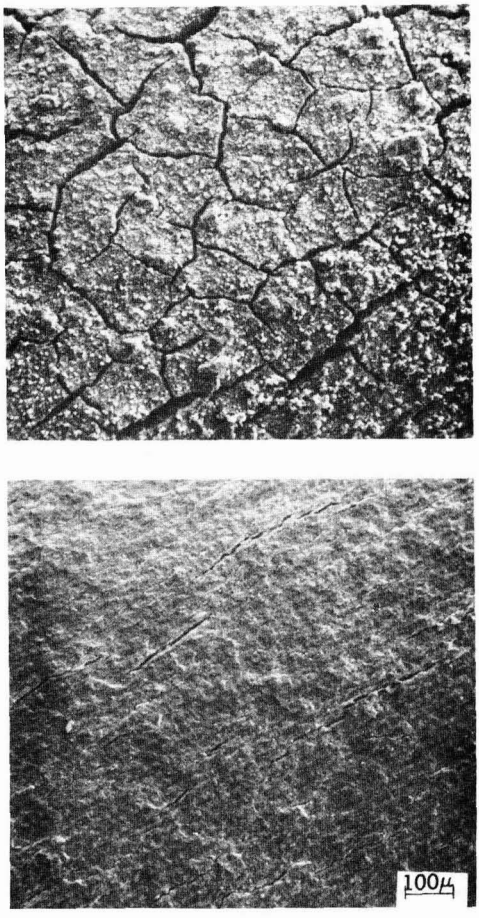


Fig. 8. Surface texture of the lead dioxide electrodes formed on (a) Pb and (b) Pb-1Sb substrate in 1.250 sp gr H_2SO_4 at 60°C after 1000 cycles.

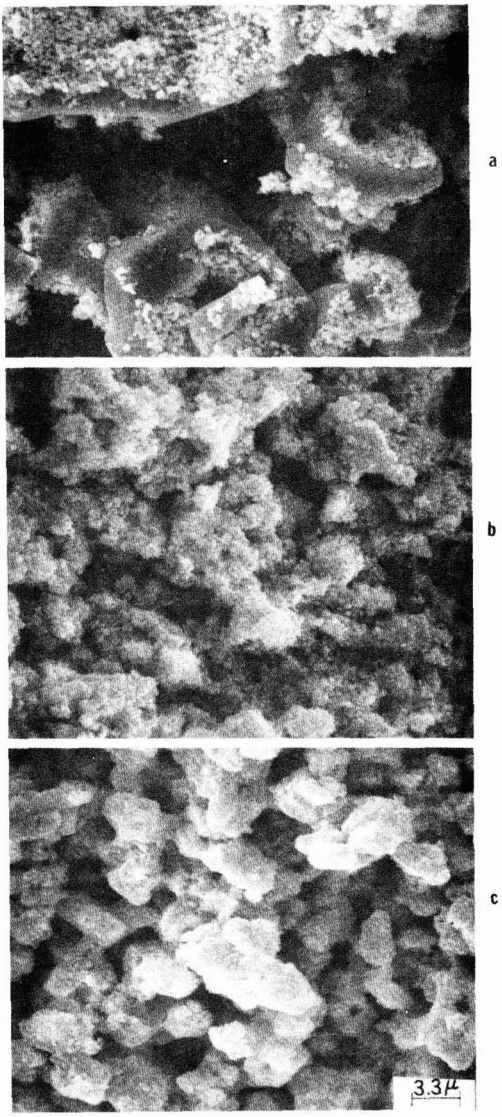


Fig. 9. The influence of antimony on the particle morphology of lead dioxide formed on (a) Pb, (b) Pb-3Sb, and (c) Pb-6Sb by linear potential sweep cycling between 975 to 1425 mV (vs. Hg/Hg_2SO_4/1.250 sp gr H_2SO_4) in 1.250 sp gr H_2SO_4 at 60°C after 1000 cycles.

In both cases the inner layer grew about 12-14 μm thick within 400 cycles. However, on subsequent cycling this was maintained well in Pb-1Sb whereas for pure lead this decreased and attained a steady-state value at a much lower level. This is demonstrated in Fig. 12 from the plot of the inner layer thickness *vs.* cycle number for Pb, Pb-1Sb, and Pb-3Sb electrodes. No significant variation in inner layer thickness between Pb-1Sb and Pb-3Sb is noted. Figure 13 is a graphical plot of electrode diameter with cycle numbers for Pb, Pb-1Sb, and Pb-3Sb electrodes. The electrode diameter is found to follow a linear relationship with cycle numbers for all three types of electrodes tested with correlation coefficient of 0.990 or better. The negative slope of the linear correlation is the

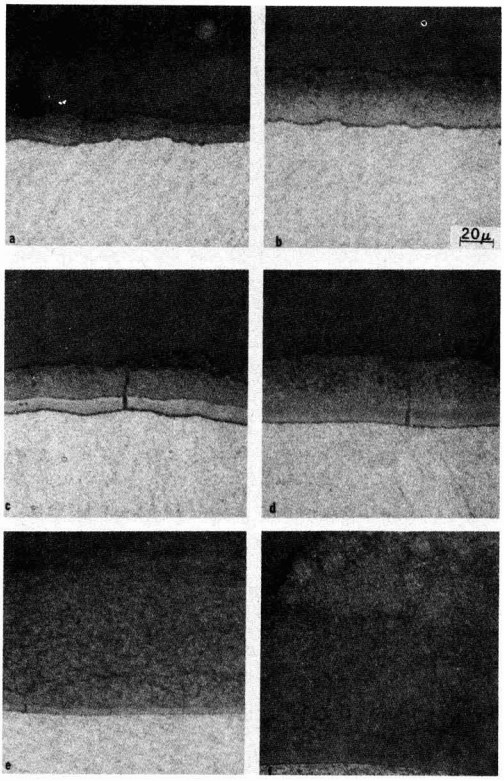


Fig. 10. Growth of lead dioxide layers on lead by linear potential sweep cycling between 975 and 1425 mV (vs. $Hg/Hg_2SO_4/1.250$ sp gr H_2SO_4) in 1.250 sp gr H_2SO_4 at 60°C. (a) 100, (b) 400, (c) 800, (d) 1200, (e) 2400, and (f) 5000 cycles.

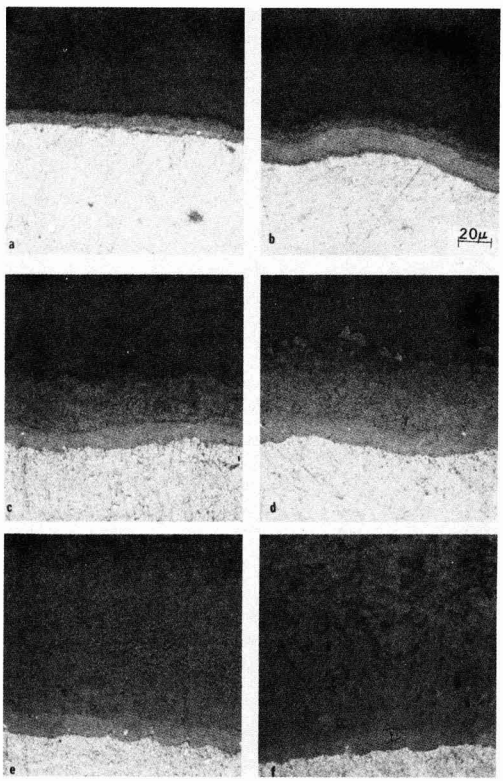


Fig. 11. Growth of lead dioxide layers on Pb-1Sb electrode by linear potential sweep cycling between 975 to 1425 mV (vs. $Hg/Hg_2SO_4/1.250$ sp gr) in 1.250 sp gr H_2SO_4 at 60°C. (a) 100, (b) 400, (c) 800, (d) 1200, (e) 2400, and (f) 5000 cycles.

average corrosion rate. The corrosion rate for a pure lead electrode is 0.0565 mm/1000 cycles compared to 0.0323 and 0.0457 mm for Pb-1Sb and Pb-3Sb electrodes, respectively. The greater corrosion rate for pure lead during this cyclic corrosion process appears to be associated with the less protective nature (less thickness and cracks in the layers) of the layer. This agrees with the experimental observations made by Weininger (17) who under similar mode of cycling noted less corrosion of antimonial lead than pure lead.

Effect of phosphoric acid additive.—To monitor the effect of phosphoric acid additive on the cyclic corrosion of the lead electrode, electrodes were cycled at 60°C in 1.250 sp gr H_2SO_4 with and without 0.2% phosphoric acid. 99% pure lead wire (2.4 mm diam) obtained from Alfa Product Incorporated was used in this series of experiments. Spectrographic analysis noted 0.025% Ag as the major impurity in this electrode material.

The electrodes were cycled up to 1150 cycles and results are summarized in Table III. The amount of gross corrosion decreased by 9%, the thickness of the total corrosion product layer by 24%, and the discharge capacity by 18% in the presence of phosphoric acid additive. No substantial difference was noted in the inner layer thickness. The growth of the corrosion product or, in turn, the grid growth of the lead electrode during cycling decreased significantly in the presence of this additive. The decreased discharge capacity in the presence of the additive is partly due to the reduced amount of corrosion (Table III) and the morphology of the β-PbO_2 layer formed in the presence of the additive. A significant agglomeration of the β-PbO_2 structure has recently been noted in constant potential oxidation of lead alloys in sulfuric acid solution with phosphoric acid additive (31).

Figure 14 depicts the influence of phosphoric acid additive on the adhesion characteristics between (*i*) the grid substrate and the inner layer and (*ii*) the inner and outer corrosion product layer. Lead electrodes cycled in pure acid were noted to develop an intermediate phase between the substrate and the inner layer and a sharp transition from the inner layer to outer layer (Fig. 14a). In contrast to this, electrodes when cycled in the presence of phosphoric acid additive were noted to have a good bond between the inner layer and the substrate and a smooth transi-

Table III. Effect of phosphoric acid additive in 1.250 sp gr H_2SO_4 electrolyte on the cyclic corrosion of the lead electrode at 60°C

(Corrosion carried out by linear potential sweep cycling between 975 to 1425 mV *vs.* $Hg/Hg_2SO_4/1.250$ sp gr H_2SO_4)

Electrolyte	1.250 sp gr H_2SO_4	1.250 sp gr H_2SO_4 with 0.2% phosphoric acid
Weight of corrosion product, mg	157.3	151.0
Amount of lead in corrosion product from analysis of stripping solution, mg	145.2	132.0
Thickness of inner layer, μm	14 ± 6	15 ± 2
Total thickness of corrosion product layer, μm	76 ± 13	58 ± 15
Discharge capacity at 1150th cycle, C	9.211	7.596

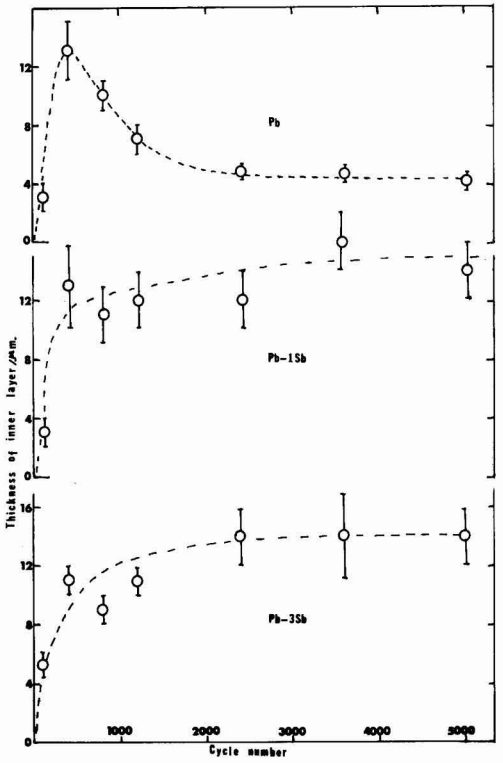


Fig. 12. The effect of cycle number on the thickness of inner layer during linear sweep cycling of (a) Pb, (b) Pb-1Sb, and (c) Pb-3Sb electrodes in 1.250 sp gr H_2SO_4 at 60°C.

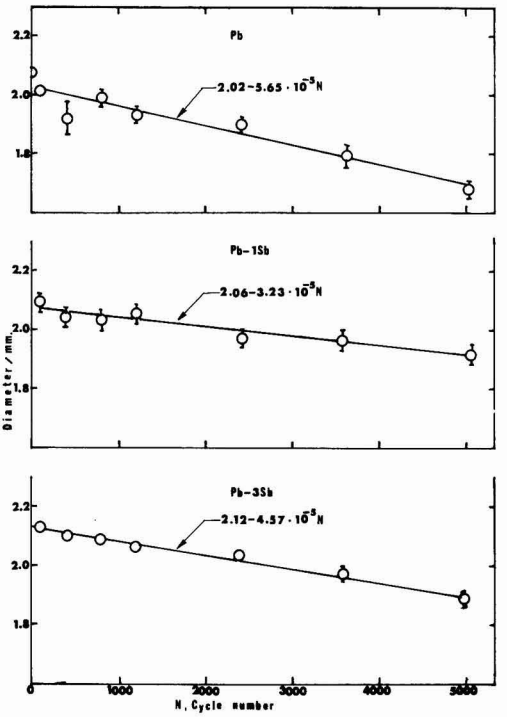


Fig. 13. The effect of cycle number on the electrode diameter during linear sweep cycling of (a) Pb, (b) Pb-1Sb, and (c) Pb-3Sb electrodes in 1.250 sp gr H_2SO_4 at 60°C.

tion from the inner dense phase to outer porous structure (Fig. 14b). Electron microprobe analysis of corroded cross section revealed high sulfur concentration at the interface between the substrate surface and inner layer for the electrodes cycled in pure electrolyte (Fig. 15). Similar examination of electrodes cycled in sulfuric acid with phosphoric acid additive exhibited no sulfur at the grid-inner layer interface and a maxima in phosphorus concentration at the interface between the inner and outer corrosion product layer (Fig. 16). This phosphorus concentration maxima coincides with the region of smooth transition between the dense inner layer and highly porous outer layer. Thus it is apparent that the presence of phosphoric acid additive promotes the adhesion between the grid substrate and inner layer and causes the smooth transition from the dense inner layer to the porous outer layer. Both of these factors appear to be responsible for promoting the cycle life of the nonantimonial lead-acid system in the presence of phosphoric acid.

Conclusions

1. Rotating disk electrode voltammetry of lead and antimonial lead in sulfuric acid indicated that the presence of antimony suppresses the sublayer corrosion and increases the oxygen overpotential.

2. Based on their cathodic discharge behavior following linear sweep cycling, corroded lead and antimonial lead electrodes undergo increasing discharge capacity with increasing antimony content.

3. The cyclically formed PbO_2 electrode is composed of a dense α-PbO_2-rich layer adjacent to the metal covered by a layer which is predominantly β-PbO_2. The steady-state thickness of the dense layer is about 14 μm on the antimonial electrode compared to 4 μm on pure lead.

4. The cyclic corrosion process of the lead dioxide electrode is influenced by the dense α-PbO_2 inner layer and its adhesion to the grid substrate.

5. The presence of antimony in the grid alloy improves the adhesion between the grid and inner layer and helps maintain the uniformity of the α-PbO_2-rich inner layer.

6. The integrity of the inner layer is enhanced by the presence of antimony in the alloy. In addition, antimony helps to promote a compact oxide layer and reduces the stress cracking of the layer.

7. The presence of antimony in the grid alloy improves the cohesion between the lead dioxide particles. This partly explains the decreased shedding of lead dioxide active mass during cycling service in the presence of antimony.

8. The formation of a nonuniform inner corrosion product layer for pure lead under cyclic corrosion may have resulted from the stress cracking of the expanding corrosion layer followed by acid permeation and sulfate formation in the crack. Formation of a sulfate barrier layer in the nonantimonial system during cycling service could result from the stress cracking and/or lack of adhesion between the inner layer and the substrate followed by acid permeation.

9. The presence of phosphoric acid as an electrolyte additive appears to improve the adhesion between the grid substrate and inner layer and between inner and outer corrosion product layer. The former appears to restrict the sulfate barrier formation whereas the latter prevents the shedding of active mass.

10. The morphology of cycled lead dioxide active mass obtained from linear sweep cycling bears a strong resemblance to the lead dioxide active mass obtained from a cycled lead acid battery. This suggests that (i)

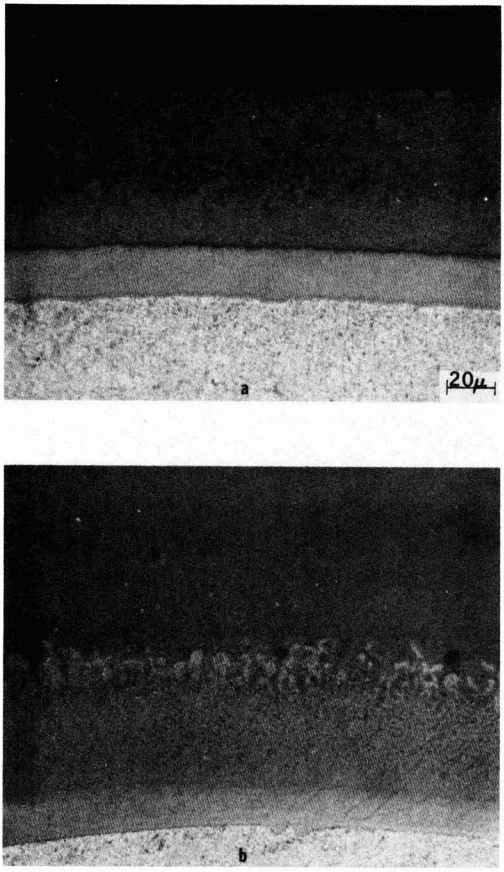


Fig. 14. The effect of phosphoric acid additive in the electrolyte on the contacts of inner layer to the substrate and to the outer layer; (a) 1.250 sp gr H_2SO_4, (b) 1.250 sp gr H_2O with 0.2 w/o H_3PO_4.

the study of the cyclic corrosion of a grid alloy and/or (*ii*) the study of the positive plate microstructure with a well-defined mode of cycling under controlled conditions could be conveniently and economically carried out by the approach followed here. This approach being simple and less influenced by the battery construction parameters may provide a clearer mechanistic understanding of the functioning of the lead dioxide electrode.

Acknowledgments

The author wishes to express his appreciation to G. Goodman and W. Tiedemann for their keen interest in this program; to W. Gentry and G. McDonald for preparation of swaged electrodes; to K. Bullock for discussion on the effect of phosphoric acid; and to A. Ortiguera for the scanning electron microscopy.

Manuscript submitted July 17, 1978; revised manuscript received Sept. 27, 1978.

Any discussion of this paper will appear in a Discussion Section to be published in the December 1979 JOURNAL. All discussions for the December 1979 Discussion Section should be submitted by Aug. 1, 1979.

Publication costs of this article were assisted by the Globe-Union Corporation.

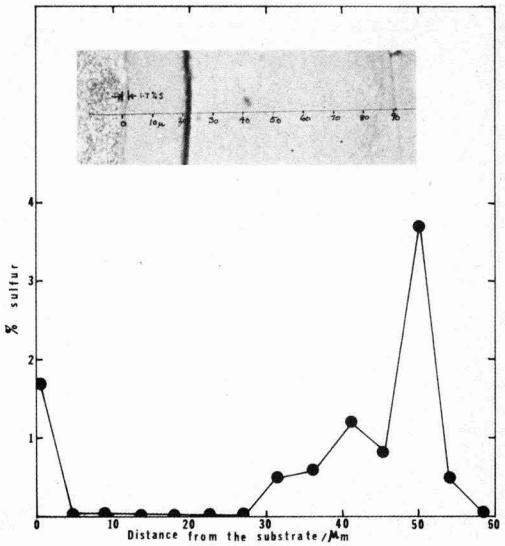


Fig. 15. Electron microprobe profile for sulfur across the lead dioxide layer formed on lead electrode by linear potential sweep cycling in 1.250 sp gr H_2SO_4 at 60°C after 1000 cycles. Measurement line in the micrograph included for increased understanding.

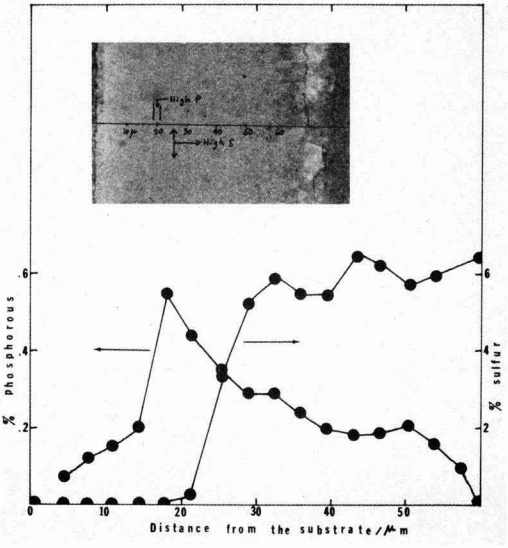


Fig. 16. Electron microprobe profile for sulfur and phosphorus across the lead dioxide layer formed on lead electrode by linear potential sweep cycling in 1.250 sp gr H_2SO_4 with 0.2 w/o H_3PO_4 at 60°C after 1000 cycles. Measurement line in the micrograph included for increased understanding.

REFERENCES

1. J. Burbank, *This Journal*, **104**, 693 (1957); **106**, 369 (1958).
2. P. Ruetschi and R. T. Angstadt, *ibid.*, **111**, 1323 (1964).
3. S. C. Barnes and R. T. Mathieson, in "Batteries 2," D. H. Collins, Editor, p. 41, Pergamon Press, New York (1965).
4. J. P. Carr and N. A. Hampson, *Chem. Rev.*, **72**, 679 (1972).

5. J. J. Lander, *This Journal*, **98**, 213, 220 (1951).
6. D. Marshall and W. Tiedemann, *ibid.*, **123**, 1849 (1976).
7. D. Pavlov and R. Popova, *Electrochim. Acta*, **15**, 1483 (1970); D. Pavlov, *ibid.*, **13**, 2051 (1968); D. Pavlov and N. Iordanov, *This Journal*, **117**, 1103 (1970); D. Pavlov, C. N. Poulieff, E. Klaja, and N. Iordanov, *ibid.*, **116**, 316 (1969).
8. P. Ruetschi, *This Journal*, **120**, 331 (1973).
9. A. C. Simon, *ibid.*, **114**, 1 (1967).
10. J. Burbank, A. C. Simon, and E. Willihnganz, in "Advances in Electrochemistry and Electrochemical Engineering," Vol. 8, P. Delahay and C. W. Tobias, Editors, John Wiley & Sons, Inc., New York (1970).
11. H. S. Panesar, in "Power Sources 3," D. H. Collins, Editor, p. 79, Oriel Press, New Castle upon Tyne (1971).
12. T. G. Chang, M. M. Wright, and E. M. L. Valeriote, in "Power Sources 6," D. H. Collins, Editor, Academic Press, London (1977).
13. T. F. Sharpe, *This Journal*, **122**, 845 (1975); **124**, 168 (1977).
14. J. P. Pohl and H. Rickert, in "Power Sources 5," D. H. Collins, Editor, p. 15, and "Power Sources 6," D. H. Collins, Editor, p. 59, Academic Press, London, New York and San Francisco.
15. H. Bode, "Lead-Acid Batteries," pp. 121-135, John Wiley & Sons, Inc., New York (1977).
16. K. R. Bullock and D. H. McClelland, *This Journal*, **124**, 1478 (1977).
17. J. L. Weininger, *J. Power Sources*, **2**, 241 (1977/1978).
18. A. C. Simon and S. M. Coulder, *This Journal*, **121**, 531 (1974).
19. W. J. Albery and W. Bruckenstein, *Trans. Faraday Soc.*, **62**, 1920 (1966).
20. H. Tamura, H. Yoneyama, C. Iwakura, and O. Ikeda, ILZRO Report on Project LE-254, March 10, 1977.
21. W. Visscher, *J. Power Sources*, **I**, 257 (1977/1978).
22. M. P. J. Brennan, B. N. Stirrup, and N. A. Hampson, *J. Appl. Electrochem.*, **4**, 49 (1974).
23. E. J. Ritchie, "Pastes and Grids for the Lead-Acid Battery," Eagle-Picher Industries, Progress Report No. 2, Combined ILZRO Research Contracts LE-82 and LE-84, December 1967.
24. J. Burbank, *This Journal*, **111**, 1112 (1964).
25. J. Burbank and E. J. Ritchie, *ibid.*, **116**, 125 (1969); **117**, 299 (1970).
26. E. Tudor, A. Weisstuch, and S. H. Dovang, *Electrochem. Technol.*, **4**, 406 (1966).
27. P. Ruetschi and B. D. Cahan, *This Journal*, **104**, 406 (1957); **105**, 369 (1958).
28. R. G. Acton, in "Power Sources," D. H. Collins, Editor, p. 133, Pergamon Press, London (1966).
29. A. C. Simon, S. M. Caulder, and J. T. Stemmle, *This Journal*, **122**, 461 (1975).
30. J. L. Dawson, M. J. Gillibrand, and J. Wilkinson, in "Power Sources 3," D. H. Collins, Editor, pp. 1-11, Pergamon Press (1971).
31. K. R. Bullock, *This Journal*, Submitted for publication.

Mechanism of Intergranular Corrosion and Pitting Corrosion of Austenitic and Duplex 308 Stainless Steel

T. M. Devine*

General Electric Company, Metallurgy Laboratory,
Corporate Research and Development Center, Schenectady, New York 12301

ABSTRACT

The influence of microstructure on the intergranular corrosion and pitting corrosion resistance of 308 stainless steel was studied as a function of the volume percent of ferrite which was varied from 0 to 15%. The all-austenitic matrix was highly susceptible to intergranular corrosion resulting from the formation of nearly continuous chromium-depleted grain boundary paths caused by the intergranular precipitation of chromium-rich $M_{23}C_6$. The presence of a critical amount and distribution of ferrite phase drastically reduced the susceptibility to intergranular corrosion. In addition to carbide precipitation, aging at 600°-700°C resulted in the decomposition of the ferrite phase into a variety of products. First the ferrite phase transformed to cellular $\gamma + M_{23}C_6$, then into single phase γ, single phase σ, and finally into a duplex $\alpha + \gamma$ structure. At 480°C the chromium possessed insufficient mobility to form $M_{23}C_6$. Instead, an extremely small and finely distributed chromium-rich precipitate, termed α', formed throughout the ferrite. From phase diagram measurements it was possible to estimate the chemical compositions and, in particular, the chromium contents of each of the phases formed during the various aging treatments. The changes in the sites of initiation of corrosion attack which accompanied the various phase changes could be satisfactorily explained on the basis of the compositions of the new phases. The phase transformations were followed by transmission electron microscopy and the corrosion attack was viewed with a scanning electron microscope.

Duplex, or two-phase austenitic-ferritic stainless steels have the interesting characteristic of being able to combine the good properties of the austenitic phase with those of the ferrite phase. For example, they have good weldability (1), workability (1, 2), high strength (1, 3, 4), high toughness (1-3), good stress corrosion cracking resistance (5, 6), and are ferromagnetic. In addition, early investigators demonstrated the superior intergranular corrosion resistance of stainless steels containing 20-40 volume percent (v/o) ferrite (7-9). Recent work has confirmed this (10-13). With the exception of these few studies little attention has been given to the effect of heat-treatments and microstructural changes on the corrosion characteristics of two-phase stainless steels. This investigation was undertaken to determine the nature and the extent of the intergranular corrosion and pitting corrosion resistances of duplex stainless steels, using 308 stainless steel as a model. This system was selected because it is the

* Electrochemical Society Active Member.
Key words: carbides, ferrite, microstructure, phase transformation.

most widely used duplex alloy and because of the range of microstructural changes which are possible in this alloy.

Experimental Procedure

The composition of the 308 stainless steel studied is given in Table I. The alloy was obtained in the form of 0.045 in. diam weld wire. The wire was sectioned into various lengths, ultrasonically cleaned in acetone and distilled water, annealed for 1 hr in argon at 1200°, 1250°, 1300°, or 1350°C, and water quenched. Specimens were then heat-treated in argon at 600° and 700°C for times of ¼-100 hr and at 480°C for 10-1000 hr and water quenched. Prior to corrosion testing, specimens were electropolished for 5 min at 2 A/cm^2 in a solution of 60% H_3PO_4 + 40% H_2SO_4 at 40°-60°C.

The specimens were evaluated for localized corrosion resistance in the modified Strauss test (according to ASTM-A262E) (14) and by anodic polarization in deoxygenated 0.1M HCl at room temperature. Specimens for anodic polarization were first electropolished as described above, soldered to an electrical test lead, and ultrasonically cleaned in acetone and distilled water. The soldered joint was masked off from the remainder of the sample with Glyptol® paint. The anodic polarization tests were conducted in a glass polarization cell which contained the specimen and two platinum-mesh counterelectrodes. A Luggin-Haber probe and salt bridge provided a low resistance path between the specimen and a saturated calomel reference electrode located in a separate beaker. The test electrolyte was deoxygenated by bubbling nitrogen through the solution at a rate of 95 cm^3/min for a minimum of 4 hr. Upon immersion in the test solution, the specimen was cathodically polarized to −1400 mV *vs.* SCE for 20 sec and then polarized in the anodic direction at a rate of 1 mV/sec, starting at a potential 100 mV lower than the corrosion potential. This particular cathodic pretreatment provided very reproducible results. Following the anodic polarization tests and the intergranular corrosion tests, the samples were examined for evidence of corrosion by optical microscopy at 250-1200×. Certain samples were further examined by scanning electron microscopy.

Galvanostatic pitting experiments were also performed in 0.1*N* HCl to aid in studying pit initiation. In this test a 1 mA/cm^2 pulse was applied for varying lengths of time while continuously monitoring the potential of the sample. The initiation of pitting was accompanied by an abrupt drop in the potential of the sample. Pit initiation rate was measured by counting the number of pits per unit area following application of a 1 mA/cm^2 anodic current for 5 min. In tests designed to study the site of pit initiation, the galvanostatic current was interrupted as soon as the potential of the specimen dropped. The sample was then immediately removed from the solution and examined in a scanning electron microscope for evidence of pitting.

Transmission electron microscopy experiments were performed on selected specimens. TEM samples were thinned in an electrolyte consisting of 62 ml $HClO_4$ + 100 ml Butylecello-solve + 137 ml H_2O + 700 ml ethyl alcohol. The specimens were examined and micrographs taken by direct electron transmission on the Siemens Elmiskop electron microscope at 125 kV. Additionally, microchemical analyses were performed on certain samples by high resolution x-ray microanalysis using a JEOL 200 keV scanning transmission electron microscope.

Results

Physical metallurgy.—Annealing 308 stainless steel at sufficiently high temperatures introduces ferrite into the microstructure. The amount of ferrite produced increases with increasing anneal temperature. A 1 hr anneal at 1350°C followed by a water quench results in the duplex microstructure depicted in Fig. 1 consisting of approximately 15 v/o ferrite as measured by area fraction. Annealing at lower temperatures produces less and less ferrite until at 1200°C the structure is 100% austenitic as shown in Fig. 2. As indicated in Fig. 1, in addition to the individual grains of ferrite, there are twin-like ferrite regions within austenite grains. The duplex structure exhibits a much finer grain size than the austenitic structure even though it was created at a higher temperature. Apparently the austenite and ferrite phases restrict each other's grain growth.

The fully austenitic structure, obtained by heat-treatment at 1200°C for 1 hr, and water quenched, is supersaturated with interstitial carbon. When aged for 1 hr at 600°C, it remained free of any precipitation. When specimens were heat-treated for 20 hr at 600°C or 1 hr at 700°C, extensive intergranular precipitation occurred as illustrated in the transmission electron micrograph in Fig. 3. The precipitates were too small to unambiguously identify them by selected area electron diffraction. However, the diffraction patterns obtained were consistent with the grain boundary precipitate being chromium-rich $M_{23}C_6$. Longer aging times at 600° and 700°C increased the amount of intergranular precipitate.

Table I. Composition of 308 stainless steel

C	Cr	Ni	Mn	P	S	Si
0.040	20.95	9.82	1.76	0.016	0.008	0.41

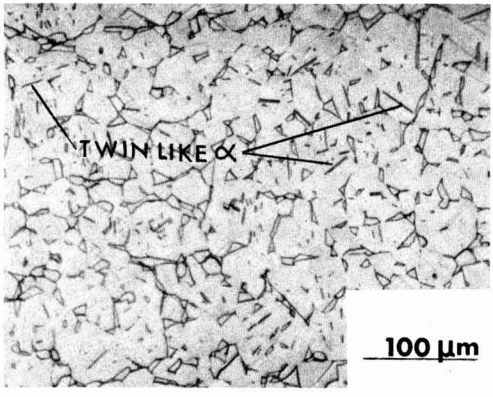


Fig. 1. Optical micrograph of 308 stainless steel heat-treated at 1350°C/1 hr, WQ.

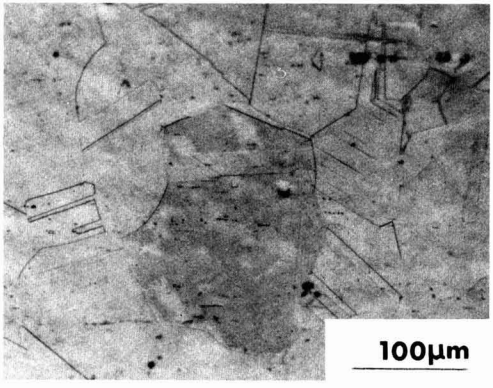


Fig. 2. Optical micrograph of 308 stainless steel heat-treated at 1200°C/1 hr, WQ.

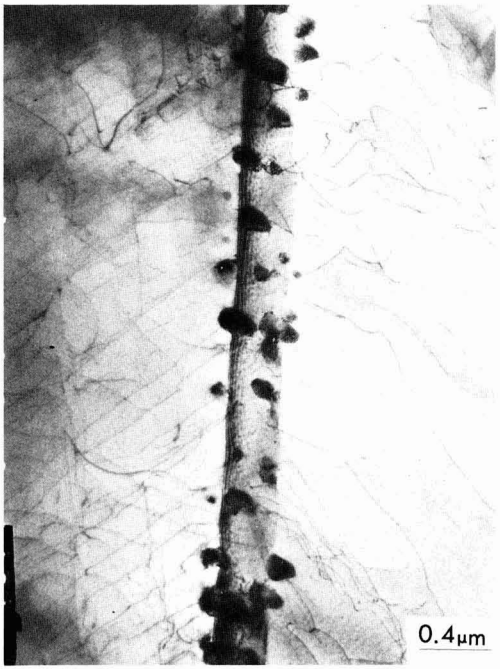


Fig. 3. Transmission electron micrograph of 308 stainless steel heat-treated at 1200°C/1 hr, WQ + 600°C/20 hr, WQ.

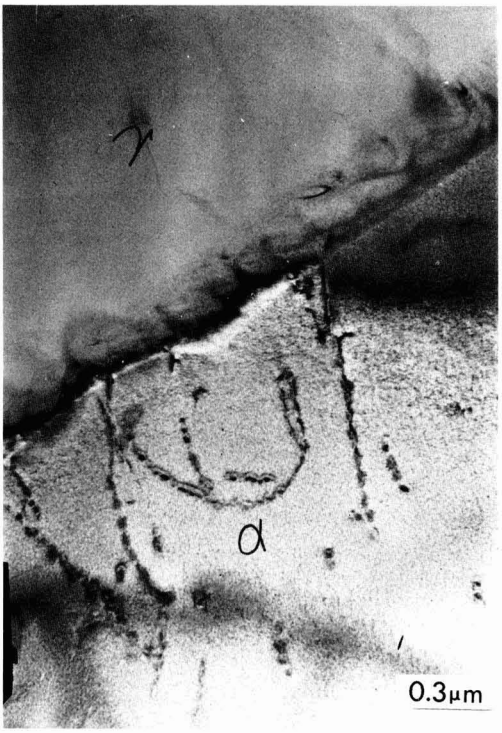


Fig. 4. Transmission electron micrograph of 308 stainless steel heat-treated at 1350°C/1 hr, WQ + 480°C/100 hr, WQ.

Aging the duplex material at 480°C for times up to 1000 hr produced no microstructural changes within the austenite grains. Similarly, no changes could be seen in the ferrite regions of 308 following 10 hr at 480°C. However, after 100 hr at 480°C significant quantities of an extremely fine precipitate could be observed within the ferrite as shown in Fig. 4. Selected area electron diffraction of the α-grains following heat-treatment for 100 and 1000 hr at 480°C indicated the presence of only bcc diffraction spots and only one set of bcc diffraction spots. These observations are consistent with the precipitate being α', a chromium-rich bcc phase whose lattice parameter is nearly identical to that of α.

Precipitation occurred in the duplex 308 stainless steel following extremely brief aging times at 600°C. As short a time as 30 min was sufficient to produce extensive precipitation. In the 8 and 15 v/o ferrite material formed by heat-treating for 1 hr at 1300° and 1350°C, respectively, the precipitation occurred exclusively along austenite-ferrite phase boundaries. In the low volume fraction ferrite material formed by heat-treating for 1 hr at 1250°C precipitation eventually occurred along austenite-austenite grain boundaries as well. Figure 5 depicts the boundary precipitation resulting from a 1 hr age at 600°C of the duplex material formed at 1350°C. The diffraction patterns were consistent with this precipitate being $M_{23}C_6$. The figure illustrates the confinement of the precipitation to the austenite-ferrite phase boundaries. Grain A was identified by selected area electron diffraction as ferrite, grains B and C were identified as austenitic. Microchemical analysis using a 200 keV JEOL scanning transmission microscope indicated the precipitate (carbide) to contain $\simeq$65 weight percent (w/o) chromium, $\simeq$30% iron, and $\simeq$2% nickel. Similar carbide precipitation occurred as a result of aging for less than 1 hr at 700°C. With further aging at 600° and 700°C, carbide precipitation continued, accompanied by decomposition of the ferrite phase. Decomposition of the fer-

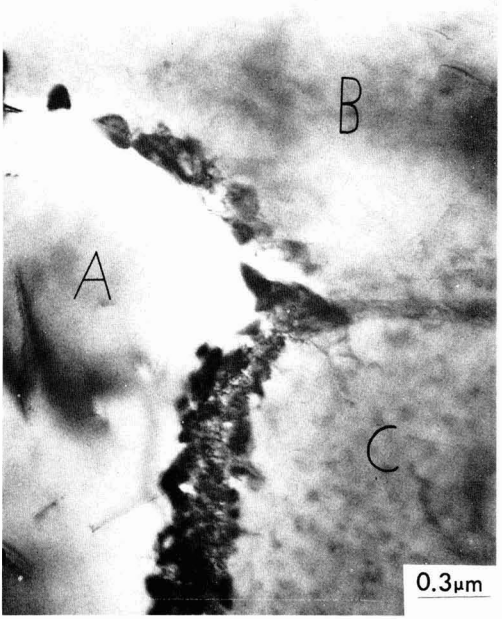


Fig. 5. Transmission electron micrograph of 308 stainless steel heat-treated at 1350°C/1 hr, WQ + 600°C/1 hr, WQ.

rite phase occurred in samples aged for only 2 hr at 600°C. As illustrated in Fig. 6 decomposition of the ferrite phase began as austenite extending into the ferrite region. Dark field microscopy revealed that the new austenite formed epitaxially with the adjacent austenite grain. As indicated in Fig. 7, a region of columnar $M_{23}C_6$ + austenite was gradually formed. The cellular $\gamma + M_{23}C_6$ zone grew deeper into the ferrite phase with continued aging. Eventually, the cellular zone ended and the ferrite decomposed into single phase austenite then into σ-phase and finally into a duplex austenite plus ferrite region as shown in Fig. 8.

Intergranular corrosion.—Figure 9 illustrates the results of A262E testing of the all-austenitic 308 stainless steel, produced by annealing at 1200°C for 1 hr, as a function of time of heat-treatment at 600° and 700°C. The results are similar to those obtained on other austenitic grades of stainless steel such as 304. A line of negative slope can be passed through the data separating the region to the left in which the material is not sensitized from the region to the right in which such heat-treatments will cause sensitization.

The A262E results as a function of heat-treatment obtained for duplex material initially annealed at 1250°C for 1 hr and water quenched were identical to those obtained for the all austenite material presented in Fig. 9. The material contained only 1-2 v/o ferrite and the results indicate that this material was at least as susceptible to intergranular corrosion as the all-austenitic material. Cracking was found along the few austenite-ferrite boundaries but also occurred extensively along the austenite-austenite grain boundaries.

Figure 10 illustrates the effect of aging on the intergranular corrosion susceptibility of the 8 v/o ferrite material. The results were the same for the 15 v/o ferrite material. In contrast to the all-austenitic material and 2 v/o ferrite material, both of which exhibited a large zone of susceptibility to intergranular corrosion, the 8 and 15 v/o ferrite alloys possessed only a small zone of susceptibility to intergranular corrosion. Also of interest is the fact that sensitization occurred quite early, 30 min, at the relatively low temperature of 600°C. The fracture surface following A262E testing

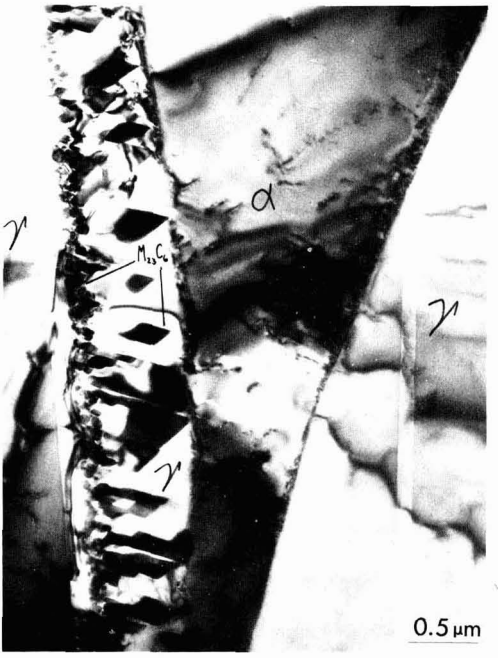


Fig. 7. Transmission electron micrograph of 308 stainless steel heat-treated at 1350°C/1 hr, WQ + 700°C/1 hr, WQ.



Fig. 6. Transmission electron micrograph of 308 stainless steel heat-treated at 1350°C/1 hr, WQ + 600°C/4 hr, WQ.



Fig. 8. Transmission electron micrograph of 308 stainless steel heat-treated at 1350°C/1 hr, WQ + 700°C/100 hr, WQ.

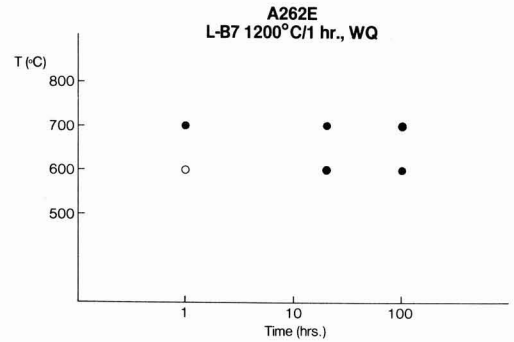


Fig. 9. Effect of aging treatment on the intergranular corrosion behavior of 308 stainless steel annealed at 1200°C/1 hr, WQ, ●, cracking; ○, no cracking.

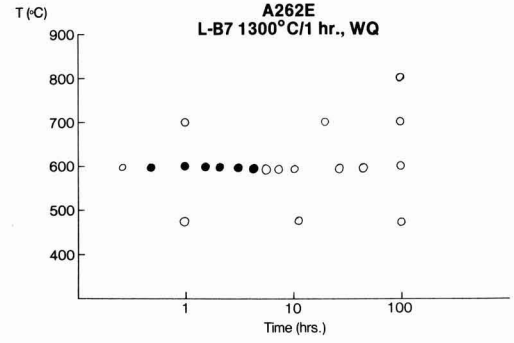


Fig. 10. Effect of aging treatment on the intergranular corrosion behavior of 308 stainless steel annealed at 1300°C/1 hr, WQ. ●, cracking; ○, no cracking.

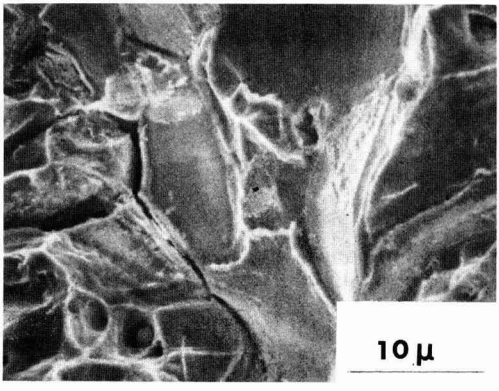


Fig. 11. Fracture surface of 308 stainless steel heat-treated at 1300°C/1 hr, WQ + 600°C/1 hr, WQ and immersed in A262E for 72 hr.

of the specimen aged for 1 hr at 600°C is illustrated in Fig. 11. Areas of grain boundary fracture can be seen. These are the result of localized corrosion along austenite-ferrite phase boundaries. Areas of ductile transgranular cracking are also apparent. These result from fracture of austenite grains and are a consequence of no carbide precipitation along austenite-austenite grain boundaries.

Figure 12 illustrates the fracture surface of the specimen annealed at 1300°C for 1 hr and aged at

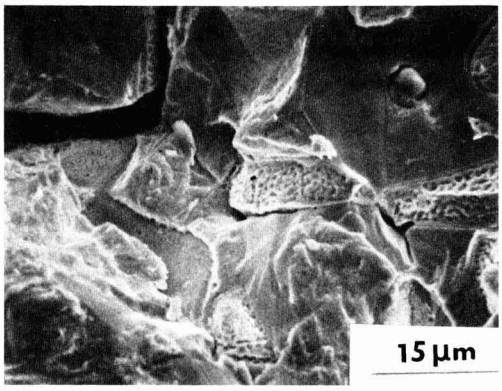


Fig. 12. Fracture surface of 308 stainless steel heat-treated at 1300°C/1hr, WQ + 600°C/5 hr, WQ and immersed in A262E for 72 hr.

600°C for 5 hr. Again, areas of grain boundary fracture and transgranular cracking can be seen. An additional feature is also apparent on this fracture surface and this is the rumpled appearance of the ferrite grains caused by the localized corrosion attack of the $\gamma + M_{23}C_6$ cellular zone. Corrosion attack in the A262E test propagated along the original austenite-ferrite boundary as indicated by the smooth, faceted appearance of the austenite grains on the fracture surface in Fig. 12. This localized attack separated the austenite grains from the $\gamma + M_{23}C_6$ cellular zone. Simultaneously the austenite within the $\gamma + M_{23}C_6$ cellular region was preferentially attacked, causing the irregular surface appearance of the ferrite grains on the fracture surface. Aging at 600°C for times longer than 6 hr results in immunity to intergranular corrosion. Nevertheless localized corrosion attack continues in selected areas of the microstructure. This is illustrated in Fig. 13 which is a scanning electron micrograph of a specimen aged at 600°C for 50 hr and then tested in A262E. The columnar $\gamma + M_{23}C_6$ zone at the original austenite-ferrite interface as well as the austenite formed within the ferrite phase have been preferentially corroded. The penetration of corrosion down the columnar $\gamma + M_{23}C_6$ zone is less than 1 grain diameter.

One rather interesting microstructural characteristic of the aged duplex samples was that carbide precipitation occurred along only 50% of the austenite-ferrite

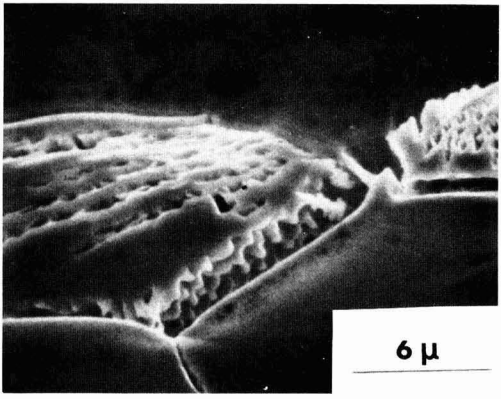


Fig. 13. Scanning electron micrograph of surface of 308 stainless steel heat-treated at 1350°C/1 hr, WQ + 600°C/50 hr, WQ and then tested in A262E.

boundaries. In addition to the ferrite regions which appeared along austenite grain boundaries, there were also ferrite regions within austenite grains. These ferrite regions were twin-like in appearance as shown in Fig. 1. There were no instances of carbide precipitation along these austenite-ferrite boundaries.

Aging the duplex material for up to 1000 hr at 480°C did not result in any intergranular corrosion attack in A262E. Nevertheless, aging for as little as 100 hr at 480°C did result in intense uniform attack of the ferrite grains themselves. Entire grains of ferrite in specimens aged at 480°C for 100 hr were completely dissolved during A262E testing.

Pitting corrosion.—Pitting potentials were obtained by potentiodynamic anodic polarization tests in 0.1*N* HCl using a potential sweep rate of 60 mV/min. The onset of pitting was indicated by an abrupt increase in corrosion rate which occurred above a certain potential. The latter was defined as the pitting potential. Following testing, each sample was carefully examined with the aid of an optical microscope at 250-1200× for evidence of localized corrosion attack. Special attention was paid to determine whether or not crevice corrosion had occurred. Samples which exhibited crevice corrosion were excluded from analysis of pitting behavior.

Table II illustrates the effect of annealing temperature on the pitting potential of 308 stainless steel. Recall that the volume percent ferrite in the alloy varies from 0 to 15% as the annealing temperature increases from 1200° to 1350°C. Regardless of the amount of ferrite present in the alloy, considerable scatter is apparent in the measured values of the pitting potential. Several samples did not pit during testing. These were assigned values of 900 mV. Transpassive behavior was exhibited at potentials above 900 mV. All specimens which pitted, regardless of annealing temperature, exhibited only a very few (~10 pits/cm^2), but large (~300 μm diam) pits. In the duplex material the pits initiated in the ferrite phase at the austenite-ferrite interface.

Regardless of annealing temperature, samples which were aged at 480°C for times of 10-1000 hr exhibited the same pitting propensity as the as-annealed material. Very low pit densities were observed, and similar values of pitting potentials were obtained. Table III illustrates the effect of aging treatment at 600° and 700°C on the pitting potential of 308 stainless steel containing different amounts of ferrite. Several points are apparent in these data. First, the scatter in the data obtained for the aged specimens was much less than that obtained for the as-annealed samples. Second, regardless of annealing temperature the pitting potential obtained on samples aged at 700°C was always greater than that obtained on samples aged at 600°C.

By comparing data in Tables II and III, it is seen that the pitting potentials of the all-austenitic material aged at 700°C were near the lower end of the range obtained for the as-annealed material. The pitting potential of the all-austenitic material decreases as the time of aging at 600°C increases from 1 to 20 hr. In fact, the specimens aged at 600°C for 1 hr behaved exactly like the as-annealed specimens. In both cases, there was a large amount of scatter in the data and the pit density following anodic polarization was very low.

Table II. Effect of annealing temperature on the pitting potential of 308 stainless steel in 0.1*N* HCl

Anneal temperature (°C/hr)	Average value of pitting potential (mV)	Difference between maximum and minimum values
1200/1	526	550
1250/1	602	460
1300/1	485	165
1350/1	418	230

Table III. Effect of aging treatment on the pitting potential of 308 stainless steel in 0.1*N* HCl

Anneal temperature (°C/hr)	Aging treatment (°C/hr)	Average value of pitting potential (mV)	Difference between maximum and minimum value
1200/1	600/1	515	595
	600/20	90	110
	600/100	136	85
	700/1	470	60
	700/20	308	15
	700/100	365	30
1250/1	600/1	240	20
	600/20	−85	10
	600/100	−125	70
	700/1	402	35
	700/20	230	24
	700/100	250	80
1300/1	600/1	195	30
	600/100	230	40
	700/1	312	35
	700/20	318	180
	700/100	284	120
1350/1	600/1	217	20
	600/10	204	16
	600/20	202	15
	600/50	295	15
	600/100	268	40
	700/1	395	20
	700/10	355	40
	700/20	362	30
	700/100	340	50

For all other aging conditions, the pits were much smaller (~20 μm diam) and the pit density was much higher (~ 10^3/cm^2) than was obtained for the as-annealed material. This was also the case for the three duplex conditions studied, namely, the pit density following anodic polarization of aged material was much greater than that obtained for the as-annealed material.

Table III indicates that the pitting potential of the low volume fraction ferrite duplex alloy formed by annealing at 1250°C for 1 hr, and water quenched (WQ), was a strong function of aging time. The pitting potential obtained by aging at either 700° or 600°C decreased as the aging time increased from 1 to 20 hr, and after 20 and 100 hr was much lower than those measured for any aging treatment of the other duplex alloys and for the all-austenitic material as well.

For the 8 and 15 v/o ferrite duplex material, in contrast to the results obtained for the all-austenitic material and the 2 v/o ferrite duplex material, the pitting potential of specimens aged at 600°C remains relatively unchanged as the aging time increases from 1 to 20 hr. The pitting potential of the 15 v/o ferrite duplex alloy increased abruptly as the aging time at 600°C increased from 20 to 50 hr.

Although the pitting potential appeared to be sensitive to aging treatment, the most dramatic change in pitting behavior during anodic polarization affected by aging was the change in pit density. To study this effect more closely, galvanostatic pitting experiments were conducted to measure pit initiation rate and to determine the site of pit initiation as a function of aging treatment. The onset of pitting was signaled by a precipitous drop of ~ 1V in the potential of the sample.

A 5 min application of a 1 mA/cm^2 pulse in 0.1*N* HCl to the as-annealed austenitic and duplex conditions of 308 stainless steel did not result in pit initiation. Similarly, no pits were initiated in specimens aged at 480°C for times up to 1000 hr. Aging at higher temperatures, however, had a dramatic effect on pitting behavior.

Figure 14 illustrates the effect of aging at 600°C on the pit initiation rate of all-austenitic 308 stainless steel. Specimens aged for 1 hr at 600°C exhibited the same behavior as the as-annealed material and were free of pits following testing. Aging for 20 or more hours at 600°C, however, resulted in a drastic increase in pitting. As depicted in Fig. 15, the pits initiated at the grain boundaries. The pits propagated rapidly down the grain boundaries resulting in grain drop-

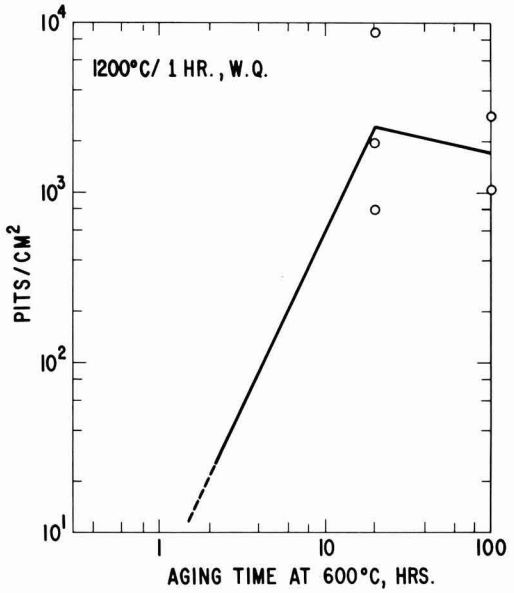


Fig. 14. Influence of aging treatment on the pit initiation rate in 0.1*N* HCl of 308 stainless steel annealed at 1200°C/1 hr, WQ.

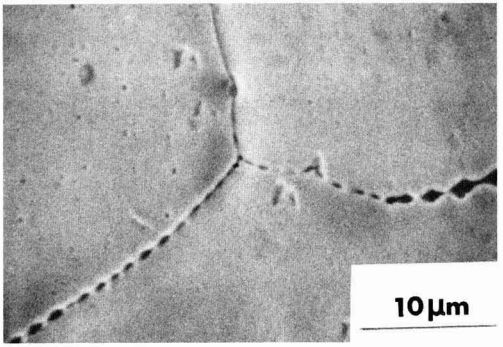


Fig. 15. Pit initiation at grain boundaries in sample of 308 stainless steel heat-treated at 1200°C/1 hr, WQ + 600°C/20 hr, WQ and galvanostatically corroded at 1 mA/cm² for 3 sec.

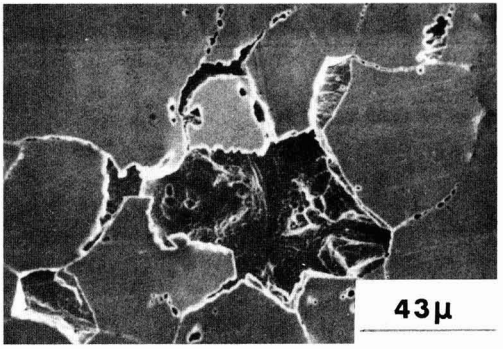


Fig. 16. Appearance of sample of 308 stainless steel heat-treated at 1200°C/1 hr, WQ + 600°C/20 hr, WQ and galvanostatically corroded at 1 mA/cm² for 5 min.

ping as shown in Fig. 16. Aging for 100 hr at 600°C resulted in similar behavior. Pits initiated at grain boundaries and propagated down grain boundaries as well as into the grain interiors.

Figure 17 summarizes the effect of aging time at 600°C on the 8 and 15 v/o ferrite duplex 308 stainless steel. In contrast to the all-austenitic material, the pit initiation rate was very high at very short aging times and decreased somewhat abruptly after aging for 8-10 hr. Whereas the pit initiation site for the all-austenitic material remained constant with aging time, namely, along the grain boundaries, the pit initiation site of the duplex alloys was a strong function of aging time. Aging for ¼-2 hr at 600°C resulted in pits initiating in the austenite phase at the austenite-ferrite interface, as shown in Fig. 18. Aging for 3 hr or more resulted in the decomposition of the ferrite phase into lamellar $\gamma + M_{23}C_6$, beginning at the austenite-ferrite interface. It was not possible to unambiguously identify the precise site of pit initiation in samples aged for 3-10 hr at 600°C. The lamellar $\gamma + M_{23}C_6$ zone was so small in these instances and the pit propagation rate so rapid that pits had grown in the austenite phase at the austenite-ferrite interface as well as in the austenite phase in the two-phase lamellar $\gamma + M_{23}C_6$ region, as

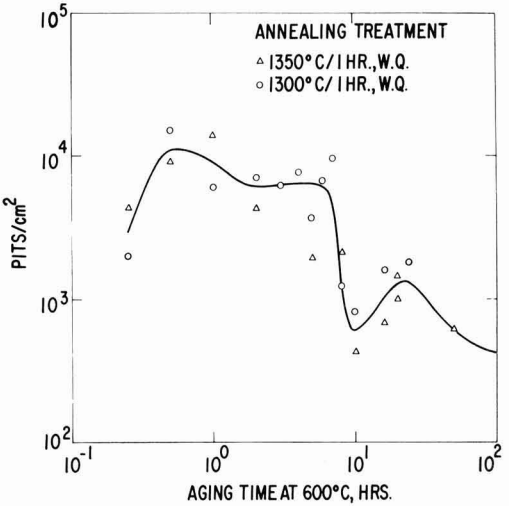


Fig. 17. Influence of aging time at 600°C on the pit initiation rate in 0.1*N* HCl of 308 stainless steel annealed at 1300°C/1 hr, WQ and 1350°C/1 hr, WQ.

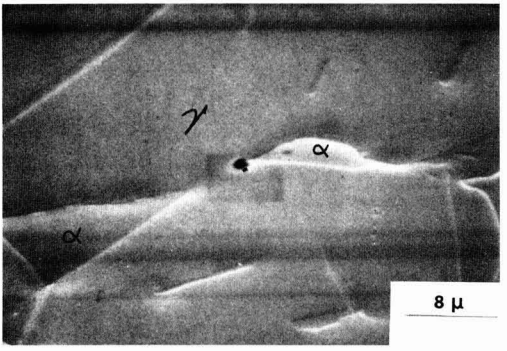


Fig. 18. Pit initiation in austenite at austenite-ferrite boundaries in sample of 308 stainless steel heat-treated at 1350°C/1 hr, WQ + 600°C/1 hr, WQ.

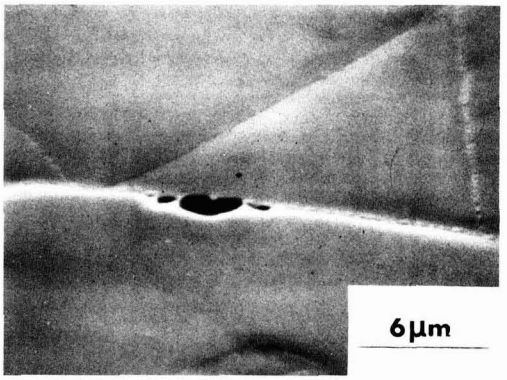


Fig. 19. Pit initiation at austenite-ferrite boundaries in sample of 308 stainless steel heat-treated at 1350°C/1 hr, WQ + 600°C/5 hr, WQ.

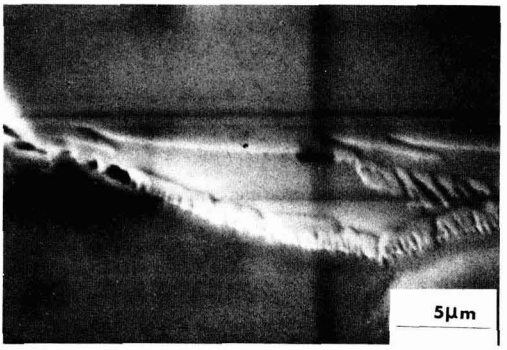


Fig. 20. Pit initiation in austenite phase in cellular $\gamma + M_{23}C_6$ zone in sample of 308 stainless steel heat-treated at 1350°C/1 hr WQ + 700°C/1 hr, WQ.

shown in Fig. 19. Consequently, the pits either initiated in the austenite phase at the original austenite-ferrite interface and then propagated into the austenite phase in the two-phase $\gamma + M_{23}C_6$ region, or vice versa. With longer aging times the ferrite continued to decompose and the lamellar $\gamma + M_{23}C_6$ region was easily distinguishable. Here, as shown in Fig. 20, pits could clearly be seen initiating in the $\gamma + M_{23}C_6$ region. As detailed in the Physical Metallurgy section, the ferrite phase decomposed sequentially into columnar $\gamma + M_{23}C_6$, single phase austenite, followed by single phase σ, and finally into duplex austenite plus ferrite. The final stages of the decomposition into σ and $\alpha + \gamma$ began after approximately 50 hr at 600°C. Pits initiated in these specimens in the two phase $\gamma + M_{23}C_6$ region and propagated into the austenite phase leaving the remaining ferrite phase unattacked as was the case for specimens aged for greater than ~10 hr. Approximately 50% of the pits formed in specimens aged for 100 hr at 600°C also initiated in the $\gamma + M_{23}C_6$ region. The remainder initiated in the newly formed duplex $\alpha + \gamma$ region and propagated through the entire, former all-ferrite region.

The pit initiation rate as a function of aging time at 600°C for the 2 v/o ferrite duplex 308 stainless steel is presented in Fig. 21. Pits initiated preferentially at the austenite-ferrite interface after a 1 hr age and within the $\gamma + M_{23}C_6$ region after 20 hr. In the latter aging conditions pits also eventually formed along austenite-austenite grain boundaries.

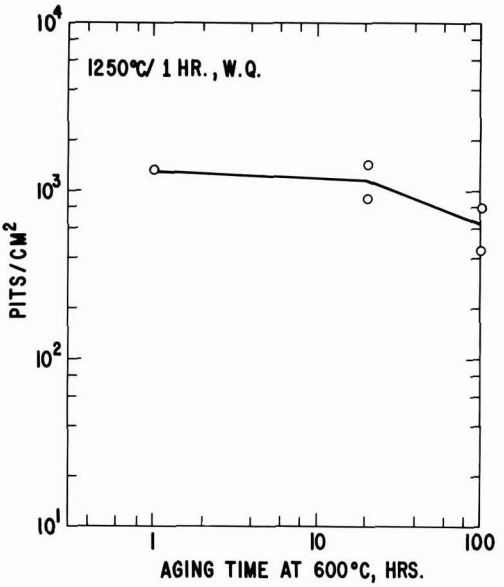


Fig. 21. Influence of aging time at 600°C on the pit initiation rate in 0.1*N* HCl of 308 stainless steel annealed at 1250°C/1 hr, WQ.

Discussion

Physical metallurgy.—From the high temperature annealing experiments it is clear that the equilibrium structure of the matrix phase of 308 stainless steel is austenitic below 1200°C. At higher temperatures increasing amounts of ferrite are stable. From available phase diagrams, the equilibrium structure of 308 stainless steel at 600°-700°C is $\gamma + M_{23}C_6$ (15). Consequently, if the duplex structures were aged for sufficiently long periods of time at these temperatures, they would eventually transform into the equilibrium $\gamma + M_{23}C_6$ structure. The composition of the ferrite phase obtained from microprobe measurements is such that its equilibrium structure at 600°C consists of α, γ, $M_{23}C_6$, and σ as shown in the phase diagram in Fig. 22. Although the bulk alloy composition dictates an equilibrium structure of $\gamma + M_{23}C_6$, the ferrite phase first decomposes to a metastable structure of α, γ, $M_{23}C_6$, and σ.

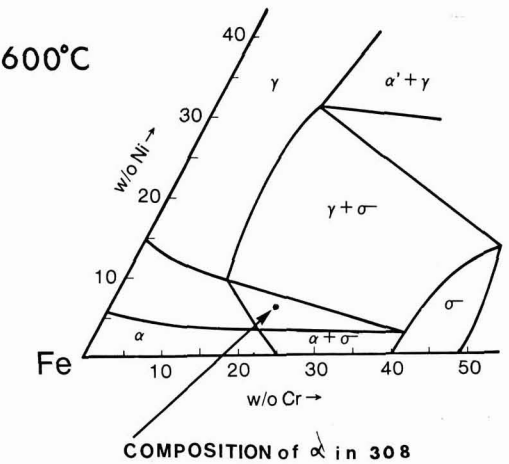


Fig. 22. Section of Fe-Ni-Cr ternary diagram at 600°C

The decomposition of the ferrite phase is accelerated by its chromium depletion caused by the early precipitation of $M_{23}C_6$ along the austenite-ferrite boundaries. In the 8 and 15 v/o ferrite duplex stainless steel, $M_{23}C_6$ precipitation occurs exclusively along the austenite-ferrite boundaries. The austenite-austenite grain boundaries were free of $M_{23}C_6$ precipitation. This results because chromium diffusion is the rate-controlling step in the precipitation reaction. Since the diffusivity of chromium in the ferrite phase is approximately 1000 times greater than in the austenite at 600°C (16) $M_{23}C_6$ forms first along austenite-ferrite boundaries (there are no ferrite-ferrite boundaries as each ferrite region is a single grain) probably by both chromium and carbon diffusing from the ferrite. The available carbon content of the ferrite is quickly exhausted and subsequent carbon comes almost exclusively from the austenite. This depletes the austenite of carbon. The feasibility of carbon depletion of the austenite is demonstrated by the fact that carbon in austenite at 600°C has a characteristic 1.2 hr diffusion distance of 35 μm, which is the average grain size. Thus, the austenite-austenite grain boundaries are free of $M_{23}C_6$ precipitation. The chromium and iron in the $M_{23}C_6$ precipitate is supplied principally by the ferrite phase. The decomposition of the ferrite phase initiates at the γ-$M_{23}C_6$-α interface since this ferrite is the most unstable because of its low chromium content as it lies in the chromium-depleted zone produced by the $M_{23}C_6$ precipitate. The α decomposes to cellular $M_{23}C_6 + \gamma$. This is because chromium diffusion (probably in the austenite phase) is the rate-determining step in the transformation. Consequently, the over-all reaction rate is speeded up by shortening the chromium diffusion distance and enhancing boundary diffusion. This is achieved by cellular precipitation of the $M_{23}C_6$ and austenite. From the phase diagram in Fig. 22, we can estimate the maximum chromium content of the austenite phase in the cellular $\gamma + M_{23}C_6$ product to be approximately 14 w/o chromium. This is the chromium content of the austenite phase in the three phase $\gamma + \alpha + \sigma$ region of the Fe-Ni-Cr ternary diagram at 600°C depicted in Fig. 22. It should also be the maximum amount of chromium which can be dissolved in the austenite phase in the three phase $\alpha + \gamma + M_{23}C_6$ region of the Fe-Cr-Ni-C quarternary since the solubility of carbon in γ is so low at 600°C. Consequently, the austenite phase in the $\gamma + M_{23}C_6$ cellular product has a rather low chromium content.

The initial decomposition of the ferrite phase into cellular $\gamma + M_{23}C_6$ is halted when the available carbon content of the ferrite phase is exhausted. Subsequent decomposition of the ferrite phase occurs by direct transformation into austenite. The latter transformation occurs with a significant amount of chromium rejection into the remaining untransformed ferrite so that an abrupt drop-off in chromium concentration occurs at the ferrite-austenite interface. The chromium-enriched ferrite phase at the austenite-ferrite interface then transforms to σ, containing approximately 40 w/o chromium and 4 w/o nickel (14). The remaining ferrite phase transforms to duplex $\alpha + \gamma$. From the Fe-Ni-Cr ternary diagram in Fig. 22, this γ phase contains at most 14 w/o chromium.

The lack of carbide precipitation along many of the austenite-ferrite boundaries in the duplex material is quite interesting (Fig. 7). The fact that carbide precipitation was never observed along the austenite-ferrite interface formed between the austenite matrix and the intergranular, twin-like ferrite regions leads one to speculate that all austenite-ferrite boundaries which are free of carbide precipitation are low energy boundaries. If indeed carbide precipitation is confined to high energy austenite-ferrite boundaries then one explanation for the phenomenon would be that nucleation occurs along high energy boundaries so as to minimize strain-energy in the lattice and/or precipitate.

At 480°C chromium has insufficient mobility for $M_{23}C_6$ to form. Instead aging at 480°C results in the ferrite phase transforming to a metastable structure of $\alpha + \alpha'$. The latter is a chromium-rich bcc phase which is responsible for the embrittlement of ferritic stainless steels aged at this temperature (17). α' may form by either a nucleation and growth process or by spinodal decomposition (18, 19). From the transmission electron microscopy, the α' precipitates appear to be approximately 30Å in diameter and spaced approximately 50Å apart. No effort was made in this program to determine the composition of α'. Other investigators have estimated the composition of α' to be around 70% chromium (20).

Intergranular corrosion.—The A262E results obtained on the all-austenitic 308 stainless steel are quite consistent with those results reported for other grades of austenitic stainless steel such as 304. The cause of intergranular corrosion is no doubt the same as that in 304, namely, the presence of chromium-depleted zones lying along grain boundaries caused by the intergranular precipitation of $M_{23}C_6$ (21). This is consistent with the transmission electron microscopy results which indicated a one-to-one correspondence between the presence of intergranular precipitation and intergranular corrosion susceptibility.

Observing the effect of heat-treatment on the intergranular corrosion resistance in A262E of the 8 and 15 v/o ferrite-containing duplex material produced by heat-treating at 1300°C for 1 hr and 1350°C for 1 hr, respectively, and WQ, there are three principal questions to be answered. First, why does sensitization occur so readily during short time anneals at low temperatures, *e.g.*, 600°C for ½ hr. Second, why does intergranular corrosion occur exclusively along austenite-ferrite boundaries. And third, what mechanism is responsible for the immunity of duplex stainless steel to intergranular corrosion following longer time ages at 600°C, *i.e.*, greater than 6 hr?

As discussed in the Physical Metallurgy section $M_{23}C_6$ precipitation occurs exclusively along the α-γ boundaries in the 8 and 15 v/o ferrite duplex stainless steels. Since the austenite-austenite grain boundaries are free of $M_{23}C_6$ precipitates and their accompanying chromium-depleted zones, the austenite-austenite grain boundaries are immune to intergranular corrosion. Although the chromium in the $M_{23}C_6$ precipitates is supplied principally by the ferrite phase, a small but significant amount of chromium is contributed by the austenite phase. In fact, the small amount of chromium contributed by the austenite phase creates a small (in width) chromium-depleted zone in the austenite at the original austenite-ferrite interface. Although the chromium-depleted zone in the austenite phase is very narrow, the amount of chromium in the austenite at the austenite-$M_{23}C_6$ interface is less than that in the ferrite at the ferrite-$M_{23}C_6$ interface and it is the narrow chromium-depleted zone in the austenite phase that causes intergranular corrosion along the austenite-ferrite boundaries in A262E. This is indicated by the pitting corrosion experiments in which pits always initiated in the austenite at the austenite-ferrite interface in material which was susceptible to intergranular corrosion. That the pits initiated on the austenite side of the interface indicates that this region possessed the lowest chromium content.

The aging times at 600° and 700°C which result in the decomposition of the ferrite phase into cellular $\gamma + M_{23}C_6$ nearly coincide with the aging treatments which confer immunity to intergranular corrosion on the alloy. However, the separation of the $M_{23}C_6$ carbides from the α-γ interface which occurs during the decomposition of the ferrite phase is not responsible for the immunity of the alloy to intergranular corrosion. Indeed, the decomposition of the ferrite into

cellular $\gamma + M_{23}C_6$ occurs after aging at 600°C for times greater than 4 hr while intergranular corrosion attack continues with aging times up to 6 hr. The smooth, featureless appearance of the austenite grains on the fracture surface of the specimen aged at 600°C for 6 hr indicates that the corrosion attack, even in the samples in which the ferrite has begun to decompose, occurs within the austenite phase along the original austenite-ferrite interface. Were the corrosion attack occurring along the cellular $\gamma + M_{23}C_6/\alpha$ interface, for example, the austenite grain boundary surface would not be smooth but would show some indication of the presence of the cellular $\gamma + M_{23}C_6$. The ferrite grain boundary surface is highly rumpled because of the localized corrosion attack of the austenite phase in the cellular $\gamma + M_{23}C_6$ zone. The latter occurs because of the low chromium content of the austenite phase ($\lesssim$14% Cr from the above calculation) in the cellular $\gamma + M_{23}C_6$. Immunity to intergranular corrosion occurs when the small chromium-depleted zone in the austenite phase at the original austenite-ferrite interface, is replenished with a critical amount of chromium required to restore the corrosion resistance of the area. This healing of the chromium-depleted zone in such a short time ($\sim$7 hr) is made possible by virtue of the unusually small width of the zone. The zone is narrow because the carbon content of the austenite phase was exhausted before sufficient time was permitted for chromium diffusion in the austenite phase to result in any significant loss of chromium. The bulk of the carbon was tied up as $M_{23}C_6$ by chromium supplied from the ferrite phase. Only a small amount of chromium from the austenite reacted with carbon to form $M_{23}C_6$. Consequently, it was relatively easy for subsequent chromium diffusion in the austenite to replenish the small chromium-depleted zone. It is worth emphasizing that the small austenitic chromium-depleted zone was healed by chromium coming from the interior of the austenite grain and not by chromium coming from the decomposing chromium-rich ferrite phase. The latter is true since pit initiation studies on material heat-treated for times longer than 6 hr at 600°C revealed that pits initiated preferentially in the austenite phase in the cellular $\gamma + M_{23}C_6$ zone. If healing was accomplished by chromium coming from the ferrite phase, such chromium would first heal the low chromium austenite in the cellular $\gamma + M_{23}C_6$ zone.

The 2 v/o ferrite duplex 308 stainless steel exhibited essentially the same intergranular corrosion behavior as the all-austenitic material. There was insufficient austenite-ferrite boundary area to tie up all of the available carbon as $M_{23}C_6$ along austenite-ferrite boundaries. Intergranular carbide precipitation occurred along austenite-austenite grain boundaries which resulted in chromium depletion and susceptibility of these boundaries to localized attack in A262E. This result emphasizes the need for a critical amount and distribution of ferrite throughout the austenite matrix in order that the carbon in the austenite be within easy access of an α-γ boundary so that the carbon supply of the austenite can be quickly exhausted by reacting with chromium and iron in the ferrite to form $M_{23}C_6$ along α-γ boundaries.

The accelerated, uniform dissolution of the ferrite phase, which occurs in duplex samples heat-treated for 100 hr or more at 480°C and immersed in A262E is the result of α' precipitation. The formation of this chromium-rich precipitate results in chromium depletion of the matrix. Sufficient chromium depletion has occurred to prevent passivation in the A262E test solution. It is interesting to note that the formation of α' did not result in enhanced susceptibility to pitting corrosion as samples heat-treated at 480°C were as resistant to pitting attack as the fully annealed specimens. Apparently chromium depletion has a greater effect on passivation tendencies (as is measured in A262E) than on passivation breakdown (as is measured by pitting tests).

Pitting corrosion.—Previous investigators have demonstrated the enhanced pitting corrosion resistance accompanying increased chromium additions to ferrous base alloys (22). Consequently, lowering the chromium content in an area by, for example, a phase transformation should increase the pitting susceptibility of that region. In fact, Rarey and Aronson have already demonstrated the enhanced pitting susceptibility of a ferritic stainless steel following the formation of chromium-depleted zones adjacent to carbide precipitates (23). Given the phase transformations which occur in austenitic and duplex 308 stainless steel during aging at 480°C-700°C, marked changes in pitting resistance should result from such heat-treatments. And, in fact, this is what the pitting potential and pit initiation results reported in this study have shown.

The galvanostatic pit initiation tests were by far the most sensitive to aging treatments. Both the site of pitting and the pit initiation rate varied strongly with the aging temperature and time. While a significant difference existed between the pitting potentials of the annealed and aged materials and between the pitting potentials of samples aged at different temperatures, there was little effect of aging time on the pitting potential. Furthermore, the large scatter in the measured values of the pitting potential of the as-annealed material requires that many measurements of the pitting potential be made in order to confirm the presence of a sensitized microstructure.

The poor reproducibility in the pitting potentials measured for the as-annealed conditions probably results from the lack of reproducibility in the pit initiation site. Pitting probably initiates in the as-annealed material at highly soluble inclusions such as manganese sulfides as was shown by Eklund for 316 stainless steel (24). The inclusions dissolve out and the aggressive solution produced, which now fills the void once occupied by the inclusion, results in propagation of the corrosion attack into the metal matrix. Samples in which pitting did not occur during anodic polarization were probably free of such inclusions. The lack of reproducibility in the size and shape of such inclusions probably contributes to the scatter in the pitting potentials.

In the as-annealed duplex material pits appear to initiate preferentially in the ferrite at the austenite-ferrite interface. This may be the result of a high concentration of sulfur at the interface or a high density of sulfides along the interface. This results from the sulfur preferentially partitioning into the ferrite phase during the high temperature anneal due to the lower activity coefficient of sulfur in ferrite than in austenite (activity coefficient of sulfur in austenite is 4 times that in ferrite at 1365°C) (25). During quenching, sulfur in the ferrite phase segregates to the austenite-ferrite interface or sulfides precipitate out of the supersaturated ferrite phase along the austenite-ferrite boundary.

Aging austenitic and duplex specimens of 308 stainless steel at 600° and 700°C resulted in a marked decrease in the scatter of the measured values of the pitting potential as well as a decrease in its numerical value. In addition, the pit density was orders of magnitude greater in aged samples than in as-annealed samples. In fact, by far the most dramatic influence of aging treatment on the pitting behavior was the drastic increase in pit density as a result of aging. The influence of aging treatment on pit density was more closely examined by means of the galvanostatic pit test.

Streicher (26) has shown that the number of pits is not a function of the potential of the sample but rather is a function of the corrosion current density. The relative pit initiation rates of different materials, therefore, can be determined by galvanostatically corroding sam-

ples at a relatively high anodic current density for a specified length of time. As in the anodic polarization test a dramatic increase in pit density was observed in the galvanostatic pit test as a result of aging. The galvanostatic pitting test was evidently a less aggressive test than the anodic polarization test. In the former, pitting never occurred in as-annealed samples whereas pits usually formed during the latter test, albeit only a very low pit density was exhibited.

Aging the all-austenitic 308 stainless steel at 600°C for 1 hr did not result in any increase in pitting susceptibility. No pitting occurred during the galvanostatic corrosion test. This behavior was exactly the same as that of the as-annealed material. This is similar to the pitting potential measurements in which the behavior of the as-annealed material and that aged for 1 hr at 600°C was the same, namely, relatively high values of pitting potential, relatively large scatter in the measured values of the pitting potential, and very low pit density following anodic polarization. These results are consistent with the transmission electron microscopy which revealed no intergranular precipitation and with the A262E findings which indicated heat-treating for 1 hr at 600°C did not cause intergranular corrosion.

Increasing the aging time at 600°C to 20 hr dramatically increased the pit initiation rate to $\sim 10^4$ pits/cm^2 as measured by the galvanostatic pit corrosion test. By interrupting the applied current immediately after pitting began the first pits were seen to initiate in the grain boundaries. Undoubtedly these pits were forming in the chromium-depleted zones adjacent to the intergranular precipitates of $M_{23}C_6$. Similar behavior was observed for the samples aged for 100 hr at 600°C and for samples aged even for as little as 1 hr at 700°C. The pits propagated rapidly down the chromium-depleted grain boundaries resulting in grain dropping as shown in Fig. 16. These results are again consistent with the A262E results which indicated aging at 600°C for 20 hr or longer and at 700°C for more than 1 hr resulted in severe intergranlar corrosion attack. Several points are of interest in the pitting potentials measured on samples aged for any time at 700°C and for 20 hr or more at 600°C. First, the amount of scatter in the pitting potentials measured for these aged conditions is much less than that obtained for the as-annealed condition. Second, the value of the pitting potential is lower for these aged conditions than for the as-annealed condition. And, finally, the pitting potential of material aged at 700°C is greater than that of material aged at 600°C. Since the pitting potential is a measure of the resistance of the passive film to initiation of breakdown, the lower pitting potential resulting from aging is due to the chromium-depleted zones formed adjacent to the intergranular carbides which are more susceptible to pitting than is the matrix. The latter, in fact, is presumably strongly resistant to pitting with pits actually forming at inclusions and then growing (by a crevice corrosion-type mechanism) into the matrix. The pitting potentials of the aged conditions are more reproducible than those for the as-annealed conditions because the pit initiation site of the aged material, namely, the chromium-depleted zone, is a more reproducible defect than the pit initiation site of the as-annealed material. That the pitting potentials measured on samples aged at 700°C are greater than those measured for samples aged for 20 hr or more at 600°C is as predicted from thermodynamic considerations (10). Due to the temperature dependencies of the carbon and chromium activities as well as to the equilibrium constant for the formation of $M_{23}C_6$, the chromium content in the matrix at the precipitate matrix interface is lower during precipitation at 600°C than at 700°C. The lower chromium content results in greater pitting susceptibility and a lower pitting potential (22).

As the aging time at 600°C increased from 30 min to 10 hr the narrow chromium-depleted zone in the austenite at the austenite-ferrite interface in the 8 and 15 v/o ferrite alloys was replenished with chromium and the site of pit initiation shifted to the austenite region within the two-phase columnar $\gamma + M_{23}C_6$ zone. This austenite region is susceptible to pitting since its chromium level is less than 14 w/o as discussed in the previous section (Fig. 22). With longer aging times the remaining ferrite phase began to transform to σ-phase and to duplex austenite plus ferrite. Corresponding to this microstructural change, the pit initiation site shifted from the columnar $\gamma + M_{23}C_6$ zone to within the austenite phase in the duplex austenite plus ferrite region formed in the transformed ferrite.

The pitting potential of the 15 v/o ferrite duplex material increased by $\simeq$90 mV as the aging time at 600°C increased from 20 to 50 hr. Other than this no changes in pitting potential of the duplex material were observed to accompany the major microstructural changes which were occurring. Consequently, the pitting potential is an inadequate parameter to study the microstructural changes which occur during aging at 600° and 700°C.

In addition to the pitting which occurred at the austenite-ferrite interface and within the transformed ferrite phase of aged samples, pits also initiated at austenite-austenite grain boundaries in the 308 stainless steel containing only 2 v/o ferrite. These pits apparently initiated in the chromium-depleted zones adjacent to $M_{23}C_6$ carbides which formed along austenite-austenite grain boundaries as well as along austenite-ferrite boundaries in the 2 v/o ferrite duplex material.

Summary

Annealing 308 stainless steel at temperatures greater than 1200°C results in the introduction of ferrite into the austenitic matrix. The amount of ferrite formed increases with the temperature. At 1350°C 15 v/o ferrite is formed. Below 1200°C the matrix structure is 100% austenitic. Annealing at 1200°C and water quenching produces a 100% austenitic structure supersaturated with carbon. Aging this material at an intermediate temperature of 600°C results in the intergranular precipitation of chromium-rich $M_{23}C_6$. A chromium-depleted zone is formed adjacent to the intergranular precipitate which results in susceptibility to intergranular corrosion attack in boiling acidified copper-copper sulfate solution (A262E) and grain boundary pitting in 0.1*N* HCl.

Whereas $M_{23}C_6$ precipitation occurs intergranularly during aging of austenitic 308 stainless steel, $M_{23}C_6$ precipitation is exclusively confined to austenite-ferrite boundaries in duplex 308 stainless steel containing a critical amount and distribution of ferrite. In such structures, because most of the chromium in the carbide comes from the ferrite phase and only a very small amount comes from the austenite phase, a chromium-depleted zone is formed within the austenite phase at the austenite-carbide interface which is susceptible to localized corrosion attack but which is very narrow compared to that which exists in sensitized austenitic stainless steel. Continued aging for only 7 hr at 600°C replenishes the narrow chromium-depleted zone so that it is no longer susceptible to corrosion attack in the A262E test. Similar healing of the much wider chromium-depleted zone formed in fully austenitic 308 stainless steel does not occur even after 100 hr at 600°C.

In addition to the precipitation of $M_{23}C_6$ along austenite-ferrite boundaries, aging at 600°C results in decomposition of the ferrite phase into cellular $\gamma + M_{23}C_6$, single-phase austenite, σ-phase, and duplex austenite plus ferrite. The corrosion behavior of these new phases is consistent with their chemical compositions as estimated from phase diagrams.

When duplex 308 stainless steel is aged at 480°C an extremely fine chromium-rich precipitate, α', forms throughout the ferrite. The chromium depletion of the ferrite phase resulting from the α' precipitation causes corrosion of the ferrite regions in A262E test.

Two major points are made by this research. First, the corrosion behavior of 308 duplex stainless steel is a very strong function of the microstructure. Second, the presence of a critical amount and distribution of ferrite can dramatically restrict the intergranular corrosion susceptibility of austenitic stainless steel.

Acknowledgments

It is a pleasure to thank the following people for their skilled contributions to this research. Miss B. J. Drummond conducted the intergranular corrosion and anodic polarization tests. Miss A. Ritter performed the transmission electron microscopy. Many helpful discussions were conducted with Drs. M. G. Benz, M. R. Jackson. and H. D. Solomon. Drs. A. J. Gianuzzi and R. Proebstle reviewed the manuscript. Financial support for this research was provided in part by the Electric Power Research Institute.

Manuscript submitted May 15, 1978; revised manuscript received Oct. 16, 1978.

Any discussion of this paper will appear in a Discussion Section to be published in the December 1979 JOURNAL. All discussions for the December 1979 Discussion Section should be submitted by Aug. 1, 1979.

Publication costs of this article were assisted by General Electric Company.

REFERENCES

1. R. C. Gibson, H. W. Hayden, and J. H. Brophy, *Trans. ASM*, **61**, 85 (1968).
2. H. F. Merrick, H. W. Hayden, and R. C. Gibson, *Metall. Trans.*, **4**, 827 (1973).
3. H. W. Hayden and S. Floreen, *Trans. ASM*, **61**, 489 (1968).
4. S. Floreen and H. W. Hayden, *ibid.*, **61**, 489 (1968).
5. D. A. Vermilyea, *Corrosion*, **31**, 421 (1975).
6. G. Ito, T. Ishihara, and Y. Shimizu, in Proceedings of the 4th International Conference on Corrosion, Tokyo, p. 75 (1971).
7. P. Payson, *Trans. AIME*, **100**, 306 (1932).
8. L. B. Pfeil and D. G. Jones, *J. Iron Steel Inst. London*, 337 (1933).
9. V. R. Scherer, G. Riedrich, and G. Hoch, *Archiv. Eisenhüttenwes.*, 1 (1939).
10. C. S. Tedmon, D. A. Vermilyea, and J. H. Rosolowski, *This Journal*, **118**, 192 (1971).
11. D. A. Vermilyea, *Corrosion*, **31**, 421 (1975).
12. T. M. Devine, "The Effect of Microstructure on the Stress Corrosion Cracking Susceptibility of Austenitic and Duplex Stainless Steels," Corrosion 77, San Francisco, March 14-16, 1977.
13. W. L. Clarke, J. C. Danko, and G. M. Gordon, in "Corrosion Problems in Energy Conversion and Generation," C. S. Tedmon, Jr., Editor, p. 410, The Electrochemical Society Softbound Symposium Series, Princeton, N.J. (1974).
14. ASTM Designation A262-70.
15. "Metals Handbook," Vol. 8, 8th ed., American Society for Metals (1973).
16. L. H. Van Vlack, "Materials Science for Engineers," p. 169, Addison-Wesley, Philippines (1970).
17. P. J. Grobner, *Metall. Trans.*, **4**, 251 (1973).
18. R. Lagneborg, *Trans. ASM*, **60**, 67 (1967).
19. H. D. Solomon and L. Levinson, Accepted for publication in *Acta Metallurgica*.
20. R. M. Fisher, E. J. Dulis, and K. G. Carroll, *Trans. AIME*, 690 (1953).
21. E. C. Bain, R. H. Aborn, and J. J. B. Rutherford, *Trans. Am. Soc. Steel Treating*, **21**, 481 (1933).
22. J. Horvath and H. H. Uhlig, *This Journal*, **115**, 791 (1968).
23. C. R. Rarey and A. H. Aronson, *Corrosion*, **28**, 255 (1972).
24. G. Eklund, *This Journal*, **121**, 467 (1974).
25. M. Hansen, "Constitution of Binary Alloys," p. 705, McGraw-Hill Book Co., New York (1958).
26. M. A. Streicher, *This Journal*, **103**, 375 (1956).

Inhibition of the Crevice Corrosion of Iron in Chloride Solutions by Chromate

E. McCafferty*

Naval Research Laboratory, Washington, D.C. 20375

ABSTRACT

The crevice corrosion of iron in neutral solutions is promoted by chloride ions and inhibited by chromate. For any given concentration of chloride in the range investigated (10^{-4}-0.6 M/l), the crevice corrosion of iron can be inhibited by using a sufficient amount of chromate, with the concentration of chromate required decreasing with the concentration of chloride. A linear relationship is observed between the logarithm of the chloride ion activity and the logarithm of the minimum activity of chromate ion required for protection against crevice corrosion. This relationship is explained on the basis of competitive adsorption between aggressive (Cl^-) and inhibitive ($CrO_4^=$) ions within the crevice, with each ion adsorbing according to a Temkin isotherm. The steady-state electrode potential of corroding iron within crevices is -620 to -660 mV *vs.* Ag/AgCl, independent of bulk solution composition and in reasonable agreement with the thermodynamic value calculated for an iron crevice or pit.

Much more attention has been paid to the inhibition of pitting than of crevice corrosion. For example, the effect of chromate on the pitting of iron and steel has been the subject of a number of investigations (1-4), as compared to only a few studies on the use of chromates to prevent crevice corrosion (5, 6). Rosenfeld and Marshakov (5, 7) have shown that inhibitor concentrations required to prevent crevice corrosion of iron are much higher than those needed for inhibition in the bulk electrolyte. Previous work (6) has shown that the rate of crevice corrosion depends on the concentrations of both chromate and chloride ions.

The information available from crevice corrosion inhibition studies has been less detailed and quantitative

* Electrochemical Society Active Member.
Key words: crevice corrosion, iron, inhibition, chromate, adsorption.

than that obtained from pitting studies. In the latter case, quantitative relationships have been observed between the pitting potential and the concentration of inhibitive or aggressive ions (3, 8, 9). In addition, there is a well-defined relationship between the concentration of aggressive ion and the minimum concentration of inhibitor required to prevent pitting (1, 2, 4, 8, 10).

The purpose of this communication is to extend our previous work (6) on model, well-defined systems in order to better understand the role of a typical inhibitor (Na_2CrO_4) in preventing crevice corrosion.

Experimental

The crevice device and corrosion cell shown in Fig. 1 were the same as used previously (6). Corrosion rates were determined by measuring the current produced between iron within the crevice coupled to an external iron electrode having free access to the electrolyte. The crevice and external electrodes were Ferrovac E high purity iron machined from the same bar. The crevice iron electrode was circular shaped (1¼ in. diam, 7.9 cm^2) and the external iron electrode was ring shaped (approx. 50 cm^2 exposed area). Details involving the electrode holders, crevice assembly, and measurement of electrode potentials within the crevice have been described previously (6).

Both the crevice and external iron electrodes were dry polished through 3/0 emery papers. Immediately before use, both iron pieces were given a final polish so that the iron surface was covered with the usual air-formed oxide film of approximately 10-25Å thickness (11).

The crevice was formed by positioning the optically polished bottom surface of the glass disk a measured distance above the iron surface by means of a micrometer attached to the disk top. The glass disk was rotated into place down through the solution, so that the crevice electrolyte contained the same concentration of inhibitor as in the bulk. This procedure eliminated the problem of diffusion of inhibitor from the bulk into the crevice. A fixed crevice height of 0.25 mm (10 mils) was used throughout this study. This clearance was chosen because it is less than the thickness of the oxygen diffusion layer (6, 7). In addition, this value lies in the range of crevice heights observed by Rosenfeld and Marshakov to give maximum corrosion intensity for iron in the presence of several inorganic inhibitors (5).

In a typical experiment, when the crevice height was set, both the crevice and external iron electrodes were left uncoupled for 15 min. At 15 min time, the two parts were short-circuited using the potentiostat in the two-electrode configuration (12), which essentially uses the potentiostat as a zero resistance ammeter. Electrode potentials of internal and external iron and the current between the two parts were measured for approximately 48 hr of coupling.

During all experiments, the cell electrolyte was open to the air and quiescent. All solutions were prepared from reagent grade chemicals and distilled water prepared in a Barnstead still.

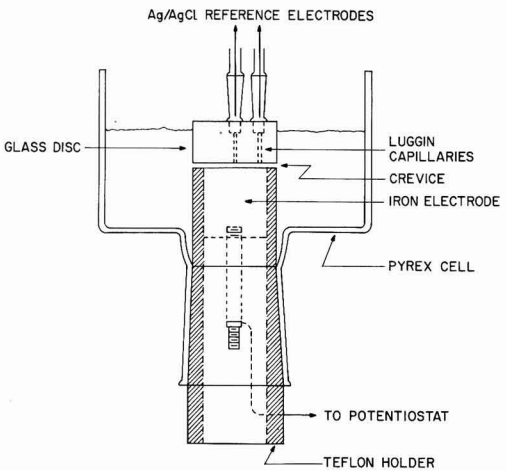


Fig. 1. The crevice corrosion cell. (Micrometer assembly and external iron electrode not shown).

Results

Results for a typical experiment are shown in Fig. 2. During the first 15 min of the experiment when the crevice iron and external iron were uncoupled, the electrode potential of the internal iron was more active (negative) due to oxygen depletion within the crevice (6, 13). Upon coupling, corrosion currents usually increased with time to a maximum, and then decreased.

Figure 3 shows the corrosion current between the internal crevice iron and external open iron for 0.6M NaCl with various amounts of added chromate. It can be seen that crevice corrosion is inhibited by adding a sufficient amount of chromate. For more dilute chloride solutions, a smaller amount of chromate is required for protection. Figure 4 shows the effect of both chloride and chromate concentrations on the crevice corrosion rate. In general, the crevice corrosion current decreases with increasing chromate and decreasing chloride concentrations. Figure 5 shows that the various $CrO_4^=/Cl^-$ solutions studied can be mapped into distinct regimes of crevice corrosion or inhibition. For any given concentration of Cl^- in the range investigated (10^{-4}-0.6 M/l), crevice corrosion can be inhibited by using the appropriate minimum amount of $CrO_4^=$ required.

Figure 6 shows the results in Fig. 5 plotted on the basis of ion activities, rather than concentrations. Activity coefficients for sodium chromate and sodium chloride in the mixed electrolyte were calculated from Harned's rule, using Harned rule coefficients for NaCl/Na_2SO_4 mixtures (14). This approximation was made because Na_2CrO_4 and Na_2SO_4 have similar activity co-

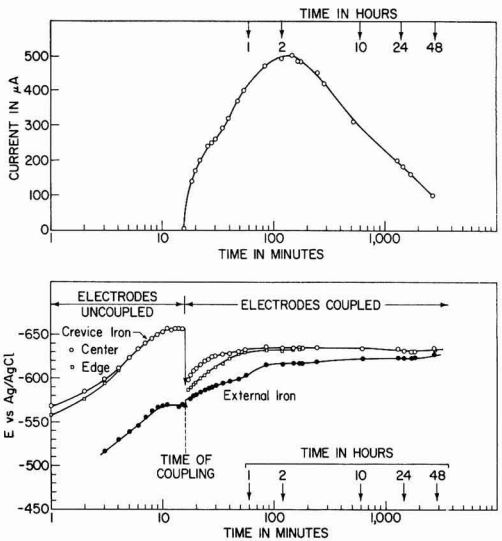


Fig. 2. Crevice corrosion current and electrode potential behavior for the couple: Iron (crevice)/iron (external) in 0.003M Na_2CrO_4 + 0.6M NaCl. (Crevice height = 0.25 mm, area of crevice iron = 7.9 cm^2, area of external iron electrode ≅ 50 cm^2.

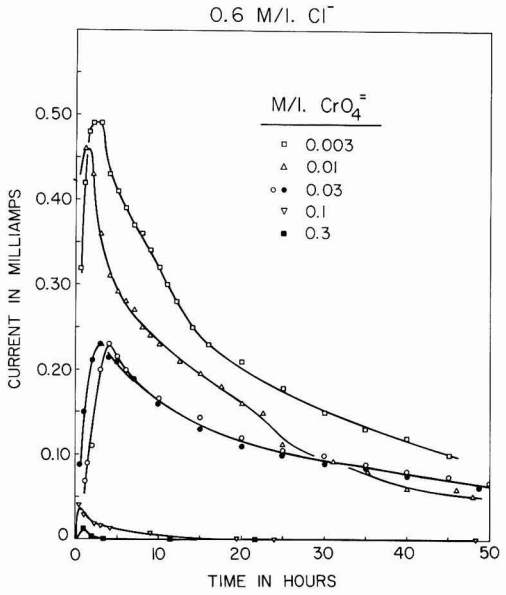


Fig. 3. Effect of chromate on the crevice corrosion of iron for a fixed chloride concentration of 0.6 M/l. (Crevice height = 0.25 mm, area of crevice iron electrode = 7.9 cm², area of outer iron electrode ≅ 50 cm².)

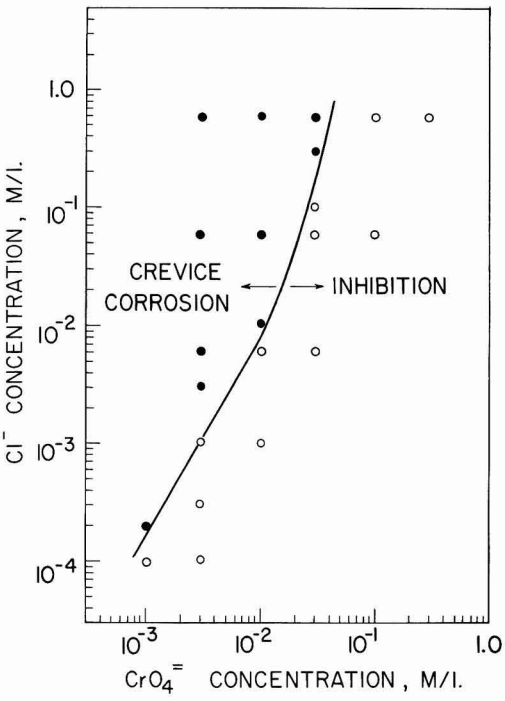


Fig. 5. Regimes of crevice corrosion and inhibition of iron in 0.25 mm crevices in chromate/chloride solutions. (Solid points indicate crevice corrosion and open points indicate inhibition.)

efficients in simple aqueous solutions (15). From Fig. 6, the border line separating the regions of crevice corrosion and inhibition is a straight line given by

$$\frac{d \log a_{Cl^-}}{d \log a_{CrO_4^=}} = \text{constant} = 2.3 \qquad [1]$$

Figure 7 shows crevice potential-time curves for 0.6M Cl^- corresponding to the current-time curves in Fig. 3. The electrode potential of iron in the crevice reached a steady-state value in each case. For the chromate concentrations where crevice corrosion occurred (0.003, 0.01, and 0.03 M/l), the electrode potential of the corroding iron was −0.630 to −0.660 mV *vs.* Ag/AgCl (five separate runs).

Figure 8 shows potential-time curves for a different Cl^- concentration (0.006 M/l) with various amounts of added chromate. Again, the steady-state potential for crevice corrosion was approximately −0.630 mV *vs.* Ag/AgCl, with more positive potentials produced by concentrations of $CrO_4^=$ which provided protection.

The crevice potentials plotted in Fig. 7 and 8 are those at the crevice center. However, in all cases, there was little difference (0-10 mV) between the potentials at the crevice center and crevice edge after 50 hr.

Figure 9 shows the steady-state electrode potentials at the crevice center for the various solutions investigated. If the crevice iron corroded, the electrode potential was −0.620 to −0.660 mV *vs.* Ag/AgCl regardless of the bulk concentration of the electrolyte. Crevices which were protected displayed potentials more positive than −0.620 mV *vs.* Ag/AgCl.

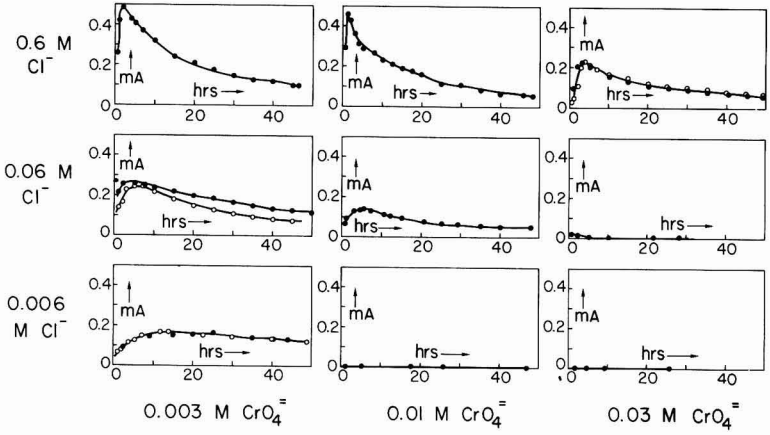


Fig. 4. Effect of chloride and chromate on the crevice corrosion of iron. Crevice height = 0.25 mm, area of crevice iron electrode = 7.9 cm², area of outer iron electrode ≅ 50 cm². (Open and closed data points indicate duplicate runs.)

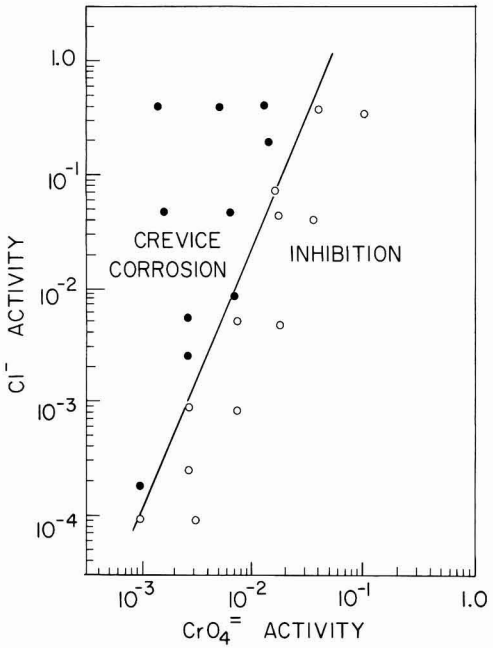


Fig. 6. Data of Fig. 5 replotted on an activity basis

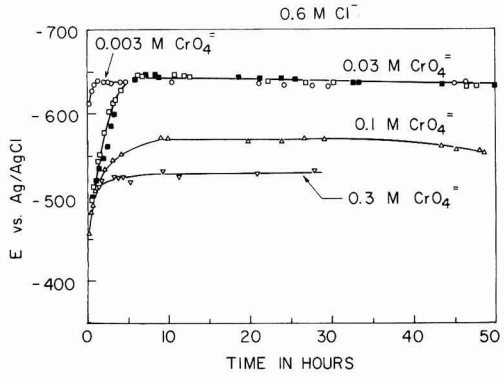


Fig. 7. Electrode potentials of iron in crevices in 0.6M NaCl with different amounts of added chromate. (Open and closed data points indicate duplicate runs.)

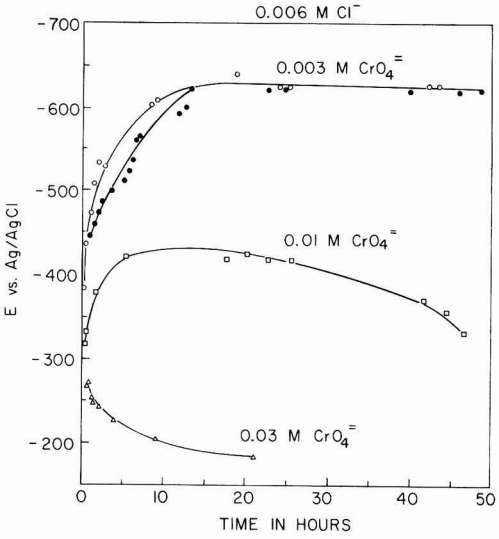


Fig. 8. Electrode potentials of iron in crevices in 0.006M NaCl with different amounts of added chromate. (Open and closed data points indicate duplicate runs.)

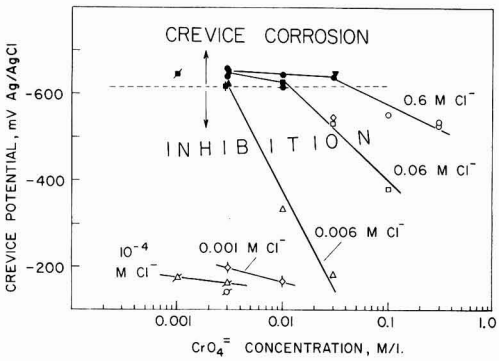


Fig. 9. Electrode potential of iron within crevices. Closed symbols indicate crevice corrosion and open symbols indicate protection. Chloride concentrations not labeled on the figure are: ▼ 0.3 M; ◇ 0.1 M; —●— 0.01M; ▮ 0.003 M; ○ 3 × 10^{-4}M; ◢ 2 × 10^{-4} M.

Discussion

The present results show that there is a critical minimum concentration of chromate required to inhibit the crevice corrosion of iron in the presence of a given concentration of chloride ion. More specifically, there is a linear log/log relationship between the activity of the aggressive ion (Cl^-) and the minimum activity of inhibitive ion ($CrO_4^=$) that can just give protection (Fig. 6). Analogous results were first obtained with iron by Matsuda and Uhlig (1) for the case of pitting corrosion. This same general relationship has been observed in free electrolytes containing various aggressive and inhibitive ions, including $Cl^-/CrO_4^=$ mixtures (2, 4, 8, 10, 16-18).

Matsuda and Uhlig (1) have interpreted the linear log/log plots obtained for pitting on the basis of competitive adsorption between inhibitive and aggressive ions. Evidence supporting the competitive adsorption mechanism has been summarized by Leckie and Uhlig (8), Kolotyrkin (19) and Rosenfeld (20). This same explanation can also be proposed for the case of crevice corrosion because of the similarities between these two forms of localized corrosion. Rosenfeld (20) suggests that the pitting of stainless steels is a type of crevice corrosion in which the porous cap of corrosion products above a pit acts like a small crevice. Both pitting and crevice corrosion propagate due to the development of a local internal acidity resulting from the restricted exchange of bulk and local electrolytes (21).

Thus, if chromate adsorption predominates within the crevice, passive film formation of Cr_2O_3 or $Cr(OH)_3$ can follow (22-25). However, if the adsorption of chloride ions predominates, then crevice corrosion ensues.

Matsuda and Uhlig (1) described the adsorption process in terms of the empirical Freundlich isotherm, which has no theoretical basis. More recently, Strehblow and Titze (9) have applied the Langmuir iso-

therm to the competitive adsorption between inhibitive and aggressive anions in the case of pitting corrosion. For adsorption of the aggressive ion

$$\frac{\theta_A}{1-\theta_A-\theta_I} = K'_A(a_{A^-})\ e^{\Delta H_{ads,A}/RT}\ e^{\gamma_A z_A FE/RT} \quad [2]$$

where θ_A and θ_I are the surface coverages of aggressive and inhibitive ions, respectively, a_{A^-} the bulk activity of aggressive anion, $\Delta H_{ads,A}$ the heat of adsorption of the aggressive ion, and E the electrode potential across the interface. The factor γ_A (not to be confused with activity coefficients) takes into account the fact that the specifically adsorbed anions move through only part of the potential drop across the interface (9).

If the heat of adsorption ΔH_{ads} is independent of coverage, Eq. [2] yields the usual Langmuir isotherm for charged intermediates (26), modified to account for the coadsorption of two species. More likely, however, the heat of adsorption decreases with coverage due to: (*i*) *a priori* heterogeneity of surface sites having a distribution of energies; and (*ii*) lateral repulsive interactions between neighboring adsorbed anions. The "induced heterogeneity" model of Boudert discussed by Conway and Gileadi (27) is not applicable because the "metal" surface in the present work is oxide covered rather than bare. A reasonable approach to include factors (*i*) and (*ii*) above is provided through use of the Temkin isotherm (26, 28), which assumes the heat of adsorption decreases linearly with coverage. Temkin isotherms have been reported for the adsorption of halides and of various organic molecules on iron (29-32).

If only one adsorbed species is involved

$$\Delta H_{ads} = \Delta H^\circ - r\theta \quad [3]$$

where ΔH° is the initial heat of adsorption and r is the Temkin parameter. For the coadsorption of two species, two different models are applicable depending on whether the aggressive ion adsorbs in patches or uniformly.

Patchwise adsorption model.—If the chloride ion adsorbs in patches or clusters, then the adsorption of chloride and of chromate will be independent of each other for most coverages. That is

$$\Delta H_{ads,A} = \Delta H^\circ_A - r_A\theta_A \quad [4]$$

and

$$\Delta H_{ads,I} = \Delta H^\circ_I - r_I\theta_I \quad [5]$$

Use of Eq. [4] in Eq. [2] gives

$$\frac{\theta_A}{1-\theta_A-\theta_I} = K(a_{A^-})\ e^{-r_A\theta_A/RT}\ e^{\gamma_A z_A/RT} \quad [6]$$

where $K_A = K'_A\, e^{\Delta H^\circ_A/RT}$. Taking logarithms and using the usual approximation that at intermediate coverages $\ln [\theta_A/(1-\theta_A-\theta_I)] << r_A\theta_A/RT$ gives the Temkin isotherm

$$\theta_A = \frac{2.303\,RT}{r_A}\log K_A + \frac{2.303\,RT}{r_A}\log a_{A^-} + \frac{\gamma_A z_A FE}{r_A} \quad [7]$$

Similarly

$$\theta_I = \frac{2.303\,RT}{r_I}\log K_I + \frac{2.303\,RT}{r_I}\log a_{I^-} + \frac{\gamma_I z_I FE}{r_I} \quad [8]$$

According to Fig. 7-9, the electrode potential for crevice corrosion is approx. −620 mV (Ag/AgCl) in all instances. With $E = E_{active}$, Eq. [7] and [8] combine to give

$$\frac{1}{r_A}\log a_{A^-} - \left(\frac{\theta_A}{\theta_I}\right)\frac{1}{r_I}\log a_{I^-} = \left(\frac{\theta_A}{\theta_I}\right)\frac{1}{r_I}\log K_I - \frac{1}{r_A}\log K_A + \left(\frac{\theta_A}{\theta_I}\cdot\frac{\gamma_I z_I}{r_I} - \frac{\gamma_A z_A}{r_A}\right)\frac{FE_{active}}{2.303\,RT} \quad [9]$$

Uhlig and co-workers (1, 8, 10) have proposed that pitting initiates when there is a critical ratio in the surface coverages of aggressive to inhibitive ions. This same effect can result in passive film breakdown within crevices (although the critical ratios are probably different in the two forms of localized corrosion). In the patchwise adsorption model, breakdown will occur at certain specific sites within the crevice and then spread to other areas as crevice acidification occurs. If there is a critical ratio in the coverages of adsorbed chloride to adsorbed chromate which leads to passive film breakdown

$$\frac{\theta_A}{\theta_I} = \Theta_{crit} \quad [10]$$

then Eq. (9) gives

$$\frac{d\log a_{A^-}}{d\log a_{I^-}} = \Theta_{crit}\frac{r_A}{r_I} \quad [11]$$

which has the form of Eq. [1].

Uniform adsorption model.—If the adsorption of Cl^- and $CrO_4^=$ ions is more uniform than patchwise, each surface species will affect the adsorption of the other. Here, the heat of adsorption of a given species will vary with the total coverage θ_T

$$\Delta H_{ads,A} = \Delta H^\circ_A - s_A\theta_T \quad [12]$$

and

$$\Delta H_{ads,I} = \Delta H^\circ_I - s_I\theta_T \quad [13]$$

where $\theta_T = \theta_A + \theta_I$ and s_A and s_I are the Temkin parameters. Use of Eq. [12] and [13] gives the pair of equations

$$\theta_T = \frac{2.303\,RT}{s_A}\log K_A + \frac{2.303\,RT}{s_A}\log a_{A^-} + \frac{\gamma_A z_A FE}{s_A} \quad [14]$$

and

$$\theta_T = \frac{2.303\,RT}{s_I}\log K_I + \frac{2.303\,RT}{s_I}\log a_{I^-} + \frac{\gamma_I z_I FE}{s_I} \quad [15]$$

in place of Eq. [7] and [8]. With $E = E_{active}$, Eq. [14] and [15] combine to give

$$\frac{1}{s_A}\log a_{A^-} - \frac{1}{s_I}\log a_{I^-} = \frac{1}{s_I}\log K_I - \frac{1}{s_A}\log K_A + \left(\frac{\gamma_I z_I}{s_I} - \frac{\gamma_A z_A}{s_A}\right)\frac{FE_{active}}{2.303\,RT} \quad [16]$$

Taking differentials gives

$$\frac{d\log a_{A^-}}{d\log a_{I^-}} = \frac{s_A}{s_I} \quad [17]$$

which also has the form of Eq. [1]. In the uniform adsorption model, it is not necessary to explicitly assume a critical ratio of adsorbed aggressive ions to adsorbed inhibitive ions. However, this idea is implicit in the concept of the critical active potential E_{active}.

Electrode potentials in crevices.—According to Fig. 9, the electrode potential of corroding iron in crevices

Table I. Electrode potential of corroding iron in crevices

Investigator(s)	System	V vs. Ag/AgCl
A. Pourbaix (33)	Iron in scaled-up crevices in various chloride solutions	$-0.62 \rightarrow -0.67$
Petersen, Soltz, and Mairs (34)	Synthetic pit on steel in natural seawater	-0.66
Present Investigation	Real-size crevices in various chloride-chromate solutions	$-0.62 \rightarrow -0.67$
M. Pourbaix (35)	$Fe/Fe_3O_4/FeCl_2 \cdot 4H_2O$ (calculated)	-0.590

is -0.62 to -0.66V *vs.* Ag/AgCl, regardless of the bulk concentration of the electrolyte. These values are in agreement with the results of other investigations (33, 34), as listed in Table I. In addition, the least active potential for crevice corrosion (-0.62V *vs.* Ag/AgCl) is only slightly different than the thermodynamic value calculated by Pourbaix (35). Based on thermodynamic considerations, Pourbaix has proposed that the internal contents of a stress-corrosion crack, corroding crevice, or corrosion pit on iron or steel consists of magnetite-covered base metal in contact with the local electrolyte, a saturated solution of ferrous chloride. The calculated thermodynamic electrode potential for this system of $Fe/Fe_3O_4/FeCl_2 \cdot 4H_2O$ is -0.590V *vs.* Ag/AgCl. The slight difference between this value and the observed electrode potentials could be due to iR drops in the measured potentials or to nonthermodynamic conditions in the crevice. Satler and Van Muylder (36) have shown that the electrode potential of iron in deaerated $FeCl_2$ solutions is more positive than -0.590V (Ag/AgCl) for solutions which are not saturated in $FeCl_2$. Chloride concentrations of 3-6 (37) and 3-12N (38) have been reported within pits on stainless steels. However, these pits were activated by considerable galvanostatic or potentiostatic treatment.

Summary

1. For a constant chloride concentration, the rate of crevice corrosion of iron decreases with increasing chromate concentration until complete protection is attained by using a sufficient amount of $CrO_4^=$ inhibitor.

2. The lesser the Cl^- concentration, the lesser the concentration of $CrO_4^=$ required for inhibition of crevice corrosion.

3. The minimum activity of $CrO_4^=$ required for inhibition is related to the activity of chloride by: $d \log a_{Cl^-}/d \log a_{CrO_4^=} =$ constant.

4. This relationship is explained by the competitive adsorption within the crevice between inhibitive ($CrO_4^=$) and aggressive (Cl^-) ions, with each ion adsorbing according to a Temkin isotherm. If adsorption of the inhibitive ion predominates, passive film formation results; but predominant adsorption of the aggressive ion leads to crevice corrosion.

5. The electrode potential of corroding iron within crevices is -620 to -660 mV *vs.* Ag/AgCl, in reasonable agreement with the thermodynamic value calculated by Pourbaix.

Acknowledgment

The author is grateful to the Office of Naval Research for financial support of this project.

Manuscript submitted July 31, 1978; revised manuscript received Oct. 6, 1978.

Any discussion of this paper will appear in a Discussion Section to be published in the December 1979 JOURNAL. All discussions for the December 1979 Discussion Section should be submitted by Aug. 1, 1979.

Publication costs of this article were assisted by Naval Research Laboratory.

REFERENCES

1. S. Matsuda and H. H. Uhlig, *This Journal*, **111**, 156 (1964).
2. A. D. Mercer and I. R. Jenkins, *Br. Corros. J.*, **3**, 130 (1968).
3. K. S. Rajagopalan and K. S. Venu, *Corrosion (Houston)*, **27**, 506 (1971).
4. V. K. Gouda and S. M. Sayed, *Corros. Sci.*, **13**, 841 (1973).
5. I. L. Rosenfeld and I. K. Marshakov, *Zh. Fiz. Khim.*, **31**, 72 (1957).
6. E. McCafferty, *This Journal*, **121**, 1007 (1974).
7. I. L. Rosenfeld and I. K. Marshakov, *Corrosion (Houston)*, **20**, 115t (1964).
8. H. P. Leckie and H. H. Uhlig, *This Journal*, **113**, 1262 (1966).
9. H. H. Strehblow and B. Titze, *Corros. Sci.*, **17**, 461 (1977).
10. H. H. Uhlig and J. R. Gilman, *Corrosion (Houston)*, **20**, 289t (1964).
11. P. B. Sewell, C. D. Stockbridge, and M. Cohen, *This Journal*, **108**, 933 (1961).
12. J. Dévay, B. Lengyel, Jr., and L. Meszáros, *Acta Chim. Acad. Sci. Hung.*, **62**, 157 (1969).
13. Yu. M. Korovin and I. B. Ulanovskii, *Corrosion (Houston)*, **22**, 16 (1966).
14. J. N. Butler, P. T. Hsu, and J. C. Synnott, *J. Phys. Chem.*, **71**, 910 (1967).
15. H. S. Harned and B. B. Owen, "The Physical Chemistry of Electrolytic Solutions," Reinhold Publishing Corp., New York (1958).
16. D. M. Brasher and A. D. Mercer, *Br. Corros. J.*, **3**, 120 (1968).
17. A. D. Mercer, I. R. Jenkins, and J. E. Rhoades-Brown, *ibid.*, **3**, 136 (1968).
18. D. M. Brasher, D. Reichenberg, and A. D. Mercer, *Br. Corros. J.*, **3**, 144 (1968).
19. Ja. M. Kolotyrkin, *This Journal*, **108**, 209 (1961).
20. I. L. Rosenfeld, "Proceedings of the Fifth International Congress on Metallic Corrosion," Japan, 1972, p. 53, NACE, Houston, Texas (1974).
21. B. F. Brown, *Corrosion (Houston)*, **26**, 249 (1970).
22. D. M. Brasher and A. H. Kingsbury, *Trans. Faraday Soc.*, **54**, 1214 (1958).
23. D. M. Brasher and A. D. Mercer, *ibid.*, **61**, 803 (1965).
24. E. S. Ivanov, *Prot. Metals USSR*, **7**, 164 (1971).
25. Z. Szklarska-Smialowska and R. W. Staehle, *This Journal*, **121**, 1146 (1974).
26. E. Gileadi, E. Kirowa-Eisner, and J. Penciner, "Interfacial Electrochemistry," p. 78 ff, Addison-Wesley Publishing Co., Reading, Mass. (1975).
27. B. E. Conway and E. Gileadi, *Trans. Faraday Soc.*, **58**, 2493 (1962).
28. E. Gileadi, "Electrosorption," p. 1, Plenum Press, New York (1967).
29. I. A. Ammar, S. Darwish, M. Etman, and W. Khalil, *Electrochim. Acta*, **13**, 603 (1968).
30. Z. A. Iofa, Y. A. Nikoforova, and V. V. Batrakov, "Proceedings of the Third International Congress on Metallic Corrosion," 1966, Vol. 2, p. 40, Moscow, (1969).
31. N. Hackerman and E. McCafferty, "Proceedings of the Fifth International Congress on Metallic Corrosion," Tokyo, 1972, p. 542, NACE, Houston, Texas (1974).
32. R. R. Annand, R. M. Hurd, and N. Hackerman, *This Journal*, **112**, 144 (1965).
33. A. Pourbaix, *Corrosion (Houston)*, **27**, 449 (1971).
34. C. W. Petersen, G. C. Soltz, and K. Mairs, *ibid.*, **30**, 366 (1974).
35. M. Pourbaix, "Localized Corrosion," p. 12, NACE, Houston (1974).
36. L. Sathler and J. Van Muylder, *Rapp. Tech. CEBELCOR*, RT. 224, March 1975.
37. T. Suzuki, M. Yamabe, and Y. Kitamura, *Corrosion (Houston)*, **29**, 18 (1973).
38. J. Mankowski and Z. Szklarska-Smialowska, *Corrosion Sci.*, **15**, 493 (1975).

The Chemical State of Cobalt in Cobalt-Hardened Gold Electrodeposits

H. Leidheiser, Jr.,* A. Vértes, M. L. Varsányi, and I. Czakó-Nagy

Center for Surface and Coatings Research, Lehigh University, Bethlehem, Pennsylvania and Institute of Physical Chemistry and Radiology, Lorand Eötvös University, Budapest, Hungary

ABSTRACT

Cobalt-hardened gold electrodeposits were prepared from all-citrate and mixed citrate-phosphate gold-plating baths doped with ^{57}Co. Mössbauer emission spectra revealed the presence of elemental cobalt, β-CoOOH, and an unidentified species (probably a cyanide) in the gold deposit.

Gold electrodeposits have wide applicability in the electronics industry in protecting substrates from corrosion. In many cases the gold electroplate is hardened by the codeposition of cobalt to the extent of 0.3-1.6 atomic percent (a/o). Such cobalt-hardened gold deposits have satisfactory contact resistances and exhibit serviceable wear resistance (1). Although these deposits are extensively used commercially, the chemical nature of the cobalt in the gold deposit has not been determined. We have addressed ourselves to this problem using ^{57}Co emission Mössbauer spectroscopy. A previous study in which the emission spectra of a large number of cobalt oxides and cobalt oxyhydroxides had been determined (2) provided an excellent background for this work. The fact that cobalt-hardened gold electrodeposits contain significant amounts of carbon, oxygen, nitrogen, and hydrogen (3) and that nonmetallic inclusions have been observed in transmission electron microscopy (4) provided additional stimulus to perform such studies.

Experimental

The plating baths utilized to form the gold deposits were proprietary solutions that are used commercially. The facts that are known about the composition of the plating baths are given in Table I. Three different plating solutions were used. One was a mixed phosphate-citrate bath and the other two were all-citrate baths. Cobalt was added as the sulfate in one all-citrate bath and as a proprietary chelate in the other two baths. Radioactive cobalt (^{57}Co) was added to 10 ml of each bath as the chloride so as to achieve an activity of approximately 1 mCi. The deposit thickness in all cases was equivalent to 15 ± 3 mg of gold/cm^2 and the substrate was copper foil, $15 \times 15 \times 0.05$ mm. The conditions of deposition for each sample are given in Table I.

The principles of emission Mössbauer spectroscopy utilizing ^{57}Co have been given previously (5) and will thus not be repeated here. The absorber used was $K_4[Fe(CN)_6] \cdot 3H_2O$ enriched in ^{57}Fe which has an isomer shift, δ, equal to -0.047 mm/sec relative to natural iron at 298°K. All values of δ mentioned in the paper are given with respect to iron.

* Electrochemical Society Active Member.
* Key words: gold electrodeposit, Mössbauer spectroscopy, CoOOH.

Results

The Mössbauer spectra of the gold electrodeposits recorded immediately after deposition exhibited a broad band with a complex shape and a width at half-maximum (Γ) of 1.3-1.6 mm/sec. Computer analysis of the components of the spectrum yielded the most satisfactory fit on the basis of six or more lines. The number of options in interpreting a spectrum was so large that it did not appear useful to attempt quantitative interpretation of the spectra. The values of Γ decreased dramatically with aging time at room temperature as shown in Table II.

The spectra obtained after aging for 10-35 days were interpreted on the basis of 3 components, the data for which are summarized in Table III. The spectrum and the computer fit are given in Fig. 1 and 2 for two deposits after aging at room temperature for 15 days. The deposit shown in Fig. 2 was cooled to 78°K and the spectrum show in Fig. 3 was obtained. No evidence of magnetic hyperfine splitting was detected.

A single heat-treatment experiment was performed in order to determine the fate of the cobalt species after such heat-treatment. Sample No. 3 was annealed for 24 hr at 400°C in a nitrogen atmosphere and was cooled slowly to room temperature. The spectrum of the resulting sample is shown in Fig. 4a. Computer analysis yielded single line components with Mössbauer parameters of $\delta_1 = -1.12$ mm/sec and $\Gamma_1 = 0.72$

Table II. Values of the width at half-maximum of the broad peak as a function of aging time

Sample No.	Aging time (days)	Γ (mm/sec)
1	1	1.34
	14	0.98
	35	0.93
2	2	1.46
	17	0.95
3	1	1.29
	15	1.06
4	3	1.59
	10	0.98

Table I. Composition of plating solutions and deposition conditions

Sample identification	Trade name and composition of the plating solution		Current density (mA/cm^2)	Temp. (°C)	pH	Time of deposition (min)
1	Orosene-80	Citrate-phosphate electrolyte, 16.4 mg Au/ml as $KAu(CN)_2$ and 1320 ppm Co as Co-chelate	10	32	4.9	30
2	Autronex-CI	All citrate system, 8.2 mg/ml Au as $KAu(CN)_2$ 264 ppm Co as $CoSO_4$	10	32	4.3	30
3	Orosene-80D	All citrate system, 16.4 mg Au/ml as $KAu(CN)_2$ 1320 ppm Co as Co-chelate	10	50	4.7	30
4	Orosene-80	Citrate-phosphate electrolyte, 16.4 mg Au/ml as $KAu(CN)_2$ and 1320 ppm Co as Co-chelate	1	32	4.9	300

Table III. Mössbauer parameters of the spectra after aging at room temperature

Sample No.	δ_1 (mm/sec)	ΔE_1 (mm/sec)	Γ_1 (mm/sec)	η_1 (%)	$(A\%)_1$	δ_2 (mm/sec)	ΔE_2 (mm/sec)	Γ_2 (mm/sec)	η_2 (%)	$(A\%)_2$	δ_3 (mm/sec)	ΔE_3 (mm/sec)	Γ_3 (mm/sec)	η_3 (%)	$(A\%)_3$
1	−0.69	0	0.78	12.5	70.7	−0.44	1.06	0.51	0.50	3.7	−0.02	0.72	0.90	1.51	25.6
2	−0.66	0	0.80	20.99	92.9	−0.51	0.97	0.22	2.26	5.5	−0.11	0.60	0.22	0.81	1.6
3	−0.63	0	0.77	14.42	76.0	−0.53	0 95	0.33	4.07	18.4	−0.06	0.84	0.29	1.40	5.6
4	−0.60	0	0.72	10.42	63.5	−0.52	0.91	0.31	2.19	11.5	−0.01	1.15	0.84	1.76	25.0

The δ values are relative to natural iron. The error range of the tabulated δ values is $\pm$ 0.03 mm/sec.

η is the intensity of the lines: $100\frac{N_\infty - N_v}{N_\infty}$, where N_∞ and N_v are the numbers of counts in one channel at $v = \infty$ velocity and at the minimum of the line, respectively.

A is the area of the line as a percentage of the whole area.

mm/sec; $\delta_2 = -0.48$ mm/sec and $\Gamma_2 = 0.88$ mm/sec. The spectrum of the heat-treated deposit determined at 78°K is shown in Fig. 4b. The spectrum was interpreted on the basis of two six-line components plus other lines of low intensity.

Discussion

The large changes observed in the spectrum after aging of the gold electrodeposits at room temperature indicate that many of the cobalt atoms in the deposit immediately after deposition are in metastable sites and rearrangments in crystallographic site take place. The broad peak observed shortly after deposition had values of Γ in the range of 1.3-1.6 mm/sec which decreased to 0.9 to 1.1 mm/sec after aging for 10-35 days as shown in Table II. The relatively large width of the lines is explained by the slightly different environments of cobalt atoms since x-ray diffraction studies indicate the presence of structural inhomogeneities, such as stacking faults, in gold electrodeposits prepared from solutions containing cobalt and other metallic ions (6, 7). The spectrum obtained shortly after deposition probably represents a summation of changes that occurred while the spectrum was being recorded since it generally required 16-48 hr to obtain satisfactory spectra.

The interpretation of Mössbauer spectra when several components are present always results in a degree of uncertainty. The ability to obtain computer fits is determined by the restrictions that are placed on the curve-fitting procedure. Much trial and error is involved and the final conclusions are based on internal consistency and consistency with independent experimental observations. The spectra obtained in this study are interpreted on the basis of three components present in all electrodeposits that were studied. It is recognized that other interpretations of the data are possible and we shall point these out when appropriate. The main spectral component was a single line with $\delta = -0.60$ to -0.69 mm/sec and $\Gamma = 0.7$-0.8 mm/sec. The species responsible for this line is cobalt in substitutional sites in the gold lattice since the normal value of δ for ^{57}Co in substitutional sites in gold is -0.62 to -0.63 mm/sec (8, 9). Violet and Borg (10, 11) have studied the state of iron in evaporated films of gold using Mössbauer spectroscopy. They obtained complex spectra when the iron concentration was in the range of 1.7-10.5 a/o. They interpreted their spectra in terms of two species (*i*) iron atoms with one or more iron nearest neighbors, and (*ii*) iron atoms with no iron nearest neighbors. An explanation of the spectra such as shown in Fig. 1 and 2 on this basis appears unlikely because the cobalt concentration in the deposits prepared in this study were lower than the iron concentrations used by Violet and Borg.

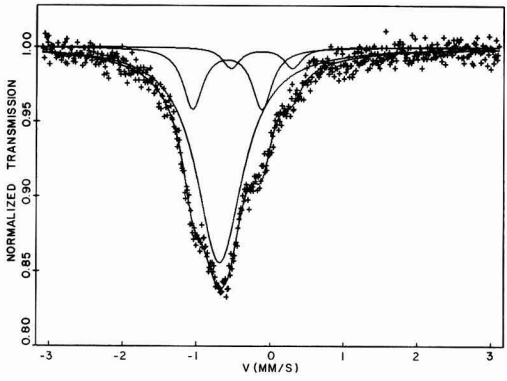


Fig. 1. Mössbauer spectrum of specimen No. 4 recorded 10 days after deposition.

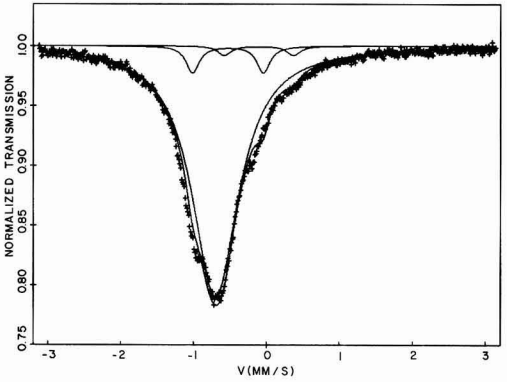


Fig. 2. Mössbauer spectrum of sample No. 2 recorded 15 days after deposition.

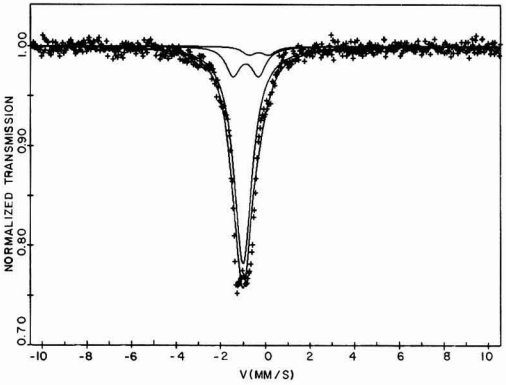


Fig. 3. Mössbauer spectrum of aged specimen No. 2 at 78°K

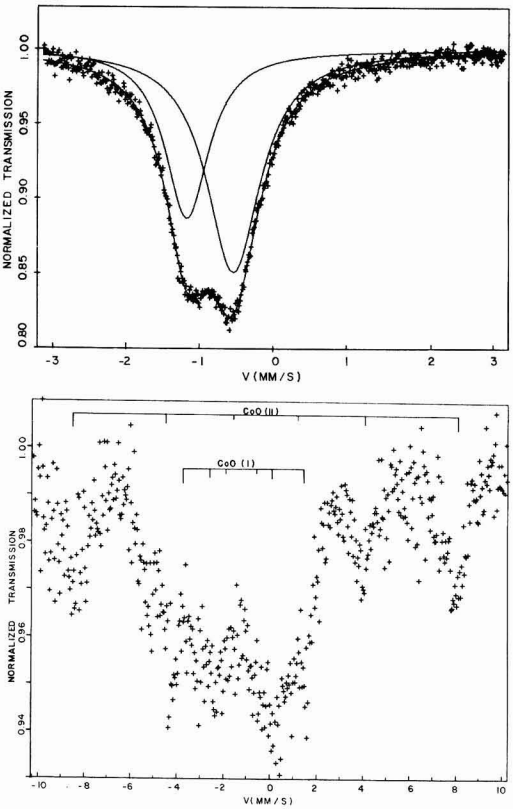


Fig. 4. Mössbauer spectra of aged specimen No. 3 after a 24 hr heat-treatment at 400°C in a nitrogen atmosphere. (a) At room temperature, and (b) at 78°K.

The second spectral component consists of a species with $\delta = -0.44$ to -0.53 mm/sec and a quadrupole splitting of 0.91-1.06 mm/sec. Previous emission Mössbauer studies of many different hydroxides, oxides, and oxyhydroxides of cobalt (2) lead us to interpret this species as β-CoOOH. This material, obtained in a pure state by anodic oxidation of electrochemically deposited $Co(OH)_2$, has Mössbauer parameters of $\delta = -0.48$ mm/sec and $\Delta E = 0.81$ mm/sec. The larger value for ΔE for the species present in the electrodeposit is presumably a result of the more asymmetrical environment within the gold host lattice. The larger value of ΔE thus would be consistent with a very small particle size for the CoOOH within the electrodeposit, in agreement with the observations of Okinaka and Nakahara (4). The simultaneous presence in the deposit of elemental cobalt and a Co(III) species appears inconsistent on the basis of the strong reducing conditions existing at the cathode. Our interpretation of this finding is that the CoOOH is formed at the anode by oxidation of Co(II) and is carried to the cathode and occluded during deposition. Apparently reduction of CoOOH to metallic cobalt or a Co(II) species is incomplete and a small amount of this oxyhydroxide retains its chemical integrity during and after inclusion in the deposit.

The CoOOH species was found in all deposits and the fraction of the total area under the Mössbauer peaks ranged from 4 to 18%. It appears reasonable to assume that the Debye Waller factors of the cobalt and CoOOH species are approximately the same on the basis of the fact that the relative area fractions did not change significantly when the spectrum was recorded with the specimen at room temperature or at 78°K. On this basis the area fraction should be proportional to the fraction of cobalt atoms existing in the elemental form (component No. 1) and in CoOOH (component No. 2). The amount of oxygen combined in CoOOH is thus calculated to be in the range of 0.006-0.03 weight percent (w/o) for the four samples given in Table III assuming a total cobalt concentration in the deposit of approximately 1%. This range is reasonable based on the measurements of Raub, Knödler, and Lendvay (3) which indicate a total oxygen content in cobalt-hardened gold deposits of the order of 0.05 w/o. It is likely that some oxygen in the deposit exists in a chemical form other than CoOOH.

The third component in the spectrum had values of $\delta = -0.01$ to -0.11 mm/sec and a wide range of ΔE from 0.60 to 1.15 mm/sec. Since the area under the peak was approximately 25% for this species in specimens 1 and 4, both of which were prepared in the citrate-phosphate electrolyte, it is tempting to associate this component with a Co species containing phosphate in these two preparations. Specimens 2 and 3, prepared in the all-citrate bath, had values of Γ equal to 0.22 and 0.29 mm/sec, whereas specimens 1 and 4, prepared in the mixed phosphate-citrate bath, had much larger values of Γ equal to 0.84 and 0.90 mm/sec. It is thus suspected that this component is an ionic cobalt species complexed in different ways depending upon the composition of the plating bath. It is possible that the doublet may result from the daughter Fe(IV) state of iron as a consequence of an Auger cascade (5) or from a low-spin state of daughter Fe(II) and Fe(III) resulting from an environment containing the CN^- ion. The Mössbauer emission spectrum of $Co(CN)_2$ has more than 50% of its area located in the 0 ± 0.6 mm/sec velocity range (12). It is worth noting that Okinaka, Koch, Wolowodiuk, and Blessington (13) have reported isolating $Co_3[Co(CN)_6]_2$ and $K_3Co(CN)_6$ from cobalt-hardened gold electrodeposits.,

No magnetic hyperfine splitting was observed in the Mössbauer spectrum of sample No. 3 taken at 78°K (see Fig. 3). The absence of such hyperfine splitting suggests that cobalt in the atomic state is not sufficiently aggregated to yield a magnetic spectrum. Thus all the evidence is consistent with the fact that cobalt exists as individual atoms, probably substitutional in the gold lattice, and that cobalt is probably not the sole cause of hardening.

The Mössbauer spectrum obtained after heat-treatment of the gold deposit at 400° in a nitrogen atmosphere, shown in Fig. 4a, consists of two broad lines with δ values of -1.12 and -0.48 mm/sec and Γ values of 0.72 and 0.88 mm/sec, respectively. The -1.12 mm/sec isomer shift belongs to the Fe(II) oxidation state and the lack of major quadrupole splitting is evidence for cubic symmetry of the Fe(II) site. The isomer shift of -0.48 mm/sec is attributed to the Fe(III) state of iron. This state of iron is not unequivocal evidence that the parent cobalt species was also Co(III) since the higher oxidation state may be a consequence of an Auger cascade taking place after electron capture by Co(II). It is well known that the Mössbauer emission spectrum of CoO exhibits parameters characteristic of both the Fe(II) and Fe(III) oxidation states. The relative concentrations of these two species are a function of the number of vacancies in the CoO lattice (14-18). An increase in concentration of vacancies increases the fraction of Fe(III) present because of the trapping of the electrons by the anion vacancies. The Mössbauer spectrum obtained at 78°K of the heat-treated deposit consists of the superposition of two sextets characteristic of Fe(II) and Fe(III) and several other lines. The values of the internal magnetic fields calculated from the six-line spectra are 170 kOe for Fe(II) and 530 kOe for Fe(III). These values are in agreement with experimental values obtained by Ok

and Mullen (14) for CoO. The other lines appear to be paramagnetic representations of the same components giving rise to the six-line spectra, but the complexity of the spectrum prevents certain identification. All the Mössbauer data are consistent with the conclusion that the major cobalt species in the heat-treated deposit is CoO, although the qualification must be made that the presence of a Co(III) species cannot be completely ruled out. These results thus confirm the observations of Thomas (19), who recently studied the oxidation kinetics of cobalt diffusing out of high current density plated gold and observed "cobalt to oxidize to what appears to be CoO."

Acknowledgment

The gold-plating baths were kindly provided by Roland Morrissey of Technic, Incorporated, to whom sincere appreciation is expressed. We are grateful to the National Science Foundation and the Hungarian Institute of Cultural Relations for the opportunity of the authors to spend time in each others' laboratories.

Manuscript submitted June 6, 1978; revised manuscript received Sept. 20, 1978.

Any discussion of this paper will appear in a Discussion Section to be published in the December 1979 JOURNAL. All discussions for the December 1979 Discussion Section should be submitted by Aug. 1, 1979.

Publication costs of this article were assisted by Lehigh University.

REFERENCES

1. M. Antler, in "Gold Plating Technology," F. H. Reid and W. Goldie, Editors, pp. 259-294, Electrochemistry Publications, Ltd., Ayr, Scotland (1974).
2. G. W. Simmons, E. Kellerman, and H. Leidheiser, Jr., "Passivity and Its Breakdown on Iron and Iron Base Alloys," R. W. Staehle and H. Okada, Editors, pp. 65-68, Natl. Assocn. Corrosion Engrs., (1976).
3. C. J. Raub, A. Knödler, and J. Lendvay, *Plat. Surf. Finish.*, **63**, 35 (1976).
4. Y. Okinaka and S. Nakahara, *This Journal*, **123**, 1284 (1976).
5. G. W. Simmons, E. Kellerman, and H. Leidheiser, Jr., *ibid.*, **123**, 1276 (1976).
6. D. G. Foulke, *Plating, (East Orange, N.J.)*, **50**, 39 (1963).
7. E. Raub, *Metall. (Berlin)*, **21**, 709 (1967).
8. W. A. Styert and R. D. Taylor, *Phys. Rev.*, **134**, A716 (1964).
9. C. F. Steen, D. G. Howard, and R. H. Nussbaum, *Solid State Commun.*, **9**, 865 (1971).
10. C. E. Violet and R. J. Borg, *Phys. Rev.*, **149**, 540 (1966).
11. C. E. Violet and R. J. Borg, *ibid.*, **162**, 608 (1967).
12. V. E. Prusakov, R. A. Shikan, B. V. Borshchagovskii, and V. J. Goldanskii, *Sov. Radiochem.*, **16**, 66 (1974).
13. Y. Okinaka, F. B. Koch, C. Wolowodiuk, and D. R. Blessington, *This Journal*, **125**, No. 8, 348C (1978).
14. H. N. Ok and J. G. Mullen, *Phys. Rev.*, **168**, 550 (1968).
15. W. Trifthauser and P. P. Craig, *Phys. Rev. Lett.*, **16**, 1161 (1966).
16. D. Schroeer and W. Trifthauser, *ibid.*, **20**, 1242 (1968).
17. H. N. Ok and J. G. Mullen, *ibid.*, **21**, 823 (1968).
18. W. R. Heleus and J. G. Mullen, *Phys. Rev.*, **B4**, 750 (1971).
19. J. H. Thomas III, *This Journal*, **125**, 898 (1978).

A Study of the Products of Ultraviolet Irradiation of Palladium-Containing Catalysts for Electroless Metal Deposition

B. K. W. Baylis, C-C. Huang, and M. Schlesinger*

Department of Physics, University of Windsor, Windsor, Ontario N9B 3P4 Canada

ABSTRACT

Ultraviolet light has a marked effect on the Sn-Pd species used in electroless metal deposition, both when Sn(II) and Sn(IV) solutions are used as the sensitizers. Some information on this effect has been gained by determining the amount of palladium washed off during the postactivation rinse. The fact that from the irradiated Sn(IV)-Pd species less Pd rinses off than from the nonirradiated indicates that the light does not simply break the bonds attaching the palladium, allowing it to be removed by rinsing. More Pd seems to be bound when Sn(II) is the sensitizer than when Sn(IV) is, indicating that the mechanisms of Sn-Pd attachment may be different. Nevertheless, whether Sn(II) or Sn(IV) was the sensitizer there remains a significant amount of palladium on the irradiated and rinsed substrate that has been altered to render it incapable of becoming catalytic in the metal plating bath.

The catalyst used for electroless metal plating of nonconducting substrates was traditionally prepared by immersion of the substrate in a Sn(II) "sensitizer" solution, followed by immersion in a Pd(II) "activator" solution. The first assumption made was that the Pd(II) reacted with the Sn(II), resulting in Sn(IV) and Pd(0). Considerable effort has been directed at definitively determining the state of the Pd after the activator step. Evidence has been presented to show on the one hand that it is Pd(0) [see Ref. (1-5)], and on the other hand that it is adsorbed or complexed Pd(II) [see Ref. (6, 7)].

Sharp and his co-workers reported in 1969 [see Ref. (1) and references therein] that u.v. light affects the sensitizing layer in some way that prevents its participation in catalyst formation. They assumed that ultraviolet light promoted the air oxidation of the Sn (II) to Sn(IV), whereby no catalyst could be

* Electrochemical Society Active Member.
Key words: electroless, palladium, sensitizer, ultraviolet irradiation.

Table I. A summary of the effects of u.v. light on Sn(IV) based catalysts

		Ni-P(H^+)	Cu(OH^-)	Ni-P(OH^-)	Co-P(OH)
Sn(IV) · Pd(II)	U.V.	No plating	Plating	No	No
	No U.V.	Plating	No	No	No

			Ni-P(OH^-)	Co-P(OH^-)	Cu(OH^-)
Sn(IV) · Pd(II)	U.V.	Acidic hypophosphite reduction	No	No	Plating
	No U.V.	Acidic hypophosphite reduction	Plating	Plating	Plating

formed with the Pd(II). In fact, this effect was used as further evidence that Sn(II) reacted with Pd(II) to form Sn(IV) and Pd(0). If only Sn(IV) were present, no redox reaction could take place.

Results obtained in our laboratory in 1972 (8) however, did not readily fit this redox mechanism. Irradiation of the species present after activation also prevented metallization, indicating that the Sn-Pd combination could be influenced by u.v. light. Further research (9) showed that u.v. light even destroys the catalytic action of the species deposited from a $SnCl_2$/$PdCl_2$/HCl solution.[1]

The observation in 1975 that aged Sn(IV) can serve as a sensitizer proved that the combination Sn(IV) · Pd(II) can indeed catalyze acidic Ni-P plating solutions (11) (Table I). This combination did not catalyze Cu plating solutions unless it had been either irradiated (11) or prereduced in an acidic hypophosphite solution (12). Irradiation of this reduced catalyst, Sn(IV)Pd(0), did not destroy its catalytic activity; both irradiated and nonirradiated Sn(IV)Pd(0) plated in a Cu plating solution.

No model has been proposed to explain the effect of u.v. light on the palladium-containing species present after activation. Irradiation can be envisioned to affect palladium in various different ways: (*i*) it can reduce Pd(II) to Pd(0) [see Ref. (13) for mechanism]; (*ii*) it can air oxidize it to Pd(IV); (*iii*) it can render Pd(0) uncatalytic; (*iv*) it can break the bonds holding the palladium (whether 0 valent or +2) on the substrate, causing it to wash off in the rinse step, and (*v*) it can dehydrate the Pd(II) to form a highly insoluble palladium oxide. The following analysis of the Pd content of the rinse water was undertaken to eliminate some of these possible mechanisms.

Experimental

All chemicals were of ACS reagent grade, supplied by Fisher or Canlab, and were used without further purification.

Baths.—The preparation of the sensitizer bath is described in detail in Ref. (14). The preparation of the Ni-P metallizing bath is described in Ref. (11). The activator was made as follows: 1g $PdCl_2$ was partially dissolved in 1 ml concentrated HCl. When 10 ml H_2O was added, the $PdCl_2$ dissolved to form solution "A." One ml of this was diluted to 50 ml for solution "B." Ten ml of solution "B" was diluted to 200 ml to make the activator baths. Finally, one more drop of HCl was necessary to keep any palladium hydroxides from precipitating over a period of days.

Procedure.—Two different slide-preparation procedures were followed:

(*i*) As in previous work, the glass microscope slides were dipped successively: 2 min in the Sn(IV) sensitizer, 1 min in a distilled water rinse, 2 min in Pd(II) activator, and then dried in air, usually with an infrared lamp. One slide in a pair was irradiated on both sides with u.v. lamp [exposure system as in Ref. (11)] for about ½ hr on each side, the other slide being allowed to stand in air for this time. The irradiated slides were washed in one beaker of distilled and deionized water (R_2-u.v.); the nonirradiated slides, in another (R_2-no u.v.). The slides were then immersed for about 20 min in Ni-P solution (11).

(*ii*) In order to set the quantity of Pd(II) that had been placed on the slide, a measured amount of activator bath (1 or 2 ml) was dropped onto one surface of the slide and allowed to dry flat. The slides were dipped into the other baths as in procedure (*i*). Only that side of the slide on which the palladium had been placed was subject to u.v. and as expected, the other side did not plate. One problem with this procedure was that if the Sn(IV)-containing slide dried even partially, the wetting of the Pd(II) solution on the slide was quite poor, and consequently, the distribution of Pd was not as even as in procedure (*i*) (dipping).

The rinse waters (both R_2-u.v. and R_2-no u.v.) were tested for Pd(II) content in two different ways. One was a standard spectrophotometric procedure using N, N-dimethyl-4-nitrosoaniline, described in Ref. (15). This procedure can determine Pd(II) concentrations of from 0.01 to 0.2 ppm.

The other test for Pd(II) involved adding Ni-P metallizing solution to the rinse water and noting when precipitation (Ni production in the bath) occurred. Sample quantities involved were 10 ml Ni-P in 30 ml rinse water. Times required for precipitation to start ranged from 20 min when the Pd(II) concentration was 0.3 ppm to days for around 0.01 ppm Pd(II).

Substrate.—All samples were prepared on Esco precleaned microscope slides. These were wiped with paper tissues before use.

Results

When procedure (*i*) was followed (the normal, dipping-only procedure) the Ni-P plated on nonirradiated sides and did not plate on the irradiated slides, as was expected. There was, however, consistently more Pd(II) present in the rinse water of the nonirradiated slides (R_2-no u.v.) than of the irradiated slides (R_2-u.v.). This result was observed both through the direct Pd(II) determination and the Ni-P precipitation test. (See Table II for sample results.)

When procedure (*ii*) was followed, u.v. irradiation was unable to affect either the plating or the amount of palladium in the rinse water if as much as 1.4 $\mu g/cm^2$ Pd(II) (*i.e.*, 8×10^{15} Pd atoms/cm^2) was dried onto the slide. If the working activator bath was di-

Table II. Results of spectrophotometric analyses and precipitation times for the second rinse (R_2) water of slides taken through procedure (*i*)

Procedure (see text)	No. of slides	Total Pd(II) in R_2* (mg)	Pd(II) in R_2 per slide (mg)	Ni-P precipitation time (min)
Sn(IV), R_1, Pd(II), dry	8	0.0294	0.0037	15
Sn(IV), R_1, Pd(II), dry, U.V.	8	0.0195	0.0024	30
Sn(II), R_1, Pd(II), dry	8	0.0026	0.00033	80
Sn(II), R_1, Pd(II), dry, U.V.	8	0.0044	0.00055	60

[1] Shipley 9F. Shipley Company, Newton, Massachusetts (10).

* The estimated error in these values is less than 0.0002.

Table III. Results of spectrophotometric analyses and precipitation times for the second rinse (R_2) water of slides taken through procedure *(ii)*

	Procedure (see text)	Pd(II) dried onto slide (mg)	Pd(II) in R_2 (mg)	Pd(II) remaining on slide + changed Pd Mg	Atoms Pd per cm^2 ($\times 10^{15}$)
	Sn(IV), R_1, Pd(II), dried	0.0054	0.0011	0.0043	0.64
1.	Sn(IV), R_1, Pd(II), dried, U.V.	0.0054	0.0005	0.0049	0.74
	Sn(IV), R_1, Pd(II), dried	0.0107	0.0064	0.0043	0.65
2.	Sn(IV), R_1, Pd(II), dried, U.V.	0.0107	0.0038	0.0069	1.03
	Sn(IV), R_1, Pd(II), dried	0.0107	0.0031	0.0075	1.14
3.	Sn(IV), R_1, Pd(II), dried, U.V.	0.0107	0.0027	0.0079	1.19
	Sn(IV), R_1, Pd(II), dried	0.054	0.025	0.029	4.3
4.	Sn(IV), R_1, Pd(II), dried, U.V.	0.054	0.023	0.030	4.6
	Pd(II), dried	0.054	0.011	0.042	6.4
5.	Sn(IV), R_1, Pd(II), dried	0.054	0.010	0.043	6.5
	Pd(II), dried	0.054	0.014	0.040	6.0
6.	Sn(IV), R_1, Pd(II), dried	0.054	0.010	0.043	6.7
	Sn(II), R_1, Pd(II), dried	0.054	0.0034	0.050	7.5
7.	Sn(II), R_1, Pd(II), dried, U.V.	0.054	0.0030	0.050	7.6

luted to 1/10 or 1/20, the palladium coverage on the slide was low enough such that marked differences due to u.v. could be noted in Ni-P plating and in the amount of palladium in the rinse waters (see Table III). Again, there was less Pd(II) in the rinse water (R_2-u.v.) used for the irradiated slides than in the rinse water (R_2-no u.v.) for the nonirradiated slides. This result should not be taken to mean that more Pd(II) remains on the irradiated slide than on the nonirradiated slide. Irradiation probably changes some of the Pd(II) to a state which is not detected in the analysis procedure. Hence the fourth column of Table III is labeled "Pd(II) remaining on slide + changed Pd."

It can be seen from Table III that both the amounts of Pd(II) rinsed off and the amounts remaining (plus changed) are dependent on the initial amount dried on. Furthermore, we found that longer or hotter drying seems also to affect the amount of palladium "remaining," *i.e.*, not rinsed off. Hence, conclusions drawn from this part of the work are restricted to comparisons of "similar" pairs of slides. Comparable pairs are bracketed in Tables II and III.

If Pd(II) is dried directly onto glass slides with no Sn(IV) being present, the amount of Pd(II) washing off during the rinse was only slightly greater than when Sn(IV) was present (see Table III). No difference could be observed when much more Pd(II) (*e.g.*, 0.107 mg) was dried on, *i.e.*, the presence or absence of Sn(IV) has no effect on such a large amount of dried-on Pd(II).

When Sn(II) was used, the amount of Pd(II) in the rinse water dropped by factors of 3-10. This effect was observed using both the dipping procedure (*i*) and the drop-on procedure (*ii*) (see Tables II and III). The effect of the u.v. light on the Pd(II) washed off was negligible when as much as 0.054 mg Pd(II) was present. For the dipped slides, an example of which can be seen in Table II, consistently more Pd(II) was found in R_2-u.v. than in R_2-no u.v. This result is the reverse of that found when Sn(IV) was the sensitizer.

Discussion and Conclusion

The fact that there is less Pd(II) in the rinse water of nonirradiated slides than of irradiated ones does not simply mean that more Pd(II) sticks to the irradiated slides. If that were the case, more Ni-P plating should occur on the irradiated slides, whereas the reverse is true. The Pd(II) analysis results would indicate that the u.v. light changes the Pd(II) in some way that prevents its subsequent reduction to Pd(0) in the plating bath (and thus prevents both Ni-P precipitation in the rinse water test and plating of Ni-P on the slides). Furthermore, this irradiated palladium can also not be complexed by N,N-dimethyl-4-nitrosoaniline to be detected spectrophotometrically. The latter condition would be fulfilled by Pd(0), but not the former. Pd(0), unless it were in a noncatalytic form, should cause both Ni-P plating on the glass slide and Ni-P precipitation in the rinse water test.

Another possibility is that the u.v. light causes the air oxidation of Pd(II) to Pd(IV), which would only be stable while bound in a complex to the slide. This species would not be observed in the spectrophotometric Pd(II) test and might not be easily reduced to Pd(0). Both statements would also hold for an insoluble palladium oxide if it were the product of the irradiation of Pd(II). Further work is necessary before a clear choice among these 3 remaining possibilities [mechanisms (*ii*), (*iii*), and (*v*)] can be made, but mechanisms (*i*) (if Pd(0) is taken to be catalytic to Ni-P) and (*iv*) would seem to have been eliminated.

As indicated above, a coverage of 8×10^{15} atoms Pd/cm^2 is too much for u.v. light to make a difference in eventual metal plating. We find that the less the amount of initial Pd dried on the slides in procedure (*ii*), the better the "contrast" in plating between irradiated and nonirradiated surfaces. The lowest coverage shown in Table III, 0.6×10^{15} atoms Pd/cm^2 for nonirradiated surface and 0.7×10^{15} atoms Pd/cm^2 for irradiated surface, is still higher than the optimum, because better contrast was obtained with dipped slides [procedure (*i*)]. The coverage remaining after the rinse can only be estimated for dipped slides because the initial quantity of Pd(II) dried on was not determined. We observed that 0.04g water adheres to one side of a dry slide after draining. Assuming the activator bath behaves similarly, about 0.08 ml Pd(II) solution remains on the slide (on both sides) after immersion and drain. This amount of solution represents 0.0043 mg Pd(II), giving a coverage of 0.178 $\mu g/cm^2$ or 1.0×10^{15} atoms Pd/cm^2. Subtracting the quantity of Pd(II) appearing in the rinse water (see Table II, first entry) results in an estimated Pd coverage remaining after the rinse of 0.15×10^{15} atoms Pd/cm^2. This value compares very well with the value 0.17×10^{15} atoms Pd/cm^2 reported by Kelly and Vondeling (16). They used radiotracer techniques to obtain this number of Pd(II) ions remaining on TiO_2 after rinsing, following immersion in a Pd(II) solution 10 times as concentrated as ours.

Similarly, using the quantity of Pd(II) that rinsed off irradiated Sn(IV)·Pd(II) (second entry in Table II), an estimated value of 0.44×10^{15} atoms Pd/cm^2 can be calculated for the sum of Pd(II) ions remaining on the substrate plus Pd which has been changed to a state other than soluble Pd(II). Kelly and Vondeling (16) report a minimum coverage of Pd(0) for the ini-

tiation of Ni-P plating of 0.03×10^{15} atoms/cm^2. Because very little Ni-P plated on the irradiated slides, it is reasonable to assume that the coverage of potentially catalytic Pd ions remaining on them was of that order. It appears from this that the u.v. radiation affects 0.44×10^{15}-0.03×10^{15} atoms/cm^2 or about 0.4×10^{15} atoms Pd/cm^2 (about half a monolayer), rendering them incapable of becoming catalytic Pd(0) in the Ni-P plating bath. As noted above, thicker layers of palladium (*e.g.*, 8×10^{15} Pd/cm^2) were not rendered inactive by u.v. irradiation. This suggests that either u.v. radiation or another necessary reactant (*e.g.*, O_2) can affect at most a monolayer of Pd(II).

The results observed when Sn(II) served as the sensitizer were quite different from those for Sn(IV) (see Table II). Much less Pd(II) was obtained in the rinse water (by a factor of nearly 10), and the rinse water for the irradiated samples regularly contained about 40 ± 20% more Pd(II). These observations suggest that Sn(II) may well bind Pd(II) better than Sn(IV) does, and may, of course, even react with it, forming Pd(0). That more Pd(II) appears in the rinse water of the irradiated samples could be interpreted to mean that irradiated Sn(II) bonds Pd(II) less well than nonirradiated Sn(II) or that u.v. radiation breaks the bonds between Pd(II) and Sn(II), allowing Pd(II) to be washed off in the rinse step.

If, however, the same assumption used above for the amounts of Pd(II) solution that will adhere to a glass slide is made, the Pd coverage on irradiated and nonirradiated slides can be estimated as before. From the Sn(II) data in Table II, the Pd coverage of nonirradiated substrate is found to be 0.93×10^{15} atoms/cm^2 and for irradiated substrate 0.88×10^{15} atoms/cm^2. If the minimum coverage for initiation of Ni-P plating is 0.03×10^{15} atoms Pd/cm^2 (8), then more than enough Pd for plating remains even on the irradiated substrate. As before, this 0.88×10^{15} atoms/cm^2 does not just represent Pd(II) adhering to the slide, but includes any palladium that is no longer soluble Pd(II). If it is assumed that the effect of the u.v. light is only to break up the Sn(IV)·Pd(0) or Sn(II)·Pd(II) species, allowing the Pd(0) or Pd(II) to be washed off, then this 0.88×10^{15} atoms/cm^2 must be Pd(0), either adhering to the slide or in the rinse water, or Pd(II) adhering to the slide. Since little plating occurs on these irradiated slides, the coverage of Pd(0) plus Pd(II) must be at most 0.03×10^{15} atoms/cm^2 (8). Thus, most of the amount would have to be Pd(0) dispersed in the rinse water. This changed Pd(0) would not be measured in the spectrophotometric test, but it would surely shorten the Ni-P precipitation time. It can be seen from Table II, however, that the Ni-P precipitation time is indeed in line with the measured Pd(II) concentration. Therefore, it is obvious that u.v. light must have an additional effect on the Sn(II)·Pd(II) or Sn(IV)·Pd(0), perhaps creating, as in the Sn(IV) case, either Pd(IV), PdO, or noncatalytic Pd(0).

De Minjer and v.d. Boom (7), using radiotracer techniques, determined a Pd coverage of 0.23×10^{15} atoms/cm^2. They used fresh 0.1 g/l Sn(II) as the sensitizer solution, which was much more dilute than our ~7 g/l $SnCl_2$ and 7.8 g/l $SnCl_4$ sensitizer solutions, although the concentration of their palladium solution (0.1 g/l) was the same as ours. Meek (5) has also determined the surface Pd(II) concentrations obtained on Sn(II) sensitized substrates, using Rutherford scattering. The Pd concentrations ranged from 4×10^{15} atoms/cm^2 upwards, depending on the Sn coverage. The higher the Sn surface concentration, the higher the Pd surface concentration. Their $SnCl_2$ concentration was 16 g/l or about twice ours, and their $PdCl_2$ was also twice as concentrated as ours. In view of the dependence of Pd surface concentration on Sn surface concentration and on the fact that Meek's Sn(II) sensitizing solution was more concentrated than ours, it is not surprising that his Pd surface concentration (4×10^{15} atoms/cm^2) is higher than our estimated Pd surface concentration of $\sim 1 \times 10^{15}$ atoms/cm^2. That the Pd value obtained by de Minjer and v.d. Boom (0.23×10^{15} atoms/cm^2) is nearer our value for Sn(IV) as sensitizer (0.15×10^{15} Pd atoms/cm^2) might suggest that such dilute Sn(II) solutions as theirs deposit mostly Sn(IV) oxides on the substrates. It has been shown (2, 17) that much more concentrated Sn(II) solutions (10 g/l $SnCl_2$) deposit 2 Sn(IV) ions for every Sn(II) ion. As reported in Ref. (2), the solubility of Sn(IV) oxide is 10^{-4}M in a solution of pH 1 (corresponding to de Minjer's sensitizer bath) and the stannous solubility is at least 5M. Hence it would not be surprising if de Minjer's sensitizing layer did in fact contain mostly Sn(IV) oxide.

Acknowledgments

We wish to thank Dr. W. J. Holland and Messrs. L. Dupuis and R. Beaupre of our Chemistry Department for helpful advice and reagents for the palladium analysis. It is also a pleasure to acknowledge the skillful assistance of Miss M. K. H. Neo in some of the Pd analyses.

Manuscript submitted June 12, 1978; revised manuscript received Oct. 6, 1978.

Any discussion of this paper will appear in a Discussion Section to be published in the December 1979 JOURNAL. All discussions for the December 1979 Discussion Section should be submitted by Aug. 1, 1979.

Publication costs of this article were assisted by the National Research Council of Canada.

REFERENCES

1. J. F. D'Amico, M. A. DeAngelo, J. F. Hendrickson, J. T. Kenney, and D. J. Sharp, *This Journal*, **118**, 1695 (1971).
2. R. L. Cohen, J. F. D'Amico, and K. W. West, *ibid.*, **118**, 2042 (1971).
3. J. F. D'Amico, F. A. Litt, and M. A. DeAngelo, *ibid.*, **119**, 956 (1972).
4. J. F. D'Amico and M. A. DeAngelo, *ibid.*, **120**, 1469 (1973).
5. R. L. Meek, *ibid.*, **122**, 1478 (1975).
6. N. Feldstein and J. A. Weiner, *ibid.*, **120**, 475 (1973).
7. C. H. de Minjer and P. F. J. v.d. Boom, *ibid.*, **120**, 1645 (1973).
8. S. L. Chow, N. E. Hedgecock, M. Schlesinger, and J. Rezek, *ibid.*, **119**, 1013 (1972).
9. M. Schlesinger and B. K. W. Baylis, *ibid.*, **121**, 1461 (1974).
10. U.S. Pat. 3,011,920 (1961).
11. B. K. W. Baylis, A. Busuttil, N. E. Hedgecock, and M. Schlesinger, *This Journal*, **123**, 348 (1976).
12. B. K. W. Baylis, N. E. Hedgecock, and M. Schlesinger, *ibid.*, **124**, 346 (1977).
13. F. Möllers, H. J. Tolle, and R. Memming, *ibid.*, **121**, 1160 (1974).
14. B. K. W. Baylis, A. Busuttil, N. E. Hedgecock, and M. Schlesinger, *ibid.*, **123**, 1376 (1976).
15. F. D. Snell and C. T. Snell, "Colorimetric Methods of Analysis," p. 530, Van Nostrand Co., Princeton, N.J. (1948).
16. J. J. Kelly and J. K. Vondeling, *This Journal*, **122**, 1103 (1975).
17. R. L. Cohen and K. W. West, *ibid.*, **119**, 433 (1972).

Mass Transfer Aspects of Electrolysis by Periodic Currents

K. Viswanathan* and H. Y. Cheh**

Department of Chemical Engineering and Applied Chemistry, Columbia University, New York, New York 10027

ABSTRACT

A general solution was obtained for the mass transfer to a rotating-disk electrode under periodic current conditions. The solution was used to derive theoretical expressions for the calculations of limiting current densities of pulsed, ramp, and saw-tooth types of currents. Experimental verification of the theoretical results was made by using a ferri-ferrocyanide system under saw-tooth current conditions.

This paper is a result of our continuing effort to study mass transfer and electrochemical kinetics in a stirred solution under non-d-c electrolysis conditions. Electrolysis by pulsed current has been presented in two recent publications (1, 2). In this paper, the mass transfer aspects of electrolysis by periodic currents are presented. A general solution based on a simple diffusion model for the mass transfer rates is derived. The results are applied to pulsed, ramp, and saw-tooth current electrolyses.

Theoretical

Assume that a rotating-disk electrode is situated in an electrolyte medium of large extent and the electrode is rotating at a constant velocity. The radius of the disk electrode and the distance between the disk electrode and the counterelectrode are both large as compared to the thickness of the Nernst diffusion layer. The number of coulombs passed during an experiment is assumed to be so small that the depletion of the reacting species in the electrolyte can be neglected. An excess of supporting electrolyte is present so that electrical migration and nonfaradaic effects are negligible. Finally, the Schmidt number of the system is much larger than unity so that the diffusion layer lies well within the momentum boundary layer. Under these conditions, the concentration of reacting species is described by the convective-diffusion equation. However, it has been shown by Viswanathan *et al.* (1) that the simple diffusion model used by Cheh (3) can predict adequately the concentration of the reacting species at the electrode surface once the flux of the reacting species is specified. The simple diffusion model neglects the convective term in the differential equation, but replaces the boundary condition at infinity by an approximate condition at the outer edge of the Nernst diffusion layer. Consequently, the concentration of the reacting species is described by the following diffusion equation

$$\frac{\partial c}{\partial t} = D\frac{\partial^2 c}{\partial z^2} \qquad [1]$$

with the boundary conditions

$$c = c_\infty \qquad \text{at } t = 0 \text{ and all } z \qquad [2]$$

$$c = c_\infty \qquad \text{at } t > 0 \text{ and } z = \delta \qquad [3]$$

$$-D\frac{\partial c}{\partial z} = \frac{i(t)}{n\mathbf{F}} \qquad \text{at } t > 0 \text{ and } z = 0 \qquad [4]$$

where c is the concentration of the reaction ion, c_∞ is its concentration in the bulk of the solution, D is its diffusion coefficient, δ is the thickness of the Nernst diffusion layer, i is the applied current density, n is the number of electrons transferred during reaction, $\mathbf{F}$ is Faraday's constant, t is time, and z is the axial coordinate extending from the electrode surface.

The applied current density is assumed to be a repetitive function of time during the on-period of the cycle and its value is zero during the off-period of the cycle. Therefore, the applied current density in Eq. [4] can be represented mathematically by

$$i(t) = f(t) \qquad \text{at } 0 < t \leq t_1,\ t_2 < t \leq t_3, \text{ etc.} \qquad [5]$$

$$i(t) = 0 \qquad \text{at } t_1 < t \leq t_2,\ t_3 < t \leq t_4, \text{ etc.} \qquad [6]$$

where $f(t)$ is a given function of t, t_1, t_3, etc. representing the end of the on-period, with t_2, t_4, etc. representing the end of the off-period. The thickness of the Nernst diffusion layer is given by Levich (4) to be

$$\delta = 1.612\left(\frac{D}{\nu}\right)^{1/3}\left(\frac{\nu}{\omega}\right)^{1/2} \qquad [7]$$

where ν is the kinematic viscosity of the electrolyte and ω is the rotation speed.

It is convenient to rewrite Eq. [1]-[6] in a dimensionless form by defining the following dimensionless parameters

$$C^* = \frac{c}{c_\infty} - 1, \quad \tau = \frac{Dt}{\delta^2} \quad \text{and} \quad \zeta = \frac{z}{\delta} \qquad [8]$$

The dimensionless equation and the boundary conditions are

$$\frac{\partial C^*}{\partial \tau} = \frac{\partial^2 C^*}{\partial \zeta^2} \qquad [9]$$

and

$$C^* = 0 \qquad \text{at } \tau = 0 \text{ and all } \zeta \qquad [10]$$

$$C^* = 0 \qquad \text{at all } \tau \text{ and } \zeta = 1 \qquad [11]$$

$$\frac{\partial C^*}{\partial \zeta} = \frac{i(t)}{(i_{dc})_l} = \mathbf{F}(\tau)$$

$$\text{at } 0 < \tau \leq \tau_1,\ \tau_2 < \tau \leq \tau_3, \text{ etc. and } \zeta = 0 \qquad [12]$$

$$\frac{\partial C^*}{\partial \zeta} = 0 \quad \text{at } \tau_1 < \tau \leq \tau_2,\ \tau_3 < \tau \leq \tau_4, \text{ etc. and } \zeta = 0 \qquad [13]$$

where

$$\tau_k = Dt_k/\delta^2 \qquad [14]$$

$$(i_{dc})_l = n\mathbf{F}Dc_\infty/\delta \qquad [15]$$

$(i_{dc})_l$ is the d-c limiting current density and $\mathbf{F}(\tau)$ is the dimensionless current density.

Equation [9] subject to boundary conditions, Eq. [10]-[13] can be solved by the Fourier series method. The concentration of the reacting species during the first cycle has been obtained originally by Miller and Gordon (5) and more recently by Tokuda and Matsuda

* Electrochemical Society Student Member.
** Electrochemical Society Active Member.
Key words: periodic current electrolysis, mass transfer, rotating disk.

(6). The dimensionless concentration can be expressed as follows

During the on-period, $0 < \tau \leq \tau_1$

$$C^*(\tau, \zeta) = -2 \sum_{n=1}^{\infty} \exp(-\mu_n^2 \tau) \cos(\mu_n \zeta) \int_0^{\tau} \exp(\mu_n^2 \alpha) \mathbf{F}(\alpha) d\alpha \quad [16]$$

During the off-period, $\tau_1 < \tau \leq \tau_2$

$$C^*(\tau, \zeta) = -2 \sum_{n=1}^{\infty} \exp[-\mu_n^2 \tau] \cos(\mu_n \zeta) \int_0^{\tau_1} \exp(\mu_n^2 \alpha) \mathbf{F}(\alpha) d\alpha \quad [17]$$

where

$$\mu_n = (2n - 1)\pi/2 \quad [18]$$

and α is a dummy variable.

The general solution consists usually of a transient and a periodic term. Cheh (3) has shown that for most electrochemical systems which involve a large number of cycles the transient term is negligible after a few cycles and only the periodic-state solution is of practical importance.

By using the Fourier-series method for subsequent cycles, the dimensionless concentration at the electrode surface C^*_i, under a periodic state condition can easily be derived as

During the on-period, $\tau_{m-1} < \tau \leq \tau_m$

$$C^*_i = -2 \sum_{n=1}^{\infty} \exp[-\mu_n^2 (\tau - \tau_{m-1}) \left\{ \int_0^{\tau - \tau_{m-1}} \exp(\mu_n^2 \alpha) \mathbf{F}(\alpha) d\alpha \right\} - 2 \sum_{n-1}^{\infty} \exp[-\mu_n^2 (\tau - \tau_{m-1})] \left\{ \int_0^{\tau_1} \exp(\mu_n^2 \alpha) \mathbf{F}(\alpha) d\alpha \right\} \frac{\exp(-\mu_n^2 \tau_c)}{[1 - \exp(-\mu_n^2 \tau_c)]} \quad [19]$$

During the off-period, $\tau_m < \tau \leq \tau_{m+1}$

$$C^*_i = -2 \sum_{n=1}^{\infty} \exp[-\mu_n^2 (\tau - \tau_m)] \left\{ \int_0^{\tau_1} \exp(\mu_n^2 \alpha) \mathbf{F}(\alpha) d\alpha \right\} \frac{\exp(-\mu_n^2 \tau_1)}{[1 - \exp(-\mu_n^2 \tau_c)]} \quad [20]$$

where τ_c is the dimensionless cycle time and m is an odd number.

The solution as given in Eq. [19] and [20] is completely general in that $\mathbf{F}(\tau)$ may represent any continuous function of time. In electrochemical applications, there are three types of $\mathbf{F}(\tau)$ which have most commonly been used. These include the pulsed current, ramp current, and harmonic current electrolyses. $\mathbf{F}(\tau)$ is a constant for pulsed current electrolysis. It is a linearly increasing function of time for ramp current electrolysis. Finally, it is a sinusoidal function of time for harmonic current electrolysis. In this paper, only the first two cases are treated. The form of the applied currents is shown schematically in Fig. 1. In these instances, C^*_i reaches its lowest value at the end of the on-period. The limiting current density which is defined as the current density which would first bring the concentration of the reacting species to a zero value at the end of the on-period under the periodic state condition can be calculated from Eq.

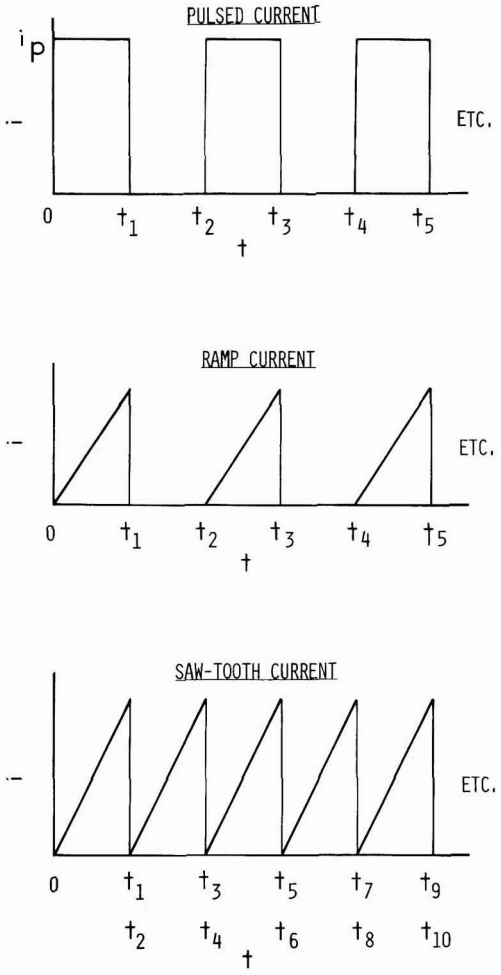


Fig. 1. Schematic diagrams of various current wave-forms

[19] and [20] by using the method outlined by Cheh (3). The results are presented as follows.

Pulsed current.—$\mathbf{F}(\tau)$ is given by

$$\mathbf{F}(\tau) = \frac{i_p}{(i_{dc})_1} = \text{constant} \quad [21]$$

where i_p is the applied pulsed current density. The pulsed limiting-current density is given by

$$\frac{(i_p)_1}{(i_{dc})_1} = \frac{1}{1 - 2 \sum_{n=1}^{\infty} \frac{1}{\mu_n^2} \frac{(\exp(-\mu_n^2 \tau_1) - \exp(-\mu_n^2 \tau_c))}{(1 - \exp(-\mu_n^2 \tau_c))}} \quad [22]$$

The application of the above equation has been discussed in some detail by Cheh (3) and more recently by Viswanathan *et al.* (1).

Ramp current.—$\mathbf{F}(\tau)$ and the ramp-limiting current density, $(i_r)_1$ are given by

$$\mathbf{F}(\tau) = \frac{kt}{(i_{dc})_1} = \left(\frac{k\delta^2}{D}\right) \frac{\tau}{(i_{dc})_1} \quad [23]$$

and

$$\frac{(i_r)_l}{(i_{dc})_l} = \frac{0.5}{\sum_{n=1}^{\infty} \frac{1}{\mu_n^2[1 - \exp(-\mu_n^2\tau_c)]} - \sum_{n=1}^{\infty} \frac{[1 - \exp(-\mu_n^2\tau_l)]}{\mu_n^4\tau_l[1 - \exp(-\mu_n^2\tau_c)]}} \quad [24]$$

where k is the rate of change of the applied current density. It is worth noting that for the present case since the applied current is a monotonically increasing function of time, the limiting current density is identified with an applied current density for which the surface concentration becomes zero at the end of the on-period. Should the rate of change of the applied current density be larger than that for the limiting current density, surface concentration may reach the value of zero at an earlier time within the on-period. It is also easy to show that as τ_l and τ_c tend to zero, the ratio $(\bar{i}_r)_l/(i_{dc})_l$ approaches unity where $(\bar{i}_r)_l$ is the time-averaged ramp-limiting current density over an entire cycle which is given by

$$\frac{(\bar{i}_r)_l}{(i_{dc})_l} = \frac{1}{\tau_c}\left[\int_0^{\tau_1} \mathbf{F}(\tau)\,d\tau\right]_l = \frac{1}{2}\frac{\tau_l}{\tau_c}\frac{(i_r)_l}{(i_{dc})_l} \quad [25]$$

Thus $(\bar{i}_r)_l$ represents in general the maximum over-all rate of electrolysis. Under the same conditions, Cheh (3) has shown that the maximum over-all rate of electrolysis for pulsed current case is equivalent to $\frac{\tau_l}{\tau_c}(i_p)_l$. Consequently, it is easy to see that $(i_r)_l$ is twice $(i_p)_l$ as τ_l and τ_c approach zero.

A common form which is used in practice is the application of saw-tooth current electrolysis. It is a special case of ramp current in that there is no off-period as indicated in Fig. 1. The ratio $(\bar{i}_r)_l/(i_{dc})_l$ *vs.* τ_c is plotted in Fig. 2 as a function of the duty cycle which is defined by the ratio τ_l/τ_c. The maximum rate of saw-tooth current electrolysis, $(\bar{i}_{st})_l$, is represented in Fig. 2 by the curve for which the duty cycle τ_l/τ_c is unity.

Experimental

Experimental verification of Eq. [22] which is the result of pulsed current electrolysis has been reported by Cheh (3) and by Viswanathan *et al.* (1). In this paper, we report the saw-tooth limiting current density experiments in a 0.01M ferricyanide, 0.01M ferrocyanide, and 0.5M K_2SO_4 solution. Certified ACS chemicals and distilled water were used in solution preparation. An Au-disk electrode of 0.461 cm^2 area was used and all experiments were carried out at 22° ± 1°C. The experimental set-up and the physical properties of the electrolyte have been reported by Viswanathan *et al.* (1). In short, the saw-tooth current was applied by feeding the triangular wave output of a Tacussel GSTP2 function generator to a Kepco PC2 power supply. The current characteristics were determined by measuring the voltage drop across a 1000Ω standard resistor connected in series to the cell. The results were recorded on a Tektronix 5103N dual trace oscilloscope. The potential difference between the RDE and the calomel reference electrode was recorded on the same oscilloscope. The only difficulty which was encountered in the present experiment was that the Tacussel GSTP2 function generator did not have the capability of producing a zero fall-period. In this work, the fall-period was set at 0.1 msec and the rise-period ranged from 50 to 200 msec, while the rotation speeds were maintained at 400, 900, and 1600 rpm. Consequently, the dimensionless cycle period, τ_c, varied from 0.0689 to 1.17.

The experimental procedure consisted of fixing a cycle period and increasing the applied current density gradually. The instantaneous saw-tooth limiting current density was measured by observing a sudden jump of the electrode potential at the end of the cycle period. The average saw-tooth limiting current density is then equal to half of the corresponding instantaneous value.

Experimental as well as theoretical results are presented in Fig. 3. The unfilled symbols represent anodic experiments, whereas the filled ones represent cathodic experiments. A comparison of these results shows that reasonable agreement has been obtained. The maximum discrepancy between the calculated values and the experimental values is 8% and the average error is about 3%.

Conclusions

A general solution based on a simple diffusion model was obtained for the concentration field of a reacting species in a rotating-disk system under periodic current conditions. Specifically, expressions for the limiting current density were derived for pulsed, ramp, and saw-tooth types of curents.

Experimental limiting current density measurements were made in a ferri-ferrocyanide system by applying the saw-tooth type of currents. A reasonable

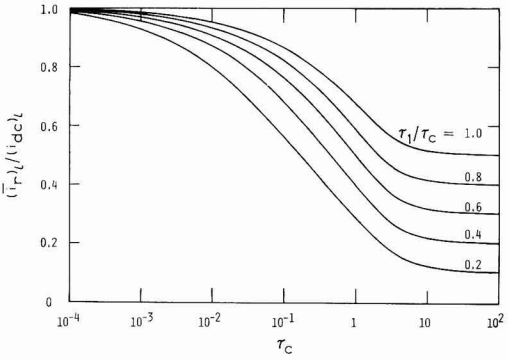


Fig. 2. Maximum rate of electrolysis using ramp currents

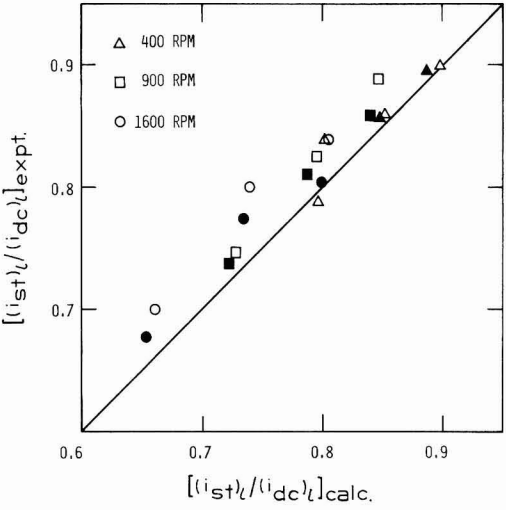


Fig. 3. Comparison between the calculated and the experimental values for the maximum rate of electrolysis using saw-tooth currents. (Filled symbols, cathodic; unfilled symbols, anodic).

agreement was obtained between the experimental measurements and theoretical predictions.

Acknowledgment

The authors wish to thank Dr. Samuel Ruben for his generous endowment of a Bergen Davis Fellowship at Columbia University, and one of us (K.V.) was the recipient of the Fellowship during the course of this work.

Manuscript submitted June 13, 1978; revised manuscript received Aug. 5, 1978.

Any discussion of this paper will appear in a Discussion Section to be published in the December 1979 JOURNAL. All discussions for the December 1979 Discussion Section should be submitted by Aug. 1, 1979.

SYMBOLS

c	concentration of reacting ion
c_z	bulk concentration of reacting ion
C^*	dimensionless concentration defined in Eq. [8]
C^*_i	periodic state concentration of the reacting ion
D	diffusion coefficient of reacting ion
$f(t)$	an arbitrary function of current density
$\mathbf{F}$	Faraday's constant
$\mathbf{F}(\tau)$	dimensionless current density defined by Eq. [12]
$i(t)$	current density
$(\bar{i}_r)_l$, $(\bar{i}_{st})_l$	average ramp limiting-current density, average saw-tooth limiting-current density
$(i_p)_l$, $(i_{dc})_l$	pulsed limiting-current density, d-c limiting-current density
k	rate of change of current density
m	an odd index
n	number of electrons transferred in reaction
t	time
t_n	defined in Fig. 1
z	axial coordinate

Greek

α	a dummy variable
δ	thickness of the Nernst diffusion layer
ζ	dimensionless axial coordinate defined in Eq. [8]
ν	kinematic viscosity
τ	dimensionless time defined in Eq. [8]
τ_1, τ_c etc.	dimensionless on-period and cycle time
ω	rotation speed

REFERENCES

1. K. Viswanathan, M. A. Farrell Epstein, and H. Y. Cheh, *This Journal*, **125**, 1772 (1978).
2. K. Viswanathan and H. Y. Cheh, *ibid.*, **125**, 1616 (1978).
3. H. Y. Cheh, *ibid.*, **118**, 551 (1971).
4. V. G. Levich, "Physiochemical Hydrodynamics," Prentice-Hall, Englewood Cliffs, N.J. (1962).
5. W. L. Miller and A. R. Gordon, *J. Phys. Chem.*, **35**, 2785 (1931).
6. K. Tokuda and H. Matsuda, *J. Electroanal. Chem. Interfacial Electrochem.*, **82**, 157 (1977).

Electrochemical Reduction of Benzal Chloride in the Presence of Carbon Dioxide

S. Wawzonek* and Jan M. Shradel

Department of Chemistry, The University of Iowa, Iowa City, Iowa 52242

ABSTRACT

The electrochemical reduction of benzal chloride in the presence of carbon dioxide in dimethylformamide formed mandelic acid, benzyl mandelate, and benzyl phenylacetate. The maximum yield of mandelic acid was 9.8% if the reduction was carried out at −2.0V and the acid was isolated as the methyl ester. Studies on the mechanism of formation of mandelic acid or its benzyl ester indicated that the intermediate α-chlorophenylacetate ion formed an α-lactone which reacts with moisture in the dimethylformamide and gives the products isolated. Phenylcarbene as an intermediate was probably a minor contributor in the formation of mandelic acid.

The electrochemical reduction of benzal chloride in the presence of carbon dioxide in dimethylformamide was investigated as a possible method for the preparation of phenylmalonic acid. Previous work on aryl and alkyl halides has involved studies of the electrochemical carboxylation of bromobenzene (1), benzyl chloride (2, 3), allyl chloride (3), bis-halomethylaromatics (4), and n-butyl halides (4). No reports on the reductive carboxylation of gem-dihalides have appeared.

Experimental

Electrolyses were carried out in a cell made from an 800 ml beaker fitted with a tube with a fritted glass disk for dispersing the carbon dioxide over the mercury pool cathode which was 7 cm diam. The anode compartment consisted of an unglazed porcelain cup 5.5 cm diam and 8 cm high. The anode consisted of a platinum mesh cylinder. The reference electrode was a mercury pool in dimethylformamide containing 0.2*M* tetrabutylammonium bromide. The cell was capped with a tight-fitting rubber stopper with appropriate openings. All electrolyses were carried out at controlled potentials using a Princeton Applied Research Model 371 Potentiostat.

* Electrochemical Society Active Member.
Key words: mandelic acid, dimethylformamide, carboxylation.

Dimethylformamide.—This solvent was dried over barium oxide and fractionally distilled from barium oxide through a zig-zag column bp 76°-78°C (43 Torr).

Benzal chloride.—This compound was purified by fractional distillation using a Vigreau column; bp 111°-112°C (0.29 Torr); n_D^{20} 1.5504.

Methyl mandelate.—A solution of benzal chloride (8.05g, 0.05 mole) in dimethylformamide (350 ml) containing tetrabutylammonium bromide (70g) was degassed for 45 min with carbon dioxide and then electrolyzed at a potential of −2.00V for 46.5 hr while carbon dioxide was passed through the solution. The initial current of 0.5A decreased to 0.09A during this period. The catholyte was separated from the mercury, treated with excess methyl iodide (20 ml), and the resulting solution was allowed to stand at room tem-

perature for 23 hr. Removal of the dimethylformamide under reduced pressure gave a solid which was triturated with ether (300 ml) and filtered. The solid was washed further with ether and the combined ether filtrates were washed sequentially with water, dilute hydrochloric acid, sodium bicarbonate solution, sodium bisulfite solution, and water. Removal of the ether after drying gave a brown oil (3.89g) which showed six components using TLC analysis on silica gel with benzene as the eluant. The oil upon distillation at 95°-170°C (0.6 Torr) gave 1.64g of a light yellow liquid. Preparative layer chromatography on silica gel using a mixture of ether (5.5 ml) and methylene chloride (94.5 ml) as a solvent gave methyl mandelate (0.82g), mp 54°-55° (5), as the major component. No dimethyl phenylmalonate could be found in the mixture.

Effect of water on the electrolysis.—A solution of benzal chloride (6.03g) in dimethylformamide (350 ml) containing tetrabutylammonium bromide (48.3g) and water (0.67g) was electrolyzed at −1.50V in the presence of carbon dioxide for 41.7 hr. The initial current of 0.135A decreased to a final value of 0.0001A.

The catholyte was separated from the mercury and the dimethylformamide was removed under reduced pressure. The resulting solid was treated with water (200 ml) and extracted with ether (200 ml).

The aqueous layer was concentrated to 100 ml and acidified with sulfuric acid. Extraction of the solution with ether (200 ml) gave a solid which, when recrystallized from a mixture of benzene and petroleum ether (bp 60°-68°), gave mandelic acid (0.13g), yield, 2.31%, mp 117°-118°C. A similar electrolysis carried out in the absence of water gave 0.32g (5.68%) of mandelic acid.

The original ether extract of the catholyte gave a light brown oil which upon distillation gave a liquid (0.97g) boiling at 145°-180°C (1 mm).

Preparative layer chromatography on silica gel using methylene chloride as a solvent gave benzyl phenylacetate (0.54g) (12.9%) and benzyl mandelate (0.14g) (3.12%); mp 91°-92°C (5). In the absence of water using a similar electrolysis the yields of benzyl mandelate and benzyl phenylacetate were 2.3 and 1.9%, respectively.

1-Phenyl-2,2,3,3-tetramethylcyclopropane.—*(i)* A solution of benzal chloride (5.64g) and tetramethylethylene (6.50g) in dimethylformamide (350 ml) containing tetrabutylammonium bromide (45.14g) was electrolyzed at −1.70V for 89.5 hr. The initial current of 0.062A decreased to a final value of 0.025A in this period.

The catholyte and anolyte were combined and extracted with pentane; tetramethylethylene and its dibromide were obtained as products. The resulting dimethylformamide solution was evaporated to dryness; the distillate by GLC analysis proved to be solely dimethylformamide. The solid obtained was triturated with ether which gave 2.34g of a liquid after treatment sequentially with water, dilute hydrochloric acid, and sodium bicarbonate solution. Analysis by gas chromatography (column, 6 ft × 0.125 in; 15% Apiezon L on 100-200 mesh Chromosorb P at 130°-250°C programmed at 6°C/min; injection port 305°, detector 325°) showed several peaks. The peak at 9.12 min was identified as 1-phenyl-2,2,3,3-tetramethylcyclopropane by comparison with an authentic sample.

(ii) A solution of 1-chloro-1-phenyl-2,2,3,3-tetramethylcyclopropane (2.0g) (6) in absolute ether (12 ml) was added to a solution of sodium (0.60g) in liquid ammonia (25 ml) and the solution was allowed to stir for 30 min. The resulting solution was cooled to −78°C and treated cautiously with solid ammonium chloride (2.0g). Removal of the ammonia was followed by the addition of water and more ether. The ether layer gave an oil which upon distillation gave 1.20g of 1-phenyl-2,2,3,3-tetramethylcyclopropane; bp 120°-121°C (4 Torr; n_D^{20}, 1.5057; *IR* (neat) 6.23 (C_6H_5), 10.60 cyclopropane), 14.26 (C_6H_5) μ; NMR ($CDCl_3$) δ 0.93 (s, 6H, $2CH_3$), 1.25 (s, 6H, $2CH_3$), 1.51 (s, 1H, CH), 7.12 (s, 5H, C_6H_5); mass spectrum m/e (relative intensity) 174 (57.4), 159 (99.4), 117 100).

Analysis.—Calculated for $C_{17}H_{18}$: C, 89.59; H, 10.41. Found: C, 89.60; H, 10.32.

Benzyl α-chlorophenylacetate.—A mixture of benzyl mandelate (3.0g) and pyridine (1 ml) was treated with thionyl chloride (4 ml) and allowed to stand at room temperature for 12 hr, and was then heated at 100° for 1 hr. The resulting solution was treated with ice water and extracted with ether. Removal of the ether gave an oil which on distillation gave benzyl α-chlorophenylacetate (1.16g); bp 180°C (2 Torr); n_D^{20}, 1.5652; *IR* (neat) 5.68 (CO), 8.63 (C-O) μ; NMR ($CDCl_3$) δ 5.10 (s, 2H, CH_2-O), 5.35 (s, 1H, CHCl), 7.00-7.60 (m, 10H, aromatic); mass spectrum m/e (relative intensity) 260 (1.2), 125 (79), 91 (100).

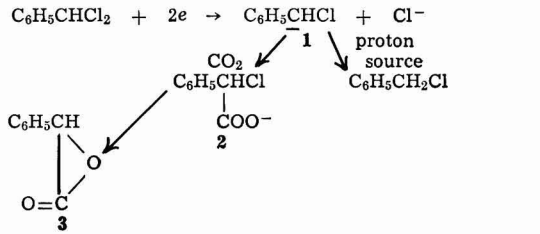
Analysis.—Calculated for $C_{15}H_{13}O_2Cl$; C, 69.10; H, 5.02. Found: C, 68.94; H, 5.02.

Results

The electrochemical reduction of benzal chloride in the presence of carbon dioxide in dimethylformamide gave mandelic acid, benzyl mandelate, and benzyl phenylacetate as the main products; no phenylmalonic acid or its derivatives was detected. The maximum yield of mandelic acid obtained was 9.8% if the electrolysis was carried out at −2.0V, and the methyl ester was formed by treating the resulting catholyte with methyl iodide. The potential was chosen on the basis of polarographic data for benzal chloride; two two-electron reduction waves are reported at −1.43 and −1.80V (Hg pool), respectively, in a 0.175*M* tetrabutylammonium bromide solution in dimethylformamide (7).

The formation of mandelic acid suggests that traces of water present in dimethylformamide are involved in the formation of this compound. Such traces of moisture are difficult to exclude from dimethylformamide, which is mildly hygroscopic, in normal operation requiring long periods of electrolysis. The use of a closed system or a dry box, which would minimize this complication, was not investigated.

Further studies were carried out to identify the intermediate which would react with water and form mandelic acid. Since the reduction proceeds stepwise, benzal chloride is converted to the anion **1**



This anion **1** can react either with carbon dioxide and form the α-chlorophenylacetate anion **2** or with a proton source and give benzyl chloride. The α-chlorophenylacetate anion can cyclize and form an α-lactone **3** which would react rapidly with water and form mandelic acid. Such a structure has been postulated as an intermediate in explaining the first-order kinetic for the hydrolysis of α-bromopropionate ion and the formation of lactic acid with retention of configuration (8). Supporting evidence for this step is the sole isolation of mandelic acid as its methyl ester from the electrolysis at −2.00V. At this potential, benzyl chloride is reduced to the benzyl carbanion which may

form toluene on protonation or phenylacetic acid on carboxylation.

In electrolyses at −1.50V, benzyl chloride is not rereduced and it interacts with anion species produced; products isolated were mandelic acid, benzyl mandelate, and benzyl phenylacetate in yields of 5.68, 2.3, and 1.9%, respectively.

The benzyl mandelate isolated results from a reaction of anion **1** with mandelic acid followed by alkylation with benzyl chloride of the mandelate ion formed

$$\underset{\mathbf{1}}{C_6H_5\overline{C}HCl} + C_6H_5CHOHCOOH \rightarrow C_6H_5CH_2Cl + C_6H_5\underset{OH}{\underset{|}{C}}HCOO^-$$

The formation of benzyl phenylacetate would involve alkylation of the anion of α-chlorophenylacetic acid, **2**, followed by an electrochemical reduction of the resulting benzyl α-chlorophenylacetate. This compound polarographically shows two reduction waves at −0.66 and −1.01V (Hg pool) in dimethylformamide containing 0.2*M* tetrabutylammonium bromide. The first wave increased with time at the expense of the second wave and is for the corresponding bromo compound formed by a displacement reaction of bromide ion on benzyl α-chlorophenylacetate.

Benzyl α-chlorophenylacetate is not a precursor of the corresponding mandelate. Direct solvolysis of benzyl α-chlorophenylacetate water does not occur since no mandelate was formed when the chloro ester was treated with water in dimethylformamide containing tetrabutylammonium bromide at room temperature for 45.5 hr.

The possibility that benzyl mandelate is formed from the chloro compound by a displacement reaction involving hydroxide ion formed from the water is precluded by the ease of electrochemical reduction of the chloro compound. The reduction potential (−1.01V) is more positive than that of benzal chloride (−1.43) and the concentration of benzyl α-chlorophenylacetate would therefore be practically nonexistent under the conditions of the electrolysis.

The reactions proposed for the formation of the products were substantiated further by the results obtained by carrying out the electrolysis of benzal chloride at −1.50V in the presence of water. Using a molar ratio of 0.12 mole of water to 0.037 mole of benzal chloride gave yields of 2.93% of mandelic acid, 3.12% of benzyl mandelate, and 12.9% of benzyl phenylacetate, respectively. These results indicate that protonation of the intermediate **1** to benzyl chloride becomes important and the resulting high concentration of benzyl chloride allows the alkylation reaction of **2** to compete favorably with the cyclization of **2** to the α-lactone **3**. The yields of benzyl phenylacetate and benzylmandelate are therefore higher than those obtained in the absence of water. The yield of mandelic acid is correspondingly lower.

Another intermediate considered which could lead to mandelic acid is phenylcarbene **4**. This species would be formed by an elimination of chloride ion from **1** and would be expected to react

$$\underset{\mathbf{1}}{C_6H_5\overline{C}HCl} \rightarrow \underset{\mathbf{4}}{C_6H_5CH} \rightarrow \underset{\mathbf{3}}{C_6H_5CHCO}$$

with carbon dioxide and form **3**. Its formation is minimal since electrolysis of benzal chloride in the presence of tetramethylethylene at −1.70V gave only trace amounts of 1-phenyl-2,2,3,3-tetramethylcyclopropane. α-chlorophenylacetate anion therefore must be the main precursor of the α-lactone and, subsequently, mandelic acid.

Acknowledgments

This paper is based on the Ph.D. Thesis of J. M. Shradel. The research was supported by National Science Foundation under Grant No. MP S74-17667. The authors wish to thank N.S.F. for this support.

Manuscript submitted July 11, 1978; revised manuscript received Sept. 6, 1978.

Any discussion of this paper will appear in a Discussion Section to be published in the December 1979 JOURNAL. All discussions for the December 1979 Discussion Section should be submitted by Aug. 1, 1979.

Publication costs of this article were assisted by National Science Foundation.

REFERENCES

1. S. Wawzonek and J. H. Wagenknecht, "Polarography," Vol. 2, p. 1035, G. J. Hills, MacMillan (1964).
2. S. Wawzonek, R. C. Duty, and J. H. Wagenknecht, *This Journal*, **111**, 74 (1964).
3. M. M. Baizer and J. L. Chruma, *J. Org. Chem.*, **37**, 1951 (1972).
4. D. A. Tysee, J. H. Wagenknecht, M. M. Baizer, and J. L. Chruma, *Tetrahedron Lett.*, 4809 (1972).
5. W. F. Barthel, J. Leon, and S. A. Hall, *J. Org. Chem.*, **15**, 485 (1954).
6. G. L. Closs and L. E. Closs, *J. Am. Chem. Soc.*, **82**, 5723 (1960).
7. S. Wawzonek and R. C. Duty, *This Journal*, **108**, 1135 (1961).
8. W. A. Cowdrey, E. D. Hughes, and C. K. Ingold, *J. Chem. Soc.*, 1243 (1937).

Electrochemical and Secular Syntheses of Derivatives of O-Carboxymethyltartronic Acid (1)*

R. C. Hallcher, D. A. White,** and M. M. Baizer**

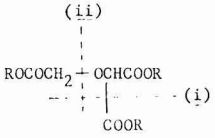
Monsanto Company, Corporate Research Laboratories, St. Louis, Missouri 63166

ABSTRACT

Routes to O-carboxymethyltartronate derivatives (**I**) involving (*a*) electrochemical carboxylation of diglycolic acid N-methylimide (**II**) and (*b*) chemical carboxylation (using a carbon dioxide equivalent) of esters of diglycolic acid (**III**) have been demonstrated. In route (*a*) tetraethyl ethenetetracarboxylate (**IV**) or 2,2'-di-*t*-butylazobenzene (**V**) were used as probases and after reaction the reduced species were reconverted to the probase by anodic (**VI**) or air (**VII**) oxidation. The product from **II** was identified as a *bis*-carboxylate (**VIII**) which on saponification or alkylation lost one molecule of carbon dioxide, giving **Ia** or **IX**, respectively.

The "world-wide efforts to find organic replacements for detergent phosphates" have been reviewed recently (2). The desired compounds must be effective, biodegradable, and inexpensive. Polycarboxylates, particularly ether polycarboxylates, promise to fulfill these requirements; within the latter category, trisodium O-carboxymethyltartronate (**Ia**) has received considerable attention.

Inspection of the structure of **I** indicates that it might be synthesized from (*i*) diglycolic acid (**IIIa**) derivatives and carbon dioxide or (*ii*) tartronic acid and acetic acid moieties. **Ia** has been prepared by direct carboxylation of disodium (**IIIb**) or dipotassium diglycolate in the presence of basic catalysts under severe conditions (3).

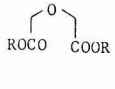


I

a, R = Na
b, R = H
c, R = C_2H_5
d, R = *n*-C_4H_9

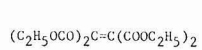


II

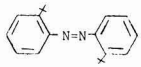


III

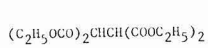
a, R = H
b, R = Na
c, R = C_2H_5
d, R = n-C_4H_9



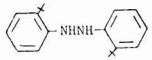
IV



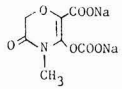
V



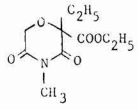
VI



VII



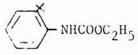
VIII



IX



X



XI

A phenoxide-mediated carboxylation of **II** followed by saponification and recovery of methylamine has also been disclosed (4); multimolar equivalents of phenoxide and a heavy recycling of phenol were involved.

The technological difficulties in these procedures prompted the quest for alternative routes to **Ia**. The work reported here involves (*a*) deprotonation of **II** by electrogenerated bases in the presence of carbon dioxide and (*b*) nonelectrochemical carboxylation of **IIIc** or **d** by a carbon dioxide equivalent. Both are illustrative and not exclusive examples of the respective approaches. In discussing both routes in one paper it is intended that organic electrochemists be provided with an unusual direct comparison of two different techniques for achieving the same objective.

The principles involved in reducing a probase (PB) to an electrogenerated base (EGB^-), using the latter to deprotonate a carbon acid (RH) to its anion (R^-) in the presence of carbon dioxide and regenerating PB from EGBH, have been discussed (5a). EGB^- must be of adequate basic strength and must not react irreversibly with carbon dioxide or PB. Application of these principles to carboxylation of a very weak carbon acid, such as **II**, has not been reported previously. Examples in which PB is **IV** or **V** are reported here.

As yet, attempted carboxylation (electrochemical or otherwise) of diglycolate esters (**IIIc, d**) have given only low yields of product. The esters are apparently less acidic than **II**. We have, therefore, examined the use of carbon dioxide equivalents, such as oxalate esters,[1] in the carboxylation of **IIIc, d**. Such equivalents can, of course, be used in the presence of stronger bases, which react irreversibly with carbon dioxide.

Experimental

Materials.—Esterification of diglycolic acid (Aldrich Chemical Company, Milwaukee, Wisconsin) with ethanol (benzenesulfonic acid catalyst) or butanol (HCl catalyst, azeotropic removal of water) afforded diethyl [70%; bp 67°-68° (0.05 mm)] or dibutyl [95%; bp 98°-99° (0.05 mm)] diglycolate. Esterification of oxalic acid dihydrate (Mallinckrodt, Incorporated, St. Louis, Missouri) and butanol (no catalyst, azeotropic removal of water) gave dibutyl oxalate [98%; bp 58°-59° (0.05 mm)]. The N-methylimide of diglycolic acid was supplied by F. W. Morgan (Monsanto Company, St. Louis, Missouri). Electrogenerated base precursors were prepared as described previously (5b). Sodium alkoxides were prepared by dissolution of sodium (1.0 g-atom) in the alcohol (1 liter). The butanol solution so obtained weighed *ca.* 770g and aliquots by weight were used. The ethanol solution was stripped until a

* Dedicated to the memory of Palle Iversen.
** Electrochemical Society Active Member.
Key words: organic, electrolysis, reduction.

[1] The condensation of esters with oxalate esters (6) and the thermal decarbonylation of the ketoesters formed (7, 8) have been reported previously. Work with other carbon dioxide equivalents will be reported elsewhere.

free-flowing powder, containing 0.3-1.0 mole of ethanol per mole of ethoxide, was obtained (completely ethanol-free sodium ethoxide was, surprisingly, not reactive). Acetonitrile and the supporting electrolyte were purified as described previously (5a). The electrochemical work was carried out in a nitrogen-filled dry box. Materials were dried *in vacuo* over phosphorus pentoxide before being transferred to the dry box.

Equipment.—The potentiostat used was a Wenking Model 70HVI-90 and the total current passed was measured with an Electrocount integrator. Analyses were obtained using a Varian T60 or A56/60 NMR spectrometer or by GLC using a 6 ft × ¼ in. stainless steel column packed with 3% OV-17 on Chromosorb W (85/100 mesh) or similar column.

Analytical procedures.—Analysis of saponified products (esters or imide) was carried out by NMR examination[2] of dry sodium salts dissolved in ice-cold 20% DCl in D_2O (Aldrich). Sodium acetate was added as a shift and integration standard. Methylene resonances were observed for **IIIb** and **Ia** at 2.20 and 2.32 ppm downfield from the sodium acetate peak (addition of *ca.* 2.1 ppm converts to Me_4Si based scale). The methine resonance of **Ia** was observed at 2.85 ppm.

Elemental analyses and NMR spectra of the products are reported in Tables I and II.

Electrocarboxylation of **II** *using probase* **IV**.—A solution of sodium bromide (3g), 18-crown-6 (2g; Aldrich[3]), and tetraethylammonium bromide (2g) in acetonitrile (150 ml) was the solvent/electrolyte system, and a typical glass H-cell was used. The catholyte (75 ml) contained **IV** (3.16g; 0.01 mole) and **II** (0.94g; 0.015 mole). The anolyte (75 ml) contained **VI** (3.18g; 0.01 mole) and sodium carbonate (4.24g; 0.04 mole). The cathode was a mercury pool (23 cm^2), the anode a platinum foil (6.5 cm^2). During reduction at −1.2V (*vs.* SCE) (initial current 180 mA, final 2 mA) in the presence of carbon dioxide at 45°-50°, **VIII** precipitated from the catholyte and it was removed by filtration. The anolyte was mixed with dry alumina (5g) for 1 hr and the carbonate, bicarbonate, and alumina were then removed by filtration. The filtered anolyte now contained probase **IV** and was charged with **II** (1.94g) and was used as the catholyte in the next electrolysis. The filtered catholyte was charged with sodium carbonate and used as the anolyte. On completion of a second similar electrolysis, product isolation, drying, and anolyte-catholyte switch were repeated. The whole process was repeated once more. Samples of the three batches of product were saponified and analyzed for **Ia**. Current efficiencies (yields) of 70% (87%), 58% (85%), and 62% (88%) were found.

Electrocarboxylation of **II** *with probase* **V**.—In the cell used above the catholyte and anolyte were each 0.2M tetraethylammonium chloride in acetonitrile (75 ml). Compound **II** (0.52g; 0.004 mole) was placed in the former and hexene (5 ml) in the latter. The cathode potential was set at −1.9V (*vs.* SCE) and anhydrous carbon dioxide was bubbled through the catholyte. Compound **V** (0.588g; 0.002 mole) in acetonitrile (10 ml) was added dropwise to the catholyte at a rate such that the current did not exceed 100 mA. After completion of the addition, electrolysis was continued until the current fell to 5 mA. Ethyl iodide (5 ml) was added to the catholyte and the mixture was stirred overnight. The solvent was evaporated, the residue triturated with ether, and the solids removed by filtration. Analysis of the evaporated ether extract showed that **IX** was formed in 58% current efficiency. Due to air oxidation during workup **V** was also found, but only *ca.* 60% of the expected amount. The remainder of this compound was detected as an approximately equimolar mixture of 2-*t*-butylaniline (**X**) and ethyl 2-*t*-butylphenylcarbamate (**XI**).

Chemical carboxylation of **IIIc**.—A mixture of **IIIc** (57g; 0.3 mole) and diethyl oxalate (43.8g; 0.3 mole) was added over 1 hr to $C_2H_5ONa \cdot C_2H_5OH$ (from Na; 0.33 g-atom) suspended in ether (500 ml) under nitrogen at 5°C. Pentane (500 ml) was added to the pale yellow solution and a gummy semisolid resulted. After trituration, the salt was filtered and washed with pentane. It amounted to 60.5g.

Hydrochloric acid (1.0*N*; 200 ml) was added to a mixture of ether (200 ml) and the salt (59.9g) dissolved in water (250 ml). The yellow color of the salt was discharged and some white solid was formed. Filtration afforded diethyl 2,4-dihydroxyfuran-2,5-dicarboxylate as a white crystalline solid (6.4g; 0.026 mole; mp 189°-190°; lit. (9) mp 189°). The aqueous layer of the filtrate was saturated with sodium chloride. The ether was separated and the aqueous layer was extracted twice with ether. The combined ether solutions were dried ($CaSO_4$), filtered, and evaporated to give the crude ketotriester (39.9g). This material (39.6g) and decolorizing charcoal (0.5g; this was not entirely necessary but led to smoother carbon monoxide evolution) were heated at 175°-177° for 28 hr. A weight loss of 5.6g was noted, and the product was only

[2] This NMR analysis method was developed by F. W. Morgan.
[3] The crown ether is added to solubilize the sodium bromide.

Table I. Elemental analyses and molecular weight (by mass spectrometer) data

Compound	Formula	Found C (%)	Found H (%)	Found M	Calculated C (%)	Calculated H (%)	Calculated M
Ic	$C_{11}H_{18}O_7$	50.3	6.8	262	50.4	6.9	262
Id*	$C_{17}H_{30}O_7$	59.2	8.8	346	58.9	8.7	346
IX*, †	$C_{10}H_{13}NO_5$	—	—	229	52.4	6.6	229
XIVa	$C_{10}H_{12}O_7$	49.3	4.9	244	49.2	5.0	244
XIVb*	$C_{14}H_{20}O_7$	56.4	7.0	300	56.0	6.7	300

* New compound.
† This compound was not obtained free of traces of crown ether and good elemental analyses were not obtained.

Table II. NMR spectra*

Compound	Ester CH_3	Ester CH_2	NMR Resonances*,† Methylene	Methine	Other
Ic	1.27 (3H, t) 1.30 (6H, t)	*ca.* 4.2 (6H, 2q)	4.30 (2H, s)	4.72 (1H, s)	
Id	0.93 (9H, t)	*ca.* 1.5 (12H, m) 4.10 (3H, t) 4.17 (6H, t)	4.28 (2H, s)	4.72 (1H, s)	3.18 (3H, s, N-CH_3), 1.72 (2H, t, CH_2), 0.95 (3H, q, CH_3)
IX	1.25 (3H, t)	4.2 (2H, q)	4.52 (2H, s)		
XIVa	1.27 (6H, t)	4.10 (4H, q)			10.30 (2H, s) (OH)‡
XIVb	0.97 (6H, t)	*ca.* 1.6 (8H, m) 4.33 (4H, t)			7.35 (2H, s) (OH)‡

* Measured in $CDCl_3$ [except **XIVa** (d^6 — DMSO)] with internal $(CH_3)_4Si$ at 60 MHz. Shifts are shown in ppm downfield from standard. The relative area, multiplicity are shown in parentheses.
† Abbreviations: s = singlet, t = triplet, q = quartet, m = multiplet.
‡ Resonance was broad and exchanged with D_2O.

slightly discolored. The charcoal was removed by filtration, using ether for washing. The filtered solution was washed with sodium bisulfite solution [from sodium metabisulfite (1.9g; 0.01 mole) and water (20 ml)] to remove any unreacted ketotriester. The ether solution was dried ($CaSO_4$), filtered, and evaporated. The residual liquid (31.8g) was distilled to give a colorless liquid [27.0g; bp 110°-120° (0.1 mm)] from which further furan crystallized. This was removed by filtration (0.7g; mp 189°-190°) and the liquid was redistilled to give pure **Ic** [24.4g; 0.093 mole; bp 103°-105° (0.05 mm)]. The yield based on **IIIc** is 32%.

Chemical carboxylation of **IIId**.—Sodium butoxide in butanol (77.0g; 0.1 mole) and **IIId** (24.6g; 0.1 mole) were added simultaneously to dibutyl oxalate (40.4g; 0.2 mole) at −5° under nitrogen over 1 hr. Butanol was removed at 30°-40° *in vacuo* and collected in a trap at −78° (77.5g; calculated 82.2g). The yellow liquid residue was cooled to 0°C and hydrochloric acid (1.0*N*; 105 ml) was added over 20m. The organic layer was separated. The aqueous layer was extracted twice with methylene chloride. The combined organic layer and washings were dried ($CaSO_4$), filtered, and evaporated, giving a pale yellow liquid (58.5g; calculated 57.6g). This was heated under nitrogen at 200°-205° for 16 hr, giving a slightly brown oil (55.2g). GLC analysis, using butyl propionate as an internal standard, showed it to contain **Id** (0.050 mole),[4] unchanged **IIId** (0.041 mole), and unchanged dibutyl oxalate (0.130 mole). Based on **IIId** consumed, the yield is 85%.

The product [bp 140°-145° (0.05 mm)] was obtained by fractional distillation of the crude product. From other experiments, which did not employ an excess of oxalate ester, dibutyl 3,4-dihydroxyfuran-2,5-dicarboxylate was isolated as white crystals (mp 138°-141°).

Results and Discussion

Electrochemical reactions.—Tetraethyl ethenetetracarboxylate (**IV**) meets all the requirements for a probase cited above. Reduction of **IV** is a divided cell in acetonitrile containing **II**, sodium bromide, and 18-crown-6 leads to precipitation of **VIII** (Eq. [1], [2]) in the cathode compartment. Simultaneously, the anodically generated bromine regenerates the probase from tetraethyl ethanetetracarboxylate (**VI**) placed in the anode compartment (Eq. [3], [4]). Sodium carbonate also in the anode

$$\underset{\textbf{IV}}{C_2X_4} + 2e^- \rightarrow C_2X_4^{2-} \qquad (X = COOC_2H_5) \qquad [1]$$

$$C_2X_4^{2-} + \textbf{II} + 2Na^+ + 2CO_2 \rightarrow \underset{\textbf{VI}}{C_2X_4H_2} + \textbf{VIII} \qquad [2]$$

$$2Br^- \rightarrow Br_2 + 2e^- \qquad [3]$$

$$\textbf{VI} + Br_2 \rightarrow \textbf{IV} + 2HBr \qquad [4]$$

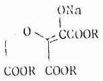
$$2HBr + 2Na_2CO_3 \rightarrow 2NaHCO_3 + 2NaBr \qquad [5]$$

$$\textbf{II} + 2CO_2 + 2Na_2CO_3 \rightarrow \textbf{VIII} + 2NaHCO_3 \qquad [6]$$

compartment serves both to remove HBr and as a source of sodium ions (Eq. [5]). The over-all reaction is summarized by Eq. [6]. After electrolysis, the product **VIII** is obtained by filtration of the catholyte, and the desired product (**Ia**) can be obtained by saponification of **VIII**. As the summary equation (Eq. [6]) shows, reagents other than carbon dioxide and sodium carbonate are not consumed and can be recycled.

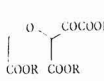
2,2′-Di-*t*-butylazobenzene is less effective as a probase in the present reaction. Its reduction in the presence of **II** and carbon dioxide in acetonitrile containing tetraethylammonium chloride leads to a salt similar to **VIII**. Being a tetraalkylammonium salt, it remains in solution but has been identified by alkylation with ethyl iodide which gives compound **IX**. This workup is carried out in air and the hydrazobenzene (**VII**) is conveniently regenerated during this procedure. However, the recovery is not complete and *ca.* 40% of azobenzene charged appears to be converted to an equimolar mixture of the aniline (**X**) and the carboxylated aniline (**XI**). Thus, with a carbon acid as weak as **II**, cleavage and carboxylation of the electrogenerated base appear to compete with deprotonation of the substrate, and the azobenzene (**V**) does not entirely fulfill the requirement that the electrogenerated base should not react irreversibly with carbon dioxide.

Chemical reactions.—Reaction of diethyl diglycolate, diethyl oxalate, and sodium ethoxide in ether leads to a clear solution from which pentane precipitates a yellow salt in 60-65% yield [based on the expected formulation (**XIIa**)].



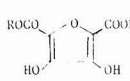
XII

a, R = C_2H_5
b, R = n-C_4H_9



XIII

a, R = C_2H_5
b, R = n-C_4H_9



XIV

a, R = C_2H_5
b, R = n-C_4H_9

It is, however, a mixture and acidification gives the furan (**XIVa**; 10-20%) in addition to the desired ketotriester (**XIIIa**; 55-65%). The solid furan is largely insoluble in the ketotriester and most of it can be removed by filtration of the crude product. The residual furan is not easily separated by distillation, and the most convenient procedure is to simply decarbonylate the crude undistilled ketotriester. The furan remains unchanged and can be more easily separated by distillation at this point. The over-all yield of **Ic** based on **IIIc** is, however, only 32%.

This procedure has several deficiencies, such as (*a*) the low over-all yield, (*b*) the difficulty of precipitating and handling the intermediate salt, and (*c*) the use of a relatively expensive base—sodium ethoxide, which is ordinarily obtained from sodium metal. Yield losses are due to (*i*) formation of an unidentified diglycolate ester self-condensation product which is not precipitated by pentane, (*ii*) losses to the aqueous layer on acidification, and (*iii*) furan formation. These problems have been alleviated by (*a*) use of butyl rather than ethyl esters (water solubility of products is not appreciable), (*b*) use of sodium butoxide solution in butanol (which can be prepared by azeotropic removal of water from sodium hydroxide dissolved in butanol), (*c*) use of an appropriate order of addition and excess oxalate ester (to minimize diglycolate ester self-condensation), (*d*) stripping of butanol prior to acidification (to displace equilibria in favor of product formation), and (*e*) acidification of the total reaction mixture without attempting isolation of the salt. This procedure gives a mixture of unchanged diglycolate and oxalate esters, small amounts of the furan, and the ketotriester. On heating at 190°-205° the first three remain unchanged and the ketotriester is decarbonylated. Separation by distillation may then be effected. Yields of 85% based on diglycolate ester consumed have been obtained in this way.

Conclusions

Two acceptable procedures for the conversion of diglycolic and derivatives to O-carboxymethyltartronate derivatives emerge from the present work. These are the electrochemical carboxylation of the imide (**II**) using tetraethyl ethenetetracarboxylate (**IV**) as the probase and the chemical reaction of dibutyl diglycolate, dibutyl oxalate, and sodium butoxide in butanol. In both cases the ultimate base (sodium carbonate or sodium hydroxide) is inexpensive, and the more expensive base which actually deprotonates the substrate

[4] 0.049 mole by saponification and NMR analysis of the dry sodium salt.

(reduced **IV** or sodium butoxide) need not be used in stoichiometric quantities.

For economic reasons it is desirable to utilize carbon dioxide itself rather than an equivalent as the carboxylating agent, and so the electrochemical procedure is preferred. Work on the use of an undivided cell, which would allow a much more convenient probase regeneration procedure, is in progress and will be reported in due course.

Manuscript submitted July 31, 1978; revised manuscript received Sept. 23, 1978.

Any discussion of this paper will appear in a Discussion Section to be published in the December 1979 JOURNAL. All discussions for the December 1979 Discussion Section should be submitted by Aug. 1, 1979.

Publication costs of this article were assisted by the Monsanto Company.

REFERENCES

1. D. Ginsberg, "A Plea for a Renaissance of a Humanistic Style in Scientific Papers," *Nouveau J. de Chim.*, **1**, 4 (1977).
2. M. M. Crutchfield, *J. Am. Oil Chem. Soc.*, **55**, 58 (1978).
3. H. J. Krause, Ger. Pat. 2,449,899 (1975); *C.A.*, **84**, 16760 (1976); Ger. Pat. 2,449,957 (1975); *C.A.*, **84**, 16761 (1976).
4. D. Ruest, R. Kidwell, and C. Y. Shen, U.S. Pat. 4,059,579 (1977).
5. (a) R. C. Hallcher, M. M. Baizer, and D. A. White, U.S. Pat. 4,072,583 (1978); (b) R. C. Hallcher and M. M. Baizer, *Justus Liebigs Ann. Chem.*, 737 (1977).
6. W. Wislicenus, *Ann. Chem.*, **246**, 306 (1888).
7. D. L. Watson, *Proc. R. Soc. London, Ser. A*, **108**, 132 (1925); *C.A.*, **19**, 2478 (1925).
8. S. C. Roy, *Proc. R. Soc. London, Ser. A*, **110**, 543 (1926); *C.A.*, **20**, 1936 (1926).
9. T. B. Johnson and C. O. Johns, *Am. Chem. J.*, **36**, 290 (1906).

Properties of RuO_x Working Electrodes in Nonaqueous Solvents

D. R. Rolison, K. Kuo, M. Umana, D. Brundage, and Royce W. Murray

Kenan Laboratories of Chemistry, University of North Carolina, Chapel Hill, North Carolina 27514

ABSTRACT

Reactions intrinsic to RuO_x electrodes in water are quenched in aprotic media and RuO_x is a well-behaved working electrode for electrochemistry of solutions of metal bipyridyls, methyl viologen, ferrocene, tetrathiafulvalene, and nitroaromatics. Follow-up reactions of nitroaromatic radicals are especially sensitive to water at RuO_x surfaces. Electrochemical properties are correlated to XPES-determined surface composition.

Electrochemical properties and applications of metal oxide electrodes have become important in recent years. Noteworthy is the catalytic efficacy of mixed oxide anodes containing ruthenium and other noble metals in the chloralkali industry (1, 2), and the photoassisted water oxidation demonstrated by Honda (3) at TiO_2 anodes.

Our interest in metal oxide electrodes stems from the discovery (4-6) that chloro- and alkoxysilanes react readily with their surfaces. The stable metal oxide electrode-silicon bond permits the covalent attachment of chemical reagents to the oxide electrode surfaces, dubbed then "chemically modified electrodes." Stable redox couples are particularly interesting immobilized reagents; it is possible to observe electrochemical reactions of these. It appears (5, 7) that electrochemical properties of immobilized redox couples mimic those of their solution analogs, at least with respect to thermodynamic formal potentials.

Metal oxide electrodes which have been chemically modified using organosilane reagents include SnO_2, TiO_2, Pt/PtO, Au/Au oxide, and RuO_2 (4-6, 8-12). Many of the redox couples whose immobilization would be interesting have electrochemistry best observed in nonaqueous solvents. Previous studies and applications of RuO_x electrodes appear to have been confined to aqueous media (13-17), and our experiments then included characterization of RuO_x as a nonaqueous working electrode, using solution redox couples. Since RuO_x is an electrode material of general interest, we describe here a study of RuO_x electrodes in nonaqueous media plus x-ray photoelectron spectroscopy (XPES) of RuO_x electrodes as we prepare them.

Experimental

Preparation of electrodes.—RuO_x electrodes are generally prepared by brushing a solution of $RuCl_3$ on Ti metal followed by baking (16-20), which produces adherent coatings of high roughness. Seeking lower roughness on chemically modified electrodes, we do not use the brush and bake approach. Instead, spray and chemical vapor deposition procedures are employed.

Spray electrodes.—A dilute (typical $10^{-2}M$) butanol $RuCl_3$ solution (Matthey Bishop, Incorporated) is aspirated onto a ¼ in. diam Ti (Alfa/Ventron) disk heated sufficiently (~200°C) for prompt evaporation of the solvent carrier. A thin coating applied in this manner is baked in air at 400°-450°C for 30-60 min. This procedure is repeated for up to 12 times (most typically 3-5) to build up a RuO_x film of the desired thickness. Electrodes with thin coatings have a royal blue coloration, thicker coatings become blue-gray then black. The blue-gray appearance is *ca.* 1-2 μm film. Repeated application of very thin films and use of short aspiration periods and dilute $RuCl_3$ solutions leads to the most adherent RuO_x films and to the lowest apparent roughness, as judged by electrochemical background currents. Quality of the aspirator device is important; that used initially in this work (a modest craft/hobby air brush) and which produced most of the electrochemically characterized electrodes, produces less smooth surfaces than the device currently in use (Badger Model 150XF air brush). A *ca.* 1 min spray from the latter aspirator (by a given operator) was calibrated at 100 ± 30Å RuO_2 using careful microweighings. The sprayed electrodes have shiny surfaces and are used without polishing.

Chemically vapor deposited (CVD) electrodes.—A vapor transport procedure is based on sublimation of ruthenium acetylacetoneate, $Ru(C_5H_7O_2)_3$, (RIC/ROC) at 190°C. A gas transport system similar to that of Bard (21) mixes ruthenium acetylacetonate vapor carried by a dry N_2 stream, with water-saturated N_2 (50°C), in a concentric delivery tube arrangement positioned approximately 2 cm over the heated (~250°C) Ti disk substrate. The ruthenium acetylacetonate is introduced into the subliming chamber after preliminary adjustment of the gas flow. Deposition of partially hydrolyzed ruthenium acetylacetonate on the heated Ti disk was continued until a thin red-brown coating appeared, which was baked at 450°C for 30 min. The procedure can be repeated to build up a highly reflective, smooth, black RuO_x coating on the Ti disk.

Prior to application of RuO_x films by either of the above procedures, the Ti base is polished with 5 μm alumina and 1 μm diamond paste, successively, to a mirror finish, and then cleaned ultrasonically. The finished RuO_x electrode is mounted for electrochemical study on the tip of a ¼ in. (OD) glass tube using Torr-Seal (Varian) as adhesive and to mask the disk edges.

Electrochemical experiments.—Electrochemical experiments were carried out in conventional nonaqueous cells equipped with Luggin reference electrode capillary to NaCl-saturated SCE, concentric auxiliary wire electrode, and operated at ambient laboratory temperature (22°C). No *iR* compensation was employed.

Chemicals.—The aprotic solvents CH_3CN (MCB, spectroquality), DMSO (Fisher, ACS certified), and DMF (Fisher, ACS certified) were predried over molecular sieves. Propylene carbonate (Eastman) was used without further purification. Tetraethylammonium perchlorate (TEAP) was prepared from the bromide salt and successively recrystallized three times from distilled, deionized water.

Ferrocene (Aldrich), *o*-chloranil (Eastman), tetrathiafulvalene (Aldrich), and methylviologen were used as received. *cis*-Dichloro-*bis*-bipyridylruthenium(II) was prepared using a general procedure obtained from Professor D. G. Whitten. *Tris*-bipyridylruthenium(II) perchlorate was prepared by refluxing $RuCl_3$ with a 10% excess of 2,2′-bipyridine (Aldrich) in EtOH for 2 days. The EtOH was removed, the residue dissolved in H_2O, the salt precipitated with sodium perchlorate and filtered. The crude $Ru(bpy)_3(ClO_4)_2$ was chromatographed on alumina, eluted with CH_3CN, and precipitated with a minimum amount of ether. The solid was then recrystallized from EtOH. *Tris*-bipyridylchromium(III) perchlorate was prepared by washing a solution of chromic perchlorate (G. F. Smith) through a Zn-amalgam column with 0.1*N* $HClO_4$ into a solution containing excess 2,2′-bipyridine. The solution was air oxidized and the resulting yellow $Cr(bpy)_3(ClO_4)_3$ filtered and recrystallized from EtOH.

X-ray photoelectron spectra.—XPES spectra were obtained using a du Pont Model 650B electron spectrometer. RuO_x samples were introduced directly from the laboratory atmosphere and, to avoid Ar beam reduction effects, were observed without sputter-cleaning. Some samples were mounted on the spectrometer probe using conducting Ag paint to establish good electrical contact with the spectrometer; on these contaminant C 1s appeared at 284.8 eV and there was no evidence of surface charging. Other samples were mounted using double side tape and corrected to C 1s as 284.8 eV.

Results and Discussion

Background currents.—Background cyclic voltammograms of spray and CVD RuO_x electrodes are illustrated in Fig. 1 for 0.1*M* Et_4NClO_4/DMF and 0.1*M* Et_4NClO_4/DMSO. Potential limits indicated for these and propylene carbonate and acetonitrile solvents correspond to 50 μA background current. The RuO_x electrode background limits, potential limits, and current levels are clearly competitive with those at platinum in these solvents.

It is known that Pt anodic potential limits in, for instance, acetonitrile are considerably extended by rigorous exclusion of water. Whether analogous potential limit extensions are achieved on RuO_x working electrodes under anhydrous or other special conditions is untested.

Potential limits and background current levels vary somewhat on RuO_x electrodes prepared ostensibly by the same procedure and differ between electrodes prepared by spray and CVD procedures. This is thought at least in part to reflect variations in surface roughness. Typically, CVD electrodes exhibit somewhat lower background currents (Fig. 1, higher optical reflectivity suggests lower roughness). Spray electrodes prepared using coarse aspiration, thick coatings per aspiration/baking cycle, or with inexperience, often

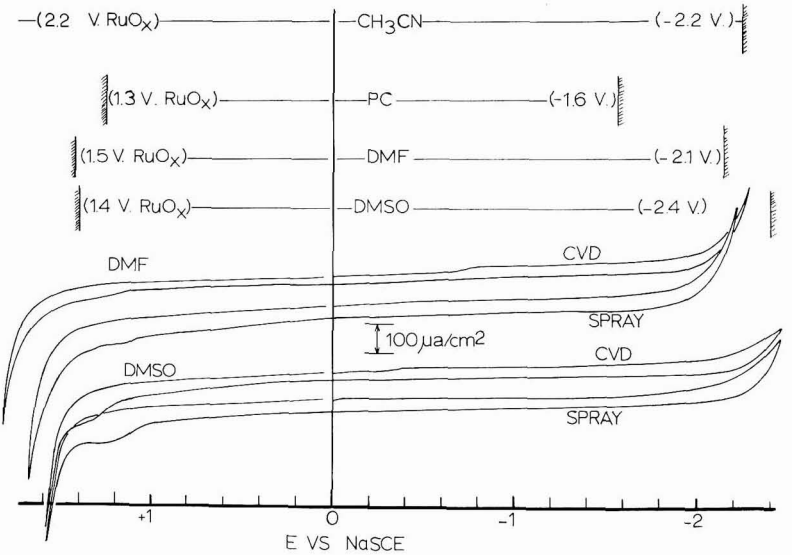


Fig. 1. Background cyclic voltammograms for spray and CVD RuO_x electrodes in DMSO and DMF, 0.1M TEAP. Potential limits for CH_3CN, PC, DMF, and DMSO expressed at 50 μA background current.

show substantial background currents. Such high roughness electrodes are less desirable when accurate definition of solution reactant mass transfer is important, and in studies of chemically immobilized substances. On the other hand, high roughness is desirable for solution reactant electrode reactions controlled by available active surface area.

Cyclic voltammograms at RuO_x film electrodes in aqueous media exhibit large background current levels, of the order of 1 mA/cm² [Fig. 2, in Ref. (14)], 10-25 times larger than typical values in Fig. 1. The aqueous studies (13-17, 22) also report distinct surface waves in the anodic potential region. These waves and the large background currents observed at other potentials are ascribed (14) to alterations of the oxidation state of surface and subsurface ruthenium sites in the electrode. Recent evidence favors surface rather than bulk processes (16).

Spray and CVD RuO_x electrodes in nonaqueous solvents exhibit neither electrode-related surface waves nor the large background current levels typical of aqueous media. This in part is attributed to the lower surface roughness thought to exist on electrodes as we prepare them. Electrodes used (14) in aqueous studies have roughness factors estimated at 60-80; judging from background (double layer) currents the roughness of our materials is perhaps 10× less. The absence of electrode surface waves or any obvious redox change in the electrode itself on potential sweeping in nonaqueous media is understandable in that proton transfer will accompany a change in Ru oxidation state and the solvents employed are aprotic. Thus, any intrinsic electrochemical activity of the RuO_x electrode itself is quenched in aprotic nonaqueous solvents. It is worth keeping in mind that electrochemical reactions of solution reactants which liberate or consume protons in the aprotic medium can conceivably indirectly provoke concurrent electrode oxidation state changes by generating acidic or basic interfacial solutions.

Detailed consequences of bonding of organosilane reagents to RuO_x surfaces on the background current levels and potential limits have not been adequately investigated in water or aprotic media. Some effects have been noticed in nonaqueous experiments.

Model redox couples.—The eight solution redox couples examined were chosen for electrochemical (fast charge transfer) and chemical (stable reactant and product) reversibility on Pt working electrodes. Such couples comprise an important class of systems for covalent electrode surface attachment studies. Included in particular were reactants thought to be simple outer sphere in heterogeneous electron transfer [$Ru(bipy)_3^{2+}$ (23) and a nitrobenzene (24)]. A large number of electrode specimens has been prepared, but a limited subset was employed for the model studies to facilitate comparisons of reactions.

To compare behavior in different nonaqueous media and to compare spray and CVD RuO_x electrodes, cyclic voltammetry of methyl viologen and tetrathiafulvalene was examined in CH_3CN, DMSO, DMF, and propylene carbonate (PC) solvents. The same pair of spray (electrode A) and CVD (electrode B) RuO_x electrode specimens used to illustrate background voltammograms (Fig. 1) was employed for these experiments. Current-potential responses are shown in Fig. 2 and numerical data are shown in Table I.

Table I. Comparison of electrochemical parameters for electrode reactions on Pt and RuO_x working electrodes

Reactant		Solvent	$E^{0'}$, V *vs.* NaSCE: RuO_x spray (CVD)	$E^{0'}$, V *vs.* NaSCE: Pt	$E^{0'}$, V *vs.* NaSCE: Lit	ΔE_p, mV: RuO_x spray (CVD)	ΔE_p, mV: Pt	$i_{p,c}/i_{p,a}$: RuO_x spray (CVD)	$i_{p,c}/i_{p,a}$: Pt	$\frac{i_p}{AC\nu^{1/2}}\times 10^{-3}$, A · cm · sec$^{1/2}$ / $\nu^{1/2}$ · mole: RuO_x spray (CVD)	Pt
Tetrathiafulvalene	(+/0)	CH_3CN	0.32 (0.33)[c]	0.32	0.33[k]	90 (82)	74	1.17 (0.93)	0.92	1.09 (1.26)	1.17
	(2+/+)		0.69 (0.70)[c]	0.69	0.70	108 (83)	71	— (1.02)	1.04		
Tetrathiafulvalene	(+/0)	DMSO	0.37 (0.37)[c]	0.38		108 (105)	90	1.01 (0.97)	0.99	0.56 (0.56)	0.53
	(2+/+)		0.58 (0.58)[c]	0.58		150 (110)	97				
Tetrathiafulvalene	(+/0)	DMF	0.40 (0.41)[c]	0.40		80 (90)	68	0.98 (0.99)	1.06	0.89 (0.80)	0.84
	(2+/+)		0.64 (0.65)[c]	0.64		80 (116)	63				
Tetrathiafulvalene	(+/0)	PC	0.31 (0.31)[c]	0.31		92 (89)	86	0.98 (0.98)	1.00	0.50 (0.52)	0.52
	(2+/+)		0.65 (0.65)	0.65		95 (93)	83	1.15 (1.08)	0.84		
Methyl viologen	(2+/+)	CH_3CN	−0.43 (−0.43)[c]	−0.42		74 (65)	68	0.79 (0.73)	0.79	0.79 (0.79)	
	(+/0)		−0.84 (−0.83)[c]	−0.83		71 (66)	54				
Methyl viologen	(2+/+)	DMSO	−0.44 (−0.44)[c]	−0.44		83 (70)	74	1.00 (0.98)	0.80	0.30 (0.33)	0.31
	(+/0)		−0.79 (−0.73)[c]	−0.79		89 (74)	75				
Methyl viologen	(2+/+)	PC	−0.48 (−0.48)[c]	−0.48		93 (85)	80	1.06 (1.05)	0.91	0.31 (0.32)	0.31
	(+/0)		−0.87 (−0.86)[c]	−0.86		99 (87)	73				
$Ru(bipy)_2Cl_2$	(+/0)	CH_3CN	0.32[d]	0.31	0.31[e]	60 ± 5	53 ± 6	1.04	1.00	0.91	0.78
$Ru(bipy)_3^{2+}$	(3+/2+)	CH_3CN	1.28[d]	1.27	1.29[e]	69 ± 11	63 ± 3	0.98	0.95	0.81	0.81
	(2+/+)		−1.33	−1.34	−1.33	63 ± 3	60	1.08	1.04	1.04	0.80
	(+/0)		−1.52	−1.53	−1.52	65 ± 7	67 ± 11	0.94	0.97		
	(0/1−)		−1.75		−1.77	68 ± 8		1.06	0.98		
$Cr(bipy)_3^{3+}$	(3+/2+)	CH_3CN	−0.24[d]	−0.24	−0.21[f]	67 ± 11	60	1.04	1.05	0.93	0.74
	(2+/+)		−0.76	−0.76	−0.72	71 ± 8	57	1.03	1.00	1.02	0.78
	(+/0)		−1.31	−1.32	−1.28	75 ± 15	60	1.06	1.01		
	(0/1−)		−1.93		−1.91	60					
Ferrocene	(+/0)	CH_3CN	0.32[d]	0.32	0.32[g]	116 ± 8[a]	95[a]	0.96	0.99	1.04	1.10
o-Chloranil	(0/−1)	CH_3CN	+0.10[d]	0.10	−0.01[g,h]	52 ± 6	50	1.09	1.01	2.08	1.61
	(−1/−2)		−0.49	−0.48	−0.80	152 ± 47	57	1.00	1.00	1.21	1.45
Propyl-3,5-dinitro-benzamide	(0/−1)	DMSO	−0.67[d]	−0.67	−0.65[i]	180[b]	56 ± 7	1.16	0.96	0.37	0.27
	(−1/−2)		−1.12	−1.07	−1.06	251	62 ± 3	1.16	1.04	0.26	0.26
Propyl-3,5-dinitro-benzamide	(0/−1)	CH_3CN	−0.80[d]	−0.79		243 ± 40[b]	78	1.00	0.96	0.66	0.91
	(−1/−2)		−1.22	−1.15		287 ± 37	105	1.16	1.05	0.56	0.74
Butyl-3,5-dinitro-benzamide	(0/−1)	CH_3CN	−0.83[j]	−0.84		80	67	0.96	0.96	0.91	1.32
	(−1/−2)		−1.20	−1.21		99	71	1.43	1.16	0.96	1.02

[a] Subsequent experiments with improved cell design gave ΔE = 89-95 on RuO_x electrodes F and G and 69 mV on Pt.
[b] Wave definition especially second wave varies greatly with different RuO_x electrode; reaction on metal oxides also sensitive to traces of H_2O and O_2. See text. ΔE_p has been observed as *ca.* 60 mV on a number of RuO_x electrodes.
[c] Electrodes A and B.
[d] Average of electrodes C, D, and E.
[e] D. J. Salmon, Ph.D. Dissertation, University of North Carolina (1977).
[f] Ref. (25).
[g] Ref. (26).
[h] $E_{1/2}$ values.
[i] Ref. (5).
[j] These data were obtained on a different RuO_x electrode than electrodes C-E and are included to illustrate the variability of the nitroaromatic results on RuO_2.
[k] Ref. (30).

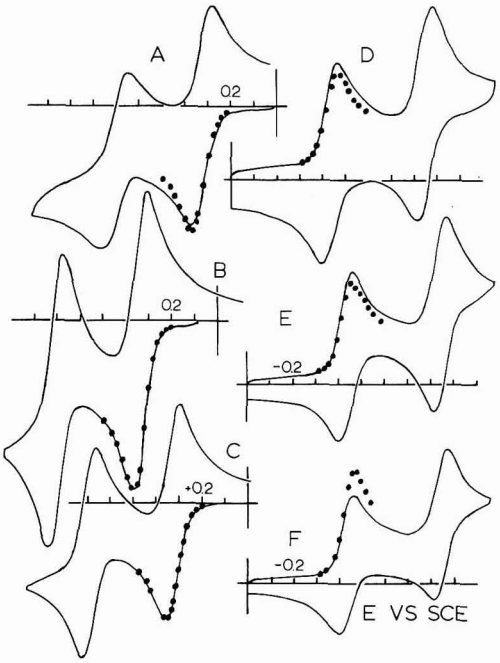


Fig. 2. Cyclic voltammograms and Nicholson-Shain theoretical shape fit for spray and CVD RuO_x and Pt electrodes. Curve A: 0.50 mmole TTF in CH_3CN, 0.1M TEAP, electrode A, 100 mV/sec; curve B: 0.664 mmole TTF in CH_3CN, 0.1M TEAP, electrode B, 80 mV/sec; curve C: 0.664 mmole TTF in CH_3CN, 0.1M TEAP, Pt electrode, 100 mV/sec; Curve D: 0.216 mmole methylviologen in CH_3CN, 0.1M TEAP, electrode A, 65 mV/sec; curve E: 0.216 mmole methylviologen in CH_3CN, 0.1M TEAP, electrode B, 65 mV/sec; curve F: 0.216 mmoles methylviologen in CH_3CN, 0.1M TEAP, Pt electrode, 200 mV/sec.

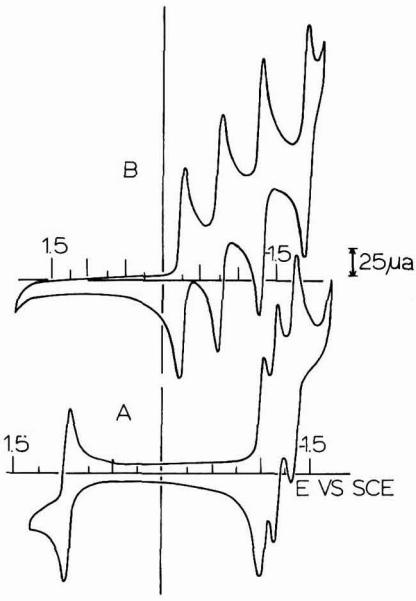


Fig. 3. Cyclic voltammograms of bipyridyl complexes at RuO_x. Curve A: 1 mmole $Ru(bpy)_3(ClO_4)_2$ in CH_3CN, 0.1M TEAP, electrode *E*, 100 mV/sec; curve B: 1 mmole $Cr(bpy)_3(ClO_4)_3$ in CH_3CN, 0.1M TEAP electrode D, 100 mV/sec.

Six other redox couples were examined in CH_3CN solvent using a set of three simultaneously prepared spray RuO_x electrodes (electrodes C, D, and E). The numerical data presented in Table I for bipyridyl complexes, ferrocene, o-chloranil, and nitrobenzamide are averages of the very similar responses of these three electrodes. Figure 3 illustrates cyclic voltammograms for the two bipyridyl complexes. The spray and CVD electrodes A and B used for methyl viologen and tetrathiafulvalene bore relatively thick (black) coatings of RuO_x; the three spray electrodes C-E were thinner (royal blue) coatings. In all cases comparative cyclic voltammetric data on a Pt disk electrode were collected simultaneously in the experiments with the RuO_x electrodes (Table I). For the most part the cyclic voltammetric data in the table correspond to a fixed (typically 0.1 V/sec) sweep rate. Experiments on time dependence of the electrode reactions are discussed later.

Comparison of formal potentials ($E^{\circ\prime}$) of the various couples on RuO_x and Pt electrodes (Table I) shows excellent agreement between the two electrode materials. Likewise, the ratio of cathodic and anodic peak currents is, with due consideration to background current correction and the presence of multiple waves, acceptably close to unity throughout the table for RuO_x and Pt. $E^{\circ\prime}$ for $Cr(bipy)_3^{3+}$ reductions on Pt and RuO_x in CH_3CN agree quite well with literature values. In DMSO $Cr(bipy)_3^{3+}$ electrochemistry is complicated on both Pt and RuO_x by product adsorption phenomena.

These results show that, for these electrode reactions, product stability is unaffected by use of a RuO_x electrode surface; *e.g.*, that in nonaqueous solvents RuO_x electrodes do not display any general effect of surface-catalyzed adsorption, product decay, etc. Exceptions to such "*inert electron source/sink*" RuO_x electrode behavior doubtless exist just as they do for Pt; the present results hint of such for the nitrobenzamide. Electrochemistry of nitrobenzamide on RuO_x is considered later.

Transient behavior.—Mass transfer characteristics of the RuO_x electrodes were first examined with cyclic voltammetric scan rate variation. Over a modest scan rate range (0.05-0.15 V/sec) $i_p/v^{1/2}$ was constant to within a few percent. When normalized to electrode area and reactant concentration, the resulting voltammetric constant is in generally good agreement between the different RuO_x electrodes and Pt (Table I) and furthermore in a given solvent (*e.g.*, CH_3CN) has similar values for the set of $n = 1$ reactions. Calculated diffusion coefficients from RuO_x data agree reasonably well with literature values on Pt where these are available.

A more exacting mass transfer examination was carried out using potential step chronoamperometry on two spray RuO_x electrodes (electrodes F and G) prepared subsequent to the preceding ones and at different times and with reduced surface area (masked with Torr-Seal) to minimize ohmic effects, so that transient currents even in the millisecond region did not exceed 0.5 mA. Figure 4 illustrates the 0.001-5 sec response (electrode F) for oxidation of $Ru(bipy)_3^{2+}$ in CH_3CN at a potential well positive of $E^{\circ\prime}$, analyzed in the usual way (27). Using $D = 9.2 \times 10^{-6}$ cm²/sec in CH_3CN,[1] an electrode area of 0.023 cm² is obtained from the average slope of Fig. 4, in acceptable agreement with the estimated (slightly irregular circle) 0.028 cm² geometrical electrode area. In a blank potential step experiment (supporting electrolyte only) at this RuO_x electrode, the background current at +1.6V decayed much more slowly (50-100 msec) than did that at a Pt electrode in the same cell (<20 msec),

[1] D calculated from $i_{p,a}$ for $Ru(bpy)_3^{2+/3+}$ from cyclic voltammetric Pt electrode data.

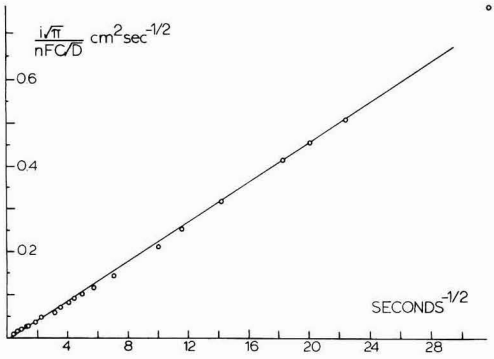


Fig. 4. Chronoamperometric current parameter vs. $t^{-1/2}$ for sprayed RuO$_x$ electrode F. 1 mmole Ru(bpy)$_3$(ClO$_4$)$_2$ in CH$_3$CN, 0.1M TEAP. Potential step 1.00V-1.53V. Linear regressed slope gives area = 0.023 cm^2.

and was 5-10× larger. The current-(time)$^{-1/2}$ data of Fig. 4 is uncorrected for background and the short-time curvature is ascribed to the background component. Lessened background and faster decay in potential steps at less anodic potentials suggest that the slow decay of background at +1.6V is due to a faradaic component.

The background effect was more prominent in a replicate of the Fig. 4 experiment using RuO$_x$ electrode G; curvature was severe for $t < 30$ msec. At longer times (0.03-10 sec), the current-(time)$^{1/2}$ relation was, however, quite linear and the electrode area obtained from the slope (0.04 cm^2) again agreed with actual (0.032 cm^2) geometrical area. The current-(time)$^{-1/2}$ response of electrode G was linear over 0.003-1 sec in a potential step (to +0.5V) experiment in 1 mmole ferrocene/CH$_3$CN.

Over-all, the potential step results are those expected for linear mass transport at RuO$_x$ electrodes down to *ca.* 10 msec. This time corresponds to a diffusion layer depth of *ca.* 2×10^{-4} cm. At sufficiently short electrolysis time, diffusional linearity is (in principle) expected to break down owing to microscopic nonplanarity (roughness) of the RuO$_x$ surface. Inasmuch as the spray-prepared RuO$_x$ electrodes are estimated to have thickness *ca.* a few microns or less, their texture is expectedly then somewhat below that detectable on mass transport grounds at the achieved electrolysis times.

Reversibility.—The first wave of tetrathiafulvalene and methyl viologen on RuO$_x$ electrodes A and B and on Pt is compared in Fig. 2 with that expected for an ideal reversible system (28). The theoretical curves (circles) were calculated using literature diffusion coefficients.[2] For tetrathiafulvalene, correspondence is excellent on Pt and on the CVD RuO$_x$ electrode B. The experimental current-potential wave on the spray RuO$_x$ electrode A is less sharp than theory which is probably due to the pseudoreversible character (ΔE_p = 90 mV, Table I) of the tetrathiafulvalene reaction on this electrode. The reduction of methyl viologen on both RuO$_x$ electrodes is more reversible and as seen in the figure its shape matches theory quite well. (The mismatch in absolute i_p merely reflects mismatch to $AD_{lit.}^{1/2}$.)

Reversibility properties of the model electrode reactions as reflected in cyclic voltammetric ΔE_p values are of some interest due to the dearth of literature information on RuO$_x$ for organic reactants and in nonaqueous media. The reversibility results proved to be quite varied.

[2] D(TTF) from Ref. (29). D(methyl-viologen) from Ref. (30).

For methyl viologen reduction and tetrathiafulvalene oxidation, the electrode A and B data of Table I indicate that these reactions are generally more reversible on CVD as compared to spray RuO$_x$ electrodes.

Reductions and oxidations of the ruthenium and chromium bipyridyls exhibit fast charge transfer rates on Pt electrodes. These electrode reactions gave within experimental error 60 mV ΔE_p values on all RuO$_x$ electrodes tested (including numerous others besides electrodes C-E in Table I), see Fig. 3. It is notable that Ru(bipy)$_3^{2+}$ oxidation at quite positive potentials and its reduction at rather negative potentials both exhibit ideal reversible (60 mV ΔE_p, i_p ratios = 1.0) behavior. Such absence of rectifying character is unexpected if these RuO$_x$ electrodes behave as n-type semiconductors, a property ascribed to RuO$_x$ electrodes by Kuhn and Mortimer (20).

Charge transfer behavior of several couples, notably tetrathiafulvalene, methyl viologen, and ferrocene, tended to be pseudoreversible to reversible on Pt, depending on solvent, and relatively less reversible (larger ΔE_p) on spray and CVD RuO$_x$ electrodes than on Pt. The degree of pseudoreversibility of these reactions varied among different preparations of (spray) RuO$_x$ electrodes. Electrodes prepared in the same "batch" (*e.g.*, C-E) behave identically. We have difficulty in identifying the variable(s) of RuO$_x$ electrode preparation controlling this pseudoreversibility but it does appear that spray electrodes prepared with very fine aspiration of dilute solutions with successive applications of thin layers produce the lowest ΔE_p separations. Supplementary ΔE_p data for ferrocene oxidation on electrode F, which was prepared in this manner using the higher quality aspiration device (Experimental) is given for example in Table I (footnote).

Several cyclic voltammograms for 3,5-dinitrobenzamide reduction in CH$_3$CN are shown in Fig. 5. The two one-electron reduction steps for this species on Pt in DMSO are reversible and pseudoreversible in CH$_3$CN. The reaction is, however, exceptionally variable on RuO$_x$ electrodes especially the second wave. On electrodes C-E (the same specimens on which the metal bipyridyls are reversibly reduced at similar potentials), the nitroaromatic reaction was very poorly reversible (Table I). On other specimens, apparently those with thicker RuO$_x$ films, the reaction can be considerably better behaved (Table I). An early set of electrodes produced essentially reversible behavior (5). The nitrobenzamide reaction on RuO$_x$ is very sensitive to solvent water contaminant. This is illustrated in Fig. 5 where an initial poorly reversible (for

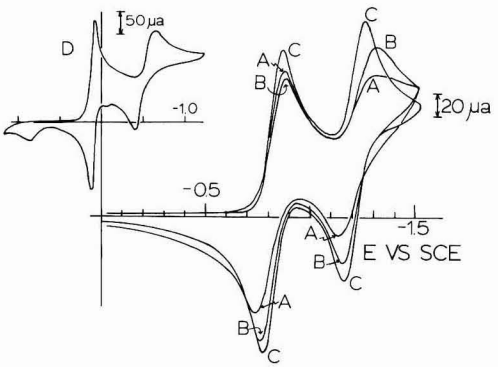


Fig. 5. Cyclic voltammograms (100 mV/sec) on spray and CVD RuO$_x$. Curves A-C: 1 mmole propyl-3,5-dinitrobenzamide in CH$_3$CN, 0.1M TEAP, (electrode A). Curve A: initial; curve B: after adding activated alumina and further degassing; curve C: after 30 min contact with alumina; curve D: 1 mmole o-chloranil in CH$_3$CN, 0.1M TEAP (electrode D).

the second wave) cyclic voltammogram in conventionally dried (molecular sieve) solvent was gradually (30 min) transformed into a much more reversible reaction upon *in situ* drying with Al_2O_3 powder (activated at 450°C). The first reduction wave for o-chloranil is equally reversible on Pt and RuO_x electrodes, but the second wave is decidedly irreversible on RuO_x (Fig. 5). A water sensitivity again exists.

We have in other studies (31) observed nitrobenzamide reduction to be both charge transfer and chemically irreversible on SnO_2 electrode surfaces, in DMSO or CH_3CN, in either solution or chemically immobilized state. Nitrobenzamide immobilized on RuO_x (and PtO) electrodes (5, 6) is more stable but decays after 50-200 cyclic reduction-oxidations. This background plus the water effect of Fig. 5 leads us to suggest that specific chemical interactions may exist between the surfaces of certain metal oxide electrodes and chemically basic organic reduction products such as radical ions. These interactions, absent on "clean" Pt electrodes, may promote proton transfer or hydrogen-bonding processes and slow charge transfer kinetics. The surface catalytic behavior of RuO_x electrodes toward organic reductions appears to be a subject deserving continued study.

X-ray photoelectron spectroscopy (XPES).—RuO_x spray electrodes were systematically examined by XPES in an attempt to correlate thus-obtained surface compositional data with preparation details and electrochemical properties.

The most definitive existing study of ruthenium oxides by XPES is that by Kim and Winograd (32), who report that the $3d_{5/2}$ band of RuO_2 powder (280.7 eV binding energy) prepared by 900°C thermal decomposition of bulk $RuCl_2 \cdot 3H_2O$ in air exhibits a high binding energy (282.5 eV) shoulder. They attribute this band to the equivalent of *ca.* four layers of RuO_3 present as defect structure on the RuO_2 surface. The associated O 1s band for RuO_2 lies at 529.4 eV; a O 1s shoulder at 530.7 eV was ascribed to the RuO_3. Hydrated RuO_2 and carbonate contaminated RuO_2 exhibited Ru $3d_{5/2}$ at 281.4 eV and O 1s at 530.5 both of which bands reverted to the RuO_2 280.7 and 529.4 eV bands on 130°C heating. Augustynski *et al.* (33) have detected RuO_3 on paint and bake RuO_x anodes by graphical resolution of Ru 3p. Pizzini *et al.* (19) determined by bulk analysis a $RuO_{2.1}Cl_{0.2}$ composition for thermal decomposition at 400°C. The chlorine residue observed by Pizzini was confirmed by Tamura (34) in a secondary ion mass spectroscopic experiment; sputtering revealed surface oxygen richness and chlorine deficit as compared to the electrode interior.

Table II. XPES results for spray RuO_x electrodes

Binding energies		
Ru	$3d_{5/2}$	280.9[a] ± 0.1 eV[a]
		282.2[b] ± 0.2[b]
Ru	$3p_{3/2}$	463.1
O	1s	529.2 ± 0.1[c]
		530.5 ± 0.1
		532.2 ± 0.2
Cl	$2p_{1/2,3/2}$	197.9[d]
Ti	$2p_{3/2}$	458.5[e]
C	1s	284.8
Band intensities		
N_{Cl}/N_{Ru} = 0.11 ± 0.03[f]		
O 1s/Ru $3p_{3/2}$ = 2.32 ± 0.26 (12 samples, no Ti band)		
N_O/N_{Ru} = 4.6 ± 0.5[g]		
$N_{O(529.2)}/N_{Ru(280.9)}$ = 2.3[h]		
O 1s/(Ru $3p_{3/2}$ + Ti $2p_{1/2}$) = 2.09 ± 0.30 (12 samples with Ti band)		

[a] Obtained on sample in good electrical contact with spectrometer (Ag paint) on which C 1s observed at a noncharged 284.8 eV. Identical B.E. observed on samples mounted with insulating sticky tape and corrected for charge using C 1s. Experimental uncertainty ± 0.1 eV.

[b] Observed as weak band in valley between Ru 3d 280.9 eV and C 1s 284.8 eV bands on a few samples.

[c] Relative intensity of three O 1s bands averages 1.4:1.7:1.9, respectively. Band at 532.2 eV broader (2.5 eV) than band at 529.2 eV (1.4 eV). These data taken from electrodes exhibiting no Ti 2p.

[d] Highly variable intensity.

[e] Present on *ca.* one-third of the *ca.* 35 electrodes studied. Its presence does not appear to shift other element B.E.

[f] Intensity converted to apparent atom ratio using relative sensitivity Cl/Ru 3p = 0.79 obtained from experiments on Ru-Cl compounds (31).

[g] Intensity converted to apparent atom ratio using relative sensitivity O/Ru 3p = 0.50 based on cross sections (35). Intensity is sum of the three O 1s bands.

[h] Intensity converted to apparent atom ratio using relative sensitivity O/Ru $3d_{5/2}$ = 0.38 based on cross sections (35). Intensities are resolved O 1s at 529.2 and Ru $3d_{5/2}$ at 280.9.

XPES spectra of spray RuO_x electrodes are shown in Fig. 6. Binding energies and (area) intensities are given in Table II. The O 1s band is multiple; curve-fitting studies indicate it is best represented as three overlapping bands with binding energies 532.2, 530.5, and 529.2 eV and somewhat variable relative intensities 1:1.7:1.4. Observation of Ru $3d_{5/2}$ in our spectrometer is complicated by the adjacent C 1s, but the electrodes clearly show a band at 280.9 eV. This band and the O 1s at 529.2 are in excellent agreement with Kim and Winograd (32) for RuO_2. On some electrodes (Fig. 6) an additional Ru $3d_{5/2}$ band was apparent; curve fitting assigned a binding energy of 282.2 eV to this species. This binding energy plus the observed 530.5 eV O 1s band are close to those values assigned (32) to RuO_3 (*e.g.*, 282.5 and 530.7 eV). The 532.2 eV O 1s band (9) may be surface metal hydroxyl and/or

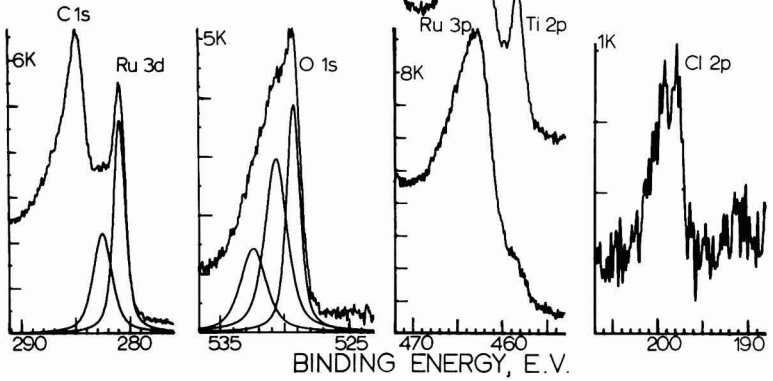


Fig. 6. XPES spectra of indicated elements on RuO_x film on Ti base. Least squares curve fitting used to resolve Ru $3d_{5/2}$ band into Ru(VI) and Ru(IV) components and to resolve O 1s into three species. Ru $3p_{3/2}$, Ti $2p_{3/2}$ panel: upper spectrum shows a different sample with higher Ti surface content.

adsorbed water. All electrodes display a broad Ru $3p_{3/2}$ band at 463 eV; curve fitting for RuO_2 and RuO_3 was not attempted.

A Cl 2p band with inorganic chloride B.E. (36) is almost always observable. The chloride residue on RuO_x surfaces varies considerably from sample to sample with no obvious correlation with baking temperature (from 400°-475°C) or time (beyond about 30 min). The average surface Cl/Ru stoichiometry is 0.11 (Table II). According to Tamura's data (34), interior Cl/Ru could be *ca.* 2× higher than the surface value. Experiments performed late in this study demonstrated that holding the Ti disk at high temperature (*ca.* 350°C) during the spray aspiration step deletes the residual Cl 2p band and makes Ti 2p (*vide infra*) more common.

We do not have an accurate experimental calibration of relative O 1s/Ru $3p_{3/2}$ sensitivity. Use of theoretical cross sections yields an average surface O/Ru atom ratio of 4.6 including all three O 1s bands in the calculation. The average O/Ru is *ca.* 3.4 if the 532.2 eV O 1s band is excluded. The "RuO_2" surface on either basis is oxygen rich as expected for RuO_3 being present as well. The resolved 529.2 eV O 1s and 280.9 eV Ru $3d_{5/2}$ bands exhibit the expected relative intensities for RuO_2 (Table II).

Many spray RuO_x electrodes exhibit a Ti 2p band (Fig. 6) at 458.5 eV, a B.E. consistent with TiO_2 (37). The 70.7 eV difference between this and the (529.2 eV) O 1s band agrees with the 71.5 eV separation characteristic of TiO_2. The Ti band was uncommon on spray RuO_x electrodes judged by their preparation to bear thicker (blue-gray or black) films and was common on thin (royal blue electrodes C-E being examples) films.

The correlation between coating film thickness and the Ti 2p band might reflect imperfect spray coverage of the Ti metal substrate. However, Ti bands still appeared on several specimens receiving a total of 12 thin spray coatings (3 per baking cycle). Also, relatively cool electrodes receiving an aspirated spray coating of the $RuCl_3$ solution but not baked show no Ti band. The average surface stoichiometry on such electrodes is estimated as $RuO_{2.3}Cl_{1.8}$ which is reasonable. These results make it likely that events during baking not spray coating result in exposure of Ti. Considerable mechanical reconstruction of the surface must accompany the thermal decomposition process and it is plausible that exposure of Ti substrate (oxidized to TiO_2) results. TiO_2 and RuO_2 form mixed oxides and it is also possible that some bulk or grain boundary migration of Ti into the RuO_x film occurs. The latter, interesting process has been suggested before (20), but we have not been able to secure unambiguous proof of it.

Discussion

The interesting aspects of surface composition deduced from the XPES data are (*i*) confirmation of RuO_2 on the surface by binding energy correlation, (*ii*) a second pair of ruthenium and oxygen states consistent with RuO_3, (*iii*) appearance of Ti on some spray electrodes, and (*iv*) residual surface chloride. Interesting effects observed in nonaqueous electrochemistry at RuO_x electrodes include besides the generally well-behaved working electrode properties, apparently slower charge transfer rates on RuO_x as compared to Pt for couples such as ferrocene, tetrathiafulvalene, and methyl viologen, and surface interactions specific to certain electrode reactions (*e.g.*, nitroaromatic). Correlations, or lack thereof, between these several factors are examined now.

We have been unable thus far to discern any clear correlation between RuO_x film thickness, or appearance of surface Ti, with electrochemical properties of solution species in nonaqueous solvents. It seems that the XPES-detected Ti surface sites are either adequate electronic substitutes for Ru in electrochemical surface electron transfer, or the mass transport distances in the electrochemical experiment to properly conductive Ru sites are insignificantly long. A dominating semiconducting character due to TiO_2 (or to the chloride content) is ruled out by the $Ru(bipy)_3^{2+}$ behavior which is reversible on both RuO_x and Pt at highly negative and positive potentials.

The residual chloride content of RuO_x electrodes is highest in the interior (34), and the electrical conductivity of RuO_2 is known (19) to depend on residual chloride. Thus residual chloride could conceivably produce ohmic charge transport effects in the RuO_x electrodes. Electrode reactions with high charge transfer rate [*e.g.*, $Ru(bipy)_3^{2+}$, $Cr(bipy)_3^{3+}$] are ideally (reversibly) behaved on RuO_x whereas slower reactions (*e.g.*, tetrathiafulvalene, methylviologen, ferrocene) experience more kinetic limitations on RuO_x as compared to Pt. Such behavior is more consistent with a RuO_x surface resistive phenomenon than with a bulk oxide resistance. The latter, as any ohmic effect, should affect all model reactions more or less identically. On this basis we are inclined not to attribute any observed electrochemical phenomena to conductivity effects of internal chloride. Surface chloride sites may act as chemically active sites, on the other hand (33).

The XPES results for Ru $3d_{5/2}$ at 280.9 eV and O 1s at 529.2 eV are in good agreement with RuO_2 results of Kim and Winograd (32). A second species, which according to the binding energies is RuO_3, also appears. The role of RuO_3 in chlorine anode efficacy has been speculated upon (33). We are inclined to suggest that the RuO_3 may constitute a charge transfer resistive element at the RuO_x surface. Whether the RuO_x surface is uniformly covered by a thick RuO_3 film or a RuO_2/RuO_3 defect structure is unknown. If for instance only a few electronically conducting (electron transfer favoring) RuO_2 patches actually exist at the surface, the electrode reaction current density at those sites would be much greater than that imagined from the electrode geometrical area. The consequences would be minimal for very fast electrode reactions [*e.g.*, $Ru(bipy)_3^{2+}$] able to sustain high current densities without departure from electrochemical equilibrium, but noticeable for electrode reactions with intrinsically slower rates such as ferrocene, tetrathiafulvalene, or methylviologen. Finally we should note that if an RuO_3 structure on the electrode has in fact electrochemical consequences, it is possible that residual surface chloride could, indirectly, affect electrochemistry through influence on the distribution or extent to which RuO_3 becomes formed.

Acknowledgment

This research was assisted by the National Science Foundation. The authors gratefully acknowledge assistance of D. F. Smith in bandfitting.

Manuscript submitted June 19, 1978; revised manuscript received Aug. 31, 1978.

Any discussion of this paper will appear in a Discussion Section to be published in the December 1979 JOURNAL. All discussions for the December 1979 Discussion Section should be submitted by Aug. 1, 1979.

Publication costs of this article were assisted by the University of North Carolina.

REFERENCES

1. South African Pat. 68/7482, 68/7371. German Pat. 2,021,422 (1969); 2,014,746, 1,915,951 (1970). British Pat. 1,206,863 (1970).
2. O. DeNora, *Chem. Ing. Tech.*, **42**, 222 (1970); **43**, 182 (1971).
3. A. Fujishima, K. Kohayakawa, and K. Honda, *This Journal*, **122**, 1487 (1975); A. Fujishima and K. Honda, *Nature*, **238**, 37 (1972).
4. P. R. Moses, L. Wier, and R. W. Murray, *Anal. Chem.*, **47**, 1882 (1975).
5. P. R. Moses and R. W. Murray, *J. Electroanal. Chem.*, **77**, 393 (1977).

6. J. R. Lenhard and R. W. Murray, *ibid.*, **78**, 195 (1977).
7. J. R. Lenhard, R. D. Rocklin, H. Abruna, K. W. Willman, K. N. Kuo, and R. W. Murray, *J. Am. Chem. Soc.*, **100**, 5213 (1978).
8. P. R. Moses and R. W. Murray, *ibid.*, **98**, 7435 (1976).
9. P. R. Moses, L. M. Wier, J. C. Lennox, H. O. Finklea, J. R. Lenhard, and R. W. Murray, *Anal. Chem.*, **50**, 576 (1978).
10. M. S. Wrighton, R. G. Austin, A. B. Bocarsly, J. M. Bolts, O. Haas, K. D. Legg, L. Nadjo, and M. C. Palazzotto, *J. Electroanal. Chem.*, **87**, 429 (1978).
11. R. J. Burt, G. J. Leigh, and C. J. Pickett, *Chem. Commun.*, 940 (1976).
12. A. Diaz, *J. Am. Chem. Soc.*, **99**, 5838 (1977).
13. D. Galizzioli, F. Tantardini, and S. Trasatti, *J. Appl. Electrochem.*, **4**, 57 (1975); **5**, 203 (1975).
14. W. O'Grady, C. Iwakura, J. Huang, and E. Yeager, "Electrocatalysis," M. W. Breiter, Editor, p. 286, The Electrochemical Society Softbound Symposium Series, Princeton, N.J. (1974).
15. T. Arikado, C. Iwakura, and H. Tamura, *Electrochim. Acta*, **22**, 513 (1977).
16. L. D. Burke, O. J. Murphy, and J. F. O'Neill, *J. Electroanal. Chem.*, **81**, 394 (1977).
17. E. K. Spasskaya, Yu. B. Makarychev, A. A. Yakovleva, and L. M. Yakimenko, *Electrokhimiya*, **13**, 327 (1977).
18. S. Trasatti and G. Buzzanca, *J. Electroanal. Chem.*, **29**, App. 1 (1971).
19. S. Pizzini, G. Buzzanca, C. Mari. L. Rossi, and S. Torchio, *Mater. Res. Bull.*, **7**, 449 (1972).
20. A. T. Kuhn and C. J. Mortimer, *This Journal*, **120**, 231 (1973).
21. K. L. Hardee and A. J. Bard, *ibid.*, **122**, 739 (1975).
22. J. Horkans and M. W. Shafer, *ibid.*, **124**, 1202 (1977).
23. C. Creutz and N. Sutin, *J. Am. Chem. Soc.*, **99**, 241 (1977).
24. M. E. Peover, "Electrochemistry of Aromatic Hydrocarbons and Related Substances," in Vol. 2, "Electroanalytical Chemistry," A. J. Bard, Editor, pp. 9-11, Marcel Dekker, Inc., New York (1967).
25. C. M. Hughes and D. J. Macero, *Inorg. Chem.*, **15**, 2040 (1976).
26. L. Meites and P. Zuman, "Electrochemical Data," Part 1, Vol. A, Wiley-Interscience, New York (1974).
27. "Techniques of Chemistry," Vol. 1, "Physical Methods of Chemistry," Part IIa, A. Weissberger and B. W. Rossiter, Editors, p. 591, Wiley-Interscience, New York (1977).
28. R. S. Nicholson and I. Shain, *Anal. Chem.*, **36**, 706 (1964).
29. D. L. Coffen, J. Q. Chambers, D. R. Williams, P. E. Garrett, and N. D. Canfield, *J. Am. Chem. Soc.*, **93**, 2258 (1973).
30. G. Gruver, T. Osa, and T. Kuwana, U.S. Army Research Symposium, Durham, N.C. (1968).
31. L. M. Wier, Ph.D. Dissertation, University of North Carolina (1977).
32. K. S. Kim and N. Winograd, *J. Catal.*, **35**, 66 (1974).
33. J. Augustynski, L. Balsenc, and J. Hinden, *This Journal*, **125**, 1093 (1978).
34. C. Iwakura, H. Tada, and H. Tamura, *Electrochim. Acta.*, **22**, 217 (1977).
35. J. H. Scofield, Lawrence Livermore Laboratory, Report No. UCRL-51326.
36. T. A. Carlson, "Photoelectron and Auger Spectroscopy," p. 358, Plenum Press, New York (1975).
37. L. Ramquist, K. Hamrin, G. Johansson, A. Fahlmen, and C. Nording, *J. Phys. Chem. Solids*, **30**, 1835 (1969); V. J. Nefecov, Y. V. Salyn, A. A. Chertkov, and L. N. Padurets, *Russ. J. Inorg. Chem., (English translation)*, **19**, 785 (1974).

Electrogenerated Chemiluminescence

34. Photo-Induced Electrogenerated Chemiluminescence and Up-Conversion at Semiconductor Electrodes

J. D. Luttmer* and Allen J. Bard**

Department of Chemistry, The University of Texas at Austin, Austin, Texas 78712

ABSTRACT

Photosensitized oxidations or reductions at p- and n-type GaAs and InP semiconductor electrodes of aromatic species in aprotic solvents leading to electrogenerated chemiluminescence (ECL) are described. The energy of the irradiating light equal to the bandgap energy of the semiconductor and the electrical energy input couple to produce excited states which eventually produce emission at shorter wavelengths. Intense ECL is observed by alternately generating radical cations and radical anions at an illuminated semiconductor electrode with smaller potential excursions than required on metal (platinum) electrodes.

Photoassisted electrode processes of a number of species (*e.g.*, aromatic hydrocarbons and heterocyclic compounds) at semiconductor electrodes in aprotic solvents have been described (1-5). These studies have demonstrated that electrochemical oxidations at n-type semiconductors occur at less positive potentials (or reductions at p-type semiconductors at less negative potentials) than are required to carry out the same process at an inert metal (*e.g.*, Pt) electrode. These processes thus involve the partial conversion of light energy to chemical energy in the electrogenerated species. When the electrogenerated species (*e.g.*, radical ions) are capable of undergoing homogeneous electron transfer reactions near the electrode surface to produce excited states, electrogenerated chemiluminescence (ECL) results. Hence the over-all scheme involves coupling of the input light energy and electrical energy to produce an output emission of higher energy (or "up-conversion"). Such a scheme was initially suggested by Nicholson (6), but prior to this report was never reduced to practice. A previous report from this laboratory described a similar experiment where the photoinduced reduction of 9,10-dichloro-9,10-dihydro-9,10 diphenyl-anthracene ($DPACl_2$) on p-Si irradiated with red light in acetonitrile (7) produced violet emission. There, however, emission is observed only upon reduction of $DPACl_2$ via a chemical-

* Electrochemical Society Student Member.
** Electrochemical Society Active Member.
Key words: photoluminescence, visible, voltammetry, energy conversion.

electrochemical mechanism (8), and much of the energy of the emitting light may be attributed to the chemical energy of $DPACl_2$ moiety itself, which is not regenerated in the over-all process.

The ECL scheme usually involves production and annihilation of radical ion species at metal electrodes by an electron-transfer mechanism (9, 10)

$$\text{(cathodic step)} \quad A + e \rightleftharpoons A^{\cdot -} \quad (E^\circ_{A/A^{\cdot -}}) \quad [1]$$

$$\text{(anodic step)} \quad D - e \rightleftharpoons D^{\cdot +} \quad (E^\circ_{D^{\cdot +}/D}) \quad [2]$$

$$A^{\cdot -} + D^{\cdot +} \rightarrow {}^3A^* \text{ (or } {}^1A^*) + D \quad [3]$$

$${}^3A^* + {}^3A^* \rightarrow {}^1A^* + A \quad [4]$$

$${}^1A^* \rightarrow A + h\nu \quad [5]$$

where A represents an electron acceptor (*e.g.*, an aromatic hydrocarbon) and D represents an electron donor (*e.g.*, an aromatic hydrocarbon or amine). Formation of excited states of D and exciplexes are also possible during the ion-annihilation reaction, Eq. [4], but are omitted, since they are not important in the reactions to be described here. When the ECL reaction is carried out on a semiconductor electrode, two new features emerge. First, the semiconductor/liquid interface behaves like a Schottky junction and shows diode-like behavior. This results in anodic reactions occurring positive of the flatband potential, V_{fb}, being blocked at n-type materials and cathodic reactions occurring negative of V_{fb} being blocked at p-type materials (11). Thus irradiation of the electrode is required to allow generation of both $A^{\cdot -}$ and $D^{\cdot +}$ and observe emission. Secondly, irradiation of the semiconductor photoassists the electrochemical process, so that oxidations at irradiated n-type electrodes occur at potentials less positive than $E^\circ_{D^{\cdot +}/D}$ and reductions at irradiated p-type electrodes occur at potentials less negative than $E^\circ_{A/A^{\cdot -}}$. Details of ECL experiments at several semiconductor electrodes incorporating these features are reported here.

Experimental

Acetonitrile (ACN; Spectroquality, Matheson, Coleman and Bell) was refluxed over fresh CaH_2 powder for 8 hr followed by fractional distillation under dry nitrogen. The middle fraction was transferred to a vacuum line and subjected to four freeze-pump-thaw cycles to remove dissolved gases. The solvent was then vacuum distilled into a storage flask containing molecular sieves (Linde 4A) activated by heating under high vacuum at 400°C for 72 hr. Benzene (BZ; Spectroquality, Matheson, Coleman and Bell) was refluxed over potassium for 24 hr under dry nitrogen, distilled, and subjected to four freeze-pump-thaw cycles. The solvent was vacuum distilled into a storage flask containing Na-K alloy.

Tetra-n-butylammonium perchlorate (TBAP; Southwestern Analytical Chemicals) and rubrene (RUB; Aldrich) were purified as previously described (8). Chrysene (CHR; Aldrich) was treated with maleic anhydride, chromatographed on an alumina column, and recrystallized repeatedly from benzene. Fluoranthene (FLU; Zone Refined, Aldrich) and perylene (PER; Gold Label, Aldrich) were used as received. 9,10-Diphenylanthracene (DPA; Gold Label, Aldrich) was sublimed and zone refined. 10-Methylphenothiazine (10-MP; Eastman) and tetracene (TET; Eastman) were purified by multiple recrystallizations from benzene. Pyrene (PYR; Eastman) was recrystallized from ethanol and sublimed twice. N,N,N',N'-tetramethyl-p-phenylenediamine (TMPD) was prepared and purified as previously reported (12). p-(9-Anthranyl)-N,N-dimethylaniline (DMAA), generously provided by Dr. Kingo Itaya, was used as received.

N- and p-type InP and GaAs semiconductor electrodes were prepared as previously reported (13, 14). V_{fb} of the semiconductor electrodes was determined by photocurrent onset measurements and Schottky-Mott plots. GaAs and InP semiconductor electrodes were etched in H_2SO_4-30% H_2O_2-H_2O (3:1:1) for 5-10 sec and then in 6*M* HCl for 30 sec (GaAs) or 5 sec (InP). The electrodes were then rinsed with H_2O and ethanol, and dried immediately under vacuum at room temperature.

The electrochemical ECL cell was of conventional design (12) and incorporated semiconductor and Pt wire-working electrodes. The Ag wire quasireference electrode was shielded in a Teflon jacket having a porous Vycor plug. The auxiliary electrode consisted of a large Pt foil in the bulk solution. The cell, containing radical ion precursor compounds and supporting electrolyte, was assembled and evacuated 5-18 hr at high vacuum. Solvent was added by vacuum distillation. Solutions typically contained 1-3 *mM* A and D and 0.1*M* TBAP as supporting electrolyte. The electrochemical and spectroscopic apparatus and techniques utilized have previously been reported (12, 13). Illumination of the semiconductor electrodes was accomplished with either a 3 mW He-Ne laser or a 650W tungsten-halogen lamp incorporating Ditric Company infrared pass (<1.7 eV) filters. A $CuSO_4$ solution filter was typically used to eliminate stray infrared light incident on the photomultiplier tube.

Results

The semiconductors studied and their properties are given in Table I, and the spectroscopic and electrochemical properties of the donor and acceptor molecules of the ECL systems are given in Table II.

N-type semiconductors.—Typical electrochemical behavior on n-type semiconductor electrodes is given in Fig. 1 and 2. In the dark, virtually no current flows at potentials positive of V_{fb}. At potentials negative of V_{fb}, however, the semiconductor electrode becomes degenerate (11) and shows cyclic voltammetric (cv) behavior similar to that on a metal electrode. Thus redox couples located negative of V_{fb} (*e.g.*, DPA, FLU) show reversible cv waves. When the n-type semiconductor

Table I. Semiconductor electrode properties

Electrode	E_g (eV)*	V_{fb}**	Area (cm²)
n-InP	1.27	−1.0 ± 0.2	0.22
n-GaAs	1.43	−1.0 ± 0.2	0.12
p-InP	1.27	+0.0 ± 0.2	0.15
p-GaAs	1.43	+0.1 ± 0.2	0.11

* Bandgap energy.
** Flatband potential, volts *vs.* SCE in acetonitrile.

Table II. Electrochemical and spectroscopic properties

Compound	$E_{1/2}$ $(R/R^{\cdot +})$*	$E_{1/2}$ $(R/R^{\cdot -})$*	E_s (eV)	E_T (eV)
N,N,N',N'-tetramethyl p-phenylenediamine (TMPD)	0.20, 0.77	—	3.1 (15)	2.38 (15)
10-methylpheno-thiazine (10-MP)	0.79	—	2.9 (15)	2.4 (15)
9,10-diphenyl-anthracene (DPA)	1.28	−1.84	3.06 (16)	1.77 (17)
fluoranthene (FLU)	—	−1.74	3.4 (17)	2.30 (17)
rubrene (RUB)	0.94**	−1.43**	2.36 (18)	1.2 (18)
p-(9-anthranyl)-N,N-dimethylaniline (DMAA)	0.75	−2.00	2.52 (19)	—
perylene (PER)	1.14	−1.63	2.85 (17)	1.52 (17)
pyrene (PYR)	1.31	−2.05	3.34 (17)	2.10 (17)
tetracene (TET)	1.02**	−1.58**	2.60 (17)	1.27 (17)
chrysene (CHR)	1.56	−2.25	3.4 (17)	2.48 (17)

* Volts *vs.* SCE in acetonitrile unless otherwise noted.
** Acetonitrile-benzene mixed solvent.

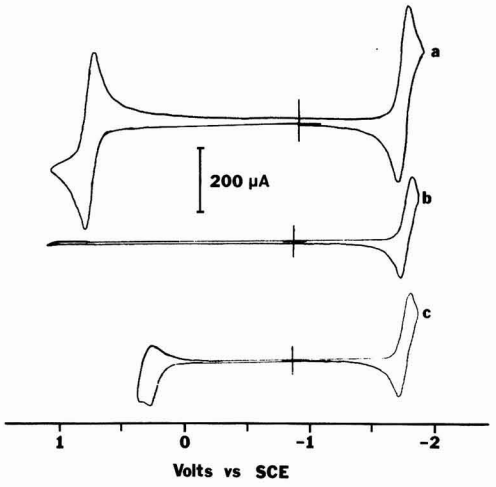


Fig. 1. Cyclic voltammetry of ~3 mM 10 MP and 3 mM FLU in 0.1M TBAP/ACN; scan rate, 200 mV/sec. (a) On platinum; (b) on n-InP in the dark; (c) on illuminated (3 mW He-Ne laser) n-InP.

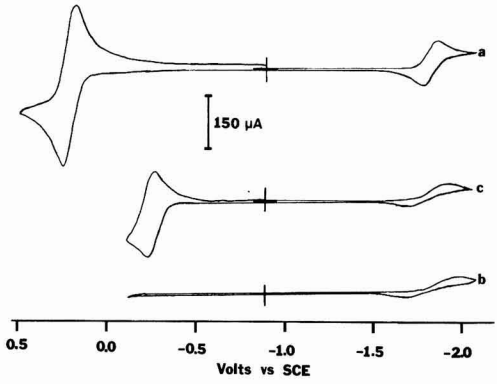


Fig. 2. Cyclic voltammetry of ~2.5 mM TMPD and 1 mM DPA in 0.1M TBAP/ACN; scan rate, 200 mV/sec. (a) On platinum; (b) on n-GaAs in the dark; (c) on illuminated (3 mW He-Ne laser) n-GaAs.

electrode is illuminated with light of greater energy than the bandgap energy (Eg), electrons are excited into the conduction band and holes produced in the valence band can be populated by electron transfer from suitable solution species. This process is most efficient at potentials positive of V_{fb} where the photoproduced holes accumulate at the semiconductor-solution interface. The photoinduced oxidation of species with solution energy levels located at potentials more positive than the valence band edge (E_v) is not expected since a hole produced at energy E_v would not be sufficiently energetic. Such a phenomenon was observed here, however, A similar photoeffect on oxidations occurring negative of V_{fb} was found in a previous study at GaAs electrodes (14) and was ascribed to production of a film on the electrode surface upon reduction which effectively formed a solid/solid junction adding a bias under illumination. Such an effect cannot be occurring here, since a photoeffect is found for the D/D^+ wave, but not at the A^-/A one. An alternate explanation rests on a change in the surface of the electrode which shifts the value of V_{fb} toward more positive values (Fig. 3). Effectively then, illumination of the n-type semiconductor electrode with bandgap energy light results in the oxidation of the solution species D at less positive potentials than those where this species is reversibly oxidized on metal electrodes. This "negative overpotential" effect (7, 14) is the basis for solar energy conversion utilizing electrochemical systems.

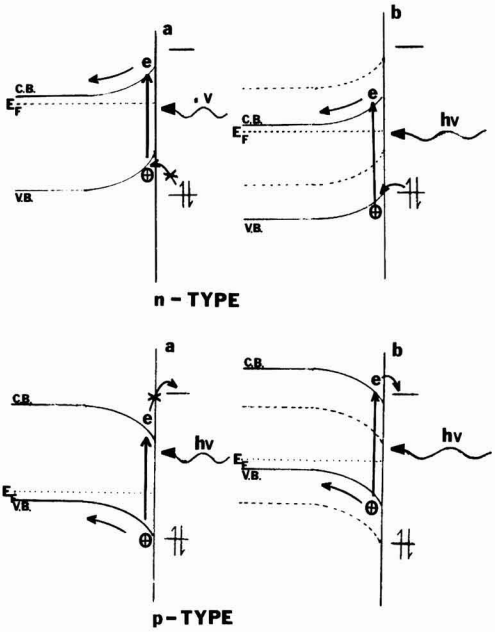


Fig. 3. Shift of conduction and valence band energies upon film formation: (a) prior to film formation; (b) film formation allowing electron transfer upon photoexcitation of the semiconductor electrode.

A typical experiment involving photoinduced ECL at an n-type semiconductor electrode is shown in Fig. 4. The initial potential is established where no current flows until the electrode is illuminated, whereupon an anodic current flows and the oxidized species is produced at the electrode. Stepping the potential to negative values to form the reduced species results in in-

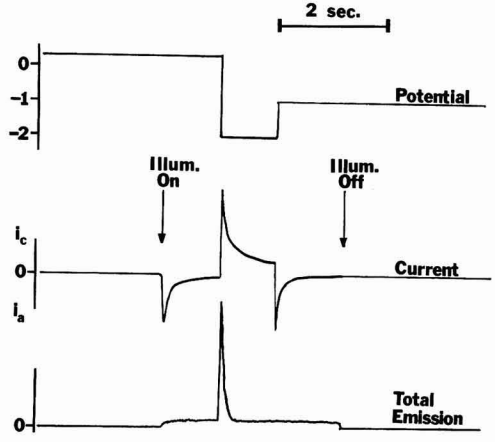


Fig. 4. Potential-, current-, and emission-time profiles illustrating photoinduced oxidation of 10 MP and reduction of FLU on n-InP yielding ECL. Illumination of n-InP with 3 mW He-Ne laser.

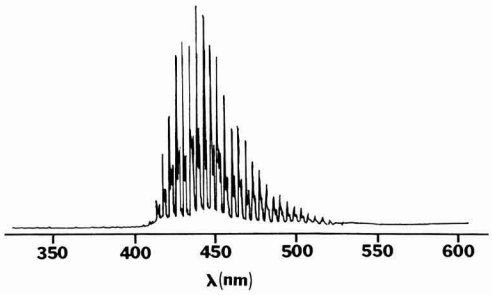


Fig. 5. Uncorrected ECL spectrum of ~2 mM TMPD and 1 mM DPA on n-InP illuminated with 3 mW He-Le laser. Potential pulsed from −0.05 to −2.0V vs. SCE at 1 Hz.

tense ECL as the radical ions annihilate in the diffusion layer adjacent the electrode. Pulsing the semiconductor electrode potential between these potential limits results in pulses of ECL emission when the electrode was illuminated with bandgap energy light (>1.4 eV). With these same potential excursions, no emission was observed on a platinum electrode, because the potential limits were insufficient to produce D^+ and A^- with photoassistance. A typical ECL spectrum obtained by scanning the emission wavelength during repetitive pulsing under irradiation is shown in Fig. 5.

The potential dependence of the emission was ascertained by employing anodic linear potential sweeps from potentials where the reduced species is formed toward positive values, as previously described (13) (Fig. 6). Under dark conditions, virtually no emission is observed at the semiconductor until the electrode potential reaches very positive potentials. The semiconductor electrode illuminated with bandgap energy light, however, gives emission at potentials less positive than those necessary for emission on platinum.

The ECL emission observed in all of the cases examined (Table III) was quite bright, visible to the eye in a well-illuminated room, and comparable to the emission observed on platinum electrodes when using larger potential excursions. Although the ECL of systems utilizing easily oxidizable species (*e.g.*, TMPD) was quite stable with continuous potentiostatic pulsing and illumination, less stability was found with species oxidized at more positive potentials. For example, although an initial ECL pulse with RUB on n-InP was intense (and easily visible), the intensity rapidly decayed upon further pulsing, probably because of oxi-

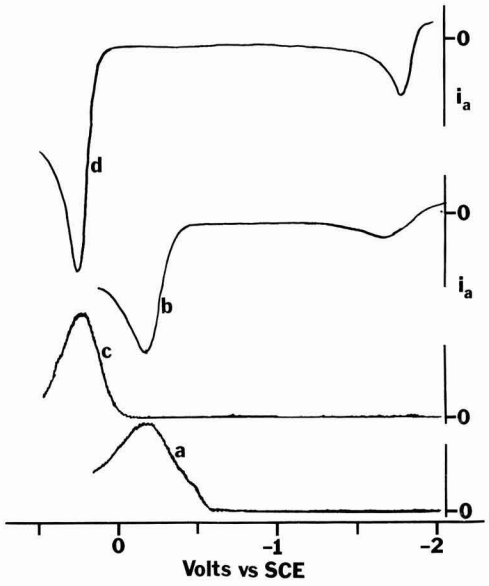


Fig. 6. ECL- and current-potential curves observed by anodic linear potential sweep voltammetry at 2 V/sec with 3 mM TMPD and 1 mM DPA in 0.1M TBAP/ACN. (a) ECL intensity; and (b) current obtained on n-InP illuminated with $h\nu < 1.7$ eV.; (c) ECL; and (d) current obtained on platinum.

dation of the semiconductor lattice (14). Electrode stability was similarly adversely affected by traces of H_2O when less rigorously dehydrated solvent was used. Under these conditions, the photoinduced oxidation of the semiconductor lattice was found to occur at less positive potentials and resulted in the accumulation of an electrically insulating film on the semiconductor electrode surface.

P-type semiconductors.—The electrochemical behavior at p-type semiconductor electrodes was analogous to that found with n-type electrodes. Typical cyclic voltammograms are shown in Fig. 7 and 8. Unlike oxidations at the n-type material, some current attributable to dark reduction of the substrate is observed at the p-type material, but only at potentials negative of where the reduction wave is found at Pt. Oxidations at potentials positive of V_{fb} occur readily and the electrode shows essentially metallic behavior.

Table III. Summary of ECL experiments on the photoinduced up-conversion at p- and n-type InP and GaAs

Electrode	System	Oxidation**		Reduction**		ΔE_{ECL}***	Emission	Comments†
		E_{p_a}	E_{p_c}	E_{p_c}	E_{p_a}			
n-GaAs	TMPD/DPA	−0.38	−0.34			1.5-1.7	Blue	Stable, bright, $\Delta E_{ECL} < E_T$
		−0.17	+0.09					
	10-MP/DPA	0.25	0.28			2.1-2.2	Blue	Moderately stable, bright emission
	DMAA	0.16	—			2.1-2.3	Yellow	Bright intramolecular exciplex emission, cation unstable
n-InP	10-MP/FLU	0.29	0.29			2.0-2.1	Blue	Mod. stable, bright, $\Delta E_{ECL} < E_T$
	RUB	0.52	0.47			1.9-2.1	Yellow	Bright, unstable
	TMPD/DPA	−0.22	−0.17			1.9-2.1	Blue	Stable, bright
		0.29	0.30					
p-GaAs	10-MP/FLU			−1.45	−1.48	2.2-2.4	Blue	Stable, bright, $E_{ECL} \leq E_T$
	PER			−1.18	−1.31	2.2-2.5	Blue	Bright, mod. stable, cooxidation of electrode
	DPA			−1.46	−1.52	2.7-2.8	Blue	Bright, unstable, cooxidation of electrode
p-InP	PER			−1.30	−1.06	2.3-2.5	Blue	Bright, mod. stable, some oxidation of InP
	DPA			−1.37	−1.14	2.6-2.8	Blue	Bright, unstable, cooxidation of InP

* 0.1M TBAP/acetonitrile solution.
** Current peak potentials, volts *vs.* SCE. Electrode illuminated with $h\nu < 1.7$ eV.
*** Potential excursions needed to obtain ECL on illuminated semiconductor electrode.
† Stability refers to semiconductor electrode with respect to degradation.

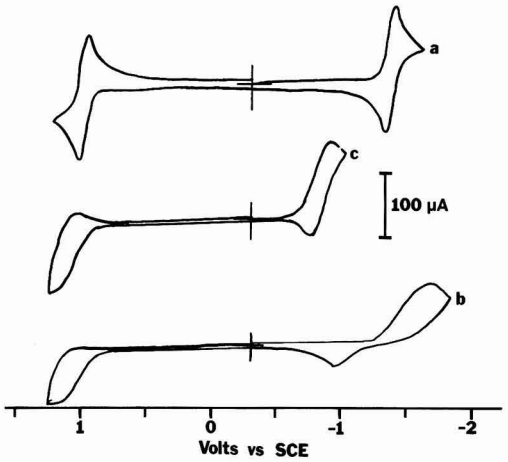


Fig. 7. Cyclic voltammetry of 1 mM RUB in 0.1M TBAP/ACN-BZ(1:1); scan rate, 200 mV/sec. (a) On platinum; (b) on p-InP in the dark; (c) on p-InP illuminated with $h\nu < 1.7$ eV.

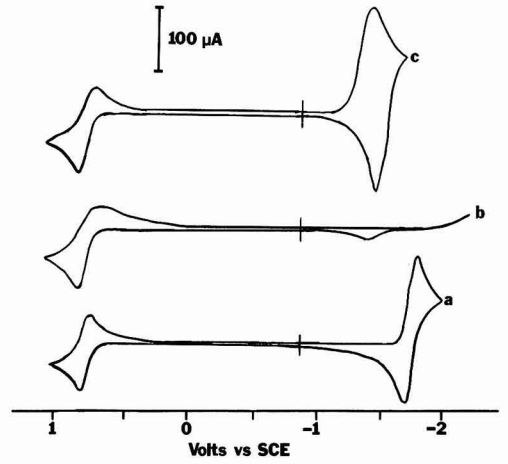


Fig. 8. Cyclic voltammetry of ~2.5 mM FLU and 1.5 mM 10-MP in 0.1M TBAP/ACN; scan rate, 200 mV/sec. (a) On platinum; (b) on p-GaAs in the dark; (c) on p-GaAs illuminated with $h\nu < 1.7$ eV.

When the electrode at potentials negative of V_{fb} is illuminated with bandgap energy light, electrons excited into the conduction band can reduce the solution acceptor species. Again, some surface phenomenon which allows the photoinduced reduction of suitable solution species with solution energy levels above the conduction band edge with a considerable "negative overpotential" must be involved (14).

The ECL results with p-type semiconductor electrodes are summarized in Table III; a typical experiment is shown in Fig. 9. Although the reduced species (FLU here) could be generated in the dark at very negative potentials (*i.e.*, beyond *ca.* −2.5V), the $A^{-\cdot}$ was typically generated at potentials positive of where it is thermodynamically accessible on platinum by illuminating the semiconductor electrode. As illustrated, no ECL could be observed on platinum under these conditions.

The ECL from the systems examined was quite intense and visible to the eye. Species with rather

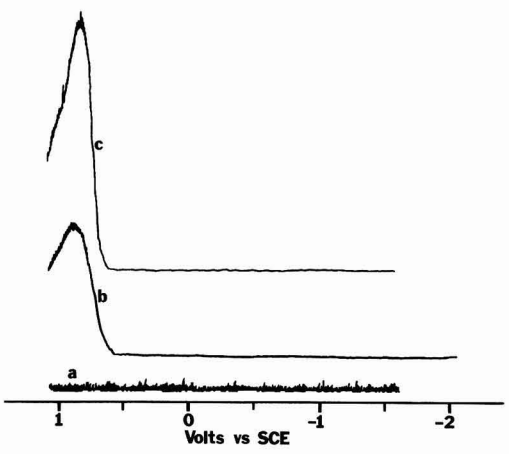


Fig. 9. ECL-potential curve obtained by anodic linear potential sweep voltammetry at 2 V/sec with 2.5 mM FLU and 1.5 mM 10-MP in 0.1M TBAP/ACN. (a) On platinum from −1.60V *vs.* SCE (Gain, ×100); (b) on platinum from −2.1V *vs.* SCE; (c) on p-GaAs illuminated with 3 mW He-Ne laser from −1.60V *vs.* SCE.

positive $E_{1/2}(R/R^{+\cdot})$ values were oxidized concurrently with the semiconductor electrode lattice and in these systems the ECL intensity tended to degrade with continuous pulsing. For example, the oxidation of DPA occurs at potentials where semiconductor lattice oxidation is observed and the ECL emission with this system was rather short-lived. A system employing 10-MP which has a somewhat less positive $E_{1/2}(R/R^{+\cdot})$ value was quite stable with continuous potential pulsing and illumination of the p-type semiconductor electrodes examined however. As observed on the n-type semiconductor electrodes, traces of H_2O had a deleterious effect upon the semiconductor electrode stability, especially when rather positive potentials were applied to the electrode.

Discussion

The results presented here demonstrate that up-conversion by the ECL-semiconductor electrode scheme, in a process where no material is consumed (except perhaps by parasitic side reactions), is possible. Moreover, photoassistance of the electrode process allows a coupling of the light energy and electrical energy input to produce emission at an energy where neither the light nor electrical energy alone would be sufficient. In the systems examined negative overpotentials of 400-600 mV could be attained. While it is true that the triplet-triplet annihilation step, Eq. [4], was responsible for the energy gain, in some of the cases examined neither the potential stimulus nor the energy of the illumination light alone was sufficient to populate the lowest triplet level. For example, for the 10 MP FLU system at n-InP, E_T for FLU is 2.30 eV, while the applied potential to the system was only 2.0-2.1V.

The results reported here suggest that the fabrication of devices employing small bandgap (<1.5 eV) semiconductor electrodes to up-convert near infrared light to higher energy light in the visible region may be possible. The emitted light was quite intense and the semiconductor electrodes were quite stable under strictly anhydrous conditions upon repeated cycling, although most ECL systems are known to degrade over a very long time period. A device built on these principles would require rather low voltages (~3V) and would have a spacial resolution determined by the narrow width of the radical ion annihilation zone.

Acknowledgment

We gratefully acknowledge the Army Research Office and the National Science Foundation for the support of this research. We are indebted to Paul Kohl for the flatband potential measurements and many helpful discussions concerning this work.

Manuscript submitted May 17, 1978; revised manuscript received July 19, 1978.

Any discussion of this paper will appear in a Discussion Section to be published in the December 1979 JOURNAL. All discussions for the December 1979 Discussion Section should be submitted by Aug. 1, 1979.

Publication costs of this article were assisted by the University of Texas at Austin.

REFERENCES

1. S. N. Frank and A. J. Bard, *J. Am. Chem. Soc.*, **97**, 7427 (1975).
2. D. Laser and A. J. Bard, *J. Phys. Chem.*, **80**, 459 (1976).
3. P. A. Kohl and A. J. Bard, *J. Am. Chem. Soc.*, **99**, 7531 (1977).
4. R. Landsberg, P. Janietz, and R. Dehmlow, *Z. Phys. Chem. (Leipzig)*, **257**, 657 (1976).
5. K. Nakatani and H. Tsubomura, *Bull. Chem. Soc. Jpn.*, **50**, 783 (1977).
6. M. M. Nicholson, *This Journal*, **119**, 461 (1972).
7. D. Laser and A. J. Bard, *Chem. Phys. Lett.*, **34**, 605 (1975).
8. K. G. Boto and A. J. Bard, *J. Electroanal. Chem. Interfacial Electrochem.*, **65**, 945 (1975).
9. L. R. Faulkner, in "MTP Int. Rev. Sci. Phys. Chem. Ser. Two," Vol. 9, D. R. Herschbach, Editor, Chap. 6, and ref. therein, Medical and Technical Publ. Co., Ltd., Lancaster, England (1976).
10. L. R. Faulkner and A. J. Bard, in "Electroanalytical Chemistry," Vol. 10, A. J. Bard, Editor, Chap. 1 and ref. therein, Marcel Dekker, Inc., New York (1977).
11. H. Gerischer, in "Advances in Electrochemistry and Electrochemical Engineering," Vol. 1, P. Delahay and C. Tobias, Editors, Chap. 4, Interscience, New York (1961); H. Gerischer, in Physical Chemistry," Vol. 9A, H. Eyring, D. Henderson, and W. Jost, Editors, Chap. 5, Academic Press, New York (1970); H. Gerischer, *Photochem. Photobiol.*, **16**, 243 (1972); H. Gerischer, *Ber. Bunsenges. Phys. Chem.*, **77**, 771 (1973); H. Gerischer, *J. Electroanal. Chem. Interfacial Electrochem.*, **58**, 263 (1975).
12. L. R. Faulkner, H. Tachikawa, and A. J. Bard, *J. Am. Chem. Soc.*, **94**, 691 (1972).
13. J. D. Luttmer and A. J. Bard, *This Journal*, **125**, 1423 (1978).
14. P. A. Kohl and A. J. Bard, Paper submitted to *ibid.*
15. S. M. Park, Ph.D. Dissertation, University of Texas at Austin (1975).
16. C. P. Keszthelyi, A. T. Kessel, W. B. Edwards, and G. D. Clark, *Proc. Louis. Acad. Sci.*, **39**, 65 (1976).
17. S. L. Murov, "Handbook of Photochemistry," Marcel Dekker, New York (1973).
18. D. K. K. Liu and L. R. Faulkner, *J. Am. Chem. Soc.*, **99**, 4594 (1977).
19. K. Itaya and S. Toshima, *Chem. Phys. Lett.*, **51**, 447 (1977).

Semiconductor Properties of Iron Oxide Electrodes

S. M. Wilhelm,* K. S. Yun, L. W. Ballenger,* and N. Hackerman*****

Department of Chemistry, Rice University, Houston, Texas 77001

ABSTRACT

The semiconductor electrode properties of thermally grown iron oxide and anodic oxide films on iron are compared. The bandgaps are 2.1 and 1.9 eV, respectively. Donor densities and flatband potentials are reported. Measurement of the currents produced by chopped illumination ($f \leq 100$ Hz) has allowed evaluation of electrode parameters and determination of reaction pathways.

The recent interest in iron oxide electrodes centers around their potential application to photoassisted electrolysis of water. These materials are promising because of their relatively narrow bandgap and of possible use because of their stability. The n-type polycrystalline αFe_2O_3 (1-5) behaves much as does single crystal αFe_2O_3 (6) (see Table I, Part A) and has the advantage of being easy to prepare.

The anodic oxide or passive film on iron is also reported to be a semiconductor (7-9) (see Table I, Part B). Photocurrent data, however, has not been reported. In the present investigation, the semiconducting character of thermally grown polycrystalline iron oxide and anodically produced oxide films on iron are compared directly with regard to photocurrent, differential capacitance, and polarization measurements.

Experimental

All measurements were made in a solution 0.075*N* in H_3BO_3, 0.075*N* in $Na_2B_4O_7$, and 1*N* in $NaNO_3$ (pH 8.4). The $K_3Fe(CN)_6/K_4Fe(CN)_6$ couple was added in certain experiments. All solutions were prepared from triply distilled water and were saturated with purified N_2. All chemicals were reagent grade or better.

A two compartment Pyrex cell containing a platinum gauze counterelectrode and a saturated calomel reference electrode (SCE) was used. All potentials are reported *vs.* SCE. The working electrode was approximately 0.5 cm from a Pyrex window through which the light was focused on the electrode surface in photocurrent experiments.

Electrodes were constructed from zone-refined iron (99.99% Fe). The thermally grown iron oxide electrodes were prepared as described previously (5). The bare metal electrodes were polished to a mirror finish and cleaned with methanol prior to use. For each working electrode a 0.5-1.0 cm^2 planar surface was exposed to solution by insulating the rest of the electrode with silicone adhesive (Dow Corning). Anodic oxide films were formed by first cathodically reducing any air formed oxide at -0.80V in pH 8.4 buffer solution for 1 hr, replacing with fresh solution under nitrogen and then polarizing at $+0.80$V for 12 hr. The film thickness was estimated by galvanostatic reduction (10).

The photocurrent measurements (Fig. 1) employed a 200W tungsten lamp for polychromatic experiments.

* Electrochemical Society Student Member.
** Electrochemical Society Active Member.
*** Electrochemical Society Honorary Member.
Key words: passivity, photocurrent, electrolysis, ion oxides.

Table I. Semiconductor/electrochemical parameters for αFe_2O_3 and anodic oxide electrodes

Part A αFe_2O_3	Electrolyte	pH	V_{FB} (V vs. SCE)	E_g (eV)	N_D (cm^{-3})
1. CVD αFe_2O_3 (1, 2)	0.25M Na_2SO_4	9	−0.1	2.2	
2. Polycrystalline αFe_2O_3 (3, 4)	0.5M KCl, borate buffer	8.9	−0.34	2.2	10^{18}
3. Thermally grown iron oxide (5)	1M $NaNO_3$, borate buffer	8.4		1.4	
4. Single crystal αFe_2O_3	1M sodium acetate	8.6	−0.41	2.2	10^{17}
5. Thermally grown iron oxide*	1M $NaNO_3$, borate buffer	8.4	−0.31	2.1	10^{17}
Part B anodic oxide					
6. Anodic oxide (8)	1M $NaNO_3$, borate buffer	8.4	−0.34	1.6	10^{20}
7. Anodic oxide (9)	1M $NaNO_3$, borate buffer	8.4	−0.30		10^{21}
8. Anodic oxide*	1M $NaNO_3$, borate buffer	8.4	−0.26	1.9	10^{20}

* This paper.

The light was filtered with Oriel short pass and long pass filters. A 0.25m Jarrell-Ash monochrometer equipped with a 250W tungsten-iodide light source and 25 nm/min motor drive was used to obtain photocurrent-wavelength curves. The incident light was chopped with a Princeton Applied Research (PAR) Model 125 chopper at 100 Hz. The potentiostat output was amplified with a PAR Model 128A lock-in amplifier. In certain experiments the light was manually chopped by turning the lamp on and off and the current recorded directly without lock-in amplification.

Relative light intensities (I/I_o) were measured with an Oriel Model 7010 radiometer. I_o was arbitrarily chosen as the output of the monochrometer at $\lambda = 500$ nm. Relative intensities for other light sources and/or wavelengths were calculated from measured diode currents and corrected for detector sensitivity. For differential capacitance measurements a General Radio Model 1603-A Z-Y bridge at 1000 Hz was employed.

Results and Discussion

Oxides formed by heating iron in air consist of an inner Fe_3O_4 layer and an outer Fe_2O_3 layer (11, 12). Electron microscope examination of a lateral section of the thermal oxide showed that the thickness was about 3μ. The resolution was insufficient to determine the thickness of the αFe_2O_3 layer, however, Hussey *et al.* (11) reported that the ferric oxide amounted to only 1-3% of the total oxide thickness. Thus the thickness of the αFe_2O_3 layer would be approximately 0.1μ.

Anodic oxides also consist of an inner Fe_3O_4 layer and an outer γFe_2O_3 layer (13, 14). The thickness of the anodic oxide was determined by galvanostatic reduction to be approximately 30Å. No attempt has been made to analyze for specific impurity concentrations in either oxide beyond the donor densities reported.

Bandgap.—The dependence of photocurrent (i_p) on wavelength is illustrated in Fig. 2. The electrodes were polarized at + 0.80V and scanning was toward longer wavelengths. The portion of the current due only to illumination was recorded continuously by lock-in amplification. The initial increase in i_p is due to increasing transmission of the long pass filter used in the experiment to eliminate second order diffraction from the monochrometer grating. From extrapolated points a' (590 nm) and b' (646 nm), an energy difference between the valence and conduction bands (E_g) of 2.1 and 1.9 eV (±0.05 eV) is obtained for the thermal oxide and anodic oxide, respectively.

The electronic transition around 2 eV for both anodic and thermal oxides corresponds to excitation within the d-state manifold of the Fe^{+3} ion ($e_g \rightarrow t_{2g}$, spin inversion) (15). The predominantly *d* character of the valence band (e_g levels) may explain the unusual stability of these oxides to photodecomposition (16). It should be noted that a minimum energy for observation of i_p does not necessarily give a strict measurement of E_g. This is especially true for the anodic oxide in which the thickness of the γFe_2O_3 layer may be comparable to the absorption depth. The value of 1.9 eV for E_g of the anodic oxide is, however, close to the value of 1.6 eV estimated by Stimming and Schultze (8).

The value of 2.1 eV for E_g of the thermal oxide disagrees significantly with the value of 1.4 eV given previously (5). Although both experiments were performed in this laboratory, no explanation for the discrepancy has yet been found. The present measurement is quite reproducible and does not depend on the method of electrode preparation or the oxidation temperature. Oxides formed by heating iron in a gas flame or in an electric furnace (600°C) give identical results.

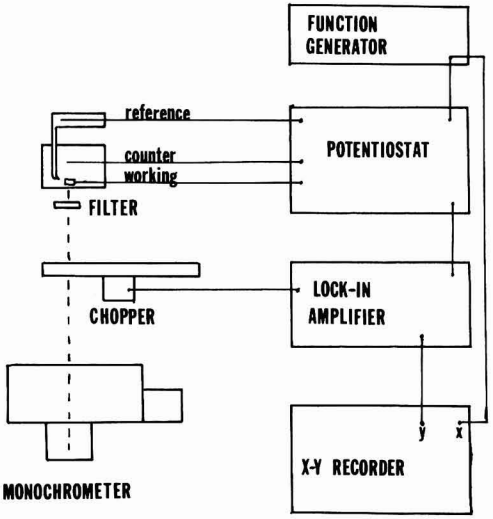


Fig. 1. Experimental apparatus for photocurrent measurements

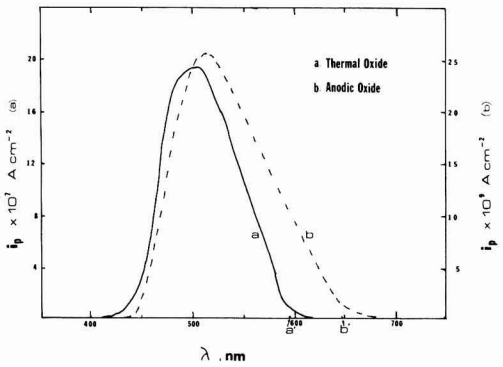


Fig. 2. Photocurrent *vs.* wavelength; chopping rate 100 Hz; scan rate 25 nm/min; $I = I_o$.

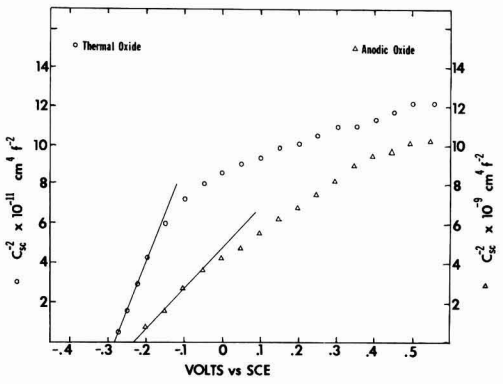


Fig. 3. Mott-Schottky plots for thermal and anodic oxides; frequency 1 kHz; pH 8.4.

Differential capacitance.—For the Mott-Schottky plots (Fig. 3) the space charge capacitance (C_{SC}) was calculated by assuming a constant Helmholtz capacitance (C_H) of 20 μf (17, 18) and employing the relations (19)

$$1/C = 1/C_{SC} + 1/C_H \quad [1]$$

$$1/C_{SC} = 2(q\epsilon\epsilon_0 N_D)^{-1}(V - V_{FB} - kT/q) \quad [2]$$

Donor densities ($N_D = 2 \times 10^{17}$/cm^3, thermal oxide; $N_D = 3 \times 10^{20}$/cm^3, anodic oxide) were obtained from the slope of the C_{SC}^{-2} *vs.* V curve. A dielectric constant (ϵ) of 12 was used in calculating N_D of the anodic oxide. The use of this value allows direct comparison with previously reported capacitance data (8) and is close to the dielectric constant of pure γFe_2O_3 ($\epsilon = 10$) (20). Similarly, $\epsilon = 100$ for the thermal oxide was chosen to allow direct comparison with Quinn (6) ($\epsilon = 120$) and Kennedy (4) ($\epsilon = 80$). Flatband potentials ($V_{FB} = -0.31$V, thermal oxide; $V_{FB} = -0.26$V, anodic oxide) were obtained from the intercept of the C_{SC}^{-2} *vs.* V curve by subtracting kT/q (25 mV).

Measurement of N_D is complicated by partial compensation in the oxide. The donor densities reported do not correspond to impurity concentrations but rather only approximate the nonstoichiometry (Fe^{+2}) of the space charge region. The capacitance measurements also show a significant frequency dependence. The nature of this dependence is complex and will be discussed in detail in a future publication (21).

Kennedy and Frese (3) have interpreted the change in slope (−0.1V) for polycrystalline αFe_2O_3 as being due to a critical voltage for the ionization of a deep donor 0.6 eV below the conduction band. It should be noted that a similar change in slope occurs for the anodic oxide at about 0.0V *vs.* SCE.

Photocurrent measurements.—The photocurrent response of the thermal oxide measured with the lock-in amplifier exhibits a linear dependence on electrode potential (Fig. 4). The intercept at −0.6V does not correspond to V_{FB}. At slower chopping rates (0.5 Hz) a transient photocurrent is observed which persists to −0.60V (Fig. 5, curve b) and is identical to that observed by Bard (2). The same transient photocurrents are also observed at the anodic oxide but are smaller (0.1-0.5 μA, $I = 3I_0$) in magnitude (Fig. 5, curve a). At fast chopping rates the lock-in amplifier photocurrent detection system does not distinguish between transient photocurrents (i_p^{ta}, anodic; i_p^{tc}, cathodic) and steady-state photocurrents (i_p^{ss}) and hence must be used with caution in evaluation of V_{FB}, etc. With low light intensities ($I = I_0$), the photocurrents at the anodic oxides (10^{-9} A/cm^2, Fig. 2) necessitate detection by phase-sensitive amplification.

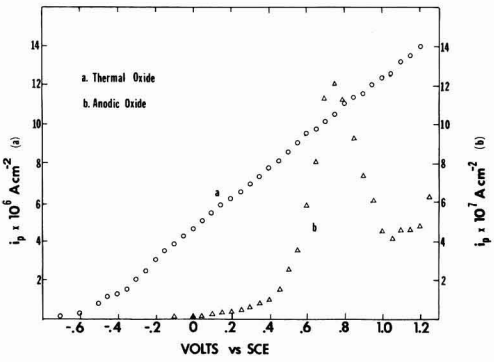


Fig. 4. Photocurrent *vs.* electrode potential; chopping rate 100 Hz; pH 8.4; $I = 3I_0$; $400 < \lambda < 900$ nm.

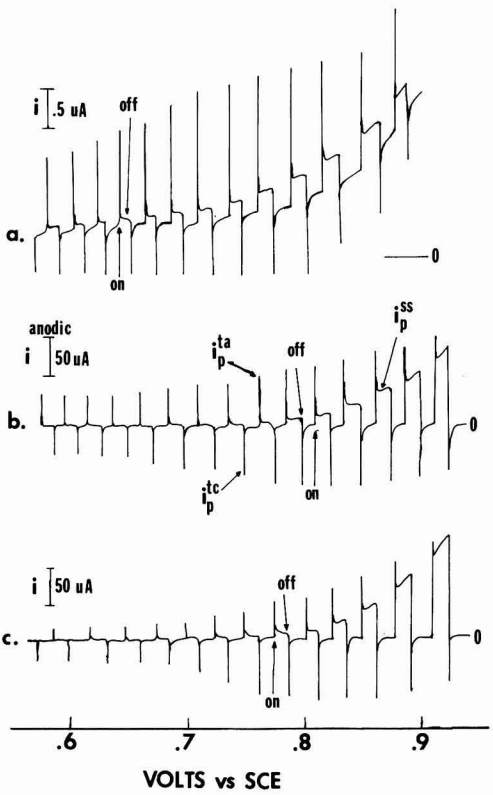


Fig. 5. Current *vs.* electrode potential, pH 8.4, potential scan +5 mV/sec; (a) anodic oxide, light manually chopped, $I = 3I_0$, $400 < \lambda < 900$ nm; (b) thermal oxide, light manually chopped; $I = 5I_0$; $400 < \lambda < 900$ nm; (c) thermal oxide; 200 mV anodic potential pulses superimposed on the linear potential ramp.

i_p^{ta} depends on wavelength exactly as does i_p^{ss} and therefore is not associated with any surface state of energy less than E_g. The transient photoresponse does not change when the solution is vigorously stirred. i_p^{ta} and i_p^{tc} are independent of i_p^{ss} in both magnitude and sign (Fig. 6, curve b). In this case, anodic current spikes and cathodic steady-state photocurrents are observed simultaneously upon illumination at potentials slightly cathodic of V_{FB} and in the presence of a reducible species [$Fe(CN)_6^{-3}$, 0.006M]. This behavior

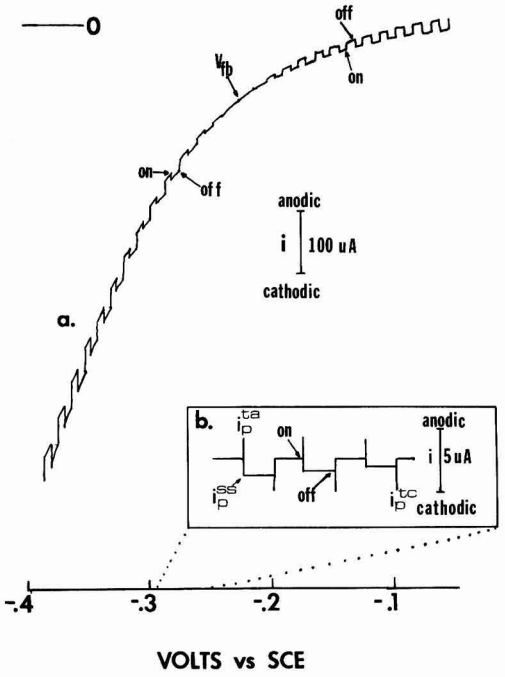


Fig. 6. Current *vs.* electrode potential for thermal oxide; pH 8.4, potential scan +5 mV/sec; $I = 5I_0$; $400 < \lambda < 900$ nm; (a) 0.025M $Fe(CN)_6^{-3}$/0.025M $Fe(CN)_6^{-4}$; (b) 0.006M $Fe(CN)_6^{-3}$/0.006M $Fe(CN)_6^{-4}$.

suggests that although i_p^{ta} and i_p^{ss} are both associated with electron-hole pair formation when the electrode is illuminated ($h\nu > E_g$), they result from different processes.

In Fig. 5, curve c, essentially the same i/V relationship is obtained by substituting 200 mV anodic potential pulses (2-3 sec duration) for the chopped illumination used to obtain curve b. Anodic potential pulses of 200 mV were chosen to approximate the effective potential-time behavior[1] of the electrode during intermittent illumination. The photovoltage ($\Delta V_p = V(\text{dark}) - V(\text{light})$ *vs.* SCE) is approximately 200 mV when measured at open circuit in pH 8.4 buffer solution.

The similarity in the curves (b, c, Fig. 5) especially in the magnitude of the steady-state currents, indicates that the alteration of the effective electrode potential by illumination produces the photocurrents observed. If holes in the valence band are not produced by the anodic potential pulses and the magnitude of the currents produced are essentially equal in both cases, it can be inferred that the holes produced by illumination do not participate as reactants in the photoassisted electrolysis.

Alternatively, if the oxide is partially compensated, substantial hole currents could exist in the dark under strong anodic bias. In this case the effect of illumination and anodic potential pulses would be equivalent in producing reactive holes at the surface. Whether the anodic dark currents are due to holes in the valence band or electron tunneling through the conduction band (see next section), the mechanism for oxidation is the same with or without light as demonstrated by the equivalency of photocurrents produced by chopped illumination and anodic potential pulses in Fig. 5. A similar argument can be applied to the photocurrents at the anodic oxides where ΔV_p is approximately 10-20 mV.

The transient photoresponse of curve b (Fig. 5) is also duplicated by the potential pulses used in curve c. The identification of i_p^{ta} and i_p^{tc} as capacitance charging (light on) and discharge (light off) follows, as this is a general feature of sudden changes in electrode potential.

It is possible to observe V_{FB} in the presence of a redox couple by a shift from cathodic to anodic photocurrents (curve a, Fig. 6). The change in sign of i_p^{ss} (−0.22V) accurately defines V_{FB}. Photocurrents at the anodic oxide were too small in the neighborhood of V_{FB} to observe a similar effect. The cathodic steady-state photocurrent is unusual for n-type semiconductors. When the conduction band is bent slightly downward, illumination increases the concentration of electrons at the surface, giving rise to an increase in the reduction current (<1% of the total current). When the bands are bent more strongly ($V < -0.45$V), the cathodic photocurrent cannot be detected.

It is generally felt that Mott-Schottky plots are not reliable for the evaluation of V_{FB}. Therefore the inversion of photocurrents should give a more accurate measure of V_{FB}. This procedure has the advantage of allowing measurement of V_{FB} in the presence of substantial Faradaic processes which complicate capacitance measurements. It does, however, require measuring small fluctuations in current.

The smaller magnitude of i_p at the anodic oxide (Fig. 4, curve b; Fig. 5, curve a) as compared with the thermal oxide is due to the smaller thickness of the space charge region and also to the smaller over-all thickness of the Fe_2O_3 layer. The lifetime of photogenerated holes is short in the bulk of the oxide and light absorbed in the space charge region is responsible for the majority of the photoresponse. The width of the space charge region of the anodic oxide is smaller due to the higher donor concentration.

There is evidence to suggest that the thickness of the anodic oxide also limits i_p. When an iron electrode was anodically oxidized (+0.80V, 1 hr) in the presence of ferrous ion (1×10^{-4}M) the photocurrent at +0.80V increased by a factor of 2(1.2-2.5 μA, $I = 3I_0$) over that of oxides formed without ferrous ion. Subsequent reduction of the film showed that the thickness was approximately 100Å. The change in i_p with time during oxidation was essentially equivalent to the film growth behavior of iron electrodes in the presence of Fe^{+2} described by Markovac and Cohen (23).

For the anodic oxide the thickness of the γFe_2O_3 layer, the absorption depth, and the Debye length are all of comparable magnitude. Strong anodic bias is necessary to transport photogenerated holes to the surface before recombination. The decrease in i_p cathodic of +0.75V (Fig. 4) results from increased hole recombination. Anodic of +0.75V, the increased concentration of nonphotogenerated holes in the valence band lowers the absorptivity of the oxide, causing a decrease in i_p. The appearance of holes (loss of compensation) at this potential is also observed by Stimming and Schultze (8).

Photocurrent *vs.* time measurements indicate that either the thickness of the oxide or its structure changes with applied potential. When a bare iron electrode (previously cathodically reduced and polarized at −0.80V) is suddenly polarized to +0.80V, i_p increases with time, achieving 70% of its final value (*ca.* 1.0 μA) within 10 sec and 95% within 10 min of the change in potential. Subsequent changing of the potential to +0.40V produces a decrease in i_p which is not instantaneous, requiring approximately 10 min to achieve 95% of its final value (*ca.* 0.1 μA). If the change in photocurrent can be correlated with a

[1] Under potentiostatic control the potential of the electrode *vs.* SCE does not change when the electrode is suddenly illuminated but the free energy of charge carriers in the electrode does change; hence the relative electrochemical potential of the electrode and solution species is altered (22). The process is equivalent to suddenly altering the electrode potential in the anodic direction.

change in thickness of the oxide, the measurement of the photoresponse may be a valuable tool in studying the kinetics of anodic film formation. This phenomenon is currently under further investigation.

Polarization curves.—The existence of an oxidation process in the dark suggests that the influence of illumination can be primarily photovoltaic with little participation of holes as reactants in producing photocurrents. The approximate position of the valance band ($+1.7 \pm 0.2$V *vs.* SCE at *p*H 8.4)[2] also supports the assumption that the valence band is not a direct participant in redox processes. Neglecting valence band participation, there are several feasible explanations as to the origin of the anodic dark currents. Due to the disordered nature of the oxides, charge transfer at grain boundaries and dislocations is possible, but is probably insufficient to explain the magnitude of the currents observed.

The kinetics of redox reactions in the dark at anodic or thermal iron oxides can be explained in terms of electron tunneling. Hardee and Bard (2) attribute the dark currents observed at CVD αFe_2O_3 electrodes to be due to tunneling across the space charge layer to the conduction band. A high donor concentration was presumed (24). The donor concentration of the thermal oxide, however, is essentially equal to that of the single crystal αFe_2O_3 electrodes (6) for which no dark currents were observed to $+2.5$V at the same *p*H. The shape of the Tafel curve (Fig. 7) has been discussed recently in terms of resonance tunneling (25). The shape of the Tafel curve can be adequately predicted by this theory. The change in slope (-0.10V) may be associated with the ionization of a deep donor (3) as indicated by the change in slope of the Mott-Schottky plot (Fig. 3). Such ionization would increase the localized donor states through which resonant tunneling is possible at potentials more anodic than -0.10V. Schmickler (25) explains this type of slope change as a transition between direct elastic tunneling and resonance tunneling.

For the anodic oxide a similar description of redox processes in terms of resonance tunneling and direct elastic tunneling has been made (26). The change in slope of the cathodic branch (Fig. 7) also occurs at approximately the same potential as the change in slope on the Mott-Schottky plot (Fig. 3).

A detailed discussion of redox processes requires a more complete analysis of the donor energy states which arise from oxygen deficiency or impurities. Knowledge of their position relative to the conduction band is essential in defining the Fermi energy and the positions of the bandedges relative to redox potentials in solution. Moreover resonance tunneling via localized donor states may be the primary mechanism of the electron transfer. The similarity in the electrochemical and semiconductor properties of thermal and anodic oxides probably lies in the fact that the donor levels caused by oxygen deficiency (Fe^{+2}) are fixed relative to the substrate (Fe_3O_4) in both cases.

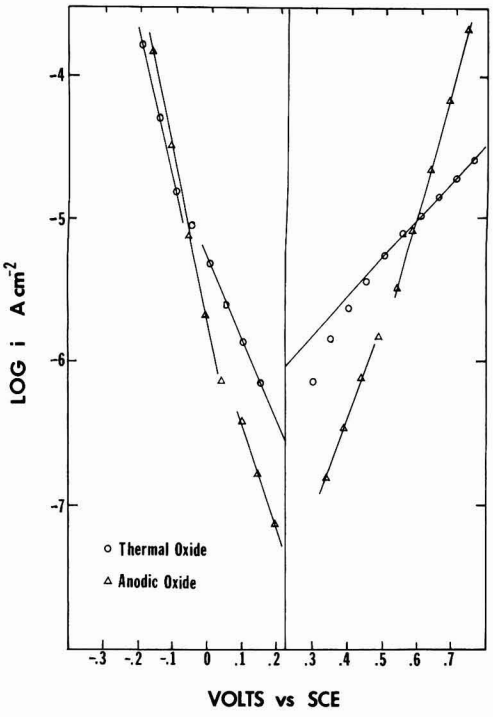


Fig. 7. Polarization curves for thermal and anodic oxides; 0.10M $Fe(CN)_6^{-3}$/0.10M $Fe(CN)_6^{-4}$; *p*H 8.4; in the dark; 1 mV/sec anodic to cathodic potential scan.

Publication costs of this article were assisted by Rice University.

Acknowledgments

The authors wish to thank the Robert A. Welch Foundation of Houston, Texas, for financial support of this research. They also wish to thank the American Iron and Steel Institute and Battelle Memorial Institute for the generous donation of the zone-refined iron used in this study.

Manuscript submitted Aug. 11, 1978; revised manuscript received Oct. 19, 1978.

Any discussion of this paper will appear in a Discussion Section to be published in the December 1979 JOURNAL. All discussions for the December 1979 Discussion Section should be submitted by Aug. 1, 1979.

[2] The position of the valence band follows from V_{fb} and E_g if we assume the Fermi energy to be close (0.1 eV) to the conduction band.

REFERENCES

1. K. L. Hardee and A. J. Bard, *This Journal*, **123**, 1024 (1976).
2. K. L. Hardee and A. J. Bard, *ibid.*, **124**, 215 (1977).
3. J. H. Kennedy and K. W. Freese, *ibid.*, **125**, 723 (1978).
4. J. H. Kennedy and K. W. Freese, *ibid.*, **125**, 709 (1978).
5. L.-S. R. Yeh and N. Hackerman, *ibid.*, **124**, 833 (1977).
6. R. K. Quinn, R. D. Nasby, and R. J. Baughman, *Mater. Res. Bull.*, **11**, 1011 (1976).
7. R. V. Moshtev, *Electrochim. Acta*, **16**, 2039 (1971).
8. U. Stimming and J. W. Schultze, *Ber. Bunsenges. Phys. Chem.*, **80**, 1297 (1976).
9. F. Delnik and N. Hackerman, in "Proceedings of the Fourth International Symposium on Passivity," Arlie, Virginia, 1977, The Electrochemical Society (1978).
10. M. Cohen and K. Hashimoto, *This Journal*, **121**, 42 (1974).
11. R. J. Hussey, G. I. Sproule, D. Caplan, and M. J. Graham, *Oxid. Met.*, **11**, 65 (1977).
12. D. Caplan and M. Cohen, *Corros. Sci.*, **6**, 321 (1966).
13. M. Nagayama and M. Cohen, *This Journal*, **109**, 781 (1962).
14. J. O'M Bockris, M. A. Genshaw, V. Brusic, and M. Wroblowa, *Electrochim. Acta*, **16**, 1859 (1971).
15. K. A. Wickersheim and R. A. Leferne, *J. Chem. Phys.*, **36**, 844 (1962).
16. H. Tributsch, *This Journal*, **125**, 1086 (1978).
17. N. E. Wisdom and N. Hackerman, *ibid.*, **110**, 318 (1963).
18. P. C. Grahame, *Chem. Rev.*, **41**, 441 (1947).
19. R. DeGrvse, W. P. Gomes, F. Cardon, and J. Vennik, *This Journal*, **122**, 711 (1975).
20. O. Jantzen, *Z. Angew Physik*, **18**, 560 (1965).
21. K. S. Yun, S. M. Wilhelm, S. Kapusta, and N. Hack-

erman, Submitted to *This Journal* (1978).
22. H. Gerischer, *ibid.*, **113**, 1174 (1966).
23. V. Markovac and M. Cohen, *ibid.*, **114**, 674 (1967).
24. B. Pettinger, H. R. Schöppel, and H. Gerischer, *Ber. Bunsenges. Phys. Chem.*, **78**, 450 (1974).
25. W. Schmickler, *ibid.*, **82**, 477 (1978).
26. W. Schmickler, *J. Electroanal. Chem. Interfacial Electrochem.*, **82**, 65 (1977).

An A-C Admittance Study of the Platinum/Sulfuric Acid Interface

S. H. Glarum* and J. H. Marshall

Bell Laboratories, Murray Hill, New Jersey 07974

ABSTRACT

Apparatus for the measurement of the a-c admittance of electrodes using sweep-frequency techniques is described. Measurements of the Pt/1.0*N* H_2SO_4 interface are reported for the hydrogen adsorption, double-layer, and oxide regions. Rotating disk electrodes were used, and necessary corrections for nonuniform current distributions are discussed. A single relaxation time closely characterizes the hydrogen adsorption process at all potentials. No evidence for Faradaic processes was evident in either the double-layer or oxide regions, but the double layer capacitance exhibits a dispersion resembling that of a diffusional process.

Alternating-current studies can provide a powerful tool for examining electrode reactions. Numerous theoretical models have been analyzed in recent years, testifying to the potential of a-c techniques (1-3). Despite this promise, progress on the experimental front has been slow, and the effective application of a-c techniques to electrochemistry has been limited (4). Certainly a major difficulty is the time required to amass sufficient data for a thorough experimental study. The frequency response of an electrode-electrolyte interface is conveniently described by a complex plane plot of the interfacial admittance. Construction of a complete plot requires a minimum of 20-30 data points spanning at least three frequency decades. Since electrode processes are potential dependent, a rigorous study necessitates measurements taken over a range of closely spaced potentials. The majority of electrode interfaces cannot be expected to remain physically invariant during an extended measuring period, and obtaining reproducible a-c data with solid electrodes is a serious experimental problem.

We have constructed apparatus based on sweep-frequency techniques to explore the usefulness of a-c measurements over the range 0.02 Hz-150 kHz. Three decades can be swept in 1-2 sec (at high frequencies), permitting the rapid and automatic accumulation of data at essentially a continuous set of frequencies. A rotating-disk electrode and a commercial potentiostat are employed, and conventional current-voltage experiments can be carried on concurrently.

The system chosen for initial examination was the Pt/H_2SO_4 electrode. The quasi-static characteristics of this electrode are well known (5-10), and a-c studies using diverse techniques are available for comparisons (11-21). In spite of the attention this electrode has attracted, interpretations for many of its interesting features have not been resolved. This report covers the hydrogen adsorption, double layer, and oxide regions of the Pt electrode in 1*N* H_2SO_4 at 23°C and frequencies between 100 Hz and 150 kHz. Numerically our results are consistent with the majority of data published, but the more complete information available offers added insights into the processes occurring in this fundamental system.

* Electrochemical Society Active Member.
Key words: impedance, adsorption, kinetics.

Experimental

Apparatus.—The equipment for sweep-frequency measurements is built around the PAR Model 173 potentiostat, the Exact Model 7071 function generator, and the PAR Model 129A two-phase lock-in amplifier (Fig. 1). Logarithmic frequency sweeping is desirable for efficient experimentation. A PAR Model 175 programmer was used for potential cycling, and a Nicolet Model 1072 signal averager for rapid data acquisition. A TI 960A minicomputer, interfaced to the 1072, expedited data analysis and control of the experiments.

The 129A is not able to track rapidly changing frequencies, and special interfaces had to be built on circuit boards within both the function generator and the lock-in amplifier (Fig. 2). The generator board constructs a 4 pulse/cycle signal, corresponding to 0°, 90°, 180°, and 270° references. The nominal pulse width is 0.3 μsec. Every fourth pulse is 1.0 μsec long, permitting identification of the 0° pulse. The pulses were derived from the square-wave and triangular-wave signals internally available. The lock-in board decodes this

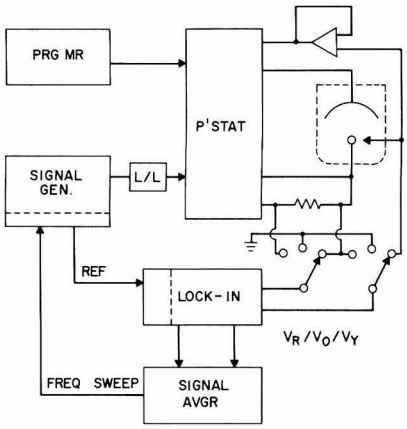


Fig. 1. Block diagram of apparatus for sweep-frequency measurement of electrode admittance (L/L, lead-lag network).

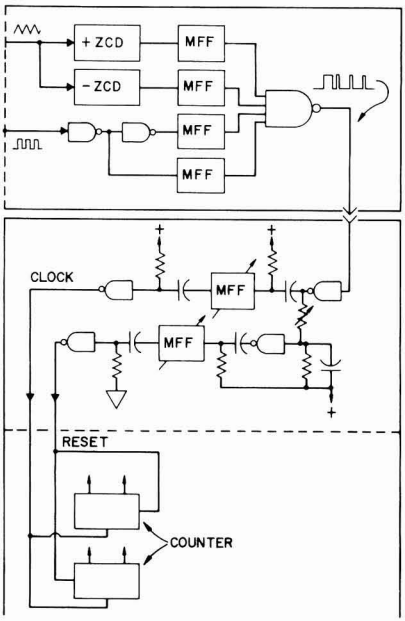


Fig. 2. Interface circuitry for the signal generator and the lock-in amplifier (ZCD, zero-crossing detector; MFF, monostable flip-flop).

reference. The 0° pulses are selected by a pulse-length discriminator and used to reset the ÷4 counter which supplies gating signals for the phase detector circuitry. The leading edge of each pulse is differentiated, delayed 1-2 μsec to compensate for the response of the amplifier stages, and then used to clock the counter. This arrangement functions quite satisfactorily from the highest frequencies (180 kHz) set by the pulse length, to essentially d-c. Limiting low frequency response is determined by the *R-C* coupled amplifiers in the lock-in front end. Although not required for this work, the useful frequency limit was lowered to 0.02 Hz by shunting all but the input coupling capacitor, and the addition of null adjustments for each d-c amplifier.

If the frequency response of the potentiostat were flat, complex plane plots of electrode admittance would be directly obtained on connection of the current output jack of the potentiostat to the lock-in input. Although the feedback amplifiers in the unit have intrinsic response times of 1-2 μsec, analysis shows that these times are magnified by cell impedances, and serious errors can occur at even a few kHz. Wiring inductances further complicate high frequency measurements on low impedance circuits.

To overcome these difficulties an external resistor (1-20Ω) was inserted in series with the working electrode. Measurements were made of the frequency-dependent potential V_R across this resistance and of the potential V_Y between the reference and working electrodes. After subtraction of the frequency-dependent offset potential of the phase detector output circuitry, the electrode admittance was found from the complex ratio V_R/V_Y.

Ideally V_Y should be frequency independent, but the response of the potentiostat leads to substantial attenuation at high frequencies. To keep the magnitude of V_Y within reasonable bounds, an adjustable lead-lag network was added to insure that V_Y remained approximately 2 mV (rms) over the working frequency range.

Tests with simple *R-C* circuits showed that admittance accuracies of 0.2% were possible in controlled situations. At high frequencies the dominant error is due to lead inductance. Measurements for the experimental wiring geometry gave effective series inductance and resistance values of 0.29 μHz and 0.05Ω.

Working electrode.—The prime requirement for a working electrode in systematic studies is a reproducible surface. Important secondary considerations are its size and shape. We selected rotating-disk electrodes for this work. Their flat surface permits repeated mechanical polishing, and their known hydrodynamic behavior is important when mass transport analysis is required. The useful frequency range of a disk electrode is inversely proportional to its radius and a nominal time constant is $\tau = \pi aC/4\kappa$, where a is the disk radius, C the double layer capacitance per unit area, and κ, the electrolyte conductivity. For the system studied $C \simeq 50\ \mu fd/cm^2$ and $\kappa = 0.22$ mho/cm, giving $\tau \simeq 14$ μsec, or an equivalent frequency of 10 kHz. Accurate measurements could be made to frequencies an order of magnitude higher, allowing evaluation of the primary conductivity of the cell. The major drawback to the use of disk electrodes is the nonuniformity of their current distribution. The consequences of this effect can be taken into account mathematically, and disk electrodes are quite suitable for accurate a-c experimentation.

The electrodes were constructed from ¼ in. stainless steel rods to which 30 mil platinum sheets were silver-soldered. The rod was then turned down to 0.0625 in. diam for a distance of ¼ in. A Teflon cylindrical sheath was thermally fitted to the shaft and formed a mold about the electrode which was then filled with epoxy resin. After curing, the Teflon was turned to its final shape, leaving a ⅝ in. mantle near the electrode. The face of the electrode was ground and polished with a series of alumina abrasives, finishing with 0.05 μm gamma alumina on Gamal microcloth. This final polishing was used for renewal of the electrode surface prior to daily runs. It was necessary to encase the exposed portion of the steel shaft in Teflon sleeving to minimize leakage currents and contamination from spattered solution.

The electrolytic cell.—The cell is an adaptation of the PAR No. 9300/01 assembly. The five ports were fitted with working, reference, and counterelectrodes, a gas sparger, and a gas outlet tube. The SCE reference electrode was connected to the cell through thick-wall capillary tubing and a Teflon stopcock. The d-c resistance of this path, in conjunction with the input capacitance of the electrometer, limited the over-all frequency response of the reference probe. A Teflon-insulated platinum wire, exposed only at its tip, was placed alongside the capillary and connected to the electrometer input through a capacitor (22). This electrode provided a high frequency reference signal, while the capillary took care of d-c needs.

In principle, electrolyte resistance can be minimized by positioning the reference close to the disk. In practice this makes the data sensitive to the actual location of the reference and may alter the current distribution pattern assumed for analysis. A reference point was therefore chosen 15 mm off-axis in the plane of the disk. The theoretical cell constant for this configuration differs by only 3% from its value for infinite separation, and lies well within the asymptotic region where the electrode may be accurately approximated as a point source (23). All measurements were taken at a nominal 23°C.

Reagents.—Seventeen-megohm water for both solution preparation and general housekeeping came from a recirculating Millipore Super-Q system with 0.22 μm input and output filters, and carbon and ion-exchange cartridges. 1.00*N* (±3%) H_2SO_4 was prepared by dilution of ultrapure acid (J. T. Baker, Ul-

trex). Solutions were deoxygenated with tank argon. The use of plastic or rubber tubing for gas connections was avoided to prevent organic contamination.

Experimental procedure.—After electrode polishing, the cell was assembled and deoxygenated. A flow of argon was maintained over the surface during the experimental period. Prior to measurement the electrode was cycled for 2 hr between −0.01 and 1.34 V_h while rotating 100 rad/sec. Current voltage curves (Fig. 3) reached a reproducible steady state, and integration of the anodic sweep in the hydrogen adsorption region gave 440 $\mu C/cm^2$.

Electrode capacitance at 100 Hz was also measured during cyclic voltammetry sweeps. Integration of *C-V* curves gave only 280 $\mu C/cm^2$. These experiments were repeated at scan rates of 100, 50, 20, 10, and 5 mV/sec, alternating *I-V* and *C-V* measurements. The former gave, respectively, 445, 443, 436, 422, and 450 $\mu C/cm^2$. while the latter yielded 287, 282, 275, 282, and 274 $\mu C/cm^2$. When the measuring frequency was reduced to 5 or 10 Hz, *C-V* integrations increased to 315 $\mu C/cm^2$, but residual low frequency dispersions do not appear to be a likely explanation for the discrepancy between *C-V* and *I-V* results. Corresponding tests with a 14 μF capacitor differed by only 2% ruling out experimental error. The shapes of both *C-V* and *I-V* curves are quite similar, although the minor intermediate peak seen in *I-V* sweeps was not evident in the a-c data, and normalized plots would be similar (13). Subtraction of the a-c capacitance from the *I-V* curve leaves a broad plateau of about 500 $\mu F/cm^2$ (apparent area) extending between 0.05 and 0.24 V_h. The associated charge presumably indicates an irreversible component in hydrogen desorption. Surface roughness factors have in the past been calculated using either integration of *I-V* or *C-V* plots. In view of the inequivalence of these procedures, we have normalized our data in terms of the geometric area of the electrode.

For admittance measurements electrode rotation was stopped, the potential sweep was halted on its anodic scan, and 32 frequency sweeps of V_R were stored in the signal averager (16 triangular cycles). This took approximately 30 sec. V_Y was then similarly measured, and finally the base line signal was determined. Cycling resumed for a period of at least 10 min. During this interval admittances were calculated and data at selected frequencies were then stored on tape for subsequent analysis. Frequency drifts (1%) are probably the greatest source of error in the calculation of reactive parameters.

Because of irreversible changes in the electrode, it is not apparent that the condition of the electrode is constant during measurement. The 100 Hz capacitance was monitored when cycling was halted. Decreases of less than 2% occurred in the hydrogen adsorption and double layer regions during the measurement interval. A drop of 30% was seen in the oxide plateau region. Most took place within the first 5 sec. In actual experiments a 10 sec delay was required for switching and resetting after the sweep had halted, and the decrease during data taking was less than 5%.

Analysis

Admittances calculated from the ratio V_R/V_Y were corrected for series inductance and resistance associated with the wiring. Corrections for the nonuniform distribution of current at a disk electrode were then necessary. It has been previously shown that the measured cell admittance, Y_m^*, is related to the electrode admittance, Y_e^*, by

$$\Gamma = \Gamma_o \left(1 + \sum \frac{\alpha_i}{1 + \Gamma\beta_i}\right)^{-1} \quad [1]$$

where

$$\Gamma_o = Y_\infty/Y_m^*$$

$$\Gamma = Y_\infty/Y_e^* \quad [2]$$

and Y_∞ is the limiting high frequency or primary conductance of the cell. The coefficients (α_i, β_i) were found by variational analysis (24).

In terms of the electrolyte conductivity, κ, and the disk radius, a (23)

$$Y_\infty = 4\kappa a \quad [3]$$

Evaluation of Y_∞, which should be independent of disk potential, was most accurately made in the oxide region. The value found, 0.219 mho/cm, is in satisfactory agreement with the known conductivity of 1.0*N* H_2SO_4 (25).

With Y_∞ in hand, Eq. [1] can be solved for Γ by an iterative procedure, choosing Γ_o as an initial estimate for Γ. A three-term expansion in Eq. [1] was used. Complex plane plots were then made of the corrected cell admittance

$$Y^* = Y_\infty/(1 + \Gamma) \quad [4]$$

which corresponds to the true electrode admittance in series with a conductance Y_∞. The importance of these corrections is shown in Fig. 4 for data taken at 1.35 V_h. Uncorrected data reveal a depressed circular arc, skewed to low frequencies. The corrected plot lies close to the semicircle characteristic of a series *R-C* circuit.

Above 0.45 V_h complex plane plots show only minor deviations from simple *R-C* response, and plots were made of the complex capacitance, $C^* = Y_e^*/i\omega$ (Fig. 5). These reveal a significant dispersion within the double layer region. Extrapolation to high frequencies indicates capacitances of 35-45 $\mu F/cm^2$ (geometric area). This value increases to ~80 $\mu F/cm^2$ in the oxide region. A quantitative comparison with published data is precluded by the considerable effects of dispersion, roughness, and the irreversible relaxation seen during sweep measurements (16, 17, 20, 21). Our values are in qualitative agreement with such data when one attempts to compensate for these factors by considering the manner in which results were calculated in these references. If current density distribution corrections are omitted, a large additional high fre-

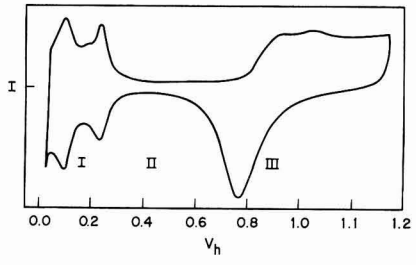


Fig. 3. Current-voltage curve for Pt/1*N* H_2SO_4 electrode indicating the hydrogen adsorption (I), double layer (II) and oxide regions (III) studied.

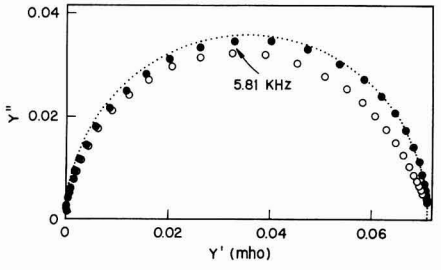


Fig. 4. Complex-plane admittance plots before (○) and after (●) corrections for the current distribution at a disk electrode. The dashed line is a semicircle. Data were taken at 1.35 V_h.

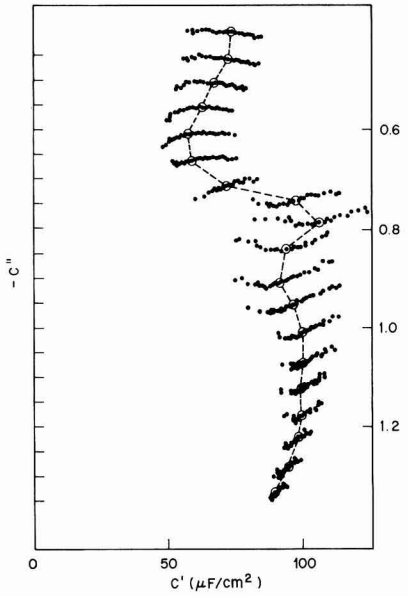


Fig. 5. Complex capacitance dispersions in the double layer and oxide regions. The locus of 10 kHz points is shown by the dashed line.

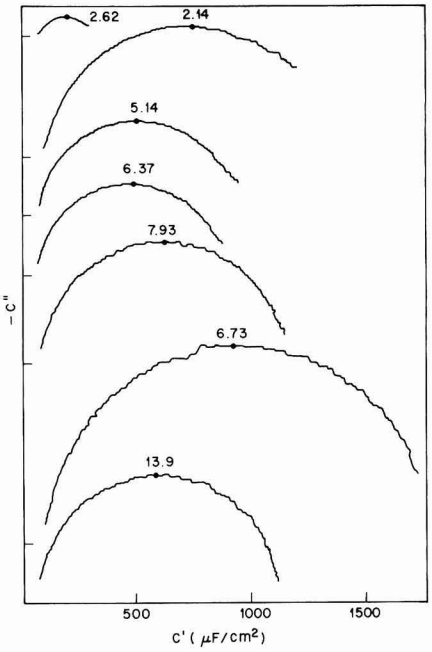


Fig. 6. Complex capacitance plots in the hydrogen adsorption region. Approximately 100 points are shown, permitting a continuous plot. From top to bottom, V_h = 0.30, 0.24, 0.20, 0.18, 0.14, 0.10, and 0.04V. The frequencies of data points near the maxima are given in kHz.

quency dispersion appears, and, at 1.35 V_h the extrapolated high frequency capacitance is reduced to ~40 μF/cm².

Below 0.45 V_h hydrogen adsorption significantly alters the electrode response. Plots of C^* in this region reveal semicircular loci with high frequency intercepts of order 50 μF/cm², corresponding to double layer capacitance values (Fig. 6). Above 0.25 V_h the shape shifts to a circular arc with approximately 45° intercepts, and the dispersion in C^* rapidly approaches its form in the double layer region.

To examine the hydrogen adsorption region in closer detail, plots (Fig. 7) were also made of $(Y_e^* - i\omega C_\infty)$, where C_∞ is the high frequency, double layer capacitance. Below 0.2 V_h the shape of these plots is insensitive to the choice of C_∞. At higher potentials it was convenient to select values such that these plots took off at 45°, corresponding to the 45° high frequency intercepts seen in C^* plots of this region (Fig. 6).

The near semicircularity of the plots in Fig. 6 and 7 below 0.25 V_h demonstrates that the hydrogen adsorption process is closely described by a single series R-C circuit as originally proposed by Dolin and Ershler (11). Values for C and $G = 1/R$ were calculated from C^* data for points ranging across the maxima. The agreement of these capacitance determinations with separate low frequency measurements and the magnitude of the high frequency intercepts in Fig. 6 indicate that no major additional dispersion is associated with hydrogen adsorption. The monotonic variation of G across the hydrogen region is particularly interesting, and there appears to be a correlation between G and the degree of surface coverage.

Published studies show no consistent behavior for this function. Dolin and Ershler found a constant value of 3.4 mho/cm² below 0.20 V_h in a 1N solution (11). Breiter reports a constant value of 30-35 mho/cm² at these potentials in 8N acid (12, 13), while in 1N acid he calculated a functional dependence showing two peaks which reached a maximum value of 25-30 mho/cm² near full coverage (14). Luk'yanycheva *et al.* found G to increase monotonically, reaching a maximum value of 20 mho/cm² for a 1N solution (16, 17),

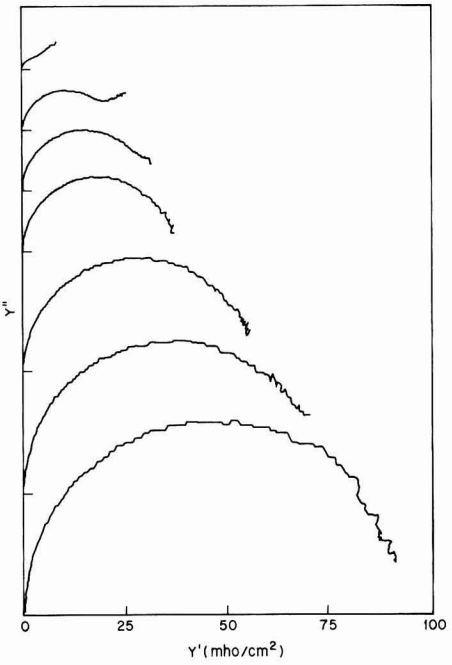


Fig. 7. Complex admittance plots of the data in Fig. 6

and recently a value of 1.7 mho/cm² has been reported for a 1N solution at 0.15 V_h (18). Our results agree

most closely with those of Luk'yanycheva when an allowance for surface roughness is included.

Discussion

Hydrogen adsorption region.—An elementary model describing the hydrogen adsorption region could involve diffusion of hydrogen ions to the electrode, followed by charge-transfer at a rate dependent on surface coverage. The current density is proportional to the difference in anodic and cathodic rate constants

$$i = Q_o \frac{d\theta}{dt} = \mathbf{F}[k_a(\eta,\theta) - k_c(\eta,\theta,H^+(0))] \quad [5]$$

which in turn depend on the fractional surface coverage, θ, the electrode potential, η, and the surface concentration of H^+ ions. An equivalent circuit can be derived by treating the a-c modulation as a small perturbation on η, θ, and $H^+(0)$, *i.e.*, $\eta = \bar{\eta} + \Delta\eta \exp(i\omega t)$ (3) and using the Warburg solution for one-dimensional diffusion

$$\Delta H^+(0) + (Q_o/\mathbf{F})\sqrt{i\omega/D}\,\Delta\theta = 0 \quad [6]$$

The result is a series circuit composed of conductive, Warburg, and capacitive admittances

$$Y_G = \partial\bar{i}/\partial\eta$$
$$Y_W = -\sqrt{i\omega D}\,(\partial\bar{i}/\partial\eta)/(\partial\bar{i}/\partial H^+)$$
$$Y_C = i\omega Q_o(\partial\bar{i}/\partial\eta)/(\partial\bar{i}/\partial\theta) \quad [7]$$

For Langmuir adsorption

$$\bar{k}_a = (2i_o/\mathbf{F})\,\theta \exp[(1-\alpha)e(\eta-\eta_o)/kT]$$
$$\bar{k}_c = (2i_o/\mathbf{F})\,(1-\theta)\exp[-\alpha e(\eta-\eta_o)/kT] \quad [8]$$

where α is a charge-transfer asymmetry factor, and for $\eta = \eta_o$, $\theta = \frac{1}{2}$, and i_o is the exchange current density. In the absence of d-c flow, $\bar{k}_a = \bar{k}_c$ and

$$Y_G = 2i_o(e/kT)\theta^\alpha(1-\theta)^{1-\alpha}$$
$$Y_W = \sqrt{i\omega D}\,\mathbf{F}(e/kT)[H^+]$$
$$Y_C = i\omega Q_o(e/kT)\theta(1-\theta) \quad [9]$$

The Warburg admittance can be estimated. At all frequencies its expected value considerably exceeds measured admittances, and it should not have detectable consequences at the concentration used in this work.

There are three salient features to the a-c behavior of the hydrogen adsorption region: the potential variations of Y_C and Y_G, and the shape of the complex plane plot of the electrode's response. The dependence of $Y_C/i\omega$ on potential resembles the differential capacitance seen in linear sweep experiments and is equivalent to the low frequency a-c capacitance measured in cyclic sweeps. Y_C reflects only equilibrium properties and is independent of kinetic parameters.

The semicircular shape of complex plane plots for the hydrogen adsorption process is equivalent to a simple series R-C circuit. Such a circuit has been implicitly assumed in the past, although Dolin and Ershler have recognized that it is formally incompatible with heterogeneous adsorption models (11).

Two interpretations for the hydrogen adsorption maxima have been proposed. Will concluded from single crystal studies that intrinsic heterogeneous adsorptions on different crystal planes were responsible (7), and his results have been recently confirmed by Hubbard *et al.* (26). An alternative model, "induced heterogeneity," has been offered by Conway *et al.* (10, 27), which supposes that coverage-dependent changes in substrate-adsorbate interactions are responsible. In the former instance, at a given coverage, distinct types of adsorbed atoms coexist, and two or more independent, parallel kinetic processes occur. In the latter instance, adsorbed atoms can be nominally equivalent, although the properties of an atom would change with potential and coverage.

For a true heterogeneous process the admittance may be described by the parallel superposition of series R-C circuits (11), and, assuming a distribution of Langmuir adsorptions

$$Y = i\omega(e/kT)\sum_\lambda a_\lambda Q_{o\lambda}\frac{\theta_\lambda(1-\theta_\lambda)}{1 + i\omega(Q_{o\lambda}/2i_{o\lambda})\theta_\lambda^{(1-\alpha_\lambda)}(1-\theta_\lambda)^{\alpha_\lambda}} \quad [10]$$

where α_λ is the surface fraction occupied by sites λ.

If two parallel, independent adsorption processes are invoked to explain the multiple capacitive maxima, then, at some intermediate potential for which both processes contribute equally to the total capacitance ($\sim$0.18 V_h), the complex capacitance should reveal two dispersions, equal in magnitude. Should the two relaxation times be nearly equal, complex-plane plots would differ only slightly from true semicircles. By either graphical or numerical analysis of C^* data, the experimental results can be empirically fit to circular arcs with centers slightly depressed below the real axis. The angle of depression varies gradually from less than 1° at 0.04 V_h to 9° at 0.24 V_h, and ranges from 4° to 6° in the capacitive overlap region of 0.16-0.20 V_h.

Calculated plots for the superposition of two equal dispersions with a 2:1 relaxation time ratio are reasonably represented by a circular-arc function depressed 6°. For 3:1 and 4:1 ratios this angle rapidly increases to 14° and 23°. For higher ratios the circular-arc description is inadequate. The curve flattens, and for ratios greater than 7:1 two maxima can be resolved in the complex plane.

For $\alpha = 0.5$, the relaxation time of a given adsorption is symmetric about $\theta = 0.5$, and the ratio of the two relaxation times is roughly given by the ratio computed from values for each maximum. From Fig. 8 a 3:1 ratio is directly obtained, and a somewhat higher value would follow if one attempted to account for overlap effects on G. The experimental data are not consistent with such a large ratio and do not show a maximum deviation from semicircular behavior in the overlap region which superposition predicts.

A more critical test is given by a complex-plane analysis of the admittance function. Analogous to the behavior of C^*, Y^* should also reveal two relaxations. The dispersion amplitudes and relaxation times in this instance are given by

$$\Delta Y = (2ei_o/kT)\theta^\alpha(1-\theta)^{1-\alpha}$$
$$\tau = (Q_o/2i_o)\theta^{1-\alpha}(1-\theta)^\alpha \quad [11]$$

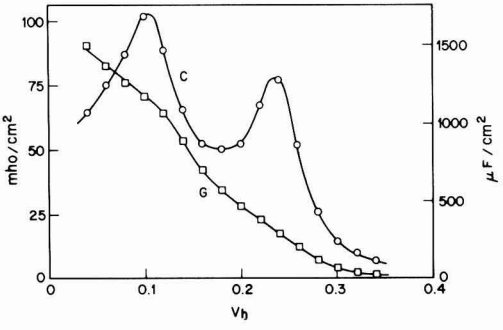


Fig. 8. Variation with potential of the conductance and capacitance associated with the dispersion in the hydrogen adsorption region.

At some intermediate potential both processes contribute equally to G, although this potential region is less evident than in the case of C^*, depending strongly on α. For $\alpha = 0.5$, it follows that the relaxation time ratio varies as the square of the exchange current ratio at a potential where two equal amplitude dispersions are expected in Y^* plots. Consequently the latter offers a more sensitive test than C^* plots when the principal difference between two processes is in their exchange currents.

For $\alpha = 0.5$ the superposition model leads to equal dispersions with at least a 10:1 relaxation time ratio at some potential in Y^* plots. The experimental data (Fig. 7) can be empirically fit to circular arcs, with depression angles ranging from 1° to 6° across the adsorption region, and show no indications of two relaxations. At the higher potentials, double layer relaxation is responsible for high frequency deviations from semicircular behavior. The magnitude of this deviation is not discernibly potential dependent and extends well into the double layer region where hydrogen adsorption is nil.

The function $G(\eta)$ does not show the maxima expected for $\alpha = 0.5$, and one might consider the case $\alpha = 1$ which leads to a monotonic curve (Eq. [9]). Straight-forward numerical analysis shows that C^* and Y^* plots should still reveal two dispersions at intermediate potentials. We are forced to conclude that the data are incompatible with the predictions of models based on a simple superposition of parallel Langmuir processes. The distributions of relaxation times which may be inferred from slight deviations from semicircular complex-plane plots are too narrow to be reconciled with such models.

For a homogeneous process the expected single relaxation time is in accord with experiment. The variation of capacitance with potential, however, does certainly not agree with a simple adsorption isotherm. Although Breiter has pointed out that the superposition of two Langmuir functions gives a reasonable fit to the data (28). A generalization of the Langmuir isotherm

$$(1 - \theta)/\theta = \exp e(\eta - \eta_0)/kT \qquad [12]$$

can be forced to fit capacitance data if η_0 is assumed to be a function of θ, and this function is plotted in Fig. 9. Formally $\eta_0(\theta)$ can be viewed as the deviation of the free energy of adsorption from that of a Langmuir model. The sigmoidal portion of the curve is responsible for the dual maxima. This function does not appear to be overly remarkable, but it is evident that minor modifications can have profound influences on differential adsorption isotherms, for the Frumkin isotherm, corresponding to a linear function, shows but one maximum.

If the Langmuir rate expressions (Eq. [3]) are modified so that η_0 is θ dependent, the expression for Y_G is unchanged. A plot of ln $[G/(1 - \theta)]$ *vs.* ln $[\theta/(1 - \theta)]$ is linear below 0.24 V_h, and from its slope, $\alpha \simeq 0.95$. The related parallel between G and $\int CdV$ has already been noted. At low surface coverage a plot of ln G *vs.* η is also linear, yielding $\alpha \simeq 0.6_5$, in agreement with a similar analysis by Honz and Nemec (15).

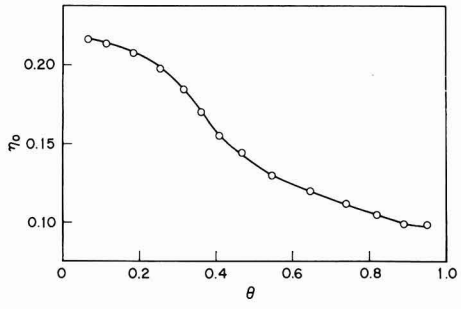


Fig. 9. Variation of the effective Langmuir potential, η_0 (Eq. [12]), with surface coverage.

At low coverage ($\theta < 0.2$) behavior is typical of that expected for a simple redox/adsorption process. At higher coverage a more involved interpretation is necessary. A mechanistic explanation for a shift in α would involve an intermediate, H*

$$H^+ \overset{e^-}{\rightleftarrows} H^* \rightleftarrows H_a \qquad [13]$$

with rate control shifting from the charge-transfer step at low coverage to the second step at higher coverage. In such a model [H*] must increase exponentially with decreasing potential, and the charge-transfer reaction should contribute to the high frequency capacitance. The absence of a noticeable change in this parameter implies a very small [H*], (<1%), and consequently an extremely large exchange current (>100 A/cm²) for the charge-transfer step, as the net exchange-current density is ~ 1 A/cm² when $\theta \simeq 1$.

A more speculative hypothesis is that the charge-transfer step remains rate determining at all coverages, but that the influence of the metal-electrolyte potential difference varies with coverage. Assume transfer occurs with a proton of H_3O^+ in contact with Pt and that potentials within the adsorption plane are determined by species on the surface. At low coverage ions and water molecules will form a polarizable layer. At high coverage hydrogen atoms will, because of large exchange currents with the substrate, create a non-polarizable layer. In the latter instance the layer-metal potential difference will not be affected by a changing electrolyte potential and $\alpha \simeq 1$.

We see no satisfactory way to rationalize the a-c response observed throughout the hydrogen adsorption region with heterogeneous adsorption models. The coverage-dependent, multiple relaxation times predicted by such models differ significantly enough so that, at some potentials, deviations from single relaxation time behavior would be apparent. Results are in accord with homogeneous adsorption models, or, more precisely, models for which adsorbed atoms are kinetically equivalent on the 10^{-4}-10^{-5} sec time scale of the experiments. In principle, as Dolin and Ershler have pointed out (11), rapid surface diffusion makes a heterogeneous process appear homogeneous, for rapid exchange renders all adsorbed atoms equivalent. Such a hypothesis would reconcile the single crystal and a-c studies but would require quite mobile hydrogen atoms because of the times and distances involved.

Finally the recent studies of hydrogen adsorption for single crystal platinum surfaces by Christmann, Ertl, and Pignet merit special attention (29). Desorption experiments on 111 faces revealed two distinct and approximately equal states of adsorbed hydrogen, with desorption energies differing by about 3 kcal/mole (125 mV). Induced heterogeneity was deemed the most probable explanation. Although the usual caveats regarding comparisons of high vacuum and electrochemical studies must be observed, their results appear quite similar to electrochemical findings, and their conclusions are in accord with our interpretation of a-c response measurements.

Double layer and oxide regions.—Electrode response in these regions can be described by a complex capacitance

$$C^* = Y_e^*/i\omega = C_0 + \frac{C_1}{1 + \sqrt{i\omega\tau}} \qquad [14]$$

This behavior also extends well into the hydrogen adsorption region. The contribution of the C_1 term leads to departures from semicircular complex plane plots. These deviations are quite small in the oxide region,

and the data are not sufficiently robust to allow accurate evaluations of C_0, C_1, and τ.

Within the double layer region $C_0 \simeq C_1$ and τ varies, with increasing potential, from 2 to 100 μsec. When oxide formation commences, both C_0 and C_1 increase, roughly doubling. As oxide coverage increases the observed dispersion in C^* decreases, until at 1.35 V_h the variation between 100 kHz and 200 Hz is only $\pm$ 3%. Evidence of a dispersion in C^* at this potential is still apparent in Fig. 5, but whether the apparent narrowing is due to a decrease in C_1 or a further increase in τ cannot be unambiguously decided.

Equation [14] has the functional form expected if a portion of the double layer capacitance were diffusion controlled. Assuming the electrode charge to be a function of potential and a concentration parameter, x

$$C_1 = (\partial Q/\partial \eta)_x$$
$$\sqrt{D\tau} = \frac{1}{\mathbf{F}} (\partial Q/\partial x)_\eta \qquad [15]$$

The magnitudes of C_1 and τ require $x > 10^{-4}$M, ruling out impurity effects, but the large changes in τ in the double layer region are inconsistent with this simple model. Alternative explanations invoking current distribution and/or surface roughness effects also appear implausible (30). These effects should be most apparent at the higher frequencies, and their absence at high potentials is a convincing demonstration of the adequacy of our current density correction procedure.

Previous studies using cyclic voltammetry/a-c techniques have suggested the existence of a reversible faradaic process at the beginning of oxide layer formation (19, 20).

We have repeated such experiments and obtained similar results. In part the changes may be explained by an increase in the complex double layer capacitance and a subsequent shift of the double layer relaxation time to lower frequencies. Plots of C^* in this region (Fig. 5) show no indications of the semicircle which would characterize a simple faradaic process. One cannot, however, exclude the possibility of a dispersion occurring principally at frequencies below 100 Hz or during the interval between the time cycling halted and measurement was initiated when, as previously noted, a significant drop in 100 Hz response occurred.

Hypotheses concerning the origin of the dispersion in the double layer and oxide regions require more information than is presently available. The data suggest that a process kinetically similar to diffusion is occurring near the electrode, but bulk diffusion appears improbable. More detailed studies varying the composition of the double layer are indicated, and low frequency dispersions would be better studied with larger electrodes.

Summary

Detailed a-c admittance measurements, particularly when combined with d-c or potential sweep experiments, are a valuable technique for the study of electrode kinetics. Complex plane plots of data after a deconvolution removing electrolyte resistance and/or a high frequency capacitance (Fig. 5-7) are convenient for viewing the information content of the data and avoid the pitfalls of model presumption followed by numerical processing.

This study of the Pt/H_2SO_4 electrode has touched on the irreversible/reversible aspects of the hydrogen adsorption process and the kinetics and possible mechanism of this process. A diffusion-like dispersion of the electrode capacitance was observed throughout the double layer and oxide regions which we cannot account for by either impurity effects or experimental artifacts. Further measurements of the effects of temperature and varying electrolyte composition may clarify questions raised by this report.

Manuscript submitted Jan. 13, 1978; revised manuscript received Oct. 1, 1978.

Any discussion of this paper will appear in a Discussion Section to be published in the December 1979 JOURNAL. All discussions for the December 1979 Discussion Section should be submitted by Aug. 1, 1979.

Publication costs of this article were assisted by Bell Laboratories.

REFERENCES

1. K. J. Vetter, "Electrochemical Kinetics," Academic Press, New York (1967).
2. M. Sluyters-Rehback and J. H. Rehback, in "Electroanalytical Chemistry," Vol. 4, A. J. Bard, Editor, p. 1, Marcel Dekker, New York (1970).
3. R. D. Armstrong, R. E. Firman, and H. R. Thirsk, *Faraday Discuss. Chem. Soc.*, **56**, 244 (1973).
4. R. D. Armstrong, M. F. Bell, and A. A. Metcalfe, *J. Electroanal. Chem.*, **77**, 287 (1977); G. Blanc, I. Epelboin, C. Gabrielli, and M. Keddam, *ibid.*, **62**, 59 (1975).
5. A. N. Frumkin, in "Advances in Electrochemistry and Electrochemical Engineering," Vol. 3, P. Delahay, Editor, p. 287, Interscience, New York (1963).
6. F. G. Will and C. A. Knorr, *Z. Elektrochem.*, **64**, 258 (1960).
7. F. G. Will, *This Journal*, **112**, 451 (1965).
8. B. S. Bagotskii, Yu. B. Vassiliev, and I. I. Pyshnograeva, *Electrochim. Acta*, **16**, 2141 (1971).
9. H. Angerstein-Kozlowska, B. E. Conway, and W. B. A. Sharp, *J. Electroanal. Chem.*, **43**, 9 (1973).
10. H. Angerstein-Kozlowska, W. B. A. Sharp, and B. E. Conway, in "Electrocatalysis," M. W. Breiter, Editor, p. 94, The Electrochemical Society Softbound Symposium Series, Princeton, N.J. (1974).
11. P. Dolin and B. Ershler, *Acta Physicochim. URSS*, **13**, 747 (1940).
12. M. Breiter, H. Kammermaier, and C. A. Knorr, *Z. Elektrochem.*, **60**, 37 (1956).
13. M. Breiter, in "Transactions of the Symposium on Electrode Processes," E. Yeager, Editor, p. 307, John Wiley & Sons, Inc., New York (1961).
14. M. W. Breiter, *J. Phys. Chem.*, **68**, 2249 (1964).
15. J. Honz and L. Nemec, *Collect. Czech. Chem. Commun.*, **34**, 2030 (1969).
16. V. I. Luk'yanycheva, E. M. Strochkova, and V. S. Bagotskii, *Electrokhimiya*, **6**, 701 (1970).
17. V. I. Luk'yanycheva, E. M. Strochkova, V. S. Bagotskii, and L. L. Knots, *ibid.*, **7**, 267 (1971).
18. T. Ohsaka, Y. Sawada, T. Yoshida, and K. Nihei, *This Journal*, **123**, 1339 (1976).
19. M. W. Breiter, *J. Electroanal. Chem.*, **7**, 38 (1964).
20. B. E. Conway and S. Gottesfeld, *J. Chem. Soc., Faraday Trans. 1*, **69**, 1090 (1973).
21. M. Rosen, D. R. Flinn, and S. Schuldiner, *This Journal*, **116**, 1112 (1969).
22. C. C. Herrmann, G. P. Perrault, and A. A. Pilla, *Anal. Chem.*, **40**, 1173 (1968).
23. J. Newman, *This Journal*, **113**, 501 (1966).
24. S. H. Glarum, *ibid.*, **124**, 518 (1977).
25. R. Haase, P.-F. Sauermann, and K.-H. Ducker, *Z. Phys. Chem.*, **48**, 206 (1966).
26. A. T. Hubbard, R. M. Ishikawa, and J. Katekaru, *J. Electroanal. Chem.*, **86**, 271 (1978).
27. B. E. Conway, H. Angerstein-Kozlowska, and F. C. Ho, *J. Vac. Sci. Technol.*, **14**, 351 (1977).
28. M. W. Breiter, *J. Electroanal. Chem.*, **8**, 449 (1964).
29. K. Christmann, G. Ertl, and T. Pignet, *Surf. Sci.*, **54**, 365 (1976).
30. R. de Levie, *Electrochim. Acta*, **10**, 113 (1965).

Sinusoidal Hydrodynamic Voltammetry at the Rotating Disk Electrode

I. Theory of Electron Transfer Kinetics

Koichi Tokuda*,[1] **and Stanley Bruckenstein**

Chemistry Department, State University of New York at Buffalo, Buffalo, New York 14214

ABSTRACT

The case of mixed electron transfer and convective-diffusion control is treated for the sinusoidally hydrodynamically modulated rotating disk electrode (SHMRDE). The complexity of the physical situation required that numerical techniques be used to solve the problem. Methods for determining the standard rate constant from SHMRDE data are described.

Theoretical and experimental studies involving the sinusoidally hydrodynamically modulated rotating disk electrode (SHMRDE) were originated and have been exploited by Miller and Bruckenstein (1-4). Their earlier hydrodynamic modulation work is based on the assumption that the Levich equation describes the modulated current, and thus the equations derived are valid only for very slow modulation (1-3). In other words, when the angular velocity, ω, of the rotating disk electrode (RDE) is controlled about a center speed ω_o according to

$$\omega^{1/2} = \omega_o^{1/2} + \Delta\omega^{1/2} \cos \sigma t = \omega_o^{1/2} (1 + \epsilon \cos \omega_o p t) \quad [1]$$

where $\Delta\omega^{1/2}$ is the maximum deviation of $\omega^{1/2}$ from $\omega_o^{1/2}$

$$\epsilon = \Delta\omega^{1/2}/\omega_o^{1/2} \quad [2]$$

and

$$p = \sigma/\omega_o \quad [3]$$

those earlier equations hold only when p is very small. From the experimental point of view, experiments using rather fast potential scan rates are desirable because they minimize the possibility of contamination of the electrode surface with impurities, and the electronic signal processing is simpler. Thus, larger values of σ are required if faster potential scans are to be used in order to maintain a relatively constant potential during one cycle of modulation. For these reasons, further theoretical work describing the modulated current response for large values of p is of interest.

In a previous paper (4) we have shown that for wide range of value of p the current for a purely convective diffusion-controlled process at frequency σ can be expressed by

$$i_l = i_{\omega l} + \Delta i_l \cos (\sigma t - \phi_l) \quad [4]$$

where Δi_l is the modulated limiting current response at σ, ϕ_l is the phase shift of Δi_l with respect to $\omega^{1/2}$, $i_{\omega l}$ is the convective-diffusion limiting current at ω_o, and i_l is the total time varying limiting current produced by ω. The results of the numerical solution of this problem depend on p and the Schmidt number, Sc = ν/D (ν = kinematic viscosity, D = diffusion coefficient), and are given in the tables in terms of ϕ_l and the limiting amplitude response, A_l, where

$$A_l = \frac{\Delta i_l/\Delta\omega^{1/2}}{i_{\omega l}/\omega_o^{1/2}} = \frac{\Delta i_l}{\epsilon i_{\omega l}} \quad [5]$$

Excellent agreement between the theoretical and experimental values was obtained for the ranges of p (0-1.0) and Sc (100-2100) investigated.

* Electrochemical Society Active Member.

[1] Present address: Department of Electronic Chemistry, Graduate School at Nagatsuta, Tokyo Institute of Technology, Midoriku, Yokohama 227, Japan.

Key words: cell, kinetics.

In this report we treat the general case of mixed electron transfer and convective-diffusion control and obtain the general relationships among the total time varying current, i, the modulated current, Δi, the average current (d-c component), i_{ω_o}, potential, relevant species concentrations, and kinetic and transport parameters.

As was the case in the convective-diffusion limiting response, the kinetic current response has the form

$$i = i_{\omega_o} + \Delta i \cos (\sigma t - \phi)$$

and the kinetic amplitude response, A, is given by

$$A = \frac{\Delta i}{\epsilon i_{\omega_o}}$$

Theoretical

We consider the process

$$\mathrm{Ox} + ne \underset{\overleftarrow{k}}{\overset{\vec{k}}{\rightleftarrows}} \mathrm{Red} \quad [6]$$

with standard rate constant k_o and standard potential E^o, and assume that there exists only the oxidized form, Ox, in the bulk of the solution. According to the usual kinetic theory of the electrode process, the general rate equation is given by

$$i = n\mathbf{F}S (\vec{k}C_{\mathrm{Ox}}^s - \overleftarrow{k}C_{\mathrm{Red}}^s) \quad [7]$$

with

$$\vec{k} = k_o \exp[-\alpha(n\mathbf{F}/RT)(E - E^o)] \quad [8]$$

$$\overleftarrow{k} = k_o \exp[(1 - \alpha)(n\mathbf{F}/RT)(E - E^o)] \quad [9]$$

where S is the surface area of the disk electrode ($= \pi r^2$), C_{Ox}^s and C_{Red}^s denote the concentrations of the species Ox and Red at the electrode surface, respectively, and α is the cathodic transfer coefficient.

In order to get the complete expression for the current-potential curves, the convective diffusion equation

$$\frac{\partial C_j}{\partial t} = D_j \frac{\partial^2 C_j}{\partial z^2} - w \frac{\partial C_j}{\partial z} \quad (j = \mathrm{Ox \text{ or } Red}) \quad [10]$$

must be solved, where w is the normal component of the fluid velocity. For the case of a sinusoidal $\omega^{1/2}$-modulation given by Eq. [1] and [2], the expression for w has been given by Eq. [20] and [21][2] of a previous paper (4).

In the same way as used for the limiting current case (4), we can find the solutions of the convective diffusion Eq. [10], which have the form

[2] $w = w_o \{1 + \epsilon (a_{01} \cos \sigma t + a_{10} \sin \sigma t) + \epsilon^2 (\ldots) + \ldots\}$.
$w_o = -0.51023 (\omega_o^3/\nu)^{1/2} z^2 (1 - 0.65327\eta_o + 0.20121\eta_o^2)$.
$\eta_o = (\omega_o/\nu)^{1/2} z$.

$$C_{Ox} = C_{Ox}^{o}u(z,t) = C_{Ox}^{o}[u_0(z) + \epsilon\{u_{01}(z)\cos\sigma t + u_{10}(z)\sin\sigma t\} + \ldots] \quad [11]$$

$$C_{Red} = C_{Ox}^{o}v(z,t) = C_{Ox}^{o}[v_0(z) + \epsilon\{v_{01}(z)\cos\sigma t + v_{10}(z)\sin\sigma t\} + \ldots] \quad [12]$$

where C_{Ox}^{o} is the concentration of Ox in the bulk of the solution.

We followed a method similar to that described in the previous paper (4) and used the following variables

$$\xi_j = z/\delta_j \quad [13]$$

$$\delta_j = [3D_j(\nu/\omega_o^3)^{1/2}/0.51023]^{1/3} \quad [14]$$

$$\lambda = k_o e^{-\alpha\zeta}(1 + e^{\zeta})\gamma^{-\alpha}\delta_{Ox}/D_{Ox} \quad [15]$$

$$\zeta = (n\mathbf{F}/RT)(E - E_{1/2}^{r}) \quad [16]$$

$$\gamma = (\delta_{Ox}/\delta_{Red})(D_{Red}/D_{Ox})\{I_{Ox}(\infty)/I_{Red}(\infty)\} \quad [17]$$

$$\theta = e^{\alpha\zeta}\gamma^{\alpha}D_{Ox}/k_o\delta_{Ox}I_{Ox}(\infty) \quad [18]$$

where

$$I_j(\infty) = 0.89294 + 0.26610Sc_j^{-1/3} + 0.12960Sc_j^{-2/3} \quad [19]$$

The details of the mathematics leading to the numerical solution are given in the Appendix. A List of Symbols used and their definition or physical significance is given following the Appendix.

Relationships between A, A_l, and λ.—Values of A and ϕ were calculated for Sc = 400, 1000, 1400, and 2100 and p = 0.05, 0.1, 0.2, 0.4, and 0.6 (and for 0.1 and 0.5 for two Sc values). A/A_l are plotted against log λ in Fig. 1. It was found out that λ can be expressed approximately within a maximum error of 4% by

$$\lambda = r_1\left(\frac{A}{A_l - A}\right)^{r_2} \quad [20]$$

Values of log r_1 are given in Table I and of r_2 in Table II and were obtained by least squares fittings of calculated λ-values at constant p and Sc to Eq. [20]. Further, it was confirmed that for the range of p (0.2-1.0) and Sc (100-2100) λ can be given approximately within a maximum error of 5% and usually within 2%, by

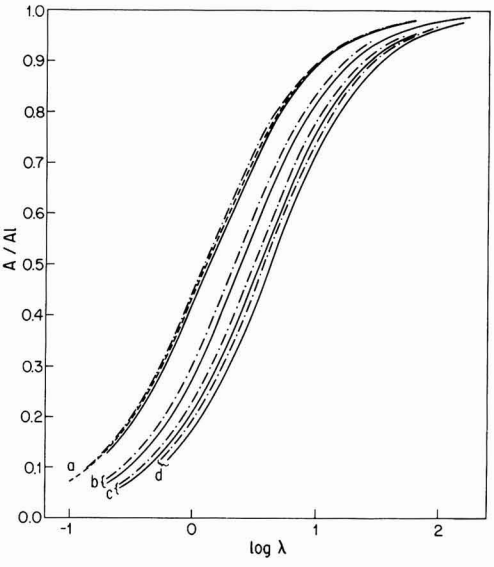


Fig. 1. Plot of A/A_l vs. log λ. a, p = 0.05; b, p = 0.2, c, p = 0.4; d, p = 0.6. Sc values: ——— 2100, —·—·— 1000, - - - - 1400.

Table I. Values of log r_1 in Eq. [20]

	p						
Sc	0.05	0.1	0.2	0.3	0.4	0.5	0.6
2100	0.11413	0.23087	0.38694	0.47936	0.54259	0.59101	0.63119
1800	0.10776	0.22088	0.37557		0.52991		0.62050
1600	0.10306		0.36652		0.52163		0.61186
1400	0.09772	0.20395	0.35649		0.51056		0.60203
1000	0.08640	0.18166	0.33089	0.42336	0.48787	0.53628	0.57666
400	0.06200	0.13034	0.26260		0.42047	0.47001	0.51010

Table II. Values of r_2 in Eq. [20]

	p						
Sc	0.05	0.1	0.2	0.3	0.4	0.5	0.6
2100	0.97440	0.95284	0.94357	0.93863	0.93715	0.94120	0.93773
1800	0.97562	0.95092	0.94355		0.93943		0.94189
1600	0.97777		0.94596		0.94153		0.94368
1400	0.97923	0.95401	0.94479		0.94019		0.93729
1000	0.98112	0.95591	0.94696	0.93742	0.93744	0.93850	0.93670
400	0.98760	0.96769	0.94566		0.93928	0.93778	0.94016

$$\lambda = 1.521p^{0.512}Sc^{0.169}\left(\frac{A}{A_l - A}\right)^{0.941} \quad [21]$$

We next consider three cases according to the rate of the electrode processes.

Reversible case: fast electron transfer.—Dividing both sides of Eq. [A-34] and [A-35] (derived in the Appendix) by k_o, then letting $k_o \to \infty$ and assuming $D_{Ox} = D_{Red}$, gives

$$U_{01}(0)(1 + e^{\zeta}) = 0, \quad U_{10}(0)(1 + e^{\zeta}) = 0 \quad [22]$$

Using Eq. [A-27] and [A-28] of the Appendix, we have, in general, for reversible redox processes

$$u_{01}(0) = u_{10}(0) = v_{01}(0) = v_{10}(0) \quad [23]$$

a result that shows that the boundary conditions for Eq. [A-2], [A-3], [A-5], and [A-6] in the Appendix, which describe the entire Δi-E curve, are exactly the same as those for the limiting current case solved in the previous paper (4). That is, for the reversible case

$$\Delta i = A_l\epsilon i_{\omega_o} \quad [24]$$

Using Eq. [A-25] and the relation $\theta = 0$, gives

$$\Delta i/\Delta i_l = i_{\omega_o}/i_{\omega ol} = 1/(1 + e^{\zeta}) \quad [25]$$

This equation indicates that the normalized Δi-E curve coincides with the normalized i-E curve. Therefore, the reversible half-wave potential for the Δi-E curve, $(E_{1/2}^{r})_{mod}$, agrees with the conventional reversible half-wave potential, $E_{1/2}^{r}$

$$(E_{1/2}^{r})_{mod} = E_{1/2}^{r} = E^{o} + (RT/n\mathbf{F})\ln\gamma = E^{o} + (RT/n\mathbf{F})\ln(D_{Red}/D_{Ox})^{2/3} + (RT/n\mathbf{F})\ln[I_{Ox}(\infty)/I_{Red}(\infty)] \quad [26]$$

Totally irreversible case.—For an extremely slow electron transfer reduction process, we need only consider the cathodic reaction. Then $e^{\zeta} << 1$ and λ is approximately

$$\lambda = k_o e^{-\alpha\zeta}\gamma^{-\alpha}\delta_{Ox}/D_{Ox} = \vec{k}\delta_{Ox}/D_{Ox} \quad [27]$$

and

$$\theta = e^{\alpha\zeta}\gamma^{\alpha}D_{Ox}/k_o\delta_{Ox}I_{Ox}(\infty) = 1/\lambda I_{Ox}(\infty) \quad [28]$$

From Eq. [A-25], we have

$$\frac{i_{\omega_o}}{i_{\omega ol}} = \frac{\lambda I_{Ox}(\infty)}{\lambda I_{Ox}(\infty) + 1} = \frac{k_o e^{-\alpha\zeta}\gamma^{-\alpha}\delta_{Ox}I_{Ox}(\infty)/D_{Ox}}{[k_o e^{-\alpha\zeta}\gamma^{-\alpha}\delta_{Ox}I_{Ox}(\infty)/D_{Ox}] + 1} \quad [29]$$

or

$$E = E_{1/2}^{irr} - \frac{RT}{\alpha n\mathbf{F}}\ln\frac{i_{\omega_o}}{i_{\omega ol} - i_{\omega_o}} \quad [30]$$

with

$$E_{1/2}^{irr} = E^o + (RT/\alpha n\mathbf{F})[\ln k_o + \ln\{\delta_{Ox} I_{Ox}(\infty)/D_{Ox}\}] \quad [31]$$

For anodic reaction there are analogous equations.

An expression relating the modulated current with potential is found by using Eq. [20]

$$\frac{\Delta i}{\Delta i_l} = \frac{i_{\omega_o}}{i_{\omega l}} \frac{A}{A_l} = \left(\frac{\lambda I_{Ox}(\infty)}{\lambda I_{Ox}(\infty) + 1}\right)\left(\frac{(\lambda/r_1)^{1/r_2}}{(\lambda/r_1)^{1/r_2} + 1}\right) \quad [32]$$

In Fig. 2, A/A_l and $\sqrt{\Delta i/\Delta i_l}$ are plotted against log λ for Sc = 1400 and p = 0.05, 0.2, 0.4, and 0.6. The corresponding values of $E - E^o$ are shown in the abscissa. These values are calculated by use of the relation

$$E - E^o = (2.303RT/\alpha n\mathbf{F})[\log(k_o\delta_{Ox}/D_{Ox}) - \log\lambda] \quad [33]$$

and assuming T = 25°C, ν = 0.01 cm²/sec, D_{Ox} = 7.14 × 10^{-6} cm²/sec, ω_o = 3600 rpm = 377.0 rad/sec, n = 1, α = 1, and k_o = 1 × 10^{-10} cm/sec. If the value of k_o changes by a factor of 10, the potential scale shifts 0.059V.

From Fig. 2, we can see that when $p \to 0$

$$i_{\omega_o}/i_{\omega l} = \sqrt{\Delta i/\Delta i_l} \quad [34]$$

which was obtained (3) in the case of very slow modulation ($p \to 0$). In general (*i.e.*, for larger values of p), there is no simple relation between the half-wave potential for the i-E curve and the one for the Δi-E curve. However, for very slow modulation, from Eq. [34] and [30] we have

$$E_{1/2}^{irr} - (E_{1/2}^{irr})_{mod} = -0.8814RT/\alpha n\mathbf{F} \quad [35]$$

This relation has been obtained in the previous paper (3).

Quasireversible case (general case).—When the value of standard rate constant is neither very large nor very small, there is a distinctive characteristic present in A/A_l-potential curves. If we have both an experimental $i_{\omega_o}/i_{\omega l}$-$E$ curve and experimental $\Delta i/\Delta i_l$-E curve, we can calculate the experimental A/A_l-E curve using Eq. [A-41] of the Appendix. Then from Eq. [20] and [15] we have

$$\frac{A_l}{A} = 1 + \frac{1}{(\lambda/r_1)^{1/r_2}} = 1 + \left(\frac{r_1 D_{Ox}}{k_o\delta_{Ox}}\right)^{1/r_2}\left(\frac{1}{e^{-\alpha\zeta}(1+e^{\zeta})}\right)^{1/r_2} \quad [36]$$

Now, A_l/A has a maximum value when

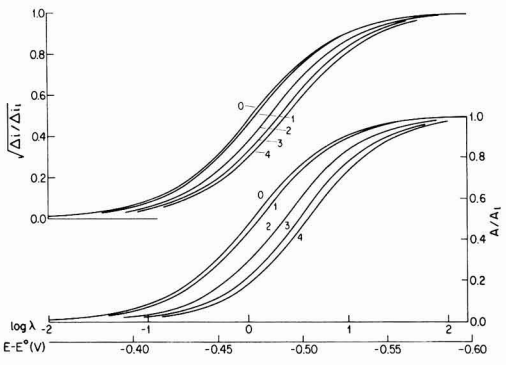


Fig. 2. Plot of normalized current functions vs. log λ (and $E - E^o$). T = 25°C, ν = 0.01 cm²/sec, D_{Ox} = 7.14 × 10^{-6} cm²/sec, ω_o = 3600 rpm (= 377.0 rad/sec), n = 1, k_o = 1 × 10^{-10} cm/sec. p values are curves 0, 0.00; 1, 0.05; 2, 0.2; 3, 0.4; and 4, 0.6.

$$e^{\zeta} = \alpha/(1-\alpha) \quad [37]$$

if $0 < \alpha < 1$. Therefore, if given the value of $E_{1/2}^r (\simeq E^o)$, we can calculate the value of α by Eq. [37], and vice versa. Then, using Eq. [36], the value of k_o can be found. Note that it was assumed $D_{Ox} = D_{Red}$ in this part of discussion, and if the actual values of D_{Ox} and D_{Red} are known, their inclusion in the numerical calculations is obvious.

In Fig. 3, some examples of $i_{\omega_o}/i_{\omega l}$-$\zeta$, $\Delta i/\Delta i_l$-ζ, and A/A_l-ζ curves are shown for Sc = 2100, p = 0.4, and k_o = 1 × 10^{-2}, 5 × 10^{-3}, and 1 × 10^{-3} cm/sec. The other values used were: α = 0.5, D_{Ox} = 5.12 × 10^{-6} cm²/sec, ν = 1.075 × 10^{-2} cm²/sec, ω_o = 900 or 1500 rpm, and σ = 12 or 20π rad/sec. Note that the slope of $\Delta i/\Delta i_l$-E curves is less steep than that of $i_{\omega_o}/i_{\omega l}$-$E$ curve and that ω-modulation emphasizes the effect of k_o. A/A_l decreases when k_o decreases at constant p and when ω_o increases at constant p.

A subsequent paper will present experimental data for the ferricyanide/ferrocyanide system and the ferric/ferrous system performed under conditions to test this aspect of the theory (5).

Plot of A_l/A against $\omega_o^{1/2r_2}$.—Substituting Eq. [14] into Eq. [36], we have

$$\frac{A_l}{A} = 1 + \left(0.5541 r_1 \frac{D_{Ox}^{2/3}}{k_o\nu^{1/6}} \frac{1}{e^{-\alpha\zeta}(1+e^{\zeta})}\right)^{1/r_2} \omega_o^{1/2r_2} \quad [38]$$

or for $0.2 \leq p \leq 1.0$

$$\frac{A_l}{A} = 1 + \left(0.843 p^{0.512} Sc^{0.169} \frac{D_{Ox}^{2/3}}{k_o\nu^{1/6}} \frac{1}{e^{-\alpha\zeta}(1+e^{\zeta})}\right)^{1.063} \omega_o^{0.531} \quad [39]$$

This equation corresponds to the Eq. [13] in Ref. (3)

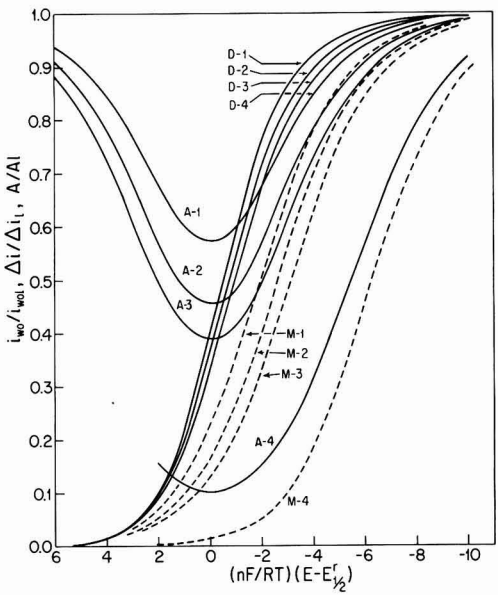


Fig. 3. Plot of normalized current functions vs. $(n\mathbf{F}/RT)(E - E_{1/2}^r)$. α = 0.5, D = 5.12 × 10^{-6} cm²/sec, ν = 1.075 × 10^{-2} cm²/sec, and p = 0.4. Curves D1-D4 are $i_{\omega_o}/i_{\omega l}$, M1-M4 are $\Delta i/\Delta i_l$, and A1-A4 are A/A_l plots. The values of k_o (cm/sec), ω_o (rpm), and σ (rad/sec) are curve 1, 1 × 10^{-2}, 1500, 20π; curve 2, 5 × 10^{-3}, 900, 12π; curve 3, 5 × 10^{-3}, 1500, 20π; curve 4, 1 × 10^{-3}, 1500, 20π.

$$\frac{1}{A} = 1 + \omega_o^{1/2}/k_E \qquad [40]$$

Equation [40] can also be derived from Eq. [A-41] of the Appendix; it has been shown that as $p \to 0$, $A_1 \to 1$, and $\Delta i/\Delta i_1 \to (i_{\omega o}/i_{\omega o1})^2$. Introducing these relations into Eq. [A-41], we have

$$\frac{1}{A} = \frac{i_{\omega o1}}{i_{\omega o}} = 1 + \frac{1}{\lambda I_{Ox}(\infty)} \qquad [41]$$

whereas we easily obtain the relation

$$\lambda I_{Ox}(\infty) = k_E/\omega_o^{1/2}$$

if we put $I_{Ox}(\infty) = \Gamma(4/3)$.

Equation [39] can also be rearranged as follows

$$\frac{A_1}{A} = 1 + \Lambda^{1.063} p^{0.544} \omega_o^{0.531} \qquad [42]$$

with

$$\Lambda = 0.843 Sc^{0.169} \frac{D_{Ox}^{2/3}}{k_o \nu^{1/6} e^{-\alpha\zeta}(1 + e^{\zeta})} \simeq \frac{0.843 D_{Ox}^{1/2}}{k_o e^{-\alpha\zeta}(1 + e^{\zeta})} \qquad [43]$$

Equation [42] suggests that the plots of A_1/A against $p^{0.544}\omega_o^{0.531}$ would give straight lines at each value of the potential in a series of the experiments changing p and ω_o. From the potential dependence of the slope given by Eq. [43], it would then be possible to determine the value of k_o.

Variation of ϕ with λ.—The phase shift in the potential region where both electron and mass transfer control are comparable is much larger than that at the potential of the convective-diffusion limiting current region. The variations of ϕ with log λ are shown in Fig. 4 for Sc = 400, 1000, and 2100 and p = 0.05, 0.2, 0.4 and 0.6. We have not found a simple equation which relates ϕ to λ, p, and Sc.

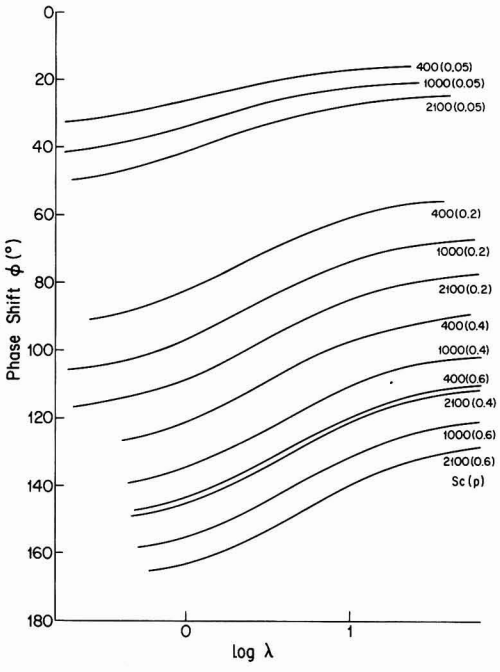


Fig. 4. Variation of phase shift with log λ. Values of Sc and p are shown for each curve in the form Sc(p).

Discussion

The theoretical treatment of the electron transfer process, Eq. [6] at a SHMRDE yielded a number of new SHM results. First, the limiting expression for very fast electron transfer, Eq. [25], demonstrates that plots of $\Delta i/\Delta i_1$ and $i_{\omega o}/i_{\omega o1}$ *vs.* E will superimpose. This result also means that the numerical tabulations given in Ref. (4) for the Δi_1 and ϕ_1 apply at all points on a Δi-E and a ϕ-E curve for a reversible system.

Despite the fact that a numerical technique was required to treat the physical situation existing at a rotating disk electrode subjected to a sinusoidal modulation in $\omega^{1/2}$, an empirical closed form expression for the modulated current response, Eq. [21], was found for the general case of mixed electron transfer and convective-diffusion control. One simple result, Eq. [37], relates the value of α to the potential at which A/A_1 is a minimum. The value of k_o can then be calculated from this piece of information using Eq. [36].

Equation [32] gives the potential dependence of the modulated current response for an extremely slow electron transfer process, while Eq. [36] relates a simple function of the modulated current response to the electrode potential. Either may be used to determine k_o.

A unique method of determining k_o is suggested by Eq. [42]. This method depends on varying σ and/or ω_o at a series of constant potentials.

Finally, the case of very slow electron transfer (the totally irreversible case) obtained previously for $p \to 0$ (3) was shown to be the limit of the mixed electron transfer solution as k_o becomes very small and $p \to 0$.

Phase angle data could not be expressed by any simple empirical expression. The numerical results are presented graphically and may be obtained in tabular form from the authors. It is clear that the variation in phase angle from the foot to the top of a voltammetric wave will be a sensitive indicator of any deviation from pure convective-diffusion control.

The experimental verification of the relationships derived for the various kinetic situations are given in Part II (5).

Conclusions

The numerical approach used to treat SHM data provides a framework for interpretation of experimental data and also serves as a standard against which future analytical techniques, based on various approximations, may be judged.

Acknowledgment

This work was supported by the Air Force Office of Scientific Research through AFOSR Grant No. 74-2572.

Manuscript submitted March 28, 1978; revised manuscript received Sept. 26, 1978.

Any discussion of this paper will appear in a Discussion Section to be published in the December 1979 JOURNAL. All discussions for the December 1979 Discussion Section should be submitted by Aug. 1, 1979.

APPENDIX

Starting with Eq. [10]-[12] and following our earlier approach (4), we obtain the set of ordinary differential equations

$$u_0'' - (\delta_{Ox} w_o/D_{Ox}) u_0' = 0 \qquad [A\text{-}1]$$

$$u_{01}'' - (\delta_{Ox} w_o/D_{Ox})(u_{01}' + a_{01} u_0') = (\delta_{Ox}^2 \sigma/D_{Ox}) u_{10} \qquad [A\text{-}2]$$

$$u_{10}'' - (\delta_{Ox} w_o/D_{Ox})(u_{10}' + a_{10} u_0') = -(\delta_{Ox}^2 \sigma/D_{Ox}) u_{01} \qquad [A\text{-}3]$$

$$v_0'' - (\delta_{Red} w_o/D_{Red}) v_0' = 0 \qquad [A\text{-}4]$$

$$v_{01}'' - (\delta_{Red} w_o/D_{Red})(v_{01}' + a_{01} v_0') = (\delta_{Red}^2 \sigma/D_{Red}) v_{10} \qquad [A\text{-}5]$$

$$v_{10}'' - (\delta_{Red} w_o/D_{Red})(v_{10}' + a_{10} v_0') = -(\delta_{Red}^2 \sigma/D_{Red}) v_{01} \qquad [A\text{-}6]$$

where the various u's and v's are functions of ξ_{Ox} and

ξ_{Red}, respectively, and primes denote differentiation with respect to ξ_j, and

$$\delta_j w_o/D_j = -3\xi_j^2 + 3.5374 Sc_j^{-1/3}\xi_j^3 - 1.9665 Sc_j^{-2/3}\xi_j^4 \quad [A-7]$$

$$\delta_j^2\sigma/D_j = 3.2576 p Sc_j^{1/3} \quad [A-8]$$

$$a_{01} = \frac{3 - 4.7165 Sc_j^{-1/3}\xi_j + 3.2775 Sc_j^{-2/3}\xi_j^2 - 0.090594 p^2}{1 - 1.1791 Sc_j^{-1/3}\xi_j + 0.6555 Sc_j^{-2/3}\xi_j^2} \quad [A-9]$$

$$a_{10} = \frac{0.8029 p}{1 - 1.1791 Sc_j^{-1/3}\xi_j + 0.6555 Sc_j^{-2/3}\xi_j^2} \quad [A-10]$$

The current is related to the fluxes of the species at the electrode surface. Thus, using Eq. [11] and [12], we have

$$\begin{aligned} i/n\mathbf{F}S &= i_{\omega_o}/n\mathbf{F}S + \Delta i \cos(\sigma t - \phi)/n\mathbf{F}S + \ldots \\ &= i_{\omega_o}/n\mathbf{F}S + i_{01}\cos\sigma t/n\mathbf{F}S + i_{10}\sin\sigma t/n\mathbf{F}S + \ldots \\ &= (D_{Ox}C_{Ox}^o/\delta_{Ox})[u_0'(0) + \epsilon\{u_{01}'(0)\cos\sigma t \\ &\quad + u_{10}'(0)\sin\sigma t\} + \ldots] = -(D_{Red}C_{Ox}^o/\delta_{Red})[v'(0) \\ &\quad + \epsilon\{v_{01}'(0)\cos\sigma t + v_{10}'(0)\sin\sigma t\} + \ldots] \end{aligned} \quad [A-11]$$

Also the current is related to the concentrations of the species at the electrode surface by Eq. [7]. Therefore

$$\begin{aligned} i/n\mathbf{F}S &= C_{Ox}^o[\{\vec{k}u_0(0) - \overleftarrow{k}v_0(0)\} + \epsilon\{\vec{k}u_{01}(0) \\ &\quad - \overleftarrow{k}v_{01}(0)\}\cos\sigma t + \epsilon\{\vec{k}u_{10}(0) - \overleftarrow{k}v_{10}(0)\}\sin\sigma t + \ldots] \end{aligned} \quad [A-12]$$

From Eq. [A-11], we have the boundary conditions for Eq. [A-1]-[A-6]

$$u_0'(0) = (\delta_{Ox}/n\mathbf{F}SD_{Ox}C_{Ox}^o)i_{\omega_o}, \qquad u_0(\infty) = 1 \quad [A-13]$$

$$v_0'(0) = -(\delta_{Red}/n\mathbf{F}SD_{Red}C_{Ox}^o)i_{\omega_o}, \qquad v_0(\infty) = 0 \quad [A-14]$$

$$u_{01}'(0) = (\delta_{Ox}/n\mathbf{F}SD_{Ox}C_{Ox}^o)(i_{01}/\epsilon), \qquad u_{01}(\infty) = 0 \quad [A-15]$$

$$u_{10}'(0) = (\delta_{Ox}/n\mathbf{F}SD_{Ox}C_{Ox}^o)(i_{10}/\epsilon), \qquad u_{10}(\infty) = 0 \quad [A-16]$$

$$v_{01}'(0) = -(\delta_{Red}/n\mathbf{F}SD_{Red}C_{Ox}^o)(i_{01}/\epsilon), \qquad v_{01}(\infty) = 0 \quad [A-17]$$

$$v_{10}'(0) = -(\delta_{Red}/n\mathbf{F}SD_{Red}C_{Ox}^o)(i_{10}/\epsilon), \qquad v_{10}(\infty) = 0 \quad [A-18]$$

Equations [A-1] and [A-4] are solved with Eq. [A-13] and [A-14] to give

$$u_0(\xi) = 1 - (\delta_{Ox}/n\mathbf{F}SD_{Ox}C_{Ox}^o)i_{\omega_o}[I_{Ox}(\infty) - I_{Ox}(\xi)] \quad [A-19]$$

$$v_0(\xi) = (\delta_{Red}/n\mathbf{F}SD_{Red}C_{Ox}^o)i_{\omega_o}[I_{Red}(\infty) - I_{Red}(\xi)] \quad [A-20]$$

where

$$\begin{aligned} I_j(\xi) &= \int_0^\xi \exp\left[\int_0^\xi (\delta_j w_o/D_j)\,d\xi\right] d\xi \\ &= \int_0^\xi \exp[-\xi^3 + 0.8843 Sc_j^{-1/3}\xi^4 - 0.3933 Sc_j^{-2/3}\xi^5]\,d\xi \end{aligned} \quad [A-21]$$

and $I_j(\infty)$ is given by Eq. [19] which was obtained from Newman's correction equation (6). (Here, the subscript to ξ was omitted for simplicity.)

From Eq. [A-11] and [A-12] we have

$$i_{\omega_o}/n\mathbf{F}S = C_{Ox}^o\{\vec{k}u_0(0) - \overleftarrow{k}v_0(0)\} \quad [A-22]$$

$$\begin{aligned} i_{01}/n\mathbf{F}S &= \epsilon C_{Ox}^o\{\vec{k}u_{01}(0) - \overleftarrow{k}v_{01}(0)\} \\ &= \epsilon(D_{Ox}C_{Ox}^o/\delta_{Ox})u_{01}'(0) = -\epsilon(D_{Red}C_{Ox}^o/\delta_{Red})v_{01}'(0) \end{aligned} \quad [A-23]$$

$$\begin{aligned} i_{10}/n\mathbf{F}S &= \epsilon C_{Ox}^o\{\vec{k}u_{10}(0) - \overleftarrow{k}v_{10}(0)\} \\ &= \epsilon(D_{Ox}C_{Ox}^o/\delta_{Ox})u_{10}'(0) = -\epsilon(D_{Red}C_{Ox}^o/\delta_{Red})v_{10}'(0) \end{aligned} \quad [A-24]$$

Substituting Eq. [A-19] and [A-20] into Eq. [A-22] and rearranging by use of Eq. [8] and [9], we get

$$\begin{aligned} i_{\omega_o} &= \frac{n\mathbf{F}S\vec{k}C_{Ox}^o}{1 + \{\delta_{Ox}I_{Ox}(\infty)/D_{Ox}\}\vec{k} + \{\delta_{Red}I_{Red}(\infty)/D_{Red}\}\overleftarrow{k}} \\ &= i_{\omega_o l}/(1 + \theta + e^\zeta) \end{aligned} \quad [A-25]$$

where $i_{\omega_o l}$ is the cathodic limiting current given by

$$i_{\omega_o l} = n\mathbf{F}SC_{Ox}^o D_{Ox}/\delta_{Ox}I_{Ox}(\infty) \quad [A-26]$$

and ζ, γ, and θ are defined by Eq. [16]-[18], respectively.

In order to calculate the modulated current, Eq. [A-2], [A-3], [A-5], and [A-6] must be solved for the boundary conditions, Eq. [A-15]-[A-18]. Since it did not appear possible to solve this set of simultaneous differential equations analytically, we employed a numerical method similar to that used in the previous paper (4). In this numerical solution, it is convenient to use the following functions

$$U_{01} = (i_{\omega_o l}/i_{\omega_o})u_{01}, \qquad V_{01} = -\gamma(i_{\omega_o l}/i_{\omega_o})v_{01} \quad [A-27]$$

$$U_{10} = (i_{\omega_o l}/i_{\omega_o})u_{10}, \qquad V_{10} = -\gamma(i_{\omega_o l}/i_{\omega_o})v_{10} \quad [A-28]$$

Then the differential equations to be solved become

$$U_{01}'' - (\delta_{Ox}w_o/D_{Ox})\{U_{01}' + a_{01}I_{Ox}'(\xi)/I_{Ox}(\infty)\} = (\delta_{Ox}^2\sigma/D_{Ox})U_{10} \quad [A-29]$$

$$U_{10}'' - (\delta_{Ox}w_o/D_{Ox})\{U_{10}' + a_{10}I_{Ox}'(\xi)/I_{Ox}(\infty)\} = -(\delta_{Ox}^2\sigma/D_{Ox})U_{01} \quad [A-30]$$

$$V_{01}'' - (\delta_{Red}w_o/D_{Red})\{V_{01}' + a_{01}I_{Red}'(\xi)/I_{Red}(\infty)\} = (\delta_{Red}^2\sigma/D_{Red})V_{10} \quad [A-31]$$

$$V_{10}'' - (\delta_{Red}w_o/D_{Red})\{V_{10}' + a_{10}I_{Red}'(\xi)/I_{Red}(\infty)\} = -(\delta_{Red}^2\sigma/D_{Red})V_{01} \quad [A-32]$$

which have exactly the same form as those in the previous paper (4).

Boundary conditions [A-15]-[A-18] convert to

$$U_{01}'(0) = i_{01}/\{i_{\omega_o}\epsilon I_{Ox}(\infty)\}, \quad V_{01}'(0) = i_{01}/\{i_{\omega_o}\epsilon I_{Red}(\infty)\}$$

$$U_{10}'(0) = i_{10}/\{i_{\omega_o}\epsilon I_{Ox}(\infty)\}, \quad V_{10}'(0) = i_{10}/\{i_{\omega_o}\epsilon I_{Red}(\infty)\}$$

$$U_{01}(\infty) = U_{10}(\infty) = V_{01}(\infty) = V_{10}(\infty) = 0 \quad [A-33]$$

From Eq. [A-23] and [A-24], using Eq. [8], [9], [16], [17], [A-27], and [A-28], we have

$$U_{01}'(0) = (k_o e^{-\alpha\zeta}\gamma^{-\alpha}\delta_{Ox}/D_{Ox})\{U_{01}(0) + e^\zeta V_{01}(0)\} \quad [A-34]$$

$$U_{10}'(0) = (k_o e^{-\alpha\zeta}\gamma^{-\alpha}\delta_{Ox}/D_{Ox})\{U_{10}(0) + e^\zeta V_{10}(0)\} \quad [A-35]$$

If we assume $D_{Ox} = D_{Red} = D$, then $I_{Ox}(\infty) = I_{Red}(\infty)$, $\delta_{Ox} = \delta_{Red} = \delta$, $\gamma = 1$ and Eq. [A-29] and [A-30] are identical to Eq. [A-31] and [A-32], respectively, that is, $U_{01} = V_{01}$ and $U_{10} = V_{10}$. Thus, from Eq. [A-34] and [A-35] we have

$$\frac{U_{01}'(0)}{U_{01}(0)} = \frac{U_{10}'(0)}{U_{10}(0)} = \lambda \quad [A-36]$$

$$\lambda = k_o e^{-\alpha\zeta}(1 + e^\zeta)\gamma^{-\alpha}\delta_{Ox}/D_{Ox} = k_o e^{-\alpha\zeta}(1 + e^\zeta)\delta/D \quad [A-37]$$

The numerical calculations were carried out as follows: For a set of values of p and Sc, we select a value of $U_{01}'(0)$. Then we chose a trial value of $U_{10}'(0)$, and solved Eq. [A-29] and [A-30] to obtain the values of $U_{01}(0)$ and $U_{10}(0)$. If Eq. [A-36] was not satisfied, a new trial value of $U_{10}'(0)$ was chosen and the procedure repeated until Eq. [A-36] was satisfied to within a tolerance of 0.01% or less.

From Eq. [A-11], [A-23], and [A-24], we obtain

$$\Delta i = (i_{01}^2 + i_{10}^2)^{1/2}$$

$$= nFS\epsilon(D_{Ox}C_{Ox}/\delta_{Ox})\,(i_{\omega_o}/i_{\omega_{ol}})\{U_{01}'(0)^2 + U_{10}'(0)^2\}^{1/2}$$

$$= \epsilon i_{\omega_o} I_{Ox}(\infty)\{U_{01}'(0)^2 + U_{10}'(0)^2\}^{1/2} \quad [A\text{-}38]$$

$$A = \Delta i/\epsilon i_{\omega_o} = I_{Ox}(\infty)\{U_{01}'(0)^2 + U_{10}'(0)^2\}^{1/2} \quad [A\text{-}39]$$

and

$$\phi = \cos^{-1}\left(\frac{U_{01}'(0)}{[U_{01}'(0)^2 + U_{10}'(0)^2]^{1/2}}\right) \quad [A\text{-}40]$$

Comparing Eq. [A-39] with Eq. [5], we have

$$\frac{\Delta i}{\Delta i_l} = \frac{i_{\omega_o}}{i_{\omega l}}\frac{A}{A_l} \quad [A\text{-}41]$$

Equation [A-41] describes the modulated current response at the SHMRDE in terms of the conventional RDE current response, the kinetic parameters, and the modulation conditions and, as shown in the body of this paper, provides a convenient diagnostic tool.

LIST OF SYMBOLS

a_{nm}	coefficients of the time dependent components in the power series representation of the modulated normal fluid velocity (Eq. [20] and [21] (4))
A	kinetic amplitude factor (Eq. [A-39])
A_l	limiting current amplitude factor (Eq. [5])
C_j	concentration of species j at point z and time t
C_j^o	bulk concentration of species j
C_j^s	surface concentration of species j
D_j	diffusion coefficient of species j
E	electrode potential
E^o	standard electrode potential
$E_{1/2}^r$	reversible half-wave potential (Eq. [26])
$E_{1/2}^{irr}$	irreversible half-wave potential (Eq. [31])
F	Faraday's constant
i	electrode kinetic current (Eq. [7])
i_l	instantaneous RDE limiting current under sinusoidal hydrodynamic modulation
i_{ω_o}	RDE current at rotation frequency ω_o
$i_{\omega l}$	limiting RDE current at rotation frequency ω_o
Δi	amplitude of the modulated current
Δi_l	amplitude of the modulated limiting current
$I_j(\infty)$	values of integral, Eq. [A-21] at $\xi \to \infty$ for species j, obtained from Newman's correction equation (Eq. [19])
$\vec{k}$	forward electron transfer rate constant
$\overleftarrow{k}$	backward electron transfer rate constant
k_o	standard electron transfer rate constant
n	number of Faradays required to reduce one mole of Ox
p	ratio of modulation frequency to mean rotation frequency (Eq. [3])
r	disk electrode radius
r_1	tabulated values in Table I for use in Eq. [20]
r_2	tabulated values in Table II for use in Eq. [20]
R	gas constant
RDE	rotating disk electrode
S	surface area of RDE
Sc_j	Schmidt number of species j
t	time
T	absolute temperature
$u(z,t)$	normalized concentration function, C_{Ox}/C_{Ox}^o (Eq. [11])
u_{nm}	coefficients in power series representation of $u(z,t)$ (Eq. [11])
U_{nm}	current weighted value of u_{nm} (Eq. [A-27] and [A-28])
$v(z,t)$	normalized concentration function, C_{Red}/C_{Ox}^o (Eq. [12])
v_{nm}	coefficients in power series representation of $v(z,t)$ (Eq. [12])
V_{nm}	current weighted value of v_{nm} (Eq. [A-27] and [A-28]
w	instantaneous normal fluid velocity
w_o	normal fluid velocity at $\omega = \omega_o$
α	cathodic transfer coefficient
γ	correction factor for diffusion coefficient difference of Ox and Red (Eq. [17])
δ_j	Levich diffusion layer thickness of species j divided by 0.89294 (Eq. [14])
ϵ	fraction of square root of rotation speed in $\omega^{1/2}$-modulation (Eq. [2])
ζ	dimensionless potential difference (Eq. [16])
η_o	dimensionless normal distance
θ	rate of mass transfer relative to rate of electron transfer (Eq. [18])
λ	rate of electron transfer relative to rate of mass transfer (Eq. [15])
ν	kinematic viscosity
ξ_j	fraction of Levich diffusion layer thickness (Eq. [13])
σ	modulation frequency, radians/sec
ϕ	phase shift between modulated current response and modulated rotation speed
ϕ_l	value of ϕ in limiting current region
$\omega^{1/2}$	square root of the instantaneous rotation frequency, (radians/sec)$^{1/2}$
$\omega_o^{1/2}$	square root of the mean rotation frequency, (radians/sec)$^{1/2}$
$\Delta\omega^{1/2}$	maximum difference between $\omega^{1/2}$ and $\omega_o^{1/2}$

REFERENCES

1. B. Miller, M. I. Bellavance, and S. Bruckenstein, *Anal. Chem.*, **44**, 1983 (1972).
2. B. Miller and S. Bruckenstein, *ibid.*, **46**, 2026 (1974).
3. B. Miller and S. Bruckenstein, *This Journal*, **121**, 1558 (1974).
4. K. Tokuda, S. Bruckenstein, and B. Miller, *ibid.*, **122**, 1316 (1975).
5. Y. Kanzaki and S. Bruckenstein, *ibid.*, **126**, 437 (1979).
6. J. S. Newman, *J. Phys. Chem.*, **70**, 1327 (1966).

Sinusoidal Hydrodynamic Voltammetry at a Rotating Disk Electrode

II. Experimental Test of the Electron Transfer Theory

Yasushi Kanzaki*,[1] and Stanley Bruckenstein*

Chemistry Department, State University of New York at Buffalo, Buffalo, New York 14214

ABSTRACT

Sinusoidal hydrodynamic modulation (SHM) experiments were performed at a rotating disk electrode to test the theory derived previously for mixed electron transfer and convective diffusion (1). The $Fe(CN)_6^{3-}/Fe(CN)_6^{4-}$, Fe(III)/Fe(II), and Tl(III)/Tl(I) couples were studied because they represented systems ranging from fairly fast to very slow electron transfer. Agreement was obtained between theory and experiment for the modulated current and phase shift in the SHM experiment.

In Part I (1), the theory for the modulated current response of a sinusoidally hydrodynamically modulated rotating disk electrode (SHMRDE) was given for reaction [1]

$$\mathrm{Ox} + ne \underset{\overleftarrow{k}}{\overset{\vec{k}}{\rightleftarrows}} \mathrm{Red} \qquad [1]$$

for a solution containing only Ox. This theory predicts the steady-state and fundamental current response produced by an imposed angular velocity function of the form

$$\omega^{1/2} = \omega_0^{1/2} + \Delta\omega^{1/2} \cos \sigma t = \omega_0^{1/2}(1 + \epsilon \cos p\omega_0 t) \qquad [2]$$

where ω is the instantaneous angular velocity, ω_0 is the mean angular velocity, $\Delta\omega$ is the maximum perturbation from the mean, σ is the radian frequency of rotation, t is the time, ϵ is the fraction of modulation in terms of the square root of modulation $(\Delta\omega/\omega_0)^{1/2}$, and p is a dimensionless modulation frequency normalized to the mean rotation speed (σ/ω_0).

The time varying current, at a potential E, has the form

$$i = i_{\omega_0} + \Delta i \cos(\sigma t - \phi) = i_{\omega_0}[1 + \epsilon A \cos(p\omega_0 t - \phi)] \qquad [3]$$

where i_{ω_0} is the mean current, Δi is the modulated current, and ϕ is the phase shift of the current response with respect to the imposed $\omega^{1/2}$-control function. The amplitude factor A, is given by

$$A = \frac{\Delta i/\Delta\omega^{1/2}}{i_{\omega_0}/\omega_0^{1/2}} = \frac{\Delta i}{\epsilon i_{\omega_0}} \qquad [4]$$

and differs from unity for two reasons. First, for values of $p > 0$, the hydrodynamic properties of the solution lead to a decreased current response and phase shift increment. This has been discussed quantitatively elsewhere (2) and is described there in terms of convective-diffusion limiting amplitude response, A_l (designated there as A in Eq. [53]) and phase shift, ϕ_l (designated there as ϕ_l in Eq [5] and [39]). Second, the electron transfer reaction, Eq. [1], is perturbed by the time-varying concentration profiles produced by the SHM technique. The theory in Part I shows that $A \leq A_l$ and $\phi \geq \phi_l$ and relates all these quantities to the standard rate constant, k_0, to the cathodic transfer coefficient α, to the standard potential E^0, and to the various transport parameters of the system.

In this part, the theory is tested for a relatively fast system ($Fe(CN)_6^{3-}/Fe(CN)_6^{4-}$ in 0.4*M* K_2SO_4), an intermediately slow system (Fe^{3+}/Fe^{2+} in 0.2*M* H_2SO_4), and a highly irreversible system (Tl(III)/Tl(I) in 1.0*M* $HClO_4$ + 0.1*M* HCl). As reported below, we find satisfactory agreement between theory and experiment.

Experimental

Chemicals.—Milli-Q water and analytical (reagent) grade chemicals were used to prepare all solutions.

Electrochemical equipment.—An operational amplifier-based three electrode potentiostat was used. The reference electrode was a saturated calomel electrode (SCE). Analog data were recorded digitally using a calculator-based (Wang 720) control and data acquisition system. Electrode potential resolution and reproducibility was ±0.5 mV, and the current measurement accuracy was ±0.5% relative. The platinum disk electrode was 0.23 cm in diameter and was mounted on a stainless steel shaft of the same diameter. The electrode end of the shaft was insulated with epoxy resin. The electrode was polished using conventional metallurgical techniques after fabrication and repolished using 0.05 μm α alumina before each new experiment. During each experiment, the electrode was potential cycled from the anodic to the cathodic limits of the supporting electrolyte several times, and then the i-E or Δi-E curve was determined. SHM measurements were made at potential scan rates of 0.8 mV sec^{-1}, a rate selected to accommodate to the response time of the Δi measured system. Δi was measured by passing the total disk current into a tuned two pole Butterworth bandpass filter, $Q = 10$, except for $\sigma = 15$ Hz, and then to a PAR Model 129A lock-in-amplifier. The magnitude of Δi and its phase are available directly from this synchronous phase sensitive detector. The reference signal to the lock-in amplifier was supplied by the motor control signal and corrected for the small phase shift with respect to the integral tachometer generator of the Model C Servotech servomoter used to control the motor speed. The motor speed controller and motor are very similar in most aspects to those described previously (2) and had equally good performance characteristics. Center rotation speeds of 900-4900 rpm (30-70 $rpm^{1/2}$) were used with modulation amplitudes ($\Delta\omega^{1/2}$) of 1-8 $rpm^{1/2}$. Modulation frequencies varied from 2 to 15 Hz and were chosen to produce the desired value of p.

Results and Discussion

Reversible and quasireversible case.—The rate of electron transfer for the half-reaction

$$Fe(CN)_6^{3-} + e \rightleftarrows Fe(CN)_6^{4-} \qquad [5]$$

* Electrochemical Society Active Member.
[1] Present address: Department of Chemistry, Aoyama Gakuim University, Chitosedai, Setagaya-ku, Tokyo, Japan.
Key words: cell, kinetics.

is generally accepted as being fairly rapid. In potassium sulfate solution, the standard rate constant has been estimated to be 1.3×10^{-1} cm sec^{-1} (3) and 0.73×10^{-1} cm sec^{-1} (4) and in potassium chloride solutions to be 0.9×10^{-1} cm sec^{-1} and 0.52×10^{-1} cm sec^{-1} (4). Thus the i-E curve at a conventional rotating disk electrode should appear to be reversible. This is found to be the case for the reduction of 2 mM ferricyanide in 0.4M K_2SO_4 at $\omega_o = 3600$ rpm.

Equation [25] in the theoretical part (1) showed that the normalized conventional current-potential ($i_{\omega_o}/i_{\omega_{ol}}$-$E$) curve and the corresponding normalized SHM curve ($\Delta i/\Delta i_l$) should superimpose for a reversible redox couple. Therefore, a SHMRDE experiment was performed in the 2 mM ferricyanide —0.4M K_2SO_4 solution at $\omega_o = 3600$ rpm and $p = 0.033$ ($\sigma = 2$ Hz). Under these experimental conditions, no difference between the two normalized curves could be detected and the maximum experimental phase shift, ϕ_{exp}, observed in the ϕ-E curve was about 1°. The latter value approximates our estimate of the error in the absolute value of ϕ. Thus the SHMRDE experiment, under the above experimental conditions, produces a "reversible" Δi-E curve. More precisely, if we assume $k_o = 1.0 \times 10^{-1}$ cm sec^{-1}, $\alpha = 0.5$ and use the theory of Part I, we calculate that the maximum phase shift should be 0.5° and the corresponding value of A/A_1 would be 0.98. A is defined here by Eq. [4] and A_1 in (1) by Eq. [5] hence

$$A/A_1 = (\Delta i/\Delta i_l)/(i_{\omega_o}/i_{\omega_{ol}}) \qquad [6]$$

These values of A/A_1 and ϕ, are within the experimental error of a SHM experiment, and thus the Δi-E curves will be indistinguishable from reversible Δi-E curves.

As p increases the normalized SHMRDE and ϕ-E curves for the $Fe(CN)_6^{3-}/Fe(CN)_6^{4-}$ system are predicted to deviate significantly from reversible behavior. This is found to be the case at $p = 0.667$ in the above solution as is shown in Fig. 1. Also plotted is A/A_1. As shown in Fig. 3 and Eq. [37] in Part I (1), A/A_1 is a minimum when

$$E = E_{1/2^r} + \frac{RT}{n\mathbf{F}} \ln \frac{\alpha}{1-\alpha} \qquad [7]$$

where $E_{1/2^r}$ is the reversible half-wave potential.

The shape of the experimental A/A_1 *vs.* E plot in Fig. 1 is in agreement with theory, changing from one on the limiting current region to a minimum value and back again to one at the foot of the current-potential curve.

A summary of the results obtained at p-values of 0.112, 0.240, 0.667, and 1.00 are given in Table I. All data were obtained in the solutions corresponding to that used in Fig. 1. In all cases, the minimum in A/A_1 occurred within the experimental error, at the estimated values of $E_{1/2^r}$. Thus according to Eq. [7], we used $\alpha = 0.5$ in the remaining calculations. The minimum value of A/A_1 was used to calculate k_o from Eq. [36] of Part I (1). The average value of k_o is $0.08_4 \pm 0.01_9$ cm sec^{-1} and is in satisfactory agreement with previous estimates for this redox couple

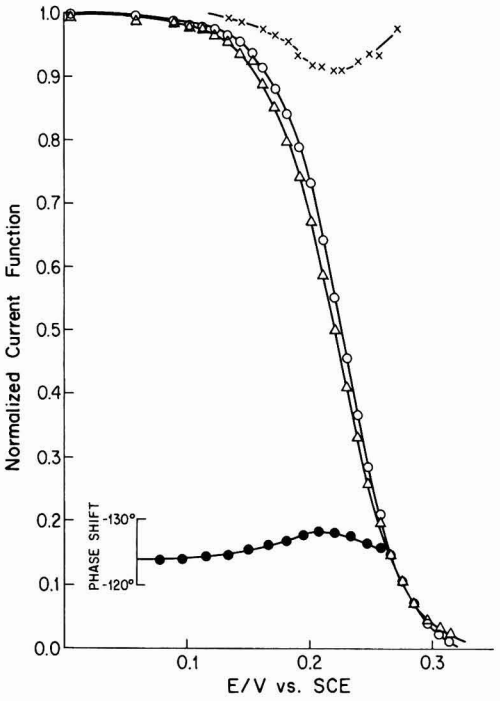


Fig. 1. Normalized current-potential curve (—○—), normalized modulated current-potential curve (—△—), A/A_1 (—×—), and corresponding phase shift (—●—) for reduction of 2 mM $Fe(CN)_6^{3-}$ in 0.4M K_2SO_4. Electrode: platinum, $\omega_o = 900$ rpm, $\sigma = 10$ Hz ($p = 0.67$). $\Delta\omega^{1/2} = 2$ rpm$^{1/2}$. Temperature 25°C.

(3, 4). As p increases, k_o appears to decrease. The reason for this trend is not known.

The SHMRDE kinetic technique is being used at its limits in this study of the $Fe(CN)_6^{3-}/Fe(CN)_6^{4-}$ system. There are only small shifts of the normalized SHMRDE curves as compared to $i_{\omega_o}/i_{\omega_{ol}}$-$E$ curves, but, as is predicted, the shifts become more pronounced as p increases.

The phase shift behavior is shown in Fig. 1 and is summarized in Table I for three p-values. The experimental phase shift values, ϕ_{exp}, agree well with the theoretical values, as shown in Table I. Note that the theoretical value of ϕ was obtained using the k_o calculated from that particular experiment.

Experimental difficulties are encountered in making A/A_1- and ϕ-measurements when Δi is less than 20% of Δi_l. The signal to noise ratio becomes unfavorable and makes Δi and ϕ_{exp} measurements less reliable.

Quasireversible case.—The reduction of 1.6 mM Fe^{3+} in 1.0M H_2SO_4 does not proceed "reversibly." One set of results obtained at the RDE ($\omega_o = 2500$ rpm) and at the SHMRDE ($p = 0.120$. $\sigma = 5$ Hz) is

Table I. $Fe(CN)_6^{3-}/Fe(CN)_6^{4-}$ system

p	ω (rpm)	σ (Hz)	A/A_1	k_o (cm sec^{-1})	Phase shift range Obs.	Phase shift range Calc.	Std. dev. in* i_d	Std. dev. in* Δi	Error† (%)
0.122	4900	10	0.94 (0.95)	1.1×10^{-1} (1.3×10^{-1})	49°-54°	49°-52°	±0.50	±0.97	41.5
0.240	2500	10	0.93	0.96×10^{-1}	80°-85°	80°-84°	±0.41	±0.43	15.7
0.667	900	10	0.91	0.75×10^{-1}	124°-128°	127°-131°	±0.43	±0.47	12.9
1.00	900	15	0.85	0.54×10^{-1}	Not detected	140°-148°	±0.44	±1.6	18.4

* Standard deviation was estimated relative to the magnitude of the limiting current.
† Error in the theory is estimated to be no more than 5% in the k_o calculation.

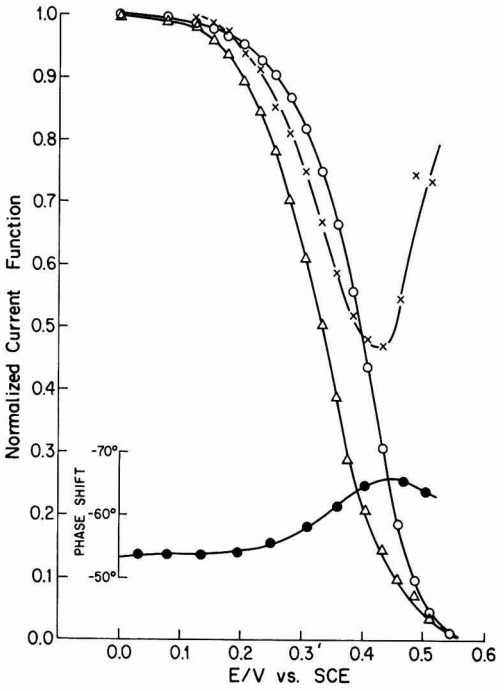


Fig. 2. Normalized current-potential curve (—○—), normalized modulated current-potential curve (—△—), A/A_1 (—×—), and corresponding phase shift (—●—) for the reduction of 1.6 mM Fe^{3+} in 1M H_2SO_4. Electrode: platinum, $\omega_0 = 2500$ rpm, $\sigma = 5$ Hz ($p = 0.12$). $\Delta\omega^{1/2} = 2$ rpm$^{1/2}$. Temperature 25°C.

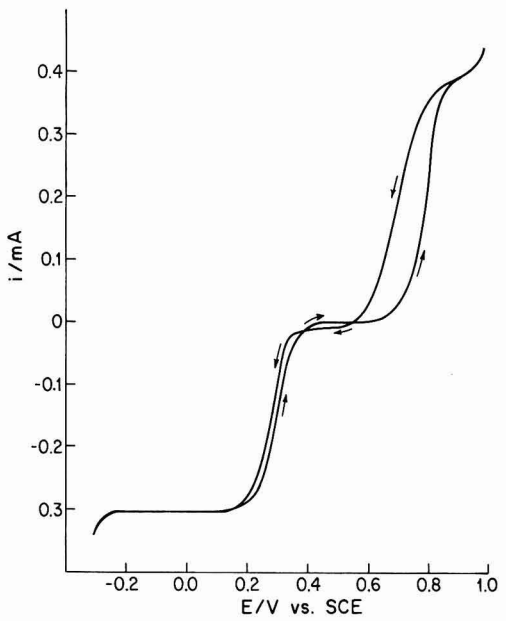


Fig. 3. Current-potential curve for Tl(III)/Tl(I)(1 mM Tl(III) + 1 mM Tl(I) in 0.1M HCl + 1M $HClO_4$. $\omega_0 = 2500$ rpm. Scan rate: 0.5 V min^{-1}. Temperature 25°C.

shown in Fig. 2. A/A_1 and ϕ have the predicted shape for a reaction having a finite rate of electron transfer rate. The results of this and similar experiments are given in Table II. Using $\alpha = 0.43$, $D = 5.26 \times 10^{-6}$ cm^2 sec^{-1}, Sc = 2100, the average value of k_o is $(4.6 \pm 0.8) \times 10^{-3}$ cm sec^{-1}. Theoretical and experimental values of ϕ are in satisfactory agreement for the smaller values of ϕ but are less than theory predicts at the larger phase shifts. Similarly, the values of k_o show an unexpected trend with p. However, the mean value of k_o is in satisfactory agreement with previously reported values (5-7). As pointed out previously (8), the measurement of k_o in this system is extremely sensitive to electrode pretreatment, and variations of the magnitude shown in Table II occur using more conventional voltammetric procedures to determine k_o (8).

Totally irreversible case.—The Tl(III)/Tl(I) couple is very irreversible in 1*M* $HClO_4$ + 0.1*M* HCl (9). This is shown clearly in Fig. 3, which is the *i-E* curve of 1 mM Tl(I) + 1 mM Tl(III) at the RDE. The oxidation wave demonstrates considerable scan-direction hysteresis, presumably as a result of the formation and removal of surface film during the potential scanning experiment. The scan direction hysteresis seen during the reduction of Tl(III) is much less and the current-potential curve was reasonably reproducible. The equilibrium potential measured with a high impedence voltmeter was +0.588V. Also, the position of the reduction and oxidation wave is characteristic of a reaction for which α is considerably different from 0.5. Taking these observations into account, we elected to analyze the *i-E* curve for the reduction of Tl(III) found during the anodic scan. The conventional plot of η *vs.* log $[i_{\omega_0}/(i_{\omega_0 l} - i_{\omega_0})]$ (Fig. 4) is linear and has a slope of 95 mV/decade, *i.e.*, if $n = 2$, $\alpha = 0.32$.

$i_{\omega_0}/i_{\omega_0 l}$ and $\Delta i/\Delta i_l$ *vs.* E curves obtained at $p = 0.05$ are shown in Fig. 5. This experiment approximates the limit of $p = 0$, for which the difference in half-wave potentials may be calculated from Eq. [35] of Part I (1). Using the value of αn found from Fig. 4, the predicted difference in the $i_{\omega_0}/i_{\omega_0 l}$ and $\Delta i/\Delta i_l$ half-wave potentials is 36 mV, as compared to the experimental value of 35 mV in Fig. 5. Also plotted in Fig. 5 is the current function $\sqrt{\Delta i/\Delta i_l}$, which in agreement with Eq. [34] in Part I (1) superimposes on the $i_{\omega_0}/i_{\omega_0 l}$ plot.

Table II. Fe(III)/Fe(II) system*

p	ω (rpm)	σ (Hz)	A/A_1	k_o (cm sec^{-1})	Phase shift range Obs.	Phase shift range Calc.	Error†‡
0.048	2500	2	0.65	6.49×10^{-3}	23°-32°	23°-33°	2.08
0.120	2500	5	0.46	4.45×10^{-3}	54°-66°	52°-75°	2.80
0.122	4900	10	0.38	4.63×10^{-3}	54°-68°	52°-79°	3.56
0.240	2500	10	0.35	4.26×10^{-3}	86°-99°	85°-115°	3.78
0.667	900	10	0.28	3.23×10^{-3}	128°-142°	130°-162°	4.35

* Standard deviation in the current-potential curve was estimated from those in $Fe(CN)_6^{3-}$ system, *i.e.*, about ±0.5%.
† Error in the theory is estimated to be about 5% in calculating k_o.
‡ Net error is about 7% or less.

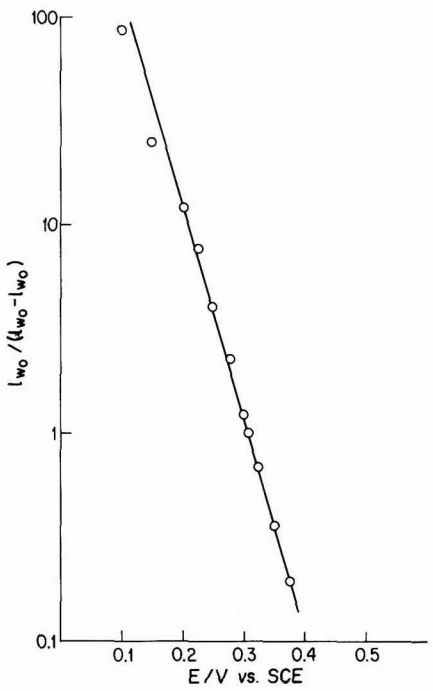


Fig. 4. Potential *vs.* log $i_{\omega_o}/(i_{\omega_{ol}} - i_{\omega_o})$ plot for the reduction of Tl(III). The plot was obtained from the anodic scan in Fig. 3.

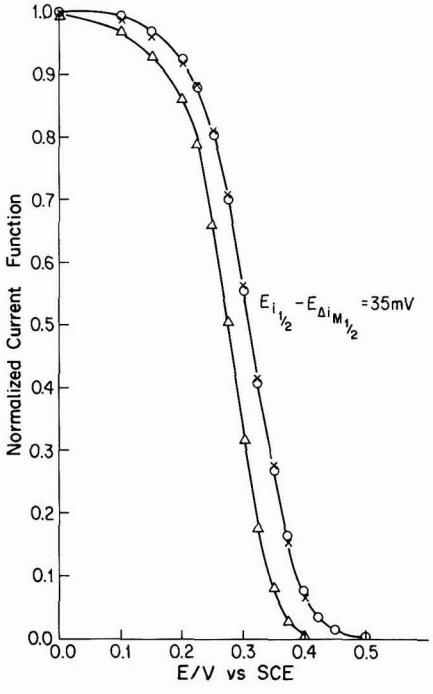


Fig. 5. Normalized current-potential curve (—○—), normalized modulated current-potential curve (—△—), and $(\Delta i/\Delta i)^{1/2}$ (—×—) for reduction of Tl(III) in $p = 0.05$. $\Delta\omega^{1/2} = 1$ rpm$^{1/2}$.

Figure 6 shows the results obtained for the previous system with $p = 0.25$. The difference between the

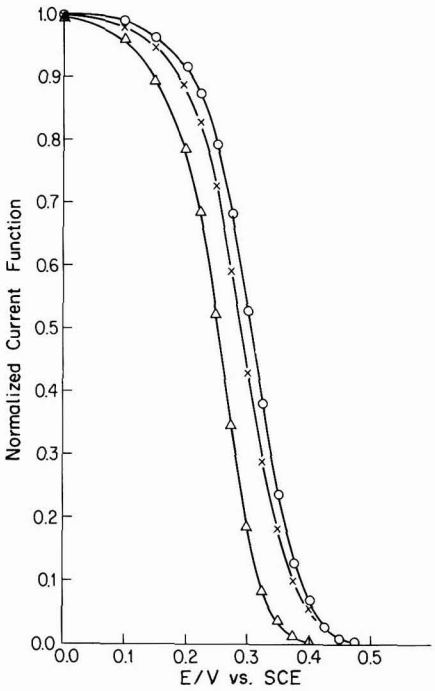


Fig. 6. Normalized current-potential curve (—○—), normalized modulated current-potential curve (—△—), $(\Delta i/\Delta i_l)^{1/2}$ (—×—) for reduction of Tl(III) in 0.1M HCl + 1M $HClO_4$. $\omega_o = 2500$ rpm, $\sigma = 10$ Hz modulation ($p = 0.24$). $\Delta\omega^{1/2} = 1$ rpm$^{1/2}$.

half-wave potentials of the $i_{\omega_o}/i_{\omega_{ol}}$ curves is ~53 mV which agrees well with the value calculated theoretically according to Part I, Eq. [29]-[33], (1). The plots of $\sqrt{\Delta i/\Delta i_l}$ and $i_{\omega_o}/i_{\omega_{ol}}$ do not superimpose, demonstrating that superposition is a limiting law for $p \to 0$.

Figure 7 demonstrates that increasing p progressively shifts the A/A_l curve cathodically with respect to the $i_{\omega_o}/i_{\omega_{ol}}$ curve for p larger than 0.048. The experimental accuracy is not sufficient to distinguish between the $i_{\omega_o}/i_{\omega_{ol}}$ and A/A_l curves for p-values less than 0.048. The shift in half-wave potentials of the $\Delta i/\Delta i_l$ curve agrees well with theory for p values greater than 0.1.

Figure 8 gives the experimental and theoretical phase shifts for the reduction of Tl(III) to Tl(I) for six p values in the range 0.024 to 1.0 over the entire Δi-E curve. Agreement is excellent on the limiting current region for $p \leq 0.50$, while the experimental results is 4° lower than theoretical value at $p = 1.0$. On the rising portion of wave, agreement is excellent between theory and experiment for $p \leq 0.12$ and is within 6° for all data for which $p \geq 0.24$.

Conclusion

The theory for mixed electron transfer and convective diffusion at the sinusoidally modulated rotating disk electrode agrees well with the experimental results for a wide range of p and k_o values. The SHMRDE technique is capable of measuring electron transfer rate constants as high as 0.1 cm sec^{-1}, since Δi-E curves are more sensitive to irreversible behavior than i-E curves. Also ϕ-E data are extremely sensitive to electron transfer kinetics.

Acknowledgments

The work was supported by the Air Force Office of Scientific Research under Grant No. 74-2572.

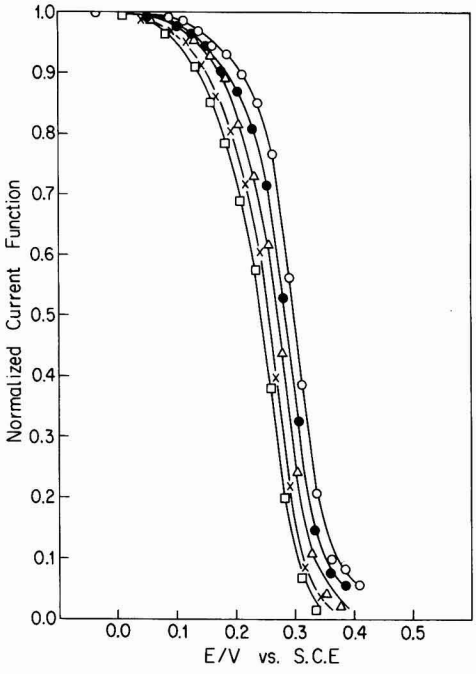


Fig. 7. A/A_l vs. E for the reduction of Tl(III) to Tl(I). The current-potential curve has been normalized with respect to the limiting current. The p values were obtained at: 2500 rpm, 1 Hz modulation ($p = 0.028$) (—○—); 2500 rpm, 2 Hz ($p = 0.048$) (—○--); 2500 rpm, 5 Hz ($p = 0.012$) (—●—): 2500 rpm, 10 Hz ($p = 0.24$) (—△—): 1200 rpm 10 Hz ($p = 0.5$) (—×—): 900 rpm, 15 Hz ($p = 1.0$ (—□—).

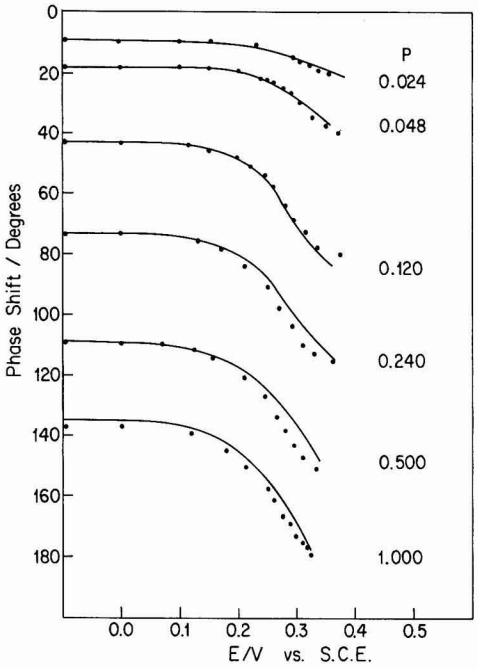


Fig. 8. Phase shift vs. E for the reduction of Tl(III) to Tl(I). The diffusion coefficient of Tl(III) determined in the solution containing 1M $HClO_4$, 0.1M HCl, and 2 mM $TlClO_4$, was 0.94 × 10^{-5} cm^2 sec^{-1}. The corresponding Schmidt number was 910. Tl(I) was electrooxidized *in situ* to Tl(III) (98%). Calculated phase shift shown as filled circles (●).

Manuscript submitted March 28, 1978; revised manuscript received Sept. 26, 1978.

Any discussion of this paper will appear in a Discussion Section to be published in the December 1979 JOURNAL. All discussions for the December 1979 Discussion Section should be submitted by Aug. 1, 1979.

REFERENCES

1. K. Tokuda and S. Bruckenstein, *This Journal*, **126**, 431 (1979).
2. K. Tokuda, S. Bruckenstein, and B. Miller, *ibid.*, **122**, 1316 (1975).
3. J. E. B. Randles and K. W. Somerton, *Trans. Faraday Soc.*, **48**, 937 (1952).
4. N. Tanaka and R. Tamamushi, *Electrochim. Acta*, **9**, 963 (1964).
5. H. P. Agarwal, *J. Electroanal. Chem.*, **5**, 236 (1963).
6. F. C. Anson, *Anal. Chem.*, **33**, 939 (1961).
7. Z. Galus and R. N. Adams, *J. Phys. Chem.*, **67**, 866 (1963).
8. B. Miller, M. I. Bellavance, and S. Bruckenstein, *This Journal*, **118**, 1082 (1971).
9. S. D. James, *Electrochim. Acta.*, **12**, 939 (1967).

Technical Note

The Composition of Anodically Formed Iron Oxide Films

M. Cohen,* D. Mitchell, and K. Hashimoto

National Research Council of Canada, Ottawa, Ontario, Canada K1A 0R9

The composition of the passive film formed on iron by anodic oxidation in neutral borate buffer solution has been the subject of numerous publications over the past few years. Nagayama and Cohen (1) showed that the films gave an electron diffraction pattern characteristic of either γ-Fe_2O_3 or Fe_3O_4. Cathodic reduction results indicated a composition of cation defect γ-Fe_2O_3 at the surface with Fe_3O_4 next to the metal. They postulated a variable composition of cubic oxide from the metal-oxide surface to the outer surface. They also showed (2) that anodic oxidation in the presence of an Fe^{++} ion led to the additional formation of γ-FeOOH by deposition from the solution. Markovac and Cohen (3) showed that γ-FeOOH could also be deposited on platinum by anodic oxidation of Fe^{++} in solutions.

Kruger *et al.* (4) examined anodic films ellipsometrically. Their results indicated that if the solution in which the anodic oxidation was performed was iron free the data could best be interpreted on the basis of the growth of a single phase oxide whose composition varied slightly across the thickness of the film. Staehle and co-workers (5), using Auger analysis, concluded that the film was duplex in nature. This conclusion had also been reached by Ord (6) using ellipsometry. In other work, Kruger (7) suggested that the film contained a small amount of hydrogen and postulated, following Bloom (8), that the outer layer of γ-Fe_2O_3 was stable only if it contained a small amount of H ($\approx$0.06%). They also pointed out that the presence of a small amount of FeOOH would account for the presence of the hydrogen.

Sato and co-workers (9) have published a number of papers on the growth and composition of the films formed in borate buffer solutions. Although their anodic oxidation was performed at pH 8.4, the cathodic reduction was done at *p*H 6.35. Earlier work by Oswin and Cohen (10) had shown that iron analyses done after cathodic reduction at this low *p*H are misleading due to the possibility of localized corrosion. Sato's current picture (9) of the passive film formed in neutral solution is a two-layer structure of "γ-Fe_2O_3" next to the metal formed by direct oxidation and γ-FeOOH at the oxide solution interface formed by deposition from Fe^{++} in solution. On the other hand, Bockris and co-workers (11) have suggested that the film is a hydrated ferrous oxide with a gel-like structure (of the composition $Fe(OH)_2 \cdot nH_2O$). They believe this is degraded to γ-Fe_2O_3 by a combination of vacuum treatment and the heating by the beam in the electron diffraction camera. This paper is an attempt to resolve some of the differences and disagreements in the above work.

* Electrochemical Society Active Member.

Key words: anodic passivity, ion oxide films, oxidation.

Experimental

A number of oxide specimens were prepared and examined using the combined techniques of reflection high energy electron diffraction (RHEED) and x-ray emission (XRE) analysis. The design and use of this equipment with oxides on metals has been described in several publications from this laboratory (12). In essence, the apparatus allows structural determination using high energy ($\approx$50 kV) electron diffraction and elemental analysis using the x-rays emitted due to bombardment by the high energy beam, or, where particular emphasis is placed on the analysis of light elements such as B or O, the use of a low energy (1800V) beam at right angles to the specimen. The penetration of both the electrons and x-rays is sufficient to allow for accurate total analysis of oxygen, for instance, in an oxide film as thick as several hundred angstroms.

The films to be examined were prepared by direct anodic oxidation of film-free iron in the neutral borate buffer solution, by anodic deposition of γ-FeOOH on platinum from a ferrous ion containing neutral perchlorate solution, and by modification of these deposited films by treatments under vacuum, at elevated temperatures, and by bombardment with the electron beam. The amount of iron in the films could be determined from the current used in their formation and the amount of oxygen corresponding to the various iron oxides could be calculated.

Results and Discussion

The compositions of films formed under various conditions are shown in Table I. The nominal oxide thicknesses were obtained by combinations of cathodic reduction, current used during anodization, and chemical analysis of the films. The thickness depended on the density of the assumed probable compound. Identification of films formed by electropolishing, anodic oxidation of iron, and anodic deposition from perchlorate solutions on platinum was made by electron diffraction. Films deposited from the ferrous-containing borate buffer solution tend to be amorphous.

Examples of films formed by anodic oxidation of iron and by anodic deposition from ferrous ion in solution are shown in Table I. The elemental analyses are those obtained by the x-ray emission technique. In the case of anodically oxidized iron the films were too thin to permit analysis for iron without interference from the underlying metal. Analyses were made for oxygen, iron, and boron on films deposited on platinum.

The oxygen content of the electropolished film corresponds to about 17Å of a mixed anhydrous Fe_3O_4-γFe_2O_3 film. This agrees with numbers obtained by cathodic reduction. The 22Å determined by oxygen analysis on the iron anodically oxidized in neutral

Table I. Anodically formed iron oxide films

Solution	Electropolish $HClO_4 \cdot HA_c$	Borate buffer pH 8.4-300 mV	BB + trace Fe^{++}	BB + Fe^{++}	ClO_4 + pH 8 + Fe^{++}
Substrate	Fe	Fe	Fe	Pt	Pt
Fe $\mu g/cm^2$	—	—	—	3.8	3.0
O	0.25	0.31	0.6	2.3	1.64
B	—	<0.005	0.012	0.31	—
Probable compound	Fe_3O_4-Fe_2O_3	"Fe_3O_4-γFe_2O_3"	"γFe_2O_3" FeOOH $FeOHB_4O_7$	γ-FeOOH $FeOHB_4O_7$ + H_2O	γFeOOH + small H_2O trace
Nominal thickness	17A	22A	?	?	114A

borate for 30 min at +0.3V (*vs.* SCE) is very close to the thickness calculated from the number of coulombs passed during the potentiostatic oxidation based on the formation of a ferric oxide. This would indicate that the amount of water in the film is quite small. If the film was composed of ferrous hydroxide as postulated by some authors (11, 13), the agreement between oxygen content of the film and coulombs passed would be much poorer. In any case the electron diffraction patterns are those of the anhydrous cubic oxide. The accuracy of the oxygen determination does not allow one to rule out completely the presence of a small amount of water or hydrated oxide in these two types of sample. In contrast to these specimens the oxide film formed in the borate buffer containing a trace of Fe^{++} contains both boron and probably hydrogen. For the same time of anodic oxidation at +0.300V the total oxygen is much larger than in the absence of ferrous ion. The extra oxygen, some of it probably as hydroxyl, is due to the deposition reaction, which in the borate buffer results in the formation of an amorphous oxide containing both boron and OH^- ion (3).

The films formed by anodic oxidation and deposition of ferrous ion always contain hydroxyl ion. Two examples of deposited films on platinum are also given in Table I. Both films were formed by anodic deposition from ferrous ion for the same length of time at +0.300V. The one formed in the borate solution was amorphous and contained both boron and more oxygen than would be expected in FeOOH. The one formed in the perchlorate solution gave a diffraction pattern of γ-FeOOH. The atomic Fe/O ratio was close to 1:2, corresponding to γ-FeOOH. Again, the accuracy of the analysis is not sufficient to rule out the presence of a small amount of water with the γ-FeOOH.

The γ-FeOOH films deposited on platinum were treated by pumping under ultrahigh vacuum, electron bombardment equivalent to that used for electron diffraction or x-ray emission measurements and heating, and any changes in oxygen content were measured by the x-ray emission technique. In some previous work (14) cathodic reduction had been used to determine changes in a γ-FeOOH film when heated in a vacuum. The results of the present experiments are shown in Table II. As can be seen, prolonged vacuum treatment (3-4 days) at room temperature and moderate electron bombardment had no measurable effect on the oxygen content. Heating to 300°C converted the γ-FeOOH to γ-Fe_2O_3. This latter identification has been reported previously (14). Heating to higher temperatures led to reduction of the γ-Fe_2O_3 to Fe_3O_4, probably by oxidizable metallic impurities in the platinum.

Table II. Treatment of deposited γ-FeOOH

	As deposited	Vacuum and electron beam	Heated to 300°C	Heated to >425°C
Fe	3.0	3.0	3.0	3.0
O	1.6	1.6	1.35	1.16
Probable compound	γFeOOH	γFeOOH	γFe_2O_3	Fe_3O_4

It has been suggested by a number of authors that electron bombardment during measurement by electron diffraction or Auger analysis can lead to a modification of the film by heating of the specimen (11, 15). Typical currents and voltages used for analyses are shown in Table III. The projected rise in temperature is based on even heating of a 1g sample. As can be seen, the projected rise of temperature of the specimen during XRE or RHEED measurements is 2°C/min, while that for Auger spectroscopy is 14°C/min. The spot size of the beam used in Auger analysis is usually much smaller than for XRE or RHEED, and hence heat dissipation into the sample may be more difficult. This may be partially offset by shorter exposure times for measurements. The 2°C/min for RHEED and XRE agrees quite well with temperature measurements of the specimen using a welded thermocouple which showed a maximum temperature rise of 2°C. This temperature rise is very small and would be insufficient to cause any changes in the oxide or hydrated oxide and disagrees with the supposition of Bockris and co-workers (11) that the anhydrous oxide is formed by degradation of a hydrated film by heating in the electron beam. The high oxygen content of the films they observed by Auger analysis was probably due to a high proportion of deposited film.

Summary

The results obtained showed that iron which is passivated in an iron-free borate buffer solution forms a substantially anhydrous "Fe_3O_4-γFe_2O_3" film. The presence of iron as ferrous ion in the solution leads to the additional formation of a mixed hydrated iron boron oxygen compound which is amorphous. The ferrous ion may be present due to the use of impure solutions or passivation in a stepwise process or with a potentiostat with a long rise time.

Hydrated ferric oxides are not dehydrated by either vacuum treatment or by the electron bombardment used during measurements. Small amounts of water or hydrates may be present in or on the films due to adsorption from the solution. However, this water probably does not play a major role in the protectiveness of the film. Of more importance are the relative amounts and distribution of the anhydrous and deposited hydrated oxides.

Manuscript submitted June 1, 1978; revised manuscript received Oct. 10, 1978.

Any discussion of this paper will appear in a Discussion Section to be published in the December 1979

Table III. Heating effects of electron beam

	Auger spec.	X-ray emission	RHEED
Amps	50×10^{-6}	8×10^{-6}	3×10^{-7}
Volts	2000	1800	50,000
Watts	0.1	0.014	0.015
Cal/min	1.4	0.2	0.21
Temp rise for 1g Fe	14°C/min	2°C/min	2°C/min

1W min-14 cal
Sp Ht of Fe-0.1 cal/gram

JOURNAL. All discussions for the December 1979 Discussion Section should be submitted by Aug. 1, 1979.

Publication costs of this article were assisted by the National Research Council of Canada.

REFERENCES

1. M. Nagayama and M. Cohen, *This Journal*, **109**, 781 (1962).
2. M. Nagayama and M. Cohen, *ibid.*, **110**, 670 (1963).
3. V. Markovac and M. Cohen, *ibid.*, **114**, 678 (1967).
4. J. Kruger and J. P. Calvert, *ibid.*, **114**, 43 (1967).
5. M. Seo, J. B. Lumsden, and R. W. Staehle, *Surf. Sci.*, **42**, 337 (1974).
6. F. C. Ho and J. L. Ord, *This Journal*, **119**, 139 (1972).
7. C. L. Foley, J. Kruger, and C. J. Bechtold, *ibid.*, **114**, 994 (1967).
8. M. C. Bloom and L. Goldenberg, *Corros. Sci.*, **5**, 623 (1965).
9. N. Sato, K. Kudo, and T. Noda, *Electrochim. Acta*, **16**, 1909 (1971).
10. H. Oswin and M. Cohen, *This Journal*, **104**, 9 (1957).
11. R. W. Revie, B. G. Baker, and J. O'M. Bockris, *ibid.*, **122**, 1460 (1975).
12. P. B. Sewell, D. F. Mitchell, and M. Cohen, *Surf. Sci.*, **33**, 535 (1972).
13. I. Epelboin, C. Gabrielli, M. Keddam, and H. Takenouti, *Electrochim. Acta*, **20**, 913 (1975).
14. M. Cohen and K. Hashimoto, *This Journal*, **121**, 42 (1974).
15. G. T. Burstein and T. P. Hoar, *Corros. Sci.*, **17**, 939 (1977).

JOURNAL OF THE ELECTROCHEMICAL SOCIETY

SOLID-STATE SCIENCE AND TECHNOLOGY

MARCH 1979

High Temperature Film Formation on Cobalt-Hardened Gold

J. H. Thomas III*,[1] and S. P. Sharma*

Bell Laboratories, Columbus, Ohio 43212

ABSTRACT

Cobalt-hardened gold electrodeposits have been thermally oxidized under dry oxidation conditions in the temperature range 150°-250°C. Auger depth profiling and ESCA are employed to characterize the surface films as a function of time and temperature. Below 175°C, only CoO is observed, as confirmed by ESCA. Above 175°C, CoO growth is observed to decrease substantially and is qualitatively related to the recrystallization phenomena of the gold deposit. In this same temperature range, potassium evolution becomes significant. ESCA and quantitative Auger indicate that the potassium may be in the form of K_2O. A model was developed using a time-of-arrival approach to characterize potassium film growth. Approximate calculations give a diffusion coefficient for potassium through gold of $\sim 1.2 \times 10^{-14}$ cm^2/sec at 200°C. This process is simply activated and has an energy of 1.25 eV. The source of potassium was speculated to be from possible decomposition of cyanide compounds trapped in voids or inclusions distributed uniformly in the gold deposit.

In a recent paper, the kinetics of cobalt diffusion out of cobalt-hardened gold electroplate was reported (1). In that study, at temperatures above ~150°C, in dry air, Auger electron spectroscopy indicated the presence of potassium on the cobalt oxide film surface. The presence of potassium [~1 atomic percent (a/o)] in electrodeposits of gold is well documented (2-4). Potassium incorporation in gold electrodeposits was first observed by Vasile and Malm (5) by spark source mass spectroscopy. More recently, Davies and Watson (3) extensively studied the effects of plating parameters on the potassium concentration of gold on plated reed relay paddles. Antler (4) has also observed potassium in electrodeposits. Estimates made by Mössbauer spectroscopy indicate that CN in the electrodeposit is not present as gold cyanides but may occur as cobalt cyanides (6). More recently, Okinaka *et al.* have demonstrated that potassium cobalt cyanide complexes exist in gold electrodeposits (7). High temperature heating produces blisters in the gold deposit which appear to be due to the decomposition of the cyanide compounds trapped in inclusions (2, 3, 8).

In this paper, the kinetics of the formation of a very thin potassium layer which forms on the surface of thermally aged (150°-250°C) cobalt-hardened gold has been investigated using Auger electron spectroscopy (AES). Kinetics of the film formation are based on an "average" time of arrival [similar to Hall's (9) analysis]. These results were used to compute an activation energy for the diffusion of potassium out of the electroplated layer. ESCA analysis of the surface film in the 150°-250°C range was performed to determine the chemical state of potassium and cobalt in this layer.

Experimental Details

Film formation and composition were obtained by Auger depth profiling techniques and ESCA (electron spectroscopy for chemical analysis). The spectrometers used were a Physical Electronics Industries Thin Film analyzer and x-ray photoelectron spectrometer equipped with a grazing electron gun. These systems are described in Ref. (10) and ftn.[2]. Auger depth profiles were obtained on the thin film analyzer using a rastered ion gun having a gold sputter rate of 16.1 Å/min in an argon atmosphere at 5×10^{-5} Torr pressure. Auger spectra were obtained at a beam energy of 3 kV at 1.8 mA emission current. The ESCA system consists of a magnesium K_α x-ray source, double pass CMA, and related electronics. The grazing angle electron gun, when used, was operated at a beam potential of 2 kV and 1.7 mA emission current. ESCA data were obtained at pass energies of 200 and 25 eV[10] and were referenced to the Au $4f_{7/2}$ line at 84 eV

Samples were obtained from a strip of spring material (CDA-725 copper alloy) electroplated from an Englehard proprietary phosphate bath with nominally 7.3 μm of cobalt-hardened gold. Electroplating was performed in a production plating system. The strip was processed by initially depositing ~2.5 μm of nickel followed by a gold flash. Hard gold was then plated to the desired thickness. The electrodeposited gold film was analyzed to consist of ~1 a/o Co by atomic absorption spectroscopy.

Samples were cleaned by vapor degreasing and were subsequently rinsed in boiling 10% H_2O_2 solution to remove organics from the gold surface prior to thermal aging. Thermal aging was performed at 150°, 175°, 200°, 225°, and 250°C for 2, 8, 24, and 48 hr. Some samples were also pulled at 36 hr. One sample was measured at

* Electrochemical Society Active Member.

[1] Present address: RCA David Sarnoff Research Center, Princeton, New Jersey 08540.

Key words: electrodeposition, oxidation, crystallization.

[2] Physical Electronics Industries, Scanning Auger Microscope, Eden Prairie, Minnesota.

each temperature and time. All aging was done in thermally stabilized ovens in laboratory air and samples were stored in a dessicator until measurements were made.

Results

AES spectra (0-1000 eV kinetic energy) for the 48 hr samples are shown in Fig. 1. These data demonstrate the changes observed in the AES spectra with thermal exposure. Measurements were performed on the thin film analyzer. Surface concentrations computed from standard sensitivity factors (11) are summarized in Table I for all times and temperatures. The signals observed vary with time and temperature, however, at 150°C, typical spectra include carbon, oxygen, chlorine, nitrogen, and cobalt with little evidence of potassium. Above 175°C for 36 hr, potassium is observed along with the other elements. It is believed that the chlorine signal arises from the cleaning procedure. At higher temperatures, copper and nickel are observed on the surface. These elements are due to the diffusion of the nickel underplate and the copper substrate material to the surface. Diffusion of these species have been studied in detail (12, 13). Inspection of the AES data indicates an increasing potassium signal with time and temperature. The chlorine and carbon signals decrease in amplitude with an increase in potassium concentration. Traces of sulfur are observed at the higher temperatures (225° and 250°C). Below 250°C, the primary surface film is composed of cobalt, potassium, and oxygen as observed earlier.

Table I. Quantitative surface analysis of aged hard gold

Temperature (°C)	Time (hr)	Element atom concentration (%) Co	O	C	Cl	S	K	Cu
150	8	14	9	43	34	—	—	—
	24	23	35	18	23	—	—	—
	48	18	19	19	44	—	—	—
175	2	24	43	22	8	—	3	—
	8	23	24	20	33	—	—	—
	24	23	57	7	12	—	—	—
	48	31	50	6	1	—	12	—
200	2	27	32	28	13	—	—	—
	8	23	35	19	12	—	11	—
	24	19	35	10	2	—	34	—
	48	14	33	6	2	—	40	6
225	2	29	38	20	13	—	—	—
	8	25	42	7	—	—	27	—
	24	17	40	2	—	—	39	3
	48	20	38	12	—	—	23	7
250	6	15	30	10	—	8	36	N/C
	24	8	22	24	—	5	40	N/C

N/C = not included in computation.

Auger depth profiling has been used to study the evolution of potassium with thermal aging. The depth profiles are shown in Fig. 2 for 175°C/48 hr and 225°C/48 hr. Typically, the cobalt oxide depth profile is observed to be predominant (1, 14). Potassium appears to be localized to the surface of the oxide film at the lower temperatures (<225°C). At 225°C/48 hr, the potassium appears to be peaked at the oxide sur-

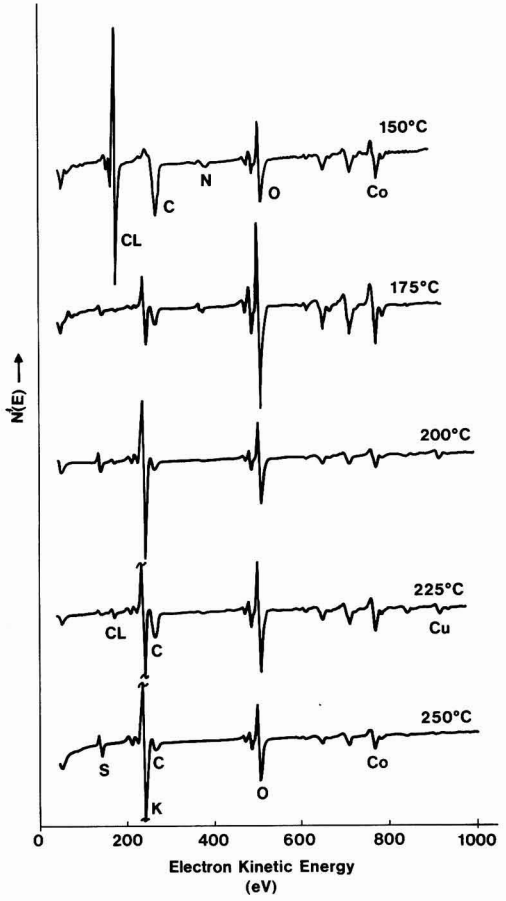


Fig. 1. Auger spectra are shown for 150°, 175°, 200°, 225°, and 250°C cobalt-hardened gold for 48 hr in a dry atmosphere.

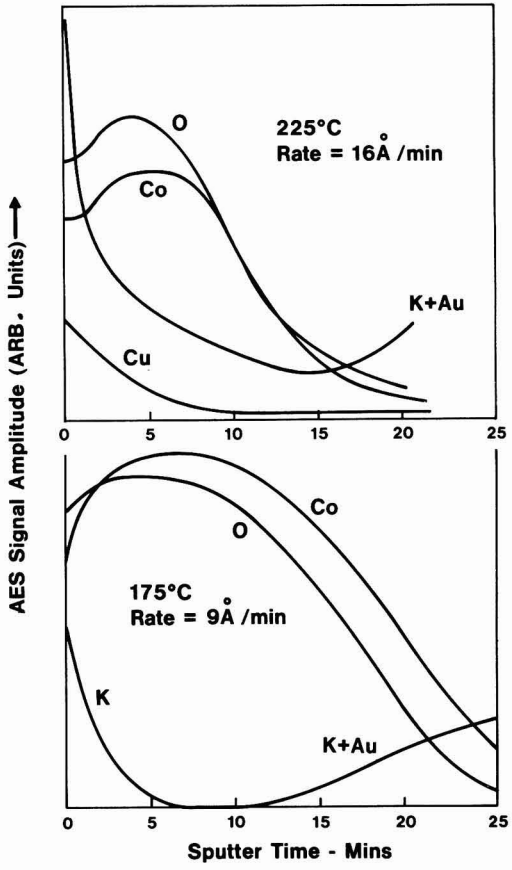


Fig. 2. Typical Auger depth profiles are shown for 175° and 225°C for 48 hr.

face and slowly decreases in magnitude through the oxide layer, indicating what appears to be a finite concentration of potassium in the oxide. This is discussed later.

Before looking at the potassium, the cobalt oxide film thickness was determined by measuring the sputter time required to reduce the cobalt Auger signal to half its peak amplitude. Cobalt diffusion out of the hard gold electroplate was studied in detail and reported in Ref. (1). In the previous paper, it was noted that the oxide film growth appeared to stop after a short time at high temperatures. By plotting the oxide film thickness as a function of thermal aging time, as shown in Fig. 3, it is clearly observed that the oxide forms rapidly on the gold surface at 200° and 225°C. No appreciable growth is observed after 24 hr at each temperature. These phenomena are discussed later.

Potassium evolution from the hard gold film can be characterized in two ways. First, one can simply use the depth profiles to measure the relative "film thickness" of the potassium layer. If the Auger potassium half-intensity point is used, film thickness can only be approximated since the interaction of the other surface species tends to perturb the peak Auger signal amplitude. For this reason, direct film thickness measurements were not made. A second approach, involving the measurement of the quantity of potassium evolved, can be used to characterize potassium evolution. The potassium peak amplitude at the surface is first normalized to the peak cobalt signal amplitude in the oxide film. In turn, this amplitude is normalized to the low energy gold Auger amplitude on the sputter-cleaned surface, providing a secondary standard if it is assumed that the cobalt oxide on each sample is similar in composition. With this information, the area under the normalized potassium profile was obtained. This is proportional to the volume of potassium evolved. The resulting amount of potassium (in arbitrary units) is plotted as a function of aging time with temperature as a parameter in Fig. 4. Detectable amounts of potassium are not evolved below 175°C, as mentioned earlier. Potassium evolved rapidly at 200° and 225°C, however, statistical data were not obtained and consequently, the curvature at 225°C may not be of physical importance. These data can be used to help characterize the physical process involved in potassium evolution.

If the potassium which is observed on the surface is assumed to come from "inclusions" of K-CN compounds randomly distributed throughout the gold electrodeposit thickness (3), then a semiquantitative model can be developed to determine an average diffusion constant for potassium in gold, and consequently can be used to determine the activation energy for the diffusion process. This approach is similar to Hall and Morabito's (9) time of arrival analyses for determining the diffusion coefficients of a species through gold deposits.

Assume that the evolved potassium reacts upon arrival at the oxide surface which we assume requires τ sec to occur, that is, an infinite sink exists at the surface at $x = L$. Potassium diffuses in the gold with a diffusion coefficient, D. From Carslaw and Jaeger (15), the concentration profile of the potassium in gold (with appropriate boundary conditions) is

$$C_K(x,t) = 4C_{ko} \sum_{n=0}^{\infty} \frac{(-1)^n}{(2n+1)\pi} \cos\frac{(2n+1)\pi x}{2L} \exp - \left[\frac{(2n+1)^2\pi^2 Dt}{4L^2}\right] \quad [1]$$

where C_K is the potassium atom concentration at (x,t) and C_{k_0} is the "initial" potassium concentration in the gold. The quantity of potassium which appears at the surface is given by

$$Q = LNC_{ko} \int_0^t D \frac{\partial C_K}{\partial x}\Bigg|_{x=L} dt \quad [2]$$

where N is the density of sites (per cubic centimeter)

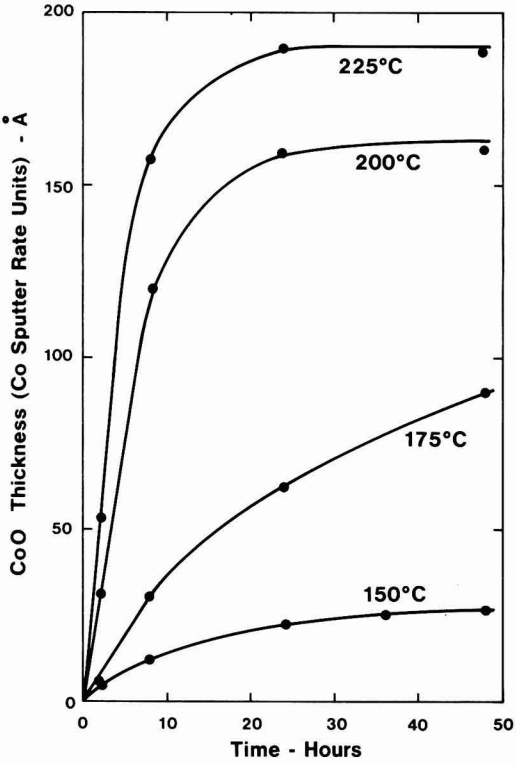


Fig. 3. Cobalt oxide thickness is shown as a function of time with temperature as a parameter. Thickness is derived from the gold sputter rate corrected to that of cobalt metal [Ref. (1)].

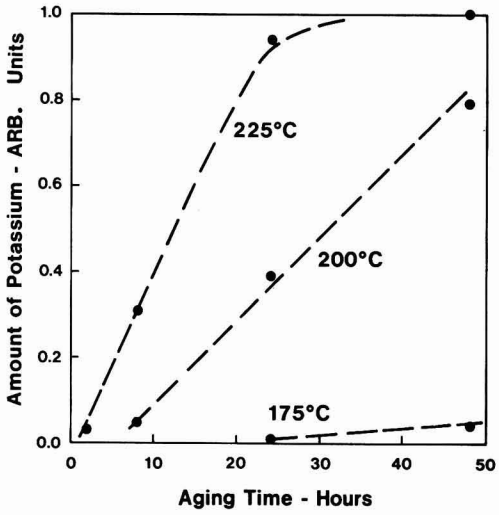


Fig. 4. The "amount" of potassium which evolves on the gold is plotted as a function of time with temperature as a parameter. The "amount," in arbitrary units, is obtained from the normalized area under the potassium depth profile.

and Q is in atoms/cm². For short times, the above integral can be approximated by

$$Q = LNC_{ko}\sqrt{\frac{4Dt}{\pi L^2}} \quad [3]$$

This solution is in fact the exact solution for a semi-infinite layer.

Following Hall and Morabito (9), it is assumed that potassium will be diluted by a factor, A, which is chosen proportional to the ratio of the planar projected inclusion area per unit surface area. This is reasonable if potassium diffuses from an inclusion to the surface by a "straight line" path. A barely detectable amount of surface atoms/cm² **F**, by Auger is

$$\mathbf{F} = AQ \quad [4]$$

Rewriting this

$$\sqrt{\frac{D\tau}{\pi}} = \frac{\mathbf{F}}{2ANC_{ko}} \quad [5]$$

where τ is the time-of-arrival of potassium on the surface. We choose $\mathbf{F} = 5$ a/o (an arbitrary concentration detectability[3] corresponding to ~1 monolayer) × 10Å (escape depth) × N as per Hall and Morabito. A, obtained by multiplying the surface inclusion density 1.14×10^{11}/cm² [from Ref. (16)] by the area of an average inclusion [50Å diam, Ref. (16)], is simply 0.023. C_{ko} is assumed to be equal to 1 a/o. Equation [5] can then be evaluated giving the following expression for the diffusion coefficient, D, for potassium in gold. The above analysis is only an order of magnitude approximation. Thus

$$D = \frac{3.3 \times 10^{-10}}{\tau} \text{ cm}^2/\text{sec} \quad [6]$$

where τ is the "time-of-arrival" for potassium.

It is significant that values of D are inversely proportional to the "time-of-arrival" for the potassium on the CoO surface independent of the choice of constants. Therefore, the relative values of D should be accurate within the limitations of the model. From a knowledge of the time at which potassium is detectable by Auger, we can approximate the value of D. If D is a simple activated process, the activation energy can be computed using an Arrhenius plot. With 5% as an arbitrary detectability limit, the times (from Fig. 4) are used to calculate the diffusion coefficient as a function of temperature. Diffusion coefficients are listed in Table II. These data are plotted on an Arrhenius plot in Fig. 5. Data presented in Fig. 5 show that D in this case is simply activated and the slope of this curve gives an activation energy of 1.25 eV for the diffusion of potassium to the surface of the gold.

ESCA Analysis

The samples aged at 250°C were studied with ESCA to determine the chemical state of the potassium found on the surface of the cobalt oxide. Over-all ESCA spectra are shown in Fig. 6 for a sample aged for 6 hr. Photoelectron lines are observed for K, N, O, C, Cu, Co, and Cl. At the same temperature, Cu increases and Ni and S appear in small concentrations. The insets on Fig. 6 show C, K, Co, and O. Line positions referenced to the Au $4f_{7/2}$ line at 84 eV are summarized in Table III.

The potassium $2p_{3/2}$ line occurs at 293.1 eV which corresponds to its ionized state, that is, K^{+1} according to the Vannerberg data (17). The cobalt $2p_{3/2}$ line occurs at 780.3 eV with a weak satellite at ~786 eV. Other investigations (14, 18) have shown this structure and position of the $2p_{3/2}$ line to correspond to either CoO or CoOOH (19). Two distinct oxygen lines are observed at 529.5 and 531.0 eV. According to

[3] This should not be confused with the bulk concentration which is defined as C_{ko} in Eq. [5].

Table II. Potassium diffusion coefficients in electroplated gold

Temperature (°C)	Time (sec) to (5 a/o K)	Diffusion coefficient (cm²/sec)
175	1.73×10^5	1.9×10^{-15}
200	2.88×10^4	1.15×10^{-14}
225	7.2×10^3	4.58×10^{-14}

McIntyre and Cook (19), the cobalt oxide oxygen line occurs at 529.6 eV and the Co $2p_{3/2}$ line has a FWHM of 2.7 eV. Our data shows that the Co $2p_{3/2}$ line has a FWHM of ~3 eV as compared with Co in CoOOH which has a FWHM of 1.8 eV. Therefore, it appears that the 529.5 eV O 1s line is due to the presence of

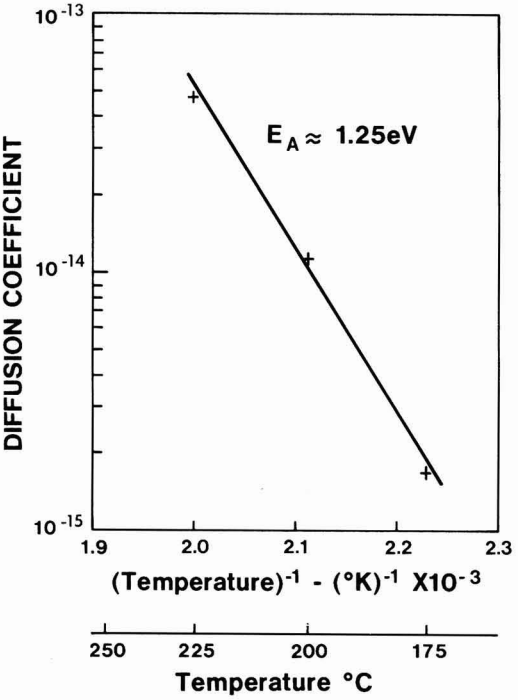


Fig. 5. The approximated diffusion coefficient for potassium in gold is plotted on an Arrhenius plot. The activation energy for this process is 1.25 eV.

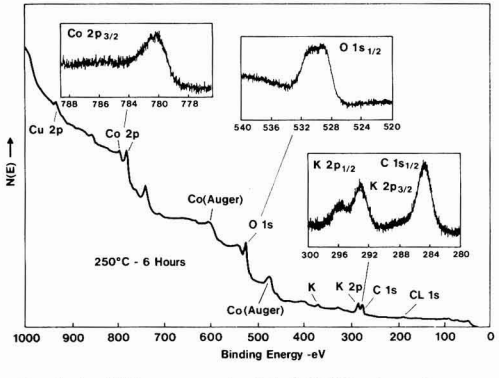


Fig. 6. An ESCA spectrum for 6 hr/250°C is shown. Insets are high resolution spectra for the Co $2p_{3/2}$, K $2p_{1/2,3/2}$, C $1s_{1/2}$, and O $1s_{1/2}$ lines.

Table III. ESCA line positions
(Ref. Au $4f_{7/2}$ at 84.0 eV)

Temperature (°C)	Time (hr)	Element (state)	Binding energy (eV)
250	6	Co $2p_{3/2}$	780.3
		O $1s_{1/2}$	529.5, 531.0
		K $2p_{3/2}$	293.1
		S 2p (Tr.)	~169 ± 0.5
		C $1s_{1/2}$	284.5

CoO. Reviewing the quantitative Auger data, we observe that the amount of Co on the immediate surface is small and the predominant species at 250°C are potassium and oxygen (about 66% of the surface composition). One should be cautious when comparing AES and ESCA signal amplitudes because of the difference in escape depths. From quantitative Auger data shown in Table I, the stoichiometric ratio of K to O is ~0.5. Subtracting out the contribution due to CoO, K_2O appears to be the surface specie, ignoring carbon, which is probably unrelated surface contamination. In Haber's study (20), the O 1s binding energy was shown to be a function of the cation oxidation state with the O 1s line in $M_2^{+1}O$ occurring near 531 eV. Thus, the oxygen line at 531 eV is probably due to the existence of K_2O on the surface, not including the possibility of CoOOH. Furthermore, from the Auger data and supporting ESCA data, namely the FWHM and positional data, it is unlikely that CoOOH is the cobalt compound but rather a simple oxide of Co^{+2}. The low amplitude of the cobalt satellite at 786 eV may indicate a more complex oxide involving cobalt. Sulfur is in the +6 state at 169 ± 1 eV as observed in Ref. (14). The data presented in Ref. (14) support the conclusions of this study if the line positions are suitably referenced.

Summary

In this study, surface analysis has shown the film to consist of cobalt oxide and potassium oxide (K_2O) type of compounds in relatively thin layers. Referenced to the gold sputter rate, the maximum potassium film thickness is approximated at ~50Å as compared with the maximum CoO thickness of ~200Å.

Cobalt oxide film formation above 175°C occurs rapidly with time and reaches a plateau region (150-200Å thickness) where film growth, within experimental error, stops at 200° and 225°C for further oxidation times, as shown in Fig. 3. At lower temperatures, the plateau region is not attained within the times for which the experiment was performed. Earlier data, presented in Ref. (1), show a similar phenomenon. Raub *et al.* (8) show in a recent paper that between 150° and 300°C, the properties of gold electroplates undergo an irreversible change. Cobalt evolution and subsequent oxidation at temperatures ranging from 100° to 250°C appear to be qualitatively related to the known recrystallization process which occurs throughout this temperature range. Kinetic growth data suggests that the reduction in grain boundary area, which acts as sites for cobalt incorporation in the gold, controls the amount of cobalt contained in the gold electrodeposit. When the grain boundary area ceases to change, CoO film growth would be controlled by the much slower process of bulk cobalt diffusion in the gold.

Potassium evolution and subsequent oxidation to what appears to be K_2O is correlated with the possible decomposition of potassium-gold-cyanide compounds trapped in voids in the deposit (22). Potassium evolved from this process diffuses from the voids through the gold with a diffusion coefficient of 1.15×10^{-14} cm²/sec at 200°C and an activation energy of 1.25 eV. These numbers were derived from a crude model based on a time-of-arrival approach assuming voids uniformly distributed throughout the deposit (9). Potassium evolution on the surface may be a precursor to the more dramatic effects, *e.g.*, blistering, observed at higher temperatures. Since the potassium is not uniformly distributed on the Au surface and the film forms on the CoO surface, it is reasonable to assume that it proceeds from discontinuities in the CoO and Au film to the surface rather than through bulk of the CoO.

Surface analysis of films formed under dry oxidation conditions shows that initially CoO is formed between 100° and 225°C [comparing data presented in this study with those presented in Ref. (1)]. Above 175°C in the range of recrystallization, what appears to be K_2O is observed on the CoO surface. Quantitative AES and ESCA data are supportive of this conclusion. Also, surface analysis shows that potassium is not uniformly distributed over the gold surface.

Acknowledgments

The authors wish to thank L. L. Hines for sample preparation and E. T. Eisenmann for his useful discussions.

Manuscript submitted May 15, 1978; revised manuscript received Sept. 30, 1978.

Any discussion of this paper will appear in a Discussion Section to be published in the December 1979 JOURNAL. All discussions for the December 1979 Discussion Section should be submitted by Feb. 1, 1979.

Publication costs of this article were assisted by Bell Laboratories.

REFERENCES

1. J. H. Thomas III, *This Journal*, **125**, 898 (1978).
2. Ch. J. Raub, A. Knodler, and J. Lendvay, *Plating Surf. Finish.*, **63**, 35 (1976).
3. T. A. Davies and P. Watson, *Plating (East Orange, N.J.)*, **60**, 1139 (1973).
4. M. Antler, *ibid.*, **60**, 468 (1973).
5. M. J. Vasile and D. L. Malm, *Anal. Chem.*, **44**, 650 (1972).
6. R. L. Cohen, K. W. West, and M. Antler, *This Journal*, **124**, 342 (1977).
7. Y. Okinaka, F. B. Koch, C. Wolowodiuk, and D. R. Blessington, Paper to be submitted to *This Journal*.
8. Ch. J. Raub, H. R. Khan, and J. Lendvay, *Gold Bull.*, **9**, 123 (1976).
9. P. M. Hall and J. M. Morabito, *Surf. Sci.*, **59**, 624 (1976).
10. P. W. Palmberg, *J. Vac. Sci. Technol.*, **13**, 214 (1976).
11. L. E. Davis, N. C. MacDonald, P. W. Palmberg, G. E. Raich, and R. E. Weber, "Handbook of Auger Electron Spectroscopy," Physical Electronics Industries, Inc., Eden Prairie, Minn. (1976).
12. P. M. Hall and J. M. Morabito, *Surf. Sci.*, **54**, 79 (1976).
13. H. G. Tompkins and M. R. Pinnel, *J. Appl. Phys.*, **48**, 3144 (1977).
14. J. H. Thomas III, *IEEE Trans. Parts, Hybrids, Packag.*, **PHP-12**, 255 (1976).
15. H. S. Carslaw and J. C. Jaeger, "Conduction of Heat in Solids," Oxford Univ. Press, London (1959).
16. R. S. Sanwald, *Metallography*, **4**, 503 (1971).
17. N. G. Vannerberg, *Chem. Scr.* **9**, 122 (1976), also L. G. Peterson and S. E. Karlsson, *Phys. Scr.*, **16**, 425 (1977).
18. T. J. Chuang, C. R. Brundle, and D. W. Rice, *Surf. Sci.*, **59**, 413 (1976).
19. N. S. McIntyre and M. G. Cook, *Anal. Chem.*, **47**, 2208 (1975).
20. J. Haber, J. Stoch, and L. Ungier, *J. Electron. Spectr.*, **9**, 459 (1976).
21. E. T. Eisenmann, *This Journal*, **124**, 1957 (1977).

In Situ Surface Analysis of the Vapor Phase Epitaxy of GaAs

J. B. Theeten and F. Hottier

Laboratoires d'Electronique et de Physique Appliquée, 94450 Limeil-Brevannes, France

ABSTRACT

The growth mechanisms of {001}, {111}Ga, and {111}As GaAs epitaxial layers are investigated by associating surface analysis techniques (ellipsometry, LEED, RHEED, and AES) with a conventional vapor phase epitaxy reactor using the GaAs-$AsCl_3$-H_2 system. The surface behavior at each step of the growth procedure (*i.e.*, the effect of the temperature, of the etching procedure, of the H_2 flow) is first examined. A semiquantitative assessment of the stable state of growth is then given and the adsorption of GaCl during growth is examined for the three substrate orientations. The results are in good agreement with the growth models based upon rate processes theory which have been proposed by Cadoret.

The vapor phase epitaxy (VPE) of gallium arsenide in the GaAs-$AsCl_3$-H_2 system is based on the following chemical equilibrium

$$GaAs + HCl \leftrightarrows GaCl + \tfrac{1}{4}\,As_4 + \tfrac{1}{2}\,H_2$$

HCl is used as a carrier agent for transferring GaAs from a solid source to a deposit. The difference in temperature between the source and the deposit is the driving force of the reaction. In contrast with the arsenic species, the gallium cannot be transported directly in its vapor form and one has to use GaCl, a more volatile gallium compound. Nevertheless, this compound remains stable at the temperature (typically 750°C) of the epitaxy. The surface of the epitaxial layer will, therefore, have to play a catalytic role in the reduction of a gallium monochloride molecule into a gallium atom able to be incorporated into the epitaxial layer. The importance of the surface has long been recognized and extensively studied from a macroscopic viewpoint (1, 2). A striking consequence of this predominant role of the surface is the strong anisotropy (1, 2) of the rate of growth as a function of the substrate crystalline orientation (up to a factor of 100 between {111}As and {111}Ga).

An investigation of the surface of an epitaxial layer at the atomic scale and during growth seemed then of paramount importance for a complete understanding of the growth mechanisms. As an attempt in this direction, we have set up an apparatus and developed a technology (3) for using surface analysis techniques in connection with a conventional VPE reactor. Details of this set up have already been published (3) and only a summary of its features will be given in Experimental. The following section discusses the behavior of the sample from its introduction at room temperature in the VPE reactor up to the moment when a stable state of growth, at 750°C, is reached. This stable state is then described in the next section and a semiquantitative assessment of the GaCl surface coverage during growth is made and compared with the models by Cadoret (4, 5).

Experimental

The chemical part of the setup is a conventional VPE system. The reaction occurs in a quartz tube where a hydrogen flow at atmospheric pressure carries the epitaxy species—HCl obtained from the decomposition of $AsCl_3$, GaCl, As_4, and As_2—from a GaAs source ($T_{source} \simeq 800$°C) to the GaAs sample ($T_{deposit} \simeq 750$°C). The temperatures are obtained with the help of a two-zone electrical furnace. Two small holes (ϕ 2 mm) have been opened in the furnace for the in-going and out-going beams of an ellipsometer. Indeed, the photon is the only possible surface probe during the epitaxial process. Furthermore, in optimum cases, 1% of a B monolayer adsorbed on an A substrate can be detected by the ellipsometry. The method is non-destructive and the use of an on-line computer makes it adequate to study fast phenomenas such as temperature effects, etching procedure, and quenching of the epitaxy.

Key words: epitaxy, surface analysis, etching.

A schematic view of our fast automatic ellipsometer is given in Fig. 1. The in-going part of the beam consists of the following sequence: a high pressure mercury lamp at the focus of a lens producing a parallel beam limited to 1 mm diam by a diaphragm, a rotating polarizer, a quarter wave plate with its slow axis at 45° from the plane of incidence. The beam then crosses the quartz tube (40 mm diam) at normal incidence and reaches the sample with an angle of incidence of 72° (for an optimum sensitivity, this angle must be in the vicinity of the Brewster angle, typically 76° for GaAs at 2 eV). The reflected beam crosses the quartz tube again at normal incidence. The state of polarization is then analyzed by a polarizer with its axis at 45° from the plane of incidence. The resulting light is measured by a photomultiplier with a 5461Å interference filter mounted on its entrance window. In order to reduce the influence of the ambient light, the reflected beam is calibrated by passing through a 150 mm cylinder closed by two ϕ 5 mm apertures. In such

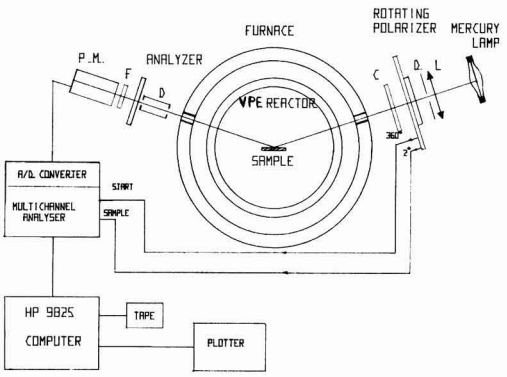


Fig. 1. The fast automatic ellipsometer operates in the rotating polarizer mode at a fixed wavelength (5461Å). The use of an on-line computer associated with a multichannel analyzer allows measurement of the angles Δ and ψ every 3 sec with an accuracy of the order of 0.05° on Δ and 0.01° on ψ.

a configuration, the intensity in the photomultiplier as a function of the angular position P of the rotating polarizer is

$$I_{PM} \propto [1 + \sin 2\psi \sin (2P - \Delta)]$$

where ψ and Δ are the ellipsometric angles of the sample. These angles describe the differences in amplitude and phase between the reflection factors of the surface for a linearly polarized light with its polarization respectively parallel ($R_{||}$) and perpendicular ($R_{\perp}$) to the plane of incidence

$$\frac{R_{||}}{R_{\perp}} = \tan(\psi) \exp(i\Delta)$$

From a practical viewpoint, bulk and surface contribution to Δ and ψ can be distinguished with the following schematic argument: adsorption of a full B monolayer over an A substrate will correspond to $\delta\psi \sim 0.1°$, $\delta\Delta \sim 1°$; large variations in $\psi(\delta\psi \sim 3°)$ are then associated with bulk changes, while a surface effect will contribute only in Δ variations with a nearly constant ψ (6).

The electronic part of the ellipsometer consists of a high precision multichannel analyzer and a desk computer. The signal from the photomultiplier passes through an 8K analog-to-digital converter and is stored in a multichannel analyzer as a function of the angular position of the polarizer (the polarizer is mounted on a wheel with a series of 180 regularly spaced teeth opened on its circumference). A pulse for the address advance input of the multichannel is produced every 2° during the rotation of the polarizer. The signal is first averaged in the multichannel and then transferred to the computer where a Fourier analysis is performed. The angles Δ and ψ are obtained every 3 sec. Standard deviations are of the order of 0.01° on ψ and 0.05° on Δ.

Such a precision of the ellipsometric angles allows the system to detect submonolayer changes on the epitaxial layer occurring in more than 3 sec. In fact, faster phenomena are not expected to occur in our atmospheric pressure VPE reactor because of hydrodynamic limitations in the gas phase. In contrast with its adequate performances in precision and rate of measurement, our ellipsometer is not able to yield absolute values of Δ and ψ. This is primarily because the light has to cross the quartz reactor twice. The geometry of the reactor and the requirements of chemistry and hydrodynamics do not allow the use of special windows. Furthermore, the position of the sample cannot be defined and reproduced very accurately. Slight misalignments are also likely to occur during the epitaxial process, especially when the temperature changes (a typical effect on Δ is discussed later). In all data discussed here, ψ and Δ will always be given on a relative basis.

Although the ellipsometry technique is quite well adapted to the surface analysis of an epitaxial process (*in situ* and in-line method), it it limited to the determination of two independent variables, ψ and Δ, which may contain many distinct contributions such as chemical and structural modifications both at the surface and in the bulk. Other surface analysis techniques are necessary to unambiguously interpret the ellipsometric information. These techniques, namely LEED, RHEED, and AES, cannot be used *in situ* since they use the electron as a probe. A "*quasi in situ*" use of these methods is nevertheless possible by transferring directly (*i.e.*, without any contact with the air) from the VPE reactor to the UHV chamber equipped with the LEED, RHEED, and AES facilities. A schematic view of the setup is given in Fig. 2. The furnace surrounding the sample can be removed in order to quench the epitaxial process. This step of the transfer process is followed with the ellipsometer.

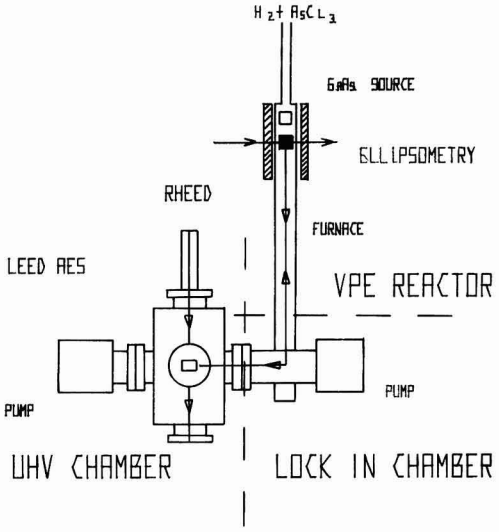


Fig. 2. Schematic view of the setup. The UHV chamber, with LEED, RHEED, and AES facilities, is attached directly to the VPE reactor. Correlation can be made between ellipsometry and electron spectroscopies.

Once the sample has reached a stable state at room temperature and under H_2 flow, it is translated toward a lock-in chamber, pumped down, and introduced into the UHV chamber. After having assessed the structure and chemistry of the surface, the sample is transferred back to its position in the VPE reactor and reexamined with the ellipsometer. A correlation is therefore possible between electron and photon spectroscopies of the surface. Indeed, such a transfer procedure modifies the sample and limitation in the assessment of submonolayer phenomena is discussed later. But such features as steps or surface roughness are not modified and can be meaningfully examined in RHEED. The UHV facilities can also be used as a preparation stage for the sample, *e.g.*, cleaning the sample prior to introduction in the VPE reactor. From this viewpoint, the epitaxy is considered as a surface treatment. Electron examinations prior and after this treatment give an over-all characterization of the epitaxial process.

Evolution of the Sample up to the Stable State of Growth

Temperature effect.—The study of the growth mechanisms implies that stable conditions have been obtained for the temperatures, the partial pressures, and the crystallinity of the layer. In reality, before reaching this ideal stable state of growth, the GaAs sample experiences a number of treatments after its introduction, at room temperature, in the VPE reactor. These treatments induce changes in the crystalline and chemical state of the substrate and determine the final success of an epitaxy. A proper assessment of these treatments is thus necessary.

The sample is first heated up to 750°C in a hydrogen flow and in the presence of a solid GaAs source maintained at 800°C. Before discussing the ellipsometric data, it must be noticed that, even without any modification of the sample, the Δ and ψ angles are temperature dependent since the band structure and therefore the refractive index of GaAs depend on the temperature. When the temperature increases, the energy gap E_g decreases, owing to the lattice expansion, with the following law (7)

$$E_g = E_0 - \frac{\alpha T^2}{T + \beta}$$

with $\alpha = 6.6643\ 10^{-4}$ and $\beta = 344°K$ for GaAs. From the viewpoint of the photon-electron interactions, a decrease in E_g corresponds to an apparent increase of the photons energy. Knowing the relation between the refractive index $\tilde{n}$ as a function of the energy E of the photon, a first approximation of the temperature dependence of $\tilde{n}$ can be determined from the above relation. As an example, when T varies from 25° to 750°C, E_g has a 0.4 eV decrease, and the apparent photon energy of a 5461Å light varies from 2.27 to 2.67 eV. The following equality will hold

$$\tilde{n}(2.27\ \text{eV}, 750°\text{C}) \equiv \tilde{n}(2.67\ \text{eV}, 25°\text{C})$$

In this approximation, one assumes that the optical transitions giving rise to the refractive index concern the same energy bands over the whole range of temperature, as is the case for a 5461Å light between 25° and 800°C. From the knowledge of $n(E)$, as shown in Fig. 3a (8, 9),[1] $n(T)$ can be obtained and therefore so can $\Delta(T)$ and $\psi(T)$, as shown in Fig. 3b. In this crude approximation, ψ varies linearly *vs.* T while Δ remains linearly constant. These behaviors are intrinsic properties of the GaAs material and will have to be subtracted from the experimental temperature dependences for determining the changes in the structure and chemistry of the sample during heat-treatment.

Typical behaviors of ψ upon temperature are shown in Fig. 4. Curves 1, 2, and 3 are successive heatings and coolings of the same GaAs(111)As sample. During the first heating up of the substrate after its introduction in the VPE reactor, an irreversible modification occurs—a decrease of 0.6° associated with the desorption of contaminants—but then a linear depen-

[1] The imaginary part of the refractive index is obtained from absorption measurements.

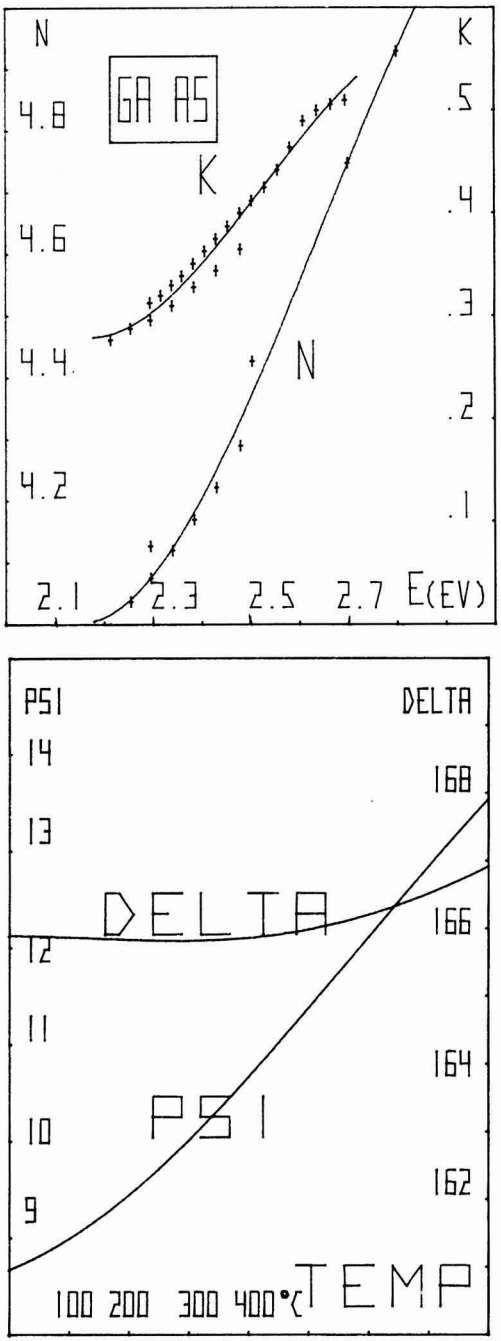


Fig. 3. Approximate evaluation of the thermal dependence of ψ and Δ. a, energy dependence of the refractive index; b, resulting ψ and Δ thermal dependence (see text).

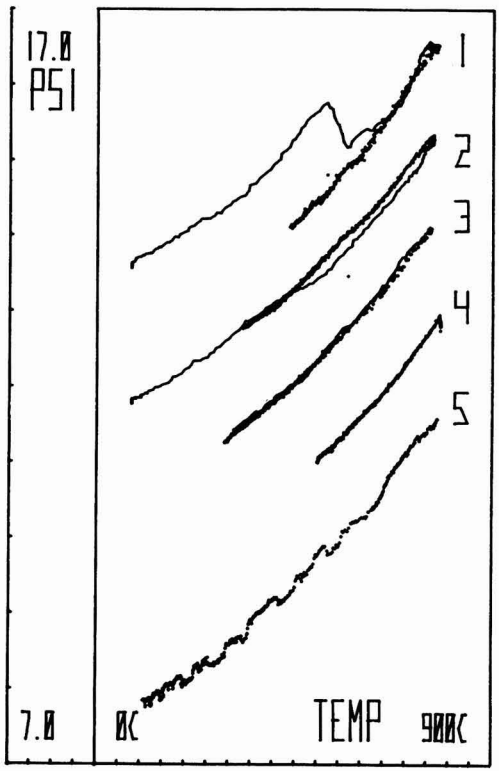
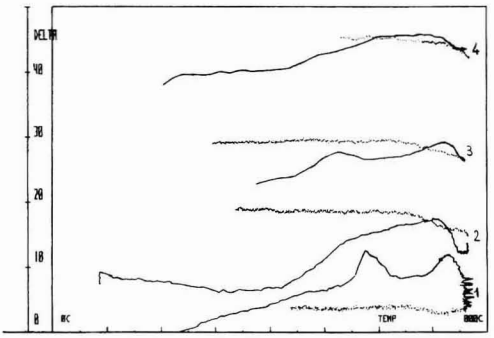


Fig. 4. ψ Evolution as a function of temperature. The full lines correspond to increasing temperatures and the dotted lines to decreasing temperatures. For clarity, the origin has been shifted in ψ for each curve. Curves 1-3 are successive cycles of the same GaAs (111)As sample; curves 4 and 5 are cooling down of an epitaxial layer on GaAs(001).

dence *vs.* T is observed. This linear behavior is reversible, as shown on curve 3, where the increasing T part and decreasing T part are superimposed. This is in good agreement with the model in Fig. 3b, and it demonstrates that a stable state is reached for the substrate. This stable state is not dependent on the substrate orientation since similar behaviors are found for epitaxial layers on GaAs(001) (curves 4 and 5).

The corresponding Δ temperature dependence is shown in Fig. 5a for the same sequence of temperature cycles from curves 1 to 4. In contrast with the ψ behavior, no reversibility is reached in Δ although the difference between increasing T and decreasing T parts tends to cancel, at least in the 500°-800°C range. For the decreasing T part of the curves, Δ is found nearly constant as expected from the model



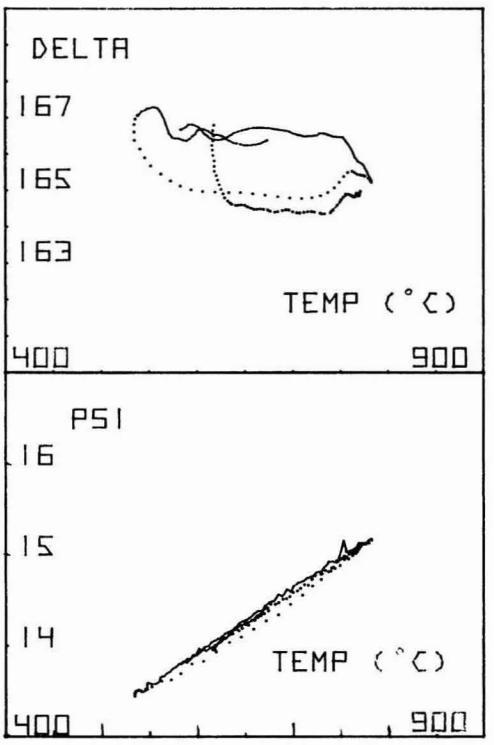


Fig. 5. a, Δ evolution as a function of temperature with the conventions as in Fig. 4. Curves 1-4 are successive cycles of the same GaAs(111)As sample; b, temperature cycles in the 500°-800°C range. The hysteresis in Δ is due to the quartz reactor (see text).

of Fig. 3b. At low temperature, adsorption occurs on the surface which lowers the Δ and makes the increasing T part different. This adsorption is removed above 500°C and the two parts tend to coincide. In fact, during these temperature cycles, another contribution to Δ changes comes from the quartz walls, as demonstrated in Fig. 5b. In this figure, the temperature of the sample (a previously deposited epitaxial layer) is varied up and down in the 500°-800°C range. ψ variations are found linear with T and no difference is seen between up and down parts. On the contrary, Δ oscillates between two levels, the higher for decreasing T and the lower for increasing T. Since the change in Δ between these two levels does not depend on the temperature, this effect cannot be due to the sample itself. This is due, rather, to changes in the temperature of the quartz tube. For increasing the temperature, the furnace is switched on and the quartz walls are heated much more rapidly than the sample. For lowering the temperature, the furnace is switched off and the quartz walls are cooled well before the sample. As mentioned above, the "window" effect (namely 2° variation in Δ) is one of the reasons why only relative measurements are possible. Apart from the low temperature adsorption and the window effect, a stable state of the substrate seems, therefore, to be reached with a behavior *vs.* temperature in good agreement with the model. Finally, as already noticed in the case of silicon (10), the ψ linear dependence in T (typically $\delta\psi = 1°$ for $\delta T = 150°C$) can be used as a rough estimate of the surface temperature.

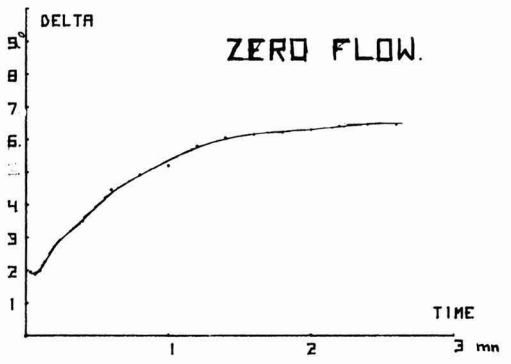
An AES examination of a sample after its heating up in the VPE reactor indicates a carbon contamination (of the order of one monolayer), a chlorine adsorption but no oxygen. LEED and RHEED patterns (1 × 1), structure, and spotty pattern in RHEED indicate a poor crystalline order at the surface. The stable state described here is therefore not associated with a clean and well-ordered GaAs surface.

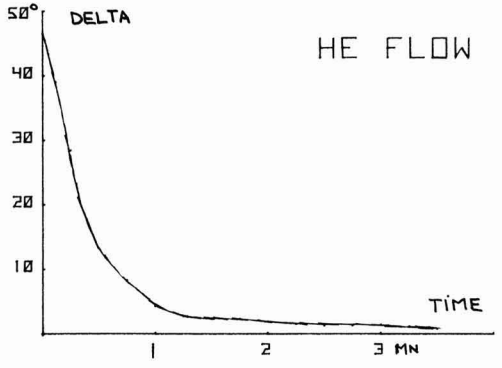
Stabilizing effect of the arsenic pressure.—The existence of such a stable state may look surprising. The GaAs surface is known to be decomposed in an ultrahigh vacuum system above 630°C (11): As_2 evaporates and Ga liquid droplets are produced. This is not the case in the VPE reactor, despite the markedly higher temperatures. Indeed, this apparent stability is due to the presence of a solid GaAs source in the VPE reactor at a still higher temperature. This source produces enough arsenic partial pressure to prevent the surface decomposition. If the sample is kept at 750°C while the source is cooled down, ψ begins to irreversibly change after a few minutes. Optical microscopy of the sample confirms the presence of Ga droplets.

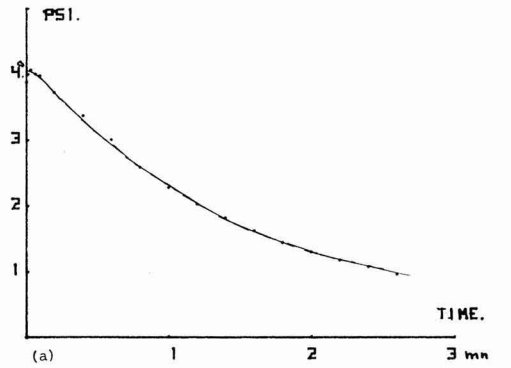
Another manifestation of the stabilizing effect of the arsenic pressure has been evidenced when cooling the substrate. The ψ and Δ evolutions are compared during the decrease of temperature for the two following conditions.

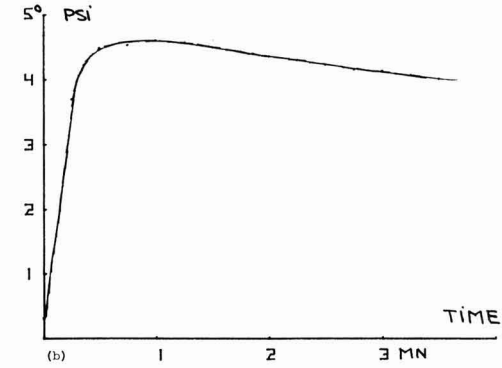
At the time $t = 0$, all the flow is stopped, the furnace is removed, and the sample cools down to the ambient temperature; ψ decays exponentially *vs.* time (Fig. 6a) (*i.e.*, linearly *vs.* T considering the cooling procedure), as is expected when there is no modifications of the substrate. By leaving a static pressure of H_2, just above the sample, this condition does not disturb the sample because a sufficient partial pressure of arsenic remains inside the reactor to stabilize the surface until its temperature is lower than 630°C (maximum temperature in UHV conditions).

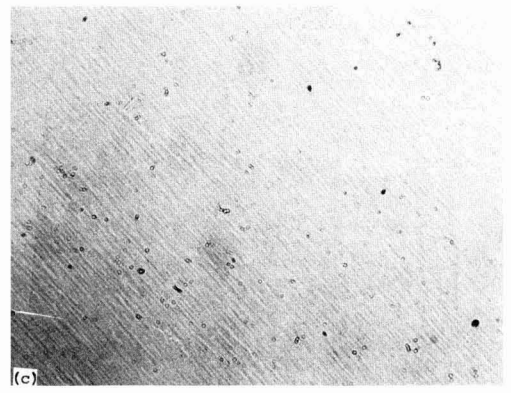
In the second condition, instead of stopping the flow, a high He flow is sent directly to the sample at $t = 0$ to cool it in a neutral gas. In that case ψ and Δ are rapidly and irreversibly modified (Fig. 6b) and Ga droplets become visible on the surface (Fig. 6d). The same experiment can be made with a high H_2 flow and an identical behavior is observed. This high flow (H_2 or He) removes the arsenic from above the sample and, when the temperature is higher than











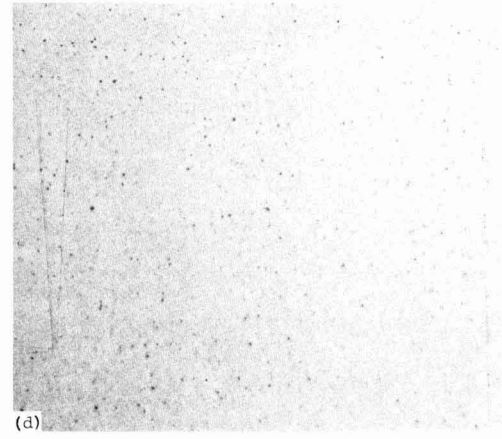


Fig. 6. Comparative Δ and ψ behaviors in a decreasing temperature step for two conditions: a, static H_2 flow; b, high He flow. The optical micrographs in the two conditions are given in c and d, respectively. The black spots in d are Ga droplets of 1 μm diam.

630°C, there is a fast evaporation of As from the surface which is no longer equilibrated with the vapor phase.

Role of the defects and contaminants.—The importance of starting the growth with a clean and well-ordered surface is clearly evidenced when comparing, in the following experiments, the evolutions of ψ and Δ for two types of sample:

Type I.—GaAs(001) sample from the atmosphere after a mechanochemical polishing which still leaves a strained layer near the surface (Fig. 7).

Type II.—Epitaxial layer on a GaAs(001) substrate deliberately reintroduced in the atmosphere for a few hours; there is a contamination layer on the surface but the epilayer is free of strain.

For the type I samples, large modifications (Fig. 7a) occur during the temperature increase. Minor desorptions (decrease in ψ associated with an increase in Δ) occur in the initial stage ($25° < T < 650°C$) and correspond to the removal of the adsorbed oxide layer. Above 650°C, two phenomena are superimposed, as seen in Fig. 7b: (*i*) an increase in ψ with a decrease in Δ, indicating the formation of a superficial layer with increasing thickness (this effect is low and tends to stop after a few minutes at 750°C); (*ii*) a sudden decay in ψ above 700°C probably due to an annealing

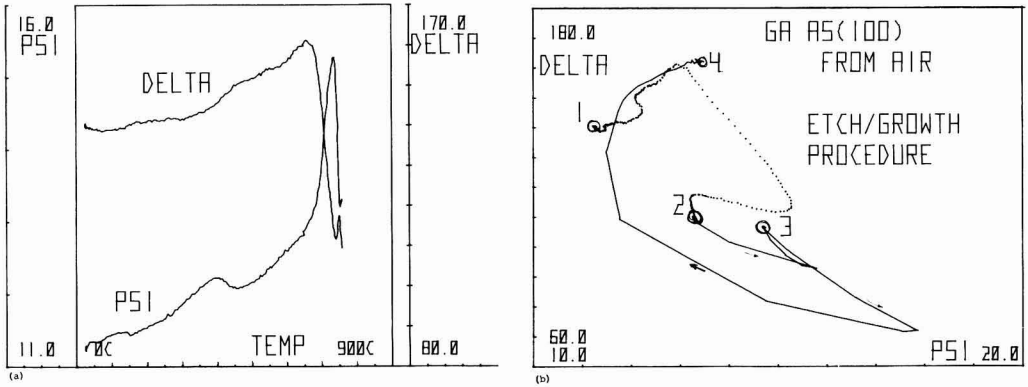


Fig. 7. Ellipsometric assessment of a GaAs(001) surface just introduced in the VPE reactor after being polished (without any heating in a reactor). a, effect of the heating step on ψ and Δ; b, effect of the etch/growth step in the (Δ, ψ) plane. The substrate is heated (between points 1 and 2), etched (between 2 and 3), and the growth starts at the point 3.

of the surface defects. This type of behavior is found reproducible and takes approximately 1000 sec in our system to reach a stable state. For a shorter period of heating up, intermediate points are reached on the line of Fig. 7b. For type II samples, the minor desorptions below 650°C are also observed. This confirms the role of the early stage of heating in removing the atmospheric contaminants. But above 650°C, ψ varies linearly and reversibly *vs.* T while Δ is nearly constant. A major difference in the surface of type I and type II samples must therefore exist.

This difference is clearly evidenced by the *in situ* etching procedure (by the use of an HCl flow). Violent reactions to the etching agent are observed on type I samples (Fig. 7b). Within a few seconds, ψ increases a number of degrees and decreases again. If the epitaxial growth starts at this moment (point 3 of Fig. 7b) by commuting the HCl flow on the source, ψ increases again quickly and then turns back more slowly up to a stable state after a few minutes (point 4 of Fig. 7b). With respect to the previous stable state under H_2 (point 2 of Fig. 7b), the modifications in ψ and Δ are $\delta\psi \simeq 0°$ and $\delta\Delta \simeq +50°$. The net effect of the etching + growth procedure can thus be described as the removal of a superficial layer (150Å typical in thickness) from a clean and well-ordered GaAs (001) surface, this effective layer corresponding to the carbon contamination and the defects. This is not at all the case for a type II sample (Fig. 8b). In a sequence of etching and growth conditions, the (ψ, Δ) point seems to move from point 2 to point 3 of Fig. 8b, both parts being close to point 1, the stable state in H_2. Only for a long etching period of the epitaxial layer, the (ψ, Δ) gradually moves to point 4 in a similar way as in Fig. 7b, only more slowly. Stopping the etching stops this movement and point 5 is the new stable state. Restarting the growth causes the (ψ, Δ) point to go back to point 6, again close to point 1.

Comparing Fig. 7b and 8b leads us to propose the following interpretation: type I and II samples are different in the number of defects present at the surface. On a polished sample, strains due to polishing are not completely removed by the heating up to 750°C and become preferential sites during the etch. Etch pits are thus formed and the surface roughness increases very rapidly with a corresponding ψ increase. When the pits are large enough to touch one another, the roughness tends to diminish. At the start of growth the high index planes revealed by the pits grow more rapidly than the (001) parts and the roughness restarts to increase and then decreases when the (001) terraces, of lower growth rate, dominate. The surface then comes back to a similarly low roughness as for the stable state in H_2 ($\delta\psi = 0°$). A RHEED examination (3) of the surface of a sample transferred at point 1, 2, or 3 of Fig. 7b confirms the role of the etching procedure by increasing the roughness. In the case of an epitaxial layer, the number of defects at the surface is markedly lower and etch pits are not induced by etching. However, a long etching time re-

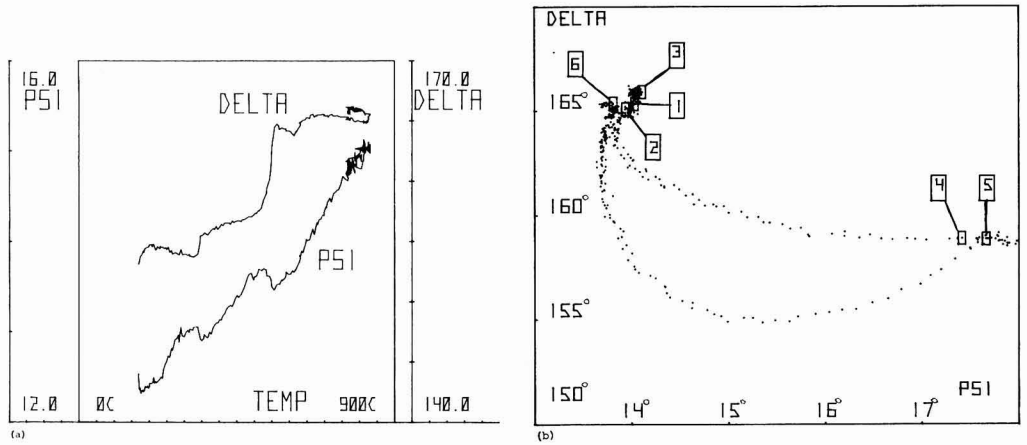


Fig. 8. Similar assessment as in Fig. 7 for a GaAs (001) epitaxial layer intentionally reintroduced into the atmosphere (see text).

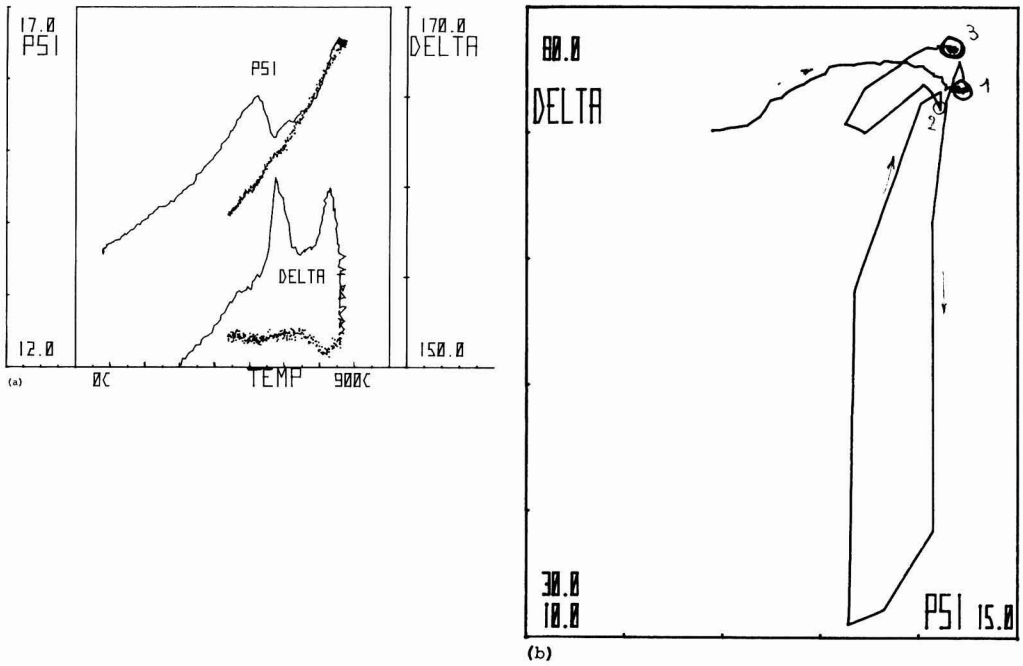


Fig. 9. a, effect of the temperature on a GaAs (111)As sample just introduced in the VPE reactor after being polished; b, effect of the etch/growth step on the same sample. The etching step is between 1 and 2 and the growth starts at the point 2; a stable state of growth is reached at 4.

moves the epitaxial layer and the defects of the underlying substrate finally turn into etch pits.

Similar results are obtained for the (111)As orientation; two types of sample have been used:

Type III.—GaAs (111)As sample from the atmosphere after mechanochemical polishing (Fig. 9).

Type IV.—Epitaxial layer on a GaAs (111)As substrate kept in the VPE reactor (Fig. 10).

A type IıI sample exhibits a marked absorption around 550°C (Fig. 9a) and then ψ behaves linearly and reversibly *vs.* T. In contrast, Δ continues to change while T is maintained at 750°C (possible formation of an "As-stabilized" structure?). The etching step again has a drastic effect on the (Δ, ψ) point (Fig. 9b). Nevertheless, ψ variations are weak and the net effect of the etching/growth procedure (point 3 as compared to point 1 in Fig. 9b) is only a 4° increase in Δ. The (111)As surface thus appears to have less defects than the (001). There still remain defects, as revealed by the etch, which are not present on epitaxial (111)As layers, these layers (Fig. 10) being nearly insensitive to the etching procedure.

In summary, the heating up in H_2 flow is not able to produce a clean and ordered surface. The etching step reveals the remaining defects by inducing pits. Several minutes of growth are necessary to recover the surface specularity and reach a "stable state of growth."

Assessment of a Stable State of Growth

Description of the model proposed by Cadoret.—Before discussing the results of our surface analysis, it is necessary to describe briefly the present model on the epitaxial growth of GaAs as given by Cadoret *et al.* (4, 5, 12, 13) and which is based on macroscopic measurements of the growth rate. In the model, growth occurs in a layer-by-layer fashion, with no three-dimensional nucleation. The kinetics of the process is limited by chemical reactions at the surface between

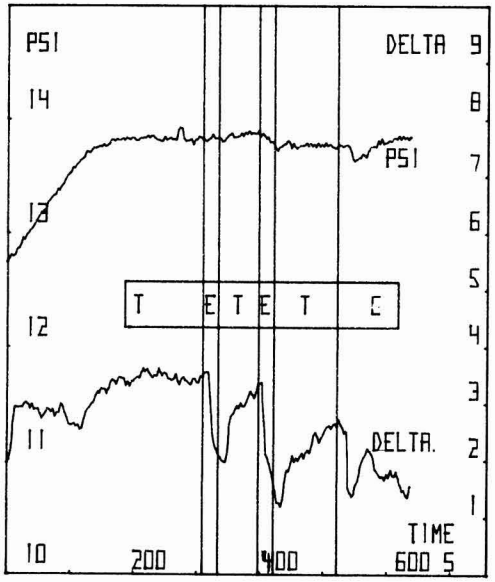


Fig. 10. Behavior of a GaAs (111)As epitaxial layer during a sequence of etch and growth conditions, E = etching conditions (HCl on the sample), T = under H_2 flow at 750°C, G = growth conditions (HCl on the source).

adsorbed species. In particular, the slowest step is the reduction of GaCl via hydrogen into a Ga atom able to be incorporated. This causes the growth rate to decrease when the partial pressure of GaCl increases (1). A significant part of the surface is occupied by not-yet-

decomposed GaCl molecules. The net effect of this GaCl coverage on the growth rate depends on the substrate orientation. On a (001) surface, each surface site is an incorporation site and GaCl molecules are chemisorbed with a low surface diffusivity. A schematic drawing of the surface during growth is given in Fig. 11. A part (θ_{Ga}) of the surface consists of bare Ga atoms. The rest of the surface is occupied by As-adsorbed atoms. Since GaCl molecules can only adsorb on As atoms, a part (θ_{AsGaCl}) of these As atoms is bonded with GaCl molecules and the rest (θ_{As}) is available. The following relation stands

$$\theta_{Ga} + \theta_{As} + \theta_{AsGaCl} = 1$$

A quantitative evaluation of these surface coverages has been done by Cadoret (4), assuming that the limiting step in the chemical reaction is the following reaction

$$(\text{As-Ga-Cl})_S + H_2 \leftrightarrows (GaAs)_S + HCl + (H)_S$$

where the subscript S stands for adsorbed species. The parameters of the model, namely, the adsorption energy of the (As-Ga-Cl) complex and the Einstein temperature of the surface (12), are adjusted by fitting the calculated growth rate with the measurements by Shaw (1). The best fit is obtained for the following adsorption energy of the (As-Ga-Cl) complex

$$\epsilon_{(100)} = -84.6 - 5.2\,\theta_{AsGaCl} \text{ (in kcal/mole)}$$

The surface coverage of AsGaCl can then be evaluated and is shown in Fig. 12 as a function of the $AsCl_3$ partial pressure for various substrate temperatures.

A Burton-Cabrera-Franck description (14) in which GaCl, As_4, and As_2 molecules (19) are first physisorbed on the terraces and then diffuse towards the steps is used. The chemisorbed As, AsGaCl, and GaAs molecules yield to the equilibrium between the kinks of the ledges and the physisorbed molecules: a very marked difference then occurs between As and Ga orientation, as shown in Fig. 13. On a (111) Ga face the GaCl bond is normal to the surface, hence parallel to the ledges, leaving the kink sites available for the As, AsGaCl, or GaAs molecule incorporation. On a (111)As face, the GaCl bond is normal to the ledge; an activation energy is necessary for the chemisorbed molecules incorporation in the kink sites. The time relaxation for this process lowered the (111)As growth rate with respect to the (111)Ga one. This model gives a good interpretation of the marked experimental anisotropy between (111)As and (111)Ga faces, namely

$$\tau_{(111)As} \ll \tau_{(111)Ga}$$

and

$$\tau_{(111)Ga} \gtrsim \tau_{(100)}$$

The last inequality is interpreted as the consequence of the adsorption energy of AsGaCl molecules on the

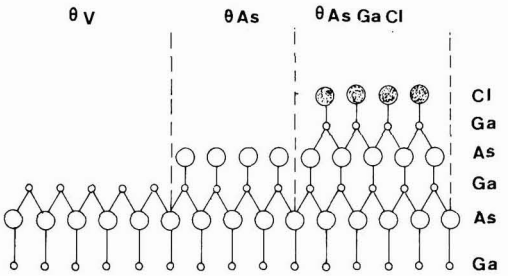


Fig. 11. Schematic surface coverage of a GaAs (001) substrate during growth.

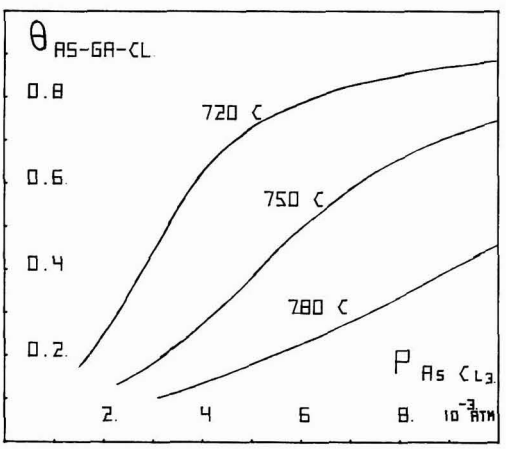


Fig. 12. Calculated adsorption isotherms of GaCl during growth on a GaAs (001) substrate (after Cadoret, private communication).

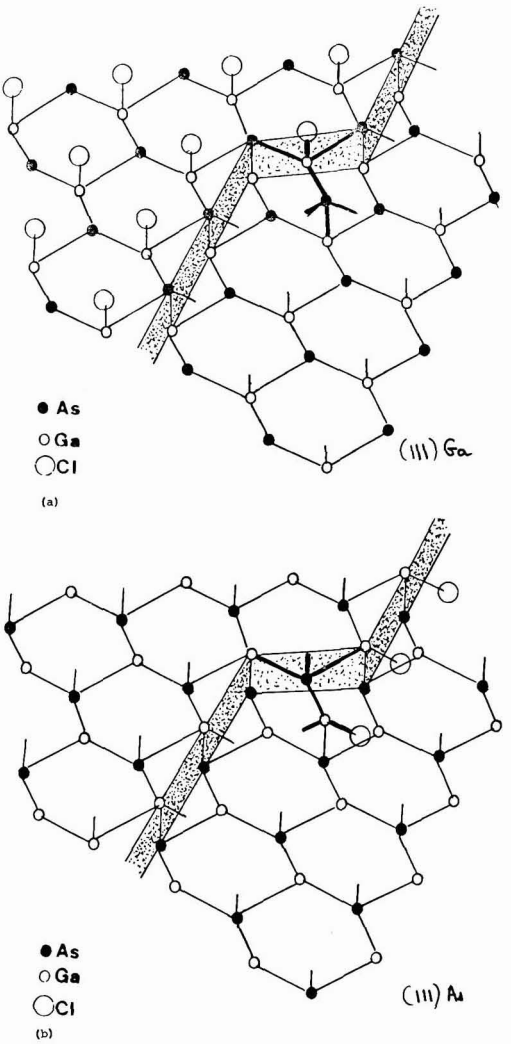


Fig. 13. a, A (As-Ga-Cl) molecule chemisorbed in a kink on a GaAs(111)Ga face; b, same case for the GaAs(111)As face.

Table I. LEED, RHEED, and AES examinations of the GaAs epitaxial layers

Orientation	Surface treatment	LEED and RHEED	Cl/As (AES peaks)
(001)	Cleaning in UHV	"Ga stabilized": C (8 × 2)	0
	Transferred during epitaxy	(1 × 2) or (1 × 1)	0.20
	Subsequent heating in UHV (500°C)	(8 × 2) or (1 × 1)	0
(111)Ga	Cleaning in UHV	"Ga stabilized": (2 × 2)	0
	Transferred during epitaxy	(1 × 1) plus 6-fold "halos" around each spot	0.14
	Subsequent heating in UHV (500°C)	(1 × 1)	0
(111)As	Cleaning in UHV	"Ga stabilized": ($\sqrt{19} \times \sqrt{19}$)	0
	Transferred during epitaxy	"As stabilized": (2 × 2)	0.1 + physisorption
	Subsequent heating in UHV (500°C)	(2 × 2)	0

(111) Ga face obtained from fitting with experimental growth rates (1)

$$\epsilon_{(111)Ga} \approx -90 - 3\theta_{AsGaCl} \text{ (in kcal/mole)}$$

Since $\epsilon_{(100)} < \epsilon_{(111)Ga}$, the limiting role of GaCl molecules is more pronounced on the (100) face with a corresponding lowering of the growth rate.

Experimental results.—A qualitative comparison with the above model can be obtained by transferring the sample from the VPE reactor directly to the UHV chamber. The results are given in Table I. The so-called "Ga and As stabilized" structures have been established, using the molecular beam epitaxy technique (15), to correspond to Ga- and As-enriched surfaces, respectively. On the (001) surface a Cl compound is found adsorbed on the surface strongly enough to survive the transfer procedure. A chlorine AES peak is obtained and the surface structure is a well-ordered (1 × 2) structure, at least at the beginning of the epitaxy. When the duration of the epitaxy is greater than a few minutes, the structure tends to be a (1 × 1). This is due to a surface roughening in the 1 μm range, observable with an optical microscope and known as the "wavelet structure" (16). This roughening induces a disorder between (1 × 2) structures at various points of the surface within the coherence length of the electron (typically 1000Å) and yields a (1 × 1) structure with a marked background. The Cl compound is desorbed when the sample is heated above 500°C in the UHV chamber. On the (111)Ga surface, a Cl compound is also found adsorbed which induces diffuse reconstruction in the LEED and RHEED pattern. This adsorption is less pronounced than for the (001) face (0.14 instead of 0.20 for the Cl/As ratio) and is also removed by heating above 500°C. On the (111)As surface, no reconstruction is observed (apart from the As-stabilized structure). The Cl AES peak is very small (0.1 instead of 0.14 or 0.20). Indeed, a chlorine AES peak is observed at the very beginning of the AES examination, but it decays very rapidly. This indicates a physisorbed Cl compound, which is desorbed by the electron beam of the AES system. These results are in good qualitative agreement with the above model: (*i*) GaAs is chemisorbed on (001) and (111)Ga surfaces and more strongly on (001); (*ii*) GaCl is physisorbed on the (111)As terraces and chemisorbed only on the ledges of the atomic steps [in fact, the Cl peak is a measurement of the number of these ledges and should depend on the misorientation of the surface to the (111)As exact orientation].

A more quantitative AES analysis has then been attempted with the idea of using the recent calibration by Chang *et al.* (17). In this paper we have attempted to map out the Ga, As, and Cl peak dependence as a function of the $AsCl_3$ partial pressure and the temperature of the substrate in order to compare with the model of Fig. 12. The Ga and As peaks have been obtained in the low energy region (20-60 eV) by a background retrieval technique of the actual AES spectrum, as shown in Fig. 14. A background of the form $y = a(b - x)^{-c} + d$ has been calculated using conventional least squares fitting. Since the escape depth of As and Ga AES electrons are, respectively, 6.9 and 5.0Å in this energy range (18), a good surface sensitivity was expected, particularly in testing the transitions between As and Ga stabilized structures. A rough estimate [assuming the same sensitivity factor for As and Ga (17)] of the Ga/As ratio is given in Table II for the various possible cases: full coverage

Table II. Evaluations from an exponential model

Type of surface		Relative intensity of AES peaks Ga	As	Ga/As	Distances between planes (Å)
(001)	Ga stabilized	2.320	2.430	0.955	As-Ga = 1.41
	As stabilized	1.750	2.981	0.587	Cl-Ga = 1.29
	Cl stabilized	1.792	2.016	0.889	
(111)Ga	Ga stabilized	2.074	2.341	0.086	As-Ga = 0.82 and 2.47
	Cl stabilized	1.603	1.942	0.825	Cl-Ga = 1.29
(111)As	Ga stabilized	2.074	1.843	1.125	As-Ga = 0.82 and 2.47
	As stabilized	1.760	2.637	0.667	

Space depth: 5.0A for Ga Auger electrons; 6.9A for As Auger electrons [after Ref. (18)].

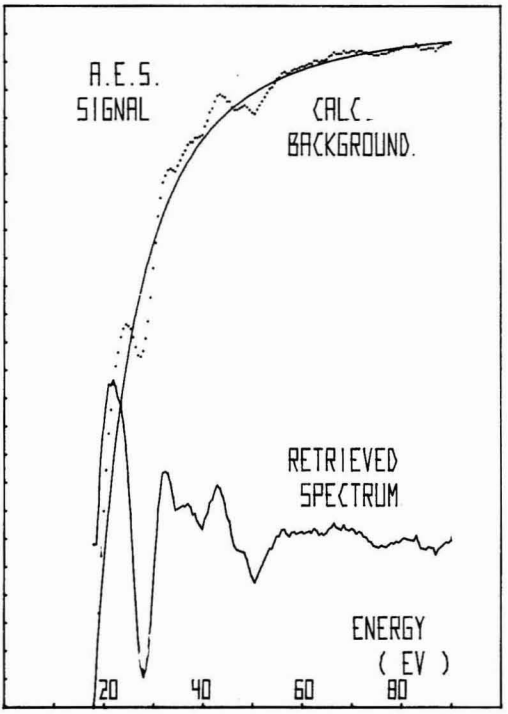


Fig. 14. Typical AES spectrum of a GaAs sample in the low energy range with the background retrieval. The double peak around 50 eV is the Ga peak, the one around 25 eV is the As peak.

of Cl, As, or Ga atoms on (001) and (111) surfaces. Unfortunately, the experimental results have not been found reproducible. For instance, the increase in the Ga/As ratio, as expected from Table II, going from a full Cl coverage to a Ga stabilized structure on (001) surface, has been found to range between 9 and 30%, depending primarily on the history of the transfer procedure. As seen in Table II, the maximum "contrast" between Cl and Ga stabilized structures is expected to be only 6%. A quantitative assessment of the chlorine adsorption is thus not possible via a transfer procedure. Clearly this transfer modifies the chemical composition of the uppermost layer and only qualitative estimates are possible.

The ellipsometry technique is not submitted to this limitation. As seen in Fig. 11, a (001) layer during growth is equivalent to less than one monolayer of chlorine atoms adsorbed on a (001)GaAs substrate. The measurement of Δ during the growth can be used to evaluate this equivalent chlorine coverage. The results are shown in Fig. 15 where Δ has been measured for three different substrate temperatures as a function of the $AsCl_3$ partial pressures on a (001) substrate. In the submonolayer region, the variation of Δ with respect to its bare substrate value, Δ_0, is known to be proportional to the surface coverage of the foreign species. In our case, the bare substrate corresponds to a small $AsCl_3$ partial pressure, *i.e.*, Δ_0 is the extrapolation of Δ at $P_{AsCl_3} = 0$. The chlorine coverage is then obtained by using the following relation

$$\Delta - \Delta_0 = -K\theta_{AsGaCl}$$

where K is a positive constant. With this correspon-

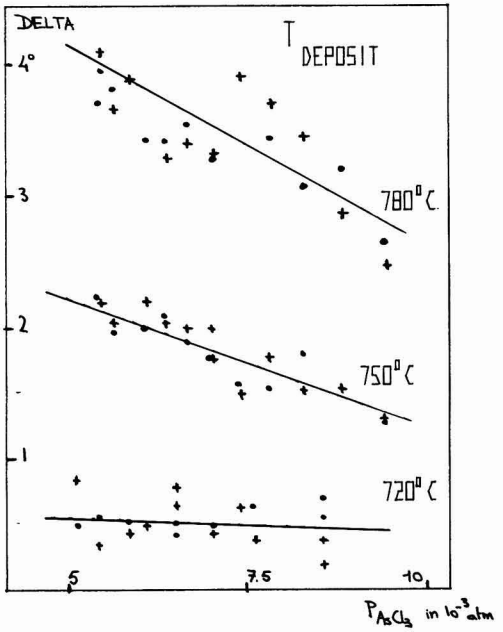
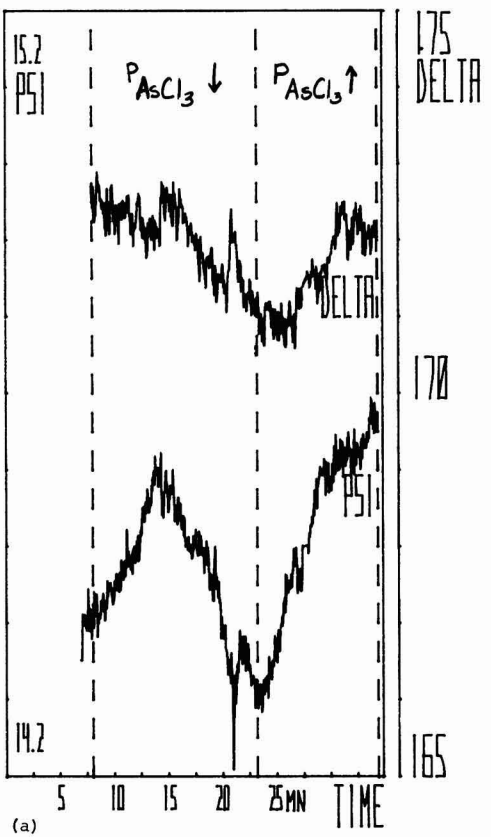


Fig. 15. Measurements of Δ as a function of the partial pressure of $AsCl_3$ for various substrate temperatures.



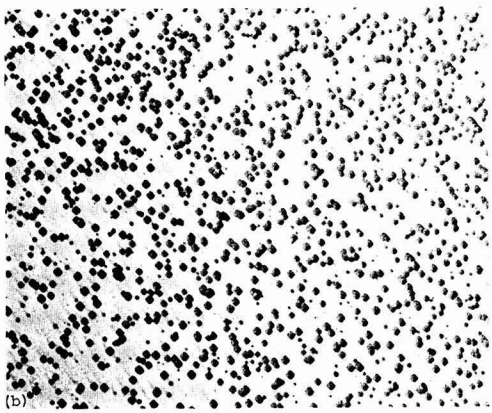


Fig. 16. a, Typical Δ and ψ variations in the case of a too fast change in the $AsCl_3$ partial pressure; b, optical micrograph of the surface morphology in this case.

dence between Δ and θ_{AsGaCl}, it is possible to compare the results of Fig. 15 to the model of Fig. 12. A good agreement is found, especially in the temperature dependence. The constant K is of the order of 3°/monolayer.

In fact, the results of Fig. 15 are obtained in the case when the partial pressure of $AsCl_3$ is modified very slowly (typically 2 hr for the 10^{-2}-5 $\times$ 10^{-3} atm range). In this case ψ is found constant within 0.03° as expected from a submonolayer model. On the contrary, if the pressure changes too rapidly, as shown in Fig. 16a (the 10^{-2}-5 $\times$ 10^{-3} atm range is explored in 15 min), an extra phenomenon is observed: ψ decreases significantly when the $AsCl_3$ partial pressure is low. An optical micrograph of the surface morphology at this stage reveals etch pits on the surface (Fig. 16b). Those defects can be eliminated by reincreasing the $AsCl_3$ partial pressure, as seen in Fig. 16a, where ψ goes back to the high pressure value.

This kinetic effect has not yet been clearly assessed but is most likely dependent on hydrodynamic phenomena inside the reactor.

Conclusion

The model of Cadoret, which is based on macroscopic measurements of the growth rate, has been qualitatively tested by surface analysis techniques. In particular, the adsorption isotherms predicted by Cadoret have been measured by ellipsometry. This technique has proved its adequacy in assessing the phenomena occurring in the CVD reactor during various treatments of the sample: (*i*) heating in H_2 flow of a polished substrate is not sufficient to produce a clean and ordered surface; (*ii*) this stable state obtained at 750°C is only possible owing to the residual partial pressure of arsenic inside the reactor; and (*iii*) an increase of the surface roughness is observed during the etching step, and the specularity of the surface is only recovered after several minutes of growth.

Manuscript submitted March 7, 1978; revised manuscript received Oct. 31, 1978.

Any discussion of this paper will appear in a Discussion Section to be published in the December 1979 JOURNAL. All discussions for the December 1979 Discussion Section should be submitted by Aug. 1, 1979.

Publication costs of this article were assisted by Laboratoires d'Electronique et de Physique Appliquée.

REFERENCES

1. D. W. Shaw, *This Journal*, **115**, 405 (1968); *ibid.*, **117**, 683 (1970).
2. L. Hollan and C. Schiller, *J. Cryst. Growth*, **13/14**, 319 (1972).
3. J. B. Theeten, F. Hottier, and H. Paradan, *Rev. Phys. Appl.*, **11**, 587 (1976).
4. R. Cadoret and M. Cadoret, *J. Cryst. Growth*, **31**, 142 (1975).
5. J. L. Laporte, M. Cadoret, and J. F. Le Men, *C. R. Acad. Sci. Paris, Ser. B*, **281**, 603 (1975).
6. For a recent review on the ellipsometry techniques, see *Surf. Sci.*, **56**, 1 (1976); see also, R. M. A. Azzam and N. M. Bashara, "Ellipsometry and Polarized Light," North-Holland, Amsterdam, The Netherlands (1977).
7. Y. P. Varshni, *Physica (Utrecht)*, **34**, 149 (1967).
8. "Semiconductors and Semimetals," Vol. 3, "Optical properties of III-V compounds," Academic Press, New York and London (1967).
9. C. Piaget and P. Guittard, Private communication.
10. M. A. Hopper, R. A. Clarke, and L. Young, *Surf. Sci.*, **56**, 472 (1976).
11. B. Goldstein, D. I. Szostak, and V. S. Ban, *ibid.*, **57**, 733 (1976).
12. J. B. Theeten, L. Hollan, and R. Cadoret, in "Crystal Growth and Materials," E. Kaldis and H. J. Scheel, Editors, Chap. 1-6, North Holland Publishing Co., Amsterdam, The Netherlands (1976).
13. R. Cadoret, Unpublished data.
14. For a recent review on the Burton, Cabrera, and Franck description, see P. Bennema and G. H. Gilmer, in "Crystal Growth, an Introduction," P. Hartman, Editor, Chap. 10, North-Holland Publishing Co., Amsterdam, The Netherlands (1973).
15. A. Y. Cho, *J. Appl. Phys.*, **42**, 2074 (1971); *ibid.*, **41**, 2781 (1970); A. Y. Cho and I. Hayashi, *Solid State Electron.*, **14**, 125 (1971).
16. See, for instance, J. V. Di Lorenzo, *J. Cryst. Growth*, **17**, 189 (1972), for typical surface morphologies evidencing the "wavelet structure."
17. C. C. Chang, P. H. Citrin, and B. Schwartz, *J. Vac. Sci. Technol.*, **14**, 943 (1977).
18. G. Ertl and J. Küppers, in "Low Energy Electron and Surface Chemistries," Chemie, Weinheim (1974).
19. R. Cadoret, M. Cadoret, and J. L. Laporte, Unpublished data.

Gas Rotational Temperature in an RF Plasma

R. A. Porter and W. R. Harshbarger[1]

Bell Laboratories, Allentown, Pennsylvania 18103

ABSTRACT

The molecular gas temperature in an rf glow discharge of N_2 was determined by analysis of the unresolved rotational structure of the emission spectrum. The emission spectrum was recorded for the rf discharge (13.56 MHz) in N_2 at a pressure of 1.0 Torr and an rf power of 1000W. Using a technique previously applied to pulse discharges in N_2 by Phillips (1), the unresolved 0′-3″ and 1′-4″ vibronic bands of the second positive system ($C^3\pi_u \rightarrow B^3\pi_g$) were analyzed. The least squares fit to these bands indicated a temperature of 595° $\pm$ 30°K. This measurement of the molecular gas temperature is applicable to the type of rf plasmas used to process semiconductor materials.

Plasma etching and deposition processes are playing an ever-increasing role in the manufacture of semiconductor devices (2-5). Because of the commercial importance of these processes, several studies have been made to characterize the physical and chemical parameters of these reactive systems. These studies have concentrated primarily on the optical emission spectra (6-9), the mass spectra (10-12), and surface chemistry of the systems (13, 14).

One plasma parameter which has not been well characterized until recently is the plasma gas temperature. However, it is impossible to fully under-

Key words: emission spectroscopy, etching, plasma deposition, semiconductor processing.

[1] Present address: Intel Corporation, Aloha, Oregon 97005.

stand the kinetics of the plasma reactions unless the temperature of the gaseous reactants is known. Recently, Oshima has reported the measurement of the gas temperature from the CO emission observed in a C_2F_6 plasma (15). His study, made at rf powers less than 100W, reports temperatures in the range of 400°-600°K.

To determine the gas temperature, Oshima analyzed the unresolved rotational structure in the CO emission produced in the C_2F_6 glow discharge (15). This technique has been widely used by spectroscopists for temperature measurements (16, 17). Nearly fifty years ago, Ornstein and van Wijk reported the gas temperature for the first negative transition of N_2^+ (18). Among many more recent studies, Molinari and co-workers have applied this same technique to the analysis of the discharge of N_2 (19, 20). They obtained a temperature of 5000°-6000°K for emission from N_2^+ and a temperature of 2800°-4000°K for emission from the $C^3\pi_u$ state of N_2. Using a technique to analyze the unresolved emission spectrum, Slovetskii and Sokolev found temperatures in the range of 680°-770°K in a tube discharge in CO_2 (21). Phillips used a similar spectral analysis technique to analyze the temporal dependence of the gas temperature in a spark discharge in N_2 (1).

This paper uses the technique described by Phillips to determine the gas temperature of molecular nitrogen, N_2. A least squares technique is used to fit the observed low resolution spectrum for emission from the second positive system ($C^3\pi_g \rightarrow B^3\pi_u$). The purpose of this paper is to demonstrate the applicability of this technique to achieve a better understanding of the types of reactive plasmas used for semiconductor manufacture.

Spectroscopic Analysis

The visible emission spectrum of N_2 in an rf discharge consists of the first positive ($B^3\pi_g \rightarrow A^3\Sigma_u^+$) and second positive ($C^3\pi_u \rightarrow B^3\pi_g$) emission systems (22, 23). This spectrum, with vibronic assignments, is shown in Fig. 1. In the present study, only the second positive system was analyzed. Since the transition is a triplet system, each band exhibits three subbands. In addition, each rotational line is split by Λ-type doubling. However, these spectroscopic distortions will be neglected for this application, because only the unresolved vibronic band shape is analyzed.

Following Phillips' analysis, the wavelength of a general rotational, vibronic transition $Cv'J'$—$Bv''J''$ is given by the formula

$$\Lambda^{Cv'J'}_{Bv''J''} = \left\{ n_a \sum_{p=0}^{4}\sum_{q=0}^{4} Y^C_{pq}(v'+1/2)^p[J'(J'+1)]^q - Y^B_{pq}(v''+1/2)^p[J''(J''+1)]^q \right\}^{-1} \quad [1]$$

For the calculations, the coefficients T_{oo}, Y_{pq} for the B and C states were taken from the work of Benesch *et al.* (24) and n_a is the refractive index of air.

The intensity of the general rotational, vibronic transition $Cv'J'$—$Bv''J''$, again given by Phillips, is

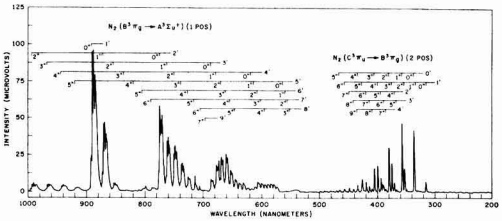


Fig. 1. Emission spectrum of N_2

$$F^{Cv'J'}_{Bv''J''} = D\frac{S_J}{T}\exp[-hcB_vJ'(J'+1)/kT] \quad [2]$$

where

$$D = h^2cB_vV^{Cv'}_{Bv''}A^{Cv'}_{Bv''}N_{Cv'}/(6k) \quad [3]$$

In the above formulation S_j is the general line strength taken for Hund's case (a) as given by Budo (25). The other parameters are: T = temperature; h = Planck constant; c = speed of light; B_v = rotational constant; k = Boltzmann constant; $A^{Cv'}_{Bv''}$ = Einstein transition probability; $N_{Cv'}$ = population; $V^{Cv'}_{Bv''}$ = transition frequency. Based on this equation the relative transition probability was calculated as a function of temperature.

Theoretically, the rotational lines have a shape that extends to infinity. As an adequate simplification, a finite band shape

$$g(\Delta\lambda) = \frac{a-(2\Delta\lambda/W)^2}{a+(a-2)(2\Delta\lambda/W)^2} \quad [4]$$

was assumed. This is a reasonable approximation to rotational line shapes. The above line shape results in a curve with a maximum of 1 at $g(0)$, a width at half maximum of W, and wings that extend to $\pm 1/2\ Wa^{1/2}$. W is taken to be the spectrometer resolution, and is fitted as a parameter along with the temperature, T. a is an arbitrary parameter, and as is seen below, the fitted parameter W strongly depends upon the arbitrary choice of a. The parameter a is associated with the intrinsic linewidth of a rotational transition.

Apparatus

For this study, the spectrum of N_2 was studied at a pressure of 1 Torr in a 13.56 MHz discharge of 1000W. The discharge was maintained in a radial flow plasma reactor with an electrode diameter of 40 cm and an interelectrode spacing of 2.5 cm (26).

The spectrum was analyzed by a 0.25m Jarrell-Ash monochromator with 0.1 mm slits and was detected with a blue-enhanced Si PIN photodiode (United Detector Technology PIN 10D-SB). With these slits the resolution of the monochromator was reported by the manufacturer to be 0.5 nm. Measurements of a well-resolved atomic transition in He ($5^3D \rightarrow 2^3P$ at 402.6 nm) gave width at half maximum of 0.4-0.6 nm, in agreement with the manufacturer's specifications. To increase the signal-to-noise ratio, the light from the plasma was chopped at 42 Hz, and the signal from the photodiode was discriminated by a lock-in amplifier at this frequency. The spectrum was recorded on a strip chart recorder as the spectrum was scanned by the monochromator.

The photodiode sensitivity decreases markedly in the ultraviolet region of the spectra, going to zero near 300 nm. However, in the region of interest of this study, near 400 nm, the photodiode sensitivity changed by no more than 5% across the 6 nm width of a vibronic band.

Data Analysis

The intensity data from the strip chart record of the emission spectrum was read at 0.25 nm intervals. Using Eq. [1]-[4] above, the digitized emission curve was fitted by a least squares procedure for a single vibronic transition (27, 28). This fitting procedure was performed for the 0'-3" and 1'-4" transitions of the second positive system, Phillips having determined that these bands were less sensitive to self-absorption. In the analysis, the temperature and the spectrometer resolution were allowed to vary; all other parameters in Eq. [1]-[4] were fixed by spectroscopic constants, with the exception of the constant a, which was arbitrarily chosen to equal 4 as discussed below.

Figure 2 presents the observed and calculated emission band profile for the 0'-3" transition. The calcu-

lated band shapes are plotted for temperatures 900° and 300°K, as well as the value 585°K obtained through

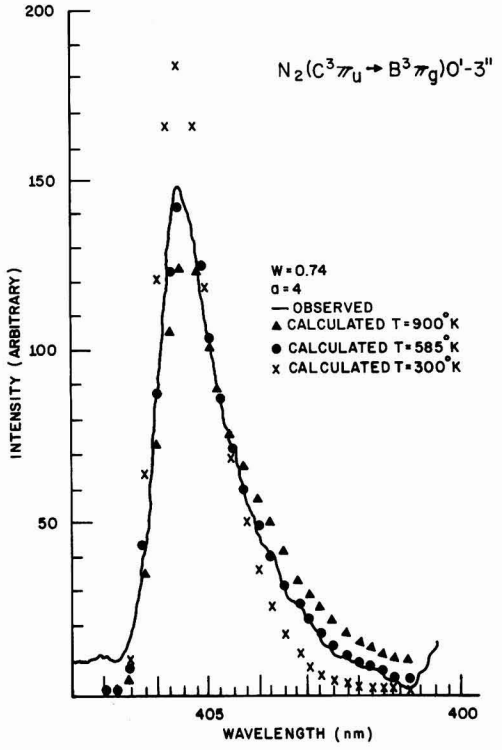


Fig. 2. Comparison of observed and calculated emission intensity for the $v' = 0 \rightarrow v'' = 3$ transition.

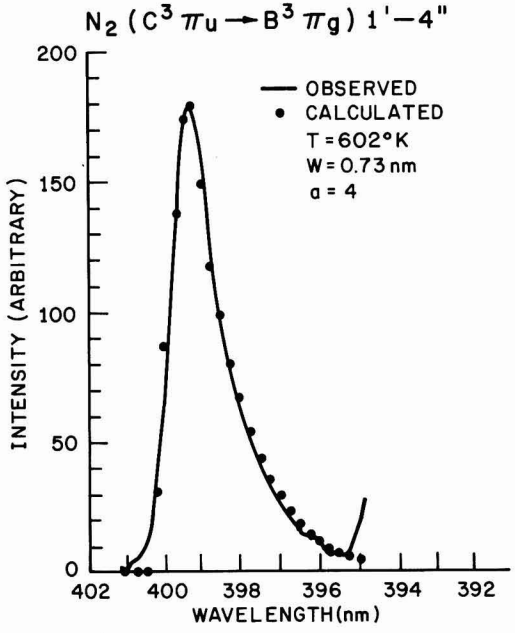


Fig. 3. Observed and calculated emission intensity of the $v' = 1 \rightarrow v'' = 4$ transition.

Table I. Iterative fit of 1'-4" vibronic band

Iteration	Temperature (°K)	Resolution (nm)	(Sum of residuals)² R^2
1	800	0.70	2446
2	573	0.74	771
3	600	0.73	725
4	602	0.73	725
5	602	0.73	725

the least squares analysis. For each calculated temperature, the area under the curve is normalized to the area of the observed transition. It is seen that as the temperature of the gas increases, the band shape is broadened, due to the larger population density in the higher rotational states. Figure 3 presents the observed and fitted emission profile for the 1'-4" transition.

The least squares procedure converged rapidly to fit the experimental data. Table I shows that in a typical run, less than 5 iterations were required to reach a minimum in the sum of the residuals squared, R^2.

Although the spectroscopic constants for this emission system are well characterized, the temperature measurement was affected by three systematic variables—the wavelength calibration, the background intensity, and the arbitrary selection of the constant a in Eq. [4].

In the spectra of Fig. 1-3, the background intensity or baseline position is not precisely determined. To determine the proper baseline position, the emission band for the 0'-3" transition was fitted in an iterative process as a function of the baseline position. This analysis is shown in Fig. 4. It is seen that R^2 is approximately a parabolic function of the baseline, while T is a linear function of the baseline position. Interpolation of Fig. 4 clearly indicates the proper baseline position. Similar analysis for the 1'-4" transition resulted in a consistent position of the baseline for the two vibronic bands.

After the proper baseline position was established, an iterative procedure was used to calibrate the wavelength. Although the monochromator is calibrated, the precision is not adequate for careful spectral measurements. In a similar manner to the baseline position measurements, the wavelength calibration was determined by an iterative procedure. Figures 5 and 6 show the dependence of R^2 and T on the wavelength calibration. Again, T is a linear function of the adjusted parameter, while R^2 shows a parabolic dependence. From the minimum in R^2, the wavelength is calibrated and T is determined. Each of the vibronic bands was

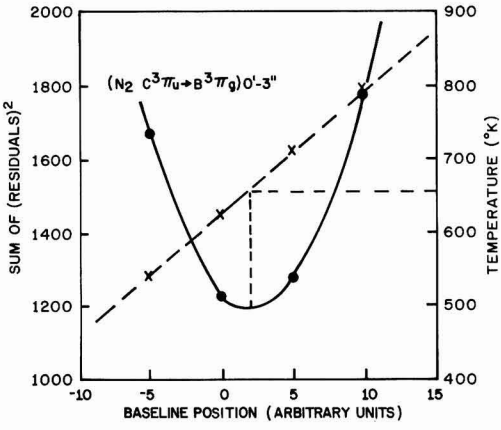


Fig. 4. Temperature dependence on the baseline position

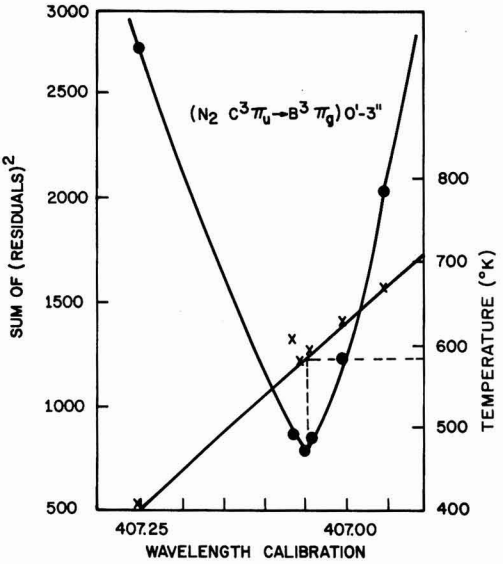


Fig. 5. Temperature dependence on the wavelength calibration for the 0'-3" transition.

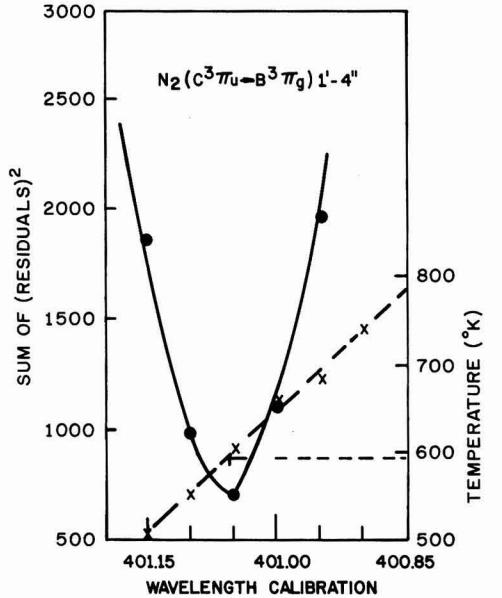


Fig. 6. Temperature dependence on the wavelength calibration for the 1'-4" transition.

fitted separately, and the positional difference of 6.0 nm between the vibronic bands is consistent with previously determined spectroscopic measurements.

Finally, the constant a in Eq. [4] was varied in an iterative manner. This constant is related to the intrinsic spectral linewidth of the individual rotational lines. The data in Table II indicate that variation in this parameter results in a change in the spectral resolution parameter, W, but has little effect on the calculated temperature. Thus, for this analysis, a is arbitrarily chosen equal to 4.

Following the above analysis, the 0'-3" and 1'-4" bands were fitted by the least squares procedure,

Table II. Dependence of calculated parameters on linewidth constant a

N_2 ($C^3\pi_u \rightarrow B^3\pi_g$) 0'-3"

a	Sum of (residuals)^2	Temperature (°K)	Spectrometer resolution (nm)
2	788	584.0	1.05
4	787	584.6	0.74
6	788	582.6	0.61
9	787	584.6	0.49

leading to temperatures of 585° and 602°K, respectively.

Discussion

One conclusion that is apparent from this study, as well as from the work of Oshima, is that the observed emission band profile is well characterized by a Boltzmann distribution for the population of molecules in the rotational levels of the excited state in the N_2 discharge. This can be understood if the primary excitation mechanism is excitation by electron collision. For this type of excitation, the angular momentum of the molecule is virtually unchanged and, thus, the distribution of molecules in the rotational levels of the upper electronic state is virtually the same as the Boltzmann distribution of the ground state. This excitation process has been established experimentally in several studies (16, 17) and is confirmed by the present work.

It is important to consider the degree to which rotational energy is converted to translational energy by relaxation processes. Using ultrasonic techniques, Kistemacher *et al.* (30) and Greenspan (31) have determined the relaxation number, the average number of collisions required to convert rotational to translational energy, near 300°K. Andersen and Hornig used shock waves for a similar determination from 300° to 400°K (32). These studies report relaxation numbers of 4-6. Since the relaxation number is essentially independent of temperature (33), the rotational relaxation time for N_2 at 1 Torr and 600°K should be approximately 50 μsec. Such a short relaxation time implies that the rotational and translational temperatures are equivalent.

As mentioned in the beginning of this paper, Oshima has reported temperature measurements in an rf plasma of C_2F_6. Using analytical techniques like those described here, he analyzed the "Ångström" system ($B^1\Sigma$-$A^1\pi$)emission of CO. In his study, the temperature was determined as a function of power over the range of 20-80W, as a function of pressure from 0.05 to 1 Torr, and as a function of gas admixtures. He reports temperatures in the range of 400°-580°K, depending on the above specified parameters, Since the present study deals with an N_2 plasma, while Oshima analyzed a C_2F_6 plasma, it is not possible to directly compare results. However, the temperature of N_2 reported here, 595°K, is quite close to the range of temperatures reported by Oshima.

The purpose of this study is to record and demonstrate that gas atoms, molecules, or radicals in the plasma are hot translationally as well as electronically. This fact is important in the consideration of the mechanisms that are involved in plasma etching or deposition processes. Several studies have reported activation energies for heterogeneous etching or deposition processes in plasma discharges (2, 5, 34, 35). In these studies, the reaction rates were determined as a function of the temperature of the substrate only. As is seen from this study the temperature of the reactant gas is much higher and is, no doubt, determined by the discharge parameters. Reported activation energies on the order of 0.5-2.5 eV should be interpreted with consideration that the gas phase reactants of the heterogeneous reaction system are hot—electronically, vibrationally, and translationally.

Manuscript submitted Jan. 24, 1978; revised manuscript received Sept. 24, 1978. This was Paper 41 presented at the Atlanta, Georgia, Meeting of the Society, Oct. 9-14, 1977.

Any discussion of this paper will appear in a Discussion Section to be published in the December 1979 JOURNAL. All discussions for the December 1979 Discussion Section should be submitted by Aug. 1, 1979.

Publication costs of this article were assisted by Bell Laboratories.

REFERENCES

1. D. M. Phillips, *J. Phys. D*, **9**, 507 (1975).
2. R. G. Poulsen, *J. Vac. Sci. Technol.*, **14**, 266 (1977).
3. R. A. H. Heinecke, *Solid State Technol.*, **21**, No. 4, 104 (1978).
4. R. L. Bersin, *ibid.*, **21**, No. 4, 117 (1978).
5. R. S. Rosler, W. C. Benzing, and J. Baldo, *ibid.*, **19**, No. 6, 45 (1976).
6. W. R. Harshbarger, R. A. Porter, T. A. Miller, and P. Norton, *Appl. Spectrosc.*, **31**, 201 (1977).
7. W. R. Harshbarger and R. A. Porter, *Solid State Technol.*, **21**, No. 4, 99 (1978).
8. E. O. Degenkolb, C. J. Mogab, M. R. Goldrick, and J. E. Griffiths, *Appl. Spectrosc.*, **30**, 520 (1976).
9. B. J. Curtis and H. J. Brunner, *This Journal*, **125**, 829 (1978).
10. G. Smolinsky and M. J. Vasile, *Int. J. Mass Spectrom. Ion Phys.*, **16**, 137 (1975).
11. G. B. Bunyard and B. A. Raby, *Solid State Technol.*, **20**, No. 12, 53 (1977).
12. Y. Horiike and M. Shibagaki, *Jpn. J. Appl. Phys.*, **15**, Suppl. 15-1, 13 (1975).
13. J. W. Coburn, H. F. Winters, and T. J. Chuang, *J. Appl. Phys.*, **48**, 3532 (1977).
14. H. F. Winters, J. W. Coburn, and E. Kay, *ibid.*, **48**, 4973 (1977).
15. M. Oshima, *Jpn. J. Appl. Phys.*, **17**, 1157 (1978).
16. G. Herzberg, "Molecular Spectra and Molecular Structure I. Spectra of Diatomic Molecules," 2nd ed., p. 205, Van Nostrand Reinhold Co., New York (1950).
17. P. W. J. M. Boumans, "Theory of Spectrochemical Excitation," p. 102, Plenum Press, New York (1966).
18. L. S. Ornstein and W. R. van Wijk, *Z. Phys.*, **49**, 315 (1928).
19. E. Molinari, *Pure Appl. Chem.*, **39**, 343 (1974).
20. F. Cramarossa and G. Ferraro, *J. Quant. Spectrosc. Radiat. Transfer*, **14**, 159 (1974).
21. D. I. Slovetskii and A. S. Sokolev, *Op. Spectrosc.*, **36**, 265 (1974).
22. A. Lofthus and P. H. Krupenie, *J. Phys. Chem. Ref. Data*, **6**, 113 (1977).
23. R. W. B. Pearse and A. G. Gaydon, "The Identification of Molecular Spectra," Fourth ed., p. 217, John Wiley & Sons, Inc., New York (1976).
24. W. Benesch, J. T. Vanderslice, S. G. Tilford, and P. G. Wilkinson, *Astrophys. J.*, **142**, 1227 (1965).
25. A. Budo, *Z. Phys.*, **105**, 579 (1937).
26. A. R. Reinberg, U.S. Pat. 3,757,733.
27. K. Hedberg and M. Iwasaki, *Acta Crystallogr.*, **17**, 269 (1964).
28. N. Arley and K. R. Buch, "Introduction to the Theory of Probability and Statistics," Chap. 12, John Wiley & Sons, New York (1950).
29. A. Jacob, *Solid State Electron.*, **20**, 479 (1977).
30. P. G. Kistemacher, A. Tom, and A. E. DeVries, *Physica*, **48**, 414 (1970).
31. M. Greenspan, *J. Acoust. Soc. Am.*, **31**, 155 (1959).
32. W. H. Andersen and D. F. Hornig, *Mol. Phys.*, **2**, 49 (1959).
33. R. Brout, *J. Chem. Phys.*, **22**, 1189 (1954).
34. C. J. Mogab, *This Journal*, **124**, 1262 (1977).
35. E. P. G. T. Van den Ven and H. Kalter, Abstract 124, p. 388, The Electrochemical Society Extended Abstracts, Spring Meeting, Washington, D.C., May 2-7, 1976.

Competitive Mechanisms in Reactive Ion Etching in a CF_4 Plasma

G. C. Schwartz,* L. B. Rothman,* and T. J. Schopen

IBM Data Systems Division, East Fishkill, Hopewell Junction, New York 12533

ABSTRACT

Studies of etch rates of sputtered SiO_2 and single crystal silicon being reactively ion etched on a silica cathode in a CF_4 plasma indicate that for SiO_2 the etching process is dominated by an ion-assisted mechanism, whereas for silicon it is usually dominated by the neutral chemical component. It is therefore expected that, with a nonerodible mask, the etched profile for SiO_2 is vertical, whereas that of silicon will usually be undercut and tapered. Scanning electron micrographs of patterns etched in SiO_2 and silicon confirm the predictions.

In reactive ion etching and sputter etching, the same rf glow discharge configuration is used. With the substrate holder acting as the cathode, ions generated in the dark space are accelerated across it and arrive at the cathode at normal incidence. The distinguishing feature of reactive ion etching is that the plasma contains chemically reactive species instead of or in addition to the inert gas used in sputter etching, and therefore the etch rate is significantly higher. Also, reactive ion etching is often much more selective than sputter etching.

In reactive ion etching, since the ions are directional, a substrate on the cathode—*i.e.*, coupled to the rf electrode—can be etched with a nonerodible mask[1] to produce vertical edges without undercutting the mask. This has been reported for SiO_2 etched in CF_4 with an aluminum mask (1) and for aluminum and its alloys etched in CCl_4 with a SiO_2 mask (2). Reactive ion etching with a nonerodible mask results in residue formation. Portions of the substrate become masked

* Electrochemical Society Active Member.
Key words: etching, sputtering, erosion.

[1] No mask is absolutely nonerodible. We define a nonerodible mask as one that has a low sputter etch rate and/or reacts with the chemical species in the plasma to form a compound whose vapor pressure is negligible and whose sputter etch rate is low. The removal rate of Al_2O_3 during reactive ion etching in CF_4 at 0.5 W/cm and 50 mTorr is 65 Å/min.

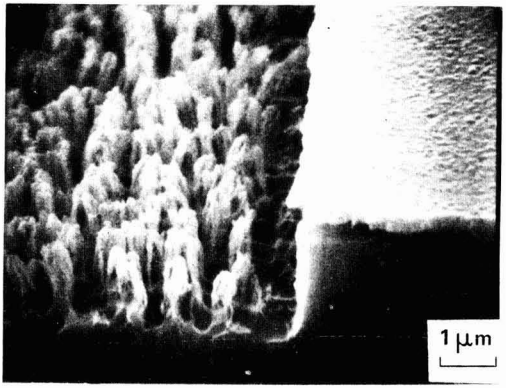


Fig. 1. Scanning electron micrograph of a fractured section of aluminum-masked sputtered SiO_2 after reactive ion etching in CF_4.

inadvertently because the etch mask is sputtered and redeposited.[2]

Figure 1 shows the nonundercut, vertical profile, and residue obtained when aluminum-masked SiO_2 is reactively ion etched in CF_4.

Previously we reported reactive ion etch rates for single crystal silicon etched in CF_4 on a substrate holder made of silica. We demonstrated the existence of a strong loading effect, *i.e.*, a decrease in the etch rate of silicon as the number of silicon wafers covering the silica plate increases; and we showed the functional dependence of the silicon etch rate on the area of silicon exposed to the plasma. By contrast, the SiO_2 etch rate decreases only slightly with increasing silicon load (3). Since the loading effect appears to be the result of depletion of active species, this suggests that neutral reactive species are more important for etching silicon than for etching SiO_2.

Earlier we also reported on etching SiO_2-coated wafers lifted into the plasma by placing them on a stack of silica disks set on the cathode (1). We call this the decoupled mode because the capacitance is increased between the substrate and the rf electrode, thereby reducing the bias at the substrate. At the same power and pressure, in the decoupled mode the etch rate of SiO_2 is significantly lower than in reactive ion etching. Moreover, the SiO_2 etches isotropically and there is no residue from an aluminum mask. This is seen in Fig. 2, which compares SiO_2 etched in the decoupled mode and in a buffered HF solution. The complete suppression of mask sputtering is evidence that the bias at the substrate is reduced substantially; in

[2] The surface of the residue was examined by Auger electron spectroscopy. When the mask had been aluminum, aluminum was detected; when the mask had been copper, copper was detected. Neither metal could be found in these areas before reactive ion etching, showing that their presence could not be attributed to improper mask fabrication. The bulk of the residue was unetched substrate, determined by means of x-ray dispersive analysis in the scanning electron microscope.

Aluminum films were analyzed by nuclear backscattering after exposure to a CF_4 plasma. To make fluorine detectable, thin (~2000Å) aluminum films were deposited on carbon disks instead of the conventional oxidized silicon substrates. The samples were placed on the cathode of a reactive ion etching system and exposed to a CF_4 plasma at a given input power, pressure, and CF_4 flow rate. Both O and F were detected at the aluminum surface. The F concentration increased and the O concentration decreased as the power input increased, keeping pressure, CF_4 flow rate, and run time constant. However, the F concentration did not change as the run time was increased from 2 to 10 min. The surface aluminum oxide appears to be converted to aluminum fluoride, as would be predicted from thermodynamic considerations. Because the vapor pressure of aluminum fluoride is low (v.p. = 1 mm at 1238°C) it is probable that the steady-state surface concentration of F is reached by balancing formation with sputtering rather than by volatilization. The same phenomenon should occur with copper. Therefore, it is probable that the residue observed with aluminum, copper and aluminum oxide masking is due to inadvertent redeposition of the corresponding sputtered fluorides.

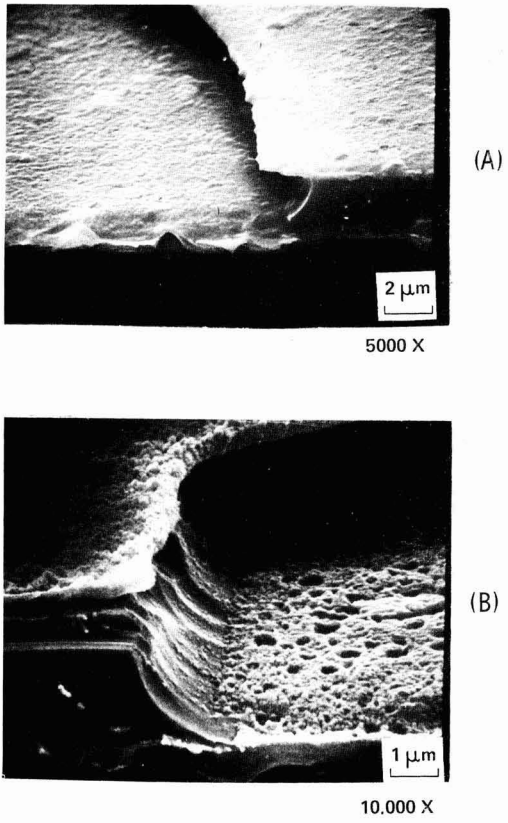


Fig. 2. Scanning electron micrographs comparing etched profiles of aluminum-masked SiO_2; fractured sections. (a) SiO_2 etched in CF_4 in the decoupled mode; (b) SiO_2 etched in buffered HF solution.

the decoupled mode ions become less important in etching SiO_2. The isotropy of etching suggests that neutral species have become more important in the process.

These earlier observations suggest that we can focus on the ion-assisted mechanism by etching in the coupled mode, and then on the neutral chemical reaction by etching in the decoupled mode. By etching with and without loading, we can observe the result of the depletion of neutral reactive species. Comparison of etch rate changes with and without coupling and loading should reveal the dominant mechanism in reactive ion etching. The validity of the method can be tested by examination of the etched profiles.

We have applied this concept to the comparison of the mechanisms of reactive ion etching of SiO_2 and silicon in CF_4.

Experimental

The system used is shown in Fig. 3. A 13.56 MHz rf generator and the impedance-matching network are connected between the water-cooled aluminum cathode and the grounded chamber enclosure. The effective chamber volume is about 45 l. The gas inlet and the pumping port are 90° apart. They are above the surface of the silica plate which is bonded to the metal cathode. The substrates to be reactively ion etched are placed on the silica plate whose area, used to convert input power to input power density, is 613 cm^2. Pressure is measured with a capacitance manometer (MKS Baratron). The sensor, placed outside the chamber, is connected to the chamber by a tube, 6.25

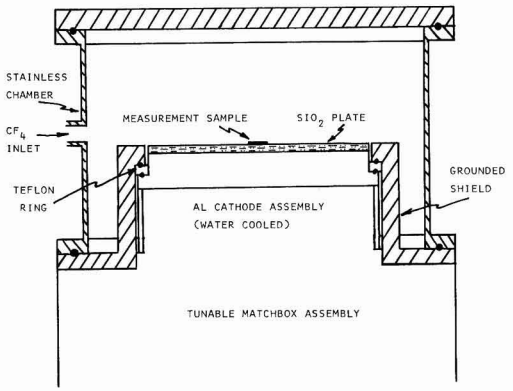


Fig. 3. The reactive ion etching system

mm diam and 20 cm long, that enters the chamber just above the gas inlet. Flow rates are measured with a Hastings Mass Flowmeter and the standard correction appropriate to the gas are used; corrected values are reported. The input flow rate of CF_4 could be varied from about 10 to 50 sccm; in these experiments it was 41 sccm.

During a run, the system pressure and the inlet flow rate are held constant. The pump speed is changed as needed to keep the flow rate the same when the pressure is varied from run to run.

The rf peak-to-peak voltage increases with increasing input power and decreases with increasing pressure. At 0.5 W/cm^2, it is about 1500V at 20 mTorr and 1200V at 80 mTorr. At 50 mTorr it increases from about 750V at 0.16 W/cm^2 input power density to about 1600V at 0.81 W/cm^2 input power density. The peak-to-peak voltage remains essentially the same when the silica cathode is covered by silicon wafers. The d-c bias on the silica surface is less than half the peak-to-peak voltage because of the capacitance of the silica plate covering the rf electrode.

The value used for input power density is the ratio of the wattmeter reading to the cathode area. From dark space voltage measurements, it has been estimated that about 20% of the input power is available for ion bombardment (4).

The surfaces of unmasked silicon and SiO_2 remain smooth during reactive ion etching in CF_4. Therefore, an interferometric method (5) can be used to measure, *in situ*, the etch rates of unmasked sputtered SiO_2 films. The incident light, $\lambda = 6328$Å, is normal to the cathode surface; the refractive index, at 6328Å, of sputtered SiO_2 is 1.467 (6). The etch rates of silicon are determined by Talystep measurement. An Al_2O_3 mask is formed on the silicon wafer by evaporation of 4000Å of Al_2O_3 through a lift-off structure. The edges of the Al_2O_3 mask are nearly vertical. After etching, the Al_2O_3 is dissolved and the step height between the masked and unmasked areas measured with a Taylor-Hobson Talystep. Although there is redeposition of sputtered mask, the residue has a negligible effect on the step height. Etch rates have been measured, in a single run, of silicon wafers masked with photoresist (which does not cause residue formation) and with Al_2O_3; within experimental error, they were the same.

Etch Rates: Results

The etch rates of sputtered SiO_2 and single crystal Si in CF_4 were measured as a function of input power at a fixed system pressure, 50 mTorr, and as a function of system pressure at two fixed input powers, 0.24 and 0.5 W/cm^2. The following cases were considered: (*i*) coupled, unloaded—one fourth of a 57 mm wafer on the silica cathode; (*ii*) coupled, loaded—silica cathode covered by close-packed silicon wafers (about 75% coverage); (*iii*) decoupled, unloaded—one fourth of a 57 mm wafer, lifted into the plasma; (*iv*) decoupled, loaded—one fourth of a wafer lifted into the plasma; silica cathode covered by close-packed silicon wafers.

The results are plotted in Fig. 4a and 4b for SiO_2 and in Fig. 5a and 5b for silicon. The etch rates for decoupled samples with loading are so low that they were omitted from the experiment of Fig. 4b.

For coupled samples, the etch rate of silicon is independent of crystal orientation, dopant, and doping level ($\sim 10^{15}$-6 $\times$ 10^{18}) with or without loading. No comparison was made for decoupled samples. As was reported earlier for SiO_2 (3), the etch rate of coupled silicon samples without loading shows no significant dependence on temperature. The etch rates of both SiO_2 and silicon have been reported to show temperature dependence for plasma etching (7, 8).

In a cursory study of the effect of adding oxygen, we obtained results that agree with those reported in the literature (9): as O_2 is added, the etch rates of silicon increase until the oxygen reaches 6-12% of the total pressure; upon any further addition, they de-

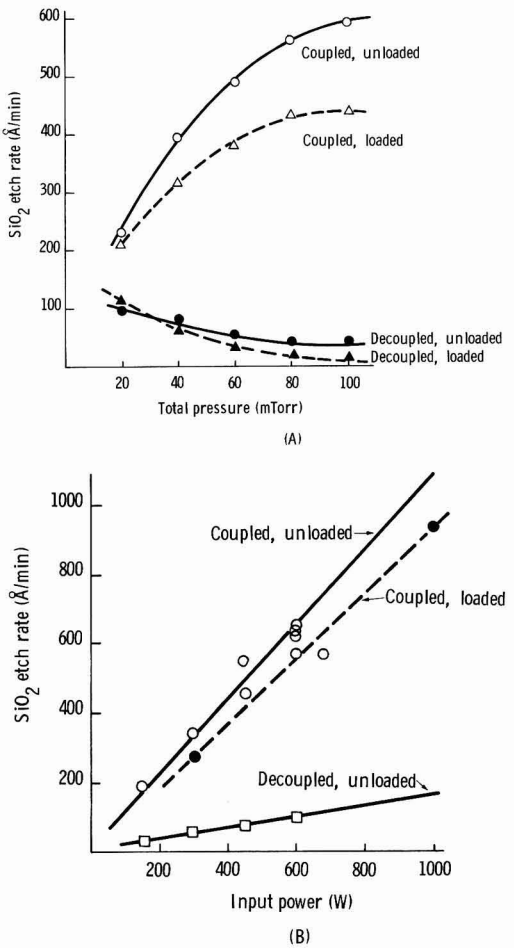


Fig. 4. Reactive ion etch rates of SiO_2 sputtered in CF_4; frequency, 13.56 MHz; input flow rate, 41 sccm CF_4; silica cathode. (a) As a function of total pressure; input power density, 0.73 W/cm^2; (b) as a function of input power; total pressure, 50 mTorr.

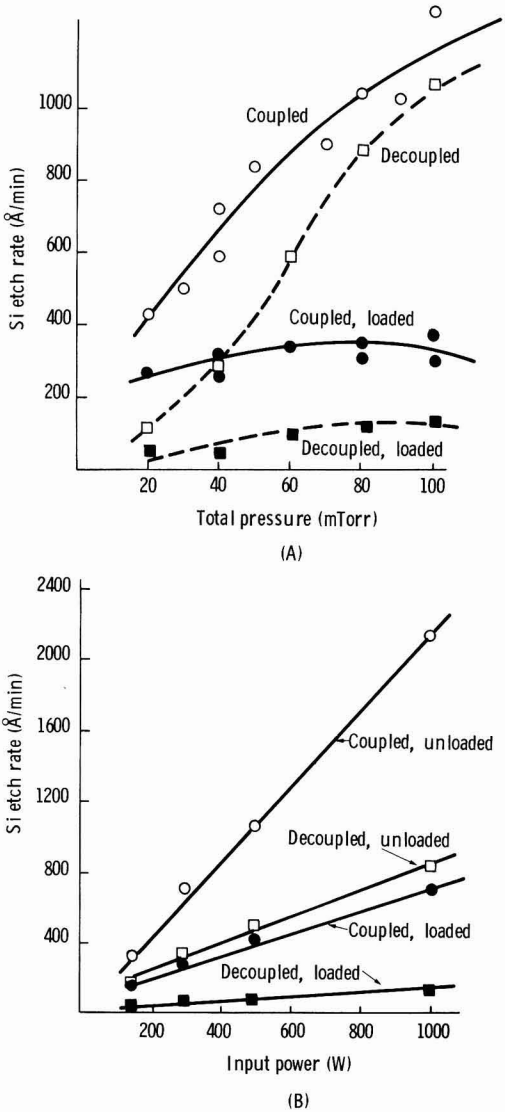


Fig. 5. Reactive ion etch rates of silicon sputtered in CF_4; frequency, 13.56 MHz; input flow rate, 41 sccm CF_4; silica cathode. (a) As a function of total pressure; input power density, 0.5 W/cm²; (b) as a function of input power; total pressure, 50 mTorr.

crease. The etch rate of silicon on a fully loaded cathode follows the same general trend.

Etch Rates: Discussion

SiO_2—At all powers and pressures, decoupling reduces the etch rate markedly, whereas loading has very little effect. This implies that the supply of neutral species is not rate-limiting and an ion-assisted mechanism is dominant. A vertical profile is therefore expected for any combination of power and pressure chosen for the reactive ion etching of SiO_2.

As analysis of Fig. 4a and 4b shows, the etch rates of coupled samples increase markedly with increasing pressure, and those of decoupled samples decrease slightly; loading has little effect. The reason why decoupled samples etch faster at lower pressure may be that increased ion energies are making the decoupling less effective; at higher pressure, gas scattering may become more important.

In summary, the dependence on pressure of the etch rate for SiO_2 is determined by whether the substrate is coupled to the cathode—that is, biased.

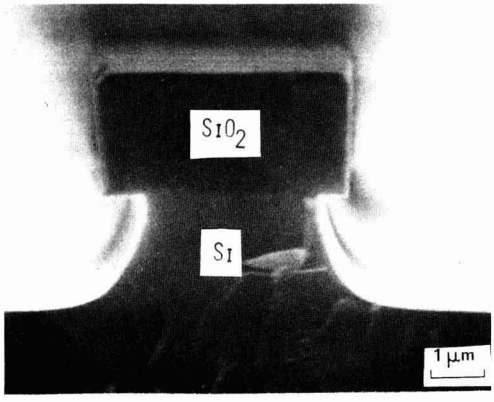
Silicon.—For silicon, unlike SiO_2, loading usually reduces the etch rate more than decoupling. This implies that etching is dominated by a mechanism involving neutral reactive species. But ions too play a role since the rate is reduced when the substrate bias is virtually eliminated. We would therefore expect the etching of silicon to be nondirectional, if not completely isotropic, with rounded and undercut profiles.

As analysis of Fig. 5a shows, the general trend in the pressure dependence of etch rates is similar for coupled and decoupled samples: without loading, the etch rate increases markedly with increasing pressure, whereas with loading it is almost independent of pressure. Therefore, the dependence on pressure of the etch rate of silicon would seem to be determined by the relative abundance of neutral species.

However, the situation is more complex than this, as a more careful examination of Fig. 5a will reveal. At 0.5 W/cm², the decoupled, unloaded curve crosses the coupled, loaded curve at 40 mTorr. Below 40 mTorr, therefore, decoupling reduces the etch rate more than loading, or, to put it another way, the etch rate is reduced more by reducing the bias than by reducing the neutral reactive species. We conclude from the earlier analysis that above 40 mTorr, neutral species dominate the reactive ion etching process, whereas below 40 mTorr the ion-assisted mechanism takes on increasing importance. This result is not completely unexpected, since, as the pressure is decreased, ion energies increase and an ion-assisted mechanism would be expected to become more important.

Etch Profiles: Results and Discussion

Figure 6 illustrates the difference between etching silicon and etching SiO_2 in a CF_4 plasma. Sputtered SiO_2, 2 μm thick, was deposited on a silicon wafer. A pattern was formed in Al_2O_3, a nonerodible mask, and the wafer was etched in 50 mTorr of CF_4 at 0.5 W/cm² on a silica cathode. When the rate monitor showed that the SiO_2 had been etched completely, the etching was allowed to continue under the same conditions. It can be seen clearly that, although the mask is beveled, the SiO_2 profile is essentially vertical. However, the profile of the silicon is rounded, and there is substantial undercutting of the mask. These same



13,500 X

Fig. 6. Scanning electron micrograph comparing profiles of silicon and SiO_2 reactively ion etched in CF_4 at 0.5 W/cm² and 50 mTorr on a silica cathode; fractured section.

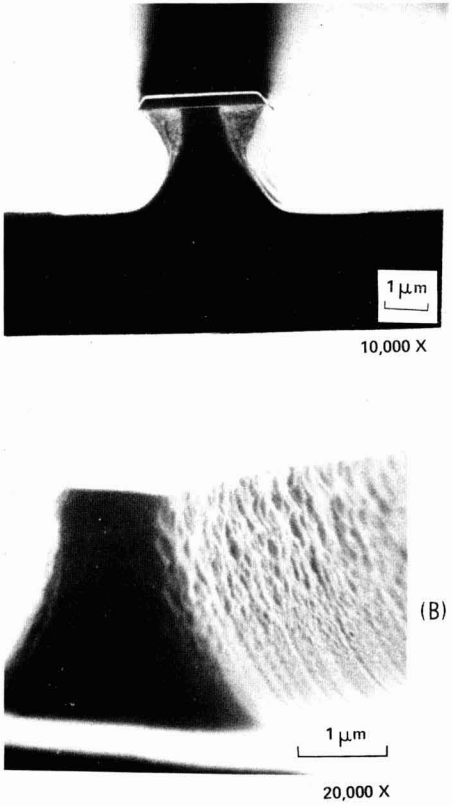


Fig. 7. Scanning electron micrographs of silicon reactively ion etched with an Al_2O_3 mask in CF_4 at 0.5 W/cm^2 and 50 mTorr on a silica cathode; fractured section. (a) With mask; (b) after dissolution of mask.

effects are obtained when the mask is applied directly to the silicon surface (Fig. 7).

Substituting a metal mask, such as aluminum, for the dielectric mask, Al_2O_3, does not change the extent of undercut (Fig. 8). For these experiments, only two properties of a mask are important; it must have a negligible erosion rate, and it must be completely resistant to deformation in the plasma so that the etch bias and true extent of undercut can be determined. When the mask etches at an appreciable rate and its profile changes during reactive ion etching, a tapered profile can be produced in any substrate. This has been shown for reactive ion etching in CF_4 with photoresist masking for silicon (10) and SiO_2 (11). The transition from dominance by the neutral chemical mechanism to dominance by the ion-assisted mechanism, deduced from the etch rate curves in Fig. 5a, can be demonstrated by examination of the profiles obtained when silicon is etched at 0.5 W/cm^2 at pressures above and below 40 mTorr. At 20 mTorr (Fig. 9a) there is no undercut; the profile has been distorted by forward-scattered mask material. At 80 mTorr (Fig. 9b) we observe severe undercutting and a rounded profile. The abrupt change in the sidewall taper during etching (compare Fig. 9b and 10b) is seen at times, but at present we do not understand the cause and cannot predict when it will happen.

Since loading substantially reduces the supply of neutral species available to each wafer, one would expect the ion-assisted mechanism to dominate. Therefore, although many combinations of power and pressure produce tapering and undercut in silicon etched on a silica cathode, the etched profile will always be vertical when silicon is etched on a silicon cathode or a fully loaded silica one. This is illustrated by a comparison of Fig. 7 and 10a where the eching conditions

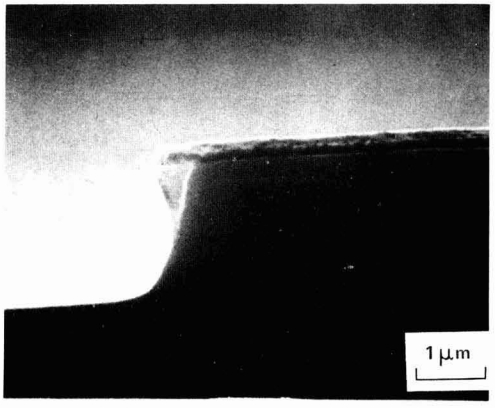


Fig. 8. Scanning electron micrograph of silicon reactively ion etched with an aluminum mask in CF_4 at 0.5 W/cm^2 and 50 mTorr on a silica cathode; fractured section.

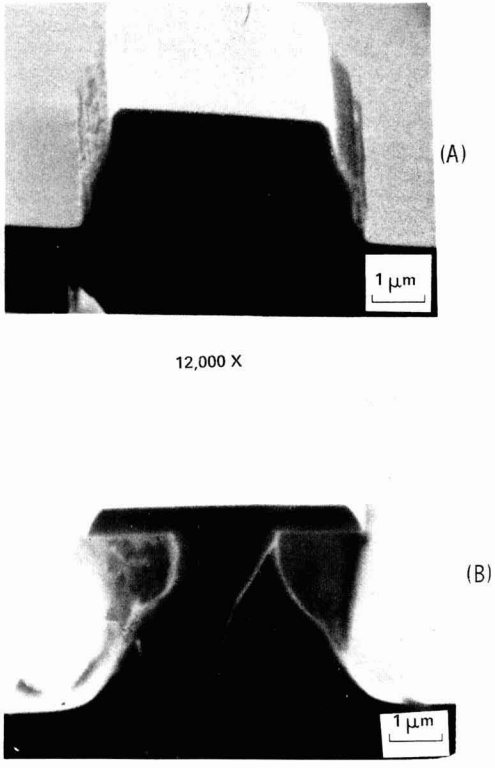


Fig. 9. Scanning electron micrographs comparing profiles of silicon reactively ion etched with an Al_2O_3 mask in CF_4 at 0.5 W/cm^2 on a silica cathode at pressures below and above the crossover point in Fig. 5a; fractured sections. (a) 20 mTorr; (b) 80 mTorr.

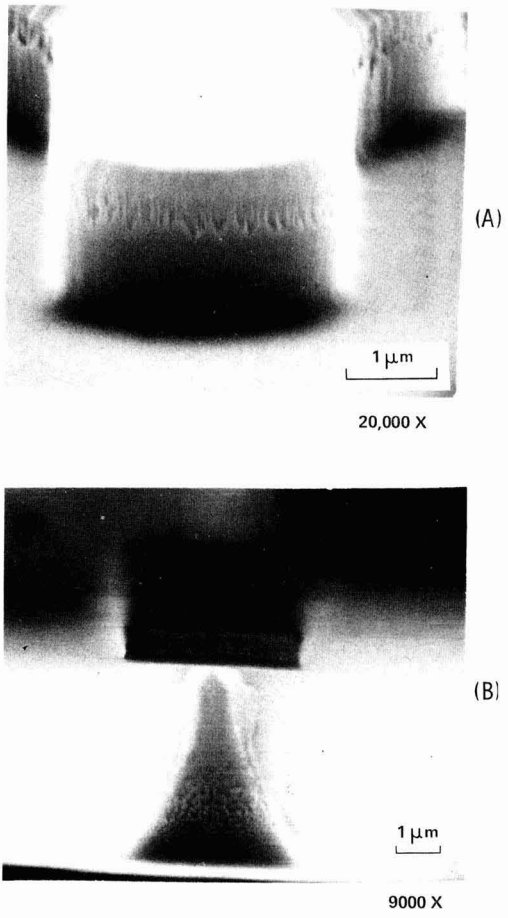


Fig. 10. Scanning electron micrograph of silicon reactively ion etched with an Al_2O_3 mask in CF_4 at 0.5 W/cm^2 and 50 mTorr when the cathode is fully loaded with silicon wafers. (a) In CF_4; (b) in CF_4/12% O_2.

are identical, except for the presence or absence of loading.

Adding oxygen to a CF_4 plasma increases the concentration of F atoms (12). Apparently the increase is so large that it compensates for the greater consumption of F by a fully loaded cathode, and therefore the neutral chemical mechanism dominates. This is illustrated by comparison of Fig. 10a and 10b, where the conditions are the same except for the addition of oxygen.

Conclusions

Examination of patterns reactively ion etched in CF_4 in silicon and SiO_2 confirms predictions based on analysis of etch rates. The reactive ion etching of SiO_2 is always dominated by an ion-assisted mechanism; the resultant profile is always vertical, and the mask is never undercut. The reactive ion etching of silicon on a silica cathode is usually dominated by a mechanism involving chemically reactive neutral species; for most operating conditions, therefore, the etch profile is not vertical, but rounded and undercut.

The loading effect observed is due to depletion of the neutral species. Because the neutral chemical component is suppressed, the ion-assisted mechanism dominates the etching process and produces vertical etch profiles in silicon. Adding oxygen markedly increases the concentration of fluorine atoms and reestablishes the chemically dominant mode, even when a silicon cathode is used.

The profile of silicon reactively ion etched in CF_4 can be changed by any process that changes the relative numbers of charged to neutral reactive species.

Manuscript submitted April 10, 1978; revised manuscript received Sept. 19, 1978. This was Paper 142 presented at the Atlanta, Georgia, Meeting of the Society, Oct. 9-14, 1977.

Any discussion of this paper will appear in a Discussion Section to be published in the December 1979 JOURNAL. All discussions for the December 1979 Discussion Section should be submitted by Aug. 1, 1979.

Publication costs of this article were assisted by IBM Corporation.

REFERENCES

1. L. B. Zielinski and G. C. Schwartz, Abstract 53, p. 117, The Electrochemical Society Extended Abstracts, Spring Meeting, Toronto, Canada, May 11-16, 1975.
2. P. M. Schaible, W. C. Metzger, and J. P. Anderson, Ext. Abst. TF9-6, 24th Nat. Symp., Am. Vac. Soc., Boston, Mass., Nov. 8-11, 1977.
3. G. C. Schwartz, L. B. Zielinski, and T. Schopen, in "Etching," H. G. Hughes and M. J. Rand, Editors, p. 122, The Electrochemical Society Softbound Symposium Series, Princeton, N.J. (1976).
4. J. Mauer, Private communication.
5. R. Glang, in "Handbook of Thin Film Technology," L. I. Maissel and R. Glang, Editors, pp. 1-115, McGraw-Hill, Inc., New York (1970).
6. W. A. Pliskin, Private communication.
7. R. G. Poulsen and M. Brochu, in "Etching," H. G. Hughes and M. J. Rand, Editors, p. 111, The Electrochemical Society Softbound Symposium Series, Princeton, N.J. (1976).
8. D. K. Lam, Abstract 147, p. 404, The Electrochemical Society Extended Abstracts, Fall Meeting, Atlanta, Georgia, Oct. 9-14, 1977.
9. N. Hosokawa, R. Matsuzaki, and T. Asamaki, *Jpn. J. Appl. Phys.*, Suppl. 2, Pt. 1, 435 (1974).
10. J. A. Bondur, *J. Vac. Sci. Technol.*, **13**, 1023 (1976).
11. H. A. Clark and E. D. Purcell, Abstract 149, p. 411, The Electrochemical Society Extended Abstracts, Fall Meeting, Atlanta, Georgia, Oct. 9-14, 1977.
12. C. J. Mogab, A. C. Adams, and D. L. Flamm, Ext. Abstract TF9-5, 24th Nat. Symp., Am. Vac. Soc., Boston, Mass., Nov. 8-11, 1977.

The Anodic Oxidation of Nickel in 1*N* H_2SO_4 Solution

M. Zamin*,[1] and M. B. Ives

Institute for Materials Research, McMaster University, Hamilton, Ontario, L8S 4M1 Canada

ABSTRACT

The anodic oxidation of nickel in 1*N* H_2SO_4 solution has been studied employing potentiostatic and galvanostatic techniques. It has been found that although a large amount of charge is consumed during anodic oxidation, only about 5% of this charge is involved in film growth. The thickness of the passive film on nickel in 1*N* H_2SO_4 is between 6-16Å for anodic oxidation times of 15-60 min. The experimental results have been used to develop a kinetic equation describing the film growth on nickel. It is shown that the logarithm of the film growth current density is inversely proportional to the charge stored in the film. The resistivity of the film suggests that the film is pure and almost stoichiometric NiO. It is suggested that the Flade potential of nickel in 1*N* H_2SO_4 corresponds to that potential, more noble than the passivation potential, at which the surface of the nickel is covered with a pore-free film of NiO and passivation is complete.

Nickel is a transition metal and, therefore, exhibits a typical active-passive phenomenon in aqueous solutions. The inhibition of dissolution at potentials more noble than the passivation potential is considered to be due to the presence of a passive film, normally believed to be an oxide (1). The function of the oxide film in inhibiting metal dissolution has often been questioned and as a result two general beliefs exist. Some investigators (2-5) believe that the oxide film inhibits corrosion by forming a physical barrier between the metal and the solution, whereas others (6, 7) are of the opinion that inhibition occurs as a result of the conversion of the precursor oxide film into an electronic conductor by the introduction of nonstoichiometry at the passivation potential.

Several investigations have been performed on the passivation behavior of nickel. Sato and Okamoto (8) proposed that the potential for the onset of passivity is the potential for the transformation from NiO to the higher oxide Ni_3O_4 when the concentration of the nickel in solution is small. This potential has been identified as the Flade potential. Polarization to higher potentials leads to oxidation and conversion of this oxide (Ni_3O_4) to Ni_2O_3. Thus, the passive oxide film on nickel may be taken to consist of either a single higher oxide Ni_3O_4 or the duplex oxide NiO and Ni_3O_4. The results of Cowan and Staehle (4) support the presence of a single oxide Ni_3O_4. In cases where the nickel electrode is directly subjected to a passive potential in H_2SO_4 solution, the passive film has been assumed (9) to be composed of NiO. The earlier estimates of the thickness of the anodic passive films on nickel were rather high (6, 10, 11). Recent work (12, 13) reveals that anodic passive films on nickel are typically 6-16Å thick.

No rate law has been derived to describe the kinetics of the passive film formation on nickel. Okamoto *et al.* (14) found that during the film growth on nickel in 1*N* H_2SO_4 the film thickness is proportional to the potential; therefore the electric field remains constant throughout the film. Later, Okamoto and Sato (15) pointed out that if the motion of the ions in the passive film is due to a high electric field, then a linear relation between film thickness and potential would be expected. Recently, Sato *et al.* (13) found that an inverse logarithmic relation was obeyed for the anodic film growth on nickel in 0.3*N* Na_2CO_3 solution (*p*H = 11.49), implying field-assisted growth.

In this study, the anodic oxidation of nickel in 1*N* H_2SO_4 solution has been studied by galvanostatic and potentiostatic techniques. The experimental results have been used to develop a kinetic equation to describe film growth on nickel. Film thickness has been determined using cathodic reduction and atomic absorption spectroscopy. Finally, the significance of the Flade potential of nickel in 1*N* H_2SO_4 solution is discussed in view of the present results and those existing in the literature.

Experimental

Materials and equipment.—0.6 cm^2 specimens were cut from a 0.1 cm thick sheet of low oxygen cathode nickel[2] using a precision wafering machine. The cut pieces were annealed in vacuum (better than 10^{-5} Torr) to yield a grain size of 0.035 mm. An electrical lead wire was attached at the center of one side with Pb-Sn solder. Specimen preparation and the cell assembly were identical to that described elsewhere (16-18). Specimens were mechanically polished to 1 μm diamond, followed by electropolishing (19) in 60% H_2SO_4 for 1 min at 0.5 A/cm^2 and then 2 min at 1.0 A/cm^2.

The 1*N* H_2SO_4 solution was prepared from reagent grade acid meeting ACS specification and distilled water. The solution was deaerated by bubbling pure dry nitrogen for a minimum period of two days prior to its use. Transfer of solution to the cell was also performed under a nitrogen atmosphere. The nitrogen gas was continuously bubbled through the cell during an experiment. All experiments were performed at 23° ± 2°C. All potentials were measured *vs.* the saturated calomel electrode (SCE) using an agar-agar salt bridge. All values of potentials are reported as recorded with no corrections being made for any junction potentials.

The polarization circuit was similar to that reported elsewhere (20). The galvanostatic circuit was composed of a 45V stabilized d-c power supply and a set of high resistances ($>10^6\Omega$) to yield various current density values. The stability in this circuit was excellent since the current (measured with a sensitivity of ±0.01 μA) remained constant during any galvanostatic experiment.

The determination of nickel in 1*N* H_2SO_4 solution was performed using a Varian Techtron Atomic Absorption Spectrophotometer (Model AA6) with a car-

* Electrochemical Society Active Member.

[1] Present address: Ontario Research Foundation, Sheridan Park, Mississauga, Ontario, L5K 1B3, Canada.

[2] Analysis in ppm by weight: Al<1; Ca—3; C—15; Cr<0.6; Co—60; Cu—8; Fe—40; Pb—8; Mg<1; Mn<0.7; P<2; Si—5; S—5; Ti<1; H_2—1.5; N_2—2; O_2—14.

bon rod atomizer (Model 63). The sensitivity of detection by this method is 0.005 ppm.

Polarization procedure.—In order to always start from a pristine metal surface, any previously formed film on the electropolished surface was removed by holding the specimen cathodically in 1*N* H_2SO_4 at −1500 mV (SCE) for 10 min. The specimen was then switched to a cathodic galvanostatic current density of 5.8 $\mu A/cm^2$ for 5 min with occasional shaking to stir the solution and disperse hydrogen bubbles from the surface. Following this treatment, the specimen was immediately polarized and never allowed to stand at open circuit.

The potentiostatic polarization was performed by anodically polarizing from −300 mV (SCE) with potentiostatic steps of 25 mV at 1 min intervals to +1600 mV (SCE). For anodic oxidation at constant current density, specimens were given a preliminary potentiostatic oxidation treatment at +400 mV (SCE) for 3 min in 1*N* H_2SO_4, after which they were switched to an appropriate anodic current density. The growth of the film was evident by the decrease in current with time at the constant potential during the preliminary oxidation and later by the increase in potential with time at the constant growth current density.

Cathodic reduction.—The film was formed at a constant potential of +600 mV (SCE) for various times and cathodically reduced at a constant current density of 2.7 $\mu A/cm^2$.

The end point of the reaction was taken as the steady-state corrosion potential, E_{corr}. In actual practice, the galvanostatic circuit was closed before the potentiostatic circuit was opened, the potentiostat compensating for the small cathodic current introduced by the reduction circuit (20). This ensured that reduction of the film would begin instantaneously with no possibility of side reactions during the short time at open circuit.

Results

Passive film thickness.—The anodic polarization curve for polycrystalline nickel in 1*N* H_2SO_4 is presented in Fig. 1 and is typical of active-passive metals. When nickel is held at a potential in the passive region, the formation of a film proceeds by the anodic dissolution of the nickel. The current density (at constant potential) decreases with time, signifying growth of the film. The charge stored in the film, which is proportional to film thickness, can be calculated by integrating the current with respect to time, if it is assumed that all the current is involved only in film growth.

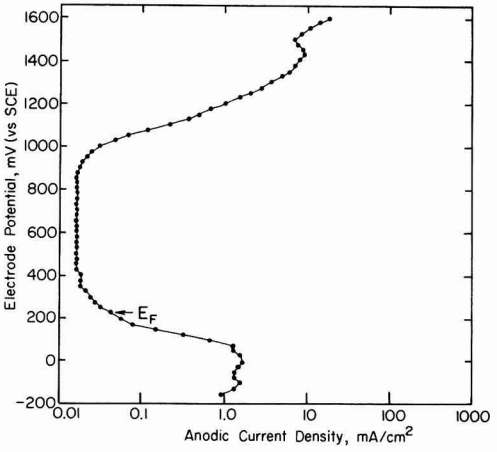


Fig. 1. Anodic polarization curve for nickel in 1*N* H_2SO_4

A large amount of charge is consumed during the anodic oxidation of nickel even in the passive region. For instance, during 3 min of preliminary potentiostatic oxidation in 1*N* H_2SO_4 at +400 mV (SCE), an average of 6.12 mC/cm^2 is consumed. If the film is assumed to be NiO, then the thickness of the film can be calculated from the analysis of Sato *et al.* (13) to be 34.7Å. Since passive films on nickel are typically 6-16Å (12, 13), it seems unlikely that all the charge associated with the anodic oxidation process corresponds to film growth. If only a part of the charge is involved in film growth, then considering the mass balance and neglecting impurity oxidation/reduction, the remainder of the charge must be associated with nickel dissolution. It thus appears that nickel dissolution is a major and important aspect of nickel passivation.

It is apparent that in order to determine the thickness of the film on nickel, the fraction of the charge corresponding to nickel present in solution must be accurately known. Since the quantity of nickel dissolved during the cathodic pretreatment could not be detected (*i.e.*, it was less than 0.005 ppm from a 0.36 cm^2 nickel electrode), the charge stored in the film, Q_f, is the total charge involved in the anodic oxidation process, Q_T, less the calculated charge corresponding to the quantity of nickel detected in solution Q_{Ni} (*i.e.*, $Q_f = Q_T - Q_{Ni}$). These results are presented in Table I.

An alternate method of determining the film thickness on nickel consists of determining the charge required to cathodically reduce at constant current density the anodically formed film. This is the charge stored in the film and can be converted to film thickness (13). The charge consumed during anodic oxidation at +600 mV (SCE) and subsequent cathodic reduction at 2.7 $\mu A/cm^2$ is presented in Table II. Cathodic reduction experiments appear to provide a more realistic estimate of the passive film thickness. Only a small fraction of the total charge involved in the anodic oxidation process goes toward film formaiton.

The cathodic reduction curves for nickel shown in Fig. 2 exhibit arrests at −50, −160, and −170 mV (SCE). Each arrest is presumably due to the reduction of a particular species. In this case, the arrest at −160 mV (SCE) appears to correspond to the reaction

Table I. The charge stored in the film during anodic oxidation of Ni in 1*N* H_2SO_4 at +600 mV for various times

Time (min)	Q_T (mC/cm^2)	Q_{Ni} (mC/cm^2)	Q_f (mC/cm^2)	x^* (Å)	Charge in film** (%)
15	24.06	22.88	1.18	6.7 ± 0.3	4.9
30	32.58	29.90	2.68	15.2 ± 0.7	8.2
60	43.46	40.63	2.83	16.1 ± 0.8	6.5

* Film thickness assuming film to be uniform and composed of NiO.
** As percentage of the total anodic charge involved in film growth.

Table II. Charge consumed during anodic oxidation of Ni in 1*N* H_2SO_4 at +600 mV and subsequent cathodic reduction at 2.7 $\mu A/cm^2$

	Passivation time		
	15 min	30 min	60 min
Anodic oxidation	23.7 mC/cm^2	33.7 mC/cm^2	43.5 mC/cm^2
Cathodic reduction	1.03 ± 0.11 mC/cm^2	2.50 ± 0.04 mC/cm^2	1.77 ± 0.01 mC/cm^2
Film thickness*	5.8 ± 0.6Å	14.2 ± 0.2Å	10.1 ± 0.1Å
Charge in film**	4.4%	7.4%	4.1%

* Assuming film to be uniform and composed of NiO.
** As percentage of the total anodic charge involved in film growth.

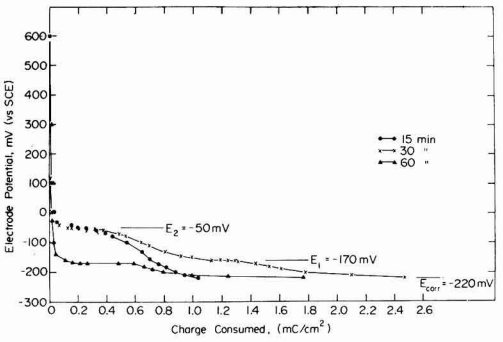


Fig. 2. Cathodic reduction curves for nickel at 2.7 μA/cm² in 1*N* H_2SO_4 for various times of anodic oxidation at +600 mV.

$$Ni + H_2O \rightleftharpoons NiO + 2H^+ + 2e \qquad [1]$$

since, from Nernst's equation (21), at the *p*H of the solution (=0.4) $E_1 = -156$ mV (SCE). Although it has not been possible to accord any reaction scheme to the other arrest potential, it is possible that it is due to a metastable complex.

Galvanostatic film growth.—It is believed by some investigators (22) that the dissolution rate of NiO in 1*N* H_2SO_4 is potential dependent, increasing with increase in potential. However, Sato and Okamoto (8) and the results of this investigation (Fig. 1) indicate that during potentiostatic polarization in 1*N* H_2SO_4 the current density in the passive region (i_p) is independent of potential (E). It is believed (23) that at this stage a steady state sets in, implying that film formation and film dissolution proceed at equal rates, *i.e.*

$$i_f = i_d = i_p \qquad [2]$$

where i_f and i_d are the film formation and film dissolution current densities.

When the film on nickel is grown under galvanostatic conditions the electrode potential increases, signifying this growth. As has already been shown, during potentiostatic film growth nickel dissolution is an important aspect of anodic oxidation and the galvanostatic film growth is no exception. The galvanostatic oxidation curves can be corrected for nickel dissolution (15, 24, 25). The corrected galvanostatic oxidation curves for nickel in 1*N* H_2SO_4 at four different current densities are presented in Fig. 3 as charge stored in the film, Q_f as a function of electrode potential. The extrapolated curves of Fig. 3 meet at +225 mV (SCE). This potential has been related to the Flade potential (E_F) by Weil (24). For nickel in 1*N* H_2SO_4, Sato and Okamoto (15) found that $E_F = +193$ mV (SCE). They also showed that

$$E - E_F = K\{(i_g - i_d)t + Q_i\} \qquad [3]$$

$$= K(Q_g + Q_i)$$

$$= KQ_f \qquad [4]$$

where Q_f = total charge in the film, i_g = measured galvanostatic growth current density, i_d = potential-independent dissolution current density, E = initial oxidation potential, K = a constant = $\partial E/\partial Q_f$, Q_i = charge stored in the film during the initial oxidation (*i.e.*, initial film thickness). Now, the initial oxidation was performed potentiostatically at +400 mV (SCE) for 3 min. Thus, $E = +400$ mV (SCE) and $E_F = +225$ mV (SCE). Hence, the charge during initial oxidation can be calculated from Eq. [3] knowing the slopes of the growth curves and their intercept on the abscissa at the various growth current densities. These results are given in Table III.

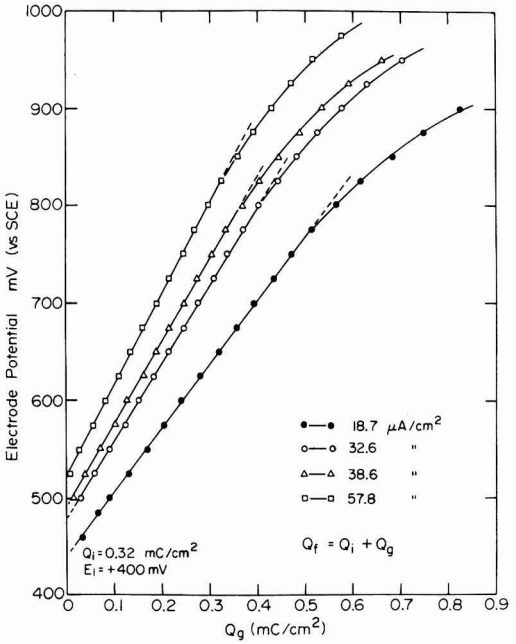


Fig. 3. Electrode potential-charge stored in film curves for nickel in 1*N* H_2SO_4 at various growth current densities. The curves are corrected for dissolution.

The average value of Q_i is 0.32 mC/cm². Potentiostatic measurements yield a total charge consumed during 3 min of anodic oxidation at +400 mV of 6.12 mC/cm² (of which only 0.32 mC/cm² or 5.25% goes toward film formation). Thus, about 95% of the charge transfer during initial oxidation in 1*N* H_2SO_4 is employed for nickel dissolution.

Discussion

Kinetics and mechanism of passive film formation on nickel.—The results for the galvanostatic oxidation of nickel in 1*N* H_2SO_4 yield a straight line when the potential (E) is plotted against the charge stored in the film (Q_f) (Fig. 3). This implies that the electric field is constant during film growth. The equation for the growth of the film under galvanostatic conditions may be written as a modification of Eq. [4] as

$$E = E_1 + KQ_f \qquad [5]$$

where E_1 is a constant. Assuming that the growth of the film obeys Ohm's law, then

$$E = i_gR = i_g\rho x \qquad [6]$$

where R = resistance of the film, ρ = resistivity of the film, i_g = growth current density, and x = film thickness. But $x = \omega Q_f$ (13) where ω = proportionality constant, and thus

$$E = i_g\rho\omega Q_f \qquad [7]$$

Table III. Estimation of the charge stored in the passive film on Ni in 1*N* H_2SO_4 during 3 min of anodic oxidation at +400 mV

i_g (μA/cm²)	Q_g (mC/cm²)	K (cm²/F)	Q_i (mC/cm²)
18.7	−0.060	675	0.32
32.6	−0.103	800	0.32
38.6	−0.112	840	0.32
57.8	−0.133	925	0.32

Average, Q_i = 0.32 mC/cm².

and from Eq. [5]

$$K = \frac{\partial E}{\partial Q_f} = i_g \omega \rho \qquad [8]$$

which implies that $K \propto i_g$. However, this is not experimentally true since K *vs.* i_g does not yield a straight line. Thus, the growth of the passive film does not exhibit a simple ohmic behavior. On the other hand, if the results of the galvanostatic oxidation are plotted as E *vs.* $\log i_g$, at constant Q_f, straight line plots are obtained (Fig. 4). In its simplest form the equation to the line may be taken as

$$\log i_g = \log \alpha + \frac{1}{b} E \qquad [9]$$

where α = constant and $b = \partial E / \partial \log i_g$ (= Tafel slope). Following the same procedure as before, it can be shown that

$$K = \frac{\partial E}{\partial Q_f} = \frac{\rho \omega b}{R} (\log i_g - \log \alpha) \qquad [10]$$

and this implies that $K \propto \log i_g$, which is observed experimentally (Fig. 5).

The equation to the line in Fig. 5 may be written as

$$\log i_g = \log K_1 + K K_2 \qquad [11]$$

where K_1 = constant and K_2 = slope of the $\log i_g$-K curve. Substituting from Eq. [5] for K into Eq. [11] and rearranging

$$\log i_g = \log K_1 - \frac{E_1 K_2}{Q_f} + \frac{K_2}{Q_f} E \qquad [12]$$

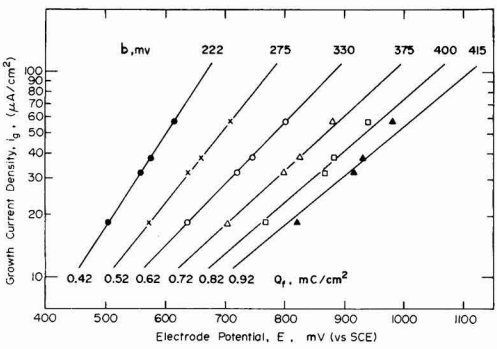


Fig. 4. Tafel plots (E — $\log i_g$) for the galvanostatic oxidation of nickel in 1*N* H_2SO_4 at various film thicknesses.

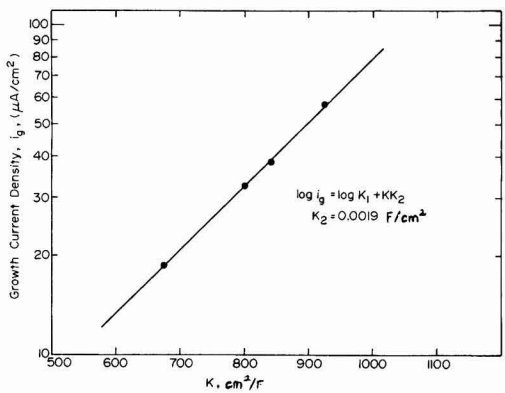


Fig. 5. *K*-log i_g plot for the galvanostatic oxidation of nickel in 1*N* H_2SO_4.

Table IV. Values of Tafel slope *b*

Q_f (mC/cm²)	$(b)_{obs}$ (mV)	$(b)_{calc}$ (mV)
0.42	222	222
0.52	275	274
0.62	330	327
0.72	375	379
0.82	400	432
0.92	415	485

Comparing Eq. [9] and [12], we have

$$\text{Tafel slope, } \frac{\partial E}{\partial \log i_g} = b = \frac{Q_f}{K_2} \qquad [13]$$

The values of the Tafel slope, b, observed in Fig. 4 and calculated from Eq. [13] at various values of Q_f, are given in Table IV. Discrepancy between the observed and the calculated values of the Tafel slopes occurs only at high values of Q_f where the variation of film thickness with potential is not linear (Fig. 3) and the present analysis is not valid. Rewriting Eq. [12] in an exponential form, we have

$$i_g = K_1 \exp \left\{ \frac{2.303 (E - E_1) K_2}{Q_f} \right\} \qquad [14]$$

This equation is identical with that assumed by Sato *et al.* (13) and implies that the field across the film remains constant. This is the basic premise of the present analysis.

Equation [14] can be integrated under the galvanostatic condition to yield an equation of the type

$$Q_f = C_1 t + C_2 \qquad [15a]$$

where C_1 and C_2 are constants. However, Eq. [14] can also be integrated under the potentiostatic condition and a rate equation of the type

$$\frac{1}{Q_f} C'_1 \ln t + C'_2 \qquad [15b]$$

as suggested by Sato *et al.* (13) can be derived. The central assumption in the conventional Mott-Cabrera (26) equation for an inverse logarithmic rate law of the type given by Eq. [15b] is that the potential drop across the film be constant. If Eq. [14] is taken to represent a modified form of the inverse logarithmic law, then the current should depend on the field applied and a plot of $\log i_g$ *vs.* $1/Q_f$ at constant potential should be linear. This is consistent with the present experimental results, as is shown in Fig. 6.

Sato *et al.* (13) also found that the anodic film growth kinetics of potentiostatic oxidation of nickel in 0.3*N* sodium carbonate solution of pH = 11.49 was in-

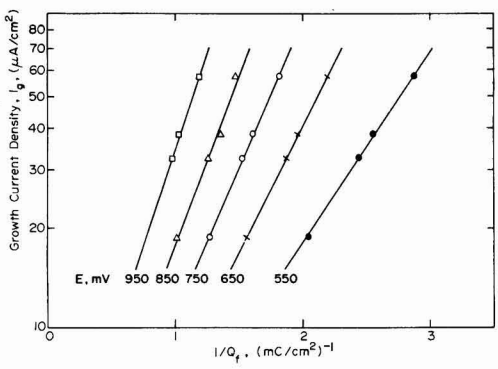


Fig. 6. $\log i_g$ — $1/Q_f$ plot for the galvanostatic oxidation of nickel in 1*N* H_2SO_4.

verse logarithmic. No derivation of the kinetic rate law was presented. Instead the potentiostatic oxidation data was arbitrarily plotted and it was found that a good fit to the inverse logarithmic law was obtained.

If $V = E - E_1$ = potential difference across the film, then Eq. [12] can be rewritten as

$$\log i_g = \log K_1 + \frac{VK_2}{Q_f} \qquad [12a]$$

The resistivity of the film can now be calculated, following Sato *et al.* (13), to be

$$\rho = \frac{R}{Q_f} = \frac{1}{K_1 K_2} = 7.1\ T\Omega\text{-cm} \qquad [16]$$

(Since a charge of 1 mC/cm² is equivalent to an NiO film of thickness 5.67Å, and the lines of Fig. 6 upon extrapolation to $1/Q_f = 0$ converge at $i_g = K_1 = 1.3$ μA/cm²). This value of the film resistivity is in good agreement with that of Sato *et al.* (13) ($\rho \approx 1\ T\Omega$-cm) calculated for nickel in sodium carbonate solution and that mentioned in the literature (27) ($\rho \approx 10\ T\Omega$-cm) for pure and almost stoichiometric NiO.

Significance of the Flade potential of nickel.—Sato and Okamoto (15) found the value of the Flade potential (E_F) of nickel in 1*N* H_2SO_4 at 40°C to be +193 mV (SCE). From the pH dependence of the Flade potential as given by Okamoto and Sato (28) for the present 1*N* H_2SO_4 solution (pH = 0.4), $E_F = +214$ mV (SCE). The value of the Flade potential as determined in the present investigation is +225 mV (SCE).

The significance of the Flade potential for nickel has remained subject to question. Okamoto and Sato (28) had suggested that the potential-determining redox reaction for the Flade potential was the conversion of NiO to Ni_3O_4. However, at a pH = 0.4 this would yield (21), $E = +631$ mV (SCE). It is therefore apparent that the Flade potential does not correspond to the conversion of NiO to Ni_3O_4 since Ni_3O_4 is thermodynamically unstable at the observed Flade potential.

In view of the present experimental data, a slightly different interpretation will be accorded to the Flade potential. The present results have suggested that the film on nickel in 1*N* H_2SO_4 is NiO, the formation potential of which has been found to be −170 mV (SCE). Thus, when passivity sets in, the surface of the nickel electrode is presumably covered with NiO. A potential value of +225 mV (SCE) on the anodic potentiostatic polarization curve of nickel in 1*N* H_2SO_4 is at the beginning of the passive region (Fig. 1). It is therefore suggested that the Flade potential corresponds to that potential, more noble than the passivation potential, at which the surface of nickel is covered with a pore-free film of NiO and passivation is complete. This interpretation of the Flade potential is also capable of explaining the data of Okamoto and Sato (15, 28).

Conclusions

As a result of this investigation the following conclusions can be made.

(*i*) A large amount of charge is consumed during the anodic oxidation of nickel in 1*N* H_2SO_4 solutions. However, only a small fraction, about 5%, of this charge is involved in film growth. The thickness of the passive film on nickel in 1*N* H_2SO_4 is between 6-16Å for anodic oxidation times of 15-60 min.

(*ii*) Galvanostatic oxidation of nickel suggests that film growth occurs under the influence of an electric field which remains constant at constant current density. The kinetics of anodic oxidation of nickel in 1*N* H_2SO_4 are of the "inverse logarithmic" type. The resistivity of the film suggests that it is pure and almost stoichiometric NiO.

(*iii*) The Flade potential of nickel in 1*N* H_2SO_4 corresponds to that potential, more noble than the passivation potential, at which the surface of nickel is covered with a pore-free film of NiO and passivation is complete.

Acknowledgments

The nickel used in this work was kindly supplied by L. A. Morris, Falconbridge Nickel Mines, Limited. The research was supported by a grant from the National Research Council of Canada.

Manuscript submitted Dec. 6, 1977; revised manuscript received Oct. 30, 1978.

Any discussion of this paper will appear in a Discussion Section to be published in the December 1979 JOURNAL. All discussions for the December 1979 Discussion Section should be submitted by Aug. 1, 1979.

Publication costs of this article were assisted by McMaster University.

REFERENCES

1. T. P. Hoar, in "The Encyclopedia of Electrochemistry," C. A. Hampel, Editor, p. 882, Reinhold Publishing Corp., New York (1964).
2. K. Schwabe and U. Ebersbach, "Proc. 4th Int. Cong. on Met. Corr.," p. 709, NACE, Washington, D.C. (1972).
3. K. Schwabe, *This Journal*, **110**, 663 (1963); *Electrochim. Acta*, **3**, 186 (1960).
4. R. L. Cowan and R. W. Staehle, *This Journal*, **118**, 557 (1971).
5. T. S. de Gromoboy and L. L. Shrier, *Electrochim. Acta*, **11**, 895 (1966).
6. A. K. N. Reddy, M. G. B. Rao, and J. O'M. Bockris, *J. Chem. Phys.*, **42**, 2246 (1965); *This Journal*, **113**, 1133 (1966).
7. A. C. Makrides, *ibid.*, **113**, 1159 (1966), and **109**, 977 (1962).
8. N. Sato and G. Okamoto, *ibid.*, **110**, 605 (1963).
9. I. A. Ammar and S. Darwish, *Electrochim. Acta*, **13**, 781 (1968).
10. L. Tronstad, *Z. Phys. Chem.*, **142**, 241 (1929).
11. K. Arnold and K. J. Vetter, *Z. Electrochem.*, **64**, 407 (1960).
12. B. MacDougall and M. Cohen, *This Journal*, **121**, 1152 (1974).
13. N. Sato, K. Kudo, and M. Miki, *J. Jpn. Inst. Metals*, **35**, 1007 (1971).
14. G. Okamoto, H. Kobayashi, M. Nagayama, and N. Sato, *Z. Electrochem.*, **62**, 775 (1958).
15. G. Okamoto and N. Sato, *J. Electrochem. Soc. Jpn.*, (overseas ed), **27**, E125 (1959).
16. M. Zamin and M. B. Ives, *Corrosion (Houston)*, **19**, 319 (1973).
17. T. Tokuda and M. B. Ives, *Corr. Sci.*, **11**, 297 (1971).
18. M. Zamin and M. B. Ives, *This Journal*, **121**, 1141 (1974).
19. T. Homma, N. N. Khoi, W. W. Smeltzer, and J. D. Embury, *J. Oxid. Metals*, **3**, 463 (1971).
20. R. F. Frankenthal, *This Journal*, **116**, 580 (1969).
21. M. Pourbaix, "Atlas of Electrochemical Equilibria in Aqueous Solutions," p. 330, Pergamon Press, New York (1966).
22. K. Nii, *Corr. Sci.*, **10**, 571 (1970).
23. G. M. Bullman and A. C. C. Tseung, *ibid.*, **12**, 415 (1972).
24. K. G. Weil, *Z. Electrochem.*, **59**, 711 (1955).
25. M. Zamin, Ph.D. Thesis, McMaster University (1976).
26. N. Cabrera and N. F. Mott, *Rep. Prog. Phys.*, **12**, 163 (1949).
27. Z. M. Jarzebski, "Oxide Semiconductors," p. 150, Pergamon Press, Warsaw (1973).
28. G. Okamoto and N. Sato, *Trans. JIM*, **1**, 16 (1960).

Photocurrents Induced by Subbandgap Illumination in a Ti-Oxide Film Electrode

D. Laser and S. Gottesfeld

Department of Chemistry, University of Tel-Aviv, Ramat-Aviv, Israel

ABSTRACT

Photocurrents induced by illumination of subbandgap photon energy in a Ti-oxide film electrode (produced by thermal oxidation of a Ti metal rod) were measured under anodic polarization with a two-beam experimental setup. The results are interpreted in terms of photon-induced electron transfers to and from active bandgap states, located at or close to the surface.

The possible role of surface states in oxidations at n-type semiconductor (SC) photoanodes has been discussed recently by various authors (1, 2). It has been concluded from experimental results and from calculations of electronic energy levels that such states may be required to allow a significant overlap with filled states of donor molecules in solution, when the energy level of the donor falls inside the SC bandgap. These surface states are thus expected to play a major role in enhancing charge-transfer across the SC-solution interface in various photoelectrooxidations, including that of water at oxide semiconductors. Another important role of such states may be the enhancement of the interaction of the SC surface with chemisorbed intermediates (3, 4). The activity of occupied bandgap states in reductions at a TiO_2 cathode (without illumination) was demonstrated by Frank and Bard (5). Morisaki *et al.* (6) and Mavroides *et al.* (7) reported results on photocurrents induced by photons of subbandgap (SBG) energy which were obtained at TiO_2 and $SrTiO_3$ photoelectrodes, respectively, when polarized cathodically to a region below the flatband potential. While such measurements may provide information on electronic states at the surface of the cathodically polarized electrode, the composition of the oxide surface (and bulk) under such negative polarizations may be somewhat different from that of the positively polarized oxide photoanode (8, 9). Mavroides [Ref. (1), p. 84] also reported measurements of SBG-induced photocapacitance and photoresistance of an anodically biased $SrTiO_3$. Heller, Chang, and Miller have recently described a two-beam experiment for identifying surface states associated with a lowering of the efficiency of the photoanodic process at CdS and CdSe electrodes (10).

We wish to report results of some measurements of photocurrents obtained with a Ti oxide photoanode which was prepared by heating a Ti metal rod to redness (for 5 min) in a butane burner flame. This Ti oxide electrode could be illuminated by a single light source of either bandgap (BG) or SBG photon energy, or by two separate sources simultaneously, one of BG and one of SBG photon energy. The results obtained seem to provide some information on the charge-transfer communication between bandgap states located at (or close to) the surface of this type of oxide electrode and the SC bands in the depletion layer. Some conclusions on the interaction of empty surface states with the donor (H_2O) molecules also seem to emerge. All these photocurrent measurements on the Ti oxide electrode were performed in an electrochemical cell under anodic polarizations, *i.e.*, under conditions directly relevant to the performance of this SC material as a photoanode.

Experimental

Figure 1 shows schematically the experimental system employed. I_1 was the BG light source (150W xenon lamp, and I_2 the SBG light source (150W Tungsten-Halogen lamp). Great care was taken, by a combination of filters, to ensure the absence of a higher photon energy component in the SBG beam. Similarly, a u.v. transmitting visible absorbing filter was used in the BG beam. When both sources of illumination were applied simultaneously, a chopper and lock-in amplifier had to be used to detect the small component of the photocurrent due to chopped SBG illumination ($\tilde{i}_{SBG}$) in the presence of the much larger photocurrents induced by the BG beam: The SBG beam was chopped by a mechanical chopper (Brookdeal, Model 9479, Berkshire, England), the internal reference signal of which (3.5V) was fed into the reference input of the lock-in amplifier. The signal input to the lock-in amplifier (Ithaco, Dynatrac 391, Ithaca, New York) was fed from the output of the current-to-voltage converter of the potentiostat (PAR Model 176, Princeton, New Jersey). This arrangement allowed measurement of the component of the photocurrent alternating at the chopping frequency and exactly in phase with the SBG light pulses, as a function of applied potential.

The Ti rod employed was of 99.9% purity (Alfa-Ventron Inorganics), the Na_2SO_4 and the H_2SO_4 were of a "suprapure" (E. Merck) quality, and the water was triply distilled. The Ti rod was inserted by pressure into a Teflon sleeve, so that only the oxide film was exposed to solution and to illumination. When the potential of this oxide electrode was varied with respect to a SCE reference while continuously illuminating the oxide with light of BG energy, the regular steady-state photocurrent *vs.* voltage wave reported before for single crystal or polycrystalline TiO_2 (11) was obtained.

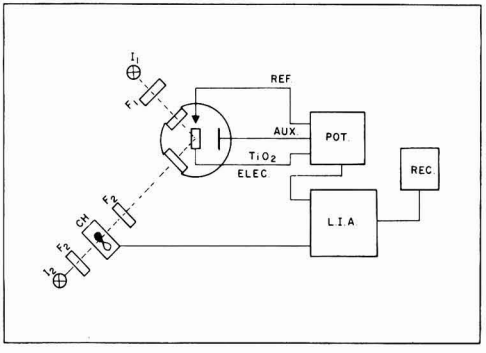


Fig. 1. Experimental setup: I_1, I_2-Xe are lamp and tungsten-halogen lamp, respectively. F_1-5 mm u.v. transmitting visible absorbing glass filter (Corning 7-51); F_2-3 mm glass filter (OG-590 Schott, Mainz, Germany) which cuts down by 10^5 any $\lambda \leq 570$ nm.

Key words: photoelectrodes, water photooxidation, surface states.

Results and Discussion

In a dark room, the periodic changes of the photocurrent induced by illumination with a single chopped beam of SBG energy could be directly recorded on a chart recorder. They are given in Fig. 2, from which it can be realized that these photoanodic currents have a much faster rise time as compared with the SBG-induced photocathodic currents reported before (6, 7). Also, the SBG-induced photoanodic currents are seen to contain a significant stationary component which does not decay during the illumination period.

The variation of the photocurrent induced by chopped SBG light ($\tilde{i}_{SBG}$) with applied potential, as well as its changes due to simultaneous irradiation with light of BG photon energy, are given in Fig. 3. The height of the $\tilde{i}_{SBG}$ plateau was found to be proportional to the intensity of the SBG beam for the intensity levels employed in our experiments (see Fig. 3); however, saturation was recorded with much stronger intensities of SBG light. The enhancement of $\tilde{i}_{SBG}$ by u.v. (BG) irradiation was not proportional to the u.v. intensity, reaching saturation for intensities slightly higher than the ones employed. The general wave-like shape of the photoanodic current *vs.* voltage curve can be seen to be similar for photocurrents induced by either SBG or BG illumination, the obvious difference being in the magnitude of the photocurrent in each case. Closer inspection reveals an inflection of $\tilde{i}_{SBG}$ at *ca.* 0.2V. In the presence of simultaneous BG irradiation this feature becomes more pronounced (see Fig. 3) and a clear "dip" appears in the anodic current wave in the potential region corresponding to the ascending branch. $\tilde{i}_{SBG}$ thus seems to contain a negative (cathodic) component in this potential region. On the other hand, simultaneous BG illumination caused a significant enhancement of the anodic photocurrent plateau induced by the chopped SBG beam at higher anodic potentials. This enhancement is the more important result in relation to the possible activity of surface states in the photoxidation of water, as discussed below. We propose the following interpretation for the measured effects:

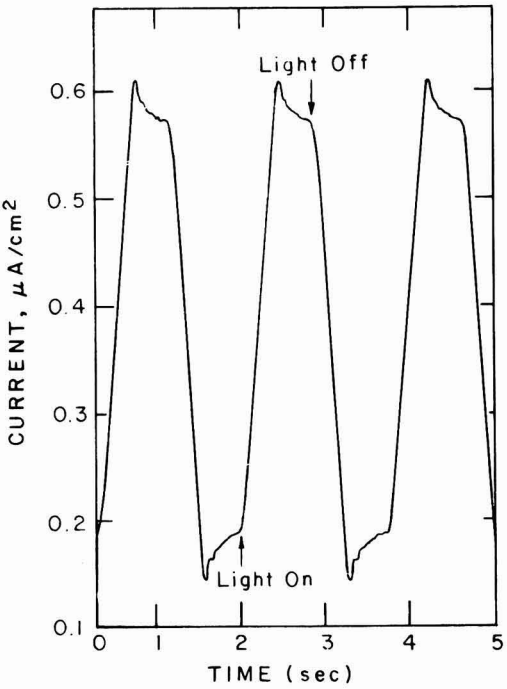


Fig. 2. The variation of photocurrent under chopped SBG illumination. The Ti oxide electrode was immersed in 0.5M Na_2SO_4, pH = 1.7 (adjusted with H_2SO_4), and under an applied potential of 1.2V *vs.* SCE. In this experiment all the power of the tungsten-halogen lamp (I_2) of wavelength ≧ 600 nm was used as the SBG illumination source. (The uniform slopes of the photocurrent *vs.* time curve are due to the mechanical chopping of a light beam of a significant cross section.)

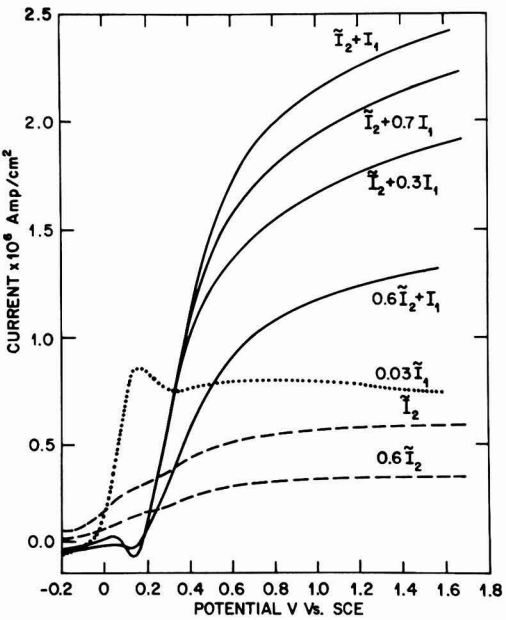


Fig. 3. Photocurrent *vs.* potential curves: dashed—recorded during chopped SBG illumination alone, at two relative intensities. (Using all the power of I_2 of λ ≧ 600 nm); dotted—recorded during chopped u.v. illumination (the u.v. beam intensity was attenuated by a diaphragm in this particular experiment to produce such small photocurrents); solid—recorded for several relative chopped SBG intensities in the presence of continuous BG (367 nm) illumination.

(i) *The cathodic transient component of* $\tilde{i}_{SBG}$.—A cathodic current transient must be the result of a limited photon-induced electron transfer in a direction from the bulk of the semiconductor toward the SC surface, *i.e.*, opposite the direction of charge flow in the main anodic photoprocess. Hence, such a transient may be due to a photon-assisted electron transfer from the valence band of the SC into empty states located at (or close to) the surface. This is schematically demonstrated in part (a) of Fig. 4. In the presence of continuous u.v. irradiation, this negative current transient becomes more pronounced, probably because some deep surface states are depopulated by the BG photons, thus increasing the probability of an electron transfer from the valence band to empty bandgap states at the surface. This explanation is in accordance with results reported by Gatos and Lagowski (12), who described an "inverted photovoltage," which was obtained for large bandgap semiconductors illuminated by light of SBG energy following u.v. irradiation. It was explained by electron transfer from the valence band into depopulated surface states (12). As the opposing field of the space charge layer in the SC increases, an electron transfer in a cathodic direction becomes less probable, and this may be the reason for the disappearance of the negative transient component

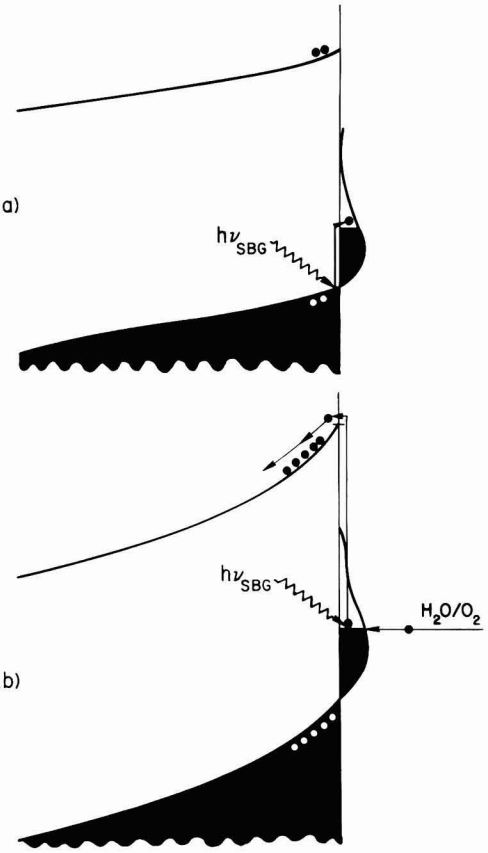


Fig. 4. Schematic representation of the possible origin of cathodic and anodic SBG photon-induced electron transfers: (a) A cathodic transient due to a photon-induced transfer from the valence band into an empty bandgap state. Such a negative current transient is expected under anodic polarizations only at small band bending and can be amplified by u.v.-induced depopulation of bandgap states. (b) An anodic current which may contain both transient and stationary components, due to a bandgap state to conduction band photon-induced electron transfer. The depopulation of such an active state may be possibly accompanied by an electron transfer from a water donor molecule. (All other electronic processes which may occur simultaneously at the illuminated oxide electrode surface were omitted for the sake of clarity.)

of $\tilde{i}_{SBG}$ at higher applied anodic potentials. Möllers *et al.* described a positive (anodic) transient current induced by a pulse of BG light in a TiO_2 photoanode in the same region of ascending photocurrent (13). We have obtained the same result with our Ti oxide material (see Fig. 3, dotted curve). This anodic transient is a mirror image of the SBG photon-induced cathodic transient described above, *i.e.*, it may be due to trapping of holes formed in the valence band by filled states at the surface (13).

(*ii*) *The enhancement of positive* $\tilde{i}_{SBG}$ *at higher anodic potentials by BG irradiation.*—The enhancement of $\tilde{i}_{SBG}$ by simultaneous u.v. irradiation is the larger and more significant effect measured. It seems to contain some clues to the possible involvement of bandgap states, located at the surface of the oxide electrode, in the water photoxidation process. The positive component of $\tilde{i}_{SBG}$ is most probably associated with photon-induced electron transfer from occupied states at (or close to) the electrode surface to states in the conduction band of the SC located in the space charge region, from which electrons can be further transferred by the depletion layer field into the bulk of the SC. This is schematically shown in part (*ii*) of Fig. 4. The positive component of i_{SBG} is thus a probe of occupied surface states which are located energetically inside the bandgap and exhibit significant charge-transfer interaction with the conduction band. The saturation of $\tilde{i}_{SBG}$ found at high intensities of SBG light seems to be associated with the limited rate of refilling of such active bandgap states. In the presence of u.v. irradiation a significant increase in the photon-induced bandgap → conduction band electron transfer is found at higher applied potentials (Fig. 3). Thus, the occupancy of some of the bandgap states seems to increase in this potential range due to the u.v. irradiation. This may be rationalized considering the following two processes:

(I) U.V.-induced photooxidation of water is expected to involve the formation of adsorbed intermediates such as OH radicals. The bonding of such radicals to the surface may result in an increase of the electron density at the SC-solution interface.

(II) Some of the electrons ejected from the valence band by u.v. photons into the conduction band may be trapped by surface states. The efficiency of such trapping is expected to decrease, however, at higher applied anodic potentials, where the stronger field in the space-charge layer will effectively drive the photoelectrons in the conduction band into the bulk of the SC. Since the measured enhancement actually increases with applied potential (Fig. 3, solid curves), the adsorption of the water-derived reaction intermediates (and, perhaps, products) seems to be the main process responsible for the apparent increased occupancy of the bandgap states induced by u.v. illumination. In any event, the energy spectrum of the enhancement of $\tilde{i}_{SBG}$ by continuous u.v. illumination seems to indicate the energetic location (with respect to the conduction bandedge) of some bandgap states located close to the surface which have a significant charge-transfer communication with the conduction band, as well as, possibly, with water molecules. As discussed above, these may be either "intrinsic" or chemisorption-induced states. From Fig. 5, which shows this spectrum, it can be seen that a significant fraction of such states is energetically located between the level of the H_2O donor molecule in solution [$\sim$ 1.3 eV below the conduction bandedge (1)] and the valence bandedge (3.2 eV below the CB edge). These states may be thus effective in the process of water photooxidation at Ti oxide electrodes. Further support for the involvement of such states in electron uptake from H_2O molecules comes from the stationary photocurrents which were measured with such Ti oxide electrodes under continuous SBG illumination (see Fig. 2): In order to maintain a stationary photoanodic current, electrons have to be transferred across the SC-solution interface at a steady rate. Considering the pure solutions employed, water seems to be the only possible electron donor. This seems to imply that water can be photooxidized at this SC material by SBG illumination via states in the gap, although the efficiency of this process is much less than that of the u.v.-induced photooxidation. This process is schematically shown in Fig. 4b. The last conclusion is in accordance with results and suggestions of Houlihan *et al.* (14), who found for Ti oxide prepared by the heating of Ti metal that the photon energy "threshold" for water photooxidation was somewhat lower than that found for single crystal TiO_2. The last authors suggested that the material obtained by thermal oxidation of Ti in a burner flame contains a number of mixed valence ("Magneli") Ti oxides. This may also explain the very broad spectrum of active bandgap states found with

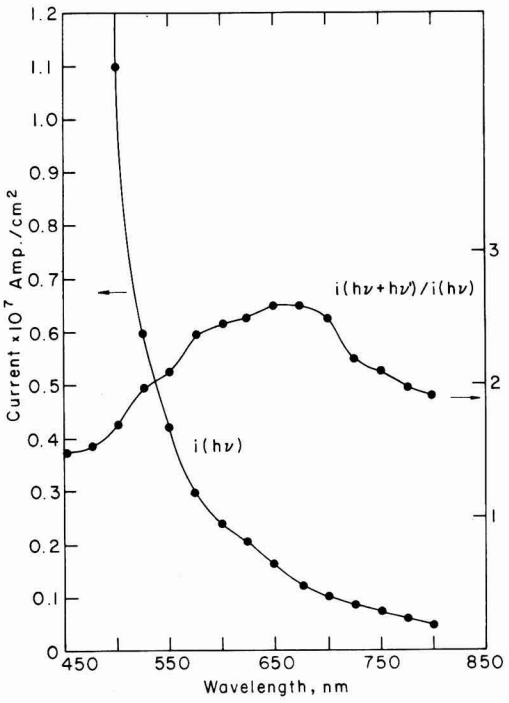


Fig. 5. The spectrum of $\tilde{i}_{SBG}$ and of its enhancement by continuous 367 nm irradiation. A Bausch & Lomb High-Intensity monochromator was used in the SBG beam in this experiment. The u.v. enhancement factor was calculated at each wavelength as: $\sim i_{SGB}$ in the presence of u.v. illumination/$\tilde{i}_{SBG}$ in the absence of u.v. illumination. This ratio is designated in the figure by: $i(h\nu + h\nu')/i(h\nu)$.

this type of oxide (Fig. 5). The introduction of active bandgap states at an appreciable density, so as to allow a relatively efficient photooxidative process through them [Fig. 4, part (b)], looks like an interesting possible solution for the lowering of photon energy thresholds of oxide semiconductor photoanodes.

Acknowledgment

Support by a grant from the U.S.-Israel Binational Science Foundation (BSF), Jerusalem, is gratefully acknowledged.

Manuscript submitted June 22, 1978; revised manuscript received Aug. 15, 1978.

Any discussion of this paper will appear in a Discussion Section to be published in the December 1979 JOURNAL. All discussions for the December 1979 Discussion Section should be submitted by Aug. 1, 1979.

REFERENCES

1. R. Memming, "Semiconductor Liquid-Junction Solar Cells," A. Heller, Editor, p. 38, (as well as other papers in Section II of the proceedings of this conference), The Electrochemical Society Softbound Symposium Series, Princeton, N.J. (1977).
2. H. Gerischer, *J. Electroanal. Chem. Interfacial Electrochem.*, **82**, 133 (1977).
3. M. Knotek, in "Electrode Materials and Processes for Energy Conversion and Storage," J. D. E. McIntyre, S. Srinvasan, and F. G. Will, Editors, p. 234, The Electrochemical Society Softbound Symposium Series, Princeton, N.J. (1977).
4. S. Gottesfeld and S. Srinivasan, *J. Electroanal. Chem. Interfacial Electrochem.*, **86**, 89 (1978).
5. S. N. Frank and A. J. Bard, *J. Am. Chem. Soc.*, **97**, 7427 (1975).
6. H. Morisaki, M. Hariya, and K. Yazawa, *Appl. Phys. Lett.*, **30**, 7 (1977).
7. J. G. Mavroides, V. E. Hemrich, H. J. Zeiger, G. Dresselhaus, J. A. Kafalas, and D. F. Kolegar, in "Electrode Materials and Processes for Energy Conversion and Storage," J. D. E. McIntyre, S. Srinivasan and F. G. Will, Editors, p. 45, The Electrochemical Society Softbound Symposium Series, Princeton, N.J. (1978).
8. D. Laser, M. Yaniv, and S. Gottesfeld, *This Journal*, **125**, 358 (1978).
9. C. K. Dyer and J. S. L. Leach, *ibid.*, **125**, 358 (1978).
10. A. Heller, K. C. Chang, and B. Miller, *ibid.*, **124**, 697 (1977).
11. A. Fujishima and K. Honda, *Nature (London)*, **238**, 37 (1972).
12. H. C. Gatos and J. Lagowski, *J. Vac. Sci. Technol.*, **10**, 130 (1973).
13. F. Möllers, H. J. Tolle, and R. Memming, *This Journal*, **121**, 1160 (1974).
14. J. F. Houlihan, D. P. Madacsi, E. J. Walsh, and L. N. Mulay, *Mater. Res. Bull*, **11**, 1191 (1976).

Defect Etch for <100> Silicon Evaluation

D. G. Schimmel

Bell Laboratories, Reading, Pennsylvania 19604

ABSTRACT

The Secco etch, 2(HF):1(0.15M $K_2Cr_2O_7$) with ultrasonic agitation, is widely used to determine dislocation densities in <100> Si. Experiments have shown that under certain conditions, the cavitation of the ultrasonics can generate anomalous defect etch pits. A new defect etch formulation was developed for evaluating <100> Si ingot material which does not require ultrasonic agitation. It consists of 2HF:1(1M CrO_3). The etching time compared to Secco etch with ultrasonics is reduced by one-half in developing etch pits of equivalent size. This composition is useful for revealing dislocations in 0.6-15 Ωcm n- and p-type silicon. In addition, dislocation etch pits are readily developed in more heavily doped <100> Si crystals using a mixture of 2HF:1(1M CrO_3):1.5(H_2O).

Sirtl etch has been widely used to reveal crystal defects in silicon, particularly for (111) surface orientations (1). The recommended compositions ranged from 0.4/0.2/1 to 0.2/0.3/1 ratios by weight of HF (H_2O free)/CrO_3/H_2O, respectively. Application of these etch formulations to (100) silicon surfaces has not been satisfactory. Secco has formulated an etch composition of 2 parts HF to 1 part 0.15M $K_2Cr_2O_7$ for revealing dislocations in (100) silicon surfaces (2). Ultrasonic agitation is required to minimize etching artifacts due to gas bubble formation during etching, and to minimize the etching time necessary to achieve easily visible and identifiable dislocation etch pits. Even with ultrasonic agitation, however, etch times of 10-20 min are required for 4-15 Ωcm p-type <100> Si and up to 45 min with a diluted Secco etch for 0.01 Ωcm p-type <100> Si.

Production <100> Si ingot material was evaluated using Secco etch as a control. Results on dislocation densities in two different etching facilities did not, however, correlate with one another. Investigation of these defect etch pit discrepancies revealed that the ultrasonic energy differed at the two facilities.

This paper describes the problem associated with defect etching using ultrasonic agitation, and presents an etch composition based on an HF-CrO_3-H_2O mixture which does not require such agitation.

Since Sirtl etch is not particularly useful for (100) surfaces (3), only Secco etch results are compared with this new etch formulation.

Experimental

Secco etch—production vs. laboratory results.—Secco-etched ingot test samples were reprocessed in the laboratory in order to verify the production facility etch pit results. The test samples were chemically repolished in 6:1:1 [HNO_3:HF:HAc (acetic acid)] to remove the original defect etch pits. They were then reetched with Secco etch, and the etch pit results were compared with those obtained in the production facility. In early comparisons correlation was good, however at a certain point in time, marked discrepancies were observed between the dislocation densities obtained in the laboratory and those obtained in the production facility. Ingot material characterized in the latter as being dislocation free (< 500 dislocations/cm²) was found to have from 5000 to 50,000 defect etch pits/cm² when evaluated in the laboratory. Characteristics of these laboratory defect etch pits are shown in Fig. 1 for two different 3 in. diam 4-15 Ωcm p-type <100> ingots. They are not representative of dislocation etch pits normally found in <100> silicon.

Ultrasonic unit comparison.—The production ultrasonic equipment used for the Secco etching employed a polypropylene tank with about ½ in. thick side walls with the transducers mounted on the outside of the walls. The laboratory ultrasonic unit, however, used a stainless steel tank which does not attenuate the transmission of ultrasonic energy as much as the thick plastic walled production equipment. During the course of this correlation study, the original laboratory unit was replaced with a new unit (40 kHz with ~180W output). The defect density discrepancies arose at about the time this new unit was placed into operation. However, regardless of the ultrasonic equipment used, test samples and etchants were always contained in plastic beakers because of the HF in the etchant and also to allow the use of smaller etch solution volumes than would be required for the ultrasonic tanks.

In order to specify the Secco etch for use, it appears necessary also to define the ultrasonic energy level employed. At the present time, however, all known methods of monitoring ultrasonic energy in solution, *i.e.*, cleaning tanks, are essentially qualitative. Conse-

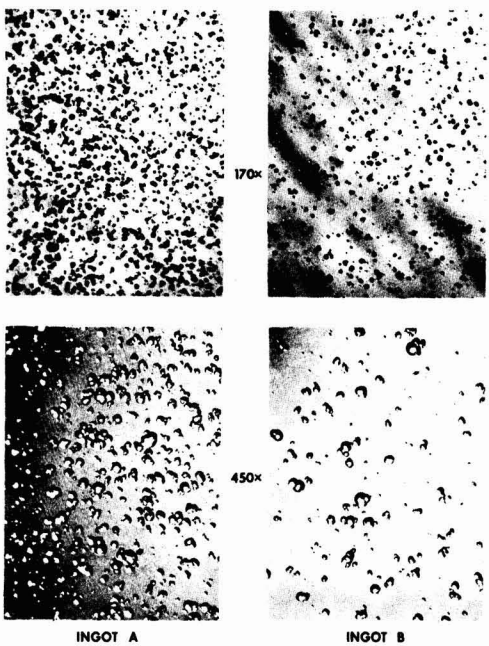


Fig. 1. Comparison of etch pit results of ingot A and ingot B (4-15 Ωcm p-type <100>). 10 min Secco etch (0.15M $K_2Cr_2O_7$) with ultrasonic agitation.

Key words: silicon etching, <100> silicon, dislocations.

quently, specifying the ultrasonic energy level for the Secco etch is very difficult, if not impossible.

New etch formulation.—One of the governing factors in defect etch pit formation is the etch rate. For a dislocation etch pit to form, the area at the dislocation must etch at a faster rate than the surrounding defect-free surface.

Ultrasonic agitation increases the etch rate of Si by enhanced solution stirring and increased solution temperature. With the HF concentration constant, variation of the Cr^{+6} (chromium) oxidizing agent concentration also affects Si etch rate. Figure 2 shows the effect of both Cr^{+6} concentration and ultrasonic agitation on the etch rate of 4-15 Ωcm p-type <100> Si. Chromic acid (CrO_3) was used to vary the Cr^{+6} concentration since $K_2Cr_2O_7$ (potassium dichromate) has a limited solubility in water (max conc. ≅ 0.17M). Since $K_2Cr_2O_7$ has 2 atoms of Cr per mole, a 0.15M $K_2Cr_2O_7$ solution is equivalent to a 0.3M solution of CrO_3 with respect to the Cr^{+6} content.

While Secco etch has been shown to decorate dislocation etch pits on (100) Si surfaces (2, 3), extended etch times with ultrasonic agitation may cause additional anomalous etch pits. An approach which suggested itself for replacing Secco etch with one etch that did not require ultrasonic agitation was to utilize equivalent etch rates. From Fig. 2, Secco etch [2 (HF):1(0.15M $K_2Cr_2O_7$)] with ultrasonics has an etch rate of ~1.65 μm/min as determined from the curve at 0.3M Cr^{+6} concentration. A close approximation of etch rate without ultrasonic agitation would involve use of a mixture containing 1M CrO_3 with ~1.75 μm/min. Thus an etch formulation of 2(HF): 1(1M CrO_3) without ultrasonic agitation should give etch pit results similar to the Secco etch with ultrasonic agitation.

Defect etch comparison.—Ideally, a comparison of defect etch solutions is to compare the etch pit results from different solutions on the same Si sample. This is possible with relatively thick samples (~ ⅛-¼ in.) from ingot material. In addition, if the test sample is taken near the tang end of the ingot, there will be a prevalence of slip dislocations which are readily identifiable and reproducible with repeated etching. Because the sample is thick it can be chemically polished repeatedly in 6:1:1 of HNO_3:HF:HAc to remove surface damage or previously decorated etch pits, and then reetched with a defect etch to again produce dislocation etch pits which can be monitored and compared with previous results.

Ingot test pieces for the etch pit comparisons were taken from the various ingots near the tang end with

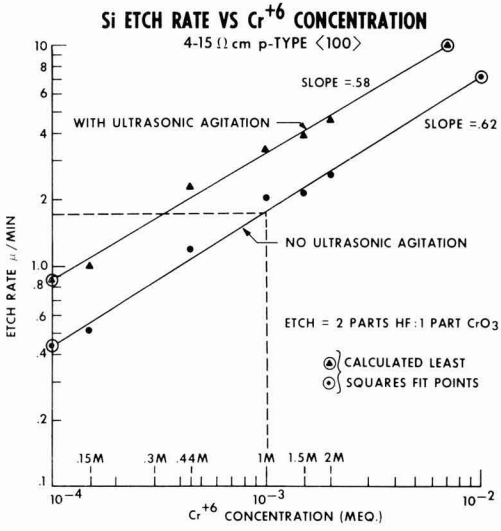


Fig. 2. Log-log plot of 4-15 Ωcm p-type <100> Si etch rate (μm/min) *vs.* Cr^{+6} concentration with and without ultrasonic agitation.

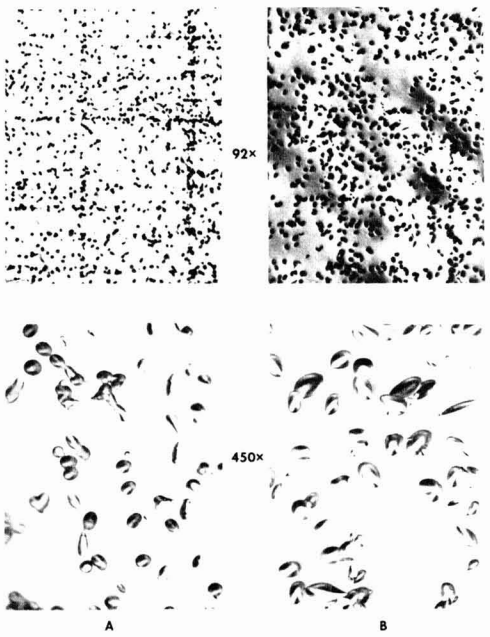


Fig. 3. Comparison of defect etch pits on same (4-15 Ωcm p-type <100>) Si ingot sample: (a) 10 min Secco etch, 2(HF): 1(0.15M $K_2Cr_2O_7$) with ultrasonic agitation; (b) 5 min etch in 2(HF):1(1M CrO_3) and no ultrasonic agitation.

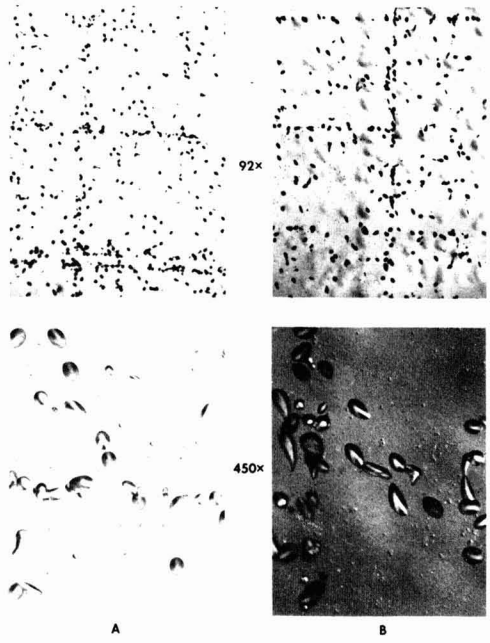


Fig. 4. Same as Fig. 3 except ingot sample is 0.6 Ωcm p-type <100>.

slip dislocations present. Figures 3 and 4 illustrate the dislocation etch pit results of the Secco etch of 2(HF):1(0.15M $K_2Cr_2O_7$) with ultrasonic agitation for 10 min *vs.* 2(HF):1(1M CrO_3) with solution agitation by beaker rotation (no ultrasonic agitation) for 5 min. Figure 3 is an etch pit comparison on 4-15 Ωcm p-type <100> and Fig. 4 is a comparison of 0.6 Ωcm p-type <100>. It is important to note that the 1M CrO_3 etch delineates dislocations which intercept the surface at shallow angles. This is demonstrated by the elongated etch pits seen in Fig. 3 and 4. It is also interesting that the 1M CrO_3 etch solution develops equivalent or larger dislocation etch pits than the Secco etch in only half the etching time even though the over-all etch rate is about the same. This was the case for all the ingot material studied.

The etch rate of Si increases with increasing doping concentration. As the etch rate increases, particularly with p-type material, Si staining becomes a problem (4). This increased etch rate of undamaged silicon without an accompanying increase in the etch rate of damaged silicon plus the heavy staining eventually obliterates any defect etch pits. It was previously found that this problem can be circumvented by dilution of the defect etch solution. Thus for 0.01 Ωcm p-type <100>, Secco etch was diluted with water to 2(HF):1(0.15M $K_2Cr_2O_7$):7(H_2O). This reduces the etch rate and minimizes the stain film formation.

Dilution *vs.* etch rate for 0.01 Ωcm p-type <100> with 2(HF):1(1M CrO_3) etchant is shown in Fig. 5. From the curve, the diluted formula of 2(HF):1(1M CrO_3):1.5(H_2O) has an etch rate of ~1.8 μm/min for 0.01 Ωcm p-type Si. This is essentially equivalent to the etch rate of the undiluted etch for 4-15 Ωcm p-type Si. Figure 6 shows the comparison of dislocation etch pits on 0.01 Ωcm p-type <100> Si for diluted Secco (2:1:7) with ultrasonic agitation for 20 min and the 5 min etch of 2(HF):1(1M CrO_3):1.5(H_2O) with solution agitation by rotating beaker only.

All of the etch pit comparisons to this point were for p-type <100> Si. However, <100> n-type Si can also be decorated and Fig. 7 shows the results of the two undiluted etchants on 0.2 Ωcm material. Defect etch pit development on n-type material is always smaller in size than for p-type and the n-type Si usually requires longer etching times to develop discernible etch pits.

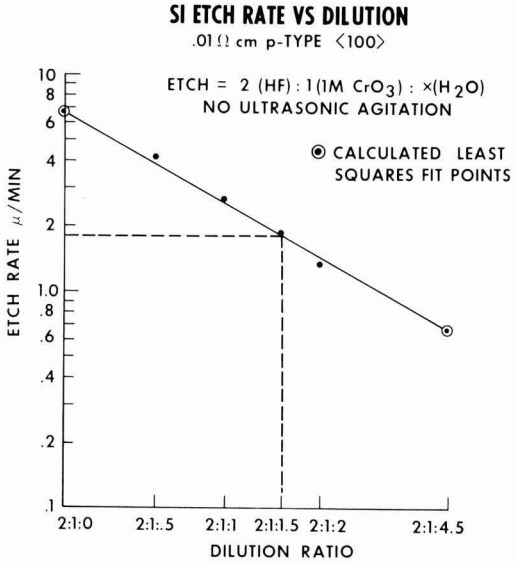


Fig. 5. Silicon etch rate of 0.01 Ωcm p-type <100> *vs.* water dilution of 2(HF):1(1M CrO_3) with no ultrasonic agitation.

All the comparison examples presented show that a 2(HF):1(1M CrO_3) etchant without ultrasonic agitation

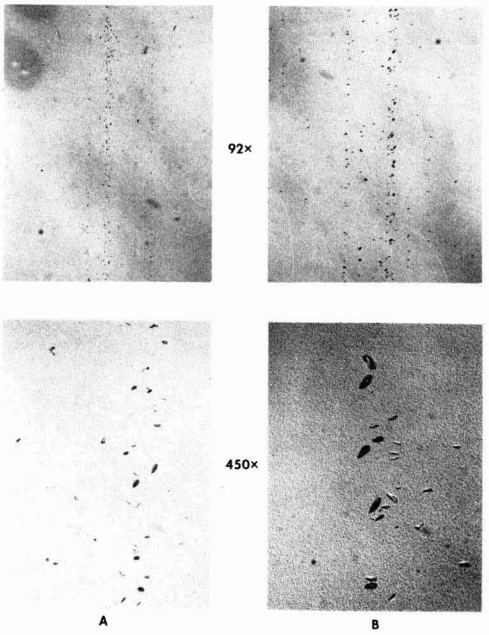


Fig. 6. Comparison of defect etch pits on same (0.01 Ωcm p-type <100>) Si ingot sample: (a) 20 min diluted Secco etch, 2(HF):1(0.15M $K_2Cr_2O_7$):7(H_2O), with ultrasonic agitation; (b) 5 min etch, 2(HF):1(1M CrO_3):1.5(H_2O) with no ultrasonic agitation.

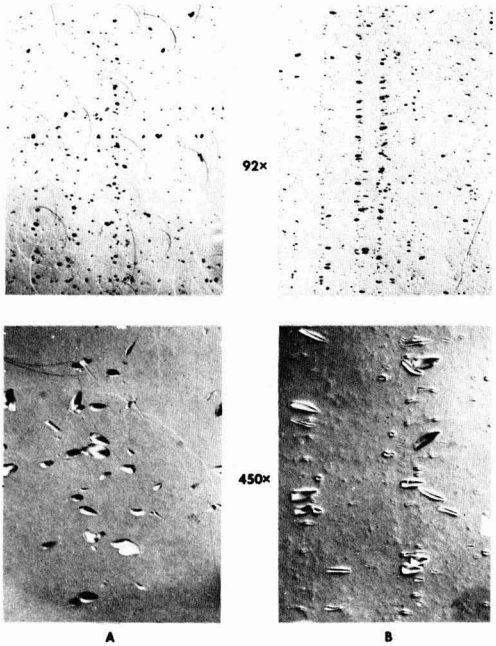


Fig. 7. Comparison of defect etch pits on same (0.2 Ωcm n-type <100>) Si ingot: (a) 20 min Secco etch, 2(HF):1(0.15M $K_2Cr_2O_7$) with ultrasonic agitation; (b) 10 min etch of 2(HF):1(1M CrO_3) with no ultrasonic agitation.

is capable of delineating dislocations in Si ingot material. It should be noted that although not shown, this etchant can and does delineate other defects such as stacking faults. The optimum etch conditions, of course, vary with the substrate resistivity and conductivity type.

Effect of ultrasonic energy.—Three identical thin-walled (~0.040 in. thick) polypropylene beakers had been used for Secco etching the 3 in. diam test ingot samples and wafers in the laboratory. Since plastic attenuates transmitted ultrasonic energy, Secco etch pit results from these beakers were compared to see if equivalent etch pit densities would result. A 3 in. diam wafer (Syton polished and cleaned) was scribed and broken into thirds. Each third of the wafer was then Secco etched for 10 min in one of the above beakers with ultrasonic agitation. The etch results varied widely, as seen in Fig. 8. Apparently, each beaker attenuated the ultrasonic energy to a different degree. However, the type of etch pits formed are similar to those shown in Fig. 1.

These apparent ultrasonic energy induced etch pits suggest two possibilities: (i) Ultrasonic energy enhances the defect etch so as to reveal defects not normally delineated; or (ii) Cavitation, depending on the energy level, generates surface damage which results in the defect etch pits seen. The second possibility is more probable and was investigated further.

A Syton polished 3 in. diam wafer was scribed and broken in half. One half was treated with ultrasonic agitation in water for 10 min using 140V input voltage rather than normal line voltage to maximize possible Si surface damage. The other half of the wafer was kept untreated as a control. Both halves of the wafer were then etched in the 2(HF):1(1M CrO_3) with no ultrasonic agitation for 5 min. The results, shown in Fig. 9, suggest strongly that excessive ultrasonic energy (cavitation level) can generate Si surface defects.

It is important to note that damage to Si surfaces in ultrasonic baths does not always occur. There appears to be a threshold at which cavitation will generate Si surface damage, as evidenced by defect etching.

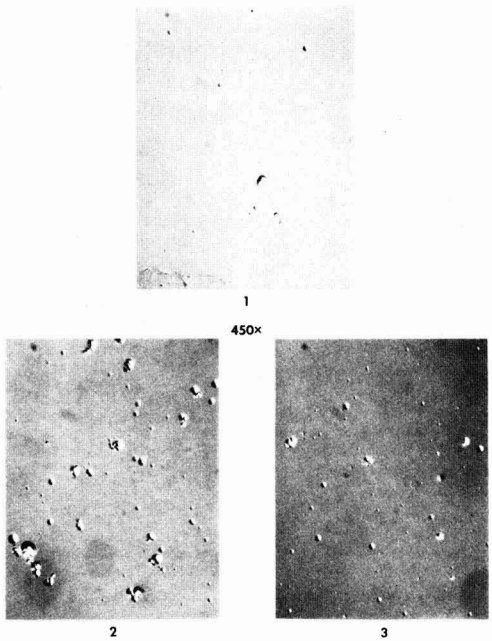


Fig. 8. Etch pit density comparison for 3 different 1000 ml Lancer polypropylene beakers with 10 min Secco etch, 2(HF):1(0.15M $K_2Cr_2O_7$), with ultrasonic agitation, one-third of same wafer in each beaker.

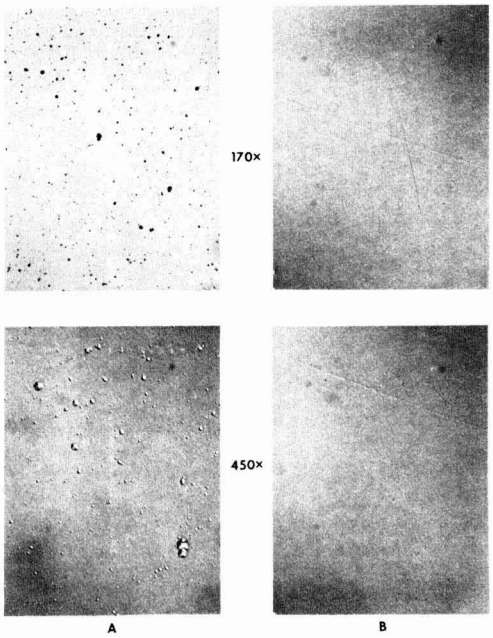


Fig. 9. Etch pit comparison of 2 halves of a 3 in. diam wafer with 5 min etch of 2(HF):1(1M CrO_3) with no ultrasonic agitation: (a) Test half pretreated 10 min in H_2O with ultrasonic agitation (140V input voltage to ultrasonic unit); (b) control half wafer had no ultrasonic pretreatment.

As a result, a recommended method for checking an ultrasonic unit is defect etching of ultrasonic-treated Si test wafers using 2(HF):1(1M CrO_3) without ultrasonics. Of course, heavily doped substrates would require the use of the water diluted etch formulation.

Defect etching of devices.—Although this paper is concerned with ingot evaluation, defect etching results on devices should also be mentioned. The presence of p-n junctions in a wafer influences and alters the etch rate of the respective doping types. As a consequence, the etch formulation described in this paper for ingot evaluation is not applicable to p-n junction diagnostics due to over etching, particularly of the p-areas.

Conclusions

A new, simple etch formulation of 2(HF):1(1M CrO_3) which does not require the use of ultrasonic agitation has been developed for <100> Si evaluation. An added bonus is the considerable reduction in etching time required over that of the Secco etch. Heavily doped <100> Si ingot material can be evaluated by a simple water dilution of the etchant to 2(HF):1(1M CrO_3):1.5(H_2O).

It has been shown that ultrasonic agitation is capable of producing Si surface damage under certain conditions.

It is also important to note that the new etch formulation developed for <100> Si evaluation is not applicable to p-n junction diagnostics.

Manuscript submitted June 2, 1978; revised manuscript received Sept. 8, 1978.

Any discussion of this paper will appear in a Discussion Section to be published in the December 1979 JOURNAL. All discussions for the December 1979 Discussion Section should be submitted by Aug. 1, 1979.

Publication costs of this article were assisted by Bell Laboratories.

REFERENCES
1. E. Sirtl and A. Adler, *Z. Metallkd.*, **52**, 529 (1961).
2. F. Secco d'Argona, *This Journal*, **119**, 948 (1972).
3. D. G. Schimmel, *ibid.*, **123**, 734 (1976).
4. D. G. Schimmel and M. J. Elkind, *ibid.*, **125**, 152 (1978).

Ion Beam Exposure of Resist Materials

Masanori Komuro, Nobufumi Atoda, and Hisazo Kawakatsu

Electrotechnical Laboratory, Tanashi, Tokyo, 188, Japan

ABSTRACT

Ion beam exposure characteristics of a positive resist, poly(methylmetacrylate) (PMMA), and a negative resist, poly(dimethylsiloxane) (PDMS), are studied. It is found that sensitivities to helium and argon ions in terms of electronic charge per unit area are much higher than in the case of electron exposure. Moreover, contrasts, gradients of the exposure characteristic curves, are somewhat better in ion exposure. Using the energy deposition rate of ions calculated from an extended LSS theory, the radiation yields for cross-linking and main chain scission are estimated. The radiation yields caused by collisions of the incident ion with electrons in the polymer are nearly equal to those in electron exposure. On the other hand, the radiation yields caused by nuclear collisions are one-half in PMMA and one-fifth in PDMS as large as the radiation yields in electron exposure. In order to investigate applicability of ion exposure to the lithographic process, a simple pattern of 2.7 μm width slit is duplicated. From the cross-sectional views observed with a scanning electron microscope, it is found that high fidelity and high resolution pattern forming is possible. A fabricating method of proximity contact between a mask and a resist film is proposed.

Lithographic performances in electron-beam or x-ray lithography depend on the interaction of the radiation with resist materials. The sensitivity of the resist, which limits the fabrication speed, is related to the energy transferred to the resist and the over-all efficiency of conversion of this energy to chemical changes such as main chain scission in positive resist and cross-linking in negative resist. The resolution depends on the lateral spread of the incoming radiation and the contrast of the resist which determines the spatial response. A high resolution pattern with submicron dimensions has been successfully produced in electron lithography, owing to the understanding of electron scattering and the use of a high contrast resist, poly(methylmetacrylate) (PMMA) (1). It is, however, a difficult problem to optimize both sensitivity and resolution simultaneously.

Chemical changes of resist materials can be induced effectively also by ion beam exposure. The amount of energy deposited per unit path length of ion beam is much greater than that of electron beam. Therefore, sensitivity to ion beam measured in terms of incident charge per unit area is expected to be higher, as suggested by Seliger *et al.* (2). High resolution can be also expected, since the lateral spread of ion beam in resist film is much less than in the case of electron beam. Thus the ion beam exposure of resists has possibility as a new lithographic technique of high resolution and of high fabrication rate, although the use may be limited at the present stage because of the difficulty of fine focusing down to 1 μm diam as a scanning exposure system and the difficulty of making a see-through mask as a pattern duplication system.

In the present work, ion exposure characteristics of the positive resist, PMMA, and a negative resist, poly(dimethylsiloxane) (PDMS), are studied. The acceleration energy of the ion is so chosen that the projected range is comparable to or more than the resist thickness. For a detailed investigation of the sensitivity, the radiation yield, defined as the number of chemical events per 100 eV absorbed, is estimated on the basis of energy deposition rate calculated by use of the LSS (Lindhard, Sharff, and Shiøtt) theory (3). The energy dissipation of ion beam is caused by electronic and nuclear collisions. Since effects of the two components are considered to be different from each other, radiation yields corresponding to both components are estimated separately. As a lithographic process, duplication of a simple pattern is attempted, and an application to proximity contact between a mask and a resist film is proposed.

Key words: lithography, radiation yield, pattern duplication, sensitivity, resolution.

Theoretical Basis

When resist polymers are exposed to ionizing radiation such as an accelerated charged particle and x-ray, main chain scission and/or cross-linking are induced to the extent according to the amount of energy deposited by the radiation (4). Thus, the sensitivity in terms of the commonly used definition of electronic charge per unit area is closely related to energy dissipation of the radiation. The number of chemical events associated with energy dissipation is conventionally described in terms of the G-value.

To estimate the G-value in ion exposure, energy dissipation rate of ion beam as a function of the penetration depth z is calculated from the extended LSS theory proposed by Brice (5, 6). According to his treatment, the first-order solution of the projected range and the root mean square spread parallel to the projected range are obtained and energy deposition caused by electronic and nuclear collisions, $S_{el}(z)$ and $S_n(z)$, respectively, is computed on the assumption that the spatial distribution for the ions is gaussian. The calculated results for PMMA are shown in Fig. 1 with the depth dose function of electron beam, $S(z)$, calculated from the formula proposed by Hoff and Everhart (7). It is shown in the figure that the energy deposition rates of the ions are about 100 times as large as that of electron beam. Further, the energy deposition curves for the ions show strong dependence on the penetration depth into the resist film. This implies that regarding the fragmented average molecular weight as a constant value over the resist film is not necessarily valid in the case of exposure by the ion

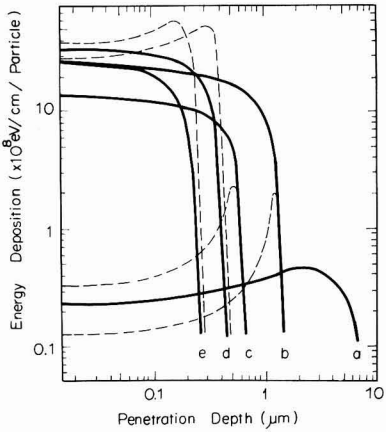


Fig. 1. Calculated curves of energy deposition rate in PMMA resist as a function of the penetration depth. (a) 20 kV electron, (b) 200 kV He^+, (c) 60 kV He^+, (d) 250 kV Ar^+, and (e) 150 kV Ar^+. For the curves of the ions, solid and broken lines are of electronic and of nuclear collision loss, respectively.

with the acceleration energy adopted here. The procedures to estimate the G-values of positive and negative resist in ion exposure are described in the following sections.

Positive resist.—In a positive resist, a formula relating the average molecular weight M_f obtainable after ion exposure to the energy deposition rate can be derived in the similar way as in electron exposure. In electron exposure, the formula is (8)

$$M_f = \frac{M_n}{1 + KqG(s)S(z)} \quad [1]$$

with

$$K = M_n/e\rho N_A 100$$

where M_n is the initial number average molecular weight, e the electronic charge, q the exposure dose, N_A the Avogadro number, ρ the density of the resist, and $G(s)$ the radiation yield for chain scission in electron exposure.

In ion exposure, the interaction of the ion with the resist polymer consists of two components: the electronic collision and the nuclear collision. The two components are presumably different in contribution to chemical events, and energy deposition rates corresponding to those are also different in the dependence on the penetration depth as seen in Fig. 1. Thus, in the present work, the radiation yield is separated into two components and consequently the number of chain scissions is given by the summation of the contribution from the two components. As a result

$$M_f = \frac{M_n}{1 + Kq\{G_{el}(s)S_{el}(z) + G_n(s)S_n(z)\}} \quad [2]$$

where $G_{el}(s)$ and $G_n(s)$ are the radiation yields for chain scission caused by electronic collisions and nuclear collisions, respectively.

Solubility rate of polymer with relatively low molecular weight M can be expressed as $\beta M^{-\alpha}$ (9). For PMMA with molecular weight up to 2×10^5, Greeneich (10) has found more precise formula, $R_o + \beta M^{-\alpha}$, where R_o, β, and α are empirically determined. When a resist film is so thin that $S(z)$, $S_{el}(z)$, and $S_n(z)$ are regarded as constants, the resist thickness removed after the development is simply obtained by the product of the solubility rate and the development time T. As the film thickness becomes thicker, the dependence of energy deposition rate on the penetration depth cannot be neglected. Then the fragmented molecular weight and the solubility rate should be treated as a function of z. In such a case, the relationship between T and the dissolved thickness d becomes (10, 11)

$$T = \int_0^d \frac{dz}{R_o + \beta M_f(z)^{-\alpha}} \quad [3]$$

where PMMA film is assumed to be dissolved successively from the resist surface in developer.

Using $G(s)$ obtained in electron exposure (4), the constants, R_o, β, and α, are given from the comparison of Eq. [3] with the experimental relationships between T and d. Then the G-values of ions are determined.

Negative resist.—Negative resist is cross-linked and converted to insoluble gels by electron or ion irradiation, so that the desired patterns are delineated in the resist. The cross-linking coefficient, the average number of cross-linked sites per molecule of weight average molecular weight, is related to the ion beam exposure dose q in the same way as in electron exposure (8, 12)

$$\delta = K'q\{G_{el}(cl)S_{el}(z) + G_n(cl)S_n(z)\} \quad [4]$$

with

$$K' = M_w/e\rho N_A 50$$

where $G_{el}(cl)$ and $G_n(cl)$ are radiation yields for cross-linking caused by electronic and nuclear collisions, respectively, and M_w the weight average molecular weight of the negative resist. When the value of δ at the interface between the resist and the substrate becomes more than a critical value, gel point, an insoluble film is left on the substrate after the development (13). Since the gel point is independent of incident radiation, the relationship between the gel dose q_{me}, defined as the minimum dose necessary to form the insoluble film on the substrate in electron exposure, and q_{mi}, that in ion exposure, is derived as

$$G(cl)q_{me}S(d_o) = G_{el}(cl)q_{mi}S_{el}(d_o) + G_n(cl)q_{mi}S_n(d_o) \quad [5]$$

where $G(cl)$ is the radiation yield for cross-linking in electron exposure and d_o the initial film thickness. Since the magnitude of $S_{el}(d_o)$ and $S_n(d_o)$ depends strongly on primary ion species, accelerating voltage and initial film thickness, the ratios of $G_{el}(cl)$ and $G_n(cl)$ to $G(cl)$ can be separately obtained from the values of q_{mi} measured under the different experimental conditions.

Experimental Procedures

The PMMA used here had an average molecular weight of 1.85×10^5 and was dissolved in trichloroethylene (TCE). Sample films were prepared by conventional spin-coating on an aluminum film evaporated on glass plates and prebaked for 30 min at 170°C. After exposure to electron or ion beam, the samples were developed in methyl isobutyl ketone (MIBK) at 25°C. Periodically the samples were removed out of the solvent and the thickness difference between the exposed and the unexposed area was measured by a stylus profilometer (Talystep). Figure 2 shows a dependence of the dissolved thickness on a development period, where the sample is irradiated with the electron dose of 1.7×10^{-5} C/cm². It is ascertained from this figure that the interrupted development and measurement results in the same feature of the dissolution curve. The dissolved thickness measured from the initial film surface was obtained by adding the thickness loss in the unexposed area to the values determined above.

The PDMS (14) of an average molecular weight of 6.1×10^5 was dissolved in TCE and then spin-coated on the same substrate as used for PMMA samples. After electron or ion exposure, the samples were developed in TCE for more than 2 min. The remaining resist thickness was measured by Talystep after evap-

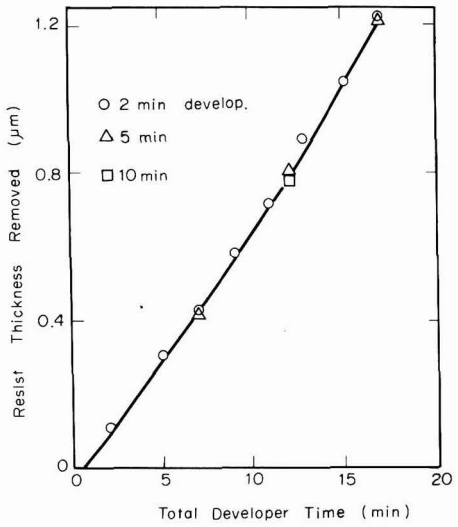


Fig. 2. A dependence of the dissolved thickness on a development period. The PMMA sample is irradiated with 1.7×10^{-5} C/cm².

orating an aluminum film of about 800Å in order to avoid deformation of the resist by the stylus.

A scanning electron microscope was used for electron irradiation experiments at an accelerating voltage of 20 kV and the typical area of 10^{-2} cm² was exposed. For ion irradiation, an ion implantation system was used and helium and argon ions were chosen as light and heavy ion species which are chemically inactive.

Results and Discussion

The positive resist PMMA.—Figure 3 shows the experimental curves of the resist thickness removed after the development time of 2 min *vs.* the incident dose of electron, He^+ and Ar^+, where the initial film thickness is 0.21 μm. It is observed that the sensitivities to He^+ and Ar^+ are about 60 and 100 times, respectively, as high as that to electron. At the same time, the contrasts are also high in ion exposure.

The development constants, R_o, β, and α, are determined from electron exposure experiments. Figure 4 shows the resist thickness removed as a function of the development time at various electron doses. The best fit between theoretical curves calculated from Eq. [3] and the experimental results is found when $R_o = 84$ Å/min, $\beta = 3.9 \times 10^8$ Å/min, and $\alpha = 1.41$, using a value of 1.9 events/100 eV for the radiation yield $G(s)$ (4). In Fig. 4, 5, and 8, it is found that dissolution begins after an induction period, and the time lag for dissolution becomes long with the decrease in exposure dose. The phenomenon has been also reported

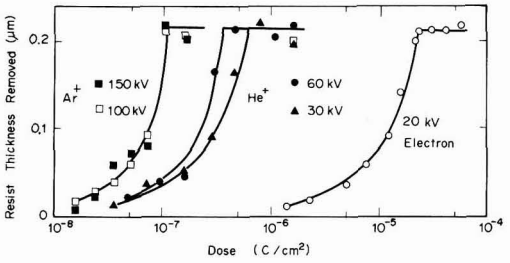


Fig. 3. Exposure characteristics of PMMA resist with electron and ion irradiation.

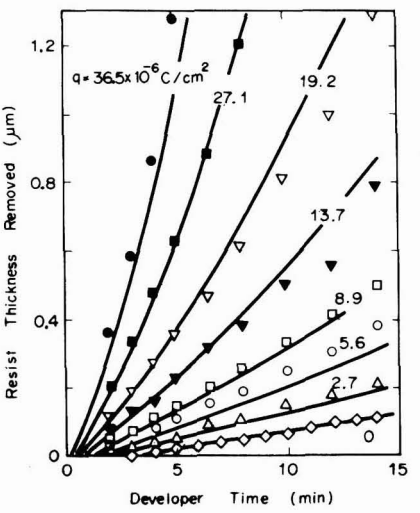


Fig. 4. Experimental and theoretical dissolution characteristics of PMMA at various doses of 20 kV electron. Solid lines are the theoretical curves calculated as $G(s) = 1.9$ events/100 eV, $R_o = 84$ Å/min, $\beta = 3.9 \times 10^8$ Å/min, and $\alpha = 1.41$.

for PMMA by Greeneich (10) and Kuroda (15). Description of the details such as a dependence on molecular weight will be published elsewhere. Here, the solubility rate is defined in the nearly linear portion after the starting time of dissolution and in the calculation of T from Eq. [3] the lag time obtained from the experimental data is simply added.

Using the values of the development constants thus determined, the radiation yields in ion exposure are in turn obtained in the same way as in the electron exposure described above. Figure 5 shows the relationship between the resist thickness removed and the development time at various doses of 200 kV He^+. Since the energy deposition by 200 kV He^+ is almost due to the electronic component as shown in Fig. 1, $G_{el}(s)$ can be determined on the assumption that

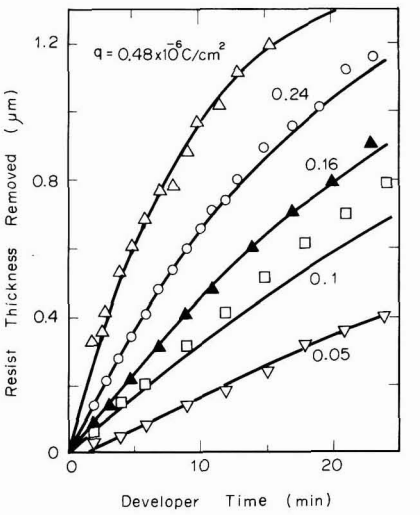


Fig. 5. Experimental and theoretical dissolution characteristics of PMMA at various doses of 200 kV He^+. The curves are calculated as $G_{el}(s) = 1.7$ and $S_n(z) = 0$.

$S_n(z) = 0$. The best fit of experimental points with theoretical curves from Eq. [3] is obtained when $G_{el}(s) = 1.7$. The curves in Fig. 5 are calculated ones using $G_{el}(s) = 1.7$. In the case of Ar^+ irradiation, the nuclear energy loss is larger than the electronic component. Therefore, $G_n(s)$ is determined by comparison of theoretical calculation with the experiments of 150 kV Ar^+ using $G_{el}(s) = 1.7$. The results are shown in Fig. 6, where theoretical curves are calculated for $G_n(s) = 0.9$.

The obtained values of $G_{el}(s)$ and $G_n(s)$ are in turn compared with experiments under different conditions for verification. Figures 7 and 8 are the dissolution characteristics to 60 kV He^+ and 250 kV Ar^+, respectively where solid lines are the calculated curves by use of $G_{el}(s) = 1.7$ and $G_n(s) = 0.9$. The calculated results agree very well with the measured results and, hence, the validity of the G-values obtained here is supported, although the values are not confirmed by a direct measurement of the molecular weight.

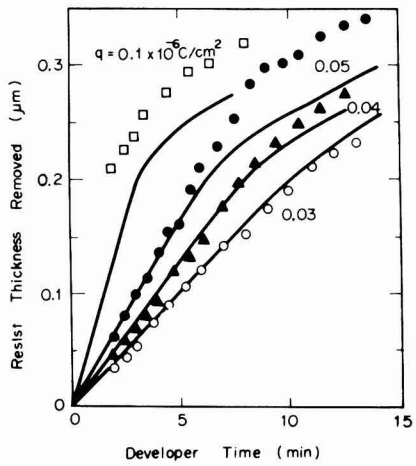


Fig. 6. Experimental and theoretical dissolution characteristics of PMMA at various doses of 150 kV Ar^+. The curves are calculated as $G_{el}(s) = 1.7$ and $G_n(s) = 0.9$.

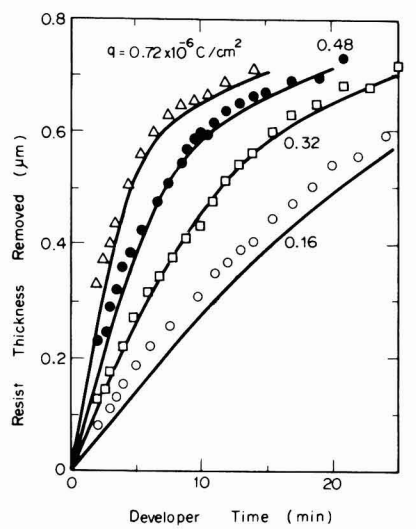


Fig. 7. Experimental and theoretical dissolution characteristics of PMMA at various doses of 60 kV He^+. The curves are calculated by use of $G_{el}(s) = 1.7$ and $G_n(s) = 0.9$.

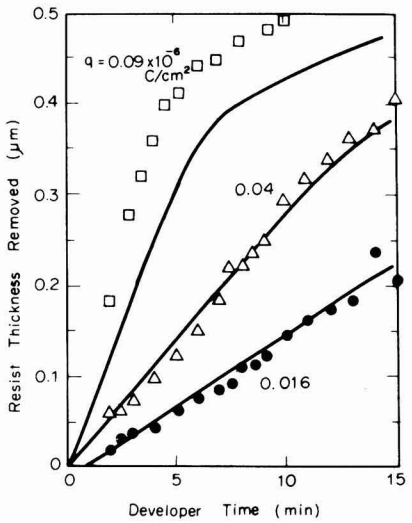


Fig. 8. Experimental and theoretical dissolution characteristics of PMMA at various doses of 250 kV Ar^+. The curves are calculated by use of $G_{el}(s) = 1.7$ and $G_n(s) = 0.9$.

The negative resist PDMS.—Figure 9 shows the exposure characteristics of PDMS resist to electron and ions, where the ordinate is the remaining resist thickness normalized to the initial film thickness. The sensitivities to 200 kV He^+ and 250 kV Ar^+ are higher than that to electron beam, as in the case of PMMA resist. However, PDMS exposed to 60 kV He^+ shows quite lower sensitivity, but high contrast. This is due to the fact that the ion has shorter projected range compared with the initial film thickness. The calculated projected range of 60 kV He^+ in PDMS is 0.738 μm and less than the film thickness 1 μm, so that the energy deposition rate at the interface becomes fairly small.

The gel doses q_m obtained from Fig. 9 and the energy depositions at the interface are listed in Table I. Figure 10 shows the relation of the electronic energy deposition at the gel dose *vs.* the nuclear. As expected from the theoretical consideration, almost linear relationship is observed. From this linear relation and Eq. [5], we obtain $G_{el}(cl)/G(cl) = 1.1$ and $G_n(cl)/G(cl) = 0.2$. The magnitude of $G_{el}(cl)$ and

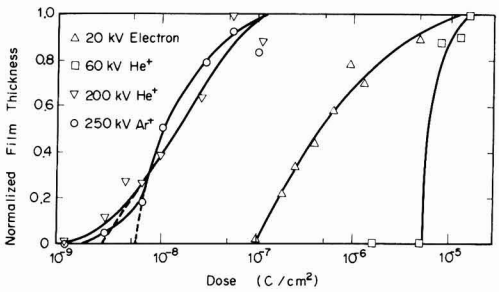


Fig. 9. Exposure characteristics of PDMS resist with electron and ion irradiation. The remaining resist thickness is normalized to the initial film thickness of 1 μm for 20 kV electron and 60 kV He^+, 0.5 μm for 250 kV Ar^+, and 1.1 μm for 200 kV He^+.

Table I. The gel doses of PDMS resist and the calculated values of the electronic and the nuclear energy deposition rate at the interface

Incident radiation	d_0 (μm)	q_m (C/cm^2)	$S_{el}(d_0)$ ($\times 10^8$ eV/cm/particle)	$S_n(d_0)$ ($\times 10^8$ eV/cm/particle)
20 kV electron	1.0	1×10^{-7}	0.278	—
60 kV He$^+$	1.0	5.2×10^{-6}	3.7×10^{-3}	1.1×10^{-2}
100 kV He$^+$	1.0	6.8×10^{-9}	3.4	1.7
200 kV He$^+$	1.1	2.4×10^{-9}	9.0	0.3
250 kV Ar$^+$	0.5	5.4×10^{-9}	2.0	14.0

Table II. The radiation yields for PMMA and PDMS resists exposed to electron and ion beam (events/100 eV)

Resist	Electron G	Ion G_{el}	Ion G_n	Ion G_{el}/G	Ion G_n/G
PMMA	1.9 (4)	1.7	0.9	0.9	0.5
PDMS	2.2 (15, 16)	2.4	0.4	1.1	0.2

G_n(cl) are calculated from G(cl) = 2.2 events/100 eV obtained by 800 kV electron irradiation (16, 17).

Discussion.—The values of G_{el} and G_n obtained here are summarized in Table II. Here, G_{el}'s are nearly equal to G of each resist, but G_n is one-half in PMMA and one-fifth in PDMS in comparison with G of each resist.

It is, in general, considered that the number of the scission or the cross-linking reactions produced directly by collisions of the incident ion with electrons in polymer is very little and most of them are produced by means of secondary effects, secondary electrons and excited electrons formed through the relaxation process of the primary excited states. This means that the number of chemical reactions induced by electronic collisions are independent of the kind of incident particle. In fact, Thompson *et al.* (18) have obtained similar results for several resist materials, making a comparison between the sensitivities in electron beam and x-ray. On the other hand, energy deposited through nuclear collisions is finally partitioned into three parts: (*i*) the atomic vibration, (*ii*) the atomic displacement, and (*iii*) the electronic excitations produced by the knock-on atoms. The first term is not effective for the chemical reactions. The third contributes to the same chemical reactions as the electronic collision case. The chemical events caused by the second term depend on the location of the displaced atom in the molecule. If radicals are produced by the displacement of side chain atoms, the chemical reactions follow the type of the resist, and the contribution to G_n is additive. On the other hand, if cross-linked atoms or atoms on the main chain are displaced, the chain scission is induced even in the negative resist, resulting in reductive contribution to G_n(cl). Although a qualitative interpretation is thus given for the difference in radiation yields between ion and electron irradiation and for the difference in contribution of the nuclear component between PMMA and PDMS, quantitative analysis of the individual process is needed for more detailed discussion.

Application

Pattern duplication.—On the basis of the first-order solution of the projected range, the projected standard deviation and the lateral standard deviation calculated from the method given in Ref. (5) and (6), contours of equi-energy deposition are obtained as shown in Fig. 11. Here, PMMA film with thickness of 1.3 μm is assumed to be exposed to 200 kV He$^+$ through a 2 μm width slit contacting closely to the resist surface and the reflection of ions from the substrate is not considered. The extent of undercutting from the slit edge is less than 0.3 μm even in the contour where energy deposition, normalized to the maximum value at the resist surface, decreases to 0.01. Therefore, high resolution pattern forming can be expected by use of the ion exposure.

In order to evaluate the practicability, experiments of pattern duplication are carried out. Resist films are exposed to He$^+$ through a 2.7 μm width slit located 100 μm distant from the resist surface. Cross sections of developed patterns are observed with a scanning electron microscope. Duplicated patterns in PMMA films with 1.3 μm thickness by use of 200 kV He$^+$ are shown in Fig. 12, together with those obtained by 20 kV electron for comparison. Exposure doses are about 1.2 and 4.5 times the critical dose in each case. (The critical dose is defined as the minimum dose necessary to perfectly dissolve the resist by the development time of 2 min in this work.) It is shown in Fig. 12 that the width of the pattern duplicated with ion dose of 1.6 $\times$ 10^{-6} C/cm^2 is almost the same as the original slit width and even at the higher dose increase in width is less than 1 μm, in contrast with the case of electron exposure where the pattern width reaches over twice the original slit width. Furthermore, the aspect of the side wall is almost perpendicular to the substrate. Figure 13 shows the same slit pattern duplicated in PDMS film of 1 μm thickness by use of 100 kV He$^+$. Exposure doses are nearly equal to the saturation dose and 3.4 times the saturation dose, where the saturation dose is defined as exposure charge density per square centimeter required to insolubilize the initial film thickness just completely. In electron lithography by use of

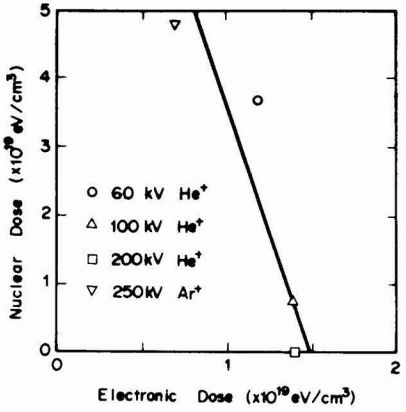


Fig. 10. The relationship between the electronic and the nuclear energy deposition at the interface necessary to form the insoluble film on the substrate.

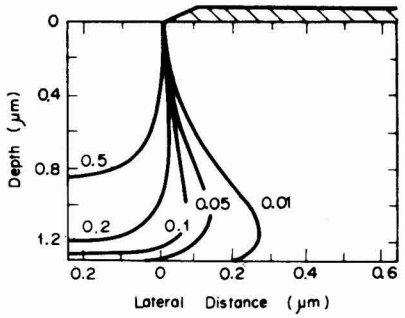


Fig. 11. Calculated contours of equi-energy deposition in PMMA resist exposed to 200 kV He$^+$. The values are normalized to the maximum energy deposition rate, 24.8 $\times$ 10^8 eV/cm, at the resist surface.

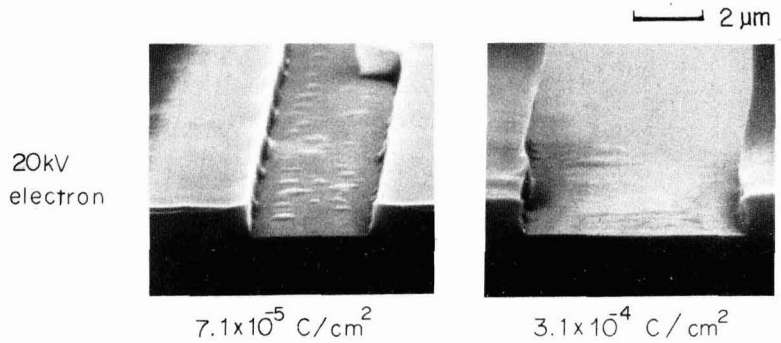
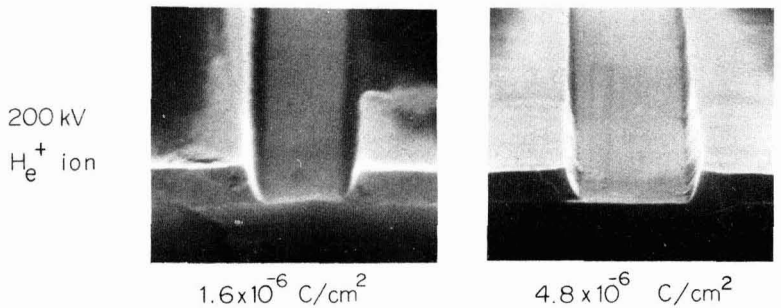


Fig. 12. Profiles of 1.3 μm PMMA film exposed through the 2.7 μm width slit.



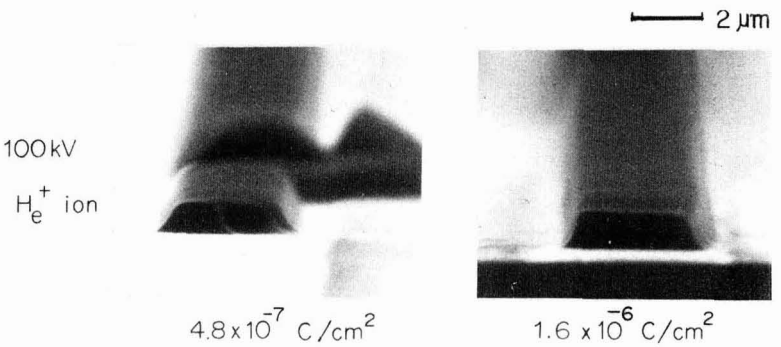


Fig. 13. Profiles of 1 μm PDMS film exposed through the 2.7 μm width slit.

negative resist, exposure with a dose which results in 50% thickness remaining or less is preferable for high resolution work (19). If the dose is greater than this value, especially in the saturation region, increase in pattern width and tailing of the pattern edge become significant (13, 20). On the contrary, in ion exposure the pattern size changes only slightly with increase in exposure dose as shown in Fig. 10 and the width of the tailing at the edge is less than about 0.5 μm, being much less than that in electron exposure.

In these experiments, the projected range of the incident ion is comparable to the film thickness. Consequently, the energy of the ion beam is almost transferred to the resist film. Even in this case, the lateral spread of the ion in the resist film is less than 0.5 μm, which implies that the problem such as a proximity effect in electron beam lithography will be avoided in ion exposure. Thus, it can be concluded that ion exposure has inherently a capability of high writing speed and of high resolution.

It is considered that the ions passing through the resist film will produce a problem of damage in the substrate material. In these experiments, the mean energy of the ions bombarding the substrate is evaluated as a few kilovolts, and the ion dose is less than an order of 10^{13} ions/cm^2. Therefore, the effect is only to produce very light damage near the substrate surface. When the substrate material is covered with an amorphous layer such as SiO_2, any problems are not introduced. Even if this is not the case, damages will be so light that they can be annealed at low temperature (21).

Application.—Figure 14 shows the dissolution characteristics of PMMA resist exposed to 60 kV He^+, in which the thickness loss in the unexposed area is not corrected. The thickness difference becomes a constant value with increasing the development time, since the resist layer over the projected range suffers only a slight damage. This fact implies that an accurate fabrication of the resist in the direction of the depth is possible by use of ion exposure. For example, it can be applied to proximity contact between a mask and a resist film in a pattern printing process like x-ray exposure. Schematic diagrams of the technical

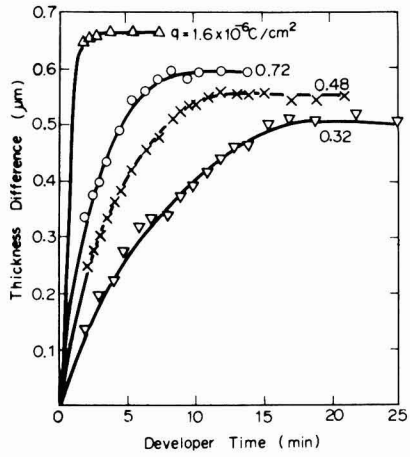


Fig. 14. Dissolution characteristics of 1.3 μm PMMA resist exposed to 60 kV He^+. Thickness loss in the unexposed area is not added.

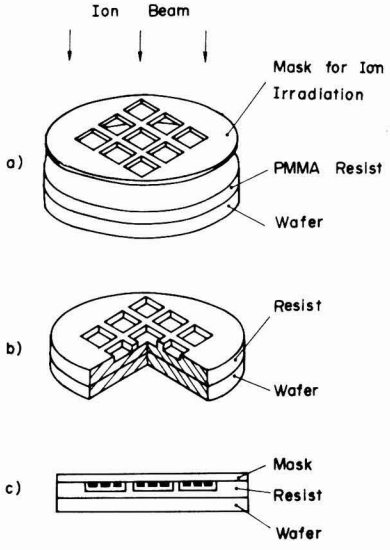


Fig. 15. Schematic diagrams indicating the procedure of proximity contact.

procedure for this purpose are shown in Fig. 15. A positive resist coated on a wafer is first exposed to an ion beam through a reticulate mask whose square is corresponding to a chip area. After a development, the resist has a cross section like Fig. 15(b). The protruding parts of the resist in this sketch will support a mask at a uniform and minute distance as seen in Fig. 15(c), so that a proximity gap will be kept constantly on the whole region of the mask and, moreover, the micropattern on the mask will be prevented from being injured. Thus, it is feasible to prolong the life of the mask and also precisely fabricate the micropattern in a simple way.

Conclusion

The exposure characteristics of the positive resist, PMMA, and the negative resist, PDMS, for helium and argon ion irradiation are studied and the following results are obtained.

1. The sensitivities of the resists in ion exposure, measured in terms of electronic charge density, are over ten times as high as in electron exposure. According to the estimation of the radiation yields on the basis of the calculations of energy deposition rate, it is found that the high sensitivity is mainly due to the fact that the energy deposition rate of the ion beam is much greater than that of electron exposure.
2. The radiation yields for cross-linking and chain scission caused by electronic collisions of ion are nearly equal to those in electron exposure.
3. The radiation yields caused by nuclear collisions are one-half in PMMA and one-fifth in PDMS in comparison with the radiation yields in electron exposure.
4. From the aspects of the patterns duplicated through the 2.7 μm width slit, it is verified that high fidelity and high resolution pattern forming is possible by use of ion beam.
5. The application to proximity contact between a mask and a resist film is proposed.

Acknowledgment

The authors would like to thank Dr. T. Tsurushima and H. Tanoue of Electrotechnical Laboratory for their useful discussions and for the use of the ion implantation system.

Manuscript submitted March 29, 1978; revised manuscript received Oct. 2, 1978.

Any discussion of this paper will appear in a Discussion Section to be published in the December 1979 JOURNAL. All discussions for the December 1979 Discussion Section should be submitted by Aug. 1, 1979.

Publication costs of this article were assisted by the Electrotechnical Laboratory.

LIST OF SYMBOLS

z	the penetration depth into a resist, μm
$S(z)$	the energy deposition rate of the electron beam at depth z, eV/cm
$S_{el}(z)$, $S_n(z)$	the energy deposition rates of the ion beam caused by electronic and nuclear collisions, eV/cm
M_n, M_f	the initial and the fragmented number average molecular weight of PMMA resist
e	the electronic charge, C
ρ	the density of a resist, g/cm³
N_A	the Avogadro's number, molecules/mole
K	the constant in the formula for the fragmented molecular weight, cm³/C
q	the exposure dose, C/cm²
$G(s)$	the radiation yield for main chain scission in electron exposure, events/100 eV
$G_{el}(s)$, $G_n(s)$	the radiation yields for main chain scission caused by electronic and nuclear collisions in ion exposure, events/100 eV
M	the number average molecular weight of a positive resist
R_o, β, α	the development constants, Å/min, Å/min, and no dimension, respectively
d	the resist thickness removed after development, μm
T	the development time, min
δ	the cross-linking coefficient, sites/molecule
K'	the constant in the formula for the cross-linking coefficient, cm³/C
$G(cl)$	the radiation yield for cross-linking in electron exposure events/100 eV
$G_{el}(cl)$, $G_n(cl)$	the radiation yields for cross-linking caused by electronic and nuclear collisions in ion exposure, events/100 eV
M_w	the weight average molecular weight of PDMS resist
q_{me}, q_{mi}	the gel doses in electron and ion exposure, C/cm²
d_o	the initial film thickness of PDMS resist, μm

REFERENCES

1. M. Hatzakis and A. N. Broers, in "Record of 11th Symposium on Electron, Ion, and Laser Beam Technology," p. 337, San Francisco Press, San Francisco (1971).

2. R. L. Seliger and W. P. Fleming, *J. Appl. Phys.*, **45**, 1416 (1974).
3. J. Lindhard, M. Sharff, and H. E. Shiøtt, *Mat. Fys. Medd. Dan. Vid. Selsk.*, **33**, No. 14 (1963).
4. A. Chaprio, "Radiation Chemistry of Polymeric Systems," John Wiley & Sons, Inc., New York (1962).
5. D. K. Brice, *Rad. Effect*, **6**, 77 (1970).
6. D. K. Brice, *ibid.*, **16**, 227 (1971).
7. P. H. Hoff and T. E. Everhart, in "Record of 10th Symposium on Electron, Ion, Laser Beam Technology," p. 454, San Francisco Press, San Francisco (1969).
8. H. Y. Ku and L. C. Scala, *This Journal*, **116**, 980 (1969).
9. K. Ueberreiter, in "Diffusion in Polymer," J. Crank and G. S. Park, Editors, p. 239, Academic Press, London (1968).
10. J. S. Greeneich, *This Journal*, **122**, 970 (1975).
11. C. H. Ting, in "Record of 11th Symposium on Electron, Ion, and Laser Beam Technology," p. 345, San Francisco Press, San Francisco (1971).
12. N. Atoda and H. Kawakatsu, *This Journal*, **123**, 1519 (1976).
13. R. D. Heidenreich, L. F. Thompson, F. D. Feit, and C. M. Melliar-Smith, *J. Appl. Phys.*, **44**, 4039 (1973).
14. Y. Yatsui, T. Tanaka, and K. Umehara, *This Journal*, **116**, 94 (1969).
15. T. Kuroda, in Proceedings of 7th International Conference on Electron and Ion Beam Science and Technology, p. 256, The Electrochemical Society, Princeton, N.J. (1976).
16. L. E. St. Pierre, H. A. Dewhurst, and A. M. Bueche, *J. Polym. Sci.*, **36**, 105 (1959).
17. W. Barnes, H. A. Dewhurst, R. W. Kilb, and L. E. St. Pierre, *ibid.*, **36**, 525 (1959).
18. L. F. Thompson, E. D. Feit, M. J. Bowden, P. V. Lenzo, and E. G. Spencer, *This Journal*, **121**, 1500 (1974).
19. L. F. Thompson, J. P. Ballantyne, and E. D. Feit, *J. Vac. Sci. Technol.*, **12**, 1280 (1975).
20. M. Hatzakis, *This Journal*, **116**, 1033 (1969).
21. J. W. Mayer, L. Erikkson, and J. A. Davies, "Ion Implantation in Semiconductors," p. 65, Academic Press, New York and London (1970).

Effusion Studies of the Vaporization/Decomposition of Potassium Sulfate

K. H. Lau, D. Cubicciotti,* and D. L. Hildenbrand

SRI International, Menlo Park, California 94025

ABSTRACT

The vaporization of K_2SO_4 was studied by the torsion-effusion method and by mass spectrometry in the range 1180°-1280°K, from which the total pressure, molecular weight, and composition of the effusing vapor were determined. Both the sublimation process $K_2SO_4(s) = K_2SO_2(g)$ and the decomposition process $K_2SO_4(s) = 2K(g) + SO_2(g) + O_2(g)$ contribute to the vaporization flux, with the sublimation pressure about 63% of the total pressure in the range of our measurements. The directly measured vapor molecular weights are in good agreement with values deduced from the magnitudes of the sublimation and decomposition pressures. A small but reproducible variation of pressure with effusion orifice area was observed, equivalent to an upper bound of 0.03 to the over-all sublimation coefficient. Second law slope heats derived from the temperature dependence of parent K^+ and SO_2^+ ions were in close agreement with each other and with the heat of decomposition calculated from established thermochemical data. Similar measurements on parent $K_2SO_4^+$ showed the temperature dependence of sublimation and decomposition pressures to be virtually identical. The heat of sublimation of $K_2SO_4(g)$ at 298°K was determined as 86.5 ± 1.5 kcal/mole, leading to the standard heat of formation $\Delta Hf_{298}^\circ(K_2SO_4, g) = -257.0 \pm 1.5$ kcal/mole. From the slope heat and the absolute pressure, one evaluates the entropy $S^\circ_{1200}(K_2SO_4, g) = 135.8 \pm 1.2$ cal/deg mole.

Metal sulfate chemistry plays a central role in a number of developing technologies such as sulfur removal from combustion gases, thermochemical generation of hydrogen from water, and coal-fired MHD power generation. In most of these applications, the high temperature vaporization/decomposition behavior of sulfates is of particular concern, but not enough is known about the basic thermodynamics and kinetics to treat the technological problems adequately. Much of the literature data are conflicting and of uncertain accuracy. The status of the vaporization data for K_2SO_4, recently reviewed by Eliezer and Howald (1), is a case in point. Reported pressures vary by more than an order of magnitude, and the relative contributions of molecular sublimation and decomposition to the total pressure have not been defined clearly. For example, only recently Atkins and Gingerich (2) reported from matrix infrared spectra that no decomposition was detected for $K_2SO_4(s)$ near the melting point, although it was observable for Na_2SO_4; Ficalora and co-workers (3), on the other hand, reported that the decomposition process $K_2SO_4(s) = 2K(g) + SO_2(g) + O_2(g)$ was readily observable by mass spectrometry and presented results indicating the decomposition pressure to exceed the sublimation pressure by a factor of about 2.5. The reader is referred to the paper of Eliezer and Howald (1) for a review of the previous vaporization studies on K_2SO_4.

In the effusion studies reported here, a somewhat different approach was taken over those reported earlier. Vapor pressures were determined by the torsion-effusion method, a purely mechanical technique that requires no knowledge of vapor composition to evaluate total pressure. These observations were augmented by simultaneous mass effusion rate measurements, thereby allowing one to evaluate the average molecular weight of effusing vapor and to derive valuable information about vapor composition.

* Electrochemical Society Active Member.

Additionally the mass spectrum of K_2SO_4 vapor was studied in detail and thermodynamic data were derived for the two modes of vaporization.

Experimental

The torsion-effusion apparatus and the associated microbalance have been described previously (4, 5) along with details of the experimental technique and the methods of data evaluation (6). Effusion cells fabricated from Pt-30% Rh alloy were used for the studies on K_2SO_4. Each cell assembly consisted of two separate vertically aligned sample chambers, 0.80 cm diam and 2.4 cm long, mounted on the suspension rod so that the orifice moment arms were about 0.8 cm. Two different orifice sizes were used, 0.06 and 0.11 cm diam. Originally, the sample chambers were sealed with Pt-Rh covers, but the seal could not be made sufficiently tight to preclude a certain amount of vapor leakage. Interestingly enough, this slight amount of leakage had no detectable effect on the measured torsion pressures, as evidenced by measurements on several standards. However, the total effusion mass loss and the vapor molecular weight were seriously affected, and another type of closure had to be devised. Tapered alumina plugs, carefully machined to fit, proved to be satisfactory and were used for all of the studies reported here. When the performance was checked against the well-known vapor pressure of KCl, both cells gave results within 5% of the values reported by Pugh and Barrow (7). In addition, the cell used in the mass effusion rate determinations yielded vapor molecular weights for KCl that agreed with the established values within a few percent. In the work on K_2SO_4, the Pt-Rh cells sealed with tapered alumina plugs yielded highly reproducible results and proved to be entirely satisfactory in every respect.

Studies of the K_2SO_4 vapor mass spectrum were carried out with the 12 in. radius, 60° sector magnetic instrument equipped with a Knudsen cell source (8, 9). A platinum effusion cell, 1 cm ID and 1.2 cm long with a 0.15 cm diam orifice, was fabricated from thin sheet material. The platinum cell fitted snugly inside a nickel holder with a 1 cm long internal cavity open at the top. The junction of a Pt, Pt-13% Rh thermocouple was clamped to the outside surface of the nickel holder near the top with an adjustable nickel band. Power input to the cell assembly was provided by a bifilar-wound molybdenum resistance heater, fashioned from 0.25 cm diam Mo rod into a helix of 2 cm ID and 4 cm length. Ionization efficiency curves were recorded automatically on an X-Y plotter, using the arrangement described previously (9). All measurements of the temperature dependence of pressure and ion intensity were made by varying the temperature randomly. However the data are tabulated in order of ascending temperature so that trends may be more easily noted.

All of the measurements reported here were made on a Mallinkrodt A. R. grade sample of K_2SO_4 with nominal purity of 99.9%. No obvious impurities were detected in the vapor mass spectrum. Furthermore, in heating the sample into the range of the torsion-effusion measurements, essentially no outgassing was observed. X-ray diffraction patterns taken before and after the measurements showed only the presence of the low temperature orthorhombic form of K_2SO_4, although our measurements at 1180°-1280°K were assumed to be on the equilibrium hexagonal form. As a check on vaporization stoichiometry, a sample of K_2SO_4 was vaporized at 1300°K under vacuum until about 30% of the original material remained. The residual material was dissolved in water and titrated for alkalinity, sulfite, and sulfide ions; in each instance the results were negative, indicating that K_2SO_4 vaporizes congruently.

Table I. Total vapor pressure of K_2SO_4(s)

(Torsion-effusion method)

Cell PR-1		Cell PR-2		
T (°K)	P (atm) × 10^6	T (°K)	P (atm) × 10^6	$\overline{M}$
1179.6	0.298	1201.4	0.762	
1189.1	0.370	1212.0	0.984	
1191.6	0.415	1213.4	1.015	
1194.3	0.452	1213.8	1.038	
1197.2	0.465	1217.1	1.122	
1201.6	0.534	1222.1	1.270	
1204.2	0.582	1224.8	1.377	
1212.2	0.717	1233.5	1.719	
1228.9	1.091	1235.8	1.776	
1229.8	1.089	1239.0	1.981	
1232.2	1.177	1244.9	2.242	119.3
1233.2	1.174	1249.3	2.531	114.2
1235.9	1.285	1256.4	2.976	
1248.9	1.776	1257.4	3.125	104.6
1252.5	1.944	1259.5	3.258	
1252.5	1.892	1261.9	3.409	113.4
1255.4	2.039	1268.4	4.032	102.9
1256.1	2.097	1270.4	4.206	
		1273.8	4.587	106.4
log P (atm) = (7.398 ± 0.079)- (16,426 ± 94)/T		log P (atm) = (7.685 ± 0.052)- (16,593 ± 66)/T		

Cell	d (cm)*	ΣCa (cm²)†
PR-1	0.11	1.68×10^{-2}
PR-2	0.06	5.08×10^{-3}

* d = orifice diameter.
† ΣCa = effective orifice area.

Results

Total vapor pressures.—A summary of the torsion-effusion total vapor pressures obtained with cells PR-1 and PR-2 and the vapor molecular weight data obtained with PR-2 are given in Table I. As seen from a plot of the pressure data, shown in Fig. 1, the pressures measured with the 0.06 cm diam orifice are about 40% higher than those determined with the larger orifice. This difference was reproduced to within a few percent in a second independent series of measurements with each cell. We attribute the effect to undersaturation of the vapor, resulting from

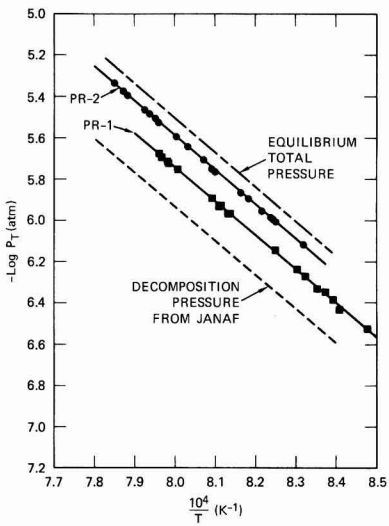


Fig. 1. Total pressure over K_2SO_4(s) measured with two platinum-rhodium effusion cells, showing relation to extrapolated equilibrium pressure and calculated pressure for decomposition process $K_2SO_4(s) = 2K(g) + SO_2(g) + O_2(g)$.

a kinetic barrier to the vaporization process. Extrapolation of the data to zero orifice area, using the Whitman-Motzfeldt model (5, 10-12), leads to the derived equilibrium pressures shown in Fig. 1.

The vapor molecular weight data listed in Table I are reasonably consistent, yielding the average value $M = 110 \pm 5$, independent of temperature. Our experimental value of M is lower than the molecular weight of K_2SO_4 (174.3), but it is significantly higher than the value $M = 44.3$ that would obtain solely for the decomposition process

$$K_2SO_4(s) = 2K(g) + SO_2(g) + O_2(g) \quad [1]$$

observed by Ficalora and co-workers (3) by mass spectrometry. It should be noted that the partial pressures of the gaseous decomposition products in the effusion cell differ from those in a closed, equilibrium system because of the requirement that the effusion rates be such as to leave the composition of the residual sulfate unchanged. Thus the partial pressures of $K(g)$, $SO_2(g)$, and $O_2(g)$ in the cell are in the ratio 2.21/1.41/1.00 rather than 2/1/1. Undersaturation of the vapor does not affect the validity of the vapor molecular weight determinations. It is clear from these results that both molecular sublimation and decomposition are major contributors to the total vaporization flux and to the resultant total effusion pressure.

Vapor mass spectrum.—In order to check these findings and to obtain more quantitative information, the vapor mass spectrum was examined. In Table II are listed the threshold appearance potential (AP) of the ions observed, the neutral precursors inferred, and the relative ion intensities at 5 eV above threshold. The ions K^+ and SO_2^+ are formed by simple ionization processes near threshold, since the threshold energies agree closely with the spectroscopic ionization potentials (IP) of the corresponding neutrals, $IP(K) = 4.34$ eV and $IP(SO_2) = 12.34$ eV. It was difficult to obtain an accurate AP for beam O_2^+ in the presence of normal background O_2^+, but the value was near 12 eV, close to the ionization potential of O_2. In view of its relatively low AP, $K_2SO_4^+$ is also a parent ion; our value of $AP(K_2SO_4^+)$, the result of several determinations, is 1 eV higher than that reported by Ficalora *et al.* (3). On the other hand, K_2O^+ is clearly a fragment ion, since it is expected that $IP(K_2O) \cong IP(K)$. In line with this, Gusarov and Gorokhov (13) have reported an approximate value of 5 eV for $IP(K_2O)$. Although Ficalora *et al.* (3) reported observation of "small concentrations of SO_3^+" over $K_2SO_4(s)$, we detected no SO_3 in spite of a careful search. However, the value $AP(SO_3^+) = 11.0 \pm 0.5$ eV reported by Ficalora *et al.* (3) is appreciably lower than the ionization potential of SO_3 determined by photoelectron spectroscopy, 12.82 ± 0.03 eV (14, 15), leaving some doubt that SO_3 was actually observed. Clarifying the role of SO_3 in the vaporization process is important since in previous studies on $MgSO_4(s)$ (5) and $ZnSO_4(s)$ (16), a large kinetic barrier retarded the evolution of the major equilibrium species SO_2 and O_2 and led to a vapor rich in SO_3.

Table II. Appearance potentials and relative intensities of ions in mass spectrum of K_2SO_4 vapor

Ion	AP (eV)	Neutral	I^+ (AP + 5 eV)*
K^+	4.5 ± 0.3	K	73.2
K_2O^+	11.5 ± 0.5	K_2SO_4	0.8
$K_2SO_4^+$	$8\ 4 \pm 0.3$	K_2SO_4	8.8
SO_2^+	12.4 ± 0.5	SO_2	6.6
O_2^+	—	O_2	2.5

* Relative intensities measured at 5 eV above the appearance potential of the ion.

On the basis of the observed ion signals and the AP data, we conclude that the major species in the vapor effusing from $K_2SO_4(s)$ are K_2SO_4, K, SO_2, and O_2, in accord with the observations of Ficalora *et al.* (3). In another mass spectrometric study, Kosugi (17) did not report the observation of $K_2SO_4^+$ and concluded erroneously that the gaseous decomposition products were K_2O, SO_2, and O_2. It is difficult to obtain an accurate measure of vapor composition from the mass spectrum alone, because of uncertainty over the relative ionization cross sections of the various species, and also over possible interference from the effect of fragmentation on species such as K^+. The latter effect is believed to be minimized in the mass spectrum of Table II, obtained at a small excess ionizing energy. The ionization efficiency curve of K^+ showed no discernible fragmentation onset between 5 and 15 eV, although above 15 eV there was an upward inflection that could be attributed to a second ionization process. Considering the possible range of ionization cross sections, the mass spectrum is not inconsistent with a vapor containing approximately comparable amounts of the gaseous species K_2SO_4, K, SO_2, and O_2. On the basis of the mass spectrometric evidence, it is concluded that the molecular sublimation process

$$K_2SO_4(s) = K_2SO_4(g) \quad [2]$$

and the decomposition reaction [1] are both of importance in the over-all vaporization process. The quantitative determination of vapor composition and its bearing on the vapor mass spectrum are discussed later in the paper.

As an aid in distinguishing between the two principal vaporization processes and in obtaining second law sublimation data specifically for $K_2SO_4(g)$, the temperature dependences of the intensities of $K_2SO_4^+$, K^+, and SO_2^+ were measured over the range 1170°-1300°K. In one run, the intensities of K^+ (7 eV), $K_2SO_4^+$ (15 eV), and SO_2^+ (17 eV) were measured at a given temperature with the indicated ionizing energies, after which the temperature was changed and the process repeated. For the second run, K^+ was determined at 7 and 30 eV for each temperature level. And in the third run, $K_2SO_4^+$ at 15 eV was measured at a series of temperatures. Second law heats were derived from least squares analysis of log (I^+T) as a function of reciprocal temperature, with the results shown in Table III. There is remarkably little variation among the slope heats of the three ions, nor does K^+ show any detectable variation with excess ionizing energy. The values for K^+ and SO_2^+ agree closely with the corresponding slope heat of 75.1 ± 0.3 kcal/mole at 1230°K calculated from accurate thermochemical data (18) for reaction [1]. In addition, the mass spectrometric results are in accord with the slope heats derived from the total pressures determined by the torsion method, $\Delta H_{1222} = 75.2 \pm 0.4$ kcal/mole (cell PR-1) and $\Delta H_{1240} = 75.9 \pm 0.3$ kcal/mole (cell PR-2).

Normally, ion species showing the same temperature dependence within experimental error are assigned to a common neutral precursor. For K_2SO_4 vapor, however, the evidence is clear that the partial

Table III. Second law slope heats derived from ion temperature dependences

Ion	Electron energy (eV)	Data points	T_{avg} (°K)	ΔH_T (kcal/mole)
$K_2SO_4^+$	15	9	1218	76.3 ± 2.0
	15	10	1252	73.9 ± 0.3
K^+	7	9	1218	76.0 ± 1.0
	7	9	1241	74.4 ± 0.7
	30	10	1245	74.1 ± 1.6
SO_2^+	17	9	1218	76.2 ± 0.8

pressure of $K_2SO_4(g)$ simply has a temperature dependence very close to those of $K(g)$ and $SO_2(g)$, *i.e.*, the sublimation and decomposition processes have nearly equal temperature coefficients. The principal evidence for this is the observation that the parent K^+ and SO_2^+ slope heats are very close to those observed for $K_2SO_4^+$ and the total pressures, in addition to agreeing well with the value calculated from thermochemical data for the decomposition process, reaction [1]. Moreover, parent K^+ at 7 eV ionizing energy and K^+ at 30 eV, which must include some fragmentation of K_2SO_4, show essentially the same temperature dependence. Our conclusions regarding the temperature coefficients of reactions [1] and [2] differ from those of Eliezer and Howald (1), who concluded that the fraction of decomposition increased with temperature. However, the data available at that time were not of sufficient accuracy to establish the point with certainty.

Determination of vapor composition.—Since the principal vaporization processes are now clearly established, it is possible to use the total pressure data to determine vapor composition quantitatively and to compare the result with the directly measured vapor molecular weight. The data used in this evaluation are summarized in Table IV, where P_T is the equilibrium total pressure over $K_2SO_4(s)$ obtained from the Whitman-Motzfeldt extrapolation to zero orifice area, P_D is the calculated pressure corresponding to the decomposition reaction [1] evaluated from thermochemical data (18), and $P_{K_2SO_4} = P_T - P_D$. As seen from Fig. 1 and Table IV, $P_T \cong 2.7P_D$. If one considers the sublimation/decomposition of K_2SO_4 denoted by the expression

$$K_2SO_4(s) = (1-b)K_2SO_4(g) + 2bK(g) + bSO_2(g) + bO_2(g) \quad [3]$$

then the average molecular weight $\overline{M}$ can be related to b and the molecular weights M of the gaseous species by the equation

$$\overline{M} = \left[\frac{(1-b)M^{1/2}_{K_2SO_4} + 2bM^{1/2}_{K} + bM^{1/2}_{SO_2} + bM^{1/2}_{O_2}}{(1-b)M_{K_2SO_4} + 2bM_K + bM_{SO_2} + bM_{O_2}}\right]^{-2} \quad [4]$$

Equation [4] follows from the expression for the average molecular weight of a multicomponent effusing vapor

$$\overline{M} = [\Sigma m_i M_i^{-1/2}]^{-2} \quad [5]$$

where m and M are the mass fraction and molecular weight of the i gaseous species. In turn, the partial pressure of $K_2SO_4(g)$ and the total equilibrium pressure P_T are related to b by the expression

$$\frac{P_{K_2SO_4}}{P_T} = \left[\frac{(1-b)M^{1/2}_{K_2SO_4}}{(1-b)M^{1/2}_{K_2SO_4} + 2bM^{1/2}_{K} + bM^{1/2}_{SO_2} + bM^{1/2}_{O_2}}\right] \quad [6]$$

From the values of $P_{K_2SO_4}$ and P_T in Table IV and Eq. [4] and [6], it follows that in the range of our measurements $(P_{K_2SO_4})/P_T) = 0.63 \pm 0.01$, $b = 0.230 \pm 0.004$, and $\overline{M} = 116 \pm 1$. This value of $\overline{M}$ deduced from the pressure measurements alone is in excellent agreement with our directly determined vapor molecular weights shown in Table I which yield $\overline{M} = 110 \pm 5$, providing strong corroboration for our interpretation of vapor composition.

Table IV. Derived vaporization data for $K_2SO_4(s)$

T (°K)	$P_T \times 10^7$ (atm)	$P_D \times 10^7$ (atm)	$P_{K_2SO_4} \times 10^7$ (atm)
1180	5.07	1.94	3.13
1200	8.74	3.31	5.43
1220	14.79	5.55	9.24
1240	24.60	9.16	15.44
1260	40.26	14.88	25.38
1280	64.90	23.85	41.05
1300	103.08	37.55	65.53

All of our experimental results are consistent with the interpretation that, over the range 1180°-1280°K, $K_2SO_4(s)$ vaporizes by the simultaneous decomposition and sublimation processes and that the molecular sublimation pressure of $K_2SO_4(g)$ accounts for 63% of the total pressure under these conditions. Within experimental error, the sublimation and decomposition pressures have the same temperature dependence. The small differences between the temperature coefficients of the measured pressures and the calculated decomposition pressures in Table IV are not significant.

Thermodynamics of $K_2SO_4(g)$.—In converting the slope heats to standard reference temperature and in subsequent third law calculations, the thermodynamic functions of $K_2SO_4(s)$ were taken from the JANAF Thermochemical Tables (18) while those of $K_2SO_4(g)$ were taken from tables prepared by Gurvich *et al.* (19), listed partially in Table V. The functions for $K_2SO_4(s)$ are based on accurate thermal measurements but those for $K_2SO_4(g)$ are calculated from spectroscopic constants that are partially estimated. Consequently, Gurvich *et al.* (19) estimate the uncertainty in the free energy function (Φ_T) for $K_2SO_4(g)$ to be about 3 cal/deg mole at 1000°K. We believe that the uncertainties in entropy and free energy functions are larger than those in the heat capacity and heat content functions so that the effect on second law calculations will be smaller than that on third law values.

The most straightforward value for the heat of sublimation of $K_2SO_4(g)$ can be derived from the mass spectrometric studies of the temperature dependence of the $K_2SO_4^+$ intensity, the results of which are shown in Table III. The two slope heats for $K_2SO_4^+$ were converted to 298°K using the aforementioned functions, leading to the results $\Delta H°_{298}$ (2) = 87.4 and 85.5 kcal/mole for the direct sublimation process. The average value $\Delta H°_{298}$ (2) = 86.5 kcal/mole, with estimated uncertainty of ±1.5 kcal/mole, is selected as the best value for the heat of sublimation of $K_2SO_4(g)$ from the present research. This result then yields the standard heat of formation $\Delta Hf°_{298}(K_2SO_4, g) = 86.5 - 343.5 = -257.0 \pm 1.5$ kcal/mole. Our value is somewhat less negative than

Table V. Thermodynamic functions of $K_2SO_4(g)$*

T (K)	$\Phi°_T$ (cal/deg mole)	$H°_T - H°_{298}$ (kcal/mole)	$S°_T$ (cal/deg mole)
298.15	87.28	0	87.28
300	87.28	0.05	87.44
400	88.34	2.82	95.39
500	90.44	5.86	102.17
600	92.90	9.09	108.05
700	95.44	12.45	113.23
800	97.96	15.90	117.83
900	100.40	19.41	121.96
1000	102.74	22.97	125.71
1100	104.99	26.56	129.14
1200	107.14	30.18	132.29
1300	109.19	33.83	135.21
1400	111.14	37.50	137.92
1500	113.01	41.17	140.46

$(H°_{298} - H°_0 = 5.34$ kcal/mole

$$\Phi°_T = S°_T - \left(\frac{H°_T - H°_{298}}{T}\right)$$

* From Ref. (19).

the selected value of Eliezer and Howald (1) (−261.2 kcal/mole) but should be more accurate since it is derived from a relatively complete and internally consistent set of results. The recent effusion measurements of Gorokhov (20) yield a second law heat of sublimation of K_2SO_4 at 298°K (86.9 ± 1.6 kcal/mole) in good agreement with the value reported here, while those of Plante (21) (80.2 ± 0.9 and 81.1 ± 2.0 kcal/mole) are somewhat lower. Earlier effusion data on $K_2SO_4(s)$ (3, 22, 23) discussed by Eliezer and Howald (1), lead to corresponding second law heats ranging from 60 to 83 kcal/mole. The vapor pressure data for liquid K_2SO_4, summarized in Ref. (1), are too discordant to be correlated with our data for the solid, so that we prefer to derive the data for $K_2SO_4(g)$ from the present measurements alone.

The molecular sublimation pressures of $K_2SO_4(g)$ derived from our measurements as described earlier are summarized in Table IV. Third law calculations yield the average heat of sublimation ΔH°_{298} (2) = 81.9 kcal/mole, with an estimated uncertainty of ±5 kcal/mole because of the uncertainties in the spectroscopic constants and thermodynamic functions of $K_2SO_4(g)$. For this reason, we prefer the second law data and the results derived therefrom. An idea of the spread in absolute sublimation pressures resulting from the various investigations can be noted from the data in Table VI, where the values are seen to range over a factor of 30. The discrepancies are very large for a relatively simple measurement and must arise largely from errors in temperature measurement and in experimental technique. However, the three most recent determinations are in fairly good agreement. We estimate an over-all uncertainty of 10% in our total pressure measurements and a maximum uncertainty of 25% in the calculated decomposition pressures (reaction [1]); this is equivalent to an over-all uncertainty of 27% in our derived $K_2SO_4(g)$ pressures.

Discussion

The reproducible effect of effusion orifice area on observed pressure is a clear indication that the overall vaporization process is hindered kinetically. From the slope and intercept of the Whitman-Motzfeldt plot (*i.e.*, a plot of reciprocal of observed pressure *vs.* effective orifice area), we calculate that the product of vaporization coefficient and vaporizing surface area, αA, is about 0.012. This, of course, involves the usual assumptions implicit in the Whitman-Motzfeldt model (10-12), but over the years these assumptions and the model itself have been shown to have a certain degree of validity. An approximate value $\alpha \leq 0.03$ then can be derived by setting the cell cross-sectional area as a lower limit to A. Other sulfate dissociative vaporization reactions such as $MgSO_4(s) = MgO(s) + SO_3(g)$ and $MSO_4(s) = MO(s) + SO_2(g) + 1/2\,O_2(g)$, where M = Mg, Ca, were found to have α values of ≤ 0.044 and ≤ 0.0027, respectively (5). The data are not sufficient to determine the degree of undersaturation in the separate sublimation and decomposition processes, but previous results (5) on $MgSO_4$ and $CaSO_4$, and the absence of a detectable orifice-size effect in effusion studies (24) of Rb_2SO_4 and Cs_2SO_4, where molecular sulfate species predominate, suggests that the kinetic barrier is associated with the decomposition process. This seems likely in view of the substantial orientational effects, i.e., changes in bond length and angle, involved in the emission of the SO_2 and O_2 gaseous species from the lattice sulfate ion. Our implicit assumption that both decomposition and sublimation processes are undersaturated to the same degree, however, introduces no significant uncertainty in the derived results.

The absolute entropy of $K_2SO_4(g)$ at 1200°K is evaluated as 135.8 ± 1.2 cal/deg mole from the second law heat of sublimation ΔH°_{1200} (sub) = 75.6 ± 1.5 kcal/mole, the absolute pressure P_{1200} (K_2SO_4, g) = 5.43 × 10^{-7} atm, and the entropy of $K_2SO_4(s)$, S°_{1200} = 101.5 ± 0.3 cal/deg mole. Our experimental entropy is 3.3 cal/deg mole larger than that calculated by Gurvich *et al.* (19) from spectroscopic and molecular constants but is within the probable uncertainty of the statistical calculation. Although the recent spectroscopic work of Atkins and Gingerich (2) corroborates most of the observed vibrational frequencies assigned by Gurvich *et al.* (19), the entropy comparison suggests that several of the estimated frequencies are too high. The experimental second law entropy should prove useful in refining the calculated functions when additional spectroscopic data become available.

As will be noted from the mass spectrum in Table II and the vapor composition data deduced here, the detection efficiency for K(g) at low ionizing energies is about an order of magnitude larger than that for $K_2SO_4(g)$. This effect probably is due primarily to differences in the ionization cross sections of the species. The alkali atoms, with their lone s shell valence electrons, are known to have substantially higher cross sections than neighboring closed-shell atoms. On this basis, one could rationalize an ionization cross section for K(g) that is 5-10 times larger than that of the closed-shell ionic structure $[K^+(SO_4^=)K^+](g)$. Instrumental factors such as ion transmission and collection efficiencies also could affect the $K^+/K_2SO_4^+$ ratio, although to a lesser extent. For the present purposes we prefer not to dwell on this point, since so little is known about the ionization cross sections of large ionic molecules such as K_2SO_4. Determination of the relative cross sections of these species would be an interesting study in itself and could perhaps be made with a $K_2SO_4(s)$ effusion source now that the composition of the vapor is established.

The trend in the relative importance of the sublimation and decomposition processes of the alkali sulfates has been noted previously (3), with decomposition alone observed for Li_2SO_4 and Na_2SO_4 (3) and predominately molecular sublimation for Rb_2SO_4 and Cs_2SO_4 (3, 24). As described here, K_2SO_4 is an intermediate case. A quantitative comparison of the two vaporization processes for each of the sulfates at a common temperature of 1200°K is given in Table VII, along with pertinent thermochemical data. The decomposition pressures of $Na_2SO_4(s)$ and $K_2SO_4(s)$ were calculated from data in the JANAF Tables (18), while those of Rb_2SO_4 and Cs_2SO_4 were calculated

Table VI. Comparison of $K_2SO_4(g)$ sublimation pressures at 1200°K

Investigators	P (K_2SO_4, g, 1200°K) × 10^7 (atm)	Ref.
Kroger and Stratmann*	38.6	(22)
Ficalora *et al.*	1.33	(3)
Halstead	38.9	(23)
Gorokhov	4.80	(20)
Plante	6.33	(21)
Lau *et al.*	5.43 ± 1.50	This work

* Pt cell data only.

Table VII. Vaporization data for alkali sulfates at 1200°K

$M_2SO_4(s)$	P_{1200} (sub)* × 10^7 (atm)	P_{1200} (decomp)† × 10^7 (atm)	ΔH°_{1200} (sub)* (kcal/mole)	ΔS°_{1200} (sub)* (cal/deg mole)
Na_2SO_4	0.80	5.2	80.1‡	34.3‡
K_2SO_4	5.4	3.3	75.6	34.3
Rb_2SO_4	13.0	4.7	76.8	37.1
Cs_2SO_4	87.0	8.3	70.3	35.4

* For process $M_2SO_4(s) = M_2SO_4(g)$.
† For process $M_2SO_4(s) = 2M(g) + SO_2(g) + O_2(g)$.
‡ From extrapolation of data beyond mp of 1157°K.

from the thermal functions of the solids given by Cubicciotti (24), data for the elements (25), and the heats of formation of the solid sulfates (26, 27). The heats, entropies, and sublimation pressures of Na_2SO_4, Rb_2SO_4, and Cs_2SO_4 were taken from the work of Cubicciotti (24, 28). For $Na_2SO_4(s)$, with a melting point of 1157°K, data for the solid were extrapolated to 1200°K for purposes of comparison. An inspection of Table VII shows that the decomposition pressures at 1200°K vary only slightly in going through the series from Na to Cs, while the molecular sublimation pressures increase by two orders of magnitude. And since the table also shows that the entropies of sublimation are reasonably constant, the increase in sublimation pressure down the series can be attributed primarily to the corresponding decrease in the heat of sublimation. This latter effect might arise from increasing repulsions between adjacent metal ions in the $M^+(SO_4^=)M^+$ solid configuration as atomic number and size of the metal ion increase. It is not clear why $Na_2SO_4(g)$ was not detected by mass spectrometry in the vapor over $Na_2SO_4(s)$ (3), since the data indicate that the molecular sublimation pressure is approximately 13% of the total pressure.

Note Added in Proof

Kohl *et al.* have indeed observed $Na_2SO_4(g)$ by mass spectrometry and provide derived thermochemical data for the gaseous sulfate (29).

Acknowledgment

We gratefully acknowledge the assistance of D. R. Knittel with the torsion-effusion measurements and of A. C. Scott with the analysis of the effusion cell residues. This research was supported by the Office of Basic Energy Sciences, U.S. Department of Energy.

Manuscript submitted June 26, 1978; revised manuscript received Sept. 23, 1978.

Any discussion of this paper will appear in a Discussion Section to be published in the December 1979 JOURNAL. All discussions for the December 1979 Discussion Section should be submitted by Aug. 1, 1979.

Publication costs of this article were assisted by SRI International.

REFERENCES

1. I. Eliezer and R. A. Howald, *J. Chem. Phys.*, **65**, 3053 (1976).
2. R. M. Atkins and K. A. Gingerich, *Chem. Phys. Lett.*, **53**, 347 (1978).
3. P. J. Ficalora, O. M. Uy, D. W. Muenow, and J. L. Margrave, *J. Am. Ceram. Soc.*, **51**, 574 (1968).
4. D. L. Hildebrand and D. T. Knight, *J. Chem. Phys.*, **51**, 1260 (1969).
5. K. H. Lau, D. Cubicciotti, and D. L. Hildenbrand, *ibid.*, **66**, 4532 (1977).
6. D. L. Hildenbrand and W. F. Hall, *J. Phys. Chem.*, **67**, 888 (1963); **68**, 989 (1964).
7. A. C. P. Pugh and R. F. Barrow, *Trans. Faraday Soc.*, **54**, 671 (1957).
8. D. L. Hildenbrand, *J. Chem. Phys.*, **48**, 3657 (1968); **52**, 5751 (1970).
9. D. L. Hildenbrand, *Int. J. Mass Spectrom. Ion Phys.*, **4**, 75 (1970), **7**, 255 (1971).
10. C. I. Whitman, *J. Chem. Phys.*, **20**, 161 (1952).
11. K. Motzfeldt, *J. Phys. Chem.*, **59**, 139 (1955).
12. J. H. Stern and N. W. Gregory, *ibid.*, **61**, 1226 (1957).
13. A. V. Gusarov and L. N. Gorokhov, *High Temp. (USSR)*, **4**, 558 (1966).
14. G. W. Mines and R. K. Thomas, *Proc. R. Soc. London, Ser. A*, **336**, 335 (1974).
15. D. S. Alderdice and R. N. Dixon, *J. Chem. Soc., Faraday Trans. 2*, **72**, 372 (1976).
16. K. H. Lau and D. L. Hildenbrand, Unpublished data.
17. T. Kosugi, *Bull. Chem. Soc. Jpn.*, **45**, 15 (1972).
18. JANAF Thermochemical Tables, NSRDS-NBS 37, 2nd ed., U.S. Govt. Printing Office, Washington, D.C. (1971).
19. L. V. Gurvich, O. V. Dorofeeva, and V. S. Yungman, in Proceedings of the Conference on High Temperature Science Related to Open-Cycle, Coal-Fired MHD Systems, Argonne National Lab. Report ANL-77-21 (1977).
20. L. N. Gorokhov, Annual Report, Institute for High Temperatures, Academy of Sciences, USSR (1975).
21. E. R. Plante, Private communication.
22. C. Kroger and J. Stratmann, *Glastechn. Ber.*, **34**, 311 (1961).
23. W. D. Halstead, *Trans. Faraday Soc.*, **66**, 1966 (1970).
24. D. Cubicciotti, *High Temp. Sci.*, **3**, 349 (1971).
25. R. Hultgren, P. D. Desai, D. T. Hawkins, M. Gleiser, K. K. Kelley, and D. D. Wagman, "Selected Thermodynamic Properties of the Elements," American Society for Metals, Cleveland (1973).
26. D. D. Wagman, W. H. Evans, V. B. Parker, and R. H. Schumm, Nat. Bur. Std. Rep. NBSIR 76-1034 (April 1976).
27. O. Kubaschewski and E. L. Evans, "Metallurgical Thermochemistry," 3rd ed., Pergamon, New York (1958).
28. D. Cubicciotti and F. J. Kenneshea, *High Temp. Sci.*, **4**, 32 (1972).
29. F. J. Kohl, C. A. Stearns, and G. C. Fryburg, in "Metal-Slag-Gas Reactions and Processes," Z. A. Foroulis, and W. W. Smelzer, Editors, p. 649, The Electrochemical Society Softbound Symposium Series, Princeton, N.J. (1975).

Technical Note

Temperature Dependence of the Reaction of Hydrogen with Highly Reactive Uranium Powders

J. L. Stakebake

Rockwell International, Rocky Flats Plant, Golden, Colorado 80401

Studies are being conducted to determine the kinetics for reactions involving hydrogen and reactive metal powders. For uranium powders the reaction is

$$U + \frac{3}{2}H_2 \rightleftharpoons UH_3 \qquad [1]$$

Key words: adsorption, kinetics, metals, thermodynamics.

During the investigation the effect of temperature was determined in 26.6 kPa (200 Torr) of hydrogen in the temperature range 50°-250°C. Each run was conducted on a single sample with a uniform surface area produced by hydriding and dehydriding the sample. After each run, the metal powder was retrieved by dehydriding under vacuum at 200°-300°C. Progress of the

reaction was followed with a Cahn Model 100 vacuum microbalance (1). Temperature measurements were made with a thermocouple located adjacent to the sample and showed no temperature excursions greater than ±5°C.

One of the kinetic models being used to evaluate the data is a progressive conversion model (1). The first-order rate expression where the rate of reaction is proportional to the amount of uranium powder available is given by

$$W_t = W_m (1 - e^{-kt}) \quad [2]$$

where W_t is the hydrogen reacted at time t, W_m is the maximum hydrogen reacted, and k is the first-order rate constant.

A comparison of the first-order rate constants at various temperatures revealed an unusual inverse temperature dependence. As the temperature was increased, the rate of reaction decreased. An Arrhenius plot of this data is shown in Fig. 1. Analysis of the Arrhenius equation

$$k = Ae^{-Q/RT} \quad [3]$$

resulted in an apparent activation energy of −1.59 ± 0.24 kcal/mole. This type of behavior has been observed before for uranium powder (2), wire (3), and coupons (4), and also for plutonium powders (5).

At temperatures above 225°C the decomposition of uranium hydride is substantial and the total rate is a function of both the forward and reverse rates. This would explain the results observed for wire and larger coupons. At the low temperatures employed in this work, as well as that of Condon and Larson (2), another factor must be involved. In both cases, the reaction rates continued to increase as the temperature was decreased to as low as 0°C in case of the Condon and Larson study. Hydrogen pressures were substantially above the decomposition pressure of the hydride so the reverse reaction would have little effect. In order to offer a possible explanation for the observed temperature dependence, one can evaluate the effect of temperature on various steps of the reaction. These steps include: (*i*) hydrogen adsorption; (*ii*) dissociation of the hydrogen molecule; (*iii*) surface or bulk diffusion; (*iv*) reaction with the uranium. Steps (*ii*), (*iii*), and (*iv*) all have positive temperature coefficients. Dissociation of hydrogen in step (*ii*) occurs rapidly with very small activation energies. This step may in fact be inseparable from the adsorption step. Step (*iii*), which involves diffusion, is also a rapid step. For the size of uranium particles being used, the diffusion of hydrogen is so fast that it plays virtually no role in controlling the reaction rate (6). Reaction of hydrogen with uranium is activated but the activation energy is likely very small. This leaves only step (*i*), the adsorption of hydrogen, to possess an inverse temperature dependence.

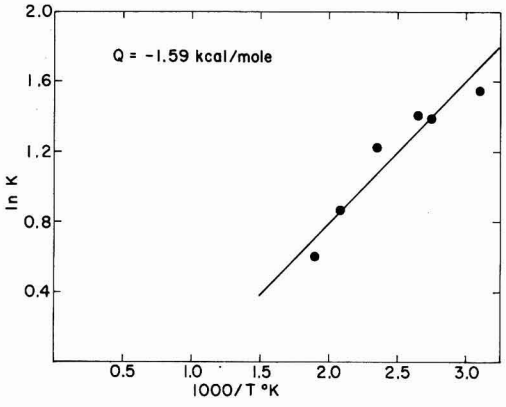


Fig. 1. Arrhenius plot of the first-order rate constants for the reaction of hydrogen with uranium powder at 26.6 kPa hydrogen pressure.

According to the kinetic theory of gases, the number of molecules striking a surface per second is

$$\frac{dN}{dt} = \frac{P}{(2\pi mkT)^{1/2}} \quad [4]$$

where P is the measured pressure, m the mass, and T the temperature of the gas molecules. The actual rate of adsorption is influenced by the sticking probability, s, which is given by

$$s = \sigma f(\theta) e^{-E/RT} \quad [5]$$

where σ is the condensation coefficient and $f(\theta)$ is a function of the surface coverage. Combining Eq. [4] and [5], the rate of activated adsorption becomes

$$r_a = \frac{\sigma P}{(2\pi mkT)^{1/2}} f(\theta) e^{-E/RT} \quad [6]$$

The temperature dependence of the rate for activated adsorption is dominated by the exponential, $e^{-E/RT}$. This means that the rate of adsorption will increase with temperature, however, for nonactivated adsorption the sticking probability will be constant or independent of temperature. The temperature dependence of the rate of adsorption will then be determined by $\sigma P/(2\pi mkT)^{1/2}$ which results in an increasing rate with decreasing temperature. Hydrogen adsorption on metals generally falls into the latter category where the adsorption is extremely fast and nonactivated.

If step (*i*) happens to be the rate-controlling step, then the temperature dependence of the rate of adsorption will be responsible for the decrease in the over-all rate of reaction with increasing temperature. If step (*i*) is not the rate-controlling step it may still be responsible for the inverse temperature behavior. This could be brought about if the adsorption of hydrogen is a near-equilibrium process with a negative ΔH. Under these conditions the free energy change, ΔG, will be approximately zero and the entropy change, ΔS, will be negative. If the heat of adsorption, ΔH, is greater than the activation energy for the subsequent rate-controlling step, then the over-all reaction rate will have an inverse temperature dependence.

In either case, the step responsible for the inverse temperature dependence is the adsorption of hydrogen. Whether or not this type of behavior is common to less reactive gas-powder systems is unknown.

Acknowledgment

This work was performed under the auspices of a contract with the U.S. Department of Energy.

Manuscript submitted Aug. 11, 1978; revised manuscript received Oct. 9, 1978.

Any discussion of this paper will appear in a Discussion Section to be published in the December 1979 JOURNAL. All discussions for the December 1979 Discussion Section should be submitted by Aug. 1, 1979.

Publication costs of this article were assisted by Rockwell International.

REFERENCES

1. J. L. Stakebake, Paper submitted to *This Journal*.
2. J. B. Condon and E. A. Larson, *J. Chem. Phys.*, **59**, 855 (1973).
3. J. E. Burke and C. S. Smith, U.S.A.E.C. Report LA-37, Nov. 1943; J. J. Katz and E. Rabinowitch, "The Chemistry of Uranium," Part I, p. 193 ff, McGraw-Hill Book Co., Inc., New York (1951).
4. W. M. Albrecht and M. W. Mallet, *This Journal*, **103**, 404 (1956).
5. J. L. Stakebake, Unpublished data (1978).
6. J. B. Condon, R. A. Strehlow, and G. L. Powell, *Anal. Chem.*, **43**, 1448 (1971).

JOURNAL OF THE ELECTROCHEMICAL SOCIETY

ACCELERATED

—BRIEF COMMUNICATIONS—

MARCH 1979

Vanadium Oxide Cathode Materials for Secondary Lithium Cells

D. W. Murphy,* P. A. Christian, F. J. DiSalvo, and J. N. Carides

Bell Laboratories, Murray Hill, New Jersey 07974

The reversible topochemical reaction of various transition metal chalcogenides and oxides with lithium may be utilized as the cathodic reaction in high energy density, ambient temperature, secondary batteries(1-6). The half-cell reaction is given in Eq. [1].

$$MX_n + aLi^+ + ae = Li_aMX_n \qquad [1]$$

Several chalcogenides studied in recent years appear to be promising candidates. However, the most studied oxides, V_2O_5 (7) and MoO_3(4), are less suitable because of low electronic conductivity, irreversible reduction at moderate potentials, and (for V_2O_5) electrolyte oxidation on recharge. We recently illustrated the importance of both electronic conductivity and unit cell volume to the topochemical incorporation of lithium by transition metal oxides with rutile related structures(8). These results suggested that the unit cell volumes of the first row transition metal rutiles are too small to incorporate lithium at significant rates. Improvement in lithium incorporation by anatase TiO_2 (9), γ-MnO_2 (10), and several chromium oxides (11) compared to their rutile forms may be attributed to the lower density of the former. We have found that V_6O_{13}, which is metallic and has an open structure, is an excellent cathode material for secondary lithium cells.

The V_6O_{13} ($VO_{2.167}$) used was prepared either by the stoichiometric reaction of V_2O_5 and V metal at 650 °C or by the thermal decomposition of NH_4VO_3 below 450 °C in an inert atmosphere. The latter procedure affords vanadium oxide with stoichiometries ranging from $VO_{2.17}$ to $VO_{2.20}$. Both methods yield materials with similar x-ray powder diffraction patterns. The characteristic metal-insulator transition in the magnetic susceptibility of V_6O_{13} near 150 °K (12) is broadened in samples prepared from NH_4VO_3. The range of particle sizes determined by SEM is 10 to 50 μm for the stoichiometric product and 1 to 5 μm for the NH_4VO_3 decomposition product.

Preliminary cycle data for Li/$LiAsF_6$, propylene carbonate (PC)/V_6O_{13} cells are shown in Fig. 1. Small test cells (13) containing stoichiometric V_6O_{13} (Fig. 1a) have capacities corres-

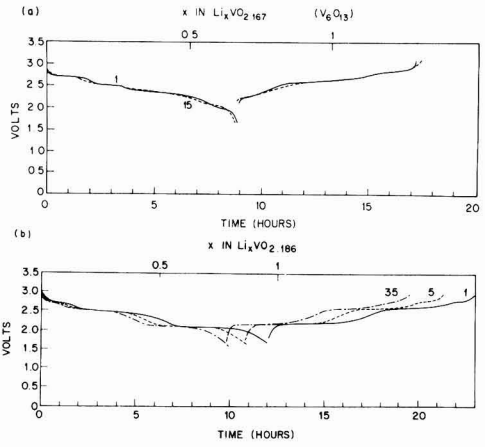


Fig. 1. (a) Voltage of a Li/1M $LiAsF_6$, PC/V_6O_{13} cell, constructed as in Ref. 13, containing 8.5 mg. V_6O_{13} prepared from V_2O_5 and V at 650 °C. The cell was cycled at 0.2 mA. Solid curve is first cycle and the dashed curve is the fifteenth. (b) Voltage of a Li/$LiAsF_6$,PC/$VO_{2.186}$ cell containing 7.95 mg. $VO_{2.186}$, prepared by thermal decomposition of NH_4VO_3, mixed with 7.95 mg. graphite cycled at 0.2 mA. Cycle numbers are indicated.

*Electrochemical Society Active Member.
Key words: batteries, topochemistry.

ponding to 0.55 to 0.65 Li/V in the range 2.8 to 2.2 volts and exhibit a sharp cutoff (i.e., no further capacity above 0.1 volts). Cells containing the NH_4VO_3 decomposition product (Fig. 1b) exhibit additional capacity near 2.1 volts such that their total capacity is near 1.0 Li/V. Cells containing the NH_4VO_3 decomposition product which had been annealed at 650 °C for 8 to 12 hours behaved similarly to those in Fig. 1a.

Chemical lithiation by n-BuLi in hexane at room temperature suggests a limit of 0.68 Li/V for the material from the stoichiometric reaction and ~1.25 Li/V for the NH_4VO_3 decomposition product. The x-ray powder diffraction patterns of $Li_xV_6O_{13}$ indicate multiphase behavior for $x<3$ and a non-stoichiometric single phase for $x>3$, in which there is a gradual increase in the b parameter of the monoclinic unit cell. For x=4 the unit cell parameters are:

a=11.89Å b=3.98Å c=10.24Å =100.4°

while for V_6O_{13} (14):

a=11.92Å b=3.68Å c=10.14Å =100.87°

Because the measured electronic conductivity (pressed pellet) of $Li_xV_6O_{13}$ decreases rapidly for $x>4$, graphite was added to the cathode to reduce polarization in the high capacity cells.

The V_6O_{13} structure (14) is shown in Fig. 2. The structure consists of alternating double and single zig-zag chains of distorted VO_6 octahedra interconnected by corner shared oxygens and infinite channels along [010]. The

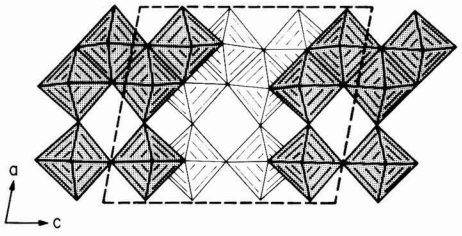


Fig. 2. The structure of V_6O_{13} projected on (010) showing interconnected single and double zig-zag chains and channels for lithium diffusion.

smallest structural element or "bottleneck" through which a lithium ion must diffuse is a square plane of oxygen atoms, which Hong (15) has suggested as optimal for lithium ion conduction in oxides. The lithium ions in $Li_xV_6O_{13}$ most likely occupy square pyramidal sites located between the single and double chains. There are eight such sites per V_6O_{13} formula unit. Similar sites are occupied by Li in the bronze, $Li_{0.3}V_2O_5$ (16). While V_2O_5 is thought to incorporate lithium with cleavage of strongly polarized V=O—V bonds (1), no such readily cleavable V-O bonds are present in V_6O_{13}.

We have also tested the suitability of several other vanadium oxides as cathode materials in lithium cells. The metastable VO_2(B) (17), thought to consist of V_6O_{13}-like zig-zag double chains interconnected by corner shared oxygens, incorporates ~0.5 Li both electrochemically and from n-BuLi. V_3O_7 reversibly incorporates 0.33 Li/V above 2.5 volts, and also exhibits substantial irreversible capacity above 2.0 volts. Appreciable capacity was obtained with V_4O_9 (approximately 0.75 Li/V), although these cells exhibited poor rechargeability. Our results with V_2O_5 are substantially in agreement with those of Walk and Gore (7).

We attribute the higher capacity of cells made from the NH_4VO_3 decomposition product largely to its smaller particle size. The behavior of these cells operated at -10 °C is similar to that shown in Fig. 1a. Additional capacity, similar to that in Fig. 1b, is obtained at 70 °C for cells containing stoichiometric V_6O_{13}.

Based on the n-BuLi stoichiometry of 1.25 Li/V and an average voltage of 2.2 volts, the theoretical energy density of the Li/V_6O_{13} cell is 800 whr/Kg. This large theoretical energy density and the excellent rechargeability make V_6O_{13} an exceptional lithium cathode material.

ACKNOWLEDGMENT

The authors are indebted to F. A. Trumbore for SEM photographs and helpful discussions, and to J. V. Waszczak for technical assistance.

REFERENCES

1. M. S. Whittingham, This Journal, 123, 315 (1976).
2. D. W. Murphy and F. A. Trumbore, J. Crystal Growth, 39, 185 (1977).
3. G. L. Holleck and J. R. Driscoll, Electrochimica Acta., 22, 647 (1977).
4. J. O. Besenhard and R. Schollhorn, J. Power Sources, 1, 267 (1976).
5. B. C. H. Steele, in "Superionic Conductors," p. 47, G. D. Mahan and W. L. Roth, Ed., Plenum Press, New York (1976).
6. M. S. Whittingham, Prog. in Solid State Chem., 12, 1,(1978).
7. C. R. Walk and J. S. Gore, Paper No. 27 presented at the Electrochemical Society Mtg., Toronto, May 11-16, 1975.
8. D. W. Murphy, F. J. DiSalvo, and J. N. Carides, Mat. Res. Bull., in press.
9. M. S. Whittingham and M. B. Dines, This Journal, 124, 1388 (1977).
10. H. Ikeda, T. Saito, and H. Tamura, Manganese Dioxide Symp. Proceeding, 1, 384 (1975).
11. J. O. Besenhard and R Schollhorn, This Journal, 124, 968 (1977).
12. A. C. Gossard, F. J. DiSalvo, L. C. Erich, J. P. Remeika, and H. Yasuoka, Phys. Rev. B, 10, 4178 (1974).
13. D. W. Murphy, J. N. Carides, F. J. DiSalvo, C. Cros, and J. V. Waszczak, Mat. Res. Bull., 12, 825 (1977).
14. K. A. Wilhelmi, K. Waltersson, and L. Kihlborg, Acta Chem. Scand., 25, 2675 (1971).
15. H. Y. P. Hong, J Solid State Chem., in press.
16. A. Hardy, J. Galy, A. Casalot, and M. Pouchard, Bull. Soc. Chim. Fr., 1056 (1965).
17. F. Theobald, R. Cabala, J. Bernard, J. Solid State Chem., 17, 431 (1976).

Manuscript submitted Nov. 16, 1978; revised manuscript received Dec. 22, 1978.

Publication costs of this article were assisted by Bell Laboratories.

Selective Chlorination with a Cyclodextrin-Modified Electrode

Tomokazu Matsue, Masamichi Fujihira, and Tetsuo Osa

Pharmaceutical Institute, Tohoku University, Aobayama, Sendai, 980, Japan

Cyclodextrins, cyclic 1,4-linked D-glucopyranose oligomers, have characteristics of forming inclusion complexes with many organic compounds in aqueous solution (1), and are studied in various fields owing to their catalytic abilities as enzyme models (2,3). Breslow et al. reported the selective chlorination in the presence of α-cyclodextrin (α-CD) (4) and methylated α-CD (5) in solution. Being compared with homogeneous reactions, heterogeneous reactions, especially electrolyses with chemically modified electrodes (CMEs), can make reaction products separate easily and facilitate stereospecific reactions since random motions of reagents will be restricted by the surface structure of electrodes. With such advantages, the organic modified electrodes have been developed since Miller et al. (6), but the stereospecific electrolyses with CMEs have scarcely been reported (7,8). In this paper, we report the selective chlorination of anisole with α-CD chemically modified (α-CD-CME) and α-CD adsorbed graphite electrodes (α-CD-AE).

The α-CD-CME was prepared as shown in scheme 1. The graphite electrodes (Tokai Carbon Co. G 2080) for electrolyses (20x30x2 mm) and for ESCA measurements (5x17x2 mm) were oxidized with $K_2Cr_2O_7$ for 1 hr, and treated with $SOCl_2$ for 1 day, and then reacted with α-CD in pyridine. After a week, the electrodes were removed from the solution and washed with water repeatedly. The reduced graphite electrode was prepared by reducing the oxidized electrode with $LiAlH_4$ in THF for 2 days. The α-CD-AE was prepared by dipping the oxidized electrode in 0.1 M α-CD aqueous solution for 1 day.

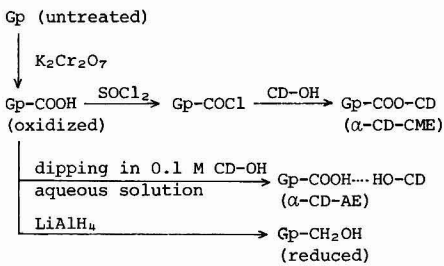
In ESCA spectrum of the α-CD-CME, strong peaks for O 1s at 530.5 eV and for C 1s at 285 eV were appeared as same as the spectrum of the oxidized one (no treatment of α-CD). But, in narrow ESCA spectrum of the α-CD-CME for C 1s, there appeared a new peak at 286.5 eV in addition to the main peak of 285 eV. The peak was assigned to carbon atoms in α-CD because they adjoin oxygen atoms of high electronegativity.

The anodic chlorination of anisole proceeds presumably in the presence of α-CD (4) as shown in scheme 2. When electrolysis is performed in the presence of α-CD, p-isomer may be formed selectively since o-positions of anisole are blocked by the inner wall of α-CD structure (9). All electrolyses were performed at 1.1 V vs. SCE and at constant temperature (20°C) in divided H-type cell, and the electrolyte was 10^{-3} M anisole and 0.5 M NaCl aqueous solution. After electrolysis, the anolyte was extracted with ether, and the ether solution was concentrated to analyze by gas chromatography.

The ratios of p- to o-isomer obtained with electrodes possessing various surface derivatizations are shown in Table I. From these data, it can be seen that the chlorination position of anisole was greatly affected by the surface derivatizations. The oxidized electrode showed the lowest ratio, and the reduced one gave slightly higher ratio than the oxidized one, which was, however, changed gradually to lower value due to the oxidation of the surface by repeating of electrolyses. By performing chemical modification and adsorption of α-CD on the graphite surfaces, these ratios became high level. Especially the α-CD-AE yielded the p-isomer more than 96 %. When the above two types of electrodes were dipped in water, the p-:o- ratio on the α-CD-AE remained high level (>10) for a few days, but fell down gradually owing to the desorption of α-CD to the bulk of the solution, and reached to 5.4 after 17 days. On the other hand, the ratio on the α-CD-CME remained high level (≈10) even after a month. These phenomena led us to the conclusion that the desorption of α-CD from the electrode surface is very slow because of the porosity of the graphite electrodes, and ester linkage between α-CD and the graphite electrode in the α-CD-CME is considerably stable. When these two types of electrodes showing high selectivity were treated with $K_2Cr_2O_7$ for 2

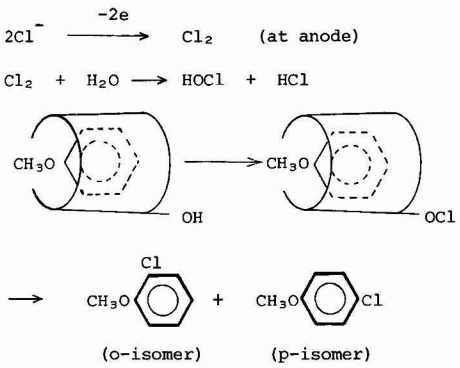
*Electrochemical Society Active Member

Key words: anisole, α-cyclodextrin, chemically modified electrode, chlorination.



Gp; graphite electrode
CD-OH; α-cyclodextrin

Scheme 1. Synthetic procedures of various surface derivatizations.



Scheme 2. Mechanism of anodic chlorination of anisole in the presence of α-CD.

Table I. p-:o- Isomer ratios of chloroanisole with various graphite electrodes.

untreated	7.1
oxidized	3.5
reduced	4.2
α-CD-CME	17.8
α-CD-AE	>25

hrs, these ratios were decreased below 8.0 since the α-CD on the graphite surfaces was removed by the oxidation.

Although the high selectivity of the homogeneous reaction between HOCl and anisole in the presence of α-CD in aqueous solution has already been reported by Breslow et al. (4), the homogeneous reaction has such disadvantages as requirement of a great deal of α-CD to realize a high selectivity in the bulk of the solution and difficulty in the separation of the reaction products from the solution. On the other hand, these disadvantages in homogeneous reaction are greatly improved by using the α-CD-CME.

Electrode reactions are heterogeneous one and they have catalytic abilities to a certain extent. This kind of study on CMEs can be developed as an approach of the biological models to enzymes or membranes.

Acknowlegement.-- This work was partially supported by a Grant-in-Aid for Science Research from the Ministry of Education.

REFERENCES

1. F. Cramer and F. M. Henglein, Quart. Revs. (London), 68, 649 (1956).
2. F. Cramer and W. Kampe, Tetrahedron Letters, 353 (1962).
3. M. L. Bender, R. L. VanEtten, G. A. Clows, and J. M. Sebastain, J. Amer. Chem. Soc., 88, 2318 (1966).
4. R. Breslow and P. Campbell, ibid, 91, 3085, (1969).
5. R. Breslow, H. Kohn, and B. Siegel, Tetrahedron Letters, 1645 (1976).
6. B. F. Watkins, J. R. Behling, E. Kariv, and L. L. Miller, J. Amer. Chem. Soc., 97, 3549 (1975).
7. B. E. Firth, L. L. Miller, M. Mitani, T. Rogers, J. Lennox, and R. W. Murray, ibid, 98, 8271 (1976).
8. B. E. Firth and L. L. Miller, ibid, 98, 8272 (1976).
9. T. Osa, T. Matsue, and M. Fujihira, Heterocycles, 6, 1833 (1977).

Manuscript submitted Oct. 17, 1978; revised manuscript received Jan. 8, 1979.

Publication costs of this article were assisted by Tohoku University.

On the Initial Oxidation Rate of Silicon

A. G. Revesz

COMSAT Laboratories, Clarksburg, Maryland 20734

It has been suggested in a recent paper (1) that the growth of thin (<200 Å) SiO_2 films on silicon is more linear and the oxide film is less protective if the thermal oxidation is performed in dry O_2 rather than in H_2O containing ambients. This has been attributed to micropores in the SiO_2 film. It is shown in this note that (1) some of these conclusions are not justified by the experimental results; (2) some reported ideas and results have been misrepresented, and (3) some of the few valid conclusions have already been reached by others.

Apparently, the conclusion that oxidation in dry O_2 is more linear than in a N_2-H_2O mixture (2000 ppm H_2O) was inferred from the observation that the standard deviation of the linear fit between oxidation time and oxide thickness is less for the former than the latter. However, this is an insufficient measure of the goodness of the fit (i.e., the probability that a linear fit is not due to chance) as it simply indicates the spread of the data around the curve. With respect to linearity, the comparison should have been done on the basis of the significance or confidence levels of the slopes (2) which are not given in Reference 1. In fact, the linear fit seems to be rather poor as the slopes of the thickness-time curve for oxidation in dry O_2 at 893°C can be estimated from Figure 1 in Reference 1 as ~3.3 Å/min. below ~70 Å and 2.3 Å/min. above ~130 Å. The average of these two values happens to be 2.8 which is the rate constant obtained by the linear fit, and, as such, supposedly valid from ~20 Å up to 200 Å. Except for the curve of oxidation in H_2O-N_2 at 780°C, all the curves in Reference 1 exhibit a similar behavior. This observation indicates that, as has been suggested earlier (3), a linear-parabolic relationship is probably more appropriate for the initial oxide growth than the linear rate law.

Even if the oxidation in dry O_2 were more linear than in the particular H_2O-N_2 mixture, this is not necessarily true for oxidation in H_2O containing ambients with different H_2O concentrations. For example, the time required to grow 150 Å thick oxide on (100) silicon in steam (where, similarly to the case of dry O_2, the mole fraction of the oxidizing agent is unity rather than ~2 x 10^{-3} as in the case of the H_2O-N_2 mixture) at 912°C can be calculated from $t = ax + bx^2$ where $a = 2.68 \times 10^{-2}$ min/Å, $b = 2.6 \times 10^{-6}$ min/Å^2, and x = oxide thickness (4) as $t = 4.28 + 5.83 \times 10^{-2} = 4.34$ min. Thus, the oxide growth under these conditions is practically linear. The time is, of course, much less than the ~50 min. required in the case of dry O_2 at 893°C. Thus, the conclusion that the initial regime of oxidation is more linear for dry O_2 than H_2O containing ambient is not generally valid.

The other conclusion that oxide films grown in dry O_2 are less protective than those grown in a H_2O containing ambient is not fully justified, either. To wit, the difference in the dielectric breakdown behavior of the 150 Å thick SiO_2 films grown in dry O_2 and H_2O-N_2 could be due to the large difference in the oxidation time: ~50 min. for dry O_2 and ~160 min. for N_2-H_2O at 893°C [from Figure 1 in Reference 1]. It is expected that the defect structures of the oxide films grown with such different rates would be different even without considering the presence of OH.

Key words: silicon, oxidation, SiO_2 film

In view of the poor linear fit

it is ironic that two pertinent published works have been summarily dismissed in Reference 1: one (3) because it "does not consider the possible curve fitting error associated with assuming a linear-parabolic initial regime" and the other (5) for "insufficient data to analyze for the determination of a best fit."

It is very significant that the slopes (i.e. the oxidation rates) were evaluated segment by segment in Reference 3, and the conclusion that the initial oxidation follows a linear-parabolic rate law was obtained from the rate vs. thickness rather than time vs. thickness curves. The other work (5) contains a very detailed statistical analysis of the data (12, 16, 15 and 8 points at four different temperatures) covering the thickness range of 55 to 4500 Å. The significance level of the curve fitting is given there, and it shows that the probability of chance occurrence of the linear-parabolic fit is less than 10^{-7}. This indicates that even a single linear-parabolic rate law (assumed to be valid even at the beginning of the oxidation) is a better approximation than the linear rate.

The concept of channel type defects in noncrystalline SiO_2 films (6) has been misinterpreted in Reference 1. The statement there that "it is difficult to reconcile the oxidation kinetics results based on more dense localized regions" is totally erroneous since it has never been suggested that the channels represent more dense regions.

What has been suggested is that channel defects might be responsible for various unique transport properties of thermally and anodically grown SiO_2 films (6). Curiously, after dismissal of the possible role of channel defects in oxide growth, it is suggested in Reference 1 that "micropores" provide a "short circuit path" during oxide growth. This is, of course, the very role that has been suggested for channels as being responsible for the extensive linear regime of oxide growth on silicon (5).

Publication costs of this article were assisted by COMSAT Laboratories.

Since it is suggested in Reference 1 that the size of the "micropores" is probably less than 20 Å, the distinction between "micropores" and channels tends to disappear. However, the concept of "micropore" collapses if their density, as suggested in Reference 1, is $\sim 10^{15}$ cm^{-2}. In this case the oxide film would contain only "micropores" as the surface density of Si atoms is of this order of magnitude. Obviously, the density of Au nuclei on the oxide surface (supposedly indicators of inhomogeneities in the oxide) is either much less than 10^{15} cm^{-2} (it is very unlikely that the electron microscopic investigations could result in this resolution) or they do not correspond to inhomogeneities in the oxide.

It should also be noted that the relationship between OH content, dielectric breakdown, dissolution rate, etc. is not as simple as implied in Reference 1. To wit, anodically grown SiO_2 films which contain 10^{20} - 10^{21} OH/cm^3 (7) have higher dissolution rates and electric conduction than thermally grown oxides [as discussed in Reference (6)] which contain less OH.

ACKNOWLEDGMENT

This paper is based on work performed at COMSAT Laboratories under the sponsorship of Communications Satellite Corporation.

REFERENCES

1. E. A. Irene, J. Electrochem. Soc. 125, 1708 (1978).
2. E. B. Wilson, An Introduction to Scientific Research, McGraw-Hill, New York, 1952, p. 269.
3. M. A. Hopper, R. A. Clarke, and L. Young, J. Electrochem. Soc. 122, 1216 (1975).
4. W. A. Pliskin, IBM Journal, May 1966, p. 198.
5. A. G. Revesz and R. J. Evans, J. Phys. Chem. Solids 30, 551 (1969).
6. A. G. Revesz, J. Non-Cryst. Solids 4, 347 (1970).
7. K. H. Beckmann and N. J. Harrick, J. Electrochem. Soc. 118, 614 (1971).

Manuscript submitted Dec. 4, 1978; revised manuscript received Dec. 20, 1978.

A New Technology for Tapered Windows in Insulating Films

Hiroshi Ono and Hiroyuki Tango

Toshiba Corporation, Toshiba Research and Development Center, Kawasaki, Japan 210

Several taper etching techniques have been developed recently for fabrication process of semiconductor devices to ensure better step converage for metallization. North et al (1) have achieved the taper etching of phosphorus-doped SiO_2 by applying ion implantation prior to photoresist coating. According to Parisi et al (2) suitable adjustments of NH_4/HF compositions and etching bath temperatures can lead to tapered windows in SiO_2. This paper describes a novel method for the taper etching utilizing the two interesting findings (3), that is (a) the surface region of insulating films exposed to CF_4- or CCl_4-plasma, or CF_4-O_2 mixture gas plasma is etched at a faster rate than that of an unexposed film, and (b) the adhesion of a photoresist to the plasma-exposed film surface is not so strong as that to unexposed film. The detailed mechanisms behind these two new phenomena have not been revealed, but can be considered as follows. The former phenomenon, (a), is almost similar to the enhanced etching behavior of damaged film by argon ion implantation. On the other hand, the latter one, (b), should be due to deposited materials, such as carbon, on the film surface during plasma etching. When either O_2 or N_2 gas was used, the taper etching phenomenon did not occur. This may suggest that gas plasma without carbon related compounds can not result in the tapering. In this paper, the novel technique is applied to engrave tapered windows in several sorts of insulating films, and also an attempt to control the taper angle of the edge profiles is described.

The processing sequence for tapered windows is shown is Fig. 1. At first, the film surface must be exposed to the plasma-excited gas prior to photoresist coating (Fig. 1 (a)). This process is most important to produce tapered steps at the edge of windows as described below. After the photoresist was coated on the film and was processed to generate photoresist image (Fig. 1 (b)), the film etching was carried out with NH_4F solution through the photoresist patterns as a mask (Fig. 1 (c)). Because of plasma exposure effect before photoresist application, the edge profiles of the film will give rise to tapering. Subsequently, the photoresist was removed (Fig. 1 (d)).

Experiments were performed on the four different silicate glasses commonly used in integrated circuits fabrication: chemically vapor deposited silicon di-oxide (CVD-SiO_2), phosphosilicate glass (PSG), thermally grown oxide (SiO_2), arsenosilicate glass (A_sSG). Two different plasma etchers were used for plasma exposure treatment. One was the CDE-II (Chemical Dry Etcher-II manufactured by Toshiba Corp.) utilizing microwave-excited active species with long life time (4). Another was the PE317 made by ETE (Etching Technique of Equipments). As etching gases, CF_4 and CCl_4 are used. When CF_4 gas was used, plasma exposure was carried out in the CDE-II under the following conditions: microwave power of 870W, the gas pressure of 0.5 Torr., and plasma exposure time of 5 min. On the other hand, in case of using CCl_4 gas, it was done in the PE317 under the following conditions: output current of 3 A, plasma exposure time of 9 min, and the gas pressure of 0.28 Torr. In Fig. 2, the eleven SEM micrographs show cross sections of window walls, where four photographs in Fig. 2 (a) are obtained from conventional etching technique without plasma exposure treatment, Figs. 2 (b)

and 2 (c) were obtained by the present taper etching technique using the CDE-II and PE317 respectively. Comparing Fig. 2 (b) and Fig. 2 (c) with Fig. 2 (a), it is evident that all the edge profiles in Fig. 2 (b) and Fig. 2 (c) have been tapered significantly. Also, note that four SEM micrographs in Fig. 2 (a) have nearly isotropic edge profiles. Furthermore, it can be seen that edge profile shown in Fig. 2 (b), and Fig. 2 (c), are so much sensitive to the kind of both the films and the gases used. In Fig. 2 (b), the taper angles of window walls with respect to the wafer surface are PSG > CVD-SiO_2, A_sSG > SiO_2, and their value are approximately 45, 32, 32, and 10° respectivefilm have the same angle. Taper angles in Fig. 2 (c), are generally smaller than those in Fig. 2 (b), where the PSG, CVD-SiO_2, and A_sSG films have the angles of 19, 15, and 15° respectively.

Other experiments were performed to examine the possibility of producing tapered steps having desired taper angles without changing a kind of etching gases and films. Plasma exposure time was chosen as an experimental parameter, and was varied in the range of 30 sec to 15 min, where CVD-SiO_2 film was used. The other parameters were the same as those in Fig. 2 (b). The results are shown in Fig. 3, and are summerized in Fig. 4, in which the taper angles are plotted as a function of plasma exposure time. Note that the taper angle becomes shallower with increasing plasma exposure time, and then reaches certain constant value. Thus, we can easily control the taper angle by only choosing an appropriate exposure time.

Features of the present taper plasma process (TAPP) are its simplicity and wide applicability including ease in controlling the taper angle. In addition, our method is very reliable and reproducible. The commercially available plasma etchers, such as IPC2004-1813SC, can also be used for plasma exposure treatment.

ACKNOWLEDGMENTS

The authors are greatful to H. Kinoshita for his operating the PE317 etcher, and to Dr. Y. Nishi for his critical reading of the manuscript.

REFERENCES

1. James C. North, Thomas E. Mcgahan, D. W. Rice, and A. C. Adams, IEEE Trans. Electron Devices, ED-25, 809 (1978).

2. G. I. Parisi, S. E. Haszko, and G. A. Rozgonyi, This Journal, 124, 917 (1977).

3. H. Ono: to be published.

4. M. Shibagaki, Y. Horiike, and T. Yamazaki, Japan, J. Appl. Phys., 17, 215 (1978).

Manuscript submitted Nov. 6, 1978; revised manuscript received Nov. 28, 1978.

Publication costs of this article were assisted by Toshiba Research and Development Center.

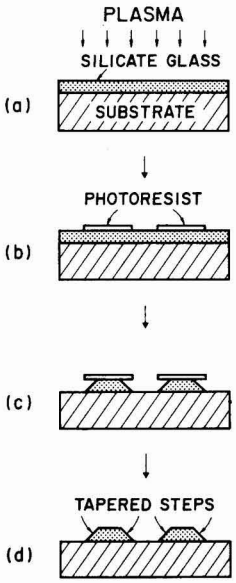


Fig. 1. Schematic processing sequence for tapered windows utilizing plasma exposure effect: (a) plasma exposure; (b) photoresist application; (c) etching in NH_4F solution; (d) photoresist removal.

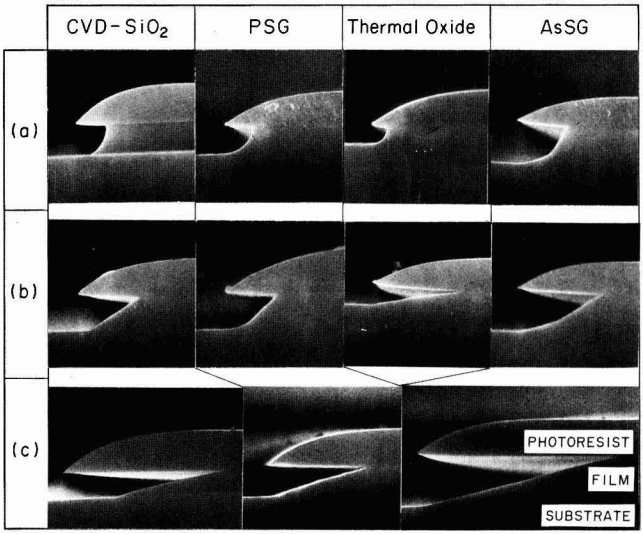


Fig. 2. SEM cross-sectional views of window walls etched in the four different films with magnification X10,000. (a) conventionally etched; (b) CF_4-plasma exposure; and (c) CCl_4-plasma exposure.

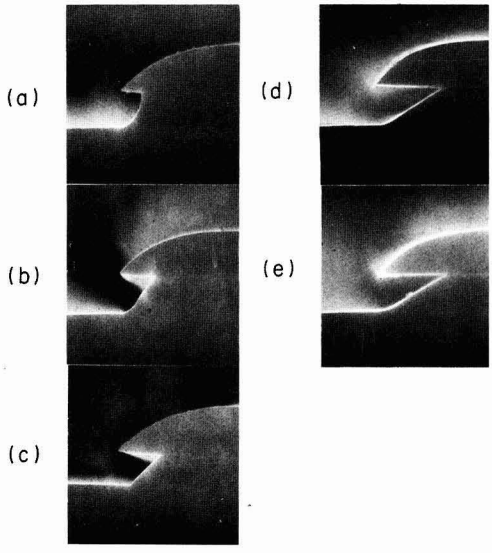


Fig. 3. SEM cross-sectional views of window walls etched in the CVD-SiO_2 film showing effects of plasma exposure time: magnification X10,000. (a) 30 sec; (b) 2 min; (c) 3 min; (d) 5 min; (e) 15 min.

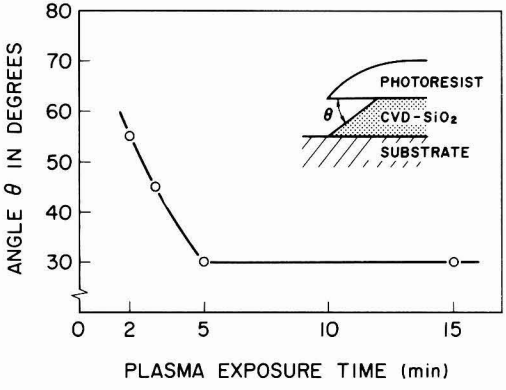


Fig. 4. Angle of window wall as a function of plasma exposure time.

JOURNAL OF THE ELECTROCHEMICAL SOCIETY

REVIEWS AND NEWS

MARCH 1979

Social Change and Future Economic Growth[1]

D. A. Vermilyea*

General Electric Company, Research and Development Center, Schenectady, New York 12309

Edward Goodrich Acheson serves as an ideal model of the innovative entrepreneurs who have contributed so remarkably to our well being. One facet of Acheson's career involved the invention, in 1891, of a new material—silicon carbide—previously unknown in nature, which remained the hardest synthetic material ever made until the discovery of boron carbide in 1929. Acheson named the new material "carborundum" and founded a company of the same name to produce it. The company prospered and grew to be one of the 500 largest U.S. industrial corporations.

The economic system in the years between Acheson's times and our own has been extremely receptive to such innovation—we take it for granted that such receptivity will continue forever. It is becoming increasingly obvious, however, that the far-reaching social changes which have accompanied the development of the affluent society since the late nineteenth century, and indeed since the beginning of the Industrial Revolution for that matter, are resulting in important changes in the economic system as well. The economy of Acheson's day no longer exists. We in the tecnnical community have generally not paid enough attention to these changes. This paper considers the nature of these social changes and the ways they will affect the future of the economy.

To a large extent the talk will be concerned with the effects of the emotional aspects of human personalities on society and on the economy. I first became interested in this subject a few years ago when I was studying the role of nuclear power in our long-term energy future. Nuclear power appeared to be the cheapest, safest, and cleanest large scale energy source available to replace oil and natural gas, and it was already technically proven. It was clear then, however, that emotional forces would play a major role in its deployment; today it seems that such forces will be decisive. It appears that, to an increasing degree, emotional forces are taking a position alongside rational technical forces in deciding the outcome of important issues. Environmentalism and the drives for decentralization and for conservation are products of these emotional forces, at least in part.

Emotional forces and impulses are fundamental and essential aspects of human personality, of course, and life would be drab indeed without them; such forces have always played an important role in human affairs. Early in the Industrial Revolution, however, and until the past few decades, their effect seems to have been supportive rather than disruptive—somehow the society had them reasonably under control. Today the emotional/rational balance is upset, and the impact of irrational elements seems divisive and negative. Pirsig, in his book "Zen and the Art of Motorcycle Maintenance," writes

> "It is the force of the irrational elements crying for assimilation that creates the bad quality, the chaotic disconnected spirit of the Twentieth Century."

It is important to understand why the emotional and the rational now seem to be out of balance—why the conflict now and not before?

This talk comprises the following major elements: the sources of social change, the nature of the changes that have occurred and are occurring, the fundamentals which control our ability to influence future directions, and the outlook: the anticipated impact on the economy and the threats and opportunities. The primary objective is to provide a comprehensive view of the current situation and of the long-term trends.

The broad conclusions are the following.

Major changes are occurring in individuals and in the social, political, and economic systems.

These changes result from growth itself, interacting with fundamental characteristics of individuals and the society.

The changes have been underway for many decades, even centuries; they are irreversible.

There is no adequate theoretical guide to modifying the natural trends.

The economy is vitally connected with the society in which it is imbedded and of which it is a part; these changes will have profound impacts on the vigor and character of the economy.

Put more succinctly: major irreversible change, inadequate theory, profound impact.

I'd like to start with a little perspective on our times. Two hundred years after the start of the Industrial Revolution we find ourselves in the remarkable and unique situation shown in Fig. 1. Throughout history it is doubtful whether per capita income ever exceeded $200 per year—about four times the minimum subsistence level—when averaged over all the people who supported the society. Affluence was for the few, and was based on the labor of serf and slave. These latter led, in Hobbes' phrase, lives that were nasty, brutish, and short. Today, in the developed world, affluence extends to the average individual, while the entire world is even moderately well off, with an average per capita income in excess of $1,000 per person. Remarkably, the growth rate which gave us this fantastically wealthy society with all its benefits was only 1.7% per year! How was such a result achieved? More important: How long will such growth continue—what will limit it, and at what level? We will return to these questions later.

The social benefits of this recent growth are enormous: we live extraordinarily well, poverty is nearly eliminated, we enjoy excellent health, we are well educated, our political and economic systems are fairly stable. But there are problems and things are

* Electrochemical Society Honorary Member.

[1] This was the Edward Goodrich Acheson Medal Award Address delivered on October 17, 1978, at the Pittsburgh, Pennsylvania, Meeting of the Society.

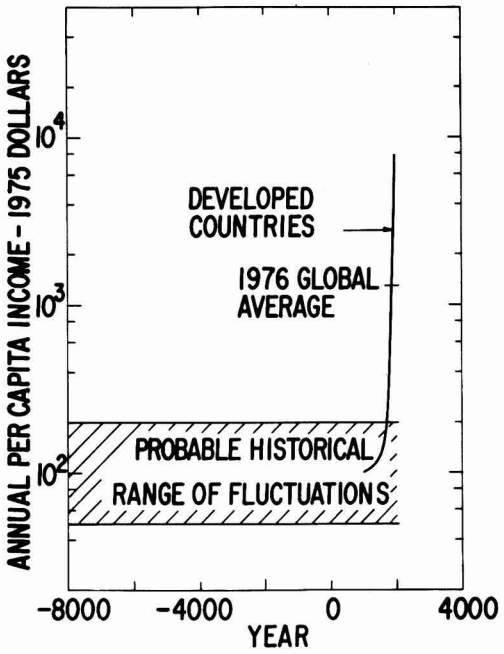


Fig. 1. The growth of affluence. Source for the 1976 global average is Kahn, Brown, and Martel (1).

changing. Some of the major forces which have driven social change are the following. First, the unrestrained free market exhibits some troublesome problems such as the tendency to encourage monopolies, unacceptable economic fluctuations, and environmental degradation; control and regulation by the central government seems to be required to prevent these difficulties. Second, the scientific sophistication which has accompanied and been encouraged by economic progress has eroded the superstitious basis of religion, and as a result, religion has become much less effective in its traditional role of controlling human irrationality. As Ellul put it in his book "Betrayal of the West," "the West is dying because it has won out over God." Urbanization and great mobility have resulted in special problems in the cities. Affluence decreases the marginal utility of wealth, and hence reduces the drive for growth. Scientific sophistication, urbanization, and affluence are perhaps the three most prominent causes of the rise in the relative importance of emotional forces. The complexity, rapid pace of change, and need for long-term planning strain individual capabilities and encourage centralization. And finally, communication and mass education result in increased social interaction and more opportunity for friction. These forces stem in large measure from growth itself, and they have been acting for a very long time.

Changes in the Political System

Now let's look at some of the changes in detail, starting with the political system. It is clear that the government plays a much more important role in today's world. Not only the size but also the functions of government have undergone major changes: whereas formerly the government served mainly as our protector and as the developer of the physical aspects of the country, to an increasing degree the government is now a producer of social goods, especially of social welfare, health, safety, and even employment. In the process it has invaded the remotest recesses of the society. Intervention by government is not new, of course, but the extent of intervention is now massive. Unfortunately, as Khrushchev put it, "Politicians are the same all over. They promise to build a bridge even where there is no river." The idea of having the government running most aspects of society is not an appealing one.

Figure 2 compares the size of the federal government to the size of the economy. Prior to 1900 the budget of the federal government seldom exceeded 3% of GNP except during wartime; today it exceeds 20%. Government at all levels now consumes about 35% of GNP as compared to 7-8% in 1900. To put it another way, government is now half as large as the private sector. It provides a major portion of the income of well over half the population, employs about 18% of the work force directly, and mandates the employment of millions more in the private sector.

Figure 3 shows recent changes in federal government expenditures. There has been a sharp decrease in expenditures for defense and a corresponding increase in payments to individuals—for social security, medicare, medicaid, pensions, welfare, and food stamps among other things. For 1975 total public expenditure for social welfare amounted to about 20% of GNP. Social welfare is not a new invention: Fig. 4 shows that such expenditures have been growing at nearly 6% per year for almost a century, and perhaps for longer.

The other major government activity I'll discuss is regulation and control, also not a new activity as shown in Fig. 5. The data are from Kauffman's book "Are Government Organizations Immortal?" The answer is that they are, but notice that they've been added at a rate which has averaged more than 2%/yr since the founding of the republic. Figure 6 shows that the addition of government agencies proceeds in bursts: fluctuations in attitudes and values result in bursts of activity which eventually subside.

Regulation is not free, unfortunately, for as Juvenal put it centuries ago "Who shall guard the guardians themselves?" Costs include the following. First, regu-

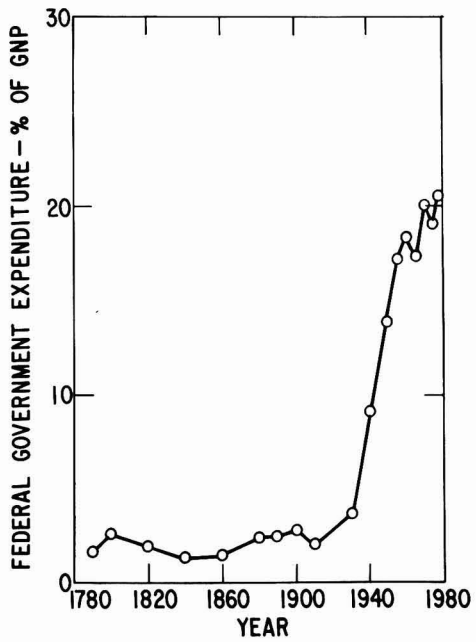


Fig. 2. The growth of federal government expenditures since 1790. The GNP between 1790 and 1874 was estimated from data in Ref. (1); other data are from Ref. (2). Wartime data excluded.

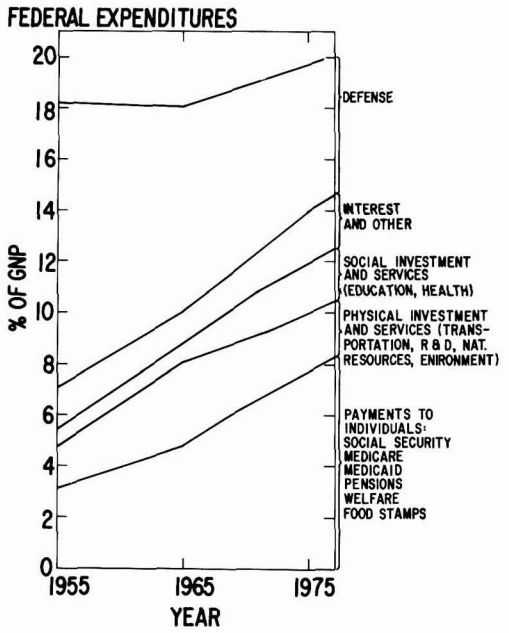


Fig. 3. Recent changes in the distribution of federal government expenditures (3).

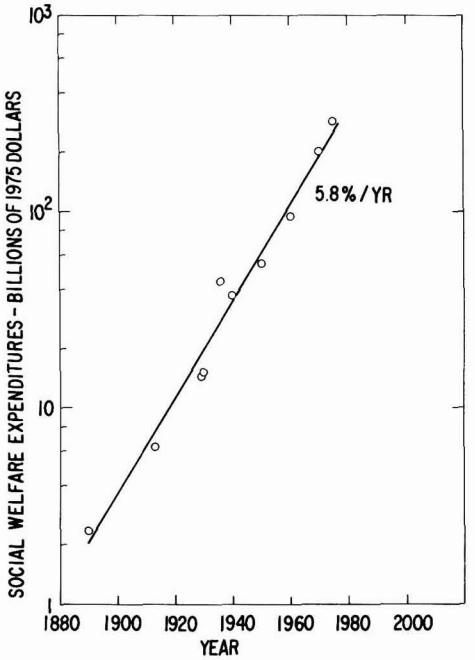


Fig. 4. Social welfare expenditures since 1885 (2)

lation may fail to achieve its objectives for a variety of reasons. The vested interest of the bureaucracy usually differs from that of the public; it turns out that regulators often protect the regulated industry to the detriment of the public; and secondary consequences may outweigh the intended benefit. Cleaning up the environment, for example, may cost jobs,

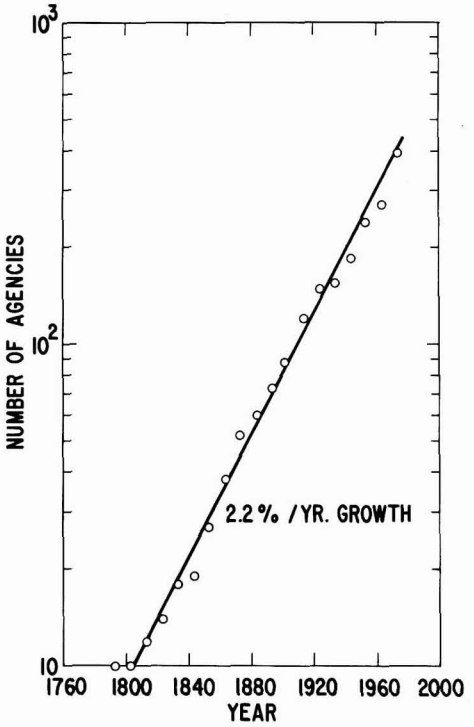


Fig. 5. Government agencies since 1790. Source: Kauffman (4)

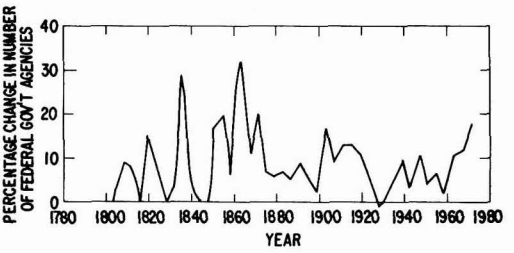


Fig. 6. The sporadic addition of federal government agencies. Source: Kauffman (4).

while in the interests of equality it has become necessary to invade privacy and categorize people by race and ethnic background. Secondly, regulation promotes inefficiency and fraud by separating responsibility from interest, promoting conflict and court contests, using coercion instead of incentives, and causing great expenditures for information. Finally, direct costs are high, both for capital expenditures and operating costs, with impacts especially severe on small businesses and nonprofit organizations.

Despite these costs, the public is reasonably satisfied with, or thinks we should spend more on, many national programs. Programs for crime control, health protection, drugs, environment, urban problems, and education were strongly favored in a 1976 survey (5), with less certainty about defense spending and helping blacks. Welfare, space exploration, and foreign oil were not in vogue. Generally, we have the government we want.

Changes in the Social System

Turning to the social system, there have been major changes in living conditions, health, working condi-

tions, income and wealth, education, and religion. I won't show any data for religion. It seems doubtful that the current revival will result in any major increase in the influence of religion.

First, some comments about living conditions. The long-term move to the cities and urban areas is not over—today more than 70% of the people live in such areas, and the trend continues, as shown in Fig. 7. Living conditions are excellent, on the average, but the family is less coherent and less stable. Marriage is commonly deferred or avoided, so that many more people live alone or in unrelated groups, while divorce is more common, so that many more children live in broken families. And, as shown in Fig. 8, fertility which has been declining erratically for more than a century is now at a level well below that needed to maintain a stable population.

Our health is excellent as shown by the improvement in life expectancy at birth, which Fig. 9 shows is still increasing steadily today. Health care is expensive, however; Fig. 10 shows that we are now spending nearly 10% of GNP to maintain our health.

Working conditions are excellent, with hours at the level people seem to prefer—about 40 hours per week—and with little heavy labor required of the work force. Figure 11 shows that affluence, as measured by personal consumption of durable goods, has been increasing at over 4%/year, more than twice the rate of per capita income. Poverty has nearly been abolished when in kind payments such as food stamps and medicaid are considered (Fig. 12).

The level of education of the population continues to improve, and more people go to college. Advanced education has increased especially rapidly as shown by the plot in Fig. 13 of doctoral degrees granted since 1920.

The generally favorable social picture is reflected in survey results: a recent Gallup poll showed 69% of the people "highly satisfied" with their lives. There is, however, a considerable amount of dissatisfaction in the society. Figure 14, taken from data in the lit-

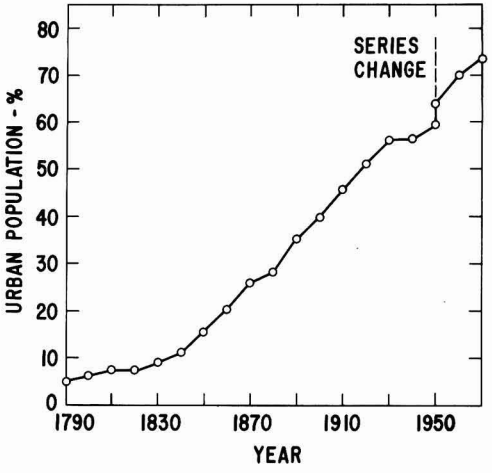


Fig. 7. The growth of urban areas since 1790 (2)

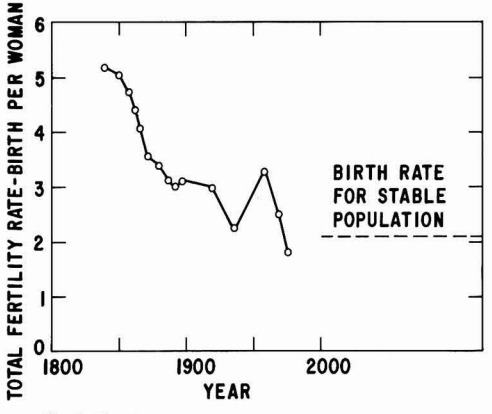


Fig. 8. The United States fertility rate since 1840 (6, 7)

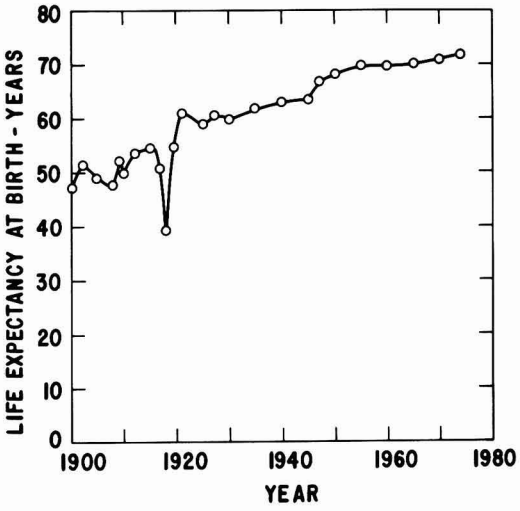


Fig. 9. Life expectancy at birth in the United States (2)

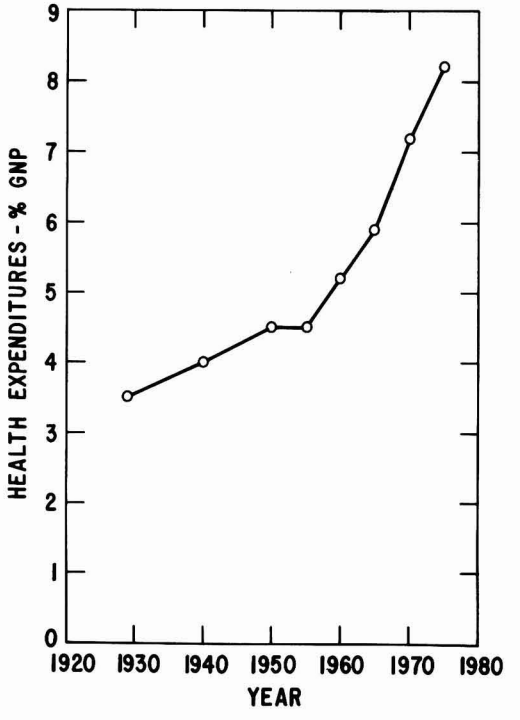


Fig. 10. The growth of expenditures for health care (2)

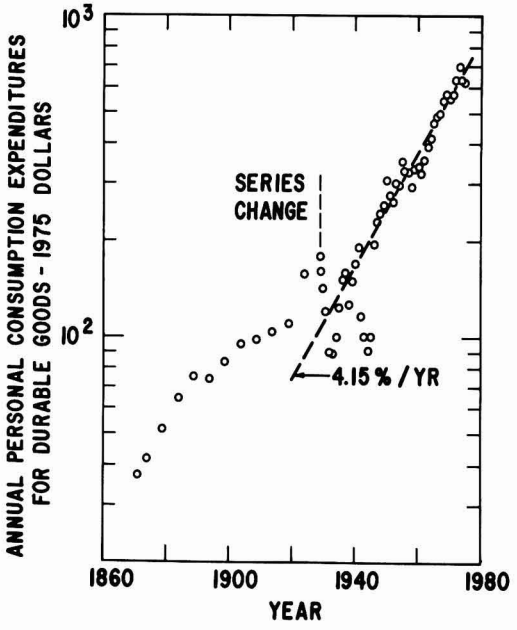


Fig. 11. Personal consumption of durable goods (2)

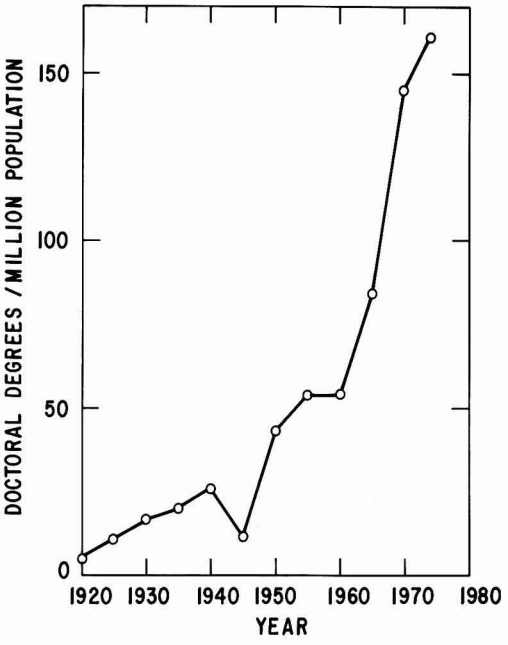


Fig. 13. Doctoral degrees in the United States (2)

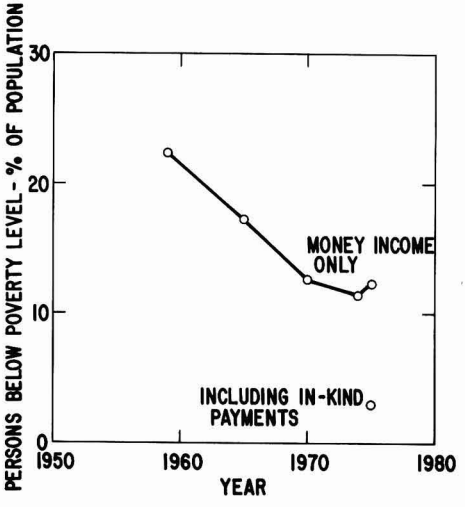


Fig. 12. Poverty in the United States (2, 8)

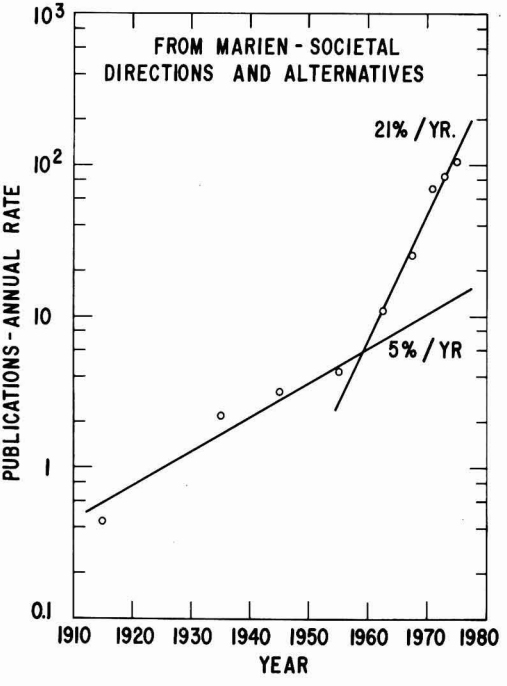


Fig. 14. The literature of social criticism. Source: Marien (9)

erature compendium by Michael Marien, shows that since about 1960 there has been a sharply increased rate of publication of critical commentary about our society.

Some major points raised by critics are the following. The decreased religious influence has resulted in the disappearance of the former consensus about fundamental values, goals, and objectives. Formerly we all agreed that bigger and richer was better, but now a substantial fraction of the people have other ideas. At the same time, norms of social behavior are less consistently followed, and it has become necessary to legislate more specific details of social interaction. Government paternalism reduces incentives, and gives rise to increased demands and expectations. The decay of the religious basis for morals has led to greater tolerance and to lower standards of behavior and performance. And finally, the strong trend toward demands for equality of result, or egalitarianism, leads to less demands on the individual for responsible social behavior and less incentive for superior performance.

In his story "Harrison Bergeron, Kurt Vonnegut (10) described the ultimate extreme of egalitarianism, in which people with abilities above the minimum level were required to wear handicaps of various kinds—buzzers in the head to confuse thought, weights and constraints to restrict movement, etc. The outcome for Harrison Bergeron, a person of truly superior capabilities, was tragic—that's no surprise if you're familiar with Vonnegut. The result of much less fully implemented egalitarianism could very well be tragic for our society as well.

By way of summary and emphasis, the most important social and political changes are centralization, secularization, affluence, and egalitarianism. The other changes which have been discussed stem at least in part from these momentous changes in the character of our society.

Consequences of Social and Political Change

The economic growth we have enjoyed has thus resulted in major changes in the social and political systems. However desirable these changes may be, they have costs. Taken together, the consequences of these political and social changes are the following. There is, first of all, a considerable loss of liberty and freedom of choice. We are no longer free to arrange for our own retirement; to care for the poor in our own way; to decide what risks we may take or what kinds of houses we may live in, etc. Secondly, with centralization of the production of social goods there are now more frequent and intense conflicts over values and social philosophy. Each individual or group feels compelled to go to the government to "get his share"—a true tragedy of the commons.

James Buchanan, in his book "The Limits of Liberty," describes the accumulation and dissipation of "social capital," the benefits to the society of having everyone behave customarily in socially benign ways. Such social capital is dissipated when people begin to cheat, and the dissipation is autocatalytic, for the more people abuse the system the more others are tempted to do so. The recent growth of the "underground economy"—cash transactions for evading taxes—is an example.

Massive overpromising has accompanied big government—social security and public pensions are excellent examples. Bureaucratic inefficiency was already discussed.

The alienation of young people and the hostility among thought leaders are especially disturbing. The extensive escape using drugs, the inward-turning withdrawal from society, increasing vandalism and violence, and the sharply increased suicide rate among teenagers reflect serious morale problems that suggest future troubles. Regarding intellectual hostility, Llewelyn King described the situation very clearly in his paper at the Uranium Institute meeting in London in July (11). King believes that there is a "new class" in American society, and writes concerning them that

> "Their class perception of American society is of a good thing gone wrong; of venal capitalism astride the stallion of technology violating the wholesomeness of America."

Their plan, again quoting King, involves

> "Turning the United States from an industrialized, centralized society into a decentralized, semiagrarian nation."

Many other authors—Irving Kristol is a notable example—have written in a similar vein about this "new class," who can be considered to be a disenfranchised elite seeking greater power in society.

Changes among Individuals

Concerning individuals, there are fewer objective data available to support contentions that change is in progress, but I believe that at least the following changes among individuals can be discerned. These changes do not affect everyone, of course, mature adults change relatively little; these changes are mostly intergenerational. But the composite, average individual is changing in these directions. First, standards of behavior and performance are lower. Examples include the decline in performance on scholastic aptitude tests, the replacement of the work ethic by the leisure ethic, the tendency to seek sensual pleasure and to have wants satisfied immediately, and the cruder, more vulgar dress and manner. An increasing proportion of the population are more dependent and less mature. An increased level of expectations and demands has accompanied the transfer to the state of responsibilities for social welfare, safety and health, and economic welfare. Lower fertility was discussed previously. Finally, the individual is less certain, less sure of the meaning of life and the significance of society, and of his contribution to it.

A comment by a financial and public-relations consultant, Sam Witchell, is interesting (12). He notes that the consequences of the lowering of standards are already well expressed in the workplace: yesterday's nonstudent is today's nonworker. "Right now" he says, "they are in the personnel office filling out application forms." They ask, according to Witchell, about benefits, vacations, salary, sick days, but do not listen to the duties of the job.

Concerning goals, some data from the National Opinion Research Corporation are presented in Table I. People in the survey thought it relatively unimportant that children try to succeed, act responsibly, or become interested in why and how things happen. The long-term trends in such attitudes are not known, but these results do not augur well for future superior performance.

Theory of Individual Behavior and Social Organization

I wish now to consider our theoretical understanding of individual behavior and of social organization. First of all, social values, goals, and attitudes reflect some kind of weighted average of the corresponding individual characteristics. It is very important, therefore, that individuals have desirable characteristics, and accordingly we must try to produce the right people. Humans, in common with many social animals, exhibit various aggressive and loving reactions which are necessary for the survival of the species; the chief task is to achieve an appropriately balanced set of these reactions. These emotional reactions arise in a complicated way from interactions between inherited characteristics and environmental forces. The debate over which is more important—nature or nurture, is an endless one; most people hold that the twig can be bent at least to some degree but accept an important inherited influence.

What kind of indoctrination is appropriate in order to produce reasonably well-balanced, mature individuals? Religion has traditionally supplied the answer, and authoritarian methods were used by the family, the schools, and the church to indoctrinate the young using moral principles supplied by and main-

Table I. Attitudes About Child Rearing—1976

How important do you think it is that a child	Important	Not mentioned	Not important
Tries to succeed	12	62	25
Is responsible	33	59	7
Is interested in why and how things happen	19	46	34

Source: National Opinion Research Center (13).

tained stable by the church. Thus were the emotional aspects of human personality kept under control and in balance. Now, with the church's authority undermined by science, we seem to be teaching the young that truth is relative, that values are a matter of taste, and that the way to behave is to look out for number one. This situation represents a modern dilemma for Western democracies: adequate indoctrination is essential but impossible.

A further requirement of individuals, young and old, is for emotional support. Such support is supplied by the family and by other important personal relationships in the community, the church, and at work, among others; all of these institutions have changed and are changing. We do not know whether adequate emotional support is now being provided.

If indoctrination and emotional support are inadequate individuals may be poorly prepared for mature social roles in a democracy. It will be a fine irony if our efforts to set people free from the authoritarianism represented in religion results in their being preprogrammed for dependence on the state.

With regard to social organization we face similar dilemmas. Authoritarianism of church and state were traditionally the rule; freedom for all is an invention of modern Western Society. Authoritarian institutions, brutal and repressive as they have often been, do provide philosophical coherence and certainty that permit firm decisions about social conduct and provide a rationale for restraining self-interest. Thus formerly the witch doctor went into a trance, or the priest prayed, or the king issued a proclamation, and action was taken. Now, having freed himself from witch doctor, priest, and king, modern democratic man must decide on some pragmatic basis what comprises appropriate action, what the citizen's duty is, and how much inequality is justified.

Can pragmatism supply adequate guidelines for action? Here we have a philosophical impasse, for the big questions of social organization are inherently disputable. For example, when is it right to injure one person to compensate another who was injured in the past by still another? That is the Bakke dilemma, which the Supreme Court was not able to answer cleanly. How much inequality is appropriate for the good of society? What "rights" does nature have: should the snail darter hold up Tellico? What is "right" concerning euthanasia, DNA research, and test tube babies? Answers to these big questions depend ultimately on our view of the relationship between man and nature. In a democracy, without a strong, common religious faith, consensus is essentially impossible.

Thus, again, we face a dilemma which is well stated by the title of Revel's book: "Can we be successful without Marx or Jesus?" It will again be a fine irony if Western democracy, which invented freedom for all, fails because it cannot find ways to limit freedom responsibility when that is necessary.

This discussion of theory can be summarized by listing the following fundamental dilemmas. First, certainty is essential but impossible. Second, indoctrination, also essential, abridges freedom, and the appropriate trade-off is not obvious. Finally there is a "Social Catch 22" which was described by Leonard Silk (14) in reviewing a book by Mishan: individuals can't be trusted to provide for themselves, but if society provides for the individuals it harms both them and itself. The recently published book "Doing Good" (15) excellently illustrates Catch 22. Theory, it seems, may not be much help in finding ways out of our difficulties.

Changes in the Economy

Let's look next at the changes in the economy that have accompanied economic growth and the social and political changes. In many respects the economy has been performing entirely normally: it is still growing at 3-4%/year, and savings, debt, and investment are all at roughly normal levels, although the quality of debt may have deteriorated. There have been some major changes and warning signals, however. We'll look especially at the shift in the balance of activities, productivity, capital formation, profitability, and inflation.

Figure 15 shows that during the past 100 years there has been a tremendous decline in agricultural employment and substantial increases in employment in government and most services, with a smaller increase in manufacturing. The sources of national income have shown similar, but smaller, shifts. Productivity gains in agriculture and in manufacturing have been generally higher than in other areas as shown in Fig. 16; differences in relative changes in employment and in sources of income are partly the result of different productivity changes among sectors.

Notice the recent change in the slope of the plot of productivity in the total private sector. Although the duration of this change is relatively short, it does represent a sharp break from the past several decades, and is cause for serious concern. Productivity gains during the recovery from the recession of 1975 have been disappointingly small. It's also worth noting that a 3%/year growth of productivity is a relatively recent phenomenon associated with the automation of farm and factory; the long-term growth has been considerably smaller.

Regarding capital formation and national wealth, data for total equity and for reproducible tangible assets show healthy growth at about the rate of GNP growth (Fig. 17). Profitability, as measured by return on capital, has fallen substantially since the postwar period however, as shown in Fig. 18, and there is concern that the future may see slower capital formation. It is disturbing that a larger fraction of our capital is being consumed by the government. It is also disturbing that we have been spending relatively less of our income on research and development since the middle sixties (Fig. 19).

Inflation is a major worry. Figure 20 shows that between 1800 and 1900 high inflation was mainly con-

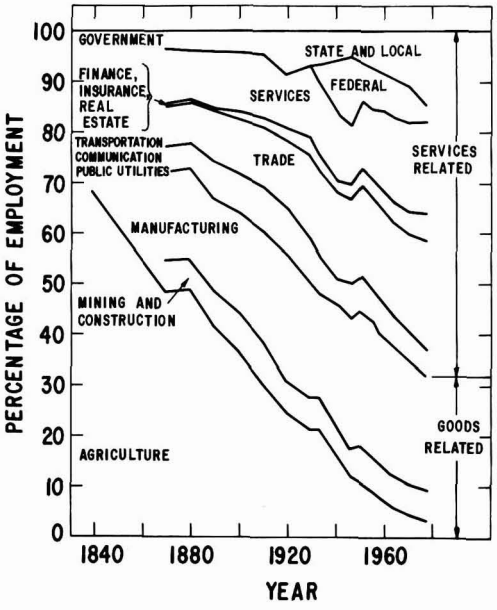


Fig. 15. Sources of employment (2)

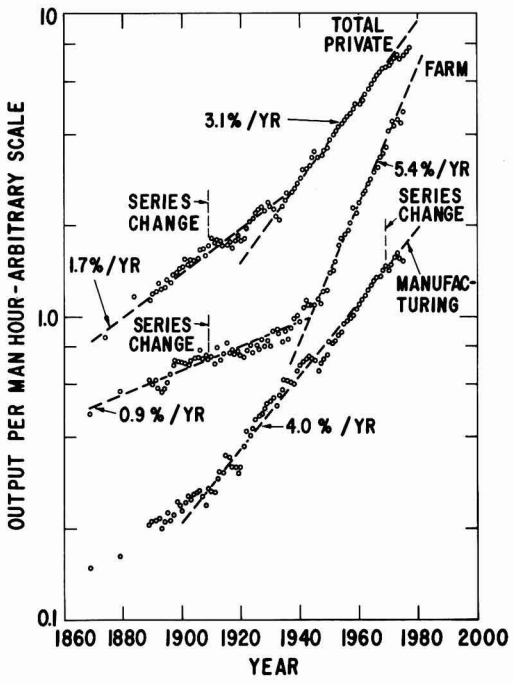


Fig. 16. Productivity in various sectors of the economy. Sources: U.S. Department of Labor and Ref. (2).

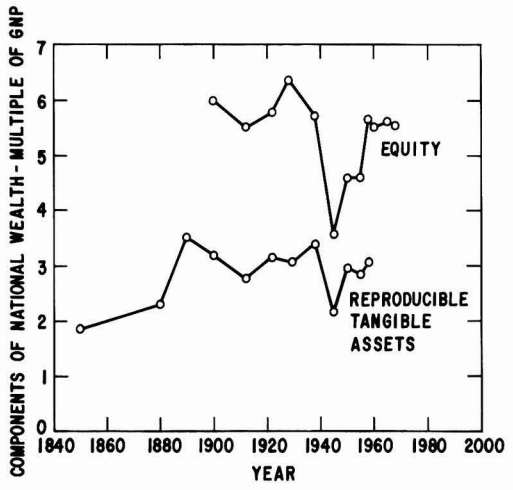


Fig. 17. Components of national wealth (2)

fined to periods of war; productivity gains brought prices back down in peacetime. Since 1900, however, that behavior has changed remarkably and, evidently, rather permanently. The average inflation rate between 1900 and 1977 was 2.6%/year while between 1933 and 1977 it was 4.6%/year.

Regardless of how one accounts for the recent surge of inflation, it is a symptom of a major problem within the society. Unless such inflation can be halted the economy faces grave difficulties in future years.

In summary, the economy has been performing reasonably well but is changing. There have been major shifts of sources of income and employment,

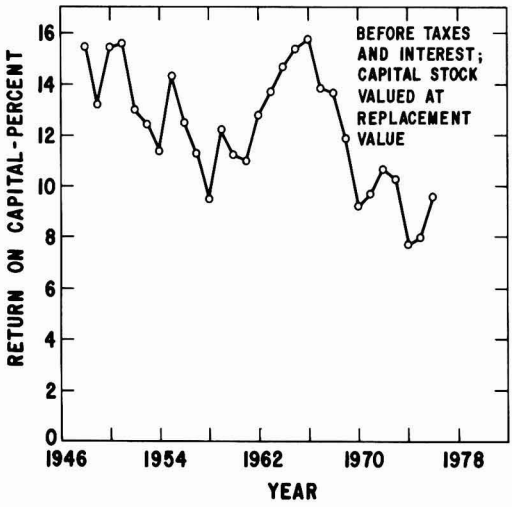


Fig. 18. Return on capital. Source: U.S. Department of Commerce (16).

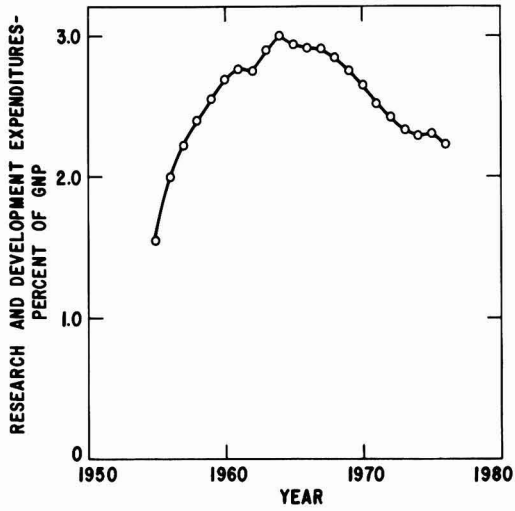


Fig. 19. Expenditures for research and development (2)

and the government plays a more important role both directly and through increased regulation and control. Problems are developing, as indicated by slowing productivity gains, unchecked inflation, and by mounting criticism of the social performance of the business community.

The Future of Society

Before considering future economic growth I'd like to talk very briefly about the future course of society, looking first at the historian's view concerning the status of Western Civilization, then at possible major social alternatives, and finally at the outlook.

A future considered likely by some is that Western Civilization is now in its death throes and that the future will see rapid decay. Toynbee's characteristics of breakdown do seem in many ways to describe modern Western Civilization (17). Alternative life styles are constantly in the news; vulgarization of the dominant minority is far advanced; we certainly have an external proletariat in the developing countries,

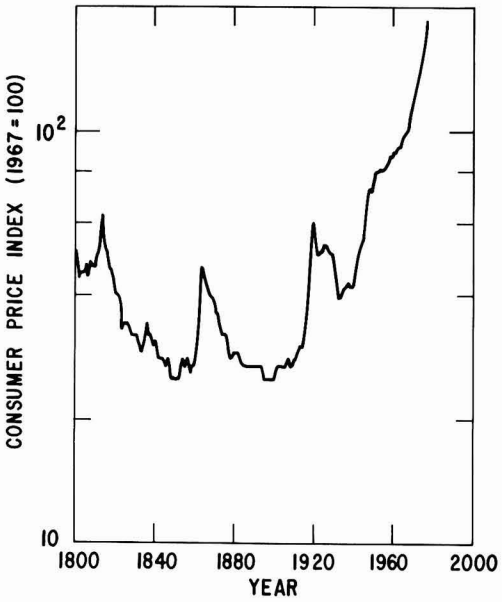


Fig. 20. Inflation since 1800 (2)

and some disadvantaged groups in the society may be considered an internal proletariat; there is a deteriorating sense of unity; the other characteristics are present to some extent. On the other hand, we do not yet have a universal state, a normal prerequisite for decline, and the United States has recently shown great vigor in response to external challenges. It is hard to believe that the end is imminent.

Could a major transformation to a more slowly growing, or stagnant, and more spiritual society take place, as Schumacher (18), Lovins (19), and Harman (20) hope? Such a change seems most unlikely: history does not provide examples of such transformations, except as part of the decline of the civilization; an example is the "Dark Ages" which followed the downfall of the Roman Civilization. The most probable future by far is a continuation of past trends to a larger, more materialistic society as proposed by Daniel Bell (21) and by Kahn and his co-workers at the Hudson Institute (1).

What will society be like in the future? It should be noted, first, that there is currently an impressive conservative reaction against the strong liberal trends of the postwar years, and the next decade should bring much less rapid social change. The long-term trend, however, is still toward further centralization and loss of liberty and freedom; more conflict and legalization; more paternalism, reduced incentives and standards, and fewer demands on individuals; and continued low fertility.

Future Economic Growth

What kind of performance can be expected from the economy of the future? Let's return to the question of what was responsible for the remarkable growth after the Industrial Revolution. There was, first of all, a strong desire for growth; that seems entirely normal for people who are not affluent: people are naturally acquisitive. The conditions which promote growth are very special, however, for only Western Society hit upon the key combination. There were three great economic inventions that made rapid growth possible: the division of labor, which led to efficiency through specialization; the market system, which mandated efficiency; and science and technology, which made it possible to overcome the law of diminishing returns. These inventions flourished in a climate that featured great personal freedom and responsibility, minimal government, simplicity, and attitudes that permitted the accumulation of great wealth and that held private property sacred. Taken all together, the system was able to take advantage of emotional aspects of human personalities—the acquisitiveness, competitiveness, greed, envy, and desire for power—and it encouraged and exploited individual differences and inquisitiveness. In addition, there were cheap resources readily available, and there was enormously important new science developed during the Enlightenment.

Today's situation is far different. Further application of the great growth inventions is hindered by current social attitudes, the climate is far more restrictive as we have discussed at length, and the desirability of growth is questioned by some. Rather than exploiting the emotional factors the system is now debilitated by their effects. Intellectual and physical resources are wasted through conflict, uncertainty, and inefficiency. On the positive side, I do not believe that growth must slow because we have run out of resources or ideas. Nuclear power is potentially cheap and abundant, and with it we can process leaner resources or even "country rock" if we have to. The possibilities for substitution, recycling, and development of new materials are tremendous. We could become the first society ever to overcome resource limitations completely. New science in biology, electronics, and astronomy is enormously impressive and has great potential. There is no obvious reason why capital could not be made available to finance developments if we wish to do so.

Let us assume, therefore, that we will avoid the worst disasters; that we will decide that modest growth is desirable and even essential; and that the mixed economy will continue to function in a modified free enterprise mode.

Denison's analysis of growth sources is a useful starting point for discussing future growth. For the years 1929-1969 Denison found that growth could be accounted for by the factors shown in Table II. The labor factor—the size and characteristics of the labor force—was the largest single contributor to growth, followed by advances of knowledge, capital formation, economies of scale, and the shift of labor away from the farms.

For the future we can expect, first of all, slower labor force growth. Figure 21 shows that the rate of population growth has been declining for nearly 100 years, and the social changes and modern technology of contraception make it probable that the slowdown will continue. Slower population and labor force growth alone will result in a substantial slowdown of economic growth.

Table II. Sources of growth of potential national income
The United States economy 1929-1969

Item	Growth rate—percent per year		
National income	3.41		
Total factor input		1.82	
Labor			1.32
Employment			1.09
Hours			−0.22
Age-sex composition			−0.05
Education			0.41
Unallocated			0.09
Capital			0.50
Output per unit of input		1.59	
Advances of knowledge and not elsewhere classified			0.92
Improved resource allocation			0.30
Economies of scale			0.36
Dwellings occupancy ratio			0.01

Source: Denison (22).

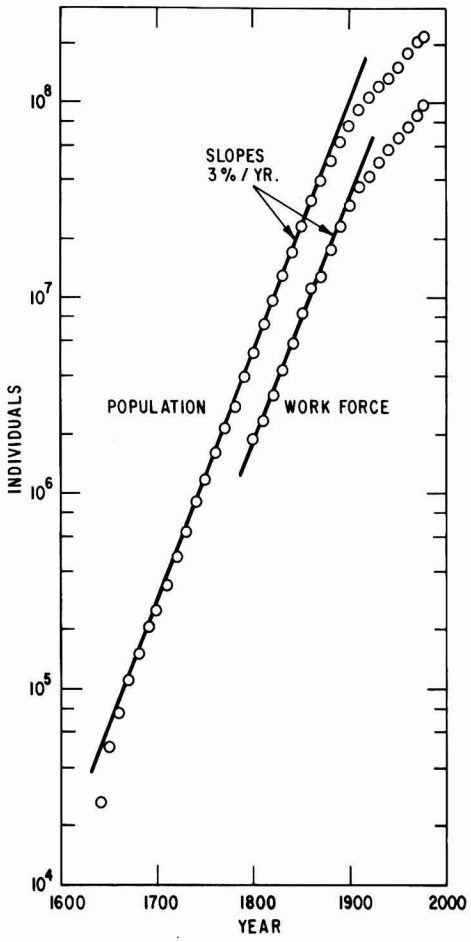


Fig. 21. The growth of the population and work force (2)

My guesses as to the future behavior of the other growth factors are shown in Table III. As the size of the population and work force stabilize, the characteristics of the work force should also tend to stabilize, as shown. Capital formation will be somewhat slower in a stagnant or slowly growing economy, and some of it will have to be dedicated to pollution control, worker health and safety, and other social concerns. Advances of knowledge will be slower because we will spend less on research and development directed to new products and processes and more on making the old ones socially acceptable. Economies of scale will be smaller in a stagnant economy, and the shift of people off the farms has been essentially completed.

Table III. Estimated future sources of growth

Item	1929-1969	Future: 1978-2025
Labor		
Employment	1.09	Decreasing to zero
Hours	−0.22	Increasing to −0.1
Age-sex composition	−0.05	Increasing to zero
Education	0.41	Decreasing to 0.2
Capital	0.5	Decreasing to 0.3
Output per unit of input		
Advances of knowledge	0.92	Decreasing to 0.5
Improved resource allocation	0.30	Zero
Economies of scale	0.36	Decreasing to 0.1
Miscellaneous	0.1	
Total	3.41	Decreasing to 1.0

Thus it is expected that during the next several decades the over-all economic growth rate will decline from more than 3%/year to close to 1%/year, with per capita income falling from 1.7%/year to about 1%/year. This optimistic result is based on the assumption that the recent sharp swing toward centralization and egalitarianism is merely a temporary fluctuation; if the recent trend should continue growth would be slower still. Just to complete the picture of the burst of growth following the Industrial Revolution, Fig. 22 shows what the full transition will look like. Per capita income in the United States will still increase by a factor ranging from two to five, depending on just exactly how the future unfolds.

Implications and Challenges

What are the implications of these changes, and how should we respond to them? As with most matters of importance there are some benefits, some problems, and some challenges to the anticipated slower economic growth. Among the benefits are less strain on resources and the environment, a less hectic pace of social change, less drastic increases in complexity, and less emotional stress among individuals. Problems include the greater difficulty of making the distribution of income and wealth more equitable and of providing for the disadvantaged in a slowly growing economy, and, for us in the technical community, the possibility of less emphasis on new science and technology to support further growth.

The major challenges that I see in the current situation are twofold. First, as we attempt to correct the imperfections in our system, it is not inevitable that we can retain the social and economic benefits we now enjoy. And second, we have in my view a moral obligation to help the rest of the world make the transition from squalor to affluence. Let me amplify each of these challenges briefly.

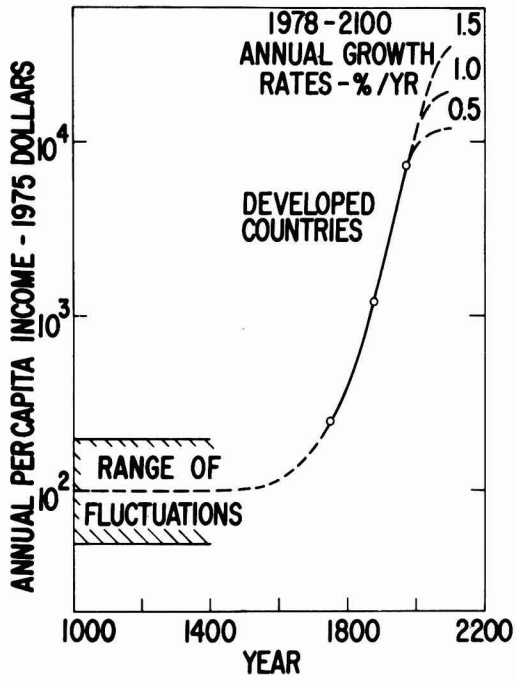


Fig. 22. Possible future growth of per capita income

The risk of losing the benefits of affluence and freedom arises because of the techniques that are being used in efforts to improve the system, and because of goals that are being set by some of our leaders. I have already discussed some of the problems, but I emphasize especially that the use of coercion rather than incentives in order to achieve regulation and control is very detrimental since it promotes inefficiency, invites evasion and court contests, and promotes rigidity rather than flexibility and innovation. Increasing centralization also leads to great inefficiency and to rigidity. Regarding goals, the drive for equality of result, or egalitarianism, contains the seeds of a major reduction in incentives throughout the system. The "new class" that wants to restrain or control completely the productive sectors of the economy and to reduce or entirely stop growth does exist, and its members are very powerful. They are great idealists as well, and think that the less desirable aspects of human behavior are largely the fault of the system and that government control of everything can fix all that. It is my view that a system which demands great leadership and extraordinary individuals is doomed to fail.

Let me quote from two of these "new class" authors: John Rawls and George Cabot Lodge. Rawls notes (23) that no one deserves natural gifts, and that it is necessary to "mitigate the arbitrary effects of the natural lottery." Lodge accepts this view, and writes (24)

> "Today, labor increasingly means skill, knowledge, education and organization. These are not owned by anybody; they are the product of the community." (Emphasis placed on last sentence).

Individualism, property rights, competition, limited state, and scientific specialization are to be replaced by communitarianism, right of membership, community need, the planning state, and holism, respectively. Regarding government, the state is to plan everything and to have enough authority to see that the plans are implemented.

Authority—there, in my view, is the real rub: I do not believe that the costs of centralization are adequately appreciated by the "new class." The teaching of history is that authoritarian regimes have always perished, usually because they indulged in gross violations of human rights. It is the chaotic, untidy freedom of Western Society that has produced the affluence we now enjoy and that has given us, for the first time in history, the chance to escape forever the Malthusian dilemma.

Our obligation to the world arises from the facts that Western Society had exploited the world's best resources, and has taught the world the way to avoid premature death. As a result, we have been partly or largely responsible for strong population growth and for consuming scarce resources, and we cannot now escape the obligation to help rectify the resulting problems. It would be craven to cower in our own corner waiting for the sky to fall and to leave the rest of the world to its own devices.

Only the United States has the necessary combination of resources, knowledge, political philosophy, and power to provide the moral and economic leadership that will be required if the world is to surmount the obstacles along the path to stability. Success in fulfilling our obligations abroad is impossible without success at home. Walter W. Rostow, in his recent book "Getting From Here To There," writes

> "Never since the 1930's have the fate of American Diplomacy and the nation's security been so closely related to the success or failure of our domestic economic policy."

These challenges, at home and abroad, are enormous, and in responding to them we may find that we not only help overcome severe problems but that we also greatly improve our own physical and emotional well-being. None of the adverse events that can be imagined is foreordained. Rigidity and inefficiency are not our inevitable lot at home. Famine is not destined to sweep the field abroad. Freedom can still prevail in the struggle against authoritarianism. While success cannot be guaranteed, and while powerful forces are at work, it seems entirely possible to me that man's noblest achievements still lie in the future, and not the past. I cannot think of anything more important for intelligent people to ponder, and I earnestly commend the further consideration of these matters to your attention.

REFERENCES

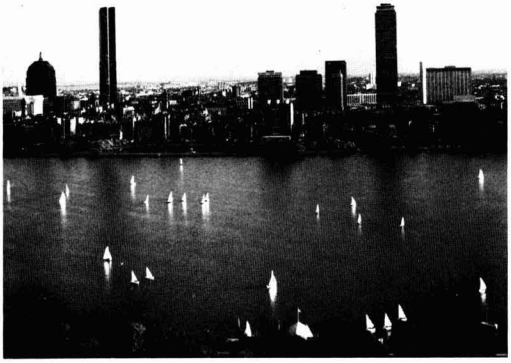
1. H. Kahn, W. Brown, and L. Martel, "The Next 200 Years," William Morrow & Co., Inc., New York (1976).
2. United States Department of Commerce, "Historical Statistics of the United States from Colonial Times to 1970," (1975); "Statistical Abstract of the United States 1977" (1978).
3. C. L. Schultze, in "Setting National Priorities," H. Owen and C. L. Schultze, Editors, Chap. 8, The Brookings Institution, Washington, D.C. (1977).
4. H. Kauffman, "Are Government Organizations Immortal?" The Brookings Institution, Washington, D.C. (1976).
5. "Social Indicators 1976," United States Department of Commerce, Washington, D.C. (1977).
6. S. Lebergott, "Manpower in Economic Growth, The American Record Since 1800," Wesleyan University Press, Middletown, Conn. (1964).
7. C. F. Westoff, *Sci. Am.*, 109 (1974).
8. M. Paglin, Conference at the Hoover Institution, Stanford Univ., Palo Alto, Calif. (1977).
9. M. Marien, "Societal Directions and Alternatives," Information for Policy Design, Lafayette, New York (1976).
10. K. Vonnegut, "Welcome to the Monkey House," Dell Publishing Co., Inc., New York (1950).
11. L. King, "Energy Daily," July 14, 1978.
12. S. Witchell, The New York Times, March 29, 1978.
13. "General Social Surveys 1977," National Opinion Research Center, Chicago, Ill. (1977).
14. L. Silk, The New York Times, February 5, 1978.
15. W. Gaylin, I. Glasser, S. Marcus, and D. Rothman, "Doing Good: The Limits of Benevolence," Pantheon Books, Inc., New York (1978).
16. Source: U.S. Department of Commerce, Presented in "Barron's, July 25, Dow Jones, New York (1978).
17. A. J. Toynbee, "A Study of History," Abridgement by D. C. Somervell, Oxford University Press, Oxford, England (1947).
18. E. F. Schumacher, "Small is Beautiful," Harper and Row, New York (1973).
19. A. B. Lovins, "Soft Energy Paths," Ballinger Pub. Co., Cambridge, Mass. (1977).
20. W. W. Harman, "An Incomplete Guide to the Future," San Francisco Book Company, San Francisco (1976).
21. D. Bell, "The Coming of Post Industrial Society: A Venture in Social Forecasting," Basic Books, Inc., New York (1973).
22. E. F. Denison, "Accounting for United States Economic Growth 1929-1969," The Brookings Institution, Washington, D.C. (1974).
23. J. Rawls, "A Theory of Justice," Harvard University Press, Cambridge, Mass. (1971).
24. G. C. Lodge, "The New American Ideology," Borzoi, Random House, New York (1974).

Erratum

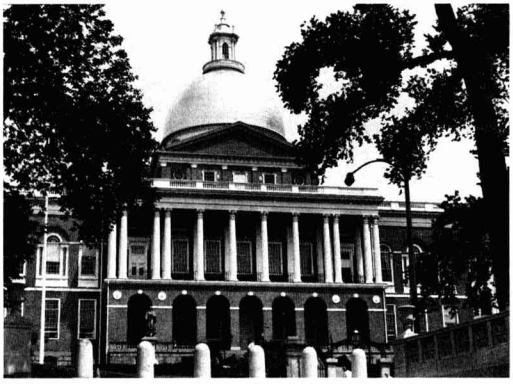
In the "Report of the Electrolytic Industries for 1977," which appeared in the November 1978 issue of the JOURNAL, Vol. 125, No. 11, pp. 455C-468C, the first sentence of the section on mercury cells on p. 457C, should read as follows:

"Membrane cells, 4 tpd chlorine capacity, replaced mercury cells in American Can of Canada Limited at Marthon, Ontario."

BUSTLING BOSTON



Begin your Boston exploration with the Prudential Building (tall building right). Topping the beautiful Boston skyline, it provides the best view and tour of Boston with its "Skywalk," a 45-minute audio-tour which familiarizes you with the view while relating local folklore and fun facts about the area.



The State House and Archives Museum is a stop you shouldn't miss. Located at the top of Beacon Hill, this historic structure was built in 1795 by Charles Bulfinch, architect of the Washington Capitol Building. Its cornerstone was laid by Samuel Adams and its archives contain the Constitution of 1780, the oldest constitution still in effect.

Boston offers an incomparable historical and cultural experience, and we hope that you won't miss this opportunity at the Society's 155th meeting in Boston to explore some of the oldest (and newest!) corners of the U.S.A.

Scanning the silhouette of the Boston skyline, you will note a juxtaposition of some of the earliest U.S. historical monuments and the world's most innovative modern architecture. In the harbor floats the Boston Tea Party Ship and Museum, where Boston's most notorious protest is dramatically recreated aboard the full-scale working replica of the Brig Beaver. The U.S.S. Constitution is a nearby neighbor, and not far away stands the birthplace of John and John Quincy Adams, simple farm homes of the second and sixth presidents of the U.S.

Travel farther and note the John Hancock building and the Prudential Center, the first major renewal project in the city. A feat of modern architecture, "The Pru" is almost a small city in itself, containing not only the 52 story Prudential Tower but various hotels, theaters, restaurants, and shops. Not far away stands a different kind of shop known as the Old Corner Book Store. Built in 1712, this was a meeting place for Longfellow, Emerson, Holmes, Harriet Beecher Stowe, Whittier, and Julia Ward Howe—authors who made Boston the "Athens of America."

Boston upholds this tradition of culture and learning today. It boasts no less than 17 universities and colleges, among which are the world-renowned Harvard University and M.I.T. In the city proper are at least 13 museums and exhibits, ranging from the Hayden Planetarium to the New England Aquarium, where more than 2000 fish are exhibited in life-like environments, to the Museum of Fine Arts, which ranks as the second most comprehensive museum in the Western Hemisphere with collections which are often unsurpassed. In addition, performing arts centers abound, and are constantly alive with the music of the famous Boston Pops or the dance of the Boston Ballet.

The revolution may be over, but Boston is still bustling with a variety of activity for all, whether you are a history buff or a lover of modern art, so we hope you will return to Boston with the Society to enjoy it once again.



The U.S.S. Constitution, better known as "Old Ironsides," now berths in Charlestown Navy Yard for a well-deserved rest. Next door, the U.S.S. Constitution Museum introduces the visitor to the history and adventures of this oldest commissioned warship afloat ("Old Ironsides" fought in 44 battles and won them all!).



There is a touch of quaintness in Boston's many colonial spots. Its history can be recognized everywhere; from its great museums and stately mansions on Beacon Hill to its waterfront and cobblestoned streets such as in Louisburg Square.

Program

Boston, Massachusetts, Meeting

THE ELECTROCHEMICAL SOCIETY, INC.

May 6-11, 1979

GENERAL INFORMATION

The 1979 Spring Meeting will be held at the Sheraton-Boston Hotel, Prudential Center, Boston, Massachusetts. In the event that you need to be contacted during the meeting, the telephone number is 617-236-2000.

A reservation card was included in the meeting announcement that was sent to all members, authors, and Technical Session Chairmen and Vice-Chairmen. Inasmuch as there are convention rates for this meeting, it is necessary for you to use the reservation card provided. If you did not receive a reservation card, please write to the Society Headquarters Office and information will be sent to you. Everyone is encouraged to use this special card. **ALL RESERVATIONS MUST BE RECEIVED AT THE SHERATON-BOSTON HOTEL NO LATER THAN APRIL 6, 1979.**

REGISTRATION

The registration area will be located in the Constitution Room Foyer on the Second Floor of the Sheraton-Boston Hotel.

Advance Registration

We suggest that all those planning to attend the 1979 Spring Meeting take advantage of ADVANCE REGISTRATION. If you need an advance registration form, please write to: Boston Meeting, The Electrochemical Society, Inc., P.O. Box 2071, Princeton, New Jersey 08540. The deadline for advance registration is April 27, 1979. Attendees who have used advance registration may pick up their packets during registration hours at a special desk.

Registration at the Meeting

The registration hours are as follows:

Sunday, May 6	4:00 P.M.	to	9:00 P.M.
Monday, May 7	7:30 A.M.	to	3:30 P.M.
Tuesday, May 8	8:00 A.M.	to	4:00 P.M.
Wednesday, May 9	8:00 A.M.	to	4:00 P.M.
Thursday, May 10	8:00 A.M.	to	4:00 P.M.
Friday, May 11	8:00 A.M.	to	10:00 A.M.

REGISTRATION FEES

All applicants and attendees are required to pay a registration fee according to the following schedule:

Technical Session Registration	
Members	$55.00
Nonmembers	80.00*
Emeritus and Honorary Members	complimentary
Members (not currently employed)	2.00
Student Members	complimentary
Student Nonmembers	2.00
Last Day Registration	
Members	15.00
Nonmembers	25.00
Ladies and Nontechnical Attendees	
Registration for Social Events	10.00

*** If a nonmember submits an Application for Admission within four months of the meeting and is subsequently elected to membership in the Society, the difference between the nonmember and member registration fee will be applied to the first year's dues.**

MEETING INFORMATION

The meeting rooms are on the Second and Third Floors. For information refer to the detailed technical session program.

Society Headquarters Office	Kent Room
Ladies Headquarters	Liberty Room C
Information/Message Center	Registration Area

GENERAL FUNCTIONS

Sunday Evening Get-Together

An informal Sunday Evening Get-Together will be held in the Constitution Room on the Second Floor from 8:00 to 10:00 P.M. All those registered for The Electrochemical Society Meeting are invited to attend.

Monday—Plenary Session

At 9:00 A.M., Monday, the Plenary Session will be held in the Grand Ballroom on the Second Floor. Philip Morrison, Massachusetts Institute of Technology, will deliver The Electrochemical Society Lecture, "Microwatts to Supernovae—and Up—."

Monday Evening Mixer

An informal social gathering will be held in the Republic Ballroom, Second Floor, from 5:30 to 7:00 P.M. Beer, soft drinks, and snacks will be served on a complimentary basis. In addition, there will be a cash bar for those who prefer mixed drinks. All meeting registrants are invited to attend.

Monday Evening Special Event

Through the courtesy of the Trustees of the Isabella Stewart Gardner Museum, we have been granted special permission for an exclusive visit to the museum for a limited number of registrants on Monday evening from 8:00 to 10:00 P.M. The Isabella Stewart Gardner Museum is a sumptuous Italian-style palace which was built in 1900 by Mrs. Gardner to house her art collection. It is located at 280 The Fenway, a short distance by taxi from the hotel. Tickets are complimentary on a "first come, first serve" basis. Tentatively, it is planned that there will be a chamber music group performing at the museum for your added enjoyment.

Tuesday

Awards and Recognition Session

An Awards and Recognition Session will begin at 4:30 P.M. in the Grand Ballroom on the Second Floor of the hotel.

The Dielectrics and Insulation Division Thomas D. Callinan Award and the Electronics Division Award will be presented. Ralph M. Hunter will be conferred an Honorary Membership in the Society, Benjamin Levich will be given the Palladium Medal which was awarded to him in 1973, and the Solid State Science and Technology Award will be presented to Morton B. Panish.

Solid State Science and Technology Award Address

Immediately following the award presentations, Morton B. Panish will deliver the Solid State Science and Technology Award Address, "III-V Heteroepitaxy and Heterostructure Lasers."

Solid State Science and Technology Award Reception

Immediately following the award address (approximately 5:45 P.M.) everyone is cordially invited to a reception in the Republic Ballroom honoring Morton B. Panish, recipient of the Solid State Science and Technology Award.

Tuesday Evening at the Boston Pops

A ***limited*** number of tickets are available for the Boston Pops Tuesday evening performance at Symphony Hall at 8:00 P.M. Tickets on the Main Floor are $11 each; tickets on the Second Balcony are $5.50 each. They will be sold on a "first come, first serve" basis, ***with advance registration only.*** Refunds will be made if your order cannot be filled.

Wednesday Evening Cocktails at the New England Aquarium

By special agreement, a private party has been arranged at the New England Aquarium for the registrants of this meeting from 6:00 to 8:00 P.M. on Wednesday evening. The New England Aquarium provides a chance to explore the magic underwater world. A special show has been scheduled for 7:00 P.M. The Aquarium is located on Boston's historic waterfront and may be reached by taxi cab. Tickets are $5.00 each which covers admission, the special 7:00 P.M. show, and predinner snacks consisting of cheeses and crackers. At the cash bar, mixed drinks will be $1.50 each, and wine or beer will be 75¢.

COMMITTEE MEETINGS

All Committee Meeting rooms are on the Third Floor of the hotel.

Sunday, May 6, 1979

3:30 P.M.—Palladium Medal Award Selection Committee, Exeter Room
5:30 P.M.—Electronics Division Planning Committee, Dalton Room
5:30 P.M.—Electronics Division Audit & Budget Committee, Clarendon Room
5:30 P.M.—Energy Technology Group Executive Committee, Gardner Room
7:00 P.M.—Council of Local Sections, Jefferson Room
8:00 P.M.—Electronics Division Executive Committee, Hampton Room
8:00 P.M.—Vittorio de Nora-Diamond Shamrock Award Selection Committee, Exeter Room

Monday, May 7, 1979

7:15 A.M.—Electrothermics and Metallurgy Division Executive Committee, Exeter Room
7:30 A.M.—Industrial Electrolytic Division Executive Committee, Clarendon Room
10:00 A.M.—Contributing Membership Committee, Board Room
10:00 A.M.—Education Committee, Dalton Room

10:00 A.M.—Electronics Division "Rump" Session Planning Subcommittee, Clarendon Room
12:15 P.M.—Dielectrics and Insulation Division Executive Committee and Planning Committee, Exeter Room
1:30 P.M.—Society Meeting Committee, Board Room
2:00 P.M.—New Technology Subcommittee, Dalton Room
4:30 P.M.—Honors and Awards Committee, Clarendon Room
4:30 P.M.—Electronics Division Award Selection Committee, Exeter Room
4:30 P.M.—Representatives to the Individual Membership Committee, Jefferson Room

Tuesday, May 8, 1979

8:00 A.M.—Editorial Committee (Breakfast Meeting), Jefferson Room
8:30 A.M.—Symposium Subcommittee, Exeter Room
9:00 A.M.—Publication Committee, Board Room
2:00 P.M.—Technical Affairs Committee, Board Room
3:00 P.M.—Financial Policy Advisory Committee, Exeter Room

Wednesday, May, 9, 1979

7:15 A.M.—Solid State Division Chairmen, Clarendon Room
7:30 A.M.—Finance Committee, Board Room
10:00 A.M.—Ways and Means Committee, Board Room
10:30 A.M.—Council of Past Presidents, Dalton Room
12:00 Noon—Electronics Division Oxide Charge Committee, Clarendon Room

Thursday, May 10, 1979

9:00 A.M.—Board of Directors, Hampton Room

LUNCHEONS AND BUSINESS MEETINGS

Monday, May 7, 1979

12:15 P.M.—Electrothermics and Metallurgy Division, Beacon C Room, Third Floor
12:15 P.M.—Electronics Division, Grand Ballroom, Second Floor (Election of Officers)
12:15 P.M.—Physical Electrochemistry Division, Independence Center, Second Floor

Tuesday, May 8, 1979

12:15 P.M.—Annual Society Luncheon and Business Meeting, Grand Ballroom, Second Floor

Wednesday, May 9, 1979

11:45 P.M.—Dielectrics and Insulation Division, Constitution Room, Second Floor, (Election of Officers) No Luncheon
12:15 P.M.—Industrial Electrolytic Division, Grand Ballroom, Second Floor
12:15 P.M.—Energy Technology Group, Independence Center, Second Floor
12:15 P.M.—Organic and Biological Electrochemistry Division, Beacon C Room, Third Floor

Thursday, May 10, 1979

12:15 P.M.—Luminescence-Electronics Division, Liberty A Room, Second Floor

TECHNICAL SESSION CHAIRMEN ORIENTATION

All Session Chairmen and Vice-Chairmen are requested to attend a breakfast meeting at 8:00 A.M. on the day of their participation in Beacon D Room on the Third Floor.

EDUCATION COMMITTEE

The Education Committee has arranged for movies to be shown on Monday, Tuesday, and Wednesday in Liberty A Room on the Second Floor. The schedule may be found in the technical session program. A brief description of each film appears on page 105C.

LADIES PROGRAM
(And Nontechnical Registrants)

The headquarters for the ladies and nontechnical registrants will be in Liberty C Room on the Second Floor of the hotel. This will be the starting point for daily activities. The ladies and nontechnical registrants are cordially invited to visit here in the morning to meet old friends and make new ones.

Sunday, May 6—On Sunday evening, the ladies and nontechnical registrants are invited to attend the Sunday Evening Get-Together which will be held in the Constitution Room on the Second Floor.

Monday, May 7—Coffee and rolls will be available in Liberty C Room from 8:30 to 9:30 A.M.

At 9:30 A.M. buses will depart for an all day trip to Plymouth, site of the Pilgrim landing and settlement. The tour will begin with a visit to the Adams Mansion in Quincy. Buses will continue to the Mayflower II, a faithful replica of the small ship which carried 102 Pilgrims to the new world. Plimoth Plantation recreates the life of the early settlers in the sixteenth and seventeenth centuries. Luncheon will be at the Governor Carver Motel. The tour will return to the hotel by 4:30 P.M. in time to freshen up for the evening mixer. Tickets for the Plymouth tour, including lunch, will be $21.00.

Tuesday, May 8—Coffee and rolls will be available in Liberty C Room from 8:30 to 9:30 A.M.

Choose one of the three walking tours of the city listed below:

Cambridge—Stroll through literary Cambridge and Harvard University. This tour will include Longfellow House, the Ware collection of Glass Flowers, Carpenter Center for the Visual Arts and the Fogg Art Museum. Take your choice of international or domestic cuisines for lunch in "The Square." There will be time for a bit of shopping before returning to the Sheraton by 4:00 P.M.

Freedom Trail—A slice of history comes alive on a tour of the highlights of Boston's Freedom Trail. This walking tour will include the Granery Burying Ground, Beacon Hill, the Old Corner Bookstore, the Old Statehouse, and Faneuil Hall. Lunch at one of the restaurants in the restored Quincy Market. Where's Boston, a multi-media presentation, will conclude this tour. Return to the Sheraton by 3:30 P.M.

Museum Tour—This tour will begin with some examples of the interesting architecture of the Back Bay. It will feature a visit to the Museum of Fine Arts with its collections of early Americana, the impressionists, Egyptian art, and others. Lunch at the museum will follow the tour. The afternoon will include the Institute of Contemporary Art, Horticultural Hall and the Boston Architectural Center. Wind up the day with some shopping along fashionable Newbury Street and return to the Sheraton by 3:30 P.M.

The cost of each tour will be $5.00, excluding lunch. Tours will provide an opportunity to enjoy a moderately priced lunch. Details will be available from your hostess.

Wednesday, May 9—Coffee and rolls will be available in Liberty C Room from 8:30 to 9:30 A.M.

Buses will depart at 9:30 A.M. for a tour of Salem. On the North Shore, Salem and Marblehead were seafaring towns. Here are the homes of merchants and shipmasters, of the witch trials, and of Nathaniel Hawthorne. After a drive through scenic Marblehead, the tour will stop to see the original painting of the "Spirit of '76" and sniff the salt air from Castle Rock. Proceed to Salem's expanded Peabody Museum where the history of Salem and its lucrative trade with the Orient are recreated. Stroll around the restored town of Salem and have lunch at the Hawthorne Inn. A visit to Derby Wharf will conclude the day. Buses will return to the Sheraton by 3:30 P.M. in plenty of time to relax before the evening program at the Aquarium. Tickets for the Salem tour, including lunch, will be $14.00.

Thursday, May 10—Coffee and rolls will be available in Liberty C Room from 8:30 to 9:30 A.M.

There are no events scheduled for this day. It is a free day for shopping or sightseeing. Please contact a hostess for assistance in arranging a visit to a particular site such as the Museum of Science, the Anesthesia exhibit at the Massachusetts General Hospital, or one of the Tuesday tours that you missed.

COST OF VARIOUS FUNCTIONS
(Other than Registration)

Sunday Evening Get-Together	Complimentary
Monday Evening Mixer	Complimentary
Monday Evening—Isabella Stewart Gardner Museum	Complimentary
Wednesday Evening at the New England Aquarium	$ 5.00
Society, Divisional and Group Luncheons (each)	6.00
Ladies and Nontechnical Registrants Activities	
Monday Plymouth Tour (including luncheon)	$21.00
Tuesday Choice of Tour (excluding luncheon)	5.00
Wednesday Salem Tour (including luncheon)	14.00

DISCUSSION

No recording will be made of oral discussion. Those contributing to the discussion of a paper and desiring their remarks to be published should send the discussion to the Publication Editor of the **Journal of the Electrochemical Society,** P.O. Box 2071, Princeton, N.J. 08540. The discussion will then be referred to the author for reply. Publication of the discussion and the comments of the author(s) depends on publication of the paper in the **Journal.**

Written discussion of a published paper should be submitted within two months following publication of the article.

EMPLOYMENT POSTERS

There will be a special bulletin board in the Registration Area for employment posters. Companies desiring to recruit employees are requested to place their announcement on this special board.

NOTE

Photographing of lantern slides, charts, etc., will be permitted unless specifically prohibited by the speaker. **PHOTO FLASH AND PHOTO FLOODS ARE PROHIBITED. Tape recordings, except on behalf of the Society, are prohibited.**

TECHNICAL SESSIONS

Monday, May 7, 1979

9:00 A.M.—Society Plenary Session, Grand Ballroom. Philip Morrison will deliver The Electrochemical Society Lecture, "Microwatts to Supernovae—and Up—."
12:15 P.M.—Electronics Division Luncheon and Business Meeting, Grand Ballroom
12:15 P.M.—Electrothermics and Metallurgy Division Luncheon and Business Meeting, Beacon C
12:15 P.M.—Physical Electrochemistry Division Luncheon and Business Meeting, Independence Center

EDUCATION COMMITTEE MOVIES

E. H. Newton, Chairman

(LIBERTY A, Second Floor)

A.M.

10:00—Corrosion in Action
10:40—Transistor Structure and Technology
11:30—Electrochemical Cells

P.M.

2:00—Think About It
2:30—Transistor Structure and Technology
3:20—Corrosion in Action
4:00—Electrochemical Reactions

BATTERY/ENERGY TECHNOLOGY GROUP

Alkaline Fuel Cell Technology

Systems, Economics

S. Srinivasan, Chairman; A. J. Appleby, Vice-Chairman

(REPUBLIC BALLROOM, Second Floor)

A.M. **Abs.**

10:00—Opening remarks by A. J. Appleby
10:10—"Progress in Alkaline Fuel Cell Technology" by K. V. Kordesch **13**
10:45—"An Alkaline Fuel Cell: Why?" by H. Van Den Broeck, M. Alfenaar, G. Spaepen, and L. Van Poucke **14**
11:10—"Factors Affecting the Economic Feasibility of Alkaline Fuel Cell Power Plants for Sweden" by T. Nilsson **15**
11:35—"Development of a 7 kW H_2/O_2 Fuel Cell Assembly with Circulating Electrolyte in a Compact Modular Design" by K. Strasser **16**

A. J. Appleby, Chairman; S. Srinivasan, Vice-Chairman

P.M. **Abs.**

2:00—"The Alkaline Fuel Cell as a Power Source for City Buses" by G. Hovestreydt, W. Keuning, M. Alfenaar, and H. Van Den Broeck **17**
2:25—"Evaluation of Improved Cathodes in Alkaline Fuel Cells" by K. V. Kordesch, S. Srinivasan, J. McBreen, E. J. Taylor, G. Kissel, and F. Kulesa **18**
2:50—"Methanol Air Fuel Cells" by O. Lindström and C. Sylwan **19**
3:15—Fifteen-minute intermission
3:30—"Water Transpiration Modeling in Alkaline Fuel Cells" by B. Schumm, Jr. **20**
3:55—"Requirements for Commercial Alkaline Fuel Cells" by D. P. Bloomfield **21**
4:20—"Computer Study of Decarbonation of Alkaline Fuel Cells" by H. H. Horowitz **22**

CORROSION

General Session

R. P. Frankenthal, Chairman; J. Kruger, Vice-Chairman

(HAMPTON, Third Floor)

A.M. **Abs.**

10:00—"Stress Corrosion Cracking of Stainless Steels in Molten $AlCl_3$-NaCl" by W. H. Smyrl **33**
10:25—"The Stress Corrosion Cracking of AISI 304 Stainless Steel in Chloride Containing Ammonium Sulfate Solutions at 220°F" by H. S. Tong and D. J. Swartz **34**
10:50—"The Electrochemical and Stress Corrosion Behavior of an Austenitic Stainless Steel in Phosphate Solutions at High Temperatures and Pressures" by H. Tischner and H. Kaesche **35**
11:15—"Hydrogen Permeation and Embrittlement in Nickel and Nickel Alloys" by M. Kurkela and R. M. Latanision **36**
11:40—"Hydrogen Profiles in Solids Measured by a New Nuclear Physical Method" by R. Doerr, E. Brauer, R. Gruner, and F. Raush **37**

J. Kruger, Chairman, R. P. Frankenthal, Vice-Chairman

P.M. **Abs.**

2:00—"Raman and Infrared Spectroscopic Studies of Aqueous Corrosion Products on Stainless Steels" by J. Keiser, C. Brown, and R. Heidersbach **38**
2:25—"Infrared and Raman Spectra of Thermal Oxidation Products Formed on Stainless Steels" by P. M. Fabis, R. H. Heidersbach, and C. Brown **39**
2:50—"Optical Studies of Polymeric Films Formed Electrochemically on Metal Electrodes" by S. Gottesfeld, M. Babai, M. Yaniv, and D. Laser **40**
3:15—Five-minute intermission
3:20—"A-C Impedance of Corroding Nickel and Iron Alloys" by M. W. Kendig and H. S. Isaacs **41**
3:45—"Corrosion by Alternating Current: A Study of Voltage Modulation on the Polarization of Mild Steel" by D-T. Chin and S. Venkatesh **42**
4:10—"The Use of Triangularly Modulated Triangular Potential Sweeps in the Study of Corrosion and Passivation Processes" by J. R. Vilche and A. J. Arvia **43**
4:35—"Effect of Fluid Flow upon Metal Repassivation in Acidic Solution" by R. C. Alkire and K. R. Weisbrod **44**

CORROSION/DIELECTRICS AND INSULATION/ELECTROTHERMICS AND METALLURGY/ENERGY TECHNOLOGY GROUP

Materials, Processes, and Characterization Techniques for Solar Energy Devices

J. A. Amick, Chairman; F. Schmid, Vice-Chairman

(CONSTITUTION ROOM, Second Floor)

A.M. **Abs.**

10:10—"A Global View of Solar Energy in Rational Units" by A. Rose **57**

Low Cost Silicon

10:55—"Progress Review of Low-Cost Processes for Polycrystalline Silicon for Solar Cells" by L. P. Hunt **58**
11:40—"Development of a Process for High Capacity Production of Solar Grade Silicon" by W. H. Reed, T. N. Meyer, and M. G. Fey **59**

G. Schnable, Chairman; H. Weaver, Vice-Chairman

P.M. **Abs.**

2:00—"Production of Silicon for Solar Cells by the Sodium Reduction of Silicon Tetrafluoride Gas" by V. K. Kapur, L. Nanis, and A. Sanjurjo **60**
2:20—"Ingot Solidification for Solar Photovoltaics" by R. G. Wolfson **61**
3:05—"Silicon Crystal Growth in Vacuum" by C. P. Khattak and F. Schmid **62**
3:25—Ten-minute intermission
3:35—"Silicon Slicing by Fixed Abrasive Slicing Technique" by F. Schmid and C. P. Khattak **63**
3:55—"Low Cost Silicon Sheet from Ingot Technologies: A Technology Projection" by A. Kran **64**
4:15—"Impurity Effects in Silicon Solar Cells" by J. R. Davis, R. H. Hopkins, P. Rai-Choudhury, P. D. Blais, A. Rohatgi, J. R. McCormick, and H. C. Mollenkopf **65**
4:50—"Chemical Impurity Analysis of Low-Cost Silicon Material for Solar Cells" by G. A. Pollock, R. Natesh, and K. M. Koliwad **66**

DIELECTRICS AND INSULATION

General Session

G. C. Schwartz, Chairman; R. G. Frieser, Vice-Chairman

(GARDNER, Third Floor)

P.M. Abs.

2:00—"Electrical Properties of SiO_2Films in Double Level Poly-Si Structures" by M. Koyanagi, T. Kamiyama, H. Sunami, and N. Hashimoto 87

2:20—"Reduction Technology of Electron and Hole Trapping Densities in Thermal SiO_2 Film" by S. Iwamatsu and Y. Tarui 88

2:40—"Electrical Confirmation of the Kooi Effect in LOCOS Structures" by D. W. Ormond and R. W. Young 89

3:00—"Cracking of Plasma Deposited Si-N Films after Subsequent Anneal" by M. Vandenberg and M. S. Hassan 90

3:20—Twenty-minute intermission

3:40—"Dielectric Properties of FeF_3 Thin Films" by A. Lachter, G. Gevers, M. Lascaud, J. Salardenne, and A. S. Barrière 91

4:00—"Thin Film Semiconductor NO_x Sensor" by S.-C. Chang 92

4:20—"Simulation of Evaporated Deposition Profiles" by W. G. Oldham, C. Sung, and A. R. Neureuther 93

4:40—"Sub 1000Å Linear Lithographic Patterns Using $Ag_2Se/GeSe_2$ Films" by K. L. Tai, L. F. Johnson, D. W. Murphy, and M. S. C. Chung 94

ELECTRONICS—SEMICONDUCTORS

Semiconductors and Other Electronic Materials

A. K. Sood, Chairman; M. B. Reine, Vice-Chairman

(GRAND BALLROOM, Second Floor)

A.M. Abs.

10:00—"Application of A-C Techniques to the Study of Lithium Diffusion in WO_3 Thin Films" by C. Ho, I. D. Raistrick, and R. A. Huggins 143

10:20—"Effect of Annealing on the Properties of Thin Films of WSi_2" by K. C. Saraswat, F. Mohammadi, and J. D. Meindl 144

10:40—"Properties of RF Sputtered, Mercury Cadmium Telluride Thin Films" by R. H. Cornely, L. Suchow, D. DeRidder, T. Gabara, and P. Diodato 145

11:00—"Silicide Formation by Laser Heating of Sputtered Refractory Metal Films on Silicon" by F. Mohammadi, K. C. Saraswat, J. Beaudouin, and J. D. Meindl 146

11:20—"Effects of Hydrogen in Amorphous Silicon Carbide Thin Films Prepared by Reactive Sputtering" by M. Le Contellec, J. Richard, A. Guivarc'h, E. Ligeon, and J. Fontenille 147

11:40—"Electrical Defects in Silicon Introduced by Sputtering" by E. Grusell, S. Berg, and L. P. Andersson 148

S. R. Butler, Chairman; B. E. Deal, Vice-Chairman

P.M. Abs.

2:00—Electronics Division Award Address
"Crystal Defects and Silicon Technology" by E. Sirtl 149

2:45—Five-minute intermission

2:50—Electronics Division Report given by B. E. Deal

3:10—"Electroluminescence in MOS Capacitors" by C. Falcony-Guajardo, F. J. Feigl, S. R. Butler, and J. B. Anthony 150

3:30—Ten-minute intermission

3:40—"Ultraviolet Ionization of Trapped Electron Centers in the MOS Oxide" by D. D. Rathman, F. J. Feigl, and S. R. Butler 151

4:00—"Interface Properties of Mo Gate MOS Structure" by H. Ishikawa, H. Tokunaga, N. Toyokura, and M. Shinoda 152

4:20—"Interface Properties of Mo and Mo/Si Gate MOS Structures" by M. Koyanagi, T. Hayashida, N. Yamamoto, and N. Hashimoto 153

4:40—"MOS Transient Capacitance: An Indicator of CCD Yield" by J. E. LaPrade, E. T. Fitzgibbons, and R. Bharat 154

ELECTROTHERMICS AND METALLURGY/ENERGY TECHNOLOGY GROUP

Characterization of Coal Combustion Products

G. J. Yurek, Chairman; H. S. Spacil, Vice-Chairman

(INDEPENDENCE-WEST, Second Floor)

A.M. Abs.

10:10—"Physical and Chemical Studies Related to the Morphogenesis of Coal Fly Ash" by G. L. Fisher 228

10:40—"Chemical Characterization of Size Fractionated Coal Fly Ash" by L. D. Hansen, D. J. Eatough, and G. L. Fisher 229

11:10—"Field Measurements of Submicron Particle Size Distributions from the Combustion of Coal" by D. S. Ensor, G. Markowski, R. G. Hooper, and R. C. Carr 230

11:30—"Fine Particle Formation in Coal Combustion" by R. C. Flagan 231

G. J. Yurek, Chairman; H. S. Spacil, Vice-Chairman

P.M. Abs.

2:05—"Submicron Fly-Ash Formation in Coal-Fired Boilers" by G. D. Ulrich 232

2:30—"Surface Processes Associated with Thermally Induced Coal Mineral Transformations: Application to Combustion Stream Cleanup" by C. D. Stinespring, D. E. Newlin, and G. W. Stewart 233

2:55—Ten-minute intermission

3:05—"Analytical Study of the Effluents from a High Temperature Entrained Flow Gasifier" by L. D. Hansen, D. J. Eatough, L. R. Phillips, R. B. Ahlgren, N. F. Mangelson, and M. L. Lee 234

3:30—"Recent Advances in the Theory and Measurement of Condensate Deposition Rates from Combustion Gases" by D. E. Rosner, K. Seshadri, F. Kohl, C. Stearns, and G. C. Fryburg 235

3:55—"Thermochemistry of a Pressurized Fluidized Bed Coal Combustor/Gas Turbine Combined Cycle" by H. S. Spacil and K. L. Luthra 236

ORGANIC AND BIOLOGICAL ELECTROCHEMISTRY

Electrochemical Microenvironment and Cell Behavior

D. Moran, Chairman; A. A. Pilla, Vice-Chairman

(INDEPENDENCE-EAST, Second Floor)

A.M. Abs.

10:00—"Cell Surface Electrochemistry and the Regulation of Tissue Growth and Repair" by A. A. Pilla 306

10:30—"Electrical Stimulation of Cartilage Cell Proliferation" by G. A. Rodan, L. A. Bourret, A. Shteyer, and L. A. Norton 307

11:00—"Modification of Cell Function by Pulsing Electromagnetic Fields" by C. A. L. Bassett, D. Moran, H. R. Chokshi, and R. Duriez 308

11:30—"Influence of Pulsating Electromagnetic Fields on Ca^{2+} Kinetics in Embryonic Chick Limb Rudiments" by J-D. Monet, J. Assailly, M-C. Weber, and A. A. Pilla 309

A. A. Pilla, Chairman; D. Moran, Vice-Chairman

P.M. Abs.

2:00—"Effect of Electromagnetically Induced Electrochemical Information on Amputated Chick Limbs In Vivo and In Vitro" by B. F. Sisken, J. F. Lafferty, I. Fowler, and A. A. Pilla 310

2:30—"Electrical Altered Adult Newt Lens Regeneration" by S. D. Smith 311

3:00—"Divalent Cations and the Development of Dormant Sponge Gemmules" by T. L. Simpson and K. M. Ostrom 312

3:30—"Gas Junction Conductance: Dependence on Internal pH" by D. C. Spray, A. L. Harris, M. V. L. Bennett, J. E. Brown, and R. B. Hanna 313

4:00—"Cathode Mediated Bone Proliferation" by J. A. Spadaro 314

4:30—"Cyclic Voltammetry of Implantable Metal Electrodes: Preliminary Studies" by M. Reichmanis 315

5:00—"The Regulation of Ion Transport by Membrane Proteins" by M. Blank 316

PHYSICAL ELECTROCHEMISTRY

The Third Symposium on Electrode Processes

E. B. Yeager, Chairman; S. Bruckenstein, Vice-Chairman

(COMMONWEALTH ROOM, Third Floor)

A.M. Abs.

10:00—Opening remarks by E. B. Yeager

10:15—"Similarities and Differences Between Electron and 323

Proton Transfers at Electrodes and in Solution" by R. A. Marcus

11:00—"Concepts in Quantum Mechanical Tunneling in Systems of Electrochemical Interest" by C. B. Duke **324**

S. Bruckenstein, Chairman, E. B. Yeager, Vice-Chairman

P.M. **Abs.**

2:00—"Some Observations of Quantum Mechanics in Electrochemical Reactions" by J. O'M. Bockris **325**

2:40—"A Model for Adsorbed States on Metal Electrodes" by W. Schmickler **326**

3:20—Ten-minute intermission

3:30—"The Measurement and Interpretation of Stochastic Effects in Electrochemistry and Bioelectrochemistry" by M. Fleischmann, C. Gabrielli, M. Labram, and A. Sattar **327**

4:10—"Coupling of Electrode Kinetics and Space Charge Dynamics in Unsupported Systems" by D. R. Franceschetti and J. R. Macdonald **328**

NEW TECHNOLOGY SUBCOMMITTEE/ELECTROTHERMICS AND METALLURGY

Superconducting Materials and Devices

R. M. Rose, Chairman; S. Foner, Vice-Chairman

(FAIRFAX A, Third Floor)

A.M. **Abs.**

10:00—"Role of Superconductivity in the Development of Magnetic Fusion Energy" by D. B. Montgomery **394**

10:25—"Superconducting Magnets for Magnetohydrodynamic Power Generation" by P. G. Marston **395**

10:50—Fifteen-minute intermission

11:05—"The Development of a Superconducting Power Transmission System" by E. B. Forsyth **396**

11:30—"High Energy Physics: The Mother of Invention for Superconductivity" by B. P. Strauss **397**

M. G. Bowman, Chairman; A. L. Giorgi, Vice-Chairman

P.M. **Abs.**

2:00—"Large Scale Applications of Superconductivity" by S. Foner and B. B. Schwartz **398**

2:25—"Fabrication of Superconducting Materials for Large Magnetic Devices" by M. Suenaga and W. B. Sampson **399**

2:50—"In Situ Technology an Alternative for the Production of Ductile Superconducting Wires" by R. Roberge, J. L. Fihey, S. Foner, E. J. McNiff, Jr., and B. B. Schwartz **400**

3:15—Fifteen-minute intermission

3:30—"The Influence of Plastic Deformation on the Residual Stress State of Multifilamentary Composites" by S. F. Cogan, D. S. Holmes, T. W. Eagar, I. M. Puffer, and R. M. Rose **401**

3:45—"High Temperature Phase Boundaries and Superconducting Properties of A15 and Chevrel Compounds" by R. Flükiger and J. L. Jorda **402**

4:10—"Neutron Irradiation of the A-15 Superconductors Nb_3Sn, Nb_3Au, and Mo_2Tc_3" by A. L. Giorgi, G. R. Stewart, and E. G. Szklarz **403**

4:25—"Transition Temperatures and Range of Composition for a New A-15 Phase in the V-Re-Tc System" by A. L. Giorgi **404**

4:40—"Information Sources for Superconductors" by C. W. Moulton **405**

Tuesday, May 8, 1979

12:15 P.M.—Annual Society Luncheon and Business Meeting, Grand Ballroom

4:30 P.M.—Awards and Recognition Session, Grand Ballroom. Morton B. Panish will deliver the Solid State Science and Technology Award Address, "III-V Heteroepitaxy and Heterostructure Lasers."

EDUCATION COMMITTEE MOVIES

E. H. Newton, Chairman

(LIBERTY A, Second Floor)

A.M.

10:00—Corrosion in Action

10:40—Transistor Structure and Technology

11:30—Electrochemical Cells

P.M.

2:00—Think About It

2:30—Transistor Structure and Technology

3:20—Corrosion in Action

4:00—Electrochemical Reactions

BATTERY/ENERGY TECHNOLOGY GROUP

Alkaline Fuel Cell Technology

Electrodes, Electrocatalysis

S. Srinivasan, Chairman; A. J. Appleby, Vice-Chairman

(REPUBLIC BALLROOM, Second Floor)

A.M. **Abs.**

9:00—"A Study of Nickel Boride as Anode Catalyst for Alkaline Fuel Cells" by C. Chuan-sin and C. Yuen-hong **23**

9:40—"Electrodes for Alkaline Hydrogen-Oxygen Fuel Cells with Nickel and Silver Catalysts" by H. Grüne **24**

10:05—"Crystallite Growing of Raney Nickel and Effect on Electrochemical Activity and Stability" by M. A. Humbert and A. Sugier **25**

10:30—Fifteen-minute intermission

10:45—"Catalysts for Alkaline Fuel Cells" by M. Bursell and G. Karlsson **26**

11:10—"Active Sites on $La_{1-x}Sr_xCoO_3$ Electrodes" by K. L. K. Yeung and A. C. C. Tseung **27**

11:35—"O_2 Reduction on Electrodeposited Pt Crystallites in Sodium Hydroxide Solution" by P. Bindra and E. Yeager **28**

Electrochemical Engineering

A. J. Appleby, Chairman, S. Srinivasan, Vice-Chairman

P.M. **Abs.**

2:00—"O_2 Reduction on Underpotential Deposited Metal Monolayers in Sodium Hydroxide" by A. Khutornoi, P. Bindra, R. Amadelli, and E. Yeager **29**

2:25—"Bimetallic Polymeric Phthalocyanines as Catalysts for Oxygen Reduction" by L. J. Gestaut, W. O. Butler, and W. A. Kovatch **30**

2:50—"Bifunctional Air-Electrode for Metal-Air Batteries" by L. Carlsson and L. Öjefors **31**

3:15—"Determination of the Rate of Chemical Decomposition of H_2O_2 by Electrocatalysts for O_2 Reduction" by F. T. B. J. van den Brink, E. Barendrecht, and W. H. M. Visscher **32**

CORROSION

General Session

R. B. Diegle, Chairman; R. M. Latanision, Vice-Chairman

(HAMPTON, Third Floor)

A.M. **Abs.**

9:00—"Electrochemical Behavior of Type 304 Stainless Steel in High Temperature, High Pressure Water" by J. B. Lee, A. K. Agrawal, and R. W. Staehle **45**

9:25—"Corrosion and Structural Characterization of Amorphous Fe-Ni-Cr-P-B Alloys" by R. B. Diegle and M. D. Merz **46**

9:50—"Study of the Corrosion of Nickel by Fluorine" by G. Gevers, A. Lachter, M. Salagoity, J. Salardenne, and A. S. Barrière **47**

10:15—Ten-minute intermission

10:25—"The Diffusion of Oxygen in the Growing Oxide and Alpha Phases during High Temperature Oxidation of Zircaloy-4" by R. E. Pawel **48**

10:50—"Steam Oxidation of Incoloy 800" by H. F. Bittner, J. T. Bell, J. D. Redman, and W. H. Christie **49**

11:15—"Thermochemical Properties of Na_2O-WO_3-SO_3 System at 1200°K" by R. Y. Lin and J. F. Elliott **50**

R. M. Latanision, Chairman; R. B. Diegle, Vice-Chairman

P.M. Abs.

2:00—"The Anodization of Superimposed Metallic Layers: Theory" by J. P. S. Pringle 51
2:20—"The Anodic Oxidation of Superimposed Niobium and Tantalum Layers: Theory" by J. P. S. Pringle 52
2:40—"The Application of Potentiostatic Pulse Method for the Determination of Critical Stress Intensity Factor for Stress Corrosion" by H. C. Chan, A. C. C. Tseung, and A. I. Onuchukwu 53
3:00—"Corrosion Resistant Amorphous Stainless Steels Containing Tungsten" by R. Wang and M. D. Merz 54
3:20—"Transient Electrochemical Behavior of Mild Steel during High Strain Corrosion Fatigue in 3.5% NaCl Solutions" by C. Patel, V. Rollins, and T. Pyle 55
3:40—"Inhibitors for the Prevention of Environmental Cracking of High Strength Aluminum Alloys in Seawater" by C. Patel 56

CORROSION/DIELECTRICS AND INSULATION/ELECTROTHERMICS AND METALLURGY/ENERGY TECHNOLOGY GROUP

Materials, Processes, and Characterization Techniques for Solar Energy Devices

Low Cost Silicon

G. Wakefield, Chairman; B. Gallagher, Vice-Chairman

(CONSTITUTION ROOM, Second Floor)

A.M. Abs.

9:00—"Silicon Ribbon Technology" by A. I. Mlavsky 67
9:45—"Long Diffusion Length Silicon Ribbon Grown by the RTR Technique" by R. N. Legge, A. Baghdadi, and R. W. Gurtler 68
10:05—"The Development and Evaluation of Materials for Resistance to Attack by Molten Silicon" by P. E. Grayson and L. A. Addington 69
10:25—Ten-minute intermission
10:35—"Silicon Photovoltaic Solar Cell Processing" by B. D. Gallagher 70
11:20—"Ion Implantation and Pulse Annealing of Back Surface Fields in Silicon Solar Cells" by A. R. Kirkpatrick, J. A. Minnucci, P. A. Iles, and S. Khemthong 71
11:40—"Optimization of Multilayer AR Coatings" by F. W. Sexton 72

Encapsulation Techniques

J. Eldridge, Chairman; H. Brandhorst, Vice-Chairman

P.M. Abs.

2:00—"The Photodegradation and Photostabilization of Polymers" by D. M. Wiles 73
2:45—"Solar Cell Encapsulation" by B. Baum, P. Willis, and E. F. Cuddihy 74

Characterization Techniques

3:05—"Evaluation of Sheet Silicon for Solar Cells" by H. Yoo, P. A. Iles, D. Tanner, and G. Pollock 75
3:25—"Solar Cell Characterization and Process Control by SPV and Current Phase-Shift Techniques" by B. L. Sopori and I. A. Lesk 76
3:45—"SAW Characterization of Photovoltaic Solar Cells" by P. Das, R. T. Webster, and B. Davari 77

DIELECTRICS AND INSULATION/ELECTRONICS

Low Temperature Processing

E. A. Irene, Chairman; R. J. Zeto, Vice-Chairman

(GARDNER, Third Floor)

A.M. Abs.

9:00—"Reduced Temperature Processing of Integrated Circuits" by B. E. Deal 95
9:30—"Reduced Oxidation Conditions for Dry Gate and Isolation Oxides on (100) Silicon Using High Pressure Oxygen" by R. J. Zeto 96
9:50—"High Pressure Thermal Oxidation of Silicon" by T. Thompson J. Wiesner, and D. Carlson 97
10:10—Ten-minute intermission
10:20—"CVD—Future Trends" by M. L. Hammond 98
10:40—"Properties of Plasma-Deposited Silicon Oxide" by M. Vandenberg 99
11:00—"Stoichiometry and the Masking Ability of LPCVD Silicon Nitride during Arsenic Diffusion" by A. Dixit, C. S. Chen, and C. E. Volk 100
11:20—"Mechanical Properties of Plasma-CVD Silicon Nitride Film" by K. Mukai, A. Hiraiwa, S. Muramatsu, S. Takahashi, and S. Harada 101

A. Jacob, Chairman; R. J. Zeto, Vice-Chairman

P.M. Abs.

2:00—"Reduction of Leakage Current of Large Area High Resistivity Silicon Photodiodes" by J. Y. M. Lee, R. D. Smith, and D. O. Massetti 102
2:20—"Low Mold Stress Epoxy Molding Compounds for Semiconductor Encapsulation" by H. Suzuki, T. Moriuchi, and M. Aizawa 103
2:40—"Laser Annealing—The Hottest Low Temperature Process in Town" by G. A. Rozgonyi 104
3:10—Recent News Papers

ELECTRONICS—SEMICONDUCTORS

Molecular Beam Epitaxy

L. L. Chang, Chairman; A. Y. Cho, Vice-Chairman

(INDEPENDENCE-WEST, Second Floor)

A.M. Abs.

9:00—"Kinetic and Surface Effects in the Growth of III-V Alloy Films by MBE" by B. A. Joyce, C. T. Foxon, J. S. Roberts 117
9:30—"Molecular Beam Epitaxy of II-VI Compound Semiconductors" by T. Yao, T. Minato, T. Sera, Y. Makita, and S. Maekawa 118
10:00—"Kinetics and Surface Interactions on Growth of InSb Thin Films by MBE" by R. Ueda and K. Tanimoto 119
10:20—Ten-minute intermission
10:30—"Effect of Lattice Mismatch on the Electronic Properties of MBE Grown InGaAs on GaAs" by C.-A. Chang, C. M. Serrano, L. L. Chang, and L. Esaki 120
10:50—"High Mobility GaAs and Cr-Doped GaAs Epitaxial Layers by MBE" by H. Morkoc and A. Y. Cho 121
11:10—"High Quality P-GaAs MBE Layers Doped by Simultaneous Low Energy Zinc Ion Irradiation" by J. C. Bean and R. Dingle 122
11:30—"The Interplay of Thermodynamics and Kinetics in MBE of Gallium Arsenide" by R. Heckingbottom, C. J. Todd, and G. J. Davies 123

ELECTRONICS—SEMICONDUCTORS

Semiconductors and Other Electronic Materials

R. O. Bell, Chairman; H. Serreze, Vice-Chairman

(GRAND BALLROOM, Second Floor)

A.M. Abs.

9:00—"Open-Tube Aluminum Diffusion" by M. Chang and A. Roesch 155
9:20—"Spin-On Arsenic Diffusion" by S. Wu and D. L. Flowers 156
9:40—"Autodoping during Silicon Liquid Phase Epitaxy" by B. J. Baliga 157
10:00—"The Application of TGZM in Power Semiconductor Product Fabrication" by M. Chang and R. Kennedy 158
10:20—"Carrier Concentration and Hall Mobility in Heavily Arsenic-Diffused Silicon" by S. Matsumoto, T. Niimi, and J. Murota 159
10:40—"D.L.T.S. and Neutron Activation Analysis Applied to a Comprehensive Study of Gold Gettering in Silicon" by D. Lecrosnier, F. Richou, J. Paugam, G. Pelous, and M. Salvi 160
11:00—"Concentration and Distribution of Oxygen and Carbon in Silicon Crystals" by H. M. Liaw 161
11:20—"The Nature of the X-Level Defect in Indium-Doped Silicon" by R. Baron, J. P. Baukus, T. C. McGill, and O. J. Marsh 162
11:40—"The Effect of Surface Charge Density on Superficial Hardness" by K. F. Beckham 163

R. Kossowsky, Chairman; W. R. Knolle, Vice-Chairman

P.M. Abs.

2:00—"Correlation of Physical and Electrical Properties of Plasma-Enhanced SiN" by K. M. Mar and G. M. Samuelson 164
2:20—"The Oxidation of Polysilicon" by W. G. Oldham, N. Chau, and N. Rovedo 165
2:40—"Densification of SIPOS" by H. R. Maxwell, Jr. and W. R. Knolle 166
3:00—"Electronic Properties of P-Doped SIPOS" by T. Adachi, K. Watanabe, S. Wakayama, and M. Kikuchi 167

3:20—"New Technology by Use of the Doped SIPOS Films" by H. Yamoto, N. Oh-uchi, H. Hayashi, T. Matsushita, and Y. Kawana **168**

Informal Discussion

Approaches to Low Cost Silicon Solar Cells

P. Rai-Choudhury, Discussion Leader

(JEFFERSON, Third Floor)

P.M.

2:00—Discussion

ENERGY TECHNOLOGY GROUP/INDUSTRIAL ELECTROLYTIC

Energy Conservation in the Industrial Electrolytic Industries

T. R. Beck, Chairman; R. C. Alkire, Vice-Chairman

(FAIRFAX A, Third Floor)

A.M. **Abs.**

9:00—"Energy Efficiency Study of Chlor-Alkali Industry" by J. B. Strauss and E. Rissmann **254**
9:35—"Energy Efficiency of Electroorganic Processes" by T. R. Beck, R. C. Alkire, and N. L. Weinberg **255**
10:10—"Energy Conservation in Aluminum Smelting" by R. W. Hyde and J. M. Parry **256**
10:45—Five-minute intermission
10:50—"Energy Incentives and Technology of Metal Recycling" by J. P. Pemsler and F. C. Brown **257**
11:25—"A Survey of Electrohydrometallurgical (Metal Winning) Processess" by R. W. Hale, W. Goldberger, B. W. Gonser, T. E. Leontis, L. E. Vaaler, and T. J. McCleer **258**

R. C. Alkire, Chairman; T. R. Beck, Vice-Chairman

P.M. **Abs.**

2:00—"Computation of Melt Velocities and Current Efficiency in Hall-Heroult Cells" by J. W. Evans and Y. Zundelvich **259**
2:20—"Energy-Saving Catalytically Active Cathodes for Caustic-Chlorine Production" by D. W. Carnell and C. R. Needes **260**
2:40—"Activated Cathodes for Reduced Power Consumption in Electrolytic Cells" by W. W. Carlin and W. B. Darlington **261**
3:00—"Reduction of Hydrogen Overpotential in a Chlorine Cell" by I. Malkin and J. R. Brannan **262**
3:20—"$NiCo_2S_4$—A Novel H_2 Evolution Electrocatalyst in Alkaline Media" by M. C. M. Man and A. C. C. Tseung **263**
3:40—"Energy Losses Occurring in and New Electrode Concepts for Alkaline Electrolyzers" by P. J. Moran, G. L. Cahen, Jr., and G. E. Stoner **264**

PHYSICAL ELECTROCHEMISTRY

The Third Symposium on Electrode Processes

B. Miller, Chairman; M. S. Wrighton, Vice-Chairman

(COMMONWEALTH ROOM, Third Floor)

A.M. **Abs.**

9:00—"Electrode Reactions of Excited Molecules" by H. Gerischer, M. T. Spitler, and F. Willig **329**
9:45—"Semiconductor Photoelectrochemical Cells" by A. J. Bard **330**
10:30—Ten-minute intermission
10:40—"The Thionine-Coated Electrode for Photogalvanic Cells" by W. J. Albery, A. W. Foulds, and A. R. Hillman **331**

J. D. E. McIntyre, Chairman; M. J. Weaver, Vice-Chairman

P.M. **Abs.**

2:00—"Kinetics of Adsorption Processes" by J. W. Schultze **332**
2:40—"Electrochemical Studies on Different Glassy Carbon Electrodes. I. Electron Transfer Kinetics" by L. Bjelica, R. Parsons, and R. M. Reeves **333**
3:20—"The Estimation of Surface Activities and Their Role in the Kinetics of Simple Electrode Reactions" by W. R. Fawcett **334**

NEW TECHNOLOGY SUBCOMMITTEE/CORROSION/DIELECTRICS AND INSULATION/ ELECTRONICS/ORGANIC AND BIOLOGICAL ELECTROCHEMISTRY

Electrochemical Modification and Monitoring of Biological Systems

L. D. Locker, Chairman; J. McHardy, Vice-Chairman

(INDEPENDENCE-EAST, Second Floor)

A.M. **Abs.**

9:00—"Oxygen Microelectrodes" by P. Pierini and E. Guilbeau **384**
9:30—"The Silver/Silver Chloride Electrode in Biomedical Monitoring" by R. Baboian, G. Haynes, and R. Robichaud **385**
10:00—"Ion-Sensing Thin-Film Transistors" by N. Alvi, I. Kaufman, and P. Pierini **386**
10:30—"The Electrochemistry of High Potential Iron-Sulfur Redox Proteins" by B. A. Feinberg and Y. K. Lau **387**
11:00—"Adaptive Cell Membrane Impedance Changes and Electrochemical Information Transfer In Vivo" by G. Cerf and A. A. Pilla **388**
11:30—"Donnan's Theory of Membrane Equilibrium: A Critical Revaluation, Theoretical and Experimental" by G. N. Ling **389**

A. A. Pilla, Chairman; F. T. Hambrecht, Vice-Chairman

P.M. **Abs.**

2:00—"In Vitro Dissolution of Pt Stimulation Electrodes" by J. McHardy, L. S. Robblee, J. M. Marston, and S. B. Brummer **390**
2:25—"In Vivo Dissolution of Pt Stimulation Electrodes" by L. S. Robblee, W. F. Agnew, L. A. Bullara, J. McHardy, and S. B. Brummer **391**
2:50—Fifteen-minute intermission
3:05—"Linear A-C Electrode Polarization Impedance Measurements on Pt and Pd Electrodes under Potential-pH Control" by M. Brownstein and R. B. Beard **392**
3:30—"D-C and A-C Linear Polarization Studies of Zinc Anodes in Biological Solutions" by N. Niazy and R. B. Beard **393**

Wednesday, May 9, 1979

12:15 P.M.—Energy Technology Group Luncheon and Business Meeting, Independence Center
12:15 P.M.—Industrial Electrolytic Division Luncheon and Business Meeting, Grand Ballroom
12:15 P.M.—Organic and Biological Electrochemistry Division Luncheon and Business Meeting, Beacon C

EDUCATION COMMITTEE MOVIES

E. H. Newton, Chairman

(LIBERTY A, Second Floor)

A.M.

10:00—Corrosion in Action
10:40—Transistor Structure and Technology
11:30—Electrochemical Cells

P.M.

2:00—Think About It
2:30—Transistor Structure and Technology
3:20—Corrosion in Action
4:00—Electrochemical Reactions

BATTERY/CORROSION/ELECTROTHERMICS AND METALLURGY/ENERGY TECHNOLOGY GROUP

High Temperature Fuel Cell Materials

H. S. Spacil, Chairman; J. Werth, Vice-Chairman

(INDEPENDENCE-WEST, Second Floor)

P.M. **Abs.**

2:05—"Materials Compatibility in a High Temperature Solid Electrolyte System" by C. Y. Yang and H. S. Isaacs **1**
2:25—"Ionic Conduction in Doped Zirconia" by D. K. Hohnke **2**
2:45—"Cathodic and Anodic Polarization Phenomena of **3**

CaO-Doped CeO_2 Electrolyte with Ag and Au Paste or Foil Electrodes" by D. Y. Wang and A. S. Nowick

3:05—"Overpotential Characteristics of Oxide Electrodes for Zirconia Fuel Cells" by H. S. Isaacs, L. J. Olmer, and G. P. Wirtz 4

3:25—Ten-minute intermission

3:35—"Dissociation of Molten Ternary Alkali Carbonates" by A. Borucka 5

3:55—"Physical and Chemical Solubilities of Fuel Cell Gases in Molten Alkali Carbonates" by A. Borucka 6

CORROSION/DIELECTRICS AND INSULATION/ELECTROTHERMICS AND METALLURGY/ENERGY TECHNOLOGY GROUP

Materials, Processes, and Characterization Techniques for Solar Energy Devices

New Technologies

T. Surek, Chairman; T. Moustakas, Vice-Chairman

(CONSTITUTION ROOM, Second Floor)

A.M. **Abs.**

9:00—"Hope for the Future—Solar Cell Materials and Processes" by D. S. Ginley and L. R. Dawson 78

9:45—"Thin Film Solar Cells" by A. K. Ghosh 79

10:30—Ten-minute intermission

10:40—"Hydrogenated Amorphous Silicon Solar Cells" by C. R. Wronski 80

11:25—"Photoelectrochemical Converter of Solar Energy: Epitaxial Layers of Alloys $Ga_xIn_{1-x}P$" by J. L. Sculfort and A. Etcheberry 81

11:45—Dielectrics and Insulation Division Business Meeting

Concentrators and Solar Thermal

V. Wells, Chairman; P. Call, Vice-Chairman

P.M. **Abs.**

2:00—"Materials for Solar Energy" by S. L. Pohlman 82

2:45—"Absorber Surfaces for Solar Receivers" by P. J. Call 83

3:30—Ten-minute intermission

3:40—"Reflectance Properties of Solar Mirror Surfaces and Problems Involved with Maintenance of High Reflectivity" by R. B. Pettit, E. P. Roth, and J. N. Sweet 84

4:25—"Corrosion Protection of Solar-Collector Heat Exchangers by Electrodeposited Organic Films" by G. H. Schnaper and V. R. Koch 85

4:45—"Fluid Corrosivity Sensor for Solar Systems" by R. Baboian and G. Haynes 86

ELECTRONICS—SEMICONDUCTORS

Molecular Beam Epitaxy

A. Y. Cho, Chairman; L. L. Chang, Vice-Chairman

(INDEPENDENCE-WEST, Second Floor)

A.M. **Abs.**

9:00—"Molecular Beam Epitaxy of IV-VI Semiconductors on IV-VI Substrates" by J. N. Walpole 124

9:25—"Silicon Molecular Beam Epitaxy" by J. C. Bean 125

9:50—"Doping of Si MBE with Simultaneous Arsenic Ion Implantation or Antimony Evaporation" by Y. Ota 126

10:10—"Selective Growth of GaAs by Molecular Beam Epitaxy" by S. Hiyamizu, T. Fujii, K. Nanbu, T. Sakurai, H. Hashimoto, and O. Ryuzan 127

10:30—Ten-minute intermission

10:40—"Optical Transmission Characteristics of MBE Grown InAs-GaSb Superlattices" by L. L. Chang, G. A. Sai-Halasz, L. Esaki, and R. L. Aggarwal 128

11:00—"Selectively Doped Semiconductor Heterostructures by Molecular Beam Epitaxy" by A. C. Gossard, W. Wiegmann, R. Dingle, and H. L. Störmer 129

11:20—"Dark and Photoinduced Transport Behavior in MBE-Grown AlGaAs-GaAs Superlattices" by R. Dingle, H. L. Störmer, L. Kopf, A. C. Gossard, and W. Wiegmann 130

11:40—"X-Ray Reflection Diffraction: A Structural Study of the GaAs-Al Interfaces" by W. C. Marra, P. Eisenberger, and A. Y. Cho 131

ELECTRONICS—SEMICONDUCTORS

Process and Device Modeling

D. A. Antoniadis, Chairman; R. W. Dutton, Vice-Chairman

(GARDNER, Third Floor)

A.M. **Abs.**

9:00—"Computer Simulation in Silicon Epitaxy" by R. Reif, R. W. Dutton, and D. A. Antoniadis 132

9:30—"Oxidation-Rate Dependence of B and P Oxidation-Enhanced Diffusions in <100> Silicon" by A. M. Lin, D. A. Antoniadis, and R. W. Dutton 133

10:00—"Oxidation-Enhanced Diffusion of Boron and Phosphorus in Silicon" by K. Taniguchi, K. Kurosawa, and M. Kashiwagi 134

10:30—"Dependence of Interface State Density on Silicon Thermal Oxidation Process Variables" by R. R. Razouk and B. E. Deal 135

11:00—"Elimination of White Ribbon by HCl Field Oxidation" by W. C. Young 136

R. W. Dutton, Chairman; D. A. Antoniadis, Vice-Chairman

P.M. **Abs.**

2:00—"Sensitivity of Electrical Parameters to Fabrication Variables for a Phosphorus Bipolar Process" by E. Khalily and R. W. Dutton 137

2:30—"A Test of the Process Modeling Program SUPREM from the Users Point of View" by D. Kranzer, W. Fichtner, E. Guerrero, and H. Ryssel 138

3:00—"Process Model and Characterization of New Submicron Channel MOS Device" by T. Yamaguchi, S. Ragsdale, M. Lust, and S. Sato 139

3:30—"Optimization of the Buried Channel for VLSI CCD's" by P. K. Chatterjee and G. W. Taylor 140

4:00—"Modeling of Thin-Film Ion-Selective Transistors" by N. Alvi, I. Kaufman, and P. Pierini 141

4:30—"A Process Monitoring and Control System" by J. W. Gaylord 142

Semiconductors and Other Electronic Materials

C. E. Volk, Chairman; J. B. Price, Vice-Chairman

(GRAND BALLROOM, Second Floor)

A.M. **Abs.**

9:00—"Oxide Isolation Process for High Density High Speed Bipolar IC's" by R. Kumar, A. K. Hochberg, J. R. Kruest, K. H. Oh, J. Rau, and G. C. Sharma 169

9:20—"Growth of High Quality Thin Oxides in Ar-O_2-HCl Gases" by W. C. Young and D. L. Henderson 170

9:40—"Charge Transport and Lattice Defects in $Co_{1-x}Mg_xO$" by E. M. Logothetis 171

10:00—"Polycrystalline Si-Schottky-I^2L (PSI^2L)—A New Technology for Low Power I^2L" by W. M. Werner 172

10:20—Twenty-minute intermission

10:40—"A Study of the Pulse Deposition of Copper Through Cylindrical Holes" by H. K. Ng, D. B. Hibbert, and A. C. C. Tseung 173

11:00—"Electrical Instability of Water-Absorbed CVD PSG Films" by T. Shirasu and Y. Kosa 174

11:20—"Hydrogen in LPCVD Polysilicon" by B. G. Bagley, P. K. Gallagher, R. E. Benenson, and C. J. Mogab 175

11:40—"LPCVD Fabrication of High Temperature Thin Film Resistors and Capacitors" by L. S. Raymond, D. J. Hamilton, W. J. Kerwin, and L. N. Nelson 176

A. Strauss, Chairman; S. Mahajan, Vice-Chairman

P.M. **Abs.**

2:00—"The Dissolution Kinetics of GaAs in Undersaturated Solutions in the Ga-Al-As System" by M. B. Small, R. Ghez, and R. M. Potemski 177

2:20—"Magnesium Doping of $Ga_{1-x}Al_xAs$" by L. R. Dawson 178

2:40—"Transmission Cathodoluminescence Study of Dislocations in GaAs and GaAlAs" by A. K. Chin, H. Temkin, and R. J. Roedel 179

3:00—"Transmission Cathodoluminescence Study of Defects in InP and InGaAsP" by H. Temkin, A. K. Chin, S. Mahajan, A. A. Ballman, W. A. Bonner, and A. G. Dentai 180

3:20—Ten-minute intermission

3:30—"The Characterization of Heavily Zinc-Doped InP Crystals" by S. Mahajan, W. A. Bonner, A. K. Chin, and D. C. Miller 181

3:50—"The Mechanism of Optically Induced Degradation in $InP/In_{1-x}Ga_xAs_yP_{1-y}$ Heterostructures" by S. Mahajan, W. D. Johnston, Jr., M. A. Pollack, and R. E. Nahory 182

—Paper withdrawn by the authors 183

4:10—"VPE Growth of InGaP/InGaAs Structures for TE Photocathodes" by R. R. Saxena, S. B. Hyder, J. S. Escher, and P. E. Gregory 184

Informal Discussion

Laser Annealing

T. O Sedgwick, Discussion Leader

(FAIRFAX B, Third Floor)

P.M.

2:00—Discussion

ELECTRONICS—LUMINESCENCE

General Session

C. F. Chenot, Chairman; M. J. Brines, Vice-Chairman

(JEFFERSON, Third Floor)

A.M. **Abs.**

9:00—"The Application of Group Theory to Luminescence" by K. H. Butler **221**

9:25—"Fast Decay U.V. Phosphor—$YAlO_3$:Ce" by T. Tomiki, T. Takeda, and T. Miyata **222**

9:50—"Luminescence of Tb-Activated Alkali Rare Earth Metaphosphate Glasses" by T. Takahashi and O. Yamada **223**

10:15—Ten-minute intermission

10:25—"Luminescence and Energy Transfer in New Complex Fluorides of Eu^{2+} and Sm^{2+}" by E. Banks and M. Shone **224**

10:50—"Cerium- and Terbium-Activated Yttrium Silicate Green Phosphors" by M. Watanabe, K. Terashima, Y. Kimura, and T. Nishimura **225**

11:15—"Ce^{+3} and Tb^{+3} Fluorescence Excited by U.V. Radiation and Fast Electrons and $Ce^{+3} \rightarrow Tb^{+3}$ Energy Transfer in α, β- and γ-$Ca_3(PO_4)_2$" by O. Bouhellal, R. Heindl, and J. Loriers **226**

11:40—"The Role of the Chromium Species in the Poly(vinyl alcohol)-Chromate Photochemical Reaction" by H. L. Van Nice and R. Farlee **227**

X-Ray Phosphors and Radiography

S. Larach, Chairman; M. Tecotzky, Vice-Chairman

(JEFFERSON, Third Floor)

P.M. **Abs.**

2:00—"Luminescence of LaOBr:Ac X-Ray Phosphors (Ac = Bi, Ce, Er, Tb-Tm, Respectively)" by J. G. Rabatin **218**

2:25—"Five Years' Experience with Rare Earth Screens" by R. Oggioni and S. Pesce **219**

2:50—"Reduced Structure Mottle in LaOBr X-Ray Intensifying Screens" by J. G. Rabatin **220**

3:15—Ten-minute intermission

Recent News Papers

M. V. Hoffman, Chairman; G. R. Gillooly, Vice-Chairman

3:25—Recent News Papers

Round Table Discussion

4:30—Round Table Discussion on
FDA Guidelines
Quantum Noise
Phosphor Stability
General Discussion

ENERGY TECHNOLOGY GROUP

General Session

Alternative Energy Overview

J. M. Woodall, Chairman; S. Srinivasan, Vice-Chairman

(REPUBLIC BALLROOM, Second Floor)

A.M. **Abs.**

9:00—"Soft vs. Hard Energy" by A. J. Appleby **237**

Electrochemical Solar Cells

9:30—"Charge Transport in a Semiconducting Electrode" by A. A. Buoncristiani **238**

9:50—"Properties of GaP Photocathodes" by D. S. Ginley and M. A. Butler **239**

10:10—"Thin Film Electrochemical Photovoltaic Cells" by H. Witzke, M. A. Russak, and J. Reichman **240**

10:30—Ten-minute intermission

10:40—"Oxide Semiconductors for Water Photoelectrolysis" by S. A. Alkaitis and R. D. Rauh **241**

11:00—"Photoelectrochemical Solar Cell Using a Fuel Cell Oxygen Cathode" by P. G. P. Ang and A. F. Sammells **242**

11:20—"A Model for Electrochemical Photovoltaic Cells" by J. Reichman **243**

11:40—"Grain Boundary Passivation and Solar Cell Improvement in Polycrystalline Silicon" by D. S. Ginley and C. H. Seager **244**

Energy Conversion and Storage

S. Srinivasan, Chairman; J. M. Woodall, Vice-Chairman

P.M. **Abs.**

2:00—"Nondestructive Testing of Electrochemical Cells" by W. C. Spindler, T. Katan, and H. F. Bauman **245**

2:20—"A Laser Raman Spectroscopic Study of Phosphoric Acid Electrolyte under Fuel Cell Operating Conditions" by W. A. Adams, C. M. Preston, M. Farrington, and P. Kruus **246**

2:40—"Synthetic Reformate Performance on Platinum in Trifluoromethanesulfonic Acid Monohydrate" by G. W. Walker and R. T. Foley **247**

3:00—"Alternate Electrolytes for Acid Fuel Cells" by S. B. Brummer, J. S. Foos, J. McHardy, J. B. McVeigh, D. E. Toland, and M. Turner **248**

3:20—Ten-minute intermission

3:30—"A Hydrogen-Bromine Fuel Cell for Energy Storage Applications" by R. S. Yeo, K. L. Hseuh, D-T. Chin, J. McBreen, and S. Srinivasan **249**

3:50—"Hydrogen and Oxygen Bubble Evolution during Electrolysis of Water" by E. Barendrecht, L. J. J. Janssen, and R. M. de Jonge **250**

4:10—"Mechanistic Study of Oxygen Evolution on $NiCo_2O_4$" by P. Rasiyah, D. B. Hibbert, and A. C. C. Tseung **251**

4:30—"Rebalance Techniques and Capacity Maintenance in Redox Flow Cell Systems" by L. H. Thaller **252**

4:50—"Electrodeposition of Minerals in Seawater: Architectural Aspects" by W. H. Hilbertz **253**

ENERGY TECHNOLOGY GROUP/ORGANIC AND BIOLOGICAL ELECTROCHEMISTRY

Energy Conversion and Storage via Biological Systems

R. K. Clayton, Chairman; A. J. Nozik, Vice-Chairman

(FAIRFAX B, Third Floor)

A.M. **Abs.**

9:00—Introductory remarks by R. K. Clayton

9:10—"Biomimetic Strategies for Solar Energy Conversion" by J. J. Katz **268**

9:45—"Photoredox Reactions of Dimeric Chlorophyll Derivatives. Modeling the Primary Events of Photosynthesis" by M. R. Wasielewski, A. G. Kostka, J. R. Norris, M. J. Pellin, and K. J. Kaufmann **269**

10:20—Five-minute intermission

10:25—"Photoelectrochemical Properties of Metalloporphyrins" by F. J. Kampas, K. Yamashita, C. K. Chang, and J. Fajer **270**

10:55—"Photo-Initiated Mediated Transport of H_3O^+ and/or OH^- across GMO Bilayers Doped with Magnesium Octaethylporphyrin" by R. C. Young, J. F. Smalley, and S. W. Feldberg **271**

11:25—"Stabilization of ZnO Surfaces for Photoelectrochemical Oxygen Production" by K. G. McGregor, J. W. Otvos, and M. Calvin **272**

ENERGY TECHNOLOGY GROUP/INDUSTRIAL ELECTROLYTIC

Energy Conservation in the Industrial Electrolytic Industries

T. R. Beck, Chairman; R. C. Alkire, Vice-Chairman

(FAIRFAX A, Third Floor)

A.M. **Abs.**

9:00—"Primary Current Distribution and Leakage Current Analysis of Hooker MX™ Membrane Cells" by D. E. Stephens, S. D. Mott, and M. Shabrang **265**

9:25—"The Photoelectrochemical Production of Chlorine" by J. Jorné **266**

9:50—"Gas Diverging Electrode in the Chlor-Alkali Membrane Cell" by J. Jorné and J. F. Louvar **267**

10:15—Ten-minute intermission

INDUSTRIAL ELECTROLYTIC

General Session

R. C. Alkire, Chairman; R. D. Varjian, Vice-Chairman

(FAIRFAX A, Third Floor)

A.M. **Abs.**

10:25—"Bubble Effects on the Solution IR Drop in a Vertical Electrolyzer under Free and Forced Convection Flow Conditions" by F. Hine and K. Murakami **281**

10:50—"Effect of Gas Evolution upon Current Distribution during Electrodeposition" by R. C. Alkire and P.-Y. Lu **282**

11:15—"Chlorine Species in the Solution Adjacent to the Anode" by I. V. Kadija **283**

11:40—"Chlorine/Caustic Soda Production in a Permselective Membrane Electrolyzer Employing Series Catholyte Flow" by R. H. Fitch, B. E. Kurtz, and C. W. Merkh **284**

R. D. Varjian, Chairman; R. C. Alkire, Vice-Chairman

P.M. **Abs.**

2:00—"An Investigation of the Electrochemical Behavior of Graphite Fiber-Polymer Composites" by G. R. Stafford, G. E. Stoner, and G. L. Cahen **285**

2:25—"Silicon and Its Alloys as a Chlorine Anode Substrate Material" by A. Martinsons, C. Welch, and H. Hoekje **286**

2:45—"Some Aspects of Silicon and Its Alloys" by C. Welch, A. Martinsons, and H. Hoekje **287**

3:10—"Linear Sweep Voltammetry of Flooded Porous Electrodes. I. First Order Irreversible Reaction" by J. A. Trainham and T. G. Stanford **288**

3:30—Five-minute intermission

3:35—"The Effect of Multiple Current Collectors on the Performance of Flow-Through Porous Electrodes" by J. J. Wu and J. A. Trainham **289**

3:55—"Multiple Reaction Sequences in Flow-Through Porous Electrodes" by R. C. Alkire and R. M. Gould **290**

4:20—"Electrodeposition of Copper and Cobalt on Fluidized Bed Electrodes" by J. W. Evans, B. J. Sabacky, and I. Masterson **291**

4:10—"Electrochemical Fluorination of Trichloroethylene and N,N-Dimethyltrifluoroacetamide" by L.-C. Hsu **292**

ORGANIC AND BIOLOGICAL ELECTROCHEMISTRY

General Session

G. Dryhurst, Chairman; J. Wagenknecht, Vice-Chairman

(INDEPENDENCE-EAST, Second Floor)

A.M. **Abs.**

9:00—"Mechanism of Electrochemical and Enzymatic Oxidation of Uric Acid" by M. Z. Wrona and G. Dryhurst **317**

9:30—"Application of Electrochemistry to the Flavoproteins Glucose Oxidase and Flavodoxin" by M. T. Stankovich **318**

10:00—"Electrochemically Activated Binding of Polycyclic Aromatic Hydrocarbons to DNA" by D. A. Tryk and S.-M. Park **319**

10:30—"Electrochemical Synthesis of N-Alkylformamides" by D. Cipris **320**

11:00—"A Chronoamperometric and Coulometric Study of 4-Substituted Catechols" by M. D. Ryan and A. Yueh **321**

11:30—"Fishes with Electric Field Detection Capabilities" by Ad. J. Kalmijn **322**

Chemically Modified Electrodes

L. L. Miller, Chairman; J. F. Evans, Vice-Chairman

(INDEPENDENCE-EAST, Second Floor)

P.M. **Abs.**

2:00—"Modified Ruthenium Electrodes and Ruthenium Modified Electrodes" by H. Abruña, K. Kuo, D. Rolison, M. Umaña, and R. W. Murray **293**

2:45—"Chemical Modification of Carbon Electrodes" by T. Osa, M. Fujihira, and T. Matsue **294**

3:30—"Chemically Derivatized n-Type Si Photoanodes: Photoelectrochemistry in Aqueous Solution" by M. S. Wrighton, A. B. Bocarsly, and E. G. Walton **295**

4:15—"Chemical Behavior of Electrode Surface Attached Molecules" by A. F. Diaz **296**

PHYSICAL ELECTROCHEMISTRY

The Third Symposium on Electrode Processes

H. Gerischer, Chairman; M. Fleischmann, Vice-Chairman

(COMMONWEALTH ROOM, Third Floor)

A.M. **Abs.**

8:30—"Factors Determining Type of Deposit in Electrocrystallization of Metals" by A. R. Despić **335**

9:10—"The Electrode Kinetics of Metal Deposition and Dissolution" by J. A. Harrison **336**

9:50—"Some Questions on the Significance of Multiple-State Underpotential Deposition and Its Dependence on Ion Adsorption" by B. E. Conway and H. Angerstein-Kozlowska **337**

10:30—Ten-minute intermission

10:40—"Studies of Underpotential Silver on Platinum and Gold" by T. M. Riedhammer, L. S. Melnicki, and S. Bruckenstein **338**

11:20—"Electrochemical Catalysis by Foreign Metal Adatoms" by J. D. E. McIntyre, S. Gottesfeld, and W. F. Peck, Jr. **339**

J. O'M. Bockris, Chairman; W. R. Fawcett, Vice-Chairman

P.M. **Abs.**

2:00—"On the Investigation of Very Fast Reactions in Electrochemistry" by Ch. Bernstein and W. Vielstich **340**

2:40—"Electrode Kinetics and Conductivity in Low Dielectric Constant Solvents" by E. Gileadi **341**

3:20—Ten-minute intermission

3:30—"Electrode Kinetics and Double Layer Structure at Solid Electrodes" by K. L. Guyer, S. W. Barr, R. J. Cave, and M. J. Weaver **342**

4:10—"Hydrogen-Involving Reactions in the Potential Region of the Alpha Phase on Smooth Palladium" by M. W. Breiter **343**

4:50—Ten-minute intermission

5:00—Special Recognition Address by V. G. Levich "Electrochemistry and Its Relation to Other Exact Sciences"

Thursday, May 10, 1979

12:15 P.M.—Luminescence-Electronics Division Luncheon, Liberty A

BATTERY/CORROSION/ELECTROTHERMICS AND METALLURGY/ENERGY TECHNOLOGY GROUP

High Temperature Fuel Cell Materials

J. Werth, Chairman; H. S. Spacil, Vice-Chairman

(INDEPENDENCE-WEST, Second Floor)

A.M. **Abs.**

9:05—"Thermal Stability of $LiAlO_2$" by P. A. Finn, K. Kinoshita, G. H. Kucera, and J. W. Sim **7**

9:25—"Thermomechanical Behavior of Lithium Aluminate/Alkali Carbonate Electrolyte Structure" by G. H. Kucera, K. Kinoshita, and R. B. Swaroop **8**

9:45—"Alternate Synthesis of Electrolyte Matrix for Molten Carbonate Fuel Cells" by R. H. Arendt and M. J. Curran **9**

10:05—"Alternate Fabrication Process for Molten Carbonate Fuel Cell Electrolyte Structures" by R. H. Arendt and M. J. Curran **10**

10:25—Ten-minute intermission

10:35—"Corrosion of Nickel and NiAl in Molten Sodium Carbonate at 900°C" by R. C. John and R. A. Rapp **11**

10:55—"Diffusional Analysis of the Monosulfide Scale on Fe-Co Alloys in H_2-H_2S Atmospheres" by D. J. Young, T. Narita, and W. W. Smeltzer **12**

ELECTRONICS—SEMICONDUCTORS

Ion Implantation

B. L. Crowder, Chairman; K. L. Wang, Vice-Chairman

(FAIRFAX A, Third Floor)

A.M. **Abs.**

9:00—"Parameters Effecting the Electrical Properties of Be and Si Implanted GaAs" by B. Molnar **105**

9:35—"Transferability of a Simple Ion Implantation Process in GaAs" by C. L. Anderson, H. L. Dunlap, B. Molnar, and J. Comas **106**

10:00—"Annealing of Ion Implanted GaAs Using a Melt Controlled Ambient" by C. L. Anderson, H. L. Dunlap, and K. V. Vaidyanathan **107**

10:25—Five-minute intermission

10:30—"Transmission Electron Microscopy Study of Si Ion-Implanted GaAs" by B. Hughes and G. H. Narayanan **108**

10:55—"Inert-Gas Bubble Formation in the Implanted Metal/Si System" by B. Y. Tsaur, Z. L. Liau, and J. W. Mayer **109**

11:20—"Ion Beam-Induced Epitaxy of Silicon" by I. Golecki, G. E. Chapman, S. S. Lau, B. Y. Tsaur, and J. W. Mayer **110**

H. J. Geipel, Chairman; B. L. Crowder, Vice-Chairman

P.M. **Abs.**

2:00—"Ion Implant Process Modeling for VLSI" by A. G. Fortino and H. J. Geipel **111**

2:40—"Abrupt Junctions by Ion-Implantation Doping of Silicon and Monitoring Damage Annealing by Laser Raman Scattering" by R. Varma, P. B. Swarup, and J. Love **112**

3:05—"Nondestructive Monitoring of Impurity Activation in Ion-Implanted Silicon by Surface Acoustic Waves" by R. Bharat, P. Das, R. T. Webster, and K. Varahramyan **113**

3:30—"Effect of Surface Contamination on SiO_2 Film by Heavy Ion Implantation" by K. Itoh, N. Horino, M. Kanegae, and T. Tsuchimoto **114**

3:55—Ten-minute intermission

4:05—"An Improved Ion-Implanted Base for Oxide-Isolated Bipolar IC's" by R. Kumar, C. S. Chen, A. K. Hochberg, M. Hunt, J. R. Kruest, K. H. Oh, and J. Rau **115**

4:30—"On the Growth of Silicon Epitaxy over Ion Implanted Buried Layers" by V. C. Kannan and G. Roper **116**

ELECTRONICS—SEMICONDUCTORS

Semiconductors and Other Electronic Materials

M. G. Buehler, Chairman; W. K. Tice, Vice-Chairman

(GRAND BALLROOM, Second Floor)

A.M. **Abs.**

9:00—"PNAF—An Efficient Silicon/Aluminum Etchant" by J. K. Pau, W. P. Ng, and J. E. Martin **185**

9:20—"Pad Materials for Chemical-Mechanical Polishing" by E. Mendel, P. Kaplan, and A. Patsis **186**

9:40—"Multiple Wafer Free Polishing. I. Machine Concept" by E. Mendel and J. Hause **187**

10:00—"Multiple Wafer Free Polishing. II. Process" by E. Mendel and J. Basi **188**

10:20—"Control of Wafer Curvature" by A. Takasu and K. Nakajima **189**

10:40—"Electrochemical Characterization of Carrier Concentration Profiles in Silicon" by C. D. Sharpe and P. Lilley **190**

11:00—"A Cross-Bridge Structure Array for Characterizing Intrachip Line Width Variations" by L. W. Linholm and M. G. Buehler **191**

11:20—"Automatic Photomask Inspection Machine" by Y. Uchiyama and D. Awamura **192**

11:40—"Design Considerations for the Integrated Gated-Diode Electrometer" by G. P. Carver and M. G. Buehler **193**

M. Coleman, Chairman; T. Surek, Vice-Chairman

P.M. **Abs.**

2:00—"Characterization of Deliberately Nickel-Doped Silicon Wafers and Solar Cells" by A. M. Salama **194**

2:20—"Creation of Defects Responsible for Photon-Induced Degradation in N^+P Silicon Solar Cells" by L. J. Cheng, D. C. Leung, and J. D. Parsons **195**

2:40—"Evaluation of Cost Effective Contact Systems for Solar Cells" by R. B. Campbell and A. Rohatgi **196**

3:00—Ten-minute intermission

3:10—"Influence on Electrode Kinetics of Shallow Diffused Semiconductor Devices" by T. A. Blaske and H. Yu **197**

3:30—"Laser Beam Analysis of Large Area a-Si:H Solar Cells" by D. L. Staebler **198**

3:50—"Amorphous II-V_2 and II-IV-V_2 Semiconductors as Possible Solar Cell Materials" by R. D. Rauh **199**

4:10—"The Effects of Substrate Temperature during Deposition on the Electromigration Failures of Al-3% Si Conductors" by F. Ichikawa and S. Ushio **200**

4:30—"Synthesis and Characterization of a Highly Conducting Organic Polymer" by K. K. Kanazawa, A. F. Diaz, G. P. Gardini, and G. B. Street **201**

ELECTRONICS

Recent News Papers

G. C. Schwartz, Chairman; D. R. Kerr, Vice-Chairman

(REPUBLIC BALLROOM, Second Floor)

A.M.

9:00—Recent News Papers

E. H. Nicollian, Chairman; D. R. Kerr, Vice-Chairman

P.M.

2:00—Recent News Papers

ELECTRONICS—LUMINESCENCE

Phosphor Efficiency and Saturation

H. Forest, Chairman; W. A. McAllister, Vice-Chairman

(JEFFERSON, Third Floor)

A.M. **Abs.**

9:00—"Review on Inefficiencies in Phosphors" by C. W. Struck **211**

10:00—"The Effects of Crystal Field and Temperature on the Photoluminescence Excitation Efficiency of Ce^{3+} in YAG" by D. J. Robbins **212**

10:25—Fifteen-minute intermission

10:40—"Observation of Emission-Intensity Loss in the Synthesis of Eu^{2+}-Activated Pyrosilicate Phosphors" by R. G. Pappalardo, C. Givens, C. F. Chenot, and R. E. Meehan **213**

11:05—"Host and Temperature Effects on Tl^{4+} Luminescence" by R. P. Burgner and W. B. White **214**

—Paper withdrawn by the authors **215**

P. N. Yocom, Chairman; R. G. Pappalardo, Vice-Chairman

P.M. **Abs.**

2:00—"Mechanisms of Current-Density Saturation in ZnS Cathodoluminescent Phosphors" by J. R. McColl **216**

2:25—"Nonlinear Quenching of Mn^{2+} Fluorescence in $Ca_5(PO_4)_3F$ under High Levels of Excitation" by F. M. Ryan and J. Murphy **217**

2:50—Ten-minute intermission

D. J. Robbins, Chairman

3:00—Round Table Discussion

ENERGY TECHNOLOGY GROUP/ORGANIC AND BIOLOGICAL ELECTROCHEMISTRY

Energy Conversion and Storage via Biological Systems

J. J. Katz, Chairman; R. K. Clayton, Vice-Chairman

(FAIRFAX B, Third Floor)

A.M. **Abs.**

9:00—"Photosynthetic Reaction Centers as Solar Cells" by R. K. Clayton **273**

9:40—"An FMN-Photosystem I Photogalvanic Cell" by E. L. Gross, S. L. Winemiller, D. Youngman, and R. L. Pan **274**

10:20—Ten-minute intermission

10:30—"The Biological Generation of Hydrogen Gas" by D. B. Knaff **275**

11:10—"Photohydrogen Production Using Biological Membranes" by J. M. Olson **276**

A. J. Nozik, Chairman; J. J. Katz, Vice-Chairman

P.M.		Abs.
2:00	"Chemical and Biological Conversion of Solar Energy" by T. B. Reed	277
	—Paper withdrawn by the authors	278
2:40	"Ethanol Production Using Microbial Cells Trapped in Polyacrylamide Gels" by R. H. Villet and J. Dillon	279
3:20	"Solar Ultraviolet Radiation: A Possible Limiting Factor of Direct Biological Conversion of Sunlight by Algae" by J. Calkins and J. A. Barcelo	280
4:10	Closing remarks by J. J. Katz	

ORGANIC AND BIOLOGICAL ELECTROCHEMISTRY

Chemically Modified Electrodes

J. F. Evans, Chairman; L. L. Miller, Vice-Chairman

(INDEPENDENCE-EAST, Second Floor)

A.M.		Abs.
9:00	"Modification of Electrode Materials Using Plasma Chemistry" by M. F. Dautartas, D. M. Ullevig, and J. F. Evans	297
9:45	"Polymer-Metal Composite Thin Films on Electrodes" by K. Doblhofer and W. Dürr	298
10:30	"Adsorbed Polymers as Electrocatalysts" by L. L. Miller, M. R. Van de Mark, G. Hostetler, and J. Kerr	299
11:15	"Coordination of Transition Metal Complexes to the Surface of Graphite Electrodes Coated with Polymeric Ligands" by N. Oyama and F. C. Anson	300

L. L. Miller, Chairman; J. F. Evans, Vice-Chairman

P.M.		Abs.
2:00	"Spectroelectrochemistry of Stable, Electroactive Polymer-Coated Electrodes" by F. B. Kaufman, A. H. Schroeder, E. M. Engler, J. Q. Chambers, and S. R. Kramer	301
2:45	"Voltammetric Investigation of Polymer Coated Electrodes" by P. J. Peerce and A. J. Bard	302
3:05	"Electrochemical Behavior of Organic 'Metal' Electrodes in Aqueous Media" by C. D. Jaeger and A. J. Bard	303
3:30	"Electrochemical and Photoelectrochemical Studies of Silane-Modified SnO_2 Electrodes" by V. R. Shepard and N. R. Armstrong	304
4:15	"Electrochemical and X-ray Photoelectron Spectroscopic Investigations of Surface Filming on Polished and Roughened Kel-F-Graphite Composition Electrodes" by J. L. Anderson, D. E. Tallman, J. E. Anderson, D. J. Chesney, and J. F. Evans	305

PHYSICAL ELECTROCHEMISTRY

The Third Symposium on Electrode Processes

R. Parsons, Chairman; B. E. Conway, Vice-Chairman

(COMMONWEALTH ROOM, Third Floor)

A.M.		Abs.
8:30	"Optical and Electrochemical Studies of Adsorbed Transition Metal Complexes and Their O_2 Electrocatalytic Properties" by E. Yeager, J. Zagal, B. Z. Nikolic, and R. R. Adžić	344
9:10	"Proton Transfer in Oxygen Reduction: A Discussion" by A. J. Appleby	345
9:50	"Models for the Photoelectrolytic Decomposition of Water at Semiconducting Oxide Anodes" by J. M. Kowalski, H. L. Tuller, and K. H. Johnson	346
10:15	"Oxygen Reduction on Platinum in Trifluoromethanesulfonic Acid and Phosphoric Acid" by W. E. O'Grady, E. J. Taylor, and S. Srinivasan	347
10:40	Ten-minute intermission	
10:50	"Some Aspects of the Reduction of Oxygen at a Platinum-Oxygen Alloy Diaphragm" by J. P. Hoare	348
11:15	"New Materials for Oxygen Reduction: Interest of Iron Naphthalocyanines" by G. Magner, M. Savy, and G. Scarbeck	349
11:40	"Effect of Glutathione on Electroreduction of Oxygen on Iron Phthalocyanine Layers" by O. Contamin, E. Levart, and M. Savy	350

M. W. Breiter, Chairman; J. A. Harrison, Vice-Chairman

P.M.		Abs.
2:00	"Mechanisms and Kinetics of O_2 Evolution at Ruthenium Oxide Electrodes" by J. F. Wolf, S. L. Soled, and A. Damjanovic	351
2:25	"In Situ LEED-Auger-Thin Layer Electrochemical Studies of the Underpotential Deposition of Pb on Au Single Crystals" by P. Hagans, A. Homa, and E. Yeager	352
2:50	"Foreign Metal Adatoms as a Probe in the Study of Some Electrocatalytic Reactions" by R. Adžić, M. Spasojević, and R. Atanasoski	353
3:15	"Yessin-Markov Shifts, E_1 Shifts of Complexes, and the Langmuir Isotherm" by R. Heyrovská	354
3:40	Twenty-minute intermission	
4:00	Round Table Discussion, E. B. Yeager, Chairman	

General Session

F. G. Will, Chairman; D. H. Mohilner, Vice-Chairman

(GARDNER, Third Floor)

A.M.		Abs.
9:00	"An Examination of the Basic Postulates of Surface Chemistry: A Variational Calculus Analysis of the Rotating-Drop Experiment" by H. M. Scholberg	362
9:20	"High Precision Computer Controlled Electrocapillary Measurements" by D. M. Mohilner and T. Kakiuchi	363
9:40	"Mass Transfer to Truncated Vertical Cylinders by Free Convection and by Rotational Forced Convection" by J. C. McClure, J. Tavakoli-Attar, and J. R. Selman	364
10:00	"Effect of Crystallite Morphology on the Conductivity of Polycrystalline Sodium β''-Alumina" by J. R. Rasmussen, A. V. Virkar, G. R. Miller, and R. S. Gordon	365
10:20	Ten-minute intermission	
10:30	"Electronic Transport in $Zr_{0.9}Y_{0.1}O_{1.95}$ Determined from a Novel Electrochemical Cell Technique" by L. C. Lee and R. N. Blumenthal	366
10:50	"Electrical Conductivity of the Solid Electrolyte System $CuCl(Al_2O_3)$" by M. R-W. Chang, K. Shahi, and J. B. Wagner, Jr.	367
11:10	"Electrical Conductivity Studies on LiI and LiI · xH_2O with and without Al_2O_3 Particles" by S. Pack, B. B. Owens, and J. B. Wagner, Jr.	368
11:30	"Electrical Conductivity of Solid AgI Containing a Dispersion of Submicron Size Al_2O_3" by K. Shahi and J. B. Wagner, Jr.	369

E. J. Cairns, Chairman; S. D. James, Vice-Chairman

P.M.		Abs.
2:00	"Evaluation of Secondary Magnesium Cells with Molten-Salt Electrolytes" by C. C. Sy, Z. Tomczuk, and M. F. Roche	370
2:20	"Reference Electrode Development for the Lithium/Metal Sulfide Battery Systems" by L. Redey and D. R. Vissers	371
2:40	"Comparison of Lithium-Boron Alloy with Pure Lithium as an Ambient Temperature Anode" by S. D. James	372
3:00	Ten-minute intermission	
3:10	"Modes of Charge and Discharge in a Single-Pore Ag/AgO Electrode" by T. Katan and K. C. Tsai	373
3:30	"Zinc-Electrode Current Efficiency in Zinc-Chlorine Hydrate Batteries. I. Theoretical Aspects" by G. L. Henriksen, S. Kodali, J. Jorné, and C. J. Warde	374
3:50	"Zinc-Electrode Current Efficiency in Zinc-Chlorine Hydrate Batteries. III. Natural Convection during Electrodeposition" by S. Kodali, J. Jorné, and G. L. Henriksen	375

Friday, May 11, 1979

ELECTRONICS—SEMICONDUCTORS

Semiconductors and Other Electronic Materials

P. Rai-Choudhury, Chairman; K. V. Ravi, Vice-Chairman

(GRAND BALLROOM, Second Floor)

A.M. Abs.

9:00—"Precipitation of Oxygen in Silicon Crystals: A Heterogeneous Process" by A. J. R. de Kock and W. M. van de Wijgert 202

9:20—"Self-Consistent Calculation of the Jahn-Teller Distorted Vacancy in Silicon" by N. O. Lipari, J. Bernholc, and S. T. Pantelides 203

9:40—"Swirl Defects in Carbon-Rich Silicon" by W. C. O'Mara and D. Guidici 204

10:00—"The Dependence of the SiO_2 Defect Density on Both the Applied Electric Field and the Oxide Thickness" by A.-K. M. Zakzouk 205

10:20—Ten-minute intermission

10:30—"Residual Disorder and the Electrical Properties of Ion-Implanted and Low-Temperature Annealed Silicon" by T. Sakurai, T. Sato, S. Tatsuta, and H. Hashimoto 206

10:50—"Carrier Lifetime Enhancement in Silicon" by A. Rohatgi and P. Rai-Choudhury 207

11:10—"The Effects of Process Induced Dislocations and Phosphorus Diffusion on Minority Carrier Generation Lifetime in Silicon" by A. Y. Liang and C. J. Varker 208

11:30—"The Induced Surface Defects vs. Carrier Lifetime as a Function of Boron Planar Diffusion Sources" by S. F. Bevacqua and M. F. Chang 209

11:50—"Detection of Sputter Contamination and Sputter-Etch Residue by Ion Microprobe Analysis" by J. Andrews, L. E. Katz, and J. W. Colby 210

PHYSICAL ELECTROCHEMISTRY

The Third Symposium on Electrode Processes

H. Angerstein-Kozlowska, Chairman; M. A. Butler, Vice-Chairman

(COMMONWEALTH ROOM, Third Floor)

A.M. Abs.

9:00—"Some Common Features of Monolayer Formation on Noble Metals" by H. Angerstein-Kozlowska, B. E. Conway, B. Barnett, and J. Mozota 355

9:25—"The Influence of Inert Ions on Surface Oxide Film Formation and Reduction at Gold Electrodes" by H. Angerstein-Kozlowska, B. E. Conway, and B. Barnett 356

9:50—"Enhancement of Anodic Photocurrents at Silver Electrodes in Halide Solutions" by M. A. Butler 357

10:15—Ten-minute intermission

10:25—"Electrochemical Fundamental Researches on $Ga_xIn_{1-x}P(O \leq x \leq 1)$ Electrodes for Solar Energy Conversion" by A. M. Redon, J. Vigneron, A. M. Guinard-Baticle, and J. L. Sculfort 358

10:50—"Investigation and Evaluation of Photoelectrochemical Cells by Photothermal Spectroscopy" by G. H. Brilmyer, A. Fujishima, and A. J. Bard 359

11:15—"Evidence for Adsorption of Dimethyl Phenazine on Platinum Using A-C Diagnostics" by K. K. Kanazawa and A. F. Diaz 360

11:40—"Some Statistical Aspects of the Growth of Crystals in Corrosion, Metal Deposition, and Anodic Film Formation" by S. Fletcher, R. G. Barradas, J. D. Porter, and R. Bowie-Reed 361

General Session

A. Damjanovic, Chairman; W. E. O'Grady, Vice-Chairman

(GARDNER, Third Floor)

A.M. Abs.

9:00—"Mechanism of Anodic Oxide Film Formation at Nickel in Alkaline Solution" by J. F. Wolf, A. Damjanovic, and L.-S. Ray Yeh 376

9:20—"An 'Unusual' pH Dependence of Anodic Oxide Film Formation at Platinum in Alkaline Solutions: Mechanism of Formation" by A. Damjanovic, L.-S. Ray Yeh, and J. F. Wolf 377

9:40—"Zinc-Electrode Current Efficiency in Zinc-Chlorine Hydrate Batteries. II. Experimental Study" by A. Kermani, J. Jorné, and S. Kodali 378

10:00—"Interfacial Phenomena in Solid Electrolytes Investigated on Thin Film Samples" by Y. Danto, G. Couturier, J. Pistré, and J. Salardenne 379

10:20—Ten-minute intermission

10:30—"Kinetics of Simple Electrode Processes: A New Approach" by R. Heyrovská 380

10:50—"An Error Analysis of the Galvanostatic Double Pulse Technique" by Z. Nagy 381

11:10—"The Kinetics and Mass Transfer of Zinc Electrode in Acidic $ZnCl_2$ Solution" by J. T. Kim and J. Jorné 382

11:30—"The Development of a Grooved Periodic Morphology on Nickel-Aluminum Alloys Electropolished under Gaseous Discharge" by A. V. Lookichev and W. W. Smeltzer 383

EDUCATION COMMITTEE

Description of Movies

Continued from page 94C.

Corrosion in Action—The film was produced as an aid to the understanding of some of the electrochemical processes that result in corrosion. A knowledge of these principles will improve the basis for action in avoiding corrosion by choosing the proper materials and using them to best advantage.

Transistor Structure and Technology—The film begins with a description of how alloy junction transistor (PNP) is made and follows with a discussion of the limitation of its speed and voltage characteristics. The characteristics of PNIP and NPNN types are discussed. Fabrication of NPNN transistors is shown. Finally, there is a brief review of power handling capability and heat dissipation.

Electrochemical Cells—The film presents a basic review of electrochemical cells, their construction and operation. The time changes and reactions at electrodes and electrolyte movement are shown by means of time-lapse photography. The role of the hydrogen ion and the electromotive force series is discussed.

Think About It—The film describes the corrosion process and shows the role of zinc coatings in corrosion control.

Electrochemical Reactions—Explains in detail by animation combined with live action the transformation between chemical energy and electrochemical energy in voltaic and electrolytic cells and in storage batteries. Ionization is reviewed to show the role that electrons play in these transformations. The film pictures some important applications of electrolytic cells for electrolysis and electroplating.

The Electrochemical Society, Boston, Massachusetts, Meeting
The Sheraton Boston, May 6-11, 1979

		Monday May 7	Tuesday May 8	Wednesday May 9	Thursday May 10	Friday May 11
Grand Ballroom Second Floor	A.M.	**Electronics—** Semiconductors Semiconductors and Other Electronic Materials	**Electronics—** Semiconductors Semiconductors and Other Electronic Materials	**Electronics—** Semiconductors Semiconductors and Other Electronic Materials	**Electronics—** Semiconductors Semiconductors and Other Electronic Materials	**Electronics—** Semiconductors Semiconductors and Other Electronic Materials
	P.M.					
Republic Ballroom Second Floor	A.M.	**Battery/ETG—** Alkaline Fuel Cell Technology	**Battery/ETG—** Alkaline Fuel Cell Technology	**ETG—** General Session	**Electronics—** Recent News Papers	
	P.M.					
Constitution Room Second Floor	A.M.	**Corrosion/D&I/ E&M/ETG—** Materials, Processes, and Characterization Techniques for Solar Energy Devices	**Corrosion/D&I/ E&M/ETG—** Materials, Processes, and Characterization Techniques for Solar Energy Devices	**Corrosion/D&I/ E&M/ETG—** Materials, Processes, and Characterization Techniques for Solar Energy Devices		
	P.M.					
Independence—West Second Floor	A.M.	**E&M/ETG—** Characterization of Coal Combustion Products	**Electronics—** Semiconductors Molecular Beam Epitaxy	**Electronics—** Semiconductors Molecular Beam Epitaxy	**Battery/Corrosion/ E&M/ETG—** High Temperature Fuel Cell Materials	
	P.M.			**Battery/Corrosion/ E&M/ETG—** High Temperature Fuel Cell Materials		
Independence—East Second Floor	A.M.	**Organic and Biological Electrochemistry—** Electrochemical Microenvironment and Cell Behavior	**New Technology Subcommittee/ Corrosion/D&I/ Electronics/Organic and Biological Electrochemistry—** Electrochemical Modification and Monitoring of Biological Systems	**Organic and Biological Electrochemistry—** General Session	**Organic and Biological Electrochemistry—** Chemically Modified Electrodes	
	P.M.			**Organic and Biological Electrochemistry—** Chemically Modified Electrodes		
Liberty A Second Floor	A.M.	**Education Committee—** Movies	**Education Committee—** Movies	**Education Committee—** Movies		
	P.M.					

Commonwealth Room Third Floor	A.M. P.M.	**Physical Electrochemistry—** The Third Symposium on Electrode Processes	**Physical Electrochemistry—** The Third Symposium on Electrode Processes	**Physical Electrochemistry—** The Third Symposium on Electrode Processes	**Physical Electrochemistry—** The Third Symposium on Electrode Processes	**Physical Electrochemistry—** The Third Symposium on Electrode Processes
Fairfax A Third Floor	A.M. P.M.	**New Technology Subcommittee/E&M—** Superconducting Materials and Devices	**ETG/Industrial Electrolytic—** Energy Conservation in the Industrial Electrolytic Industries	**ETG/Industrial Electrolytic—** Energy Conservation in the Industrial Electrolytic Industries and General Session **Industrial Electrolytic—** General Session	**Electronics—** Semiconductors Ion Implantation	
Fairfax B Third Floor	A.M. P.M.			**ETG/Organic and Biological Electrochemistry—** Energy Conversion and Storage via Biological Systems **Electronics—** Informal Discussion Laser Annealing	**ETG/Organic and Biological Electrochemistry—** Energy Conversion and Storage via Biological Systems	
Gardner Third Floor	A.M. P.M.	**D&I—** General Session	**D&I/Electronics—** Low Temperature Processing	**Electronics—** Semiconductors Process and Device Modeling	**Physical Electrochemistry—** General Session	**Physical Electrochemistry—** General Session
Hampton Third Floor	A.M. P.M.	**Corrosion—** General Session	**Corrosion—** General Session			
Jefferson Third Floor	A.M. P.M.		**Electronics—** Informal Discussion Approaches to Low Cost Silicon Solar Cells	**Electronics—** Luminescence General Session **Electronics—** Luminescence X-Ray Phosphors and Radiography	**Electronics—** Luminescence Phosphor Efficiency and Saturation	

Abstracts*

BATTERY/CORROSION/ELECTROTHERMICS AND METALLURGY/ ENERGY TECHNOLOGY GROUP

High Temperature Fuel Cell Materials

Abstract No. 1

Materials Compatibility in a High Temperature Solid Electrolyte System

C. Y. Yang* and **H. S. Isaacs,** Dept. of Energy and Environment, Brookhaven National Laboratory, Upton, N.Y. 11973

In a high temperature solid-state electrochemical system, the four basic components, electrolyte, anode, cathode, and interconnector must be compatible both physically and chemically. The limiting chemical factors are cation interdiffusion, liquid phase formation, oxygen diffusion through interconnector, vaporization, decomposition, etc. This paper reports compatibility studies of yttria-stabilized-zirconia in contact with different electrode/interconnector materials at temperatures of 1600°K and up. Emphasis is on the $LaCrO_3$ based materials which have been suggested to be promising interconnection materials.

Abstract No. 2

Ionic Conduction in Doped Zirconia

D. K. Hohnke, Ford Motor Co., Dearborn, Mich. 48121

The ionic conductivity data for zirconia doped with aliovalent metal oxides, $Zr(M)O_{2-x}$, are reviewed and compared with theoretical models. Analysis of the data shows that there exists a unique and clearly discernible proportionality between the experimentally determined parameters that describe $\sigma(x,T)$ for this class of materials. The proportionality factor has the character of an entropy-like term. The significance of this relationship and its possible interpretation are discussed.

Abstract No. 3

Cathodic and Anodic Polarization Phenomena of CaO-Doped CeO_2 Electrolyte with Ag and Au Paste or Foil Electrodes

D. Y. Wang and **A. S. Nowick,** Henry Krumb School of Mines, Columbia University, New York, N.Y. 10027

Anodic and cathodic overpotentials, η, are separately measured in the range 500°-800°C as a function of current, I, using a current-interruption method and a separate reference electrode. Although the η-I curves obey the Butler-Volmer equation, the cathodic and anodic decay curves after interruption show that the observed behavior cannot be explained simply in terms of a charge-transfer mechanism, as in the case of Pt paste electrodes. The mechanism proposed involves the slow diffusion of oxygen along the interphase between electrode and electrolyte.

Abstract No. 4

Overpotential Characteristics of Oxide Electrodes for Zirconia Fuel Cells

H. S. Isaacs* and **L. J. Olmer,** Brookhaven National Laboratory, Upton, N.Y. 11973, and **G. P. Wirtz,** University of Illinois, Urbana, Ill. 61801

Electronically conducting iridium and praeseodymium oxides are being used as cathodes for fuel cells with zirconia-yttria electrolytes. A range of morphologies of these oxides have been prepared using different techniques and were studied using both a-c and d-c methods. Short polarization times with indium oxide showed characteristics similar to those observed with noble metal electrodes in air. With time the polarization currents increase as a result of changes in the oxide. Praeseodymium electrodes in conjunction with conducting current collectors showed low overvoltages. Impedance measurements to determine the electrode mechanisms and methods for electrolyte resistance losses are presented.

* An asterisk by a name indicates which author will present the paper.

Abstract No. 5

Dissociation of Molten Ternary Alkali Carbonates

A. Borucka, Borucka Research Co., Livingston, N.J. 07039

Several experimental methods and relevant details of the necessary apparatus for reliable measurements of the dissociation pressures of thermally unstable molten electrolytes, such as the ternary alkali carbonate eutectic, Li/Na/K/CO_3, are discussed. Experimental results obtained for the above melt, at temperatures from 500° to 800°C, are given along with a theoretical discussion.

Abstract No. 6

Physical and Chemical Solubilities of Fuel Cell Gases in Molten Alkali Carbonates

A. Borucka, Borucka Research Co., Livingston, N.J. 07039

A discussion is presented of the methods and apparatus used for studies of gas solubilities in thermally unstable molten salt electrolytes. The experimental results shown include the solubilities of CO_2, O_2, CO, and N_2 in the ternary eutectic, Li/Na/K/CO_3, followed by a theoretical analysis and comments.

Abstract No. 7

Thermal Stability of $LiAlO_2$

P. A. Finn,* K. Kinoshita, G. H. Kucera, and **J. W. Sim,** Argonne National Laboratory, Chemical Engineering Div., Argonne, Ill. 60439

The thermal stability of α-, β-, and γ-$LiAlO_2$ in the presence of the Li_2CO_3-K_2CO_3 eutectic (62 mole percent (m/o) Li_2CO_3-38 m/o K_2CO_3) was examined in molten carbonate fuel cells and in laboratory pot tests at 875°-975°K. The $LiAlO_2$ samples were characterized by x-ray diffraction analysis, scanning electron microscopy, surface area measurements, and particle size analyses. Experimental results obtained in tests ≤2400 hr at 925°K indicated that α- transforms to γ-$LiAlO_2$, while both β- and γ-$LiAlO_2$ appear to be stable. The rate of surface area loss of $LiAlO_2$ (α, β, γ) due to particle growth was slower in gas environments containing CO_2. Changes observed in the fuel cells were duplicated in the pot tests.

Abstract No. 8

Thermomechanical Behavior of Lithium Aluminate/Alkali Carbonate Electrolyte Structure

G. H. Kucera,* K. Kinoshita, and **R. B. Swaroop,** Argonne National Laboratory, Chemical Engineering Div., Argonne, Ill. 60439

The thermomechanical properties (thermal expansion, static creep, and structural deformation) of electrolyte structures consisting of lithium aluminate ($LiAlO_2$) and 55 w/o Li_2CO_3-K_2CO_3 (62-38 m/o) were measured in CO_2 environment in the temperature range 25° to ~650°C. The samples of $LiAlO_2$ were synthesized as powders of the three allotropes (α-, β-, and γ-) with surface areas ranging from ~7 to 80 m^2/g and a variety of particle shapes. The relationship between the thermomechanical properties of the electrolyte structure and the surface area, particle shape, and particle size distribution of the $LiAlO_2$ powders are discussed.

Abstract No. 9

Alternate Synthesis of Electrolyte Matrix for Molten Carbonate Fuel Cells

R. H. Arendt* and **M. J. Curran,** General Electric Co., Corporate Research and Development, Schenectady, N.Y. 12301

A process is presented for the preparation of the electrolyte matrix, a poorly bonded assemblage of $LiAlO_2$ crystallites, based on the use of a fugitive molten reaction medium. This medium, a molten mixture of alkali chlorides comprising as much as 75 w/o of the reacting mass, is separated from the product $LiAlO_2$ prior to the preparation of electrolyte structures. Therefore, the reaction medium may contain additional equally fugitive components to favorably modify the $LiAlO_2$ characteristics. Further, the existence of electrolyte-free $LiAlO_2$ allows this material to be beneficiated by physical or chemical means prior to being incorporated into electrolyte structures. Data on the characteristics of both the reaction and the product $LiAlO_2$ are presented.

Abstract No. 10

Alternate Fabrication Process for Molten Carbonate Fuel Cell Electrolyte Structures

R. H. Arendt* and **M. J. Curran,** General Electric Co., Corporate Research and Development, Schenectady, N.Y. 12301

A process is presented for the preparation of reinforced molten carbonate fuel cell electrolyte structures which does not involve a hot-pressing operation. This process is based on the use of an electrolyte-free $LiAlO_2$ matrix material of predetermined, tailored characteristics. The matrix is fabricated into a "blank" using conventional ceramic techniques. The "blank" is subsequently infiltrated under controlled conditions with molten electrolyte of any desired composition and to any specific electrolyte content.

Abstract No. 11

Corrosion of Nickel and NiAl in Molten Sodium Carbonate at 900°C

R. C. John and **R. A. Rapp,** Ohio State University, Columbus, Ohio 43210

The hot corrosion of nickel and NiAl in molten sodium carbonate at 900°C has been studied. Reference electrodes of $Au/Na_2CO_3 + 0.97O_2 + 0.03CO_2$ in a beta-alumina tube and Pt/O_2 (1 atm) in a zirconia tube were used to evaluate the acid-base nature and oxygen activities of the melt. These electrodes were also useful in determining the solubility of $NaAlO_2$ and NiO in the carbonate as functions of P_{O_2} and a_{Na_2O} (or P_{CO_2}). The measured corrosion rates of NiAl, Ni-200, and Ni-270 were correlated with the solubilities.

Abstract No. 12

Diffusional Analysis of the Monosulfide Scale on Fe-Co Alloys in H_2-H_2S Atmospheres

D. J. Young, T. Narita, and **W. W. Smeltzer,** Dept. of Metallurgy and Materials Science, McMaster University, Hamilton, Ont., Canada L8S 4M1

A ternary diffusion model is invoked to interpret the diffusional growth of the monosulfide scale formed on Fe-Co alloys containing 10-60 a/o Co in H_2-H_2S atmospheres. The concentration profiles across the sulfide scales were determined by using electron probe microanalyzer. Two kinds of computation procedures were adopted for calculating concentration and sulfur activity profiles. Both results obtained show that the relative self-diffusivity (P) of cobalt to iron in the sulfide is not constant but varies with the sulfide composition. By making use of an empirical P-function best-fitting calculated and observed concentration profiles were in good agreement for all alloys used. A more modified random shooting computation method is proposed to gain the complete description for monophase scale growth on binary alloys using diffusional and compositional results without any sulfidation data.

BATTERY/ENERGY TECHNOLOGY GROUP

Alkaline Fuel Cell Technology

Abstract No. 13

Progress in Alkaline Fuel Cell Technology

K. V. Kordesch, Technical University of Graz, Institute for Inorganic-Chemical Technology, Graz, Austria

Alkaline fuel cell work has declined in the USA, compared to Europe. Using reformed fuels instead of hydrogen is a big factor for utility applications but not for the operation of electric vehicles or small power units. The CO_2-removal from the air is not restrictive. Combining secondary batteries with fuel cells looks attractive. This paper discusses feasibility studies and expectations in respect to electrocatalysts, performance, and operational lifetimes.

Abstract No. 14

An Alkaline Fuel Cell: Why?

H. Van Den Broeck,* M. Alfenaar, G. Spaepen, and **L. Van Poucke,** ELENCO N.V., Mol, Belgium

After a first three-year phase (1976-1978) of ELENCO'S program on alkaline fuel cells, the Belgian and Dutch partners in ELENCO have decided to finance further technical development for a second phase of three years. This paper discusses the basis of this decision and hence touches upon the alkaline fuel cell technology, manufacturing cost, CO_2-removal, potential application areas, and corresponding market assessments.

Abstract No. 15

Factors Affecting the Economic Feasibility of Alkaline Fuel Cell Power Plants for Sweden

T. Nilsson, The Royal Institute of Technology, Dept. of Chemical Technology, Stockholm, Sweden

A sensitivity analysis of the production cost of electricity for fuel cell power plants for biomass fuel comprizing a modified steam-iron process, air treatment equipment, alkaline fuel cells, and inverters is presented. Variables are the current density, operation pressure of the fuel cells, O and M cost of the fuel cell modules, fuel price, plant size, oxygen utilization, and types of electrodes used. C.O.E. less than 5 c/kW-hr and about 7500 Btu/kW-hr may be reached.

Abstract No. 16

Development of a 7 kW H_2/O_2 Fuel Cell Assembly with Circulating Electrolyte in a Compact Modular Design

K. Strasser, Siemens Research Laboratories, Erlangen, Germany

In continuing the development of the H_2/O_2 fuel cell with free electrolyte and supported platinum-metal-free electrodes, a 7 kW fuel cell assembly was developed. The aim of the development was to increase power density and improve the technology of the assembly. The development is based on a construction in which a 35 or 70 cell module, an electrolyte regenerator for removing water and heat, all operating control and monitoring devices and the whole channel system are integrated into a compact assembly block of modular design. The constructural features of the assembly, the operating controls and monitoring devices, the problems encountered during development as well as the results are considered in more detail.

Abstract No. 17

The Alkaline Fuel Cell as a Power Source for City Buses

G. Hovestreydt,* W. Keuning, M. Alfenaar, and **H. Van Den Broeck,** ELENCO N.V., Mol, Belgium

An economical assessment has been made of city buses with a full fuel cell or a battery-fuel cell hybrid setup. Comparisons have been made with a full secondary battery-driven bus and with combustion engine buses using fuels such as diesel, LPG, hydrogen, or methanol. Projections have been made about the potential developments and the related cost evolutions throughout the eighties and the nineties. It is concluded that the battery-alkaline fuel cell hybrid is a very promising concept.

Abstract No. 18

Evaluation of Improved Cathodes in Alkaline Fuel Cells

K. V. Kordesch, S. Srinivasan, J. McBreen, E. J. Taylor,* G. Kissel, and **F. Kulesa,** Dept. of Energy and Environment, Brookhaven National Laboratory, Upton, N.Y. 11973

Improved cathodes, obtained from Union Carbide Corporation, were evaluated in fuel cells of several configurations. These included single cells, parallel bicells, series bicells and 0.5 kW modules. New electrode designs enhance gas mass transfer and yield a 50% improvement in performance over that obtained by Kordesch in the late sixties. Cell performance under several conditions is reported. These include the effect of temperature and intermittent operation and cell performance using air and oxygen as the oxidant.

Abstract No. 19

Methanol Air Fuel Cells

O. Lindström* and **C. Sylwan,** The Royal Institute of Technology, Dept. of Chemical Technology, Stockholm, Sweden

Methanol is attracting a lot of interest in Sweden as fuel for vehicular applications in the future. A small direct

methanol air fuel cell in an electric tricycle and a fuel cell/battery hybride bus are described. Hydrogen air fuel cells are preferred in the larger application with hydrogen from methanol converters. The carbon dioxide question as well as alternative power plants are discussed.

Abstract No. 20

Water Transpiration Modeling in Alkaline Fuel Cells

B. Schumm, Jr., Union Carbide Corp., Battery Products Div., Cleveland, Ohio 44101

It is desirable in the continuous operation of aqueous electrolyte hydrogen-oxygen fuel cell batteries to remove heat and balance water formation by vapor transpiration to the feed gas streams. A sufficient partial pressure gradient must be maintained to accomplish this. The factors to be controlled and the gas diffusion models describing their relationships are discussed. Actual fuel cell battery response is reviewed.

Abstract No. 21

Requirements for Commercial Alkaline Fuel Cells

D. P. Bloomfield, Physical Sciences Inc., Woburn, Mass. 01801

The systems considerations associated with utility size fuel cell power plants impose restrictions on the alkaline fuel cell. This paper shows how power plant life, cost and efficiency objectives, and the thermal integration aspects of subsystem configuration affect the operating requirements of alkaline fuel cells.

Abstract No. 22

Computer Study of Decarbonation of Alkaline Fuel Cells

H. H. Horowitz, Exxon Research and Engineering Co., Linden, N.J. 07036

The feasibility of decarbonating the electrolyte of alkaline fuel cells run on methanol or H_2-Cl_2 mixtures derived from carbonaceous fuels was studied by computer modeling. Several schemes were examined, all based on the idea that for part of the time the acidity generated at the anode is allowed to accumulate until the CO_2 is released, while the alkali generated at the cathode is used for the power portion of the cycle. If the OH^- transference is made to approach unity during the power cycle and zero during decarbonation, then the fraction of time spent in decarbonation should equal the percentage of CO_2 in the hydrogen. The calculation showed that this figure could be approached in certain optimized decarbonation configurations without the use of expensive ion exchange membranes.

Abstract No. 23

A Study of Nickel Boride as Anode Catalyst for Alkaline Fuel Cells

C. Chuan-sin * and **C. Yuen-hong,** Laboratory of Electrochemistry, Dept. of Chemistry, Wu-han University, Wu-han, China.

The chemical, physical, and electrochemical properties of samples of nickel boride prepared by different methods are compared and related to their activity as anode catalyst. It is found that the percentage of boron retained by the catalyst should be carefully controled, while the optimal boron content depends on the method of preparation of electrodes. Some good nickel boride anodes can run more than 2500 hr without much deterioration.

Abstract No. 24

Electrodes for Alkaline Hydrogen-Oxygen Fuel Cells with Nickel and Silver Catalysts

H. Grüne, Siemens Research Laboratories, Erlangen, Germany

For alkaline hydrogen-oxygen fuel cells the comparatively cheap metals silver and nickel instead of platinum can be used as catalysts. The low exchange current densities of these materials require thick electrodes (0.3-1 mm) with long transport distances. Considerations and experiments lead to an optimized size shape of the catalyst particle. Using silver and nickel catalysts having high specific surface areas, electrodes were constructed which allow stationary current densities up to 1 A/cm^2 (H_2, air) and 2 A/cm^2 (O_2).

Abstract No. 25

Crystallite Growing of Raney Nickel and Effect on Electrochemical Activity and Stability

M. A. Humbert and **A. Sugier,** Institut Français du Pétrole, 92500 Rueil Malmaison, France

Investigations on Raney nickel used as a hydrogen electrode catalyst show that heat-treatment under controlled atmosphere or aging in concentrated KOH induces an important and rapid crystallite growth. Recrystallization occurs through ad-atom migration or reorganization, the former mechanism prevailing in KOH. The influence of crystallite size on oxide reducibility has been demonstrated and hydrogen electrochemical oxidation has been shown to be a "nondemanding" reaction for the crystallite size range studied.

Abstract No. 26

Catalysts for Alkaline Fuel Cells

M. Bursell* and **G. Karlsson,** The Royal Institute of Technology, Dept. of Chemical Technology, S-100 44 Stockholm, Sweden

Cathodes comprizing nickel screens painted with doped silver catalyst in Teflon suspension have exhibited almost only activation polarization under current load at different temperatures, KOH-concentrations, and oxygen partial pressures. With air and 5M KOH at 70°C, 0.83V *vs.* H_2-reference was obtained at 1 kA/m^2. Cathodes have also been made with, in decreasing order of activity, perovskites containing manganese, cobalt, or nickel as well as spinels as catalysts. MoTi-containing Raney nickel was among the anode catalysts studied.

Abstract No. 27

Active Sites on $La_{1-x}Sr_xCoO_3$ Oxygen Electrodes

K. L. K. Yeung* and **A. C. C. Tseung,** Dept. of Chemistry, The City University, London ECl, England

Galvanostatic oxygen stripping studies on the $La_{1-x}Sr_xCoO_3$ showed that both maximum performance and the maximum oxygen coverage occurred at $x = 0.5$. This indicates that the improvement in steady-state performance with x is due to the increase in the number of Co^{3+}/Co^{IV} couples. The results also suggest that the double exchange between the Co^{3+}/Co^{IV} couple satisfies an important condition for the splitting of the O = O bond. Crystallographic and steric considerations suggest that the number of active sites on $La_{1-x}Sr_xCoO_3$ is governed by geometric factors.

Abstract No. 28

O_2 Reduction on Electrodeposited Pt Crystallites in Sodium Hydroxide Solution

P. Bindra* and **E. Yeager,** Case Laboratories for Electrochemical Studies and Dept. of Chemistry, Case Western Reserve University, Cleveland, Ohio 44106

The rotating disk and ring-disk measurements have been carried out to study O_2 reduction on Pt crystallites in sodium hydroxide as a function of concentration and temperature. Platinum crystallites were electrodeposited on various substrates from a solution of platinum ions using the potentiostatic pulse method. Electron microscopic examination of the deposit shows the crystallites under some circumstances to be hexagonal platelets exposing the (111) surface. The effect of Pt crystallite size on O_2 reduction in alkaline media is discussed.

Abstract No. 29

O_2 Reduction on Underpotential Deposited Metal Monolayers in Sodium Hydroxide

A. Khutornoi, P. Bindra, R. Amadelli, and **E. Yeager,*** Case Laboratories for Electrochemical Studies and Dept. of Chemistry, Case Western Reserve University, Cleveland, Ohio 44106

The catalytic activity for O_2 reduction of underpotential deposited (UPD) mono- or submonolayers of various met-

als on a stable substrate have been studied using the rotating disk electrode technique. The results show that in NaOH solutions UPD layers of Cu, Ag, and Pt on gold are more active catalytic surfaces than the gold surface, which by itself is a good catalyst. The mechanism of O_2 reduction on these electrocatalytic surfaces is discussed.

Abstract No. 30

Bimetallic Polymeric Phthalocyanines as Catalysts for Oxygen Reduction

L. J. Gestaut,* W. O. Butler, and **W. A. Kovatch,** Diamond Shamrock Corp., Electrolytic Systems Div., Painesville, Ohio 44077

A series of bimetallic polymeric phthalocyanines, p(M/M')Pc, has been synthesized where M and M' are from the groups Fe, Co, Zn, and Cu. Catalytic activities for oxygen electroreduction were found to be significant for all pairings. ESCA and Auger spectra of the p(Cu/Zn)Pc polymer indicate changes in the oxidation states of the metal ions; a fractional increase being observed for the copper ion, a fractional decrease for the zinc ion.

Abstract No. 31

Bifunctional Air-Electrode for Metal-Air Batteries

L. Carlsson and **L. Öjefors,** Swedish National Development Co. (SNDC), Dept. for Energy and Environmental Technology, Åkersberga, Sweden

In order to fulfil volume and cost requirements on metal-air batteries it is necessary to use bifunctional air electrodes which also serve as counterelectrodes during charge. This twofold duty puts a very high demand on the electrode, especially the structure and catalyst. In the iron-air battery program of SNDC a 0.6 mm porous Ni-electrode with Ag catalyst has been developed for this purpose with a life of more than 100 charge-discharge cycles. In the paper design, performance, relationship Ni/Ag, structural changes, mode of failure, etc. are discussed.

Abstract No. 32

Determination of the Rate of Chemical Decomposition of H_2O_2 by Electrocatalysts for O_2 Reduction

F. T. B. J. van den Brink, E. Barendrecht, and **W. H. M. Visscher,** Laboratory for Electrochemistry, University of Technology, Eindhoven, The Netherlands

In the investigation of electrocatalytic materials suitable for the reduction of oxygen, there is a lack of knowledge of their behavior with respect to the nonelectrochemical decomposition of hydrogen peroxide. If the heterogeneous rate constant of this reaction were known, all other (potential dependent) reactions could be determined separately and a thorough insight into the mechanism of O_2 reduction could be obtained. We here describe a simple method for measuring the rate constant of the chemical H_2O_2 decomposition at electrocatalytic materials with a rotating ring disk electrode.

CORROSION

General Session

Abstract No. 33

Stress Corrosion Cracking of Stainless Steels in Molten $AlCl_3$-NaCl

W. H. Smyrl, Sandia Laboratories, Albuquerque, N.M. 87185

Stress corrosion cracking of austenitic and ferritic stainless steels is being studied in anhydrous molten $AlCl_3$-NaCl at 150°C. Cracking has been observed in Nitronic 40 (21 Cr-6 Ni-9 Mn), Nitronic 50 (22 Cr-13 Ni-5 Mn), and Nitronic 60 (17 Cr-9 Ni-9 Mn) in the heavily cold rolled condition. All the materials show a region II (stress independent) crack propagation velocity of the order of 10^{-5} cm/sec. Stress dependent (region I) crack propagation is also observed for all materials. The crack path is transgranular at high stress intensities, with a small amount of intergranular separation at low stress intensities. The effect of an imposed electrical potential is to retard (stop) the crack propagation for cathodic potentials, with little effect at anodic potentials where the materials are passive in the NaCl-saturated molten salt. These results are discussed as they relate to boiling $MgCl_2$ tests at the same temperature, and as to implications for hydrogen-induced cracking. (This work was supported by the United States Department of Energy (DOE), under Contract AT(29-1)-789.)

Abstract No. 34

The Stress Corrosion Cracking of AISI 304 Stainless Steel in Chloride Containing Ammonium Sulfate Solutions at 220°F

H. S. Tong and **D. J. Swartz,** Allied Chemical Corp., Corporate Development Center, Morristown, N.J. 07960

The straining electrode technique was used to study the stress corrosion cracking (SCC) susceptibility of AISI 304 stainless steel in chloride containing 35% $(NH_4)_2SO_4$ solutions at elevated temperature. The SCC susceptibility was evaluated from experimentally obtained quantitative expressions for the decreases of ultimate tensile strength and reduction of area in these solutions compared to inert conditions. The inhibiting effect of nitrates was also studied. Electrochemistry of the alloy-environment system is presented, and correlation between the SCC susceptibility and the electrochemical parameters are discussed.

Abstract No. 35

The Electrochemical and Stress Corrosion Behavior of an Austenitic Stainless Steel in Phosphate Solutions at High Temperatures and Pressures

H. Tischner* and **H. Kaesche,** Corrosion Laboratory, Dept. of Materials Science and Engineering, M.I.T., Cambridge, Mass. 02139

An apparatus is described which enables electrochemical and electrochemically controlled stress corrosion tests up to 300°C. All tests have been carried out with a silver/silver-phosphate reference electrode in a 0.4M Na_2HPO_4/NaH_2PO_4 solution. Polarization curves of AISI Type 304 stainless steel as well as SCC tests at rest potential and under potentiostatic control demonstrate the influence of the electrode potential and the stress on the behavior of the alloy in that kind of PWR model system. Effects of phosphate precipitates are also discussed.

Abstract No. 36

Hydrogen Permeation and Embrittlement in Nickel and Nickel Alloys

M. Kurkela* and **R. M. Latanision,** Corrosion Laboratory, Dept. of Materials Science and Engineering, M.I.T., Cambridge, Mass. 02139

Earlier work has suggested an association between intergranular cracking of nickel by hydrogen and grain boundary segregation of elements like Sn, Sb, P, and S. To test this association, permeation of hydrogen was studied as a function of grain boundary partitioning of these elements by employing the Devanathan technique and segregation examined by Auger electron spectroscopy. The transport of hydrogen by dislocation was studied by straining the specimen in a permeation experiment.

Abstract No. 37

Hydrogen Profiles in Solids Measured by a New Nuclear Physical Method

R. Doerr, E. Brauer,* R. Gruner, and **F. Raush,** Institute of Physical Chemistry, University of Frankfurt, Frankfurt am Main, Germany D 6000

Hydrogen permeation plays an important role in corrosion phenomena. A new method based on the resonant nuclear reaction between 15 nitrogen and protons which yields α particle and a characteristic 4.43 MeV γ ray can be used for hydrogen detection down to 30 ppm. Depth profiles of the hydrogen concentration can be measured with a depth resolution of 50Å in a range of 2 or 3 μm. Examples are presented of hydrogen depth profiles of palladium-coated Ti-foils, of Al, and Al alloys.

Abstract No. 38

Raman and Infrared Spectroscopic Studies of Aqueous Corrosion Products on Stainless Steels

J. Keiser,* C. Brown, and **R. Heidersbach,** Dept. of Ocean Engineering, University of Rhode Island, Kingston, R.I. 02881

Types 410, 430, 446, and 502 stainless steels were exposed to a series of electrolytes under conditions of varying temperature, pH, and electrochemical potential. *In situ* Raman spectra and infrared reflection spectra were recorded and are presented. Cells for *in situ* Raman spectroscopy are discussed along with signal averaging and data smoothing techniques necessary to enhance the signal to noise ratios obtained from thin passive films on metal surfaces.

Abstract No. 39

Infrared and Raman Spectra of Thermal Oxidation Products Formed on Stainless Steels

P. M. Fabis,* **R. H. Heidersbach,** and **C. Brown,** Dept. of Ocean Engineering, University of Rhode Island, Kingston, R.I. 02881

Type 410, 430, 446, and 502 stainless steels were exposed to air and oxygen environments at temperatures from 250° to 880° C. The infrared reflectance spectra and laser Raman spectra of the oxidation products were obtained *in situ* and are reported. Modifications to standard infrared reflectance equipment which were necessary to insure spectral reproducibility are also discussed. *In situ* infrared and Raman spectroscopy cell designs for high temperature oxidation exposures are also discussed.

Abstract No. 40

Optical Studies of Polymeric Films Formed Electrochemically on Metal Electrodes

S. Gottesfeld* (Present address: Bell Laboratories, Murray Hill, N.J. 07974), **M. Babai, M. Yaniv,** and **D. Laser,** Dept. of Chemistry, University of Tel-Aviv, Tel-Aviv, Israel

The growth and properties of polymeric films formed by the electrooxidation of phenolic compounds were investigated *in situ* by ellipsometry and reflectometry. Thick uniform films (*ca.* 1000Å) can be grown on platinum anodes. The nature of the films formed on titanium electrodes by anodization in the presence of phenolic compounds was investigated. A characteristic optical behavior which was found for oxide-covered titanium in chloride solutions is modified in the presence of the phenolic additives.

Abstract No. 41

A-C Impedance of Corroding Nickel and Iron Alloys

M. W. Kendig* and **H. S. Isaacs,** Brookhaven National Laboratory, Upton, N.Y. 11973

A-C methods offer a possible technique for monitoring the corrosion rates of metals in a wide range of aqueous systems. Measurements were carried out on nickel, alloy 600, and Type 405 stainless steel in acid solutions. The potentials of the alloys were varied potentiostatically and by the additions of hydrogen peroxide, oxygen, nitrogen, and hydrogen. The corrosion rates of the alloys during passivation and depassivation show a large hysteresis with potential. The relation between the a-c impedance and the corrosion rates during passivation and depassivation is presented.

Abstract No. 42

Corrosion by Alternating Current: A Study of Voltage Modulation on the Polarization of Mild Steel

D-T. Chin and **S. Venkatesh,*** Dept. of Chemical Engineering, Clarkson College of Technology, Potsdam, N.Y. 13676

Corrosion by alternating current has received renewed attention in recent years. In this study, the polarization of mild steel in aqueous Na_2SO_4 solution was examined with an alternating voltage (a-V) modulation method. It was found that the superimposed a-V shifted the corrosion potential of mild steel toward the active direction and destroyed the passivity of mild steel at the passive potentials. The effect of a-V was simulated numerically on a digital computer and the calculations showed a qualitative agreement with the experimental observations.

Abstract No. 43

The Use of Triangularly Modulated Triangular Potential Sweeps in the Study of Corrosion and Passivation Processes

J. R. Vilche and **A. J. Arvia,** Instituto de Investigaciones Fisicoquímicas Teoricas y Aplicadas (INIFTA), 1900 La Plata, Argentina

The electrical responses of iron, nickel, and cadmium electrodes in acid, neutral, and alkaline media under triangularly modulated triangular potential sweep perturbations are studied. The *E/I* displays exhibit characteristic splittings and fine structure which are due to the formation of different hydroxide and oxyhydroxide species within the potential range of water stability. The systematic change of frequency and amplitude of both the base and modulating signals make it possible to obtain detailed information about the corrosion and passivation behavior of metals.

Abstract No. 44

Effect of Fluid Flow upon Metal Repassivation in Acidic Solution

R. C. Alkire* and **K. R. Weisbrod,** Dept. of Chemical Engineering, University of Illinois, Urbana, Ill. 61801

Mass transfer effects upon repassivation were evaluated experimentally with use of an impinging jet electrolysis cell. Iron and cobalt specimens were studied in sulfuric and perchloric acids. Potential control was used to depassivate the metal surface and then initiate repassivation. It was found that repassivation rates could be correlated with mass transfer principles based upon the hypothesis that the electrolyte at the metal surface must be saturated with metal salt if repassivation is to occur.

Abstract No. 45

Electrochemical Behavior of Type 304 Stainless Steel in High Temperature, High Pressure Water

J. B. Lee,* Republic Steel Corp., Research Center, Independence, Ohio 44131, and **A. K. Agrawal** and **R. W. Staehle,** Dept. of Metallurgical Engineering, Ohio State University, Columbus, Ohio 43210

The electrochemical corrosion behavior of Type 304 stainless steel has been studied in a high temperature, high pressure aqueous system. The effect of dissolved oxygen on the open-circuit potential of Type 304 was measured at 250°C in a flowing autoclave system using an internal silver-silver chloride electrode. The active-passive behavior of Type 304 was investigated in dilute sodium sulfate solutions with quasisteady-state polarization curves. The kinetics of oxygen reduction on the passivated Type 304 was also studied in dilute sodium sulfate solution at 250°C. Results and discussion are presented.

Abstract No. 46

Corrosion and Structural Characterization of Amorphous Fe-Ni-Cr-P-B Alloys

R. B. Diegle,* Battelle Columbus Laboratories, Columbus, Ohio 43201, and **M. D. Merz,** Battelle Pacific Northwest Laboratories, Richland, Wash. 99352

Alloys with compositions of 47Fe-30Ni-2Cr-15P-6B and 33Fe-30Ni-16Cr-15P-6B were sputtered at a rate of about 30 μm/hr onto copper substrates. Corrosion behavior was determined by polarization and weight loss techniques in chloride media, and structure was studied by TEM, DSC, and x-ray diffraction. The sputtered deposits are essentially completely amorphous, and they exhibit the same excellent corrosion resistance as do amorphous alloys of similar compositions but prepared by melt-quenching techniques.

Abstract No. 47

Study of the Corrosion of Nickel by Fluorine

G. Gevers, A. Lachter, M. Salagoity, J. Salardenne, and **A. S. Barrière,** Laboratoire de Recherches en Electrotechnique et Physique du Solide, Université de Bordeaux I, 33405 Talence, France

Nickel is employed to protect the mechanical pieces used for the isotopic separation of the uranium gaseous phase. To describe the corrosion of nickel by fluorine we have prepared layers of NiF_2 by several techniques. The characterization of the samples is deduced from: mass spectrography; scanning electron microscopy; x-ray diffraction; backscattering of α particles and α-X reactions studies. Optical and electrical properties of NiF_2 thin films are examined.

Abstract No. 48

The Diffusion of Oxygen in the Growing Oxide and Alpha Phases during High Temperature Oxidation of Zircaloy-4

R. E. Pawel, Metals and Ceramics Div., Oak Ridge National Laboratory, Oak Ridge, Tenn. 37830

During isothermal oxidation at temperatures above the alpha/beta transition, the growth of layers of oxide and oxygen-stabilized alpha Zircaloy into the parent beta phase can be modeled in terms of an idealized multiphase, moving boundary, diffusion problem. Equations were developed that express the effective oxygen diffusion coefficients in terms of the reaction rate constants and equilibrium solubility values. This analysis was applied to recent experimental kinetic data for the steam oxidation of Zircaloy-4 to determine the oxygen diffusivities in the two-product phases over the temperature range 1000°-1500°C. These results are discussed in terms of appropriate comparisons and their usefulness and limitations in modeling oxidation experiments. (This research was sponsored by the Division of Materials Science, U.S. Department of Energy under contract W-7405-eng-26 with the Union Carbide Corporation.)

Abstract No. 49

Steam Oxidation of Incoloy 800

H. F. Bittner,* **J. T. Bell, J. D. Redman,** and **W. H. Christie,** Oak Ridge National Laboratory, Oak Ridge, Tenn. 37830

In situ formed oxides on heat exchanger materials have been proposed as barriers to tritium permeation for fusion reactor applications. To understand these barrier effects, characterization of the oxide coatings is necessary. In the present work oxides produced on Incoloy 800 tubes from tritium permeation experiments are analyzed by ion microprobe, x-ray diffraction, and optical microscopy. Results of oxidation studies on coupon samples of Incoloy 800 are presented, including effects of surface pretreatment and annealing techniques. (This research was sponsored by the Division of Materials Sciences, U.S. Department of Energy under contract W-7405-eng-26 with the Union Carbide Corporation.

Abstract No. 50

Thermochemical Properties of Na_2O-WO_3-SO_3 System at 1200°K

R. Y. Lin and **J. F. Elliott,** Dept. of Materials Science and Engineering, M.I.T., Cambridge, Mass. 02139

The activity of sodium oxide in ternary Na_2O-WO_3-SO_3 melts was measured at 1200°K by the emf cell

Pt(s), O_2(g)	Na^+	SO_2(g), O_2(g), Pt(s)
Na_2O-WO_3 melt	β-Alumina	Na_2O-WO_3-SO_3 melt

The composition of the ternary melt was determined using both standard chemical analytical methods and a thermogravimetric technique under the same conditions of temperature and gas composition as were employed in the emf measurements. Based on these data, the activity of tungsten trioxide in the melt was obtained by applying the Gibbs-Duhem equation for a three-component system.

Abstract No. 51

The Anodization of Superimposed Metallic Layers: Theory

J. P. S. Pringle, Chemistry and Materials Div., Atomic Energy of Canada Ltd., Chalk River Nuclear Laboratories, Chalk River, Ont., Canada K0J 1J0

The chief factor affecting the anodization of superimposed metal layers is oxide resistivity, which determines whether the metal order is conserved or not. Its effect will be modified, however, by consideration of transport numbers, relative metal migration rates, oxide structure, and Pilling-Bedworth ratios. These various factors are reviewed, and their effects illustrated with examples from the literature.

Abstract No. 52

The Anodic Oxidation of Superimposed Niobium and Tantalum Layers: Theory

J. P. S. Pringle, Chemistry and Materials Div., Atomic Energy of Canada Ltd., Chalk River Nuclear Laboratories, Chalk River, Ont., Canada K0J 1J0

Recent studies by Perriere *et al.* [*J. Electrochem. Soc.*, **125,** 1549-1557 (1978)] have shown that when niobium is superimposed on tantalum, the metallic order is conserved on anodization, and that when the tantalum is superimposed, it is partially inverted. The effects can be ascribed to the difference in resistivity between the two oxides, so that fingers of substrate niobium oxide penetrate a superimposed tantalum oxide layer. All ancillary observations can be explained by this hypothesis.

Abstract No. 53

The Application of Potentiostatic Pulse Method for the Determination of Critical Stress Intensity Factor for Stress Corrosion

H. C. Chan,* Faculty of Engineering, Middlesex Polytechnic, Queensway, Enfield, Middlesex, England, and **A. C. C. Tseung** and **A. I. Onuchukwu,** Dept. of Chemistry, The City University, London EC1, England

It has been shown that there is a critical value of stress intensity, K_{ISCC}, above which stress corrosion will occur, and that this corresponds to the creation of a stretch zone at the crack tip. Traditionally, K_{ISCC} is obtained by the constant loading method, which is tedious and time consuming. Using a precracked tensile specimen which is insulated at the crack tip as part of a corrosion cell, it is possible by the application of potentiostatic pulse method to detect the increase of corrosion current when new surface is exposed. From the tensile load at this instance, K_{ISCC} can be calculated. This present method will enable rapid assessment of the susceptibility of a material to stress corrosion cracking.

Abstract No. 54

Corrosion Resistant Amorphous Stainless Steels Containing Tungsten

R. Wang and **M. D. Merz,*** Battelle Pacific Northwest Laboratories, Richland, Wash. 99352

Amorphous stainless steels stabilized with additions of W were made by vapor deposition. The corrosion behavior was studied by polarization curves in chloride solutions of varying *p*H. The addition of W was found adequate to stabilize the amorphous structure and to enhance protective film formation. The material exhibited improved resistance to corrosion pitting compared to crystalline vapor-quenched stainless steel and was comparable to melt-quenched amorphous alloys stabilized with metalloids.

Abstract No. 55

Transient Electrochemical Behavior of Mild Steel during High Strain Corrosion Fatigue in 3.5% NaCl Solutions

C. Patel,* **V. Rollins,** and **T. Pyle,** Dept. of Chemistry and Metallurgy, Lanchester Polytechnic, Coventry, England

A study of the effect of low frequency high strain cyclic deformation on the kinetics of anodic and cathodic reactions occurring at a mild steel surface immersed in 3.5% aqueous chloride solution of *p*H 8.2 has been made. It has been shown that plastic deformation accelerates both the anodic and cathodic reactions and that cathodic polarization does not suppress the anodic dissolution transient until significant overpotentials are applied. However at these potentials a large cathodic transient is observed, and it seems impossible to select a potential under high strain fatigue conditions at which neither the cathodic nor the anodic reaction is accelerated by the plastic deformation.

Abstract No. 56

Inhibitors for the Prevention of Environmental Cracking of High Strength Aluminum Alloys in Seawater

C. Patel,* Dept. of Chemistry and Metallurgy, Lanchester Polytechnic, Coventry, England

The cyclic plastic straining electrode technique was employed to study the strain-enhanced dissolution behavior of Hiduminium 48 (Al-Zn-Mg alloy) in saline solutions containing various inhibitors. The precise manner in which dissolution transients varied with time and successive cycles of strain was dependent upon the following factors: the solution flow rate, the chloride concentration, the potential of the metal, the type of inhibitor in the solution, the sign of the strain reversal, the number of previous strain cycles applied, and the strain rate.

CORROSION/DIELECTRICS AND INSULATION/ELECTROTHERMICS AND METALLURGY/ENERGY TECHNOLOGY GROUP

Materials, Processes, and Characterization Techniques for Solar Energy Devices

Abstract No. 57

A Global View of Solar Energy in Rational Units

A. Rose, Universities Professor Program, Boston University, Boston, Mass. 02215

The world's energy needs, limitations, and solar sources can be arranged in a compact, meaningful table when energy is measured in fractions of the total solar flux intercepted by the earth. Furthermore, the assignment of solar efficiencies to presently existing solar energy farms and the assessment of their current energy costs provides grounds for optimism that solar voltaic cells can eventually provide a universal source of low cost energy.

Abstract No. 58

Progress Review of Low-Cost Processes for Polycrystalline Silicon for Solar Cells

L. P. Hunt, Dow Corning Corp., Solid-State Research and Development Laboratory, Hemlock, Mich. 48626

An up-to-date review is given of processes funded by the Jet Propulsion Laboratory's Low-Cost Solar Array Project sponsored by the U.S. Department of Energy. Emphasis is placed on processes that have shown the most technological progress for producing solar-grade silicon for less than $10/kg. Process comparisons are made based upon silicon cost, purity, production rate, total quantity produced, energy consumption, and the degree of technological complexity and commercial readiness.

Abstract No. 59

Development of a Process for High Capacity Production of Solar Grade Silicon

W. H. Reed, T. N. Meyer, and **M. G. Fey,** Westinghouse Power Circuit Breaker Div., Arc Heater Project, Trafford, Pa. 15085

The realization of cost effective silicon photovoltaic arrays will depend in part on the development of new methods for large capacity silicon production resulting in a factor of six lower in cost. Currently under development at Westinghouse is a program to produce silicon based on the high temperature (3000°K) sodium reduction of $SiCl_4$. This process development employs Westinghouse a-c electric arc heaters as the heat source for the reaction. Engineering analyses and detailed design of the experimental verification unit were completed, and the test system is presently being installed. Experiments are in progress to examine the reaction kinetics, reactant injection, and product separation.

Abstract No. 60

Production of Silicon for Solar Cells by the Sodium Reduction of Silicon Tetrafluoride Gas

V. K. Kapur, L. Nanis, and **A. Sanjurjo,** SRI International, Menlo Park, Calif. 94025

High purity silicon was produced by the exothermic reduction of SiF_4 gas with sodium metal. Fluosilicic acid (H_2SiF_6), a waste by-product of the fertilizer industry, was used as an inexpensive source of SiF_4 gas. The boron and phosphorus impurities in the polycrystalline silicon obtained were in the ppb level, and transition metal impurities were in the ppm level. The resistivity of the p-type silicon material was in the 0.1-0.5-cm range. Additional purification may be obtained by directional solidification or Czochralski crystal growing. This SiF_4-Na process offers a potential for producing low-cost polycrystalline silicon for solar cells.

Abstract No. 61

Ingot Solidification for Solar Photovoltaics

R. G. Wolfson, Varian, Lexington Vacuum Div., Lexington, Mass. 02173

Silicon for solar cells is produced by Czochralski growth, a process specifically refined to meet the needs of the microelectronics industry. The material requirements of solar photovoltaics, however, are less demanding, albeit different, and price is now a primary concern. The constraints of the solar industry can be satisfied by reducing the cost of ingot solidification, with some sacrifice of crystal quality. Melt replenishment during Czochralski growth and various forms of ingot casting are considered.

Abstract No. 62

Silicon Crystal Growth in Vacuum

C. P. Khattak* and **F. Schmid,** Crystal Systems, Inc., Salem, Mass. 01970

It has been found that silicon crystals grown in vacuum are saturated with carbon. The source of the problem has been identified with silicon carbide formation involving reactions of silica crucible and graphite retainer. The theoretical analysis has been confirmed experimentally using the heat exchanger method where approximately 50% reductions in carbon levels have been achieved when silica was not in contact with graphite. (This paper presents results of research performed for the Low-Cost Solar Array Project, Jet Propulsion Laboratory, California Institute of Technology, sponsored by the U.S. Department of Energy through an interagency agreement with the National Aeronautics and Space Administration.)

Abstract No. 63

Silicon Slicing by Fixed Abrasive Slicing Technique

F. Schmid* and **C. P. Khattak,** Crystal Systems, Inc., Salem, Mass. 01970

Commercial slicing techniques show either poor material utilization or have high expendable materials costs. This hinders adoption of silicon ingot growth technology for terrestrial and photovoltaic application. The multiwire fixed abrasive slicing technique, still in advanced development stage, has shown that thin wafers can be economically sliced. Twenty-five wafers per centimeter yielding 1.08 square meter of wafer per kilogram of silicon ingot have been demonstrated. The surface damage of these wafers has been 3-5 μm. (This paper presents results of research performed for the Low-Cost Solar Array Project, Jet Propulsion Laboratory, California Institute of Technology, sponsored by the U.S. Department of Energy through an interagency agreement with the National Aeronautics and Space Administration.)

Abstract No. 64

Low Cost Silicon Sheet from Ingot Technologies: A Technology Projection

A. Kran, IBM Corp., East Fishkill Facility, Hopewell Junction, N.Y. 12533

Silicon ingot forming (*e.g.*, Czochralski) and ID slicing technologies are analyzed and projected for their potential of providing low cost sheet material for photovoltaic application. Since both processing operations directly contribute to material quality, which in turn determines solar cell conversion efficiency, both ingot growth and ID slicing must be analyzed simultaneously to determine the most cost-effective approach. Using the PECAN (photovoltaic energy conversion analysis) system, the analysis projects for 1986 sheet material prices of $100/m^2 for conventional (0.25 mm thick) solar cells, and $50/m^2 for thin (0.10 mm thick) solar cells. In addition the outlook for crystal growing and slicing technology, resulting in $20/m^2 silicon sheet, is also reviewed.

Abstract No. 65

Impurity Effects in Silicon Solar Cells

J. R. Davis,* R. H. Hopkins, P. Rai-Choudhury, P. D. Blais, and **A. Rohatgi,** Westinghouse Research and Development Center, Pittsburgh, Pa. 15235, and **J. R. McCormick** and **H. C. Mollenkopf,** Dow Corning Corp., Pittsburgh, Pa. 15235

We have studied the effects on cell performance of various impurities introduced into Czochralski, float-zone, and polycrystaline silicon ingots and dendritic ribbons. Impurities were added in controlled amounts along with boron or phosphorus as primary dopants. All crystals were analyzed chemically, microstructurally, and electrically using solar cells. These data show performance loss was primarily due to degradation of the base diffusion length. An analytic model, devised from this information satisfactorily predicts cell performance from the impurity concentrations. These results permit establishing impurity tolerance limits for solar grade silicon as a function of the required cell performance.

Abstract No. 66

Chemical Impurity Analysis of Low Cost Silicon Material for Solar Cells

G. A. Pollock,* R. Natesh, and **K. M. Koliwad,** Jet Propulsion Laboratory, Pasadena, Calif. 91103

The low cost silicon sheet for terrestrial solar cells contains both structural and chemical imperfections. In order to optimize the performance of the solar cell device, it is essential to understand the interaction between the two imperfections. In addition to the interaction with structural imperfections the total impurity concentration is dependent on the nature of the low cost growth procedure. In this investigation we have used AES, ISS, and SIMS to study the distribution of impurities around structural imperfections such as grain boundaries, twins and inclusions and NAA and SSMS to study total impurity concentrations.

Abstract No. 67

Silicon Ribbon Technology

A. I. Mlavsky, Mobil Tyco Solar Energy Corp., Waltham, Mass. 02154

The very low cost which must be met by "silicon sheet" for compatibility with photovoltaic panels to sell at, say, 50¢ to 80¢ per watt has stimulated the development of a number of techniques for producing silicon directly in the form of ribbon. These techniques are reviewed briefly and a relatively detailed account is given of the status of what is thought by many to be the most advanced process, namely, edge-defined, film-fed growth ("EFG").

Abstract No. 68

Long Diffusion Length Silicon Ribbon Grown by the RTR Technique

R. N. Legge, A. Baghdadi, and **R. W. Gurtler,** Motorola, Inc., Semiconductor Group, Phoenix, Ariz. 85062

One of the approaches to low cost photovoltaic arrays is through the use of thin, polycrystalline silicon ribbon grown at high speed. The ribbon-to-ribbon (RTR) crystal growth method is one such approach which grows large-grain (~1 cm^2) polycrystalline ribbons of silicon. Unprocessed RTR grown ribbons normally exhibit minority carrier diffusion lengths of 5-15 μm. Through the use of a suitable sequence, diffusion lengths as high as 210 μm have been measured on 3-5 Ω-cm material. This value is comparable to (or exceeds) the sample thickness, allowing full utilization of the optically generated electron-hole pairs. The short-circuit currents of RTR solar cells that have been gettered during processing reflect these long diffusion lengths.

Abstract No. 69

The Development and Evaluation of Materials for Resistance to Attack by Molten Silicon

P. E. Grayson and **L. A. Addington,*** Eagle-Picher Industries, Inc. Miami Research Laboratory, Miami, Okla. 74354

The large area silicon sheet growth task objective of lowering the cost of silicon photovoltaic material requires the development of materials which exhibit improved chemical and dimensional stability in contact with molten silicon. These materials may find application as containers and/or shaping dies in processes such as edge-defined film growth. This paper describes the development and evaluation of proprietary coatings of pure silicon carbide, silicon nitride, and aluminum nitride on less pure hot pressed substrates of the respective ceramic materials. Silicon sessile drop experiments were performed on coated test specimens under controlled oxygen partial pressures. X-ray diffraction and SEM characterization was performed prior to testing. The reaction interfaces were characterized after testing with optical and scanning electron microscopy and Auger electron spectroscopy. (This work was supported by the Jet Propulsion Laboratory of the California Institute of Technology.)

Abstract No. 70

Silicon Photovoltaic Solar Cell Processing

B. D. Gallagher, Jet Propulsion Laboratory, Pasadena, Calif. 91103

The presentation describes current state-of-the-art silicon solar cell processing technology in use and/or being developed for low cost terrestrial solar modules. Processes covered under the general areas of surface preparation, junction formation, contact formation and antireflective coating application are discussed. Cost comparisons based on a JPL developed Solar Array Manufacturing Industry Simulation (SAMIS) computer program are presented for competing processes in the general areas described above.

Abstract No. 71

Ion Implantation and Pulse Annealing of Back Surface Fields in Silicon Solar Cells

A. R. Kirkpatrick and **J. A. Minnucci,** Spire Corp., Bedford, Mass. 01730, and **P. A. Iles** and **S. Khemthong,** Optical Coating Laboratory Inc., City of Industry, Calif. 91746

Back surface fields (BSF) have recently become important in the development of high-efficiency silicon solar cells. Common methods of processing to create a BSF involve thick-film aluminum ink. Ion implantation with appropriate annealing is also capable of forming effective BSF layers in wafers as thick as 0.018 in. The improved cell efficiency with introduction of implanted BSF layers is discussed and a comparison of BSF effects by aluminum alloy and by implantation are presented. (This work was supported in part under Jet Propulsion Laboratory, Contract 954786 for the U.S. Department of Energy, by NASA Contract NAS3-20823.)

Abstract No. 72

Optimization of Multilayer AR Coatings

F. W. Sexton, Sandia Laboratories, Albuquerque, N.M. 87185

A computer code to optimize multilayer AR coatings for terrestrial solar cell applications has been developed. Optimum thicknesses are determined using a sequential search technique which maximizes the integral of the product of the internal spectral response of a cell, the solar spectrum at AM1, and the transmittance of the AR coat. Results are compared to experimental and published data for several multilayer structures, as well as variable refractive index CVD nitride coats.

Abstract No. 73

The Photodegradation and Photostabilization of Polymers

D. M. Wiles, Chemistry Div., National Research Council of Canada, Ottawa, Ont. Canada K1A 0R9

Mechanisms for photodegradation of polymer systems are reviewed and the steps involved in photolytic degradation are discussed. Factors which influence the stability of polymer systems and techniques for increasing the stability of polymers for solar applications are covered. The influence of heat and ultraviolet light, as well as oxygen and moisture, on the stability of typical polymer systems are included in the presentation.

Abstract No. 74

Solar Cell Encapsulation

B. Baum, P. Willis, and **E. F. Cuddihy,** Springborn Laboratories, Inc., Enfield, Conn. 06082

The original goal of the program was to screen polymeric materials for use as 20 year life pottants for encapsulation of the solar cell. However, polymers such as fluorocarbons (or silicones) that have the required weathering resistance are

too costly to meet the LSA 1986 encapsulation goals of $8/m^2. A possible solution to this problem lies in the use of a composite consisting of a low cost pottant with poor weather resistance protected by a stable outer coating or film. Two general designs are being considered: substrate and superstrate. One substrate design consists of a rigid base, *e.g.*, a wood composite, an elastomeric pottant, such as ethylene/vinyl acetate copolymer (EVA), and u.v. stabilized acrylic cover. In the superstrate model glass is the top cover, EVA is the pottant with a white pigmented back cover film.

Abstract No. 75

Evaluation of Sheet Silicon for Solar Cells

H. Yoo, P. Iles, and **D. Tanner,** Optical Coating Laboratory, Inc., Photoelectronics Div., City of Industry, Calif. 91746 and **G. A. Pollock,** Jet Propulsion Laboratory, Pasadena, Calif. 91103

The properties required for sheet silicon suitable for solar cells are reviewed. Results are presented of a uniform evaluation of several candidate sheet-forms. These results include *I-V* parameters after a "standard" processing sequence, and their correlation with measurements of diffusion length, spectral response, dark diode characteristics, and light-spot scanning. Some limited attempts at improved processing are described. The paper indicates how such analysis can show over-all promise, and indicates specific areas of improvement for the various sheet forms.

Abstract No. 76

Solar Cell Characterization and Process Control by SPV and Current Phase-Shift Techniques

B. L. Sopori and I. A. Lesk, Motorola Inc., Solar Energy R&D, Phoenix, Ariz. 85008

This paper describes the use of surface photovoltage (SPV) and current phase-shift (CPS) techniques to measure the minority carrier diffusion length/lifetime at various stages of silicon solar cell fabrication. Improvements in the SPV method to make it suitable for high resolution mapping of diffusion length and junction depth measurement in solar cells is described. Results of application of these techniques to (*i*) solar cell process control, and (*ii*) study of the influence of defects and grain boundaries in photovoltaic processes in polycrystalline silicon are also included.

Abstract No. 77

SAW Characterization of Photovoltaic Solar Cells

P. Das, R. T. Webster, and **B. Davari,** Electrical and Systems Engineering, Rensselaer Polytechnic Institute, Troy, N.Y. 12181

Photovoltaic energy conversion can be achieved when light generates excess carriers at a p-n junction, a metal-semiconductor or a semiconductor-electrolyte junction. The conversion efficiency of these devices is degraded by the presence of interface states which act as recombination centers for excess carriers. We describe a nondestructive technique for characterizing the interface states of the solar cell using a surface acoustic wave (SAW) delay line. Analysis of the SAW attenuation and the acoustoelectric voltage reveals the properties of the interface. (This work was partially supported by ONR Contract No. N000-14-75-C-0772.)

Abstract No. 78

Hope for the Future—Solar Cell Materials and Processes

D. S. Ginley* and **L. R. Dawson,** Sandia Laboratories, Albuquerque, N.M. 87185

An assessment of some of the materials and processes envisaged for use as photovoltaics for solar energy conversion is made. Particular attention is directed toward three main areas: developed materials for use in flat-plate arrays, advanced cells for use in solar concentrator systems, and emerging materials that show potential for use in photovoltaics. Primary emphasis is directed toward the materials parameters rather than economic cost considerations. (This work was supported by the U.S. Department of Energy under Contract AT(29-1)-789.)

Abstract No. 79

Thin Film Solar Cells

A. K. Ghosh, Exxon Research and Engineering Co., Linden, N.J. 07036

Thin film polycrystalline materials, *e.g.*, Cu_2S:CdS, Si, Cu_2O, organics, etc., appear promising as low cost solar cells for flat plate collectors. A brief description of our current understanding of devices fabricated from each of these materials and of the problems associated with these devices are presented. The role of grain boundaries in relation to device performance, especially for polycrystalline silicon, is discussed. Carrier generation and transport in organic materials are different from those observed in inorganic devices. A brief theory of organic solar cells is presented.

Abstract No. 80

Hydrogenated Amorphous Silicon Solar Cells

C. R. Wronski, Exxon Research and Engineering Co., Linden, N.J. 07036

Great interest exists in hydrogenated amorphous silicon (a-SiH_x) for fabricating low cost, thin film solar cells for terrestrial use. Currently several approaches to the fabrication of this material are being studied. Significant progress is also being made in the understanding of a variety of a-SiH_x properties including those directly related to its potential as a useful solar cell material. The recent advances in amorphous silicon solar cell fabrication, and in the improved understanding of the operation of these devices are reviewed.

Abstract No. 81

Photoelectrochemical Converter of Solar Energy: Epitaxial Layers of Alloys $Ga_xIn_{1-x}P$

J. L. Sculfort,* and **A. Etcheberry,** Laboratoire d'Electrochimie Interfaciale du CNRS, Meudon-Bellevue, France

Epitaxial layers of $Ga_xIn_{1-x}P$ alloys, two or three dozen micron thick have been prepared on substrates made of GaP 111 B. Depending on the dopant it is possible to obtain either semiconductors of n type (S,N) or p type (Zn) for $1 \leq x \leq 0.9$ with an indirect transition. The electrodes, used in their native state, present rectifying properties when put in contact with the electrolyte. Under illumination, a photocurrent is obtained in an electrolyte medium, both acid or basic. The anodic dissolution of these crystals has been studied. Their behavior is close to that of pure GaP, but, however, the particular conditions of the growth play a great part in the light decomposing of the crystals (surface states, deep level donors due to traps).

Abstract No. 82

Materials for Solar Energy

S. L. Pohlman, Solar Energy Research Institute, Golden, Colo. 80401

As solar energy technology is developed, demand for materials which can survive high temperature applications increases. Materials must be characterized for thermal conversion systems which are subject to diurnal thermal cycling. The primary heat-transfer fluids used in these systems include molten salts, liquid metals, water, gases, and oils. A review of several solar energy systems, including their materials requirements and anticipated problems, is presented.

Abstract No. 83

Absorber Surfaces for Solar Receivers

P. J. Call, Materials Branch, Solar Energy Research Institute, Golden, Colo. 80401

The optical properties of the receiver surface are important for the cost-effective operation of solar thermal energy conversion systems ranging from simple passive building design to sophisticated two-axis tracking concentrators. Recent advances in absorber material development are reviewed that may potentially impact a wide range of applications: low temperature selective paints, stabilization of black chrome to 400°C, vacuum techniques for producing intermediate temperature selective absorbers (400°-700°C), and high absorptance paints for high temperatures.

Abstract No. 84

Reflectance Properties of Solar Mirror Surfaces and Problems Involved with Maintenance of High Reflectivity

R. B. Pettit, E. P. Roth,* and **J. N. Sweet,** Sandia Laboratories, Albuquerque, N.M. 87185

The maintenance of high efficiency in solar power systems requires that solar mirrors possess and maintain a high value of specular reflectance. Methods have been developed for characterizing the reflectance properties of a wide variety of candidate reflector materials, including silvered glass, metallized plastic films, polished aluminum, and various protective coatings. The degradation in reflectance caused by dirt and dust accumulation on mirror surfaces has also been investigated for some of these materials and correlated with deposited particle size distributions. (This work was supported by the Division of Solar Technology, U.S. Dept. of Energy (DOE), under Contract AT (29-1)-789.)

Abstract No. 85

Corrosion Protection of Solar-Collector Heat Exchangers by Electrodeposited Organic Films

G. H. Schnaper* and **V. R. Koch,** EIC Corp., Newton, Mass. 02158

Under normal operating conditions, solar-collector heat exchangers can experience temperatures of up to 149°C (300°F). Moreover, stagnation temperatures may exceed 204°C (400°F). Despite the presence of inhibitors, these high temperatures increase the corrosion rate of the collector metal to intolerable levels, thus reducing the lifetime of the system. We have found that by electrochemically depositing thin polymeric films on typical solar-collector materials (Cu, Fe, and Al), the corrosion rates can be substantially reduced. The kinds of monomer starting materials, the method of deposition, and corrosion test data are discussed. (This work was supported by the Department of Energy under Contract EM-78-C-04-4297.)

Abstract No. 86

Fluid Corrosivity Sensor for Solar Systems

R. Baboian and **G. Haynes,** Texas Instruments Inc., Attleboro, Mass. 02703

The corrosivity of heat-exchanging fluids depends on many factors including system design and liquid type. Frequently, systems which are compatible become incompatible due to changes in the chemistry of the heat-exchanger fluid. This paper describes a sensor capable of detecting changes which occur and lead to increased corrosivity. The sensor system is based on electrochemical principles and consists of a sensing probe, electronics package, and an indicating device.

DIELECTRICS AND INSULATION

General Session

Abstract No. 87

Electrical Properties of SiO_2 Films in Double Level Poly-Si Structures

M. Koyanagi, T. Kamiyama, H. Sunami, and **N. Hashimoto,** Hitachi Ltd., Central Research Laboratory, Kokubunji, Tokyo, Japan

It is confirmed using the *I-V* method and SEM observation that leakage currents through SiO_2 films, thermally grown on lower poly-Si electrodes, are greatly affected by both poly-Si-SiO_2 interface properties and the cross-sectional configuration of lower poly-Si electrodes. Large leakage currents flow through SiO_2 films, thermally grown on poly-Si layers at relatively low temperature, due to electron trapping at the interface and interface irregularities. It is evident that wet oxidation at relatively low temperature results in cross-sectional configuration of poly-Si with sharp edges and gives rise to lowering of breakdown voltage of SiO_2 films due to electric field enhancement at sharp edges. Consequently, dry oxidation at high temperature can realize double level poly-Si structures with high breakdown voltage between the lower poly-Si and upper poly-Si electrodes. This is because dry oxidation at high temperatures can improve the poly-Si-SiO_2 interface properties and give rise to cross-sectional configuration of poly-Si electrodes with round edges.

Abstract No. 88

Reduction Technology of Electron and Hole Trapping Densities in Thermal SiO_2 Film

S. Iwamatsu and **Y. Tarui,** VLSI Technology Research Assoc., Cooperative Laboratories, Takatsuku, Kawasakishi 213, Japan

Electron and hole trapping densities of thermal oxide film can be reduced with a new technology. This technology is based on phosphorous ion implantation to the centroids of the trappings and annealing in oxygen ambient. The trapping densities are reduced to be nearly zero, but when the sample is annealed in nitrogen ambient after phosphorous ion implantation, the trapping densities are not reduced. In these cases, trapping densities are evaluated with corona charging processes and *C-V* measurement technology.

Abstract No. 89

Electrical Confirmation of the Kooi Effect in LOCOS Structures

D. W. Ormond* and **R. W. Young,** IBM Data Systems Div., East Fishkill Facility, Hopewell Junction, N.Y. 12533

An attempt has been made to substantiate the Kooi effect (1) in LOCOS (locally oxidized silicon) structures by several electrical measurement techniques. A sharp cutoff has been observed in the high field dielectric breakdown characteristics of MOS capacitors which had a stepped oxide (*vs.* planar oxide) structure. The dependence of this breakdown phenomenon upon several pertinent parameters, *e.g.*, the thickness of the SiO_2 layer which separates the Si_3N_4 oxidation mask from underlying silicon substrate, shows agreement with the mechanism proposed by Kooi.

1. E. Kooi, J. G. van Lierop, and J. A. Appels, *This Journal*, **123,** 1117 (1976).

Abstract No. 90

Cracking of Plasma Deposited Si-N Films after Subsequent Anneal

M. Vandenberg, Sperry-Univac, St. Paul, Minn. 55165, and **M. S. Hassan,*** AMI, Santa Clara, Calif. 95051

The use of plasma deposited Si-N films as a final passivating layer requires the ability to maintain the integrity of the deposited layer over metallization after heat-treatment cycles. This paper examines the characteristics of Si-N films produced in both internal and external electrode systems which are indicative of "crack free" films. *IR* absorption, optical absorption, and Auger spectra are correlated with physical properties. Process conditions which lead to the production of "crack free" films are recommended.

Abstract No. 91

Dielectric Properties of FeF_3 Thin Films

A. Lachter, G. Gevers, M. Lascaud, J. Salardenne, and **A. S. Barriere,** Laboratoire de Recherches en Electrotechnique et Physique du Solide, Universite de Bordeaux I, 33405 Talence, France

FeF_3 thin films are obtained by different techniques. Their composition and crystallization degree, functions of the preparation conditions, are studied by x-ray diffraction, Mossbauer resonance, and backscattering of α particles. The dielectric properties of the layers are deduced from TSP and a-c measurements. It is shown that the polarization of the samples results from an electronic transfer of electrons between localized states corresponding to a lack of fluorine inside weak resistance zones separated by regions which limit the d-c conductivity.

Abstract No. 92

Thin Film Semiconductor NO_x Sensor

S.-C. Chang, GM Research Laboratories, Electronics Dept., Warren, Mich. 48090

A thin film semiconductor NO_x sensor has been fabricated by reactive rf sputtering from a tin target. The gas

detection is based on monitoring the sensor-resistance change caused by NO_x chemisorption on the sensor surface. The sensor is highly sensitive and selective toward detecting NO_x in air. The chemical composition of the film is being investigated by AES and ESCA. A simple chemisorption model is presented to explain the observed phenomena.

Abstract No. 93

Simulation of Evaporated Deposition Profiles

W. G. Oldham,* **C. Sung,** and **A. R. Neureuther,** Dept. of Electrical Engineering and Computer Sciences and the Electronics Research Laboratory, University of California, Berkeley, Calif. 94720

The general line-edge profile simulator SAMPLE has been extended to evaporated thin films. The code includes the following source-substrate geometries: (*i*) single point source, (*ii*) multiple point sources, (*iii*) hemispherical source, and point source with planetary-mounted substrate. Two-dimensional surface geometries with arbitrary shape may be specified. The simulator produces cross sections of the evaporated film coverage over the surface geometries. Examples are shown for typical spattering and planetary evaporator conditions. (This research was sponsored by the National Science Foundation Grant ENG77-14660-A01.)

Abstract No. 94

Sub 1000Å Linear Lithographic Patterns Using $Ag_2Se/GeSe_2$ Films

K. L. Tai,* **L. F. Johnson, D. W. Murphy,** and **M. S. C. Chung,** Bell Laboratories, Murray Hill, N.J. 07974

Using the $Ag_2Se/GeSe_2$ inorganic negative resist system, linear gaps of 300Å have been resolved. The resist is unique in its high contrast ($\gamma > 5$). Only aqueous solutions are used in the processing of the resist. Swelling and other materials-related distortions are totally absent and dry processing is simple and highly selective.

DIELECTRICS AND INSULATION/ELECTRONICS

Low Temperature Processing

Abstract No. 95

Reduced Temperature Processing of Integrated Circuits

B. E. Deal, Research and Development Laboratory, Fairchild Camera and Instrument Corp., Palo Alto, Calif. 94304

Current trends in integrated circuit fabrication technology appear to be toward lower processing temperatures. While several good reasons exist for limiting process temperatures to 1000°C or below, some disadvantages or problems also have been reported which are discussed. General considerations and trends in the areas of epitaxial deposition, thermal oxidation, diffusion, and chemical vapor deposition are reviewed with respect to lower temperature processing.

Abstract No. 96

Reduced Oxidation Conditions for Dry Gate and Isolation Oxides on (100) Silicon Using High Pressure Oxygen

R. J. Zeto, U.S. Army Electronics Technology and Devices Laboratory (ERADCOM), Fort Monmouth, N.J. 07703

The dry thermal oxidation of (100) silicon by 500 atm oxygen pressure (less than 1 ppm moisture) was investigated to determine practical oxidation conditions relative to the low temperature processing of silicon IC devices. Oxide growth was studied at temperatures between 685° and 885°C. Specific oxidation temperature/time conditions are presented for preparing gate oxides and obtaining oxide isolated device structures. The data are compared to dry oxidation at 1 atm and to steam oxidation at 20 atm, and are presented in terms of the linear-parabolic growth equation. An industrial equipment for automated silicon oxidation via dry high pressure oxygen is currently being fabricated by Autoclave Engineers with DARPA support.

Abstract No. 97

High Pressure Thermal Oxidation of Silicon

T. Thompson,* **J. Wiesner,** and **D. Carlson,** Applied Materials, Inc., Santa Clara, Calif. 95051, and **R. Kline,** GaSonics, Mountain View, Calif. 94043

High pressure silicon oxidation is becoming more important in the move toward low temperature wafer processing. In a production environment, the oxidation behavior must be characterized in order to accurately predict the oxide thickness *vs.* time relationship. To this end, the thermal oxidation of silicon in both pyrogenic steam and in dry O_2 has been investigated as a function of temperature and pressure in a commercially available production system. The characterization for 750°, 850°, and 920° and at 1, 5, and 10 atm pressure is presented for both (111) and (100) orientations of silicon.

Abstract No. 98

CVD—Future Trends

M. L. Hammond, Applied Materials, Inc., Santa Clara, Calif. 95051

The VSLI focus on finer geometry puts new demands on CVD technology. Historic increases in wafer diameter and wafer throughput has slowed in favor of a focus on film properties and film qualities. Autodoping and pattern shift assume new importance in epitaxial growth, while step coverage and defect density are key factors in the lower temperature CVD technologies. A higher conductivity first layer interconnect film is also essential for the new device requirements. An overview of trends in epitaxy and CVD is given with an emphasis on reduced pressure epitaxy and plasma-enhanced CVD of SiO_2.

Abstract No. 99

Properties of Plasma-Deposited Silicon Oxide

M. Vandenberg, Sperry-Univac, Saint Paul, Minn. 55165

Some properties of oxide films deposited from N_2O and SiH_4 in a rf glow discharge at low temperatures are reported. Variation of pressure, rf power, and gas phase reactant ratio are correlated to physical measurements over the temperature range of 25°-300°C. Dielectric constant and breakdown voltage are discussed with respect to processing parameters. A comparison of this film is made with CVD oxide as an intermetal dielectric.

Abstract No. 100

Stoichiometry and the Masking Ability of LPCVD Silicon Nitride during Arsenic Diffusion

A. Dixit,* **C. S. Chen,** and **C. E. Volk,** Burroughs Corp., San Diego, Calif. 92127

Masking failure of LPCVD silicon nitride films during high temperature arsenic diffusion is observed when these films are deposited with ammonia to dichlorosilane ratio <7:1 at the deposition temperature of <760°C. This masking failure is noticed after diffusion when the silicon nitride film is stripped in HF; a number of unetchable areas are left on the silicon wafer. The unetchable areas are not visible on as-deposited films. Helium backscattering data indicate that this masking failure occurs in nonstoichiometric silicon rich films.

Abstract No. 101

Mechanical Properties of Plasma-CVD Silicon Nitride Film

K. Mukai,* **A. Hiraiwa, S. Muramatsu, S. Takahashi,** and **S. Harada,** Hitachi, Ltd., Central Research Laboratory, Kokubunji, Tokyo, Japan

Highly reliable chip passivation film which has low defect density is desirable for plastic packaged integrated circuits. The defects of the film are normally cracks which are induced by mold stress of resin materials. Plasma-CVD silicon nitride film has high mechanical strength and can withstand the mold stress. Breaking energy of the film was estimated by measuring the Vickers hardness, breaking strain, and residual stress. These properties are related to the composition and density of the film.

Abstract No. 102

Reduction of Leakage Current of Large Area High Resistivity Silicon Photodiodes

J. Y. M. Lee,* **R. D. Smith,** and **D. O. Massetti,** Hughes Aircraft Co., Carlsbad, Calif. 92008

An experimental study has been made to reduce the leakage current of large area, high resistivity (p-type, 8000-15000 Ω-cm), fully depleted silicon p-i-n photodiodes. Reduction of bulk leakage current is accomplished by a low oxidation temperature, all ion-implantation process. Surface leakage current is reduced by newly developed surface passivation techniques. As a result, leakage current as low as 1 μA/cm^3 of depletion volume is achieved at 200V reverse bias. Comparison with other more conventional process is presented.

Abstract No. 103

Low Mold Stress Epoxy Molding Compounds for Semiconductor Encapsulation

H. Suzuki,* **T. Moriuchi,** and **M. Aizawa,** Nitto Electric Industrial Co., Ltd., Plastic Package for Semiconductor Development Dept., 919 Fuke-cho, Kameyama, Mie, Japan

Epoxy encapsulants which give low mold stress have been developed. The stress detective devices consist of Piezo resistors that are used to evaluate the mold stress. The influence of resin compositions and filler contents is studied. The relation between mechanical properties of the resins and mold stresses is obtained. The mold stress strongly depends on the thermal expansion coefficient, elastic modulus, and glass transition temperature. Fibrous filler decreases the stress. Moldability and reliability are also investigated.

Abstract No. 104

Laser Annealing—The Hottest Low Temperature Process in Town

G. A. Rozgonyi, Bell Laboratories, Murray Hill, N.J. 07974

High intensity pulsed and CW lasers provide a convenient source of energy which can be rapidly transferred to semiconductor materials with a high degree of spatial and temporal selectivity. This offers the option of high temperature processing in localized regions without the need for a furnace, which would slowly heat the entire wafer. This talk reviews the basic solid and liquid phase regrowth processes that occur in ion-implanted, and in deposited amorphous and polycrystalline layers. Comparisons with conventional thermal annealing and a discussion of those areas of device processing for which laser annealing may provide unique advantages are covered.

ELECTRONICS—SEMICONDUCTORS

Ion Implantation

Abstract No. 105

Parameters Effecting the Electrical Properties of Be and Si Implanted GaAs

B. Molnar, Naval Research Laboratory, Washington, D.C. 20375

In recent years considerable attention has been given to the doping of GaAs by ion implantation. The effects of some important parameters on the electrical properties of Be and Si implanted GaAs are presented in this paper. These parameters include: the temperature of annealing, the encapsulant used for protecting the GaAs during the anneal, the dose level used, and the effect of various semi-insulating GaAs substrates. To evaluate the influence of these parameters, the charge-carrier and mobility distributions have been determined from differential resistivity and Hall measurements. The significance of each parameter was evaluated by comparing the experimental distributions with the corresponding theoretical distribution. (This work was supported by the Naval Electronic Systems Command.)

Abstract No. 106

Transferability of a Simple Ion Implantation Process in GaAs

C. L. Anderson,* and **H. L. Dunlap,** Hughes Research Laboratories, Malibu, Calif. 90256, and **B. Molnar** and **J. Comas,** Naval Research Laboratory, Washington, D.C. 20375

Ion implantation of beryllium into GaAs, followed by annealing at 550°C in argon or vacuum without encapsulation, is shown to produce layers with strong p-type conductivity and high hole mobility. We have investigated the transferability of this process by electrical characterization of samples prepared independently at our two facilities. The layers produced were nearly identical in sheet resistivity, but statistically significant differences of about 15 percent were observed between the Hall effect mobilities of samples prepared at the two laboratories. An investigation employing samples from four separate ingots failed to reveal any significant effects of ingot-to-ingot variations on the electrical properties of the implanted layers. (Work supported by the Naval Electric Systems Command.)

Abstract No. 107

Annealing of Ion Implanted GaAs Using a Melt Controlled Ambient

C. L. Anderson, H. L. Dunlap, and **K. V. Vaidyanathan,*** Hughes Research Laboratories, Malibu, Calif. 90265

It is frequently necessary to anneal ion-implanted gallium arsenide at temperatures in excess of its dissociation temperature. Diffusion of the constituent elements and physical adhesion to the sample surface make the use of suitable encapsulants for high temperature anneal troublesome. In this paper we discuss the use of a procedure which permits annealing implanted GaAs without any encapsulant in a readily controllable system which employs a Ga melt saturated with GaAs as a source of As (and Ga) overpressure. Experimental results on Si- and Se-implanted GaAs covering a range of implantation and anneal parameters are discussed. (This work was supported in part by the Air Force Office of Scientific Research under contract F49620-76-C-0028.)

Abstract No. 108

Transmission Electron Microscopy Study of Si Ion-Implanted GaAs

B. Hughes* and **G. H. Narayanan,** Dept. of Materials Science, University of Southern California, University Park, Los Angeles, Calif. 90007

Transmission electron microscopy has been used to study the implantation induced defects of GaAs implanted with 10^{15}/cm^2, 200 keV, Si ions for samples in the as-implanted state and after anneals at 600° and 800°C. Stereomicroscopy and stripping were used to examine defect profiles. The results are discussed with emphasis on the prismatic dislocation loops and diffuse linear defects observed after annealing at 800°C. These defects show anomalous contrast suggesting dopant decoration. Their images are compared to computed images. A relationship between these results and low doping efficiencies for high dose n-type implants is discussed.

Abstract No. 109

Inert-Gas Bubble Formation in the Implanted Metal/Si System

B. Y. Tsaur, Z. L. Liau, and **J. W. Mayer,** California Institute of Technology, Pasadena, Calif. 91125

Gas-bubble formation has been observed by Rutherford backscattering technique and cross-sectional transmission electron microscopy as a result of inert-gas ion bombardment in a system consisting of a thin metal film (Cr, V, Ni, Ti, or Pd) evaporated on Si substrates. The gas bubbles were found to form predominantly near the interface between the Si substrate and the surface layer. With increasing ion dose, the number of gas atoms trapped in the bubbles at the interface continued to grow and the surface layer peeled off at high doses.

Abstract No. 110

Ion Beam-Induced Epitaxy of Silicon

I. Golecki,* G. E. Chapman, S. S. Lau, B. Y. Tsaur, and **J. W. Mayer,** California Institute of Technology, Pasadena, Calif. 91125

Epitaxial regrowth of an amorphous Si layer on a [100] Si crystal held at 200°-400°C is achieved under bombardment with Si, Kr, or Xe ions. Channeling measurements with MeV He ions show that the regrowth proceeds from the amorphous-crystalline interface, and has an initially linear dose dependence. The annealing beam, however, introduces additional damage centered at or beyond the ion range. Amorphous layers obtained by low temperature self-ion bombardment regrow much more readily than amorphous-deposited layers.

Abstract No. 111

Ion Implant Process Modeling for VLSI

A. G. Fortino* and **H. J. Geipel,** IBM General Technology Div., Essex Junction, Vt. 05452

VLSI complexity requires utilization of numerical process modeling to design processes that meet multiple device requirements. In this paper, we develop design procedures for obtaining accurate IGFET threshold adjust implants. The necessary physical parameters that insure accuracy of models are empirically derived; included is a discussion of techniques employed in their derivation. The thresholds predicted from this activity are found in good agreement with experimental measurements of polysilicon gate active and parasitic IGFET thresholds.

Abstract No. 112

Abrupt Junctions by Ion-Implantation Doping of Silicon and Monitoring Damage Annealing by Laser Raman Scattering

R. Varma,* Chemical Engineering Div., Argonne National Laboratory, Argonne, Ill. 60439, **P. B. Swarup,** Northampton Community College, Bethlehem, Pa. 18015, and **J. Love,** Florida Institute of Technology, Melbourne, Fla. 32901

Single crystal p- and n-type silicon wafers were ion-bombarded with keV P^+, As^+ and B^+ through oxide layers and thermally annealed. The shapes of the bands at 302, 432, 520, 620, and 820 cm^{-1} from laser Raman scattering from silicon surface layer were found to be diagnostic of damage. Correlation of band-broadening with theoretically calculated lattice damage and the application of *in situ* monitoring of lattice damage for optimal wafer annealing for solar-cell fabrication are discussed in detail.

Abstract No. 113

Nondestructive Monitoring of Impurity Activation in Ion-Implanted Silicon by Surface Acoustic Waves

R. Bharat, Rockwell International, Anaheim, Calif. 92800, and **P. Das,* R. T. Webster,** and **K. Varahramyan,** Dept. of Electrical and Systems Engineering, Rensselaer Polytechnic Institute, Troy, N.Y. 12181

Impurities introduced into a semiconductor sample by ion implantation are generally activated by a subsequent thermal treatment either in a furnace or by a laser. The effectiveness of the thermal cycle used in producing free carriers in the implanted layer can be monitored through the use of a surface-acoustic-wave (SAW) convolver, in which the SAW attenuation and the transverse acoustoelectric voltage as functions of the conductivity of the interacting semiconductor layer. Results obtained by this technique for boron-implanted silicon subjected to various annealing treatments are presented, and the potential applications of this nondestructive technique to semiconductor device fabrication discussed.

Abstract No. 114

Effect of Surface Contamination on SiO_2 Film by Heavy Ion Implantation

K. Itoh,* N. Horino, M. Kanegae, and **T. Tsuchimoto,** Computer Development Laboratories Ltd., Kodaira-Shi, Tokyo, Japan

Surface contamination of thermally oxidized silicon during ion implantation ($\sim 10^{16}/cm^2$) is analyzed by AES and IMA, and the effects to devices and their manufacturing processes are investigated. The following results are obtained: (*i*) decrease of etching rate of SiO_2 film due to knock-on implanted carbon, and (*ii*) increase of surface-state charge density (Q_{ss}, max $\sim 10^{12}/cm^2$) at Si-SiO_2 interface. The latter effect does not depend on implant dose rate but on implant time.

Abstract No. 115

An Improved Ion-Implanted Base for Oxide-Isolated Bipolar IC's

R. Kumar,* C. S. Chen, A. K. Hochberg, M. Hunt, J. R. Kruest, K. H. Oh, and **J. Rau,** Burroughs Corp., San Diego, Calif. 92127

The ion implantation of boron through shaped dielectric films has resulted in improved base characteristics required for high speed, high density, oxide-isolated bipolar integrated circuits. The technique results in the formation of an oxide-walled base structure with tight distributions of junction breakdown and low leakage characteristics. The oxide-walled base leads to the elimination of yield-limiting, parasitic Schottky diodes which are formed near the bird's beak in the contact metallization of conventional, diffused base processes due to a loss of surface junction passivation. Further increases in packing density are possible since the oxide-walled base allows the fabrication of devices with emitter regions terminated in the oxide-isolated regions.

Abstract No. 116

On the Growth of Silicon Epitaxy over Ion Implanted Buried Layers

V. C. Kannan* and **G. Roper,** Tektronix, Inc., Beaverton, Ore. 97077

When arsenic ions are implanted into silicon as a dopant source for buried layers, the subsequent annealing procedure (or BL drive) must be chosen so as to anneal out all the damage induced due to implantation without creating any secondary defects. Otherwise, the secondary defects left behind would act as nucleation centers for stacking faults and dislocation loops during the subsequent epitaxial deposition. Several process variables could be optimized to achieve a high quality epitaxy. The variables at the implantation stage are dose, dose rate, and ion energy. Some of the variables may have to be fixed according to device needs such as the final buried layer sheet resistance and junction depth. Once the dose and energy are chosen, drive procedure should be properly adopted to yield defect free buried layers. Some process variables available during growth of epi are HCl etch back and deposition temperature. In this report we present results leading to the optimization of process variables with superimposed device constraints to obtain defect free epitaxy on arsenic-implanted buried layers.

Molecular Beam Epitaxy

Abstract No. 117

Kinetic and Surface Effects in the Growth of III-V Alloy Films by MBE

B. A. Joyce, C. T. Foxon, and **J. S. Roberts,** Philips Research Laboratories, Redhill, Surrey RH1 5HA, England

The use of modulated beam techniques in conjunction with reflection electron diffraction (RHEED) to obtain kinetic information relating to growth and doping of III-V alloy films by MBE is described. Results are illustrated with reference to the growth of films of $Ga_xIn_{1-x}P$, $Ga_xIn_{1-x}As$, and $GaAs_yP_{1-y}$. The structure and composition of these films in relation to growth parameters, and the influence on optical and electrical behavior are also considered.

Abstract No. 118

Molecular Beam Epitaxy of II-VI Compound Semiconductors

T. Yao,* T. Minato, T. Sera, Y. Makita, and **S. Maekawa,** Electrotechnical Laboratory, Tanashi, Tokyo, Japan

Molecular beam epitaxy (MBE) of II-VI compound semiconductors, especially of zinc chalcogenides is re-

ported in this paper. Special emphasis is placed on the growth characteristics, the investigations on surface morphology and crystallinity, and optical and electrical properties. The advantages of MBE growth of these materials over other crystal growth methods are indicated.

Abstract No. 119

Kinetics and Surface Interactions on Growth of InSb Thin Films by MBE

R. Ueda* and **K. Tanimoto,** Dept. of Applied Physics, School of Science and Engineering, Waseda University, 3-4-1 Ohkubo, Shinjuku-ku, Tokyo, 160 Japan

The fundamental molecular processes on the substrate surfaces in the synthesis of InSb thin films have been pursued by MBE. Beam characteristics and interactions with surfaces of Si and other single crystals were studied. Nucleation and growth processes were studied by RHEED, TEM, AES, and other electron spectroscopic methods. The results obtained were compared and interpreted with conventional growth theories of thin films.

Abstract No. 120

Effect of Lattice Mismatch on the Electronic Properties of MBE Grown InGaAs on GaAs

C.-A. Chang, C. M. Serrano, L. L. Chang, and **L. Esaki,** IBM Thomas J. Watson Research Center, Yorktown Heights, N.Y. 10598

When InGaAs films are grown on GaAs using MBE, the misfit stress is known to be largely relaxed into defects. TEM studies have indicated that most such defects are confined in the vicinity of the film-substrate interface. We show that these defects have a profound effect on both the carrier concentration and the mobility of thin InGaAs films, for example, ~2000Å. For films with a thickness greater than 1 μm, much less effect has been observed. (This work was sponsored in part under ARO Contract.)

Abstract No. 121

High Mobility GaAs and Cr-Doped GaAs Epitaxial Layers by MBE

H. Morkoc, University of Illinois, Urbana, Ill. 61801, and **A. Y. Cho,** Bell Laboratories, Murray Hill, N.J. 07974

The growth of Cr-doped GaAs epitaxial layers by MBE on Cr-doped substrates in a substrate temperature range of 500°C to 650°C was investigated. The epitaxial layers were doped with Sn to a net electron concentration of about 4×10^{14} cm^{-3} to minimize the amount of Cr that was necessary to achieve semi-insulating properties. The epitaxial layers with a net electron concentration of about 4×10^{14} cm^{-3} exhibited electron mobilities of 8084 cm^2/Vsec and 105,000 cm^2/Vsec, at 300°K and 78°K respectively. The freeze-out ratio of the carriers as the temperature dropped from 300°K to 78°K was about 1% indicating very little O_2 contamination. The growth and properties of Cr-doped semi-insulating GaAs and high mobility GaAs epitaxial layers by MBE are reported. In addition, the results on the use of Cr-doped layers as a buffer layer to maintain high electron mobility in the thin epitaxial films are described.

Abstract No. 122

High Quality P-GaAs MBE Layers Doped by Simultaneous Low Energy Zinc Ion Irradiation

J. C. Bean* and **R. Dingle,** Bell Laboratories, Murray Hill, N.J. 07974

Low energy zinc ions have been incorporated in growing MBE GaAs layers producing heavily doped P-type material. As-grown layers retain a substantial amount of radiation damage as indicated by the absence of photoluminescence and low hole mobilities. A post-growth anneal yields layers with mobilities and luminescence comparable to state-of-the-art zinc-doped LPE epitaxial layers. Annealed layer quality does not depend on substrate growth temperature or ion energy over the ranges 580°-650°C and 100-3000 eV respectively. Measured zinc ion sticking coefficients increase with ion energy to a value near unity for 3 keV ions. The data suggest that the sticking coefficients are enhanced by a simple ion burial mechanism.

Abstract No. 123

The Interplay of Thermodynamics and Kinetics in MBE of Gallium Arsenide

R. Heckingbottom,* **C. J. Todd,** and **G. J. Davies,** Post Office Research Centre, Martlesham Heath, Ipswich, England IP5 7RE

The thermodynamic framework underlying the growth of doped GaAs by MBE has been examined for all common dopants. It is found in all cases that the experimental results are consistent with the thermodynamic predictions. The implications for the conventional assumption that any limitations in MBE are due to kinetic effects are considered. The results suggest that a consideration of the thermodynamic framework are as important in MBE as in other methods of crystal growth.

Abstract No. 124

Molecular Beam Epitaxy of IV-VI Semiconductors on IV-VI Substrates

J. N. Walpole, M.I.T. Lincoln Laboratory, Lexington, Mass. 02173

In most molecular beam epitaxy of IV-VI semiconductors, substrates other than the IV-VI materials have been used. Recent work with IV-VI substrates, primarily growth of (Pb, Sn) Te on PbTe, is reviewed here. Topics include growth techniques, carrier density and mobility of layers, use of foreign dopants, lattice-matched heteroepitaxy, and device results. The latter include optical waveguides, single and double heterostructure lasers, distributed feedback lasers, and closely confined homostructure lasers.

Abstract No. 125

Silicon Molecular Beam Epitaxy

J. C. Bean, Bell Laboratories, Murray Hill, N.J. 07974

Silicon molecular beam epitaxy has produced epitaxial layers with electrical and crystallographic quality comparable to CVD material. Within the films carrier mobilities equal bulk values, minority carrier lifetimes exceed 30 μsec, and dislocation densities are less than 1000/cm^2. Layers have been produced with novel hyperabrupt doping profiles and have been used in the fabrication of PIN and varactor device structures. It has been found, however, that the sticking probability of most dopants is a strong function of substrate temperature and that many dopants can segregate on the growing epitaxial surface. The control of doping profiles therefore depends critically upon the choice of dopant and on the accurate regulation of growth conditions.

Abstract No. 126

Doping of Si MBE with Simultaneous Arsenic Ion Implantation or Antimony Evaporation

Y. Ota, Bell Laboratories, Reading, Pa. 19604

High quality silicon molecular beam epitaxial films (Si-MBE) were successfully grown in an ultrahigh vacuum system with an As^+ ion source or an Sb effusion source. For the As^+ ion at 600 eV, the sticking coefficient was >0.75 at growth temperatures from 750° to 950°C, whereas that of evaporated Sb depended on the film growth temperature. Excellent arsenic doping control from 10^{14} to 10^{19} cm^{-3} was obtained. Good antimony doping control was realized from 10^{14} to high 10^{17} cm^{-3} for growth temperatures between 500° and 1050°C, respectively.

Abstract No. 127

Selective Growth of GaAs by Molecular Beam Epitaxy

S. Hiyamizu, T. Fujii, K. Nanbu, T. Sakurai, H. Hashimoto, and **O. Ryuzan,** Fujitsu Laboratories Ltd., Nakahara-ku, Kawasaki 211, Japan

Planar-type selective growth of polycrystalline and monocrystalline GaAs was achieved on a Cr-doped semi-insulating GaAs substrate, partially masked with thermal oxide of GaAs (~300Å thick), by molecular beam epitaxy. Resistivity $1 \sim 2 \times 10^6$ Ω-cm in a polycrystalline region (1 μm thick), which is nine orders of magnitude higher than that in a monocrystalline region, was maintained up to a doping level of 4×10^{18} cm^{-3} (Sn), and it decreased drastically for higher doping. Electron mobility in a narrow, stripe-shaped

monocrystalline region showed 2500 cm^2/Vsec ($n = 1.4 \times 10^{18}$ cm^{-3}) at room temperature, and did not vary even when the stripe-width decreased from 50 to 4 μm.

Abstract No. 128

Optical Transmission Characteristics of MBE Grown InAs-GaSb Superlattices

L. L. Chang, G. A. Sai-Halasz, and **L. Esaki,** IBM Thomas J. Watson Research Center, Yorktown Heights, N.Y. 10598, and **R. L. Aggarwal,** M.I.T. Francis Bitter National Magnet Lab and Dept. of Physics, Cambridge, Mass. 02139

Optical transmission measurements were performed on InAs-GaSb superlattices grown on GaSb substrates by MBE. The improved quality of the epitaxy has resulted in the observation of additional fine structure in the absorption spectra, which is believed to be due to transitions involving heavy holes at higher quantum states. Under applied magnetic fields, the spectra exhibit oscillatory characteristics due to Landau levels. The deduced energy gaps of the superlattices are consistent with those predicted theoretically. (This work was sponsored in part under ARO Contract.)

Abstract No. 129

Selectively Doped Semiconductor Heterostructures by Molecular Beam Epitaxy

A. C. Gossard, W. Wiegmann, R. Dingle, and **H. L. Störmer,** Bell Laboratories, Murray Hill, N.J. 07974

Molecular beam epitaxy has been used to grow layered semiconductor crystals in which dopant atoms are incorporated only in selected layers, producing a separation of charge carriers and impurities. A number of such GaAs/AlGaAs heterostructures, selectively doped with Si, have been made. Both single-interface structures and multiple stacks of selectively doped layers were studied. Both have shown enhanced carrier mobility and carrier lifetimes resulting from the separation of the parent dopant atoms and carriers.

Abstract No. 130

Dark and Photoinduced Transport Behavior in MBE-Grown AlGaAs-GaAs Superlattices

R. Dingle,* H. L. Störmer, L. Kopf, A. C. Gossard, and **W. Wiegmann,** Bell Laboratories, Murray Hill, N.J. 07974

Transport behavior in AlGaAs-GaAs superlattices has been studied as a function of layer thickness, barrier height, and dopant distribution. Samples in which the AlGaAs layer is doped and the GaAs layer undoped show higher mobilities than uniformly doped structures. A novel, photoinduced persistent conductivity effect is seen at low temperatures. The origin of this effect is traced to Si-induced centers in the AlGaAs layers. The role of these Si impurities in influencing the superlattice mobility has been investigated.

Abstract No. 131

X-Ray Reflection Diffraction: A Structural Study of the GaAs-Al Interfaces

W. C. Marra, P. Eisenberger, and **A. Y. Cho,** Bell Laboratories, Murray Hill, N.J. 07974

A new technique utilizing conventional x-ray diffraction in conjunction with total external reflection has provided a new and powerful tool for studying ordered interfaces and surface phenomena. It has been used in this work to study the details of the interface region of an MBE grown Al single crystal on an MBE grown GaAs single crystal substrate. A simple model including variations of the lattice parameter and disorder in the interface region is in good agreement with these experimental results.

Process and Device Modeling

Abstract No. 132

Computer Simulation in Silicon Epitaxy

R. Reif and **R. W. Dutton,** Integrated Circuits Laboratory, Stanford University, Stanford, Calif. 94305, and **D. A. Antoniadis,** Massachusetts Institute of Technology, Cambridge, Mass. 02139

A model that describes the incorporation of dopant atoms into growing silicon epitaxial films in a horizontal, atmospheric-pressure reactor has been implemented in the Stanford University IC process simulation program, SUPREM. With this model, the program is able to simulate epitaxial-layer doping profiles resulting from arbitrary time-varying dopant-gas flows by considering the important kinetics occurring in the growing epitaxial surface (*i.e.* adsorption, surface diffusion, site incorporation) and the redistribution of dopants in the solid during growth. Limitations in the simulation of front autodoping profiles is also discussed.

Abstract No. 133

Oxidation-Rate Dependence of B and P Oxidation-Enhanced Diffusions in <100> Silicon

A. M. Lin,* D. A. Antoniadis, and **R. W. Dutton,** Integrated Circuits Laboratory, Stanford Electronics Laboratories, Stanford, Calif. 94305

Oxidation enhanced diffusion (OED) of B and P are observed to vary with the oxidation rate during the oxidation of silicon. This paper describes the characteristics of this rate dependence over a range of temperatures (900°-1200°C). An extrinsic-point-defect oversaturation model of OED is presented to explain the dependence. In the model, the defects causing the OED are generated at oxidized Si surface at a rate depending on the oxidation rate during oxidation. The previously observed time dependence of OED can also be explained through the rate-dependence using this model. The correlation of OED and oxidation stacking faults is discussed based on this model.

Abstract No. 134

Oxidation-Enhanced Diffusion of Boron and Phosphorus in Silicon

K. Taniguchi,* K. Kurosawa, and **M. Kashiwagi,** NEC-Toshiba Information Systems, Inc., Kawasaki, Kanagawa, 210, Japan

The effect of oxidizing ambients on boron and phosphorus diffusion in (100) and (111) silicon is studied at 1000° and 1100°C. Both boron and phosphorus show oxidation-enhanced diffusion. The diffusion enhancement is greatly affected by variation in ambient conditions. Dry oxygen and wet oxygen differently influence the diffusion for the same oxidation rate, and the difference in the enhanced diffusion for both the ambients becomes pronounced at larger junction depth. The degree of enhancement is larger in (100) than in (111) silicon for boron, but it is larger in (111) than in (100) silicon for phosphorus at 1000°C.

Abstract No. 135

Dependence of Interface State Density on Silicon Thermal Oxidation Process Variables

R. R. Razouk and **B. E. Deal,** Research and Development Laboratory, Fairchild Camera and Instrument Corp., Palo Alto, Calif. 94304

Characterization of the process dependence of silicon oxide charge densities is important in establishing process modeling as a useful tool in advanced integrated circuit fabrication. The dependence of the structural type of interface state charge on thermal oxidation variables is presented. Those variables include silicon type (n- and p-type), silicon orientation [(100) and (111)], oxidation temperature (900°-1200°C), oxidation ambient (O_2, H_2O, HCl/O_2), and annealing/cooling ambient (O_2, N_2, Ar). The effects of pre- and post-metallization hydrogen annealing on interface state densities are discussed.

Abstract No. 136

Elimination of White Ribbon by HCl Field Oxidation

W. C. Young, Burroughs Corp., San Diego, Calif. 92127

A process for eliminating ammonia species migration to the $Si\text{-}SiO_2$ interface during silicon nitride masked field oxidation has been developed. 2% HCl in the pyrogenic oxidizing medium reacts with the NH_3 and prevents formation of silicon nitride in the active area where the gate oxide will subsequently be grown. The chemical/thermodynamic model of the process predicts the improvement in measured electrical parameters, as well as increased sort yield and reliability.

Abstract No. 137

Sensitivity of Electrical Parameters to Fabrication Variables for a Phosphorus Bipolar Process

E. Khalily* and **R. W. Dutton,** Integrated Circuits Laboratory, Stanford University, Stanford, Calif. 94305

The Process Modeling Program (SUPREM) and the Device Modeling Program (SEDAN) have been used to study the effect of process steps on the device characteristics for a bipolar transistor. A standard NPN bipolar process with phosphorus emitter is simulated, the required data have been obtained to replace the emitter diffusion by an ion implantation step, and the fabricated device has been characterized to confirm the simulation. The range of variation of the device parameters has been correlated to the deviations in the processing steps. Critical process parameters which have a dominant effect on each electrical parameter are shown.

Abstract No. 138

A Test of the Process Modeling Program SUPREM from the Users Point of View

D. Kranzer,* Siemens AG, Component Div., Munich, Germany, **W. Fichtner** and **E. Guerrero,** TU, Vienna, Austria, and **H. Ryssel,** IFT, Munich, Germany

Since the Stanford University Process Engineering Models (SUPREM) program has been available we have used SUPREM to simulate different process steps as used in modern MOS and bipolar processing. We feel that the results obtained from the experiment and simulation regarding sheet resistivity and junction depth makes an extensive comparison with experiment, on the basis of profile measurements, necessary in order to use SUPREM II effectively in process development. In this contribution we report on results concerning boron, arsenic, and arsenic-boron profiles. The experimental methods applied are: (n-α)-method, anodic oxidation in conjunction with sheet resistivity, (n-γ)-activation and Auger analysis. Concerning the boron profiles it was generally observed, that a disagreement exists in the tail region, at the interface and in the oxide. Assuming $\beta = 0$ yields a far better agreement in the tail region. The same is found for diffused samples, where the solubility limit is not exceeded. For high implanted boron doses, however, a suitable choice of β larger than 1 is required to fit the experimental results. In the case of the coupled diffusion (arsenic-boron) a surprisingly good agreement is observed in the vicinity of the arsenic-boron junction.

Abstract No. 139

Process Model and Characterization of New Submicron Channel MOS Device

S. Ragsdale,* T. Yamaguchi, M. L. Lust, and **S. Sato,** Tektronix, Inc., Applied Research Group, Beaverton, Ore. 97077

S-MOS, a new submicron channel MOS integrated circuit technology, has been developed, as has been previously reported. Devices made with this technology showed a 0.3-0.9 μm channel length. Delay times per gate were subnanosecond to two nanoseconds, and power dissipation per gate was 0.3-0.7 mW. Local oxidation techniques and the bird's beak phenomenon have been used to achieve a continuous change of oxide thickness and silicon height; through this, the channel is implanted at high energy. We discuss the process model and methods of creating different bird's beak angles. We also discuss the dependence of channel length and impurity profile on the bird's beak angle, and the channel region ion dose dependence on the drift layer.

Abstract No. 140

Optimization of the Buried Channel for VLSI CCD's

P. K. Chatterjee* and **G. W. Taylor,** Texas Instruments, Dallas, Texas 75222

The scaling of buried channel CCD's for VLSI memories involves an optimum buried channel design which comprehends the tradeoffs between charge capacity and transfer efficiency at scaled operating voltages. An analytic buried channel CCD model with Gaussian impurity distribution is used to define the optimization criteria, and a design for optimum charge capacity and transfer efficiency in scaled CCD's is described.

Abstract No. 141

Modeling of Thin-Film Ion-Selective Transistors

N. Alvi, I. Kaufman, and **P. Pierini,** Dept. of Electrical Engineering, Dept. of Chemical Engineering, and The Center for Solid State Science, Arizona State University, Tempe, Ariz. 85281

A model for the thin-film group II-VI semiconductor transistor utilized as an ion-sensitive device is formulated in terms of a two-dimensional Poisson's equation which, including all nonlinear terms, is solved numerically to give the potential distribution within the semiconductor. Effects due to the exceedingly thin semiconductor layer (90-300Å) and interface trap densities, with discreet and distributed levels, are incorporated. Voltage drops across the electrolyte-insulator interface are related to the ionic concentrations in solution. Current through the device is calculated as a function of the voltage drops across the channel. Comparison with experimental results is discussed.

Abstract No. 142

A Process Monitoring and Control System

J. W. Gaylord, RCA Laboratories, Solid State Technology Center, Somerville, N.J. 08876

An economically sound general purpose computer based system has been developed for the monitoring and control of the semiconductor manufacturing process. This system can be programmed to track and control product flow, monitor and optimize processes, enforce the maintenance of manufacturing equipment, assist production scheduling, and report production problems and status. Any or all of these functions can be implemented at a particular site. The talk describes the system and the functions currently implemented in an LSI COSMOS pilot production facility.

Semiconductors and Other Electronic Materials

Abstract No. 143

Application of A-C Techniques to the Study of Lithium Diffusion in WO_3 Thin Films

C. Ho,* I. D. Raistrick, and **R. A. Huggins,** Dept. of Materials Science and Engineering, Stanford University, Stanford, Calif. 94305

An a-c method has been developed for the study of the kinetics of lithium injection from nonaqueous liquid electrolytes into thin (1000-3000Å) films of WO_3 deposited on tin oxide-covered glass substrates. The frequency dependence of the electrode impedance was analyzed by the complex plane method. Important kinetic parameters, including the chemical diffusion coefficient, were determined as a function of lithium activity for amorphous and crystalline films.

Abstract No. 144

Effect of Annealing on the Properties of Thin Films of WSi_2

K. C. Saraswat,* F. Mohammadi, and **J. D. Meindl,** Integrated Circuits Laboratory, Stanford University, Stanford, Calif. 94305

Effect of annealing on the structure and resistivity of thin films of sputtered WSi_2 has been studied. $WSi_2/SiO_2/Si$ and $WSi_2/Si/SiO_2/Si$ films were annealed in N_2 at 600°-1000°C and resulting changes in structure of WSi_2 were studied by x-ray diffraction, SEM and optical microscope and were related to the changes in resistivity. $Al/WSi_2/SiO_2/Si$ and $Al/WSi_2/Si/SiO_2/Si$ films were annealed in N_2 at 400°-700°C and stability of the Al/WSi_2 interface was determined by studying the structure of the films.

Abstract No. 145

Properties of RF Sputtered, Mercury Cadmium Telluride Thin Films

R. H. Cornely,* L. Suchow, D. DeRidder, T. Gabara, and **P. Diodato,** New Jersey Institute of Technology, Newark, N.J. 07102

Employing large-area targets prepared by pressing powders and Hg vapor as sputtering gas, films of $(Hg_xCd_{1-x})Te$

(with $x = 0.75$) have been deposited on Si, CdTe, mica, and glass substrates. Structural, optical, and electrical properties of the films were studied by x-ray diffraction, infrared spectrophotometry, scanning electron microscopy, and Hall effect measurements, as a function of Hg vapor pressure, substrate temperature, and film deposition rate. A high degree of (111) preferred orientation has been obtained, and the location and steepness of the absorption edge indicate that the films have the same composition as the targets.

Abstract No. 146

Silicide Formation by Laser Heating of Sputtered Refractory Metal Films on Silicon

F. Mohammadi,* K. C. Saraswat, J. Beaudouin, and **J. D. Meindl,** Integrated Circuits Laboratory, Stanford University, Stanford, Calif. 94305

Thin films of refractory metals (W, Mo, Pt) were sputtered on silicon. The wafers were scanned with a Nd:YAG laser radiation operating in CW mode. The resulting films were examined by x-ray diffraction and SEM techniques. Up to certain energy density no interface reaction was observed; however, at a critical energy density the metal was completely converted into silicide. Above the critical energy density, evaporation of the metal film and severe damage to the surface of the wafer was observed.

Abstract No. 147

Effects of Hydrogen in Amorphous Silicon Carbide Thin Films Prepared by Reactive Sputtering

M. Le Contellec, J. Richard, and **A. Guivarc'h,** PMT/CPM Centre National d'Etudes des Télécommunications, Lannion, France, and **E. Ligeon,** and **J. Fontenille,** DRF Centre d'Etudes Nuclaires de Grenoble, Grenoble, France

Amorphous silicon carbide $Si_xC_yH_z$ thin films have been prepared in a wide range of composition by rf reactive sputtering of a silicon target in a gaseous mixture of Ar, CH_4, and H_2 (or D_2). Film compositions have been determined by Rutherford backscattering and ^1H (^{11}B, α) $\alpha\alpha$ nuclear reaction. Correlations have been made with infrared transmission measurements. The hydrogen content is important (for $x = y$ $0.25 < z < 0.4$) and appears to have a dominant effect on the film density, the optical gap, and the refractive index.

Abstract No. 148

Electrical Defects in Silicon Introduced by Sputtering

E. Grusell,* S. Berg, and **L. P. Andersson,** Institute of Technology, University of Uppsala, Uppsala, Sweden

Electrical properties of metal silicon junctions formed by sputtering of a metal on a silicon surface in an rf-diode sputtering system are reported. Experiments have been made on both n-type and p-type silicon, and show that the sputtering process introduces damage in the surface region. *I-V*, *C-V*, temperature activation, and DLTS experiments are described, and a theory is presented which assumes the appearance of charged centers near the surface of the semiconductor.

Abstract No. 149

Crystal Defects and Silicon Technology

E. Sirtl, Heliotronic GmbH, D-8263 Burghausen, Germany

The chronology of the development of silicon as a semiconductor always has been accompanied by progress in "defect engineering." Starting with grain boundary studies in the early rectifiers, dislocation kinetics has been the thoroughly investigated successor after efficient methods had been worked out for the growth of monocrystals. Since dislocation-free silicon became a standard material, interests have been drawn largely to the difficult subject of point-like defects. Today, some parallels in behavior can be seen already between typical microelectronic (mono) and solar-grade (poly) silicon. Finally, the weaknesses in our present basic understanding of crystal defects are elaborated.

Abstract No. 150

Electroluminescence in MOS Capacitors

C. Falcony-Guajardo,* F. J. Feigl, S. R. Butler, and **J. B. Anthony,** Sherman Fairchild Laboratory, Lehigh University, Bethlehem, Pa. 18015

We have investigated electroluminescence observed during pulsed avalanche injection of MOS capacitors. The devices incorporated 0.1-0.3 μm thick thermal oxide on (100), p-Si substrates. Constant time-average injection currents below 1 $\mu A\text{-}cm^{-2}$ were studied to times of order 10^4 sec (10^{16} electrons-cm^{-2} electron fluence across fresh oxide films). Emission intensities of 10^5-10^8 photons-$sterad^{-1}$-sec^{-1}-cm^{-2} in the wavelength region 180-650 nm were measured through semitransparent Al electrodes, using low-noise photon counting techniques. Throughout these experiments, the constant-current tracking voltage was continuously monitored and the high frequency *C-V* curve was intermittently measured. A decreasing emission intensity during the initial stages of avalanche aging was proportional to the time derivatives of both the tracking voltage and the *C-V* flatband voltage. We suggest that both the light emission and the negative oxide charge buildup are due to electron capture into impurity-related localized states in the oxide.

Abstract No. 151

Ultraviolet Ionization of Trapped Electron Centers in the MOS Oxide

D. D. Rathman,* F. J. Feigl, and **S. R. Butler,** Sherman Fairchild Laboratory, Lehigh University, Bethlehem, Pa. 18015

We have investigated the effects of ultraviolet illumination (4.5-6.7 eV photon energy) on negative trapped oxide charge Q_{OT} in MOS capacitors. The devices incorporated steam grown, 1 μm thick, unannealed SiO_2 films on (100), n-Si substrates. The oxide films and the Si surface were illuminated through semitransparent Al electrodes. Values of Q_{OT}/e up to 5×10^{12} cm^{-2} were obtained under positive bias photoinjection conditions (due to trapping of injected electrons). Q_{OT}/e could be reduced by 50% by subsequent u.v. photodepopulation under zero bias conditions (due to photoionization of the trapped electron centers). The electron trapping centers were related to H and Na impurities incorporated in the oxide layer during oxidation at 1200°C. These centers have previously been shown to be optically inactive at photon energies below 4 eV. The over-all experimental logic and results parallel recent IBM studies of electron trapping centers associated with ions implanted into the MOS oxide layer.

Abstract No. 152

Interface Properties of Mo Gate MOS Structure

H. Ishikawa, H. Tokunaga, N. Toyokura, and **M. Shinoda,** Fujitsu Laboratories Ltd., 1015 Kamikodanaka, Nakahara-ku, Kawasaki, Japan

Refractory metal films such as molybdenum offer unique advantages as gate material over conventional polysilicon for VLSI applications. Mo-SiO_2-Si interface properties such as flatband voltages, electronic work function, and interface charges were investigated as a function of various high temperature annealing in nitrogen and forming gas subsequent to deposition. We have found that the effective work function of molybdenum has been 4.7 eV due to molybdenum silicide formation at the Mo-SiO_2 interface when the Mo-SiO_2-Si structure has been annealed in forming gas in the temperature range from 700° to 1000°C. On the other hand, the structure annealed in nitrogen has varied the effective work function of molybdenum from 4.8 to 5.1 eV according to the increase of the annealing temperature from 700° to 1000°C as a result of molybdenum oxide formation.

Abstract No. 153

Interface Properties of Mo and Mo/Si Gate MOS Structures

M. Koyanagi, T. Hayashida, N. Yamamoto, and **N. Hashimoto,** Hitachi Ltd., Central Research Laboratory, Kokubunji, Tokyo, Japan

Si-SiO_2 and electrode-SiO_2 interfaces are investigated by *I-V* and *C-V* methods for Mo and Mo/Si gate MOS structures. Electron trapping centers are observed near the Si-

SiO_2 interface in Mo gate MOS structures which are not thermally annealed. Mobile ions and electron trapping centers are induced near the Mo-SiO_2 interface in structures with high temperature N_2 annealing. These mobile ions and trapping centers are not observed in structures where a thin Si_3N_4 or poly-Si film is inserted between the Mo and SiO_2 films. Accordingly, it is proposed that mobile ions, such as Na^+ and K^+, in Mo films are emitted into SiO_2 in Mo gate MOS structures by high temperature annealing. Then, trapping centers are induced near the Mo-SiO_2 interface. It is found that Mo/Si gate structures provide stable interfaces and may be applied in MOS LSI's.

Abstract No. 154

MOS Transient Capacitance: An Indicator of CCD Yield

J. E. LaPrade,* **E. T. Fitzgibbons,** and **R. Bharat,** Rockwell International, Anaheim, Calif. 92803

This paper describes the correlation obtained empirically between MOS transient capacitance characteristics and the dark-current-related performance of large-area CCD arrays, based on the data gathered for an area array (110 × 110 cells) on a cell-by-cell basis. These measurements were made both at room temperature and on cooled devices for CCD's fabricated with different process sequences, and statistically analyzed for comparison with MOS transient capacitance data gathered on the same wafers. These results establish the feasibility of using a simple test structure and procedure to rapidly predict the effects of process variations on CCD yield.

Abstract No. 155

Open-Tube Aluminum Diffusion

M. Chang and **A. Roesch,** General Electric Co., Semiconductor Products Dept., Electronics Park, Syracuse, N.Y. 13221

Aluminum is the fastest p-type diffusion species for silicon. It is always attractive to power semiconductor product manufacturers. Due to the extremely active nature of aluminum atoms at elevated temperatures, successful aluminum diffusion could only be achieved in a closed-tube system in the past. With better understanding of aluminum chemical properties, we have designed systems that can be used to perform aluminum diffusion in a real open ambient. Several devices were made with this technique. In this paper, we discuss the techniques and results of device fabrication achieved by open-tube aluminum diffusion.

Abstract No. 156

Spin-On Arsenic Diffusion

S. Wu* and **D. L. Flowers,** Motorola Inc., Semiconductor Group, Phoenix, Ariz. 85008

Deep junction (approx. 5μ) arsenic diffusions using spin-on areno-silica glasses were evaluated. Excellent repeatability can be achieved. Factors affecting the load uniformity are discussed. Oxygen concentration of the N_2-O_2 mixture used in diffusion processing was found to be an important factor in achieving doping efficiency and minimizing surface damage.

Abstract No. 157

Autodoping during Silicon Liquid Phase Epitaxy

B. J. Baliga, General Electric Co., Corporate Research and Development Center, Schenectady, N.Y. 12301

During the growth of silicon layers by vapor phase epitaxy, autodoping has been found to be a serious problem due to the transport of dopants from the substrate into the vapor phase. This paper discusses the use of silicon liquid phase epitaxial growth to eliminate autodoping problems. It has been found that autodoping can also occur during silicon liquid phase epitaxy and that it is caused by meltback of the substrate prior to epitaxial growth. The paper describes results of lateral autodoping studies and the elimination of autodoping by supersaturation of the melt.

Abstract No. 158

The Application of TGZM in Power Semiconductor Product Fabrication

M. Chang and **R. Kennedy,** General Electric Co., Semiconductor Products Dept., Electronics Park, Syracuse, N.Y. 13221

High power semiconductor devices have been fabricated with deep p-type isolation regions. By employing the temperature gradient zone melting (TGZM) technique, special device structures can be made that were not possible solely by solid-state diffusion. Various TGZM processing techniques have been developed and evaluated. Devices with blocking voltages higher than 2500V were made with TGZM isolation. Device performances as measured by carrier lifetime, blocking capability, leakage current level, and other characteristics are excellent. The detailed process of device fabrication using the TGZM technique and the resulting device characteristics are presented.

Abstract No. 159

Carrier Concentration and Hall Mobility in Heavily Arsenic-Diffused Silicon

S. Matsumoto* and **T. Niimi,** Dept. of Electrical Engineering, Keio University, Hiyoshi Yokohama, 223, Japan, and **J. Murota,** Musashino Electrical Communication Laboratories, N.T.T., Musashino, Tokyo, 180, Japan

For heavily arsenic-diffused silicon, carrier concentration n and Hall mobility μ_H are determined by sheet Hall measurement at 300°K. The relationship between total arsenic concentration C_T and n is obtained at concentrations $> 10^{20}cm^{-3}$. It is found that (*i*) μ_H does not depend on the neutral arsenic concentration, which is valued with the diffusion temperatures; and (*ii*) electrically active arsenic concentration at the diffusion temperature C_A is not equal to n, although C_A has been estimated using a $\rho - n$ curve at 300°K.

Abstract No. 160

D.L.T.S. and Neutron Activation Analysis Applied to a Comprehensive Study of Gold Gettering in Silicon

D. Lecrosnier, F. Richou, J. Paugam, G. Pelous, and **M. Salvi,** CNET, CPM/PMT, Lannion, France

The gettering of gold in silicon wafers by phosphorus diffusion or argon implantation have been studied either as a function of the surface phosphorus concentration or of argon dose and anneal temperature. For that, complementary measurement techniques were used. The gold concentration in the substrate, before and after gettering, was determined by successive etching and D.L.T.S. measurements. Such a method is able to analyze very low gold concentration (down to 10^{11} gold atoms/cm^3). From neutron activation analysis and from backscattering measurements the distribution of gettered gold was obtained and compared either to the phosphorus profile or to the argon induced defects profile. Our results are presented and discussed in view of a recently published theory on phosphorus diffusion.

Abstract No. 161

Concentration and Distribution of Oxygen and Carbon in Silicon Crystals

H. M. Liaw, Motorola, Inc., Semiconductor Research and Development Laboratories, Phoenix, Ariz. 85008

Concentration of oxygen in Czochralski-grown silicon crystals has been correlated to growth ambient from a few Torr to 1 atm. Concentration of oxygen is also affected by the ratio of crystal diameter to crucible diameter. Carbon concentration in a given crystal is approximately inversely proportional to its oxygen concentration. The distribution of oxygen is studied both in axial as well as in radial directions of the crystals. The variation of oxygen donors along the crystal ingot is also studied.

Abstract No. 162

The Nature of the X-Level Defect in Indium-Doped Silicon

R. Baron and **J. P. Baukus,*** Hughes Research Laboratories, Malibu, Calif. 90265, **T. C. McGill,** California Insti-

tute of Technology, Pasadena, Calif. 91125, and **O. J. Marsh,** Hughes Research Laboratories, Malibu, Calif. 90265

An additional acceptor level, the X level, has been reported in Si:In. We now present strong evidence that the X level is an In-C substitutional (In_s-C_s) pair. Concentrations of In, C, and X level ranging over several orders of magnitude were observed by Hall effect, photoconductive spectral response and infrared absorption. The X-level concentration follows a mass-action law with the In and C concentrations. Reversible anneal effects have been observed. The electronic properties and temperature dependence of the concentration of this center are found to be those expected for a nearest neighbor In_s-C_s pair. (This work was partially supported by the Defense Advanced Research Projects Agency and monitored by the Army Night Vision Laboratory under Contract No. DAAK 70-77-C-0082.)

Abstract No. 163

The Effect of Surface Charge Density on Superficial Hardness

K. F. Beckham,* Corrosion Laboratory, Dept. of Materials Science and Engineering, M.I.T., Cambridge, Mass. 02139

An experiment is being undertaken in order to model the mechanical behavior of semiconductor electrodes. The environment under control is the surface charge density on the electrode and the variable to be measured is surface hardness. With the technique being used—surface photovoltage spectroscopy in high vacuum—a faithful representation of the space charge region in the electrode can be attained while excluding all other parameters, such as electrolyte composition.

Abstract No. 164

Correlation of Physical and Electrical Properties of Plasma-Enhanced SiN

K. M. Mar and **G. M. Samuelson,** Motorola, Inc., Semiconductor Group, Phoenix, Ariz. 85008

The empirical relationships between Si/N ratio and other physical and electrical properties of plasma-enhanced CVD silicon nitride (SiN) films were investigated. The films were deposited in a commercially available reactor using silane or ammonia flow rate as the variable. An apparent correlation exists between the Si/N ratio and the u.v. absorption edge, refractive index, and Si-H/N-H ratio. The correlation in each case was dependent on the deposition variable. However, the correlation between Si/N ratio and high field d-c conductivity, dielectric properties, stress, and density is less apparent. Finally, there is no apparent correlation between Si/N ratio and Frenkel-Poole parameters.

Abstract No. 165

The Oxidation of Polysilicon

W. G. Oldham,* N. Chau, and **N. Rovedo,** Dept. of Electrical Engineering and Computer Sciences and the Electronics Research Laboratory, University of California, Berkeley, Calif. 94720

The oxidation of patterned polysilicon films deposited on silicon dioxide and silicon nitride has been studied by SEM analysis of cross sections. The polysilicon oxide contours have been characterized as a function of edge slope, film doping, oxidation temperature and time, and substrate type. It is found that the simple geometrical construction proposed by Kuhn explains certain features, but strain, and the relief of strain with phosphorus doping plays a major role. (This research was sponsored by the National Science Foundation Grant ENG77-14660-A01.)

Abstract No. 166

Densification of SIPOS

H. R. Maxwell, Jr.* and **W. R. Knolle,** Bell Telephone Laboratories, Inc., Reading, Pa. 19603

We have investigated the effect of high temperature anneals on the physical properties of semi-insulating polycrystalline silicon (SIPOS) films containing 25 atomic percent oxygen. Heat-treatments of 900°C or greater in inert ambients densify the film, resulting in a film thickness decrease up to 10%. The infrared transmission spectrum of the SIPOS film changes also. The film stress changes from tensile to compressive after anneal and is consistent with the infrared spectrum changes.

Abstract No. 167

Electronic Properties of P-Doped SIPOS

T. Adachi (Present address: Stanford Electronics Laboratories, McC 201, Stanford University, Stanford, Calif. 94305),* **K. Watanabe, S. Wakayama,** and **M. Kikuchi,** Sony Corp. Research Center, 174 Fujitsukacho, Hodogayaku, Yokohama 240, Japan

Semi-insulating polycrystalline silicon (SIPOS) films heavily doped with phosphorus have been prepared by CVD techniques. The Fermi level, the mobility gap, the density of states in the mobility gap, and some other properties have been investigated with electrical and optical measurements as well as electron spin resonance. The as-deposited films are semi-insulating ($\rho \sim 10^{10}$ Ω-cm), while heat-treatment around 1000°C in dry nitrogen gas increases the conductivity of the film up to ~1 Ω-cm. We explain this property of the film in terms of the Fermi level and the density of states in the mobility gap.

Abstract No. 168

New Technology by Use of the Doped SIPOS Films

H. Yamoto,* N. Oh-uchi, H. Hayashi, T. Matsushita, and **Y. Kawana,** Sony Corp., Semiconductor Div., Asahi, Atsugi 243, Japan

P- or B-doped SIPOS films have been chemically vapor deposited at 650°C from N_2-SiH_4-N_2O-PH_3 or B_2H_6, respectively. The films change to semiconductors from semi-insulating materials by heat-treatment. Their resistivities have been precisely controlled in the range of 0.01-100 Ω-cm by varying the gas phase composition, annealing temperature, and time. The doped SIPOS films can be applied to various purposes, especially to an emitter ballast resistance as well as emitter diffusion source. Stable power transistors with a fall time of 10 nsec at 10A, 400V have been successfully fabricated by employing the doped SIPOS technology.

Abstract No. 169

Oxide Isolation Process for High Density High Speed Bipolar IC's

R. Kumar,* A. K. Hochberg, J. R. Kruest, K. H. Oh, J. Rau, and **G. C. Sharma** (Present address: Chrysler Corp., Huntsville, Ala.), Burroughs Corp., San Diego, Calif. 92127

We have developed an improved technique of forming oxide isolation regions for an epi-collector bipolar integrated circuit process. The dielectrically isolated regions exhibit lower parasitic capacitances than similar devices formed by junction isolation and both the speed and density of bipolar IC's are increased significantly. A combination of silicon plasma etching and high energy ion implantation is used to form channel stop regions under the isolation oxide in a single masking step. The surface topography is planarized using special etching techniques. The fabrication variables and resulting device performances are presented.

Abstract No. 170

Growth of High Quality Thin Oxides in Ar-O_2-HCl Gases

W. C. Young* and **D. L. Henderson,** Burroughs Corp., San Diego, Calif. 92127

A method of growing thin (300-400Å) gate oxides has been developed that results in high dielectric strength (> 7 mV cm^{-1}), low pinhole counts (1/cm^2 @ 20V) and good uniformity (< 5% variation). The method involves conventional atmospheric pressure furnaces, with the exception that argon is used in the preoxidation thermal recovery phase and as the gas for postoxidation anneal. Electrical parameters of the oxide are repeatable and consistent, but not identical to conventional oxides.

Abstract No. 171

Charge Transport and Lattice Defects in $Co_{1-x}Mg_xO$

E. M. Logothetis, Ford Motor Co., Dearborn, Mich. 48121

The electrical conductivity and the thermoelectric power of $Co_{1-x}Mg_xO$ were measured in the range 700°-1100°C and at oxygen partial pressures between 1 and 10^{-20}atm. Analysis of the data suggests that for $x<0.5$-0.7, charge transport occurs by motion of itinerant carriers (holes); for $x>0.7$, a change from band conduction to hopping conduction is indicated. The conductivity data of the cobalt-rich materials are not consistent with simple point-defect models and suggest the existence of a complex defect structure.

Abstract No. 172

Polycrystalline Si-Schottky-I^2L (PSI^2L)—A New Technology for Low Power I^2L

W. M. Werner, Siemens AG, München, Germany

This paper describes a new technique using polycrystalline silicon as the electronically active material for Schottky diodes which are used for the separation of the outputs of an I^2L gate. Therewith it is possible to minimize the area of the switching transistor to a device with only one collector without regard to the number of outputs of the gate because the polySi-Schottky-diodes are outside the active transistor area. This technique leads to a reduction of the power delay product of about one decade besides significant advantages in packing density, design flexibility, and device performance.

Abstract No. 173

A Study of the Pulse Deposition of Copper Through Cylindrical Holes

H. K. Ng, D. B. Hibbert,* and **A. C. C. Tseung,** Dept. of Chemistry, The City University, London EC1, England

The disadvantages of using a $CuSO_4$ acid bath for plating copper through holes under steady-state conditions, are poor throwing power, variable thickness of deposit, and the inability to use high current density. Pulse plating can overcome these problems. Potentiostatic pulses with an on:off ratio of 1:2 and frequency of 100 A7, give the optimum deposit, superior to galvanostatic pulses. A computer model of through-hole plating was developed, and transition times calculated for different diameter holes.

Abstract No. 174

Electrical Instability of Water-Absorbed CVD PSG Films

T. Shirasu and **Y. Kosa,** Hitachi, Ltd., Musashi Works, Kodaira, Tokyo 187, Japan

Electrical characteristics of CVD PSG films were investigated using *C-V* and *I-V* methods. A new polarization phenomenon was found which was associated with water-absorbed CVD PSG films deposited on thermally oxidized silicon wafers. The polarization was observed as those films were deposited, decreased by heating above 100°C, and increased again after long-term exposure to room air ambient or water boiling. Bulk currents also vary with water absorption. Correlation between the polarization and bulk currents was investigated.

Abstract No. 175

Hydrogen in LPCVD Polysilicon

B. G. Bagley,* P. K. Gallagher, R. E. Benenson, and **C. J. Mogab,** Bell Laboratories, Murray Hill, N.J. 07974

We have used both evolved gas analysis (EGA) with line of sight mass spectroscopy and the resonant nuclear reaction $^1H(^{15}N,^4He)^{12}C$ to detect the presence of hydrogen in LPCVD polysilicon. Neither technique detected hydrogen in an as-deposited sample. Following a hydrogen anneal (½ hr at 450°C) H_2 was readily detected by EGA, the evolution beginning at 330°C (planar sample). The resonant reaction technique did not detect hydrogen (detection limit 0.2%) in the annealed sample.

Abstract No. 176

LPCVD Fabrication of High Temperature Thin Film Resistors and Capacitors

L. S. Raymond, D. J. Hamilton, W. J. Kerwin, and **L. N. Nelson,** Dept. of Electrical Engineering, The University of Arizona, Tucson, Ariz. 85721

Thin film resistors and capacitors with long term operating temperatures to 500°C are needed in high temperature geothermal well logging instrumentation. LPCVD has been utilized to deposit the thin films used in fabricating the passive components. Temperature coefficients are less than ± 100 ppm/°C over the temperature range of 25°-500°C for both the resistors and capacitors. The resistor material is grown from WF_6 and SiH_4 in hydrogen. The resistivity of the currently used material is 2500 $\mu\Omega$-cm. The capacitor dielectric is silicon nitride formed from SiH_4 and NH_3. The capacitor electrodes are tungsten.

Abstract No. 177

The Dissolution Kinetics of GaAs in Undersaturated Solutions in the Ga-Al-As System

M. B. Small,* R. Ghez, and **R. M. Potemski,** IBM Thomas J. Watson Research Center, Yorktown Heights, N.Y. 10598

The formation of heterostructures by LPE necessarily involves situations of constitutional disequilibrium when a new solution is introduced to a layer of a solid composition with which it is not in equilibrium. The transport equations which describe an idealized (static solution) situation of this type are defined. Solutions to these equations are presented for the process of "etch back epitaxy" in the (GaAl)As system. Experimental results are also presented for the same process and compared with the theoretical results.

Abstract No. 178

Magnesium Doping of $Ga_{1-x}Al_xAs$

L. R. Dawson, Sandia Laboratories, Albuquerque, N.M. 87185

The effect of growth temperature, substrate orientation, and composition (mole fraction of AlAs,x) on the incorporation of magnesium in $Ga_{1-x}Al_xAs$ grown by liquid phase epitaxy has been studied. For small values of x the distribution coefficient, k_{Mg}, and solid solubility are relatively insensitive to growth temperature (in the range of 800°-900°C) with values of 0.1 and 10^{19} cm^{-3} (corresponding to ρ ~0.005 Ω-cm), respectively. Higher values of x (up to ~0.8) show a decrease in k_{Mg}. [This work was supported by the U.S. Department of Energy under Contract AT(29-1)-789.]

Abstract No. 179

Transmission Cathodoluminescence Study of Dislocations in GaAs and GaAlAs

A. K. Chin,* H. Temkin, and **R. J. Roedel,** Bell Laboratories, Murray Hill, N.J. 07974

Using the new technique of transmission cathodoluminescence (TCL), we directly observe dislocations in GaAs substrates and GaAlAs epitaxial layers. A one to one correspondence between the TCL image of dislocations and dislocation etch pits produced by KOH etching is found on <100> oriented samples. The TCL images of dislocations are resolved to within the minority carrier diffusion length (*i.e.*, 1-2 μm in GaAs and 5-10 μm in GaAlAs). With the high resolution and high magnification of the TCL technique, we observe dislocations propagating along the (110) plane of GaAs.

Abstract No. 180

Transmission Cathodoluminescence Study of Defects in InP and InGaAsP

H. Temkin,* A. K. Chin, S. Mahajan, A. A. Ballman, W. A. Bonner, and **A. G. Dentai,** Bell Laboratories, Murray Hill, N.J. 07974

We present the results of a defect study of liquid encapsulated Czochralski grown InP substrates and InGaAsP grown by liquid phase epitaxy using the technique of transmission cathodoluminescence (TCL). The TCL image of the dislocations permits an accurate measurement of the dislocation density and an estimate of the minority carrier

diffusion length. In addition to the dislocation density, TCL examines material quality by imaging growth related defects, *e.g.*, growth striations and impurity clusters in InP and stacking faults in InGaAsP.

Abstract No. 181

The Characterization of Heavily Zinc-Doped InP Crystals

S. Mahajan,* **W. A. Bonner, A. K. Chin,** and **D. C. Miller,** Bell Laboratories, Murray Hill, N.J. 07974

Heavily zinc-doped InP crystals, grown along the <111> direction by the liquid encapsulated Czochralski technique, have been characterized by x-ray topography, transmission cathodoluminescence, and transmission electron microscopy. It is observed that heavy zinc-doping improves the perfection of crystals. However, the presence of a high density fine precipitate suggests that all of the dopant atoms are not in solid solution. This is consistent with the previous observations that for high zinc concentrations; the number of free carriers does not match the number of introduced zinc atoms.

Abstract No. 182

The Mechanism of Optically Induced Degradation in $InP/In_{1-x}Ga_xAs_yP_{1-y}$ Heterostructures

S. Mahajan,* Bell Laboratories, Murray Hill, N.J. 07974, **W. D. Johnston, Jr., M. A. Pollack,** and **R. E. Nahory,** Bell Laboratories, Holmdel, N.J. 07733

Optically degraded regions in $In_{1-x}Ga_xAs_yP_{1-y}$ layers, grown on the (001) InP substrate by liquid phase epitaxy, have been examined in detail by transmission electron microscopy. It is shown that these areas are associated with dislocation clusters or bundles which project along the <110> and <100> directions lying in the (001) plane. We conclude that the observed features develop by nonradiative recombination enhanced glide of threading and inclusion-generated dislocations present in the layers. We have also argued that the evolution of substructures seen in degraded $GaAs/Ga_{1-x}AP_xAs$ lasers can be rationalized more easily if it is assumed that glide precedes climb. This glide-climb approach has several advantages over explanations based exclusively on climb.

Abstract No. 183

Fabrication and Characteristics of LED for Optical Communications

Y. Ono, M. Mori, K. Ito, and **K. Kurata,** Hitachi, Ltd., Central Research Laboratory, Kokubunji, Tokyo, Japan

Efficient $Ga_{1-x}Al_xAs$ LED's with thick window layers have been fabricated, and their performances have reached 36.5% and 14% in external efficiencies for infrared (830 nm) and visible (710 nm) diodes. The effects of AlAs mole fraction in junction region and thickness of p-type layer for the efficiencies were examined. Frequency response strongly depends on the hole concentration in Zn-doped active layer. For application to optical analog modulation systems, the relationship between near-field emission pattern and carrier concentration in Ge-doped window layer is discussed.

Abstract No. 184

VPE Growth of InGaP/InGaAs Structures for TE Photocathodes

R. R. Saxena,* **S. B. Hyder, J. S. Escher,** and **P. E. Gregory,** Varian Associates, Palo Alto, Calif. 94303

Vapor phase epitaxial growth has been used to prepare InGaP/InGaAs/GaAs structures for use as field assisted transferred electron photocathodes for operation at 1.06 μm. Growth parameters have been established for grading InGaAs on GaAs and for the InGaP/InGaAs heterojunction growth using the hydride process. Field assisted photoemission has been demonstrated and better than 1.5% overall efficiency at 1.06 μm has been obtained with this structure.

Abstract No. 185

PNAF—An Efficient Silicon/Aluminum Etchant

J. K. Pau, W. P. Ng, and **J. E. Martin,*** Rockwell International, Microelectronic Device Div., Newport Beach, Calif. 92624

Extensive research for a suitable silicon etchant for defreckling has led to the formation and introduction of PNAF to our silicon/aluminum etch process. The selected PNAF solution contains four acids, phosphoric, nitric, acetic, and fluoboric. An appropriate composition of these four acids makes it a very efficient and attractive defreckle etchant, etching aluminum/silicon rapidly while keeping either the positive or negative photoresists intact. Being a good etchant for both aluminum and silicon, it removes the silicon freckle as well as the aluminum "snow" between metal lines. Being kind to the photoresists, the parts can always be reetched, since they are still being protected by the photoresist. This renders metal rework due to underetch practically nonexistent. Several other formulations of silicon etchants are also described and their relative merits are discussed.

Abstract No. 186

Pad Materials for Chemical-Mechanical Polishing

E. Mendel,* **P. Kaplan,** and **A. Patsis,** IBM Corp., East Fishkill Facility, Hopewell Junction, N.Y. 12533

Polishing pad materials used for chem-mech polishing have been studied. Experimental results indicate that correlation exists between pad characteristics, mechanical properties, and polishing performance. Approaches used to make pad materials are discussed in a general way, but the structural features that distinguish different pad materials are presented in considerable detail. Application of these pads for conventional, high pressure, and free polishing using chem-mech techniques are described. Factors which affect pad life and performance are identified.

Abstract No. 187

Multiple Wafer Free Polishing. I. Machine Concept

E. Mendel* and **J. Hause,** IBM Corp., East Fishkill Facility, Hopewell Junction, N.Y. 12533

The polishing machine described in this paper has been designed and developed for simultaneous chem-mech free polishing of both surfaces of silicon wafers. The main elements of the machine are (*i*) a pair of 61 cm diameter top and bottom plates which rotate in opposite directions, (*ii*) plastic carriers (nests) which have teeth around the outer edge and apertures for placement of wafers, (*iii*) an outer ring gear fixed to the machine base exterior, (*iv*) a freely rotating inner pin gear, and (*v*) a unique slurry feed system. Planetary motion of the nests, which contain the wafers, is produced by the frictional differences arising from the top and bottom surfaces of the wafers being in contact with dissimilar top and bottom polishing pads. Typically, 15 wafers, 82.5 mm diameter, are two-side free polished in 25 min.

Abstract No. 188

Multiple Wafer Free Polishing. II. Process

E. Mendel* and **J. Basi,** IBM Corp., East Fishkill Facility, Hopewell Junction, N.Y. 12533

This paper discusses multiple wafer free polishing processes developed for silicon. After polishing, both sides of the wafer are highly specular, damage free, and readily cleaned. Wafer flatness is less than 6 μm. One technique uses SiO_2-based, oxidizing-agent enhanced slurries, whereas the other employs a polishing reagent composed of NH_4F and $Cu(NO_3)_2$. We describe how the development of multiple wafer free polishing has resulted in an over-all simplification of wafer shaping process. Some parametric data are given.

Abstract No. 189

Control of Wafer Curvature

S. Takasu* and **K. Nakajima,** VLSI Cooperative Laboratories, Miyazaki, Takatsu-ku, Kawasaki, Japan

It is very important for the VLSI processes to control the curvature of wafers. A series of 1000 wafers from nine 76

mm ingots were polished on seed and bottom side alternately. The sign of the curvature of the wafers proved to depend on the polishing side of the slice. The magnitude of the curvature changed periodically corresponding to blade-dressing interval during the slicing process. In some cases, the dressing changed the sign of curvature from convex to concave or vis-a-vis. Application of this process to larger diameter, for example 125 mm wafers led to successful sign control of the wafer curvature.

Abstract No. 190

Electrochemical Characterization of Carrier Concentration Profiles in Silicon

C. D. Sharpe and **P. Lilley,*** Electrical and Electronic Engineering Laboratories, The University of Manchester, Manchester, England, M. 13 9PL

The capacitance-voltage behavior of the electrolyte-silicon interface has been investigated in relation to the silicon carrier concentration; at certain overpotentials the semiconductor depletion region approximates a Schottky barrier. A particular electrolyte has been found to yield smooth anodic dissolution of silicon in addition to *C-V* characteristics suitable for the determination of carrier concentration. Single and multiepitaxial layers (with carrier concentrations in the range 10^{15}-10^{18}cm^{-3}) have been profiled and compared with results obtained by conventional techniques.

Abstract No. 191

A Cross-Bridge Structure Array for Characterizing Intrachip Line Width Variations

L. W. Linholm* and **M. G. Buehler,** Center for Electronics and Electrical Engineering, Electron Devices Div., National Bureau of Standards, Washington, D.C. 20234

Periodic line width variations were determined by using an array of cross-bridge sheet resistors. A test pattern consisting of 53 arrays of 120 resistors each was developed. Test results indicate that periodic line width variations on the order of 0.3 μm occur within each 5.08 mm by 5.08 mm array. The variations are introduced by the optical lithography system used to fabricate the photomask. The method presented can be used to determine the performance of various lithography systems. [This work was conducted as part of the Semiconductor Technology Program at the National Bureau of Standards. This work was supported by the Defense Advanced Research Projects Agency (Order No. 2397, Program Code 7D10).]

Abstract No. 192

Automatic Photomask Inspection Machine

Y. Uchiyama and **D. Awamura,** Nippon Jidoseigyo, Ltd., c/o DNP (America), Inc., New York, N.Y. 10016

Of recent, the pattern of photomasks has become very minute, and it has become difficult to inspect the photomask with the naked eyes through a microscope. The requirement for detection level has gone up to about 1 micron in photomask inspection, and we have developed a machine which can be used at such level as well as operated on a practical and stable basis in a commercial production factory. In this machine we use a flying spot CRT and compare two adjoining chips simultaneously. In Japan, 27 such machines are in practical use and 3 in the United States. This machine is of substantial help in raising this quality of photomask.

Abstract No. 193

Design Considerations for the Integrated Gated-Diode Electrometer

G. P. Carver and **M. G. Buehler,** Electron Devices Div., National Bureau of Standards, Washington, D.C. 20234

A microelectronic test circuit composed of a gated diode and a source-follower MOSFET permits high-speed determination of extremely small leakage currents in gate-controlled diodes for materials characterization. Design criteria were developed which constrain the output to reflect diode open-circuit voltage decay characteristics and which can be used to minimize parasitic capacitance loading effects. The comparison of leakage measurements on Al-gate p-channel devices using conventional techniques with results using the test circuit illustrate the implications of the design criteria and the improved accuracy of the test circuit for determining bulk generation lifetime, surface recombination velocity, and other current leakage mechanisms. [This work was conducted as part of the Semiconductor Technology Program at the National Bureau of Standards. This work was supported in part by the Charles Stark Draper Laboratory, Inc. (order No. DL-H-139485).]

Abstract No. 194

Characterization of Deliberately Nickel-Doped Silicon Wafers and Solar Cells

A. M. Salama, California Institute of Technology, Jet Propulsion Laboratory, Pasadena, Calif. 91103

Microstructural and electrical evaluation tests were performed on nickel-doped p-type silicon single and multicrystal wafers and cells. The concentration levels of nickel in silicon were 5×10^{14}, 4×10^{15} atoms/cm^3 (single crystals) and 8×10^{15} atoms/cm^3 (multicrystal). The single crystal N/P nickel-doped solar cells of concentration 4×10^{15} atoms/cm^3, showed a degradation in the cell conversion efficiency, whereas that of the multicrystal N/P nickel-doped cells (concentration 8×10^{15} atoms/cm^3) exhibited better conversion efficiencies. The results show that this behavior is related to the size and distribution of the microstructural defects and grain boundaries in the silicon solar cells.

Abstract No. 195

Creation of Defects Responsible for Photon-Induced Degradation in N$^+$P Silicon Solar Cells

L. J. Cheng, D. C. Leung, and **J. D. Parsons,** Jet Propulsion Laboratory, Pasadena, Calif. 91103

Some terrestrial N$^+$P silicon cells exhibit photon-induced degradation effects under AMI illumination. Cells and diffused wafers without metallization which had been processed under various conditions were examined using spectral response and minority carrier diffusion length measurements. Preliminary results indicate that the creation of the defect responsible for the degradation is independent of metallization but is related to diffusion temperature and wafer arrangement in diffusion tube.

Abstract No. 196

Evaluation of Cost Effective Contact Systems for Solar Cells

R. B. Campbell* and **A. Rohatgi,** Westinghouse Advanced Energy Systems Div., Research and Development Center, Pittsburgh, Pa. 15235

Several metal contact systems for solar cells were studied as replacements for the conventional evaporated TiPdAg system. Performance was measured using solar cell parameters and detailed *I-V* curves. The evaporated TiPd electroplated Ag system gives as good results as the total evaporated system and is more cost effective. Electroplated Cu with evaporated TiPd serving as a barrier for the fast diffusing Cu is promising from the point of view of cell performance, sintering characteristics, and cost.

Abstract No. 197

Influence on Electrode Kinetics of Shallow Diffused Semiconductor Devices

T. A. Blaske and **H. Yu** (Present address: Texas Instruments, Dallas, Texas 75222),* Varo Semiconductor, Inc., Garland, Texas 75040

Effects from surface defects, surface concentration, diffusion profiles, and contact potential must all be used in the analysis of electron kinetics in shallow diffused junctions. Theoretical calculations of the *I-V* characteristics for ideal p-n junctions, Schottky barrier diodes, and shallow diffused devices are compared with ultrathin boron diffused p-n junctions. These device characteristics from such shallow diffused junctions are altered by the influence of different contact metallizations (Al, Ti, Mo) and the electrode isolation by incorporation of a very thin layer of doped polycrystalline silicon.

Abstract No. 198

Laser Beam Analysis of Large Area a-Si:H Solar Cells

D. L. Staebler, RCA Laboratories, Princeton, N.J. 08540

Schottky-barrier and PIN solar cells made with discharge produced hydrogenated amorphous silicon (a-Si:H) were analyzed with a HeNe laser. Scans of short-circuit current were taken, along with point by point checks of the illuminated *IV* curve at different laser beam positions. The latter has never been reported before for any type of cell, and is allowed here by the poor dark characteristics of a-Si:H cells. No nonuniformities were found in cells as large as 40 cm^2. (This research was prepared for the Department of Energy, Division of Solar Technology, under Contract No. EY-76-C-03-1286 and RCA Laboratories, Princeton, NJ 08540.)

Abstract No. 199

Amorphous II-V_2 and II-IV-V_2 Semiconductors as Possible Solar Cell Materials

R. D. Rauh, EIC Corp., Newton, Mass. 02158

A variety of II-V_2 and II-IV-V_2 semiconductors show a tendency to glass formation. Unlike the chalcogenide glasses, they have a rigid diamond-like local structure which may allow them to be doped, if bonding defects can first be neutralized. Numerous members of these classes of materials meet the requirements of economy and bandgap (direct, 1.1-1.6 eV) to be considered as thin film solar cell materials. Preliminary experimental results on their doping and defect compensation are presented.

Abstract No. 200

The Effects of Substrate Temperature during Deposition on the Electromigration Failures of Al-3%Si Conductors

F. Ichikawa* and **S. Ushio,** OKI Electric Industry Co., Ltd., Higashiasakawa, Hachioji, Tokyo, Japan

The effects of substrate temperature during deposition on the electromigration failures of Al-3%Si films were investigated. The lifetime of Al-3%Si films deposited at room temperature showed longer life than that of Al-3%Si deposited at 300°C. This contradicts the previous works on Al conductors. The failure modes of Al-3%Si varied significantly with substrate temperature during deposition, so the effects of substrate temperature on the grain size, crystalline orientation, and Si depth-distribution of Al-3%Si films were examined.

Abstract No. 201

Synthesis and Characterization of a Highly Conducting Organic Polymer

K. K. Kanazawa, A. F. Diaz, G. P. Gardini (Permanent address: Istituto di Chimica Organica, Universita di Parma, Parma, Italy), and **G. B. Street,** IBM Research Laboratory, San Jose, Calif. 95193

Polymerization of pyrrole was initiated by electrochemical oxidation from an acetonitrile solution, forming a highly conducting polymer overlayer. The cyclic voltammogram of ferrocene continued to appear reversible on the coated electrode. The polymer film was stripped from the electrode, and its conductivity was studied using four probe methods. The room temperature conductivity ranged from 1 to 100 $(ohm\text{-}cm)^{-1}$, depending on preparative conditions. X-ray studies and electron micrography suggest an amorphous polymer, unlike the fibrous polyacetylene $(CH)_x$.

Abstract No. 202

Precipitation of Oxygen in Silicon Crystals: A Heterogeneous Process

A. J. R. de Kock* and **W. M. van de Wijgert,** Philips Research Laboratories, Eindhoven, The Netherlands

The relationship between the as-grown perfection of dislocation-free Czochralski silicon crystals and the precipitation behavior of oxygen at elevated temperatures has been studied with x-ray transmission topography, copper decoration, preferential etching, and infrared absorption spectroscopy. Large differences in precipitation rate and precipitate distribution were observed in crystals containing swirl defects, swirl-free crystals, and crystals quenched from the melt. The results indicate that oxygen precipitation is a heterogeneous process in which grown-in thermal point defects play an essential role.

Abstract No. 203

Self-Consistent Calculation of the Jahn-Teller Distorted Vacancy in Silicon

N. O. Lipari,* **J. Bernholc,** and **S. T. Pantelides,** IBM Thomas J. Watson Research Center, Yorktown Heights, N.Y. 10598

We have previously introduced a Green's function method for the description of deep impurity and defect levels, and applied to the unrelaxed vacancy in Si. However, it is well known that the vacancy induces a significant lattice distortion and that the symmetry around the vacancy is not T_d, but, in fact, D_{2d}. Here, we report calculations of the Jahn-Teller distorted vacancy, using the tetragonal displacement values for the nearest neighbors estimated by Watkins. We find that the T_2 bound state of the unrelaxed vacancy at 0.8 eV above the valence band maximum splits into a singly degenerate B_2 state at 0.4 eV and a doubly degenerate E state at 0.9 eV. Changes in the density of states, the charge density, as well as other types of distortions are also discussed.

Abstract No. 204

Swirl Defects in Carbon-Rich Silicon

W. C. O'Mara* and **D. Guidici,** Siltec Corp., Menlo Park, Calif. 94025

Silicon crystals containing varying amounts of carbon have been examined for swirl defects by thermal oxidation and etching. Crystals were 4 in. diameter, boron-doped (100) silicon grown by the Czochralski method. Initial carbon concentration in the melt varied from 1-10 ppma. Wafers from these crystals were oxidized at 1050°C in a steam ambient for 10 hr cycles and etched using a modified Secco etch. Carbon concentration was determined by means of infrared absorption. Swirl defects were observed in wafers from carbon rich portions of ingots intentionally doped with carbon. The types of defects which comprise the swirl pattern are discussed.

Abstract No. 205

The Dependence of the SiO_2 Defect Density on Both the Applied Electric Field and the Oxide Thickness

A.-K. M. Zakzouk, Electrical Engineering Dept., College of Engineering, University of Riyadh, Riyadh, Saudi Arabia

By using liquid crystals in contact with the oxide, defective regions can be nondestructively identified. The defect density and the total leakage current density were found to be exponentially increased with the square root of the positive applied electric field. The defect diameter was found to be in the range of 0.29-0.89 μm. For oxide thicknesses above 0.2 μm the defect density exponentially decreases with increasing the oxide thickness. At thickness less than 0.2 μm the defect density increases very rapidly. The theoretical treatment resulted in good agreement with the experimental results. The space-charge density in the oxide was found to be equal to 5.6×10^{11} e/cm^2.

Abstract No. 206

Residual Disorder and the Electrical Properties of Ion-Implanted and Low-Temperature Annealed Silicon

T. Sakurai, T. Sato, S. Tatsuta, and **H. Hashimoto,** Fujitsu Laboratories Ltd., Nakaharaku, Kawasaki 211, Japan

Electrical properties of 50-90 keV Si plus 30 keV B-implanted and epitaxially regrown p^+ layers in silicon are studied as a function of the position of residual damage induced at the amorphous-crystalline interface relative to the junction. The electrical activity of implanted boron increases as the damaged layer approaches the junction, but the leakage current at the junction of which depth is 0.25 μm increases drastically when the depth of the damaged layer is deeper than about 0.15 μm.

Abstract No. 207

Carrier Lifetime Enhancement in Silicon

A. Rohatgi* and **P. Rai-Choudhury,** Westinghouse R&D Center, Pittsburgh, Pa. 15235

The effect of cooling rate, back surface damage gettering, and HCl oxidation on the minority carrier generation lifetime has been studied for Czochralski, float-zone, and neutron transmutation-doped float-zone Si. MOS capacitors were fabricated in the temperature range of 900°-1275°C in ambients containing 0-6% HCl. Data indicate that fast-cooling results in low lifetime (50-100 μsec) regardless of the back surface damage gettering (BSDG), oxidation temperature or HCl concentration. Slow cooling in N_2 combined with the BSDG gives 5-10 times enhancement in lifetime. Oxidation in 1% HCl, along with the slow cooling and BSDG, gives an additional monotonic increase in lifetime with the oxidation temperature. The study shows that proper choice of material and process can yield generation lifetimes in excess of 2 msec.

Abstract No. 208

The Effects of Process Induced Dislocations and Phosphorus Diffusion on Minority Carrier Generation Lifetime in Silicon

A. Y. Liang* and **C. J. Varker,** Motorola Inc., Semiconductor Group, Semiconductor Research and Development Laboratories, Phoenix, Ariz. 85008

In many high temperature device fabrication processes dislocation generation is virtually unavoidable. The electrical effects on pn junction devices is dependent on the generation lifetime of the minority carriers and the defect structures in the base material. MOS capacitance relaxation profiles on processed wafers can be used to investigate the electrical effects of process-induced defects. Experimental results indicate that the generation lifetime of the minority carriers depends strongly on the design of the thermal diffusion processes used to fabricate the device and the effectiveness of impurity gettering during processing. Interactions between the thermal-diffusional process and the material can produce a heavily dislocated wafer in which the generation lifetime exceeds that of the initial dislocation free material. Experimental results are presented which show the effects of thermal-diffusion processing on the minority carrier generation lifetime profiles. Additional results are presented to illustrate the minimal electrical effects of process induced dislocation in wafers which have been efficiently gettered with phosphorus.

Abstract No. 209

The Induced Surface Defects *vs.* Carrier Lifetime as a Function of Boron Planar Diffusion Sources

S. F. Bevacqua* and **M. Chang,** General Electric Co., Semiconductor Products Dept., Electronics Park, Syracuse, N.Y. 13221

The introduction of boron nitride (BN) planar diffusion sources gained wide acceptance in the industry as a means of providing greatly improved uniformity and process control in boron diffusion. Various silicon wafer surface damage and defects have been experienced as induced by BN diffusion. With the advent of a new planar ceramic boron source—boron plus (B^+)—a comprehensive study and evaluation was undertaken. Besides offering greater ease of handling and source preparation while maintaining same process control capability, far less surface damage has been found on the B^+-diffused wafers in contrast to the BN-diffused wafers. However, BN-diffused wafers tend to yield better carrier lifetime. A systematic study was done to explore and compare the induced surface damage and the resultant carrier lifetime as a function of BN and B^+ diffusion in a wide range of diffusion conditions. The detailed results and a tentative postulation are presented.

Abstract No. 210

Detection of Sputter Contamination and Sputter-Etch Residue by Ion Microprobe Analysis

J. Andrews,* Bell Laboratories, Murray Hill, N.J. 07974, **L. E. Katz,** Bell Laboratories, Allentown, Pa. 18103, and **J. W. Colby,** Kevex Corp., Burlingame, Calif. 94010

Ion microprobe analysis of a silicon integrated circuit wafer after PtSi sintering has revealed seven metallic elements contaminating the first level of sputtered Pt: Rh, Ti, Al, Mg, Na, K, and Ca. The first four were cosputtered with Pt; the origin of the alkali metals is not known. A Si ion image of the device wafer revealed excessive Si buildup in a narrow area, ~3 μm wide, framing the sintered PtSi contacts.

ELECTRONICS—LUMINESCENCE

Phosphor Efficiency and Saturation

Abstract No. 211

Review on Inefficiencies in Phosphors

C. W. Struck, RCA Laboratories, Princeton, N.J. 08540

A review is given of the current understanding of the various processes which produce the inefficiencies seen in phosphors.

Abstract No. 212

The Effects of Crystal Field and Temperature on the Photoluminescence Excitation Efficiency of Ce^{3+} in YAG

D. J. Robbins, Royal Signals & Radar Establishment, Great Malvern, Worcestershire, England

Absorption and luminescence spectra of Ce^{3+} in $Y_3Al_5O_{12}$ (YAG) have been measured at various temperatures between 4.2 and 300°K. Zero-phonon transitions have been observed and the phonon replicas correlated with lattice phonon energies. The temperature dependence of the characteristic Ce^{3+} absorption bands at 340 and 460 nm is explained in terms of a tetragonal crystal field splitting of both the $4f^1$ ground and $5d^1$ excited states of Ce^{3+}. These crystal field effects influence the pumping efficiency of YAG:Ce when used as a color-correction phosphor in high-pressure lamps.

Abstract No. 213

Observation of Loss of Emission-Intensity Loss in the Synthesis of Eu^{2+}-Activated Pyrosilicate Phosphors

R. G. Pappalardo,* C. Givens, and **C. F. Chenot,** GTE Laboratories, Waltham, Mass. 02154, and GTE-PMG Towanda, Pa. 18848

Syntheses of Eu^{2+}-activated pyrosilicate phosphors, characterized by a narrow emission band at 400 nm, occasionally produce materials of reduced efficiency and faint body-color. Both undesirable features are partially removed by an annealing treatment in air. Various spectroscopic techniques have been employed to determine the mechanisms of this efficiency loss. The reduced-efficiency phosphors exhibit additional absorption, as derived from difference reflection spectroscopy, from 200 to 500 nm. The annealing treatment removes the extra absorption peaking at 410 nm, thereby reducing the self-absorption of emission, but also converts Eu^{2+} to the trivalent state. Work is in progress to identify the centers responsible for the observed nonactive absorption of visible and u.v. radiation.

Abstract No. 214

Host and Temperature Effects on Ti^{4+} Luminescence

R. P. Burgner* and **W. B. White,** Materials Research Laboratory, The Pennsylvania State University, University Park, Pa. 16802

The temperature dependence of Ti^{4+} luminescence has been examined in a number of host materials which possess different activator site symmetries and coordination numbers. Emission position, intensity, and lifetime were found to vary significantly from host to host as well as with respect to temperature. These variations are explained in terms of phonon-assisted emission and X-alpha-SCF calculated energy levels.

Abstract No. 215

Concentration Quenching of Nd^{3+}-Luminescence in $Li(Nd_{1-x}Yb_x)P_4O_{12}$

A. Suzuki, Y. Kashiwada, and **S. Tanimizu,** Hitachi Ltd., Central Research Laboratory, Tokyo, Japan

Emission characteristics of $Li(Nd_{1-x}Yb_x)P_4O_{12}$ were measured by excitation in the Nd^{3+} levels at 800 nm. A few a/o of Yb^{3+} drastically increases the total quantum efficiency. The energy transfer probability from Nd^{3+} to Yb^{3+}, estimated from the decay rate of the Nd^{3+} emission, is not large enough to explain observed efficient emission from Yb^{3+}.

The results suggest that, by trapping excitation energy, Yb^{3+} reduces concentration quenching caused by migration of the excited state of Nd^{3+}.

Abstract No. 216

Mechanisms of Current-Density Saturation in ZnS Cathodoluminescent Phosphors

J. R. McColl, GTE Laboratories, Waltham, Mass. 02154

Two mechanisms are responsible for loss of cathodoluminescent efficiency when current density is increased in ZnS or (Zn, Cd)S activated with Cu^+ or Ag^+. The first, simple depletion of activator centers by excessive excitation, can be mitigated by raising activator concentration. The second is an excited state absorption effect: a hole bound to a Cu^+ or Ag^+ center is excited to the valence band either by direct photon absorption or by energy transfer from another excited activator center. This mechanism limits the linearity of response in a fundamental way. Experimental evidence for excited state absorption is presented.

Abstract No. 217

Nonlinear Quenching of Mn^{+2} Fluorescence in $Ca_5(PO_4)_3F$ under High Levels of Excitation

F. M. Ryan* and **J. Murphy,** Westinghouse R&D Center, Pittsburgh, Pa. 15235

The decay kinetics of Mn^{2+} fluorescence in single crystals of $Ca_5(PO_4)_3F$ have been studied. The decay in fluorescence intensity following pulsed excitation corresponds to a decay in the excited state population, N, of the form

$$\frac{dN}{dt} = -\alpha N^2 - \frac{N}{\tau}$$

where α increases with manganese concentration. These results may be explained by the model of Tolstoi and Abramov (1) in which two interacting ions, both in the excited state, can give rise to a non-radiative quenching process of the type

$$A^* + B^* \rightarrow A + B^{**}$$

1. N. A. Tolstoi and A. P. Abramov, *Opt. Spectros.*, **20,** 273 (1966).

X-Ray Phosphors and Radiography

Abstract No. 218

Luminescence of LaOBr:Ac X-Ray Phosphors (Ac = Bi, Ce, Er, Tb-Tm, Respectively)

J. G. Rabatin, General Electric Co., Cleveland, Ohio 44110

LaOBr is an effective host for several activators. Because of high x-ray absorption and absolute density, LaOBr phosphors are especially useful for x-ray screen applications in medical radiology. The present paper describes the luminescent properties, speeds, and other characteristics under x-ray excitations of the following phosphors: LaOBr:Bi; LaOBr:Ce; LaOBr:Er and LaOBr:Tm; Tb. Speeds in excess of four times $CaWO_4$ screens have been obtained. The primary emissions are in the blue and near ultraviolet regions.

Abstract No. 219

Five Year's Experience with Rare Earth Screens

R. Oggioni and **S. Pesce,** Research Laboratories, Ferrania, Savona, Italy

A comparison between rare earth and calcium tungstate screens is made with reference to their main physical properties. Performance in terms of speed and objective image quality are also compared. The main result coming from the use of rare earth intensifying screens in radiography is a strong reduction in x-ray exposure without loss in information content. The immediate benefit is a significant decrease of the dose given to the patient, but other possibilities to improve image quality are available. Some points connected with x-ray equipment are also discussed.

Abstract No. 220

Reduced Structure Mottle in LaOBr X-Ray Intensifying Screens

J. G. Rabatin, General Electric Co., Cleveland, Ohio 44110

The tendency for incipient convection cell formation during the early stages of screen drying leads to nonuniform distribution and packing of phosphor particles. The present study utilizes fine grain film for x-ray exposures, scanning electron microscope techniques, x-ray diffraction method for preferred orientation, and variations in coating parameters such as wet thickness, drying rates, and viscosity to study these convection cell tendencies and the effects on structure mottle. Some suggestions are presented for reducing structure mottle.

General Session

Abstract No. 221

The Application of Group Theory to Luminescence

K. H. Butler, Truro, Nova Scotia, Canada B2N-3L8

Group theory has an important application in explaining the spectra of phosphors. When the site symmetry of the activator is known, group theory predicts the number of bands in the excitation spectrum, also polarization, approximate wave number and relative intensity. In addition, group theory indicates the order of magnitude of decay time of emission. Examples showing agreement between theory and experimental data are presented.

Abstract No. 222

Fast Decay U.V. Phosphor—$YAlO_3$:Ce

T. Tomiki, T. Takeda and **T. Miyata,** Matsushita Research Institute Tokyo, Inc., Ikuta, Tamaku, Kawasaki, Japan

The conditions of synthesizing $YAlO_3$:Ce phosphors ($\lambda_{max} \simeq 365$ nm) were investigated. Attempts were made to eliminate visible light-emitting $Y_3Al_5O_{12}$:Ce phosphor which always coexisted in products prepared from the stoichiometric mixtures by solid-state reaction below 1600°C. A remarkable effect was observed by changing the ratio Y_2O_3:Al_2O_3 or adding mineralizers such as barium compounds to the stoichiometric mixture, and thereby $YAlO_3$:Ce phosphor, which has a radiant efficiency of 6 ~ 9% with $\tau_{1/e} \simeq 20 \sim 35$ nsec, could be prepared.

Abstract No. 223

Luminescence of Tb-Activated Alkali Rare Earth Metaphosphate Glasses

T. Takahashi* and **O. Yamada,** RCA Research Laboratories, Inc., Zushi-machi, Machida City, Tokyo 194-02 Japan

Excitation and emission spectra of Tb^{3+} were measured in alkali yttrium terbium metaphosphate glasses having the general composition $n(M_2O{\cdot}P_2O_5)[(1-x)Y_2O_3{\cdot}xTb_2O_3{\cdot}3P_2O_5]$. The Tb^{3+} emission at the 4f-5d transition bands was enhanced at a Tb concentration where the Tb^{3+}-Tb^{3+} pair population becomes maximum. The intensities of Tb^{3+} emission increased in the order of Li, Na, K when n is fixed, and with increasing alkali, when M is fixed. Sensitization of Tb^{3+} emission by Ce-codoping was also investigated.

Abstract No. 224

Luminescence and Energy Transfer in New Complex Fluorides of Eu^{2+} and Sm^{2+}

E. Banks and **M. Shone,** Department of Chemistry, Polytechnic Institute of New York, Brooklyn, N.Y. 11201

New phases of composition $EuMgF_4$, $SmMgF_4$, $SrMgF_4$ and their solid solutions have been prepared by solid-state reaction at about 900°C. All are orthorhombic, with unit cells similar to that of $BaMnF_4$, a piezoelectric compound. $EuMgF_4$ fluoresces bright blue under a HPMV lamp in a broad band peaking at 437 nm, with a broad excitation band peaking at 356 nm. The brightness in solid solutions with $SrMgF_4$ peaks at 75 mole % $EuMgF_4$ indicating that there is little concentration quenching of the Eu^{2+} emission. $SmMgF_4$ shows a weak red line emission, characteristic of Sm^{2+}, under the same excitation. The excitation spectrum

of $SmMgF_4$ is a band, peaking at about 450 nm, lying in the emission band of $EuMgF_4$. Solid solution samples $Eu_{1-x}Sm_xMgF_4$ showed only the Sm^{2+} line emission under 350 nm excitation, even for $x = 0.01$ (1 m/o $SmMgF_4$). The complete absence of Eu^{2+} emission in these samples demonstrates the complete transfer of excitation energy from Eu^{2+} to Sm^{2+} in these materials. The transfer is largely nonradiative, as shown by shortening of the Eu^{2+} fluorescent lifetime in the sample with 1 m/o $SmMgF_4$.

Abstract No. 225

Cerium- and Terbium-Activated Yttrium Silicate Green Phosphors

M. Watanabe,* K. Terashima, Y. Kimura, and **T. Nishimura,** Toshiba Corp., Electron Tube and Device Div., Kawasaki-City, Kanagawa, 210 Japan

Luminescence properties of cerium- and terbium-activated yttrium silicate green phosphors (Y_2SiO_5:Ce, Tb) were investigated. The energy transfer from cerium to terbium was observed under u.v. excitation and intense green emissions were obtained in fluorescent lamps. Fluorescent lamps with Y_2SiO_5:Ce, Tb phosphors showed higher efficacy than ever developed with green phosphors. Characteristics of three narrow spectral bands fluorescent lamps using Y_2SiO_5:Ce, Tb green phosphors are also discussed.

Abstract No. 226

Ce^{+3} and Tb^{+3} Fluorescence Excited by U.V. Radiation and Fast Electrons, and $Ce^{+3} \rightarrow Tb^{+3}$ Energy Transfer in α, β- and γ-$Ca_3(PO_4)_2$

O. Bouhellal, R. Heindl,* and **J. Loriers,** Laboratoire de Physico-Chimie des Materiaux par Techniques Avancees, Centre National de la Recherche Scientifique, Laboratoires de Bellevue, 92190 Meudon, France

The luminescence properties of β- and γ-$Ca_3(PO_4)_2$:Ce^{+3} have been reinvestigated. The emission of the charge-compensated compounds is much stronger than in the case for the uncompensated. Compensation by Na^{+1}-ions gives the best results. An efficient $Ce^{+3} \rightarrow Tb^{+3}$ energy transfer has been found in both β- and γ-$Ca_{3-2x-2y}Ce_xTb_yNa_{(x+y)}(PO_4)_2$. Both the emission and the u.v. excitation spectra, and the decay-times of Ce^{+3} and Tb^{+3} have been measured.

Abstract No. 227

The Role of the Chromium Species in the Poly(vinyl alcohol)-Chromate Photochemical Reaction

H. L. Van Nice* and **R. Farlee,** Tektronix, Inc., Beaverton, Ore. 97077

The important chromium species involved in the aqueous photochemical reaction between poly(vinyl alcohol) (PVA) and the chromate ion have been identified. The first step in the reaction is formation of a PVA-chromate ester. Upon irradiation of the ester Cr(V) is formed which disproportionates to form Cr(VI) and Cr(IV). The Cr(IV) oxidizes the PVA, and the resulting Cr(III) forms a complex with unoxidized sites of PVA molecules. The photochemical reaction in aqueous solution was found to be *p*H limited with no detectable reaction occurring above *p*H 12.

ELECTROTHERMICS AND METALLURGY/ENERGY TECHNOLOGY GROUP

Characterization of Coal Combustion Products

Abstract No. 228

Physical and Chemical Studies Related to the Morphogenesis of Coal Fly Ash

G. L. Fisher, Radiobiology Laboratory, University of California, Davis, Calif. 95616

Studies of the physical, morphological, and chemical properties of size-classified, stack-collected coal fly ash are described. Elemental analyses indicate enhanced concentration of relatively volatile elements or their oxides, as well as relatively nonvolatile elements in the finest fly ash fractions. A possible bimodal size distribution is observed for Cr, As, U, Zn, W, and Sb. Morphological studies indicate that the relative abundances of particle types are also size dependent. Electron microscopic studies indicate the complexity of fly ash surfaces and the matrix heterogeneity of individual particles. Mutagenesis studies provide insight into the physical properties of biologically active fly ash components.

Abstract No. 229

Chemical Characterization of Size Fractionated Coal Fly Ash

L. D. Hansen* and **D. J. Eatough,** Thermochemical Institute and Dept. of Chemistry, Brigham Young University, Provo, Utah 84602, and **G. L. Fisher,** Radiobiology Laboratory, University of California, Davis, Calif. 95616.

Size fractionated fly ash was obtained from the stack breeching of a major southwestern coal-fired power plant by means of a cyclone separator. A variety of analytical procedures have been used to identify the chemical species and compounds present as a function of particle size. Fluoride and sulfate have been found to increase as particle size decreases. The *p*H of water extracts was found to decrease as particle size decreased. These results have been shown to be generally applicable to coal-fired power plants by studies on ash from other plants. About 10% of the chlorine present in the size fractionated ash has been shown to be Cl^-. The chemical state of the remaining chlorine has not yet been identified. About one-half of the sulfate is decomposed to SO_2 at 200°C. The identity of the reducing agent in this reaction has not yet been determined.

Abstract No. 230

Field Measurements of Submicron Particle Size Distributions from the Combustion of Coal

D. S. Ensor* and **G. Markowski,** Meteorology Research, Inc., Altadena, Calif. 91001, and **R. G. Hooper** and **R. C. Carr,** Electric Power Research Institute, Palo Alto, Calif. 94303

During the last four years a number of large field measurements of particle size distributions have been conducted on full-scale utility boilers. Experimental techniques have included electrical aerosol size analyzers, cascade impactor (conventional and low pressure), SCM analysis, diffusion batteries, integrated light-scattering monitors, and continuous trace gas monitors. The results from four sites are reported and interpreted.

Abstract No. 231

Fine Particle Formation in Coal Combustion

R. C. Flagan, Environmental Engineering Science, California Institute of Technology, Pasadena, Calif. 91101

Two modes are observed in the particle size distribution of the aerosol leaving a pulverized coal boiler. Large ash particles of about 20 μm mass mean diameter are formed from the residual ash. A narrow peak in the particle size distribution at about 0.1 μm mean diameter appears to be produced by coagulation of very fine particles formed when volatilized ash or other vapors condense. Comparison of the chemical composition of the fine and large particles provides further evidence for the role of condensation in fine particle formation.

Abstract No. 232

Submicron Fly-Ash Formation in Coal-Fired Boilers

G. D. Ulrich, Dept. of Chemical Engineering, University of New Hampshire, Durham, N.H. 03824

According to previous work, the surface of coal-derived fly ash is enriched in volatile trace metals. This was attributed to molecular condensation. We suggest, in contrast, that volatile compounds evaporate, nucleate, and grow first as submicron aggregates before depositing on the surface of residual ash particles. Data obtained in this laboratory for oxide-synthesis flames have been employed to successfully predict the size, morphology, and composition of submicron aggregates found in fly ash.

Abstract No. 233

Surface Processes Associated with Thermally Induced Coal Mineral Transformations: Application to Combustion Stream Cleanup

C. D. Stinespring, D. E. Newlin, and **G. W. Stewart,** Morgantown Energy Technology Center, Morgantown, W. Va. 26505

Aluminosilicate mineral inclusions in coal give rise to a large number of entrained particles in coal combustion streams. The surface composition of these particles, as produced by thermal treatment of the aluminosilicate mineral inclusions, controls the heterogeneous chemistry associated with the particles. Auger studies have been performed to determine the temperature dependent surface composition of heated aluminosilicate minerals. Based on these results, several gas-surface interactions have been selected for investigation. The implications of these studies for combustion stream cleanup are discussed.

Abstract No. 234

Analytical Study of the Effluents from a High Temperature Entrained Flow Gasifier

L. D. Hansen,* D. J. Eatough, L. R. Phillips, R. B. Ahlgren, N. F. Mangelson, and **M. L. Lee,** Brigham Young University, Provo, Utah 84602

The chemical composition of the effluent streams from a laboratory scale, high temperature, pressurized, entrained flow, coal gasifier have been determined as a function of gasifier operating conditions. The conclusions of this study are: (*i*) this type of gasifier produces very little or no condensible organic material such as tars and phenols; (*ii*) the small amount of polynuclear aromatic hydrocarbons produced, ~0.001 lb/ton of coal consumed, is entirely absorbed on the fine particulates collected in the product gas scrubber water; (*iii*) the only other pollutant of much significance is ~500 ppm of H_2S in the product gas; (*iv*) increasing the pressure and the coal feed rate in the gasifier greatly improve coal conversion efficiency; and (*v*) decreasing O_2/coal ratios in the reactor increases methane and decreases H_2S in the product gas.

Abstract No. 235

Recent Advances in the Theory and Measurement of Condensate Deposition Rates from Combustion Gases

D. E. Rosner* and **K. Seshadri,** High Temperature Chemical Reaction Engineering Laboratory, Yale University, New Haven, Conn. 06520, **F. Kohl, C. Stearns,** and **G. C. Fryburg,** National Aeronautics and Space Administration, Lewis Research Center, Cleveland, Ohio 44135

Necessary recent extensions of convective diffusion theory (multicomponent transport and thermal diffusion effects) are discussed in the light of our dew point and deposition rate measurements in seeded atmospheric pressure burners. A novel interference technique, based on the remote detection of reflected laser radiation, is described for the measurement of deposition rates of optically thin inorganic materials from combustion gases. Illustrative results are presented for the deposition and growth of B_2O_3(l) films on temperature-controlled metal ribbons in convective crossflow. Emphasis is placed on two nonthermodynamic aspects of deposition: vapor (and particle) transport phenomena and chemical kinetics.

Abstract No. 236

Thermochemistry of a Pressurized Fluidized Bed Coal Combustor/Gas Turbine Combined Cycle

H. S. Spacil and **K. L. Luthra,*** General Electric Co., Corporate Research and Development, Schenectady, N.Y. 12301

A thermochemical model is presented for a pressurized fluidized bed coal combustor/gas turbine combined cycle. Thermodynamic calculations have been carried out to predict the impurity content of the hot cleaned gas. A simplified treatment is used to estimate the expected amount of condensates in the gas turbine. The calculations show that the deposition rates of alkali sulfate in the gas turbine may be about 50 times higher than those expected in a normal oil fired system. The effects of impurities in coal such as Na, K, Cl, Pb, and V that can lead to corrosive deposits in gas turbines are discussed.

ENERGY TECHNOLOGY GROUP

General Session

Abstract No. 237

Soft *vs.* Hard Energy

A. J. Appleby, Electric Power Research Institute, Palo Alto, Calif. 94303

"Hard" and "soft" energy scenarios are considered in the post-fossil fuel economy. Since all of the proposed energy sources are very capital-intensive, the importance of capital maximization is stressed. Due to the limited ability of the economy to raise capital, an elasticity effect will operate, resulting in a competition between capital intensive energy production and consumption. This will lead to automatic conservation/GNP dollar. The significance of electrochemical contributions is emphasized.

Abstract No. 238

Charge Transport in a Semiconducting Electrode

A. M. Buoncristiani, Dept. of Physics, Christopher Newport College, Newport News, Va. 23606

Photosensitive semiconductor electrodes in electrochemical cells produce photocurrents and/or catalyze electrolysis. We present a model, based on semiconductor device theory, of charge transport in the semiconductor and exchange through the interface. The model incorporates the nonlinearity of these processes and is used to study conditions limiting energy conversion, *e.g.*, saturation of current flow due to high light intensity. Numerical results describing charge distributions in the semiconductor and its effect on the electrolyte are obtained.

Abstract No. 239

Properties of GaP Photocathodes

D. S. Ginley* and **M. A. Butler,** Sandia Laboratories, Div. 5154, Albuquerque, N.M. 87185

The stability and electrical properties of Zn-doped, p-GaP photocathodes have been investigated in a number of electrolytes. The illuminated electrode is generally unstable, but the mechanism and decomposition rate appears to depend on pH and electrolyte composition. The flatband potential V_{fb} predicted from atomic electronegativities agrees with that measured by capacitance techniques at the measured PZZP of $pH_{PZZP} = 4.5$. The discrepancy between V_{fb} determined by capacitance techniques and the photocurrent onset was explored. (This work was supported by the Materials Sciences Program, Division of Basic Energy Sciences, U.S. Department of Energy under Contract AT (29-1)-789.)

Abstract No. 240

Thin Film Electrochemical Photovoltaic Cells

H. Witzke,* Optel Corp., Princeton, N.J. 08540, and **M. A. Russak** and **J. Reichman,** Grumman Aerospace Corp., Bethpage, N.Y. 11714

Electrochemical photovoltaic cells utilizing thin films of cadmium chalcogenides show potential of achieving at least 10% solar conversion efficiencies at very low cost. The best results to date have been obtained with CdSe thin films deposited by thermal co-evaporation of the elements. Details of the fabrication techniques, the effects of post-deposition processing and the results of long term stability tests are presented. Incorporation of *in situ* electrical energy storage by the use of a third electrode has also been accomplished. The problems encountered by the use of some specific storage electrode systems and potential solutions to these problems are disclosed.

Abstract No. 241

Oxide Semiconductors for Water Photoelectrolysis

S. A. Alkaitis* and **R. D. Rauh,** EIC Corp., Newton, Mass. 02158

Semiconducting oxide photoelectrodes for the photoelectrochemical decomposition of water were synthesized in order to obtain optimal bandgaps as well as flatband potentials. The effects of isomorphous substitution in photoanodes having the perovskite, corundum, and other

structures is presented. The effects of solution composition as well as electrode surface derivitization have also been investigated.

Abstract No. 242

Photoelectrochemical Solar Cell Using a Fuel Cell Oxygen Cathode

P. G. P. Ang* and **A. F. Sammells,** Institute of Gas Technology, Chicago, Ill. 60616

Oxygen evolution at an illuminated photoanode can occur at a voltage negative of the reversible oxygen potential. We have investigated n-type Fe_2O_3 and some of the mixed oxides as photoanodes. These photoanodes were relatively simple to fabricate and apparent polarization losses can be reduced by using porous surfaces. The performance characteristics of photoelectrochemical cells using several of these photoanodes together with Teflon-bonded diffusion electrodes for oxygen reduction are discussed.

Abstract No. 243

A Model for Electrochemical Photovoltaic Cells

J. Reichman, Research Dept., Grumman Aerospace Corp., Bethpage, N.Y. 11714

The classical diffusion theory for semiconductor-electrolyte solar cells is extended to include electron-hole photoregeneration in the bulk as well as space charge region of the semiconductor. Theory bears some resemblance to equations for the Schottky barrier solar cell. A more comprehensive model includes mass transfer effects in electrolyte and simple surface recombination mechanisms under quasi-equilibrium conditions. An improved model is presented which does not include quasi-equilibrium conditions. This gives better agreement under experiment.

Abstract No. 244

Grain Boundary Passivation and Solar Cell Improvement in Polycrystalline Silicon

D. S. Ginley* and **C. H. Seager,** Sandia Laboratories, Albuquerque, N.M. 87185

A technique has been developed for passivating the grain boundaries in polycrystalline silicon. Results are presented demonstrating the effectiveness of the introduction of atomic hydrogen on the electrical properties of individual grain boundaries. Initial kinetic and thermodynamic parameters for the process are discussed. Preliminary results of the treatment on prototype cells of neutron transmutation doped polysilicon are presented. Increases in cell efficiency have been observed both as a consequence of improved carrier lifetimes and larger open-circuit potentials. (This work was supported by the U.S. Department of Energy under Contract AT(29-1)-789.)

Abstract No. 245

Nondestructive Testing of Electrochemical Cells

W. C. Spindler,* Electric Power Research Institute, Palo Alto, Calif. 94303, **T. Katan** and **H. F. Bauman,** Lockheed Palo Alto Research Laboratory, Palo Alto, Calif. 94304

Nondestructive electrochemical and physicochemical perturbations are discussed which hold promise in routine evaluations of electrochemical cells by induction of diagnostic responses. Although mergence of anode and cathode behavior into inseparable combinations may introduce diagnostic difficulties, the behavior of many cells is overwhelmingly determined by one limiting electrode. Accurate prediction of performance may then be possible from computer evaluations of periodically stored responses. Methods of interpreting the semiempirical Shepherd and Peukert equations are presented.

Abstract No. 246

A Laser Raman Spectroscopic Study of Phosphoric Acid Electrolyte under Fuel Cell Operating Conditions

W. A. Adams* and **C. M. Preston,** Defence Research Establishment Ottawa, DND, Ottawa, Ont., Canada K1A 0Z4, and **M. Farrington** and **P. Kruus,** Dept. of Chemistry, Carleton University, Ottawa, Ont., Canada K1S 5B6

The performance of phosphoric acid fuel cells is found to be dependent on the acid concentration in the electrolyte, the operating temperature, and the presence of dissolved contaminants. There is some evidence that the structure of the purified acid itself close to the electrodes is an important factor in cell performance. Raman spectra of strong phosphoric acids have been obtained over a wide concentration range (dilute aqueous to 100% H_3PO_4) and temperatures from 0° to 200°C to determine which species are present. The Raman spectral evidence is compared to that available from other techniques.

Abstract No. 247

Synthetic Reformate Performance on Platinum in Trifluoromethanesulfonic Acid Monohydrate

G. W. Walker,* U.S. Army MERADCOM, Ft. Belvoir, Va. 22060, and **R. T. Foley,** Dept. of Chemistry, American University, Washington, D.C. 20016

During the past five years a number of investigators have sought to find a new electrolyte for the phosphoric acid fuel cell. The perfluoroalkylsulfonic acids, and in particular trifluoromethanesulfonic acid monohydrate (TFMSA · H_2O) have demonstrated many of the desired properties such as low vapor pressure, a nonadsorbing anion, and improved electrode kinetics. The TFMSA · H_2O studies have been continued to include the reaction of synthetic reformate (2-3% CO, 25% CO_2, H_2 balance) on platinum in the acid. Reaction kinetics of the individual constituents as well as the over-all reformate reaction have been investigated in an effort to determine the rate-limiting process.

Abstract No. 248

Alternate Electrolytes for Acid Fuel Cells

S. B. Brummer, J. S. Foos,* J. McHardy, J. B. McVeigh, D. E. Toland, and **M. Turner,** EIC Corp., Newton, Mass. 02158

The purpose of our research is to synthesize and test new electrolytes to replace phosphoric acid in fuel cells. Trifluoromethanesulfonic acid has shown promise but wets Teflon and is too volatile. As an alternate, we have studied methane di- and trisulfonic acids and their methylene-substituted halogen derivatives. We report on the preparation and properties of the parent and chloro-substituted acids as well as on progress in the synthesis of the fluoro acids. (This work was supported by the U.S. Department of Energy under Contract No. EY-76-C-03-1363.)

Abstract No. 249

A Hydrogen-Bromine Fuel Cell for Energy Storage Applications

R. S. Yeo,* Dept. of Energy and Environment, Brookhaven National Laboratory, Upton, N.Y. 11973, **K. L. Hseuh** and **D-T. Chin,** Dept. of Chemical Engineering, Clarkson College of Technology, Potsdam, N.Y. 13676, and **J. McBreen** and **S. Srinivasan,** Dept. of Energy and Environment, Brookhaven National Laboratory, Upton, N.Y. 11973

An experimental and theoretical study has been made to determine the feasibility of a hydrogen-bromine fuel cell for energy storage applications. The laboratory data were collected for the cell performance and the membrane characteristics during the charge and the discharge operations. An unsteady-state heat balance was used to predict the temperature change and the over-all electric-to-electric efficiency. The results indicate that the hydrogen-bromine system can achieve an efficiency greater than 70% when the operating cell current density is less than 200 mA/cm^2.

Abstract No. 250

Hydrogen and Oxygen Bubble Evolution during Electrolysis of Water

E. Barendrecht,* L. J. J. Janssen, and **R. M. de Jonge,** University of Technology, Laboratory of Electrochemical Technology, Eindhoven, The Netherlands

Hydrogen has been proposed as a new chemical energy carrier along with electricity. Producing hydrogen by conventional water electrolysis reveals also that bubble genesis and growth are important parameters. Therefore, bubble formation (*i.e.*, growth rate, size, frequency, active sites distribution, coverage, coalescence, etc.) at solid and transpar-

ent electrodes was studied as function of current density, pressure, temperature and convection conditions. Research was carried out with low and high speed cameras and completed with impedance measurements.

Abstract No. 251

Mechanistic Study of Oxygen Evolution on $NiCo_2O_4$

P. Rasiyah, D. B. Hibbert,* and **A. C. C. Tseung,** Dept. of Chemistry, The City University, London EC1, England

Previous studies have shown that $NiCo_2O_4$ is a very good catalyst for O_2 evolution in alkaline media. Cyclic voltammetric and coulometric studies showed that at least three surface compounds are formed between 1.1-1.5V *vs.* DHE in 5*N* KOH, 25°C. The rate follows first order kinetics; above 1.45V, O_2 is evolved which may involve the breakdown of the highest surface oxides.

Abstract No. 252

Rebalance Techniques and Capacity Maintenance in Redox Flow Cell Systems

L. H. Thaller, NASA-Lewis Research Center, Cleveland, Ohio 44135

In the NASA redox system based on acidic solutions of iron and chromium chlorides separated by an ion exchange membrane, rebalance is performed at the system rather than the single cell level. A simple, efficient, energy-producing iron-hydrogen cell has demonstrated the ability to maintain the electrochemical capacity of the cathode redox fluid in exact balance with the anode redox fluid and hold the system capacity constant with repetitive deep cycling. Rebalancing is required in all electrochemical storage concepts including conventional batteries to correct for the nonuniform cumulative inefficiencies during cycling that gradually reduce the ampere-hour capacity of the system. The rebalancing of redox stacks and the advantages of this system-level capability relative to competing systems are discussed.

Abstract No. 253

Electrodeposition of Minerals in Seawater: Architectural Aspects

W. H. Hilbertz, Marine Science Institute, The University of Texas at Austin, Austin, Texas 78712

Electrode configurations submerged in seawater and supplied with d.c. are described and material compositions accreted on the cathode, consisting mainly of $Mg(OH)_2$ and $CaCO_3$, are analyzed. Having an average strength of 4267.5 psi in compression, these electrodeposited materials can be utilized for *in situ* construction in the oceans. Projects ranging from mariculture facilities to OTEC plants and artificial islands are presented and discussed.

ENERGY TECHNOLOGY GROUP/INDUSTRIAL ELECTROLYTIC

Energy Conservation in the Industrial Electrolytic Industries

Abstract No. 254

Energy Efficiency Study of Chlor-Alkali Industry

J. B. Strauss* and **E. Rissmann,** Versar, Inc., Springfield, Va. 22151

Chlor-alkali production processes were studied as part of the DOE-ANL program on energy intensive industries. Twenty electrolytic and nonelectrolytic processes were investigated with respect to process history, scientific basis, engineering design, cost, and energy efficiency. Five processes were selected as economically competitive with and more energy efficient than current electrolytic processes. They were the membrane cell (with and without the oxygen or hydrogen cathode), Kel-Chlor, Mobay (direct electrolysis of HCl), catalytic oxidation of HCl, and a modified NH_4Cl/NO_2 process.

Abstract No. 255

Energy Efficiency of Electroorganic Processes

T. R. Beck,* Electrochemical Technology Corp., Seattle, Wash. 98107, **R. C. Alkire,** University of Illinois, Urbana, Ill. 61801, and **N. L. Weinberg,** Electrosynthesis Co., East Amherst, N.Y. 14051

The Swann Bibliography of the electroorganic literature has been searched for electroorganic synthesis techniques for organic chemicals produced at greater than 10,000 tons/yr. Flowsheets and material and energy balances were developed for those chemicals in this group which could be produced by electrochemical means. Corresponding items were developed from literature on conventional chemical processing to produce these chemicals. Over-all estimated energy requirements for the two routes are compared.

Abstract No. 256

Energy Conservation in Aluminum Smelting

R. W. Hyde and **J. M. Parry,*** Arthur D. Little, Inc., Cambridge, Mass. 02140

All primary aluminum production today is based on the Hall-Heroult electrolytic process. The electrical energy consumption is commonly 6-8 kW-hr/lb of aluminum coupled with significant thermal energy associated with the fabrication of the consumable carbon anode. This paper reviews a recently completed study of the possibility for energy conservation using alternative processes for aluminum production, for example, a direct carbothermal reduction, the subhalide and subsulfide processes. It also examines the opportunities for major improvements in the Hall-Heroult process with the use of titanium diboride cathodes and nonconsumable anodes.

Abstract No. 257

Energy Incentives and Technology of Metal Recycling

J. P. Pemsler* and **F. C. Brown,** EIC Corp., Newton, Mass. 02158

Metal recycle has been examined for those metals of interest to the electrolytic industries: aluminum, copper, nickel, magnesium, and titanium. Lead was also considered, since its major use is in batteries. Large energy savings result from secondary metal recycle. Current technology relies on sorting and physical separations followed by pyrometallurgical treatment. Hydrometallurgical processes may be feasible where low grade scrap cannot be treated by current technology or where environmental constraints require utilization of the scrap material.

Abstract No. 258

A Survey of Electrohydrometallurgical (Metal Winning) Processes

R. W. Hale, W. Goldberger, B. W. Gonser, T. E. Leontis, L. E. Vaaler,* and **T. J. McCleer,** Battelle Columbus Laboratories, Columbus, Ohio 43201

The process metallurgy of metals other than copper and aluminum were reviewed to find opportunities for reducing energy consumption through use of electrolytic methods. Approximately 90% of the energy for producing other nonferrous metals is used for magnesium, zinc, lead, chromium, manganese, and sodium. Use of a caustic leach/electrolyte for zinc electrowinning appears potentially attractive. The dendritic deposit produced lends itself to development of a continuous process. Opportunities also exist for lead, sodium, and possibly magnesium.

Abstract No. 259

Computation of Melt Velocities and Current Efficiency in Hall-Heroult Cells

J. W. Evans* and **Y. Zundelvich,** Dept. of Materials Science and Mineral Engineering, University of California, Berkeley, Calif. 94720

The paper reports on an investigation of molten cryolite and metal circulation in aluminum reduction cells. Such circulation is known to shorten the life of cell linings and is responsible for a reduction in current efficiency. Employing current densities and magnetic field strengths calculated by other workers, the turbulent velocities of metal and cryolite within the cell have been computed. Velocities were found to be in reasonable agreement with velocities measured on actual cells. A means by which the current efficiency can be predicted from the velocity computations is described.

Abstract No. 260

Energy-Saving Catalytically Active Cathodes for Caustic-Chlorine Production

D. W. Carnell* and **C. R. Needes,** E. I. du Pont de Nemours & Co., Inc., du Pont Experimental Station, Wilmington, Del. 19898

A commercially feasible catalytically active porous nickel electrode has been developed. When used as the cathode in caustic-chlorine diaphragm cells it reduces cell voltage and power consumption by 6-8%. The estimated investment for converting existing diaphragm cells to the catalytic cathode is low enough that the discounted cash flow rate is expected to be at least 15%. The cathode is also effective in reducing the power consumption of membrane cells.

Abstract No. 261

Activated Cathodes for Reduced Power Consumption in Electrolytic Cells

W. W. Carlin and **W. B. Darlington,*** PPG Industries, Inc., Chemical Div., Corpus Christi, Texas 78408

The advent of titanium anodes with electroactive coatings has resulted in a reduction of the chlorine evolution potential in chlor-alkali cells to near the thermodynamic reversible value. Now electroactive cathode coatings have been developed which achieve the same relative potential reduction for the hydrogen evolution reaction. Chlor-alkali cells with these newly developed, activated cathodes have been operated for over 18 months with a 70% reduction in cathode overpotential and a total average reduction in cell power consumption of 6%, compared to cells with untreated steel cathodes.

Abstract No. 262

Reduction of Hydrogen Overpotential in a Chlorine Cell

I. Malkin* and **J. R. Brannan,** Diamond Shamrock Corp., T. R. Evans Research Center, Painesville, Ohio 44077

Several coatings have been developed which are capable of reducing the hydrogen overpotential on a steel cathode by approximately 150 mV. This is equivalent to an energy savings of 108 kW-hr/ton. These coatings perform equally well in both diaphragm and membrane chlorine cells. Full size commercial cathode cans have been coated and continue to show this energy savings after one year of service. Ground has been broken for a commercial facility for coating cells.

Abstract No. 263

$NiCo_2S_4$—A Novel H_2 Evolution Electrocatalyst in Alkaline Media

M. C. M. Man* and **A. C. C. Tseung,** Dept. of Chemistry, The City University, London EC1, England

X-ray powder diffraction and chemical analysis confirmed that $NiCo_2S_4$ can be formed by reacting H_2S with high surface area $NiCo_2O_4$ (80 M^2/g) at 350°C for 8 hr. Teflon-bonded $NiCo_2S_4$, supported on 100 mesh nickel screens gave 1 A/cm^2 at −150 mV *vs.* DHE (dynamic hydrogen electrode). Furthermore, unlike other non-noble cathode catalysts (*e.g.*, nickel boride or Raney nickel), this catalyst is not deactivated at open circuit or exposure to air at elevated temperatures. (This study was supported by the EEC.)

Abstract No. 264

Energy Losses Occurring in and New Electrode Concepts for Alkaline Electrolyzers

P. J. Moran,* **G. L. Cahen, Jr.,** and **G. E. Stoner,** Applied Electrochemistry Laboratory, Dept. of Materials Science, University of Virginia, Charlottesville, Va. 22901

Efficient operation of hydrogen-producing alkaline electrolyzers is a prerequisite for the hydrogen energy scheme. Our research efforts attempt to increase operating efficiency by two methods. First, a minimization or elimination of time-dependent increases in cell voltage which occur at constant current and temperature would be helpful. The second method is the use of high surface area electrodes obtained from polycrystalline whiskers. Whisker electrodes can be fabricated or the whiskers can be attached to existing electrode systems.

Abstract No. 265

Primary Current Distribution and Leakage Current Analysis of Hooker MX™ Membrane Cells

D. E. Stephens,* **S. D. Mott,** and **M. Shabrang,** Hooker Chemical Co., Niagara Falls, N.Y. 14302

Computer simulation of leakage currents and the resulting effect on the current density distribution are presented for the Hooker bipolar MX™ membrane cell. Leakage current measurements have been made on full size pilot cells using target electrodes located in the various inlet and outlet ports. Design improvements to minimize leakage current losses in the MX™ cells have been made and the computer program used to predict the effect in larger bipolar cell stacks.

Abstract No. 266

The Photoelectrochemical Production of Chlorine

J. Jorné, Dept. of Chemical Engineering, Wayne State University, Detroit, Mich. 48202

Will the use of a photoelectrode in a chlor-alkali cell result in increased energy efficiency? Tungsten trioxide anode and platinum cathode were used in the electrolysis of 4M NaCl solution. The WO_3 anode, prepared by oxidation at 750°C, was illuminated by a 300W light source. The anode potential was controlled potentiostatically, and the current increase was measured upon illumination. A current density increase of 10-25% was measured upon illumination and chlorine evolution was observed at the anode.

Abstract No. 267

Gas Diverging Electrode in the Chlor-Alkali Membrane Cell

J. Jorné, Department of Chemical Engineering, Wayne State University, Detroit, Mich. 48202, and **J. F. Louvar,** BASF Wyandotte Corp., Wyandotte, Mich. 48192

The purpose of this investigation was to find an effective means of removing gas bubbles from the interelectrode space of a new chlor-alkali membrane cell. The gas evolution increases the ohmic resistance of the electrolyte and the current distribution becomes nonuniform in the vertical direction. It was observed that by using a gas diverging electrode the gas bubbles diverged to the back of the vertical electrode. Various expanded steel cathodes were very effective in diverging the H_2 gas, which resulted in a significant drop of the cell potential. The effectiveness was tested as a function of the spacing between the cathode and the membrane, current density, temperature and the geometry of the expanded metal electrodes. Gas diverging electrodes eliminate the restriction on the cell's height and can result in capital investment savings.

ENERGY TECHNOLOGY GROUP/ORGANIC AND BIOLOGICAL ELECTROCHEMISTRY

Energy Conversion and Storage via Biological Systems

Abstract No. 268

Biomimetic Strategies for Solar Energy Conversion

J. J. Katz, Chemistry Division, Argonne National Laboratory, Argonne, Ill. 60439

Sufficient progress in the understanding of chlorophyll function has been made to make efforts to mimic plant photosynthesis in the laboratory a practical proposition. Synthetic photoreactive chlorophyll species that have many of the optical and redox properties of *in vivo* photoreaction center chlorophyll can now be prepared. Progress in the direction of a biomimetic technology for solar energy conversion is described, and important questions that must still be addressed are discussed.

Abstract No. 269

Photoredox Reactions of Dimeric Chlorophyll Derivatives. Modeling the Primary Events of Photosynthesis

M. R. Wasielewski,* A. G. Kostka, and **J. R. Norris,** Chemistry Div., Argonne National Laboratory Argonne, Ill. 60439,

and **M. J. Pellin** and **K. J. Kaufmann,** Dept. of Chemistry, University of Illinois, Urbana, Ill. 61801

A series of dimeric chlorophylls have been prepared which serve as well-defined biomimetic models of reaction center chlorophyll both in green plants and in photosynthetic bacteria. These models are used to probe the photoredox properties of reaction centers as a function of dimeric chlorophyll electron donor geometry and the relative orientation of these dimers to electron acceptors, *e.g.*, pheophytins and quinones. The results of a range of photoelectrochemical, optical, and magnetic resonance experiments elucidate important features of both the kinetics and mechanism of light induced electron transfer in these systems.

Abstract No. 270

Photoelectrochemical Properties of Metalloporphyrins

F. J. Kampas,* K. Yamashita, C. K. Chang, and **J. Fajer,** Dept. of Energy and Environment, Brookhaven National Laboratory, Upton, N.Y. 11973

The photoelectrochemical properties of films of tetraphenyl-, tetrabenz-, tetrapropyl-, and octaethyl porphyrins, porphins, chlorins, co-facial diporphyrins and mesoporphyrin esters have been studied in Al/Porphyrin/Ag, and Al/Porphyrin/Fe $(CN)_6^{-3}$, $Fe(CN)_6^{-4}$/Pt cells. The dark current-voltage characteristics of the cells resemble those of a metal-insulator-semiconductor diode and are attributed to an Al-Al_2O_3-porphyrin interface. Action spectra indicate that the photoactive region is the porphyrin-aluminum electrode. For a given porphyrin ligand, quantum efficiencies of the photocurrents parallel the first oxidation potentials of the porphyrins: the more easily oxidized compounds exhibit higher quantum yields. Peak quantum yields range from 10^{-1} to 10^{-4} with power conversion efficiencies varying from 10^{-2} to 10^{-6} for wavelengths of 420-440 nm. (This work was performed under the auspices of the Division of Chemical Sciences, U.S. Department of Energy, Washington, D.C., under Contract No. EY-76-C-02-0016.)

Abstract No. 271

Photo-Initiated Mediated Transport of H_3O^+ and/or OH^- across GMO Bilayers Doped with Magnesium Octaethylporphyrin

R. C. Young, J. F. Smalley, and **S. W. Feldberg,*** Div. of Chemical Sciences, Dept. of Energy and Environment, Brookhaven National Laboratory, Upton, N.Y. 11973

Photogenerated magnesium octaethylporphyrin cation ($MgOEP^+$) in GMO bilayers is shown to mediate the transport of H_3O^+ and/or OH^-. Open-circuit experiments with a *p*H gradient across the bilayer unequivocally demonstrate that a light flash can "turn on" the membrane to H_3O^+/OH^- transport. The magnitude of this voltage response is 0.053 V/ΔpH (ΔpH = the difference in the *p*H on each side of the bilayer) indicating a highly selective process. Data from voltage clamp experiments are consistent with the predicted kinetic behavior of the classic Markin or Lauger carrier model and permit elucidation of some of the controlling rate processes. (This work was done under Contract No. EY-76-C-02-0016 with the U.S. Department of Energy.)

Abstract No. 272

Stabilization of ZnO Surfaces for Photoelectrochemical Oxygen Production

K.G. McGregor, J. W. Otvos,* and **M. Calvin,** Laboratory of Chemical Biodynamics, Lawrence Berkeley Laboratory, University of California, Berkeley, Calif. 94720

n-type ZnO is known to produce oxygen under bandgap illumination (>3 eV) at an aqueous electrolyte interface when photogenerated holes react with water. Normally, however, in a simultaneous reaction anodic dissolution of the crystal occurs with formation of Zn^{2+}. We have found that on polycrystalline sintered pellets of ZnO we can completely inhibit the dissolution with a layer of chemisorbed zinc phthalocyanine, which apparently captures the hole and prevents its reaction with bulk crystal.

Abstract No. 273

Photosynthetic Reaction Centers as Solar Cells

R. K. Clayton, Div. of Biological Sciences, Cornell University, Ithaca, N.Y. 14853

Purified bacterial reaction centers (RC's) mixed with ubiquinone (UQ) can be deposited as films. Photochemical transfer of electrons from the RC's to UQ occurs with high quantun efficiency, and the separated charges are stable against recombination for about 1-3 sec. In principle, such cells may have an over-all efficiency for solar energy conversion of 17%. The many problems that must be solved in such a device are described and discussed.

Abstract No. 274

An FMN-Photosystem I Photogalvanic Cell

E. L. Gross,* S. L. Winemiller, D. Youngman, and **R. L. Pan,** Dept. of Biochemistry, The Ohio State University, Columbus, Ohio 43210

We have constructed a photogalvanic cell using FMN and Photosystem I particles. The Photosystem I particles were placed on a filter between two compartments containing the electron donor $[K_4Fe(CN)_6]$ and the electron acceptor [FMN] respectively. The FMN side was illuminated. 300 mV were observed across a 3000Ω resistance yielding 0.1 W/m² or a power efficiency of 0.13%. This was doubled by substituting DCIP-ascorbate for the $K_4Fe(CN)_6$. Both Photosystem I photochemistry and the direct photoreduction of FMN contribute to the potential.

Abstract No. 275

The Biological Generation of Hydrogen Gas

D. B. Knaff, Dept. of Chemistry, Texas Tech University, Lubbock, Texas 79409

A considerable number of microorganisms are capable of reducing protons to hydrogen gas. Some algae can use a light-energized oxidation of water as the source of electrons for this H_2 production. Thus, in principle, a combustable fuel (distributable through existing pipelines) can be produced from an essentially inexhaustable electron donor and energy source. The biochemistry of the enzyme that catalyzes H_2 production is discussed and some practical difficulties analyzed.

Abstract No. 276

Photohydrogen Production Using Biological Membranes

J. M. Olson, Dept. of Biology, Brookhaven National Laboratory, Upton, N.Y. 11973

A device made of unit-membrane vesicles containing photochemical reaction centers and light-harvesting pigments from plants, algae, and bacteria is proposed. Photosystem-I reaction centers with hydrogenase is put into the membrane of one type vesicle, and Photosystem-II reaction centers with the water-splitting enzyme are put into the membrane of the other type vesicle. A mobile electron carrier shuttles back and forth between the two types of vesicle. (This work was supported by the U.S. Dept. of Energy.)

Abstract No. 277

Chemical and Biological Conversion of Solar Energy

T. B. Reed, Solar Energy Research Institute, Golden, Colo. 80401

Many solar conversion processes provide a transitory useful product such as heat or electricity which then must be used immediately or stored. Conversion techniques which produce chemicals or fuels have a built in storage capability that provides much greater flexibility of use. Biomass is the most exquisite example of chemical conversion of solar energy atuned to Nature's purposes, and has been the principle energy source for human kind for most of our existence. Now that our dowry of low cost oil and gas is running out, we are again discovering that there is a large store of chemical energy in biomass which we can easily tap using existing techniques. An overview of both the technical and institutional activities directed toward harnessing this energy is presented.

Abstract No. 278

Integrating Wastewater Treatment with Fuel Production Using Microalgae

J. R. Benemann* and **W. J. Oswald,** University of California, Sanitary Engineering Research Laboratory, Berkeley, Calif. 94720

Wastewater treatment with microalgae in shallow, open ponds requires a process for algal harvesting before treatment effluents can be discharged. Two relatively low-cost processes for microalgal harvesting are being developed: microstraining and bioflocculation. Both processes require control of detention time, mixing, and other parameters in pond operations. Current experience indicates that it is possible to operate microalgal ponds fed with settled sewage such that the algae will flocculate and settle within a 48 hr period. The settled algal biomass can be anaerobically digested to methane gas, with the residue disposed of on land for its fertilizer value. The supernatant of the bioflocculation-settling process can support growth of additional crops of microalgae to allow achievement of nutrient (nitrogen, phosphorus) removal.

Abstract No. 279

Ethanol Production Using Microbial Cells Trapped in Polyacrylamide Gels

R. H. Villet, Solar Energy Research Institute, Golden, Colo. 80401 and **J. Dillon,** Massey University, New Zealand

For the biological transformation of chemicals immobilized, cell technology can have advantages over conventional freely suspended cell systems: cells can be used repeatedly; products can be separated readily; continuous processing at high rates of throughput is feasible. Yeast cells for converting lactose and glucose to ethanol were immobilized in cross-linked polyacrylamide gels. Cylindrical biocatalyst particles were tested in a batch system. Rates of substrate utilization and alcohol production were measured.

Abstract No. 280

Solar Ultraviolet Radiation; A Possible Limiting Factor of Direct Biological Conversion of Sunlight by Algae

J. Calkins* and **J. A. Barcelo,** Dept. of Radiation Medicine, Albert B. Chandler Medical Center, University of Kentucky, Lexington, Ky. 40506

The possible use of algae for food and fuel has stimulated extensive research into direct bioutilization of sunlight. Algae grow rapidly, are photosynthetically efficient, and amenable to automation. However, some outdoor algal cultures have not grown as well as anticipated from laboratory studies. We note that solar u.v.-B might contribute to the problems of outdoor growth and present data on incident u.v.-B, its attenuation in natural waters and the u.v.-B sensitivity of certain algae which permits quantitative estimation of the injurious potential of solar u.v.

INDUSTRIAL ELECTROLYTIC

General Session

Abstract No. 281

Bubble Effects on the Solution *IR* Drop in a Vertical Electrolyzer under Free and Forced Convection Flow Conditions

F. Hine and **K. Murakami,** Nagoya Institute of Technology, Gokiso-cho, Showa-ku, Nagoya 466, Japan

Effects of electrolytic bubbles on the *IR* drop of caustic soda solution in a vertical cell of about 1m high were studied under both free and forced convection flow conditions. Two Luggin probes were positioned near the anode and the cathode to determine the solution *IR* drop during electrolysis. A sectioned electrode having 10 segments was employed to obtain the current distribution from the bottom to the top of cell. The superficial resistivity of the solution containing gas bubbles agreed well with Braggemann's equation. The solution *IR* drop decreased significantly when adequate conditions for solution convection was established, and hence, the anode-to-cathode gap was most important for reduction of the solution *IR*.

Abstract No. 282

Effect of Gas Evolution upon Current Distribution during Electrodeposition

R. C. Alkire and **P.-Y. Lu,*** Dept. of Chemical Engineering, University of Illinois, Urbana, Ill. 61801

The effect of electrolytic hydrogen evolution upon the mass transfer coefficient for simultaneous copper electrodeposition was studied in a cell containing a vertical sectioned cathode. It was found that the mass transfer coefficient for copper deposition depended both upon local bubble growth as well as upon convection caused by bubbles rising along the cathode. A mathematical model for the multireaction cathode process was developed based upon mass transfer and potential distribution considerations. The model was used successfully to predict the current distribution in a cell of nonuniform geometry.

Abstract No. 283

Chlorine Species in the Solution Adjacent to the Anode

I. V. Kadija, Chlor-Alkali, Olin Chemicals, Charleston, Tenn. 37310

With a rotating double ring system we have analyzed the chemical composition of the chlor-alkali anode surface solution. The pH range was between 1-7. We have been able to identify quantitatively the concentration of chlorine and some other intermediate chlorine compounds. We have followed their change in concentration against the pH changes of the operating solution. In the pH range of 6-7 we have found quantities of chlorine in the solution corresponding to chlorine pressure close to 1 atm. These findings are correlated to the two competitive reactions electrochemical generation *vs.* chemical dissolution.

Abstract No. 284

Chlorine/Caustic Soda Production in a Permselective Membrane Electrolyzer Employing Series Catholyte Flow

R. H. Fitch,* B. E. Kurtz, and **C. W. Merkh,** Allied Chemical Corp., Industrial Chemicals Div., Syracuse Technical Center, Solvay, N.Y. 13209

Series catholyte flow involves feeding the catholyte from a first cell to succeeding cells, the final caustic soda concentration being reached in the last cell. Power savings and other advantages of series catholyte flow over conventional parallel flow in the operation of a permselective membrane electrolyzer producing chlorine and caustic soda are discussed. Results of experiments with a five unit-cell commercial scale series catholyte flow electrolyzer are contrasted with results from a conventional parallel flow unit. Practical design considerations in applying series catholyte flow to a commercial electrolyzer are enumerated and the effects of process variables on performance are explored.

Abstract No. 285

An Investigation of the Electrochemical Behavior of Graphite Fiber-Polymer Composites

G. R. Stafford,* G. E. Stoner, and **G. L. Cahen, Jr.,** Applied Electrochemistry Laboratory, Dept. of Materials Science, University of Virginia, Charlottesville, Va. 22901

A composite material containing 40-60% randomly oriented graphite fibers has a specific resistivity on the order of 1-10 Ω-cm, good enough to make it a candidate for an electrode material. The fiber orientation plays a major role in both the mechanical stability and the electrochemical performance of the electrode. If the fibers are aligned perpendicularly to the surface, the solution sees a surface of mini-electrodes embedded in an inert plastic. This configuration not only offers the maximum dimensional stability, it also offers the advantage of controlling the electrode's electrochemical performance by altering the fiber size and separation.

Abstract No. 286

Silicon and Its Alloys as a Chlorine Anode Substrate Material

A. Martinsons, C. Welch,* and **H. Hoekje,** PPG Industries, Inc., Chemical Div., Barberton, Ohio 44203

Techniques were developed to cast monolithic silicon and silicon-iron alloys. These cast materials were cell tested to assess their potential as dimensionally stable chlorine anode substrates. An electrocatalytic coating of RuO_2-TiO_2 was applied to the test substrate. A silicon anode was tested successfully in excess of 413 days while a silicon-8% iron alloy anode was tested for 1050 days. Silicon alloys containing chromium, tungsten, or molybdenum were also tested, but less successfully.

Abstract No. 287

Some Aspects of Silicon and Its Alloys

C. Welch,* **A. Martinsons,** and **H. Hoekje,** PPG Industries, Inc., Chemical Div., Barberton, Ohio 44203

Silicon and its low iron alloys exhibit good valve-metal action when polarized in acidified chlorinated brine solution. The doping of silicon with boron reduces the electrical resistivity and significantly improves its chemical resistance to alkaline attack. The presence of low levels of iron results in the formation and segregation of iron disilicide phases within the silicon matrix. Attempts to increase the miscibility of the iron disilicide phases by alloying with a second metal were, in general, unsuccessful.

Abstract No. 288

Linear Sweep Voltammetry of Flooded Porous Electrodes. I. First Order Irreversible Reaction

J. A. Trainham* and **T. G. Stanford,** Chemical Engineering Group, College of Engineering, University of South Carolina, Columbia, S.C. 29208

A theoretical analysis of a flooded porous electrode subject to a linearly time varying potential is treated for the limiting case of a first order irreversible reaction when the ohmic potential drop within the electrode is ignored. External and internal mass transfer effects are included in the analysis. A Green's function technique is used to solve the governing equations for mass transfer with electrochemical reaction external and internal to the electrode. Results of the analysis when used in conjunction with experimental data allow the determination of the reaction rate per unit volume ($a\ i_{o,\ ref}$ the product of the specific interfacial area times the exchange current density).

Abstract No. 289

The Effect of Multiple Current Collectors on the Performance of Flow-Through Porous Electrodes

J. J. Wu* and **J. A. Trainham,** Chemical Engineering Group, College of Engineering, University of South Carolina, Columbia, S.C. 29208

A one-dimensional model for flow-through porous electrodes is used to predict the variation in electrode potential within the porous electrode and the effluent concentration for current collectors placed at the front and the back of the electrode. Results are presented for upstream and downstream placement of the counterelectrode relative to the fluid inlet. Analytical expressions have been developed for an electrode operating under limiting current conditions. A computer model is used to predict electrode behavior above and below the limiting current of a metal deposition reaction. Results show that the variation in electrode potential within the porous electrode can be minimized by varying the current passed at each current collector. For the limiting current case, conditions for the minimum potential variation can be predicted analytically for any set value of the solution to matrix conductivity ratio (κ/σ). The use of multiple current collectors is a technique by which the "effective" conductivity ratio can be infinitely varied.

Abstract No. 290

Multiple Reaction Sequences in Flow-Through Porous Electrodes

R. C. Alkire and **R. M. Gould,*** Dept. of Chemical Engineering, University of Illinois, Urbana, Ill. 61801

An experimental and theoretical study of multiple reaction sequences in flow-through porous electrodes has been carried out. The reaction systems investigated included copper deposition in the presence of an iron redox couple, simultaneous copper and cobalt deposition, and two-step oxidation of 9-10 diphenylanthracene. Total and partial current distributions, and reactor conversion efficiencies were measured in each system over a wide range of operating parameters. Quantitative agreement was achieved with theoretical model calculations.

Abstract No. 291

Electrodeposition of Copper and Cobalt on Fluidized Bed Electrodes

J. W. Evans,* **B. J. Sabacky,** and **I. Masterson,** Dept. of Materials Sciences and Mineral Engineering, University of California, Berkeley, Calif. 94720

Investigations of the electrodeposition of cobalt and of copper from aqueous sulfate solutions have been carried in a 100A cell. Current efficiencies and power consumptions were determined as a function of metal ion concentration, pH, temperature, bed expansion, and particle size. The results of a preliminary economic assessment of a fluidized bed cell for electrowinning of copper are presented, as are initial results from experiments using a larger (800A) cell.

Abstract No. 292

Electrochemical Fluorination of Trichloroethylene and N,N-Dimethyltrifluoroacetamide

L.-C. Hsu, National Aeronautics and Space Administration, Lewis Research Center, Cleveland, Ohio 44135

Fluorination of trichloroethylene and N,N-dimethyltrifluoroacetamide was carried out in laboratory scale in advanced "Simons" type electrochemical apparatus which could be operated automatically from ambient to 50 psi pressure. A variety of fluorine-substituted products are formed depending upon electrolysis conditions and concentrations of reactant relative to the NaF, KF, HF electrolyte. A new reaction mechanism of electrochemical fluorination of trichloroethylene is proposed. The solvency-to-fluorine content relationship of fluorinated N,N-dimethyltrifluoroacetamide is described. Potential uses of fluorinated solvents prepared in this way having functional groups are discussed.

ORGANIC AND BIOLOGICAL ELECTROCHEMISTRY

Chemically Modified Electrodes

Abstract No. 293

Modified Ruthenium Electrodes and Ruthenium Modified Electrodes

H. Abruna, K. Kuo, D. Rolison, M. Umaña, and **R. W. Murray,*** Kenan Laboratories of Chemistry, University of North Carolina, Chapel Hill, N.C. 27514

Preparation, surface analysis, and electrochemical properties of electrode surfaces based on ruthenium chemistry are discussed. Ruthenium oxide interfaces can be chemically modified in several ways, including covalent bond-forming reactions with organosilane reagents, to affix molecular surface states to the electrode surface. Surface states can be based on ruthenium complexes, and examples of chemistry used to immobilize ruthenium polypyridyl complexes on various electrode materials are given.

Abstract No. 294

Chemical Modification of Carbon Electrodes

T. Osa,* **M. Fujihira,** and **T. Matsue,** Pharmaceutical Institute, Tohoku University, Aobayama, Sendai 980, Japan

Our recent studies of chemically modified carbon electrodes (CMCE) are presented. Various kinds of chemically active groups are formed on the surface by general chemical methods such as air oxidation, reagent oxidation, reagent reduction, and nitration. Then the surface groups are covalently bound with functionally important compounds via ester, amide, ether, and C-C bonds. Some surface characterization by ESCA, electrochemical method, etc., are demonstrated. Among applications of CMCE, selective substitution reaction of aromatic compounds using cyclodextrin modified carbon electrodes are mainly discussed.

Abstract No. 295

Chemically Derivatized n-Type Si Photoanodes: Photoelectrochemistry in Aqueous Solution

M. S. Wrighton,* **A. B. Bocarsly,** and **E. G. Walton,** Dept. of Chemistry, M.I.T. Cambridge, Mass. 02139

n-Type Si suffers photoanodic surface degradation in aqueous electrolytes, but this degradation can be substantially suppressed by derivatization of the surface with hydrolytically unstable ferrocenes such as trichlorosilylferrocene, 1,1′-*bis*-(triethoxysilyl)ferrocene, or (1,1′-ferrocenediyl)dichlorosilane. The derivatized surface generally exhibits electrochemical properties reflecting oligomeric coverages of electroactive ferrocene material of up to twenty monolayers. The derivatized electrode can be used as the photoanode in a cell employing an aqueous solvent containing reductants such as I^-, $[Ru(NH_3)_6]^{2+}$, and $[Fe(CN)_6]^{4-}$. The comparison of these systems and the stability and efficiency of optical → electrical energy conversion devices based on such derivatized electrodes are discussed.

Abstract No. 296

Chemical Behavior of Electrode Surface Attached Molecules

A. F. Diaz, IBM Research Laboratory, San Jose, Calif. 95193

Our interest in the preparation of stable electrode surfaces with chemical selectivity leads us to a fundamental study of the dynamics of surface molecules in the electrochemical process. Of the several approaches we have employed for preparing modified electrode surfaces, the use of a covalently attached surface monolayer prepared by treatment of a metal oxide surface with the appropriate silyl derivative proves to be most useful. Our results from experiments designed to quantify the dynamics of the surface molecules and their influence on the electrochemical process are presented.

Abstract No. 297

Modification of Electrode Materials Using Plasma Chemistry

M. F. Dautartas, D. M. Ullevig, and **J. F. Evans,*** Dept. of Chemistry, University of Minnesota, Minneapolis, Minn. 55455

Studies of two types of plasma chemistry used to modify electrode materials are reported. The first involves the use of small molecule discharges to generate reactive sites on the electrode surface for use in subsequent conventional chemical coupling schemes (*e.g.*, free radical sites, functional groups). The second approach is to carry out plasma deposition of bound electroactive polymers onto electrode surfaces using large molecule plasma (*e.g.*, ferrocene, vinylferrocene).

Abstract No. 298

Polymer-Metal Composite Thin Films on Electrodes

K. Doblhofer* and **W. Dürr,** Fritz-Haber-Institut der Max-Planck-Gesellschaft, D-1000 Berlin 33, Germany

Polymer films with a thickness of 10-100 nm which are deposited on metal or carbon electrodes at elevated temperature with the method of glow-discharge polymerization are stable during electrolysis. The electrocatalytic activity of such films, for instance with respect to the cathodic dioxygen reduction, may be enhanced by the introduction of metallic centers in the form of ions, dispersed atoms, or metal clusters. Theoretical and experimental aspects of such composite film/electrode systems are discussed.

Abstract No. 299

Adsorbed Polymers as Electrocatalysts

L. L. Miller,* **M. R. Van de Mark, G. Hostetler,** and **J. Kerr,** Dept. of Chemistry, University of Minnesota, Minneapolis, Minn. 55455

Redox polymers have been adsorbed onto metal electrodes by dip coating. The resulting material was analyzed by x-ray photoelectron on Auger electron spectroscopy, and it was determined that rather uniform layers of 15-200Å (depending on the concentration of the dip solution) could be produced. These "polymer electrodes" are then used for electrochemistry on nonaqueous solvents. It is shown that the polymer layer can be reversibly charged and does not desorb. When it is charged it becomes more highly conductive. The charged layer acts as a catalyst for the reduction of solution species like oxygen or alkyl halides. The utility of such materials for selective electrocatalysis is discussed.

Abstract No. 300

Coordination of Transition Metal Complexes to the Surface of Graphite Electrodes Coated with Polymeric Ligands

N. Oyama and **F. C. Anson,*** California Institute of Technology, Pasadena, Calif. 91125

The attachment of polymeric materials to electrode surfaces is one means for fashioning "chemically modified electrodes." Polymeric ligands are attractive electrode modification agents because the resulting surfaces may serve as coordination sites for metal complexes. The electrochemical behavior of transition metal complexes bound to graphite electrodes that are coated with poly(4-vinylpyridine) and other polymeric ligands is described. The coated graphite electrodes extract metal complexes from extremely dilute solutions. The polymeric coatings are simple to apply and survive repeated metallation. Electrode surfaces that will accept a wide variety of metal cations seem likely to be preparable by appropriate selection of the pendant ligand groups on the polymeric molecules.

Abstract No. 301

Spectroelectrochemistry of Stable, Electroactive Polymer-Coated Electrodes

F. B. Kaufman,* **A. H. Schroeder, E. M. Engler, J. Q. Chambers** (Permanent address: University of Tennessee, Knoxville, Tenn. 37916), and **S. R. Kramer** IBM Thomas J. Watson Research Center, Yorktown Heights, N.Y. 10598

A new class of electroactive copolymers consisting of linear polychloromethyl-styrene partially functionalized with various mono-substituted donor groups can be easily spin coated from THF solution onto metallic electrodes to produce films ranging in thickness from ~50Å to >1μ. These modified electrodes have been investigated with cyclic voltammetry (CV), chronoamperometry and u.v.-VIS spectroscopy at optically transparent electrodes. The films show CV waves corresponding to electron transfer to and from the polymer-bound substituents. Thinner films have faster response times, although the ratio of equivalents of charge passed to groups present in the film is quite high and is constant for all thicknesses. Such electrodes exhibit unchanging response over many thousands of cycles and can be stored in a dry state and reused with no loss of activity. Variation of electrolyte concentration, solvent and polymer chain coverage has lead to a physical model of the rate-determining processes in the film. Physical measurements verify the uniformity of film thickness and the electrochemical behavior of solute species in contact with these electroactive films confirm complete coverage of the metallic surface devoid of pore or channel defects.

Abstract No. 302

Voltammetric Investigation of Polymer-Coated Electrodes

P. J. Peerce and **A. J. Bard,** Dept. of Chemistry, The University of Texas at Austin, Austin, Texas 78712

The electrochemical behavior of electrodes coated with various polymers, *e.g.*, poly(vinylferrocene), was studied. The homogeneity of the polymer films was probed by examining the chronoamperometric and cyclic voltammetric behavior of various redox couples in acetonitrile solution. The data were analyzed by the method of Gueshi, Tokuda, and Matsuda to determine whether electron conduction occurred through channels in the polymer film and to estimate the hole size and fractional surface coverage. Results consistent with electron transfer through small holes in the polymer layer were obtained for some of the systems studied. Cyclic voltammetric studies of the redox reactions of the polymer film itself, as well as examination of the electrode surfaces by electron spectroscopy, were also undertaken.

Abstract No. 303

Electrochemical Behavior of Organic "Metal" Electrodes in Aqueous Media

C. D. Jaeger* and **A. J. Bard,** Dept. of Chemistry, The University of Texas at Austin, Austin, Texas 78712

Electrodes of organic metallic materials, *e.g.*, TTF-TCNQ, NMP-TCNQ and TTT-TCNQ (donors TTF = tetrathiafulvalene, NMP = N-methyl phenazinium and TTT = tetrathiatetracene and acceptors TCNQ = tetracyanoquinodimethane), can be prepared as compacted pellets, single crystals, or thin films. Such electrodes were investigated in aqueous media. The potential limits of stability of the electrodes depended upon the donor or acceptor (TCNQ) compound and the supporting electrolyte. Within the stable potential region the oxidation and reduction of soluble redox couples at the electrode could be carried out. Upon exceeding the potential limits of stability of the electrode, the subsequent voltammograms showed peaks attributable to insoluble compounds of the donor or TCNQ and the supporting electrolyte.

Abstract No. 304

Electrochemical and Photoelectrochemical Studies of Silane-Modified SnO_2 Electrodes

V. R. Shepard and **N. R. Armstrong,*** Dept. of Chemistry, Analytical Div., University of Arizona, Tucson, Ariz. 85721

Attempts to irreversibly attach phthalocyanine dye molecules to silane-modified SnO_2 electrodes have been successful. The photoelectrochemical response of these electrodes has been encouraging, however the mode of attachment was unclear in our earliest experiments. More recent results indicate that adsorption as well as covalent attachment is important in the surface modification process. Results from extensive differential capacitance and voltammetric studies, in aqueous and nonaqueous media, indicated appreciable adsorption of metal phthalocyanines and metal ions to mono-, di- and tri-amine functional silanes, and the formation of a stable, reversible, redox couple on the modified SnO_2 electrode surface.

Abstract No. 305

Electrochemical and X-Ray Photoelectron Spectroscopic Investigations of Surface Filming on Polished and Roughened Kel-F-Graphite Composition Electrodes

J. L. Anderson,* **D. E. Tallman, J. E. Anderson,** and **D. J. Chesney,** Dept. of Chemistry, North Dakota State University, Fargo, N.D. 58105, and **J. F. Evans,** Dept. of Chemistry, University of Minnesota, Minneapolis, Minn. 55455

Electrochemical and x-ray photoelectron spectroscopic (XPS) techniques have been applied to characterize the surface of a composite Kel-F-graphite electrode material. Cyclic voltammetric studies consider the effects of surface treatment and solvent composition for mixed aqueous/methanolic solutions. The unusually low double-layer capacity values of these electrodes are investigated as a function of surface preparation and electrolyte concentration. Both electrochemical and XPS data indicate graphite surface modification by a thin Kel-F film on highly polished electrodes. The film is disrupted by roughening the surface.

Electrochemical Microenvironment and Cell Behavior

Abstract No. 306

Cell Surface Electrochemistry and the Regulation of Tissue Growth and Repair

A. A. Pilla, Bioelectrochemistry Laboratory, Orthopaedic Research Laboratories, Dept. of Orthopaedic Surgery and Applied Chemistry and Chemical Engineering, Columbia University, New York, N.Y. 10032

The biological response of living cells to low level pulsating current of highly specific waveform is considered. It is shown that a detailed analysis of the effect of transport coupled interfacial processes such as specific adsorption and phase transfer can provide significant insight concerning the electrochemical steps which may be involved in cell regulation. This approach has led to the configuration of a family of current waveforms designed to excite surface and/or transport in a manner specific enough to modify the kinetics of cellular processes such as development, protein synthesis, etc.

Abstract No. 307

Electrical Stimulation of Cartilage Cell Proliferation

G. A. Rodan,* L. A. Bourret, A. Shteyer, and **L. A. Norton,** University of Connecticut Health Center, School of Dental Medicine, Dept. of Oral Biology, Farmington, Conn. 06032

Electrical perturbations produced by external electric field of approximately 1000 V/cm stimulate proliferation of cartilage and bone cells growing in culture. The stimuli act both on G_1 (pre DNA synthesis) and G_2 (pre mitosis) arrested cells, in the lag, logarithmic, and density-dependent-inhibited phases of growth. Changes in cyclic nucleotides, electrolyte fluxes, and cell adherence indicate that the transduction of the electrical stimulus into a biological signal occurs at the cell membrane and involves known physiological pathways of cellular communication.

Abstract No. 308

Modification of Cell Function by Pulsing Electromagnetic Fields

C. A. L. Bassett, D. Moran, H. R. Chokshi, and **R. Duriez,** Orthopaedic Research Laboratories, College of Physicians and Surgeons, Columbia University, New York, N.Y. 10032

Pulsing electromagnetic fields have been used clinically to heal nonunions, stimulate epiphyseal growth, and fill lytic lesions in bone. This study defines the effects of different pulses on cell function in tissue culture. Isolated chondrocytes and limb rudiments from chick embryos were grown in various pulsing fields. Depending upon the waveform DNA and RNA synthesis (measured by ^3H thymidine and uridine) can be selectively altered. Furthermore, calcium kinetics of chondrocytes can be increased or decreased. (This work was supported by NIH AM-07822 and NAS-9-14931.)

Abstract No. 309

Influence of Pulsating Electromagnetic Fields on Ca^{2+} Kinetics in Embryonic Chick Limb Rudiments

J-D. Monet, J. Assailly, and **M-C. Weber,** Centre de Technologie Biomedicale SCR 4, Hopital Necker, Paris, France, and **A. A. Pilla,*** Bioelectrochemistry Laboratory, Orthopaedic Research Laboratories, Dept. of Orthopaedic Surgery and Applied Chemistry and Chemical Engineering, Columbia University, New York, NY. 10032

In order to assess the influence of induced current waveform on the efficacy of the transfer of electrochemical information to living cell membranes the rate of Ca^{2+} uptake by isolated embryonic chick limb rudiments was studied. The effect of time of exposure up to 2 hr and waveform types were examined. Typical results show that when the waveform is properly configured for surface coupled membrane transport, significant increases (20-50%) in the amount of Ca^{45} present in the limb rudiment *vs.* its contralateral control are observed. The implications of this in the therapeutic application of bone repair are discussed.

Abstract No. 310

Effect of Electro-Magnetically Induced Electrochemical Information on Amputated Chick Embryo Limbs *In Vivo* and *In Vitro*

B. F. Sisken, J. F. Lafferty, and **I. Fowler,** Wenner-Gren Research Lab and Dept. of Anatomy, University of Kentucky, Lexington, Kentucky 40506, and **A. Pilla,** Bioelectrochemistry Laboratory, Orthopaedic Research Laboratories, College of Physicians and Surgeons, Columbia University, New York, N.Y. 10032

Chicken eggs incubated for 5 days at 39°C were aseptically opened by removing a square of shell. The right forelimb of each embryo was then amputated and the egg sealed by replacing the shell. The embryos were then returned to a 39°C atmosphere to continue development; some of these eggs were placed in a plastic holder set inside an incubator fitted with 3 different devices (supplied by Electro-biology Incorporated, New Jersey) that induced

electromagnetic current of 3 different waveforms. The effect of these induced fields on the development of the amputated limb stump is presented.

Abstract No. 311

Electrical Altered Adult Newt Lens Regeneration

S. D. Smith, Dept. of Anatomy, University of Kentucky, College of Medicine, The A. B. Chandler Medical Center, Lexington, Ky. 40506

Adult newts were subjected to transcorneal lentectomy following Ms-222 anaesthesia. Tiny (1 mm) Ag-Pt bimetallic couples were implanted into the vitreous body with either the Ag(−) or Pt(+0) electrode near the dorsal margin of the iris, from which the new lens develops. Controls consisted of animals with either simple lentectomy, or lentectomy and Ag or Pt wire implants. Results indicate that the electrical currents generated affect both the rate of development and the morphology of the regenerated lenses.

Abstract No. 312

Divalent Cations and the Development of Dormant Sponge Gemmules

T. L. Simpson* and **K. M. Ostrom,** Dept. of Biology, University of Hartford, West Hartford, Conn. 06117

Dormant gemmules of the fresh water sponge *Spongilla lacustris* can be temperature stimulated to undergo germination (cell division) and hatching (cell motility). Both processes can be inhibited by appropriate concentrations of divalent cations (Zn, Mn, Ni, etc.) but not by calcium, which can overcome this inhibition. Divalent cations do not act osmotically although high concentrations (20 mosmolar) of Na^+ and K^+ may inhibit in this way. Zinc binds intracellularly both to the 600g pellet and supernatant; binding to the former is less reversible.

Abstract No. 313

Gap Junction Conductance: Dependence on Internal *p*H

D. C. Spray,* A. L. Harris, M. V. L. Bennett, J. E. Brown, and **R. B. Hanna,** Albert Einstein College of Medicine, Bronx, N.Y. 10461

Gap junctions provide low resistance pathways between cells of many tissues. Treatment of isolated pairs of blastomeres from killifish or axolotl embryos with agents expected to decrease internal *p*H (100% CO_2, acetate, proprionate) quickly and reversibly reduce junctional conductance without affecting intracellular Ca^{++} levels as measured by aequorin luminescence. Lowering of external *p*H is without effect. CO_2 uncoupling is associated with an apparent increase in P-face particle density seen in freeze fracture.

Abstract No. 314

Cathode Mediated Bone Proliferation

J. A. Spadaro, Orthopedic Research Laboratory, V. A. Medical Center, Syracuse, N.Y. 13210

Potentiostatic and galvanostatic d-c polarization curves (*in vitro* and *in vivo*) for several metal electrodes used for electrical bone stimulation, suggest that oxygen reactions mediate the increase in osteoblastic activity nearby. For current high enough to produce hydrogen evolution, necrosis has generally been reported in animal experiments. On this basis, a framework for specific mechanism(s) can be proposed for electrode-induced bone growth.

Abstract No. 315

Cyclic Voltammetry of Implantable Metal Electrodes: Preliminary Studies

M. Reichmanis, Orthopedic Research Laboratory, V.A. Medical Center, Syracuse, N.Y. 13210

The current-voltage characteristics of several commonly used implantable metal electrodes were studied by means of cyclic voltammetry. Both positive and negative potentials (*vs.* SCE) were examined at various sweep rates. Data are presented for *in vitro* and *in vivo* measurements.

Abstract No. 316

The Regulation of Ion Transport by Membrane Proteins

M. Blank, Dept. of Physiology, Columbia University, College of Physicians and Surgeons, New York, N.Y. 10032

The red cell membrane proteins, spectrin and actin, are present as a layer on the inner face of the membrane. At an interface, these proteins form films whose mechanical properties approximate those of the intact membrane. The film permeabilities to ions are on the order of 10^{-4} cm/sec, and to uncharged species they are very much greater. The ionic permeability is very sensitive to the *p*H, especially in the region of the protein isoelectric point. (This work was supported by NSF, PCM 76-11676.)

General Session

Abstract No. 317

Mechanism of Electrochemical and Enzymatic Oxidation of Uric Acid

M. Z. Wrona and **G. Dryhurst,*** Dept. of Chemistry, University of Oklahoma, Norman, Okla. 73019

The electrochemical oxidation of a number of uric acid derivatives has been studied by means of linear and cyclic sweep voltammetry, coulometry, product identification, thin-layer spectroelectro chemistry, and double potential step chronoamperometry. The electrochemical oxidation of these compounds has been carefully compared to their peroxidase-catalyzed oxidation. Spectral, electrochemical, and kinetic evidence supports the conclusion that the electrochemical oxidation mechanism is identical to the enzymatic oxidation mechanism.

Abstract No. 318

Application of Electrochemistry to the Flavoproteins Glucose Oxidase and Flavodoxin

M. T. Stankovich, Dept. of Chemistry, University of Massachusetts, Amherst, Mass. 01003

Flavodoxin and glucose oxidase catalyze electron transfer reactions; riboflavin is the active site of electron transfer. The enzymes catalyze vastly different kinds of reactions; glucose oxidase catalyzes a simultaneous two-electron transfer from glucose to oxygen; flavodoxin catalyzes nonspecific one-electron transfers from NADH. The electrochemical behavior of the enzymes has been studied in order to relate the electron transfer properties (redox potential, number of electrons transferred, kinetics) to the reaction mechanism of the two enzymes. Enzymes were studied by spectroelectrochemical techniques using mediator dyes; direct electron transfer from electrode to enzyme was studied using differential pulse polarography.

Abstract No. 319

Electrochemically Activated Binding of Polycyclic Aromatic Hydrocarbons to DNA

D. A. Tryk* and **S.-M. Park,** Dept. of Chemistry, University of New Mexico, Albuquerque, N.M. 87131

A series of carcinogenic and noncarcinogenic polycyclic aromatic hydrocarbons have been subjected to constant potential anodic electrolysis in an organic solvent phase in contact with an aqueous solution of calf thymus DNA. The extents of binding have been determined by u.v. absorption, fluorescence, and circular dichroism spectroscopy in order to evaluate a correlation between the extents of binding and the carcinogenicities. Work is being done to determine the reactive species involved and the exact nature of the binding in each case.

Abstract No. 320

Electrochemical Synthesis of N-Alkylformamides

D. Cipris, Allied Chemical Corp., Corporate Research Center, Morristown, N.J. 07960

Dimethylformamide, diethylformamide, and other mono- and disubstituted N-alkylformamides are produced

from carbon monoxide and the corresponding alkylamine by electrolysis in methanolic solution. The electrolysis is conducted in a one-compartment cell at 20°-40°C under a carbon monoxide pressure up to 100 atm. The reaction is highly dependent on the electrolyte employed. The current efficiencies exceed 100% (based on 1 **F**/mole of amide). Electrochemical generation and continuous regeneration of a catalytic species appear responsible for the observed high reaction rates and high yields of formamides. The process is described and the reaction mechanism discussed. The possible advantages over existing chemical processes are pointed out.

Abstract No. 321

A Chronoamperometric and Coulometric Study of 4-Substituted Catechols

M. D. Ryan* and **A. Yueh,** Marquette University, Milwaukee, Wis. 53233

The oxidation of 4-substituted catechols to their o-quinone was studied by the use of chronoamperometry and coulometry in order to understand the reaction mechanism of the quinone. Kinetic studies using double-potential step chronoamperometry indicate that a coupling reaction between the quinone and a catechol molecule was the main kinetic pathway. From cyclic voltammetry, no new electroactive intermediates were observed for most of the catechols. In order to obtain information on the identity of the intermediates, large scale electrolysis of catechol was performed and the identity and amount of the catechol and possible intermediates were monitored by gas or liquid chromatography. The results show that the polymerization reaction is extremely rapid once it has been initiated. An electrochemical study of some of the intermediates also confirm this conclusion. The only exception is 3,4-dihydroxypropiophenone where the intermediate is stable enough to be seen by cyclic voltammetry.

Abstract No. 322

Fishes with Electric Field Detection Capabilities

Ad. J. Kalmijn, Woods Hole Oceanographic Institution, Woods Hole, Mass. 02543

Sharks, skates, and rays are equipped with highly sensitive electroreceptors, which enable them to detect d-c and low-frequency voltage gradients as low as 0.01 μV/cm. Their electric sense plays an important part in predation where in the final attack they sharply cue in on the bioelectric fields of their prey. They also receive orientational cues from the electric fields of ocean currents and from the voltage gradients induced by their own swimming through the earth's magnetic field.

PHYSICAL ELECTROCHEMISTRY

The Third Symposium on Electrode Processes

Abstract No. 323

Similarities and Differences Between Electron and Proton Transfers at Electrodes and in Solution

R. A. Marcus, Noyes Laboratory of Chemical Physics, California Institute of Technology, Pasadena, Calif. 91125

Electron and proton transfer reactions (including the hydrogen overvoltage reaction) have in common the transfer of a light particle. Under certain conditions, Franck-Condon considerations apply to a proton transfer, just as they do to electron transfers, and the theory of the two processes is then rather similar. Under other conditions, the change in charge distribution is not so abrupt and a more conventional approach applies. The conditions are defined using potential energy surfaces and a unified treatment is described.

Abstract No. 324

Concepts in Quantum Mechanical Tunneling in Systems of Electrochemical Interest

C. B. Duke, Xerox Corp., Xerox Webster Research Laboratory, Rochester, N.Y. 14644

A survey is presented of the various tunneling mechanisms which can influence the kinetics of electron transfer in electrochemical systems. First, a consideration of the localization of the initial and final states is presented with emphasis on describing the influence of fluctuations on electron states in noncrystalline media. Second, elastic and inelastic tunneling processes, respectively, are described between various types of electron states. Third, we discuss the reversibility of tunneling transitions between localized states. These considerations permit us to survey the mechanisms for the dependence of electron transfer on molecular motions. We conclude with a brief indication of some of the problems entailed in identifying these elemental mechanisms with the actual kinetics observed in coupled electron transfer processes involving many separate independent electron-transfer steps.

Abstract No. 325

Some Observations of Quantum Mechanics in Electrochemical Reactions

J. O'M. Bockris, Dept. of Chemistry, Texas A&M University, College Station, Texas 77843

A sketch is given of the concepts which have developed in the course of work upon the quantum theory of electrode processes. The work has gone down two lines. One originated with papers by Oliphant and Moon (generally attributed to Gurney) and the other originated in a paper due to Libby. The pro's and con's attaching to each of the molecular (Oliphant) and the dielectric (Libby) approach, respectively, are discussed.

Abstract No. 326

A Model for Adsorbed States on Metal Electrodes

W. Schmickler, Institut für Physikalische Chemie der Universität Bonn, 5300 Bonn 1, Germany

The Anderson model for adsorption from the gas phase is extended to the electrochemical case. Self-consistent equations for the partial charge-transfer coefficient of an adsorbed species are derived and applied to alkali adsorption; the results are compared with experimental data. A model is presented for electron exchange between a metal/adsorbate system and a redox electrolyte. The current/potential characteristics of this process are calculated in dependence on various system parameters.

Abstract No. 327

The Measurement and Interpretation of Stochastic Effects in Electrochemistry and Bioelectrochemistry

M. Fleischmann,* C. Gabrielli, M. Labram, and **A. Sattar,** Dept. of Chemistry, The University, Southampton S09 5NH, Hants, England

The fluctuations generated by chemical reactions may be observed in at least one of two ways: first as the statistics of ensembles of transients; second by determining the autocovariance function or maybe the power spectral density of the appropriate variable assuming stationarity. Measurements on electrochemical systems using both approaches are illustrated with the following examples: (*i*) the two-dimensional nucleation and crystal growth of metals, (*ii*) the two-dimensional nucleation of pores in lipid bilayers, (*iii*) the three-dimensional nucleation and crystal growth of metals and semiconductors, (*iv*) the kinetics of lattice formation in electrocrystallization reactions, (*v*) the kinetics of electrocatalysis. It is shown that for many systems a single molecular event leads to a large realizable fluctuation [e.g., (*i*), (*ii*), (*iii*), and (*v*)] especially if the size of the system being investigated is made small. The new kinetic information which may be obtained from quantities related to the second (and higher) moments of the reaction rates is delineated.

Abstract No. 328

Coupling of Electrode Kinetics and Space Charge Dynamics in Unsupported Systems

D. R. Franceschetti and **J. R. Macdonald,*** Dept. of Physics and Astronomy, University of North Carolina, Chapel Hill, N.C. 27514

The coupling of space charge dynamics and electrode kinetics in unsupported liquid and solid material/electrode systems is discussed, with emphasis on exact theories of small-signal response and on numerical simulation of large-signal behavior for systems with and without sig-

nificant compact layers. The usefulness of small-signal response measurements on systems subject to a constant biasing potential difference is examined, and the representation of such response by equivalent circuits suitable for use in data analysis is considered.

Abstract No. 329

Electrode Reactions of Excited Molecules

H. Gerischer, M. T. Spitler, and **F. Willig,** Fritz-Haber-Institut der Max-Planck-Gesellschaft, D-1000 Berlin 33, Germany

Redox potentials of excited molecules are shifted into negative direction for reduction and into positive direction for oxidation. They can be derived from ground state redox potentials and spectroscopic data. Semiconductors and insulators can be used as a probe for the correlations between redox potentials of molecules in electrolytes and energy band positions in solids. Such correlations were investigated for a series of dyes and electrode materials. These experiments and some reasons for deviations are discussed.

Abstract No. 330

Semiconductor Photoelectrochemical Cells

A. J. Bard, Dept. of Chemistry, The University of Texas at Austin, Austin, Texas 78712

The principles of photoelectrochemical cells utilizing semiconductor electrodes are described. The results of recent studies of semiconductor electrodes in nonaqueous solvents, such as acetonitrile and liquid ammonia, are given and photovoltaic cells utilizing such solvents described. Examples of the application of electrochemical measurements with semiconductor electrodes to the design of heterogeneous photocatalytic and photosynthetic systems are also discussed.

Abstract No. 331

The Thionine-Coated Electrode for Photogalvanic Cells

W. J. Albery,* **A. W. Foulds,** and **A. R. Hillman,** Dept. of Chemistry, Imperial College, London SW7 2AY, England

The successful operation of a photogalvanic cell requires that the illuminated electrode discriminates between the photogenerated species or else the electrode merely catalyzes the back reaction. In the iron thionine cell a thionine-coated electrode can be prepared by oxidizing at 1.3V. A stable coating of up to 20 monolayers of thionine is laid down in a few minutes. Such an electrode discriminates between organic couples like thionine or quinones, but rate constants for inorganic couples such as Fe^{3+}, $Fe(CN)_6^{3-}$ or even $Ru(bpy)_3^{3+}$ are very much reduced.

Abstract No. 332

Kinetics of Adsorption Processes

J. W. Schultze, Institut für Physikalische Chemie und Quantenchemie der Freien Universität Berlin, Berlin, Germany

In most adsorption systems, the rate determining step is the transfer of a heavy particle from the outer Helmholtz plane to the metal surface. In addition to that, surface diffusion and reorientation processes can be rate determining in case of strong lateral attraction which has been found for metal monolayers. Galvanostatic and potentiostatic transients were measured in dependence on coverage and surface structure. Results are discussed for transfer processes and surface diffusion as well.

Abstract No. 333

Electrochemical Studies on Different Glassy Carbon Electrodes. I. Electron Transfer Kinetics

L. Bjelica, R. Parsons,* and **R. M. Reeves,** Laboratoire d'Electrochimie Interfaciale du C.N.R.S. Meudon-Bellevue, France

Cyclic voltammetry was used to study the kinetics of six simple electron transfer reactions at the interface glassy carbon/electrolyte solution. Carbons made at various carbonizing temperatures were studied in an attempt to relate the kinetics to solid state properties. Surface state and surface preparation are of great importance and often obscure the bulk effects. Furthermore the behavior of the electron transfer reactions appears to be specific indicating even for these reactions a marked interaction with the carbon surface.

Abstract No. 334

The Estimation of Surface Activities and Their Role in the Kinetics of Simple Electrode Reactions

W. R. Fawcett, Guelph-Waterloo Centre for Graduate Work in Chemistry, Dept. of Chemistry, University of Guelph, Guelph, Ontario, Canada N1G 2W1

The inadequacies of the traditional Frumkin model of double layer effects are considered. These include the possibility that the reaction site is not coincident with the outer Helmholtz plane, discreteness-of-charge effects related to the formation of images in the electrode and diffuse layer, and to finite reactant size, and attractive ion-ion interactions in the inner layer. The variation in electrostatic contributions to reactant and product activity are examined as a function of electrode potential and reactant distance from the electrode. Data recently obtained in this laboratory are discussed in the light of this analysis.

Abstract No. 335

Factors Determining Type of Deposit in Electrocrystallization of Metals

A. R. Despić, Faculty of Technology & Metallurgy, University of Beograd, Karnegijeva 4, 11000 Beograd, Yugoslavia

Three basic types of metal deposits are recognized: (*i*) compact layers with predominant lateral growth of crystals to coalescence, (*ii*) disperse deposits with predominant growth normal to the surface, and (*iii*) disperse deposit without any preferential direction of growth (granular deposits). Basic factors determining the type of growth are discussed. They include the effect of the substrate, effects of additives or impurities in solution, as well as the effect of slow transport of depositing ions. Different substrates have been investigated for the deposition of zinc and cadmium and the type of deposit is related to the presence or absence of underpotential deposition. It is also shown that granular growth is favored under conditions when strong adsorption of additives or impurities takes place.

Abstract No. 336

The Electrode Kinetics of Metal Deposition and Dissolution

J. A. Harrison, Dept. of Physical Chemistry, University of Newcastle upon Tyne, Newcastle upon Tyne, England

The difficulties of measuring the electrode kinetics of metal deposition reactions on real metal surfaces have largely been overcome by using a computer controlled measuring and evaluation system. A brief description of the system, which is capable of making all known types of electrode-kinetic measurement, is given. Current-potential and impedance data obtained at the rotating disk for the deposition of Cu, Cd, Zn from simple aqueous solutions are presented. Possible reaction schemes and methods of analysis of the data are discussed.

Abstract No. 337

Some Questions on the Significance of Multiple-State Underpotential Deposition and Its Dependence on Ion Adsorption

B. E. Conway and **H. Angerstein-Kozlowska,** Dept. of Chemistry, University of Ottawa, Ottawa, Ont., Canada K1N 9B4

The following questions concerning the significance of multiple-state adsorption in electrodeposited monolayers are addressed: (*i*) what is the significance of redistribution of electrodeposition of atoms amongst multiple states in the presence of various anions or cations, adsorbed or free in the double layer; (*ii*) what is the role of water adsorption and orientation; (*iii*) how are ion effects to be interpreted in relation to u.p.d. profiles for single crystal surfaces; (*iv*) what is the charge for monolayer adsorption of H in the light

of cation effects; (ν) does some intrinsic multiplicity of chemisorption states remain on single-crystal surface planes? Some general conclusions are offered.

Abstract No. 338

Studies of Underpotential Silver on Platinum and Gold

T. M. Riedhammer, L. S. Melnicki, and **S. Bruckenstein,*** Dept. of Chemistry, State University of New York at Buffalo, Buffalo, N.Y. 14214

The isotherms for underpotential deposition (UPD) of silver on polycrystalline gold and silver were determined. At potentials very anodic of the equilibrium potential for a bulk silver electrode, the UPD electrosorption valency was significantly less than unity, and approached unity only near the equilibrium potential. More than three layers of UPD silver deposit just anodic of the equilibrium potential. The reduction of oxygen and of hydrogen are inhibited by UPD silver on gold or platinum. Current-voltage curves for oxygen reduction at pure silver closely resembled those for 3-4 atom layers of UPD silver on both substrates. UPD silver on both substrates inhibits hydrogen reduction. However, the current-potential curves for hydrogen evolution at 100 atom layer thick UPD deposits occurred more readily than on pure silver.

Abstract No. 339

Electrochemical Catalysis by Foreign Metal Adatoms

J. D. E. McIntyre,* **S. Gottesfeld,** and **W. F. Peck, Jr.,** Bell Laboratories, Murray Hill, N.J. 07974

Underpotential adsorption of heavy metal atoms such as Tl, Pb, and Bi on noble and transition metal substrates markedly catalyzes several different types of electrochemical reactions, *e.g.*, electroreduction of O_2, electrooxidation of organic fuels, and electrodeposition of metals. The relative importance of both surface geometric and electronic structure factors in enhancing the reaction rates have been examined by use of combined *in situ* electrode kinetic and optical spectroscopy techniques. Owing to the simple atomic nature of the metallic adsorbates, it is proposed that investigations of such modified electrodes may provide a link between studies at the atomic level of processes occurring at solid-vacuum and solid-gas interfaces and the operation of real catalytic systems.

Abstract No. 340

On the Investigation of Very Fast Reactions in Electrochemisty

Ch. Bernstein and **W. Vielstich,*** Institute of Physical Chemistry, University of Bonn, Bonn, Germany

For the investigation of fast electrode reactions transient techniques or steady-state methods may be used. The feasibilities of the relaxation methods are limited by double layer charging and adsorption effects. The applicability of the stationary techniques depends upon the attainable mass transfer rates. A ring electrode in turbulent pipe flow represents a suitable arrangement for obtaining high rates of mass transfer up to 0.2 cm/sec. This electrode was used to measure the kinetics of the system $Fe(bipy)^{2+}/Fe(bipy)^{3+}$, the fastest charge transfer reaction in aqueous solution on platinum and to investigate the very fast dissociation reaction of the chloroacetic acid with a rate constant of 10^7 sec^{-1}.

Abstract No. 341

Electrode Kinetics and Conductivity in Low Dielectric Constant Solvents

E. Gileadi, Institute of Chemistry, Tel-Aviv University, Ramat-Aviv, Israel

Unexpectedly high conductivities have been observed in a number of low dielectric constant, nonpolar solvents. In concentrated solutions of Al_2Br_6 and KBr in aromatic hydrocarbons (which can serve as practical plating baths for aluminum), the conductivity is probably due to hopping of ions between ionic aggregates. A hopping mechanism of conductivity was confirmed for the Br^- ion in mixtures of nitrobenzene and bromine and in pure bromine. Unusually high conductivities were also observed for the bromide ion in solid bromine.

Abstract No. 342

Electrode Kinetics and Double Layer Structure at Solid Electrodes

K. L. Guyer, S. W. Barr, R. J. Cave, and **M. J. Weaver,*** Dept. of Chemistry, Michigan State University, East Lansing, Mich. 48824

The electrode kinetics of various Co(III)-$(NH_3)_5X$ complexes containing neutral and anionic ligands X have been monitored at Ag, Pt, and Au aqueous interfaces as a first step in exploring reactivity at electrocatalytic surfaces of metal complexes that are known to follow well-defined inner and outer sphere mechanisms at Hg electrodes. Most reactions proceed via rapid inner sphere pathways at clean surfaces. The rates for outer sphere pathways for each reactant were obtained at surfaces that were modified by irreversible monolayer adsorption of I^-, thiourea, and metal complexes. These results allow the factors favoring inner over outer sphere pathways to be explored in detail.

Abstract No. 343

Hydrogen-Involving Reactions in the Potential Region of the Alpha Phase on Smooth Palladium

M. W. Breiter, General Electric Co., Research and Development Center, Schenectady, N.Y. 12301

Hydrogen adsorption on smooth clean palladium is accompanied by dissolution of hydrogen in the bulk. The usefulness of potential steps, voltammetry, and impedance measurements for the distinction between adsorbed and dissolved hydrogen is discussed. Both the Volmer reaction and the transfer of hydrogen from adsorption sites to sites below the surface are relatively rapid. Isotherms of hydrogen adsorption are of the Temkin type. The linear relation between the logarithm of the concentration of dissolved hydrogen and electrode potential is interpreted.

Abstract No. 344

Optical and Electrochemical Studies of Adsorbed Transition Metal Complexes and Their O_2 Electrocatalytic Properties

E. Yeager, J. Zagal, B. Z. Nikolic, and **R. R. Adzic,** (Present address: University of Belgrade, Belgrade, Yugoslavia), Case Laboratories for Electrochemical Studies and Dept. of Chemistry, Case Western Reserve University, Cleveland, Ohio 44106

Water soluble transition metal macrocyclics such as the tetrasulfonated phthalocyanines (TSPC) are strongly adsorbed on noble metal and graphite electrodes in acid and alkaline electrolytes. The CoTSPC is a good catalyst for O_2 reduction to peroxide and the FeTSPC for the over-all 4-electron reduction. The optical properties of the adsorbed species have been examined using reflectance spectroscopy and evidence obtained for the O_2 adduct with the adsorbed complexes.

Abstract No. 345

Proton Transfer in Oxygen Reduction: A Discussion

A. J. Appleby, Electric Power Research Institute, Palo Alto, Calif. 94303

Proton transfer theories have normally only been considered in terms of hydrogen evolution. However, both electrochemical and chemical proton transfer steps are of importance in other processes, in particular oxygen reduction. The types of models and rate equations for such processes are considered from the viewpoint of the method of energy transfer to the bond to be broken. Some basic assumptions (Born-Oppenheimer, the Born-Bjerrum inertial term) are discussed.

Abstract No. 346

Models for the Photoelectrolytic Decomposition of Water at Semiconducting Oxide Anodes

J. M. Kowalski,* **H. L. Tuller,** and **K. H. Johnson,** Dept. of Materials Science and Engineering, M.I.T., Cambridge, Mass. 02139

A number of semiconducting oxide electrodes have been shown to assist in the production of hydrogen by photoelectrolytic decomposition of water. In this paper we begin by reporting on results of $X\alpha$ molecular orbital calculations

which provide insight into the electronic interaction between water and a TiO_2 semiconducting surface. We then present preliminary experimental results which provide a means for testing some of the implications of the theoretical models.

Abstract No. 347

Oxygen Reduction on Platinum in Trifluoromethanesulfonic Acid and Phosphoric Acid

W. E. O'Grady, E. J. Taylor,* and **S. Srinivasan,** Dept. of Energy and Environment, Brookhaven National Laboratory, Upton, N.Y. 11973

Rotating ring-disk studies of oxygen reduction in 25-75 v/o TFMSA and 85% H_3PO_4 have been conducted. The kinetics and mechanism have been determined on a reduced oxide free platinum surface at room temperature. In order to completely analyze the ring-disk data the viscosities, oxygen solubilities and oxygen diffusion coefficients have also been determined. A comparison of the reaction kinetics and mechanisms in these two acids is made.

Abstract No. 348

Some Aspects of the Reduction of Oxygen at a Platinum-Oxygen Alloy Diaphragm

J. P. Hoare, General Motors Research Laboratories, Electrochemistry Dept., Warren, Mich. 48090

The steady-state galvanostatic polarization curve was obtained on the front side of a Pt diaphragm in contact with O_2-stirred $2N$ H_2SO_4 solution while the back side was in contact with concentrated HNO_3. From low oxygen overvoltage (O_2-η) measurements it is shown that the rest potential is the reversible O_2 potential. The rate of O_2 reduction on the Pt-O alloy diaphragm is lower at high current densities than on a bright Pt cathode. At very high current densities the system is driven into the H_2-evolution region where the H_2-η is close to the literature values for the H_2-η on bright Pt. When the system was returned to open circuit, the rest potential returned to the normal oxygen potential after about 24 hr. This time delay represents the time required to repair the complete layer of adsorbed oxygen atoms which had been removed by the strong cathodic current.

Abstract No. 349

New Materials for Oxygen Reduction: Interest of Iron Naphthalocyanines

G. Magner, M. Savy,* and **G. Scarbeck,** Laboratoire d'Electrochimie Interfaciale du C.N.R.S., Meudon-Bellevue, France

Iron naphthalocyanine has been systhesized and characterized by x-ray diffraction, optical spectroscopy and ESR. Loadings have been prepared *in situ* on carbon black supports. They have been investigated by voltage sweep using ultrathin electrodes and ring-disk techniques. On the cathodic side the activity remains always higher than that of the support material after several cycles to oxygen evolution. Compared to a dimer of FePC, evidence for a low level of H_2O_2 production has been found.

Abstract No. 350

Effect of Glutathione on Electroreduction of Oxygen on Iron Phthalocyanine Layers

O. Contamin, E. Levart, and **M. Savy,*** Laboratoire d'Electrochimie Interfaciale du C.N.R.S., Meudon-Bellevue, France

O_2 reduction on FePc in presence of glutathione has been investigated by cyclic voltammetry and impedance technique in neutral buffered solutions. Introduction of glutathione causes an inhibition followed by an increase of the C.D. The impedance at H.F may be represented by a capacitance in parallel with a resistance. For L.F evidence for a pseudoadsorption impedance (in parallel with a transfer diffusion impedance) has been obtained; this increases with increasing cathodic polarization. Impedance variations *vs.* glutathione concentration provide information on adsorption and reduction effects.

Abstract No. 351

Mechanisms and Kinetics of O_2 Evolution at Ruthenium Oxide Electrodes

J. F. Wolf, S. L. Soled, and **A. Damjanovic,** Allied Chemical Corp., Corporate Development Center, Morristown, N.J. 07960

Kinetics of O_2 evolution are determined at ruthenium oxide electrodes, prepared in different ways, in basic solutions of different pH. For most of the electrodes, Tafel parameters, at all pH's, are close to $2.3\,RT/F$ and pH dependences, $(dV/dp\mathrm{H})_i$, to $-2.3\,RT/F$. The dependence of i_o on the oxide electrode preparation and electrode pretreatment, as well as on electrode composition are discussed. Mechanisms and the kinetics of the reaction are discussed and compared to the mechanisms and kinetics at platinum electrodes under similar conditions.

Abstract No. 352

In Situ LEED-Auger-Thin Layer Electrochemical Studies of the Underpotential Deposition of Pb on Au Single Crystals

P. Hagans, A. Homa, and **E. Yeager,** Case Laboratories for Electrochemical Studies and Dept. of Chemistry, Case Western Reserve University, Cleveland, Ohio 44106

Linear sweep voltammetry has been used to examine the underpotential deposition of Pb on Au single crystals which have been characterized by LEED and shown to be clean by Auger. The electrochemistry is accomplished using a special transfer system and a thin layer cell which uses pure Pb as the counter and reference electrode. Each low index surface exhibits distinct features on the UPD portion of the voltammograms. Following the electrochemical measurements, the single crystals with the Pb UPD layers have been reexamined with LEED and Auger. (This research was supported by ONR and NASA).

Abstract No. 353

Foreign Metal Adatoms as a Probe in the Study of Some Electrocatalytic Reactions

R. R. Adžić, M. Spasojević, and **R. Atanasoski,** Institute of Electrochemistry, ICTM, and Center for Multidisciplinary Studies, University of Belgrade, Belgrade, Yugoslavia

It has been recently shown that the foreign metal adatoms obtained by underpotential deposition can considerably change the catalytic properties of electrode surfaces. Striking catalytic and inhibitory effects have been found in several instances. Besides that, the studies of electrode reactions on surfaces modified by foreign metal adatoms offer in certain cases information on the mechanisms of reactions. This has been found for: (*i*) oxidation of formic acid on Pt, Rh, Pd and Au, (*ii*) hydrogen evolution on Pt and Au, and (*iii*) oxygen reduction on Pt. For the first reaction the catalytic effects, while for the last two, the inhibition gave some evidence on the mechanism of these reactions. A detailed account on these experiments is presented.

Abstract No. 354

Yessin-Markov Shifts, $E_{1/2}$ Shifts of Complexes, and the Langmuir Isotherm

R. Heyrovská, Na Šťáhlavce 6, Praha 6, Czechoslovakia 160 00

The experimental Yessin-Markov potential shifts, $\triangle E_m$, as well as the $E_{1/2}$ shifts of reducible metallic ions in solutions of complex forming ions adsorbable/nonadsorbable on the electrode can both be represented by an equation analogous to the Szyszkowski equation which has been already interpreted in terms of the Langmuir isotherm. It is concluded that the heterogeneous adsorption forces and the homogeneous coordination forces are of similar nature and are probably of the charge-transfer type.

Abstract No. 355

Some Common Features of Monolayer Formation on Noble Metals

H. Angerstein-Kozlowska, B. E. Conway, B. Barnett, and **J. Mozota,** Dept. of Chemistry, University of Ottawa, Ottawa, Ont., Canada K1N 9B4

Electrostatic, specific interaction, and blocking effects of electrochemically unreactive anions and cations on the initial stage of oxidation of Au, Pt, Ir, and Ru are discussed. Common features of monolayer oxide formation on noble metals are stressed in relation to observed differences which can be ascribed to different extents of competition in ion adsorbability. Factors determining these effects are distinguished.

Abstract No. 356

The Influence of Inert Ions on Surface Oxide Film Formation and Reduction at Gold Electrodes

H. Angerstein-Kozlowska, B. E. Conway, and **B. Barnett,** Dept. of Chemistry, University of Ottawa, Ottawa, Ont., Canada K1N 9B4

The kinetics of oxide film formation and reduction at Au are shown to be intimately related to ion adsorption and desorption processes. The several states of surface oxide which can be distinguished on Au are shown to be critically dependent on anion or cation adsorption, *e.g.*, in ClO_4^-, SO_4^{2-}, CO_3^{2-}, OH^-, and Ba^{++} ion solutions at various concentrations, including trace levels, and at various temperatures. Similar distinguishable states of Pt oxide films can also be demonstrated on the potentiodynamic reduction curve.

Abstract No. 357

Enhancement of Anodic Photocurrents at Silver Electrodes in Halide Solutions

M. A. Butler, Sandia Laboratories, Div. 5154, Albuquerque, N.M. 87185

Anodic photocurrents at silver electrodes, previously observed by Sass and Gerischer, may be enhanced over an order of magnitude by addition of halide ions to the electrolyte. The potential dependence and spectral response curves suggest growth of a silver halide surface layer as the mechanism for this effect. The relationship of the spectral response to the surface electronic structure is discussed. [This work was supported by the Materials Sciences Program, Division of Basic Energy Sciences, U.S. Department of Energy under Contract AT(29-1)-789.]

Abstract No. 358

Fundamental Researches on $Ga_xIn_{1-x}P$ ($0<x<1$) Electrodes for Solar Energy Conversion

A. M. Redon, J. Vigneron, A. M. Guinard-Baticle, and **J. L. Sculfort,** Laboratoire d'Electrochimie Interfaciale du CNRS, Meudon-Bellevue, France

The semiconductor series $Ga_xIn_{1-x}P$ is of interest because the bandgap can be varied between 1.3 and 2.6 eV as x varies between 0 and 1. A study of the basic physical properties of electrodes of this type in contact with various aqueous solutions has been made. The bandgap and the transition mode were obtained from the dependence of the photocurrent on the wavelength of the incident light. These measurements also yield the flatband potential which compares well with that found from impedance measurement. The bandgap corresponding to maximum efficiency has been determined. A number of redox systems were studied with the aim of blocking the anodic dissolution and of increasing the efficiency.

Abstract No. 359

Investigation and Evaluation of Photoelectrochemical Cells by Photothermal Spectroscopy

G. H. Brilmyer,* Dept. of Chemistry, University of Texas, Austin, Texas 78712, **A. Fujishima,** Dept. of Chemistry, University of Tokyo, Hongo, Bunkyo-Ku, Tokyo, Japan, and **A. J. Bard,** Dept. of Chemistry, University of Texas, Austin, Texas 78712

The photooxidations of various redox species at electrodes of the n-type semiconductors CdS, TiO_2 and GaAs (single crystal) were investigated using photothermal spectroscopy. The variation of the observed thermal changes in the electrode during the photoassisted reaction with potential could be related directly to the amount of light energy utilized. Measurements made as a function of applied potential can therefore be used to determine the quantum and power efficiencies of the over-all process without absolute calibration of the excitation source. Both empirical and theoretical treatments of this technique are discussed.

Abstract No. 360

Evidence for Adsorption of Dimethyl Phenazine on Platinum Using A-C Diagnostics

K. K. Kanazawa* and **A. F. Diaz,** IBM Research Laboratory, San Jose, Calif. 95193

The electrochemical oxidation on platinum electrodes of dimethyl phenazine was studied using ramp and a-c voltammetry. The ramp voltammograms showed a rate-dependent anodic-cathodic peak separation, the separation decreasing with increasing ramp rate. Both the fundamental and second harmonic currents contain a component in quadrature with the a-c excitation which increases linearly with frequency and a component at $\pi/4$ from the a-c excitation which increases as the square root of frequency. These results are discussed in terms of currents due to adsorbed species and due to diffusing species.

Abstract No. 361

Some Statistical Aspects of the Growth of Crystals in Corrosion, Metal Deposition, and Anodic Film Formation

S. Fletcher, R. G. Barradas, J. D. Porter, and **R. Bowie-Reed,** Dept. of Chemistry, Carleton University, Ottawa, Ont., Canada K1S 5B6

The formation of solid crystalline phases is a common feature of many electrochemical reactions including corrosion, metal deposition, and anodic and cathodic film formations. Unfortunately the problem of modeling the crystal growth processes in an accurate and verifiable way has raised a number of serious theoretical difficulties which as yet have not been resolved. Among the many difficulties we address ourselves in the present paper to three important questions: (*i*) What is the spatial distribution of growth centers, and how may this be statistically described? (*ii*) How may the growth geometry of individual crystals be recovered from experimental data? (*iii*) How do crystals of the emergent phase interact with each other and with the boundaries of the electrode? The statistics of a large number of potentiostatic experiments is then theoretically described, and we indicate how the geometries and the spatial distribution of crystals may be investigated via an analysis of the moments of the experimental (i-t) responses.

General Session

Abstract No. 362

An Examination of the Basic Postulates of Surface Chemistry: A Variational Calculus Analysis of the Rotating-Drop Experiment

H. M. Scholberg, Bedford, Mass. 01730

A rigorous demonstration is given showing that it is impossible to describe the excess energy in any surface by the use of a single parameter, the surface tension, without violating the laws of motion. The addition of a second parameter, the flexural rigidity, is shown to be adequate to explain published data on the system n-hexadecane/glycerol, and to demonstrate that for small radii of curvature, such as are present in the important industrial surfaces, the curvature parameter contributes orders of magnitude more energy to the surface than does the surface tension.

Abstract No. 363

High Precision Computer Controlled Electrocapillary Measurements

D. M. Mohilner* and **T. Kakiuchi,** Dept. of Chemistry, Colorado State University, Fort Collins, Colo. 80523

Higher precision electrocapillary measurements required for research on the temperature coefficient of electrosorption have necessitated several modifications in the design of the computer controlled capillary electrometer originally described in 1971. These modifications include increasing the number of bits of data acquired, improving the reproducibility of the electrode potential, minimizing the frequency of required cathetometer readings (the least

accurate measurement), and protecting the apparatus from vibration. The effect of each of these modifications is evaluated.

Abstract No. 364

Mass Transfer to Truncated Vertical Cylinders by Free Convection and by Rotational Forced Convection

J. C. McClure, J. Tavakoli-Attar, and **J. R. Selman,*** Dept. of Chemical Engineering, Illinois Institute of Technology, Chicago, Ill. 60616

Limiting current measurements at the horizontal end face and at the vertical curved surface of truncated cylinders are compared with values predicted by well-established correlations for free convection at vertical electrodes and for mass transfer at rotating disks and cylinders. Strong hydrodynamic interaction between the two mass-transfer surfaces is found. A correlation is presented for stagnation flow induced by free-convection streaming at the periphery of a horizontal surface (advection).

Abstract No. 365

Effect of Crystallite Morphology on the Conductivity of Polycrystalline Sodium β''-Alumina

J. R. Rasmussen,* A. V. Virkar, G. R. Miller, and **R. S. Gordon,** Ceramatec, Inc., Salt Lake City, Utah 84108

A modification of the two-layer inhomogeneous conductor model has been made which takes the crystallite morphology into account through a calculation of the average local electric field experienced by a mobile ion. In the case of a planar conductor such as β- or β''-alumina, a linear relationship exists between the measured resistivity and the depolarization factor which is a function of the crystalline morphology. High frequency, room temperature conductivity data are in excellent agreement with theory.

Abstract No. 366

Electronic Transport in $Zr_{0.9}Y_{0.1}O_{1.95}$ Determined from a Novel Electrochemical Cell Technique

L. C. Lee,* IBM Corp., Poughkeepsie, N.Y. 12602, and **R. N. Blumenthal,** Marquette University, Milwaukee, Wis. 53233

Steady-state permeation of oxygen through a yttria stabilized-zirconia electrolyte ($Zr_{0.9}Y_{0.1}O_{1.95}$) was achieved utilizing a novel electrochemical cell technique. The electron, σ_n, and hole, σ_p, conductivities of $Zr_{0.9}Y_{0.1}O_{1.95}$ were determined (at 1000° and 1050°C over a wide range of oxygen pressures) from measurements of the oxygen flux as a function of the difference in oxygen concentration across the electrolyte. Both the magnitude and P_{O_2} dependence of the electronic conductivities ($\sigma_n \propto P_{O_2}^{-1/4}$; $\sigma_p \propto P_{O_2}^{1/4}$) were in good agreement with the reported results of previous investigators who employed a d-c polarization technique. The chemical diffusivity, $\tilde{D}$, was determined from nonsteady state oxygen step change measurements utilizing the aforementioned electrochemical cell. The electron mobility, μ_n, and hole mobility, μ_p, were determined from $\tilde{D}$.

Abstract No. 367

Electrical Conductivity of the Solid Electrolyte System $CuCl(Al_2O_3)$

M. R-W. Chang,* K. Shahi, and **J. B. Wagner, Jr.,** Center for Solid State Science, Arizona State University, Tempe, Ariz. 95281

The a-c conductivity of polycrystalline CuCl containing a dispersed second phase of Al_2O_3 has been studied between 25° and 400°C. Enhanced conductivity was observed for samples containing initial particle sizes less than 1 micron, with the maximum enhancement at about 10 m/o. At low temperature, the addition of 10 m/o of 0.06 micron Al_2O_3 increased conductivity by a factor of 30. (This research was supported by NASA Contract NAS-8-32937.)

Abstract No. 368

Electrical Conductivity Studies on LiI and LiI · $x H_2O$ with and without Al_2O_3 Particles

S. Pack,* Center for Solid State Science, Arizona State University, Tempe, Ariz. 85281, **B. Owens,** Medtronics, Inc., Minneapolis, Minn. 55478, and **J. B. Wagner, Jr.,** Center for Solid State Science, Arizona State University, Tempe, Ariz. 85281

Between 25° and 128°C, the conductivity of LiI is less than that of hydrated LiI. Addition of dried Al_2O_3 particles to LiI yields no enhanced conductivity but Al_2O_3 containing traces of moisture yields enhanced conductivity. Using cells, Li|LiI or LiI (trace H_2O)|Li, the a-c and d-c conductivities are the same. This suggests that conduction is ionic and not due to water or hydronium ion. (This work was supported by a grant from the Center for Solid State Science at Arizona State University.)

Abstract No. 369

Electrical Conductivity of Solid AgI Containing a Dispersion of Submicron Size Al_2O_3

K. Shahi* and **J. B. Wagner, Jr.,** Center for Solid State Science, Arizona State University, Tempe, Ariz. 85281

The a-c conductivity of AgI containing submicron size Al_2O_3 particles has been studied between 300° and 500°K. The conductivity depends on the particle size, smaller particles resulting in larger enhancement. The conductivity *vs.* composition curve exhibits a maximum, around 30 m/o Al_2O_3. The addition of undried 30 m/o Al_2O_3 (0.06 μm) enhanced the conductivity by more than 3 orders of magnitude at room temperature. Predried Al_2O_3 enhanced the conductivity by more than 1½ orders of magnitude. (This research was supported by NASA Contract NAS-8-32937.)

Abstract No. 370

Evaluation of Secondary Magnesium Cells with Molten-Salt Electrolytes

C. C. Sy,* Z. Tomczuk, and **M. F. Roche,** Argonne National Laboratory, Chemical Engineering Div., Argonne, Ill. 60439

The purpose of this study was to develop a secondary magnesium cell employing a molten salt electrolyte. Magnesium and magnesium alloys were tested as negative electrode materials in high temperature (375°-468°C) cells employing either the KCl-NaCl-$MgCl_2$ eutectic or the LiCl-KCl-$MgCl_2$ eutectic as the electrolyte. The magnesium alloys tested were Mg_2Al_3, MgZn, Mg_2Si, Mg_2Cu, and Mg_2Pb. The positive electrode materials tested were FeS_2, TiS_2, FeO (which was not rechargeable), and NiO. The open-current voltages of the fully charged cells ranged from 1.3 to 1.8V, and their coulombic efficiencies were greater than 80%. The lifetimes of the cells were limited by magnesium dendrite formation on the negative electrodes.

Abstract No. 371

Reference Electrode Development for the Lithium/Metal Sulfide Battery Systems

L. Redey* and **D. R. Vissers,** Argonne National Laboratory, Chemical Engineering Div., Argonne, Ill. 60439

Reference electrodes are being developed at the Argonne National Laboratory for the electrochemical characterization of the large Li-Al/metal sulfide engineering cells. A practical reference electrode for this application must have a well-defined potential, be chemically inert toward the environment in which it is being used, and possess the geometry and strength required for the application. In this study five different cell couples were evaluated as potential reference electrode materials using several different electrode designs. A Ni/Ni_3S_2 reference electrode with excellent long term stability and capable of functioning as a Luggin-type capillary is described. An *in situ* technique capable of verifying the stability of the reference electrode potential also is presented.

Abstract No. 372

Comparison of Lithium-Boron Alloy with Pure Lithium as an Ambient Temperature Anode

S. D. James, Naval Surface Weapons Center, White Oak Laboratory, Electrochemistry Branch, Silver Spring, Md. 20910

This work is comparing the anodic oxidation of Li and of Li-B alloys in aprotic solvents with a view to using the alloy as an ambient temperature anode. Alloy discharge curves are being obtained as a function of discharge rate and composi-

tion of alloy and electrolyte. Useful coulombic capacities were obtained from the Li-B alloy, close to the lithium potential at room temperature. In unstirred $LiClO_4$-PC, pure Li anodes passivate at discharge rates above 2 mA · cm^{-2}. Time to passivation increases in stirred solution and at lower current densities.

Abstract No. 373

Modes of Charge and Discharge in a Single-Pore Ag/AgO Electrode

T. Katan* and **K. C. Tsai,** Lockheed Palo Alto Research Laboratory, Palo Alto, Calif. 94304

The charge-discharge behavior of a single-pore, Ag/Ag_2O/AgO electrode is examined in 10M KOH saturated with Ag_2O during repeated cycling. A 14 micron single-pore slot serves as an analog of a pore in a porous electrode. Evidence is presented that the first formation of AgO during galvanostatic charge involves a metastable, soluble AgII species before solid AgO is formed. During charge, formation of the AgII species and AgO(s) appears to be from Ag rather than from Ag_2O.

Abstract No. 374

Zinc-Electrode Current Efficiency in Zinc-Chlorine Hydrate Batteries. I. Theoretical Aspects

G. L. Henriksen* and **S. Kodali,** Energy Development Associates, A Gulf + Western Co., Madison Heights, Mich. 48071, **J. Jorné,** Chemical Engineering Dept., Wayne State University, Detroit, Mich. 48202, and **C. J. Warde,** Energy Development Associates, A Gulf + Western Co., Madison Heights, Mich. 48071

In Zn/Cl_2 batteries with flow-through porous-graphite chlorine electrodes, the major source of zinc-electrode current inefficiency is chemical reaction with chlorine dissolved in aqueous $ZnCl_2$ electrolyte. The reaction rate is controlled by mass transport of chlorine to the zinc electrode under the influence of convective flow in the interelectrode gap. Three mechanisms combine to establish a steady-state fluid-dynamic pattern in the gap during electrode position: forced convection of bulk electrolyte through the chlorine electrode, natural convection in the diffusion layer adjacent to the zinc electrode, and bubble-induced convection created by anodic generation of chlorine. Relative magnitudes of current inefficiencies attributable to these mechanisms (3-7%) and methods of superimposition are analyzed for a range of practical cell conditions to enhance the zinc-electrode current efficiency.

Abstract No. 375

Zinc-Electrode Current Efficiency in Zinc-Chlorine Hydrate Batteries. III. Natural Convection during Electrodeposition

S. Kodali,* Energy Development Associates, A Gulf + Western Co., Madison Heights, Mich. 48071, **J. Jorné,** Chemical Engineering Dept., Wayne State University, Detroit, Mich. 48202, and **G. L. Henriksen,** Energy Development Associates, A Gulf + Western Co., Madison Heights, Mich. 48071

Zinc-electrode current efficiency is investigated during electrodeposition when transport of dissolved chlorine is controlled only by natural convection in the cell gap. Mass transfer rates of ionic tracers to the zinc cathode are measured in cells having finite cell gaps between vertical-plate electrodes. Rayleigh numbers and empirical constants derived from these data are used to determine chlorine-transfer rates. For cell gaps in the range of 1-5 mm, the resultant current inefficiencies of 2-3% are a decade larger than those attributable to molecular diffusion across the gap. The influence of anodically produced bubble-induced convection on the resultant fluid-dynamic pattern in the gap also is examined. Predictions are made for enhancing zinc-electrode current efficiency.

Abstract No. 376

Mechanism of Anodic Oxide Film Formation at Nickel in Alkaline Solution

J. F. Wolf, A. Damjanovic, and **L.-S. Ray Yeh,** Allied Chemical Corp., Corporate Development Center, Morristown, N.J. 07960

The formation of an anodic film over nickel anodes in alkaline solution is studied by galvanostatic and potentiodynamic techniques. The kinetics of the film formation up to about 50Å thickness obeys the formalization of the Cabrera-Mott model of growth and leads to an exponential equation for growth rate. The observed pH dependence of the kinetics reveals, however, that two parameters, one in the frequency term and another in the exponent, are affected by OH^- concentration. This dependence is analyzed in detail, and a mechanism for the oxide film formation based on this dependence is presented.

Abstract No. 377

An "Unusual" pH Dependence of Anodic Oxide Film Formation at Platinum in Alkaline Solutions: Mechanism of Formation

A. Damjanovic, L.-S. Ray Yeh, and **J. F. Wolf,** Allied Chemical Corp., Corporate Development Center, Morristown, N.J. 07960

At platinum anodes in aqueous alkaline solutions an oxide film grows at potentials anodic to about 1.0V *vs.* RHE. From potentiodynamic and galvanostatic charging experiments it is determined that the kinetics of the film growth proceeds according to the well-known Cabrera-Mott model of high field assisted formation of ions at metal/oxide interface and their migration through the oxide phase. The observed complex dependence of growth rates on pH is, however, not in accordance with this model. It reflects a simultaneous dependence of two parameters in the rate equation on pH. The analysis of this dependence suggests that a rate determining step in the over-all process of growth is a process at the oxide/solution interface rather than at the metal/oxide interface usually assumed for the model.

Abstract No. 378

Zinc-Electrode Current Efficiency in Zinc-Chlorine Hydrate Batteries. II. Experimental Study

A. Kermani and **J. Jorné,*** Dept. of Chemical Engineering, Wayne State University, Detroit, Mich. 48202, and **S. Kodali,** Energy Development Associates, A Gulf + Western Co., Madison Heights, Mich. 48071

Zinc-electrode current efficiency during electrodeposition is investigated in a single cell over a range of operating conditions. Measured inefficiencies are due to the combined effects of several convective mechanisms which control the mass transfer rate of dissolved chlorine to the zinc electrode. They depend linearly on chlorine concentration and nonlinearly on cell gap and electrolyte flow rate through the chlorine electrode. Increased efficiencies occur between 3-4 mm cell gaps and 2-5 ml/cm^2-min electrolyte flow rates for selected conditions of electrolyte composition and temperature. The results are analyzed to determine the predominant chlorine transport mechanisms for different combinations of gap and flow rate.

Abstract No. 379

Interfacial Phenomena in Solid Electrolytes Investigated on Thin Film Samples

Y. Danto, G. Couturier, J. Pistré, and **J. Salardenne,** Laboratoire de Recherche en Electronique et Physique du Solide, Université de Bordeau I, Talence, France

This study was performed on thin film samples, a configuration allowing a better characterization of the electrode/solid electrolyte interface region. Measurements were carried out by the frequency response method, completed by a study of photoelectric and thermally stimulated currents. Anionic conductors such as βPbF_2 and $PbSnF_4$ ($\sigma \simeq 10^{-3}\Omega^{-1}cm^{-1}$ at room temperature) were used. In the case of metal-ionic conductor systems, the influence of the nature of electrode material on charge transfer processes and on contact capacitance was investigated. Semiconductor (Si)/ionic conductor interfaces were also examined. In all cases, the effects of bias and temperature were considered. Lastly, a discussion on the thermodynamical equilibrium at the contacts is given.

Abstract No. 380

Kinetics of Simple Electrode Processes: A New Approach

R. Heyrovská, Na Stáhlavce 6, Praha 6, Czechoslovakia 160 00

The Butler-Volmer equation predicts that the initial slopes $|d\eta/di|$ (polarization resistance) at low overvoltages are the same for both cathodic and anodic processes, but experiments in the literature indicate that the cathodic slopes are greater than the anodic slopes. Consequently, a pair of $\sin h$ function of η has been found to give a quantitative fit. The suggested interpretation uses only experimentally accessible physicochemical parameters. The Nernst equation and the equation for polarographic waves easily follow.

Abstract No. 381

An Error Analysis of the Galvanostatic Double Pulse Technique

Z. Nagy, Argonne National Laboratory, Chemical Engineering Div., Argonne, Ill. 60439

Two modifications of the technique are compared. In the first one the horizontal overpotential trace, $(d\eta/dt)_{t=t_m} = 0$, occurs at a fixed time after the end of the prepulse ($t_m = t_1 + \Delta t$), while in the second it occurs at a fixed ratio ($t_m = qt_1$). All previous applications of the technique tacitly have used the first modification, because at $t_m = t_1$ an inevitable inductive spike and ringing distorts the trace. The systematic errors, caused by inadequacies in the mathematical approximations, are examined in detail and are compared with random experimental errors. The errors are presented as a function of two characteristic time: the time constant of the reaction resistance-double layer capacitance system and the time constant of the reaction resistance-diffusion impedance system. It is shown that the first modification is limited for fast reactions by systematic errors and is not much better than the single pulse technique. The second modification could be used for reactions with any rate constant, in principle without upper limit, but is limited by random experimental errors.

Abstract No. 382

The Kinetics and Mass Transfer of Zinc Electrode in Acidic $ZnCl_2$ Solution

J. T. Kim (Present address: Bell Laboratories, Murray Hill, N.J. 07974) and **J. Jorné,** Dept. of Chemical Engineering, Wayne State University, Detroit Mich. 48202

The kinetics and mass transfer of zinc electrode in acidic $ZnCl_2$ solution have been investigated in order to understand and optimize its performance in the zinc-chlorine hydrate battery. The polarization of the zinc electrode was measured using a rotating hemispherical zinc electrode which is ideal for this case because its primary current distribution is uniform. Tafel behavior can be observed and exchange current densities of 1.4, 1.75, and 2.65 mA/cm^2 were determined in 0.5, 1.0, and 2.0M $ZnCl_2$ solutions, respectively. A cathodic mechanism of two consecutive one-electron transfer steps is postulated, where the first is the rate determining step. Limiting currents were measured and the diffusion coefficient 0.89×10^{-5} cm^2/sec was determined in 0.05M $ZnCl_2$ at 25°C. The surface roughness during zinc deposition was investigated in terms of the fraction of the limiting current and the micro-throwing power of the zinc deposition.

Abstract No. 383

The Development of a Grooved Periodic Morphology on Nickel-Aluminum Alloys Electropolished under Gaseous Discharge

A. V. Lookichev and **W. W. Smeltzer,*** Institute for Materials Research, McMaster University, Hamilton, Ontario, Canada L8S 4M1

Ni-Al alloys as the γ-solid solution, Ni_3Al, and NiAl were electropolished in a phosphoric acid-ethanol-water electrolyte at currents and voltages ranging up to 3.5 A/cm^2 and 30 V. Electropolishing of vertically suspended electrodes at high current densities, 2-3.5 A/cm^2, and high gas-discharge rates led to a unique vertically grooved periodic surface structure at 40-43 μm spacing. This surface morphological development is related to the formation by oxygen discharge of a "boiling" bubble layer approximating a close-packed array which moves upward such that the groove spacing is equal to the bubble radius.

NEW TECHNOLOGY SUBCOMMITTEE/CORROSION/DIELECTRICS AND INSULATION/ELECTRONICS/ ORGANIC AND BIOLOGICAL ELECTROCHEMISTRY

Electrochemical Modification and Monitoring of Biological Systems

Abstract No. 384

Oxygen Microelectrodes

P. Pierini and **E. Guilbeau,** Dept. of Chemical and Bio Engineering and The Center for Solid State Science, Arizona State University, Tempe, Ariz. 85281

Conical microelectrodes with approximately 1μ tips have been extensively used to measure oxygen concentrations polarographically in tissue. The interpretation of these measurements is made difficult by poor characteristics, such as excessive drift, aging, and the lack of a definitive limiting-current plateau. Current distributions and polarographic curves are computed, taking into account mass transfer effects, electrode kinetics, and the potential distribution in the medium. The experimental data can then be more accurately analyzed with the model since the location of a limiting current shoulder is not critical. Experimental results for several media and electrode surfaces are compared with the theory.

Abstract No. 385

The Silver/Silver Chloride Electrode in Biomedical Monitoring

R. Baboian, G. Haynes, and **R. Robichaud,** Texas Instruments Inc., Attleboro, Mass. 02703

The silver/silver chloride electrode is used widely in both laboratory and industrial applications. In the application of patient monitoring, the silver/silver chloride electrode is recognized as the most versatile and stable one. This paper describes the fundamental aspects of the silver/silver chloride electrode in biomedical environments. Electrochemical techniques were used to evaluate the characteristics of several electrode designs. Results of this study have been utilized to design an improved electrode.

Abstract No. 386

Ion-Sensing Thin-Film Transistors

N. Alvi, I. Kaufman, and **P. Pierini,** Dept. of Electrical Engineering, Dept. of Chemical Engineering, and The Center for Solid State Science, Arizona State University, Tempe, Ariz. 85281

A new microsensor device for ionic concentrations in aqueous electrolytes is described. This solid-state field-effect device is made entirely by thin-film vacuum deposition technology using polycrystalline group II-VI semiconductors. Ion selectivity is then achieved by depositing suitable solid-state membranes or gate material. Sensitivity of the thin-film transistor to sodium, potassium, and the halogen anions, and also to pH changes in the range 1-10 is demonstrated. Device design and fabrication are described, together with its performance characterization as a field effect transistor and as an electrochemical sensor. Applications for determination of pH, K^+, and Cl^- ion concentrations in blood serum and as a skin surface sensor are discussed.

Abstract No. 387

The Electrochemistry of High Potential Iron-Sulfur Redox Proteins

B. A. Feinberg* and **Y. K. Lau,** Dept. of Chemistry, The University of Wisconsin-Milwaukee, Milwaukee, Wis. 53201

Ferredoxins ($E^{o\prime} \simeq -430$ mV *vs.* SHE) and high potential iron-sulfur proteins ($E^{o\prime} \simeq +350$ mV) both have the $Fe_4S_4^*$ (S* = inorganic sulfide) cluster as the redox prosthetic group which is held by four protein sulfydryl groups. Cyclic voltammetry and other electrochemical methods were used to study the mechanism of the reactions of HiPIP at the HDME. Cyclic voltammetry of both oxidized and reduced

chromatium HiPIP gave adsorption peaks at $E_{pc} = -332$ mV and $E_{pa} = -318$ mV; $i_{pc} > i_{pa}$ and both were linear with scan rate from 0.05-10 V/sec. Peak potentials shifted as a function of pH. The apoprotein gave identical cyclic voltammetry as the holoprotein, which indicates that the cluster is not undergoing super-reduction at the HDME but rather adsorption followed by mercury-sulfur electrochemistry.

Abstract No. 388

Adaptive Cell Membrane Impedance Changes and Electrochemical Information Transfer *In Vivo*

G. Cerf* and **A. A. Pilla,** Bioelectrochemistry Laboratory, Orthopaedic Research Laboratories, Dept. of Orthopaedic Surgery, and Applied Chemistry and Chemical Engineering, Columbia University, New York, N.Y. 10032

A detailed analysis is presented of the manner by which the electrochemical microenvironment of a living cell influences the magnitude and kinetics of the potential-dependent membrane processes. Computer analysis of the Laplace plane impedance observed for the toad urinary bladder membrane system shows substantial changes in the number and value of time constants associated with passive Na^+ transport as a function of normal variations in its bladder concentration. These environmentally induced changes in membrane impedance must be considered when specific current waveforms are employed for the modification of cell function. Thus the optimal encoding of electrochemical information transfer signals will require knowledge of adaptive impedance changes associated with a cell's stage in its development and/or cycle as well as its state of function.

Abstract No. 389

Donnan's Theory of Membrane Equilibrium: A Critical Revaluation, Theoretical and Experimental

G. N. Ling, Molecular Biology Dept., Pennsylvania Hospital, Philadelphia, Pa. 19107

The validity of the membrane-pump theory of living cells, currently widely taught in many textbooks, rests upon the validity of Donnan's theory of membrane equilibrium which prescribes relationships between the electrical potential differences between two adjoining phases separated by a semipermeable membrane and the distribution ratios of permeant ions between these phases. This paper presents results of both theoretical and experimental studies of Donnan membrane theory are such and its application to the living cells. In addition, an alternative formulation is also discussed.

Abstract No. 390

In Vitro Dissolution of Pt Stimulation Electrodes

J. McHardy,* **L. S. Robblee, J. M. Marston,** and **S. B. Brummer,** EIC Corp., Newton, Mass. 02158

Appreciable dissolution of Pt electrodes can occur in saline solution during the application of "balanced biphasic" current pulses analogous to those used for neural stimulation. Referring dissolution to the net charge injected in either direction, rates in inorganic solution ranged from ≤ 10 ng Pt/C for pulses of $\pm 100\ \mu C/cm^2$ (geometric) to $\sim 10^3$ ng Pt/C for pulses of $\pm 500\ \mu C/cm^2$. In the presence of 0.02 w/o HSA protein, initial dissolution rates were similar, but they declined rapidly and approached zero within a few hours. (This work was supported by the National Institutes of Health under NINCDS Contract No. N01-NS-3-2313.)

Abstract No. 391

In Vivo Dissolution of Pt Stimulation Electrodes

L. S. Robblee,* W. F. Agnew, L. A. Bullara, J. McHardy, and **S. B. Brummer,** EIC Corp., Newton, Mass. 02158, and Huntington Institute of Applied Medical Research, Pasadena, Calif.

Implanted cortical electrodes (1.1 mm Pt disks) were stimulated for 36 hr (4 × 9 hr/day) with balanced, biphasic pulses ($\pm 100\ \mu C \cdot cm^{-2}$ geom/pulse, 50 Hz). Following stimulation, the tissue Pt concentration 0-1 mm beneath the stimulation electrodes ranged from 0.2-11.4 μg/g wet tissue weight, compared with only 0-1.3 μg Pt/g tissue at a depth of 1-2 mm. Tissue beneath unstimulated electrodes contained 0-0.6 μg Pt/g tissue. No Pt was detected in kidney or blood samples from the experimental animals. (This work was supported by the National Institutes of Health under NINCDS Contracts N01-NS-3-2313 and N01-NS-0-2275.)

Abstract No. 392

Linear A-C Electrode Polarization Impedance Measurements on Pt and Pd Electrodes under Potential-pH Control

M. Brownstein and **R. B. Beard,** Biomedical Engineering and Science Institute, Drexel University, Philadelphia, Pa. 19104

Linear a-c electrode polarization impedance measurements have been taken over the frequency range 250 Hz to 1 MHz on platinum and palladium in physiologic saline and weak electrolyte under potential and pH control over regions outlined by Pourbaix potential-pH diagrams. At low pH's in physiologic saline the rate determining mechanism appears to be adsorption while for weak electrolytes charge transfer. At higher pH's electrode impedance mapping is less consistent than at lower pH's.

Abstract No. 393

D-C and A-C Linear Polarization Studies of Zinc Anodes in Biological Solutions

N. Niazy* and **R. B. Beard,** Biomedical Engineering and Science, Drexel University, Philadelphia, Pa. 19104

D-C polarization measurements show the appearance of a region of passivity for Zn in the presence of biological organic molecules which is absent in pure NaCl solution. The results of a-c electrode impedance studies show that in the presence of the inhibitors the Zn/solution interface appear to be controlled by an absorption type process in agreement with the electrical equivalent circuit model for the adsorption controlled reaction proposed by Timmer *et al.*

NEW TECHNOLOGY SUBCOMMITTEE/ELECTROTHERMICS AND METALLURGY

Superconducting Materials and Devices

Abstract No. 394

Role of Superconductivity in the Development of Magnetic Fusion Energy

D. B. Montgomery, M.I.T., Cambridge, Mass. 02139

Recent experiments in the U.S. Fusion Program have removed two of the largest physics uncertainties in the fusion energy dream. It is now generally accepted that fusion energy will be a reality, but that the machines will involve high technology and engineering development requirements for the first wall, and for the magnets will require essentially the balance of this century. Present magnetic confinement experiments utilize resistive magnets, but future machines must utilize superconductors to achieve net power output. Even the smallest of the next generation net-power producers will utilize more than 1000 tons of superconducting material. Many of the potential designs call for niobium-tin material, whose strain tolerance in present day form is far from ideal.

Abstract No. 395

Superconducting Magnets for Magnetohydrodynamic Power Generation

P. G. Marston, Francis Bitter National Magnet Laboratory, M.I.T., Cambridge, Mass. 02139

MHD, which has been recently shown to be capable of the highest efficiencies and lowest cost of any near term energy generating technology, seems certain to be the first large scale commercial application of superconductivity. A national program is described, with scale demonstrations of critical items in 1979, aimed at the development of a broad industrial base and a new international market in the mid-1990's for coal-burning MHD/steam power plants as utilities. The technical problems are discussed, and superconducting MHD magnets in the Soviet Union and the United States are described.

Abstract No. 396

The Development of a Superconducting Power Transmission System

E. B. Forsyth, Brookhaven National Laboratory, Associated Universities, Inc., Upton, N.Y. 11973

Underground power transmission systems built with superconducting cables promise important advantages over conventional cables, however, the detailed technical design must be influenced by the economics of incorporating superconducting cables into existing networks. The development work at Brookhaven required major efforts in the fields of superconducting and dielectric materials. In particular, a low loss form of Nb_3Sn conductor was developed. Highly oriented and laminated polymeric tapes form the electric insulation. A demonstration site rated at 138 kV, 1000 MVA is under construction. (This work was supported by the U.S. Department of Energy.)

Abstract No. 397

High Energy Physics: The Mother of Invention for Superconductivity

B. P. Strauss, Fermi National Accelerator Laboratory, Batavia, Ill. 60510

About one month after the announcement of high field superconductivity in Nb_3Sn in 1961, a meeting was held at the Lawrence Berkeley Laboratory outlining a program of research and development on superconducting devices for high energy physics. This has proven to be a very special relationship which has made use of the well-known high technology content and innovative approach to problem solving associated with high energy physics. This paper interconnects the needs for highly sophisticated devices with many of the technological developments in the areas of materials as well as magnet construction and operation. The areas of technological fall-out to other areas of technology are also examined.

Abstract No. 398

Large Scale Applications of Superconductivity

S. Foner, Francis Bitter National Magnet Laboratory, M.I.T., Cambridge, Mass. 02139, and **B. B. Schwartz,*** Francis Bitter National Magnet Laboratory, M.I.T., Cambridge, Mass. 02139 and Dept. of Physics, Brooklyn College of the City Univ. of New York

We present a brief review of large scale application of superconductors to the problems energy generation and transmission, high speed magnetic levitation, computers, and special applications such as high gradient magnetic separation. We outline the special characteristics required of superconductors and their materials properties. Recent developments in new practical materials and their mechanical properties as related to critical current and stress are presented. Trends in future developments and research are discussed. (This work was supported in part by the DOE through the Plasma Fusion Center and the NSF.)

Abstract No. 399

Fabrication of Superconducting Materials for Large Magnetic Devices

M. Suenaga* and **W. B. Sampson,** Brookhaven National Laboratory, Upton, N.Y. 11973

Fabrication methods for high field (A15) superconducting conductors for large magnetic devices are reviewed. The processes which are discussed are (*i*) continuous filament processes (bronze process, external and internal diffusion processes), and (*ii*) multiply connected filament processes (casting and infiltration processes). With each process advantages, disadvantages, and achievable properties, including mechanical properties of wires, are pointed out. (This work was performed under the auspices of U.S. Department of Energy.)

Abstract No. 400

In Situ Technology an Alternative for the Production of Ductile Superconducting Wires

R. Roberge,* IREQ, Institut de Recherche de l'Hydro-Québec, Varennes, Que., Canada J0L 2P0, **J. L. Fihey, S. Foner, E. J. McNiff, Jr.,** and **B. B. Schwartz,** Francis Bitter National Magnet Laboratory and Plasma Fusion Center, M.I.T., Cambridge, Mass. 02139

Materials and conductor development are required for many large high fields superconductors applications. The *in situ* technology offers an attractive alternative to the present process for the production of ductile multifilamentary superconducting wires. The over-all critical current density of the *in situ* wires is on a par with those of conventional materials, typically 10^4 A/cm^2 at 14 tesla. Their major advantage arises from the improved mechanical properties which permit a larger strain on the composite before degradation occurs. The promises and limitations of these new emerging materials are presented.

Abstract No. 401

The Influence of Plastic Deformation on the Residual Stress State of Multifilamentary Composites

S. F. Cogan,* D. S. Holmes, T. W. Eagar, I. M. Puffer, and **R. M. Rose,** Dept. of Materials Science and Engineering, M.I.T., Cambridge, Mass. 02139

The strain dependence of the superconducting critical current, Jc, in multifilamentary A-15 composites is markedly improved by the residual stress state. This residual stress state, however, can be totally eliminated by plastic deformation in the matrix. Results are presented for multifilamentary Nb_3Sn composites which show that the removal of the residual stresses in the matrix seriously degrade subsequent Jc *vs.* strain dependence. This behavior is particularly important when considering cyclic stresses.

Abstract No. 402

High Temperature Phase Boundaries and Superconducting Properties of A15 and Chevrel Compounds

R. Flükiger* and **J. L. Jorda,** Dept. Phys. Mat. Condensee, Geneve, Switzerland

The optimum superconducting properties of high field superconductors are often obtained for compositions which are only stable at high temperatures (~1800°C). Improved direct methods for determining high temperature phase boundaries (DTA, TA on levitating samples and others) have been applied to A15 compounds and are discussed. The high temperature phase boundaries for the Chevrel compound Cu-Mo-S is presented. Superconducting properties are also used as a tool for determining high temperature phase fields.

Abstract No. 403

Neutron Irradiation of the A-15 Superconductors Nb_3Sn, Nb_3Au, and Mo_2Tc_3

A. L. Giorgi, G. R. Stewart, and **E. G. Szklarz,*** Los Alamos Scientific Laboratory, Los Alamos, N.M. 87545

Samples of the A-15 superconductors Nb_3Sn, Nb_3Au, and Mo_3Tc_3 were irradiated by high energy neutrons ($E > 1$ MeV) to a fluence of approximately 6×10^{20} neutrons cm^{-2}. A depression in superconducting transition temperature, T_c, occurred for the highly ordered Nb_3Sn and Nb_3Au samples. No change in T_c occurred in the highly disordered Mo_2Tc_3. Analogous efforts on T_c were observed when the A-15 forms of Nb_3Au and Mo_2Tc_3 were converted to the A-2 (bcc) structures of the same composition. These results are discussed in terms of the mechanisms involved in radiation induced damage and the linear chain model.

Abstract No. 404

Transition Temperatures and Range of Composition for a New A-15 Phase in the V-Re-Tc System

A. L. Giorgi, Los Alamos Scientific Laboratory, Los Alamos, N.M. 87545

A new superconducting A-15 phase was recently found in the V-Re system. The equivalent phase does not exist in the V-Tc system. However, by substitution of part of the rhenium with technetium, a stable single phase superconducting A-15 structure was found to form over a limited range having the general composition $V_{0.3}Re_{0.7-x}Tc_x$. The transition temperature, T_c, increases with increasing concentration of technetium. The method of preparation, range of composition, lattice parameters, and T_c values for this A-15 phase are presented.

Abstract No. 405

Information Sources for Superconductors

C. W. Moulton, Chemical Abstracts Service, Columbus, Ohio 43210

Coverage by *Chemical Abstracts* of the primary technical literature on superconducting materials and devices is described. Included are considerations of selection criteria, with emphasis placed on abstracting and indexing, and in-depth presentation of the information. Disciplinary distinctions as they pertain to the chemical literature, as well as the coverage overlap with other secondary sources, are discussed. Examples of abstracting and indexing practices are presented to illustrate how *Chemical Abstracts* and its adjunct services can be used for the retrieval of information.

INDEX TO AUTHORS

Abstract No.

Abruna, H. ... 293
Adachi, T. ... 167
Adams, W. A. ... 246
Addington, L. A. ... 69
Adžic, R. R. ... 344, 353
Aggarwal, R. L. ... 128
Agnew, W. F. ... 391
Agrawal, A. K. ... 45
Ahlgren, R. B. ... 234
Aizawa, M. ... 103
Albery, W. J. ... 331
Alfenaar, M. ... 14, 17
Alkaitis, S. A. ... 241
Alkire, R. C. ... 44, 255, 282, 290
Alvi, N. ... 141, 386
Amadelli, R. ... 29
Anderson, C. L. ... 106, 107
Anderson, J. E. ... 305
Anderson, J. L ... 305
Andersson, L. P. ... 148
Andrews, J. ... 210
Ang, P. G. P. ... 242
Angerstein-Kozlowska, H. 337, 355, 356
Anson, F. C. ... 300
Anthony, J. B. ... 150
Antoniadis, D. A. ... 132, 133
Appleby, A. J. ... 237, 345
Arendt, R. H. ... 9, 10
Armstrong, N. R. ... 304
Arvia, A. J. ... 43
Assailly, J. ... 309
Atanasoski, R. ... 353
Awamura, D. ... 192

Babai, M. ... 40
Baboian, R. ... 86, 385
Baghdadi, A. ... 68
Bagley, B. G. ... 175
Baliga, B. J. ... 157
Ballman, A. A. ... 180
Banks, E. ... 224
Barcelo, J. A. ... 280
Bard, A. J. ... 302, 303, 330, 359
Barendrecht, E. ... 32, 250
Barnett, B. ... 355, 356
Baron, R. ... 162
Barr, S. W. ... 342
Barradas, R. G. ... 361
Barrière, A. S. ... 47, 91
Basi, J. ... 188
Bassett, C. A. L. ... 308
Baukus, J. P. ... 162
Baum, B. ... 74
Bauman, H. F. ... 245
Bean, J. C. ... 122, 125
Beard, R. B. ... 392, 393
Beaudouin, J. ... 146
Beck, T. R. ... 255
Beckham, K. F. ... 163
Bell, J. T. ... 49
Benemann, J. R. ... 278
Benenson, R. E. ... 175
Bennett, M. V. L. ... 313
Berg, S. ... 148
Bernholc, J. ... 203
Bernstein, Ch. ... 340
Bevacqua, S. F. ... 209
Bharat, R. ... 113, 154
Bindra, P. ... 28, 29
Bittner, H. F. ... 49
Bjelica, L. ... 333
Blais, P. D. ... 65
Blank, M. ... 316
Blaske, T. A. ... 197
Bloomfield, D. P. ... 21

Abstract No.

Blumenthal, R. N. ... 366
Bocarsly, A. B. ... 295
Bockris, J. O'M. ... 325
Bonner, W. A. ... 180, 181
Borucka, A. ... 5, 6
Bouhellal, O. ... 226
Bourret, L. A. ... 307
Bowie-Reed, R. ... 361
Brannan, J. R. ... 262
Brauer, E. ... 37
Breiter, M. W. ... 343
Brilmyer, G. H. ... 359
Brown, C. ... 38, 39
Brown, F. C. ... 257
Brown, J. E. ... 313
Brownstein, M. ... 392
Bruckenstein, S. ... 338
Brummer, S. B. ... 248, 390, 391
Buehler, M. G. ... 191, 193
Bullara, L. A. ... 391
Buoncristiani, A. M. ... 238
Burgner, R. P. ... 214
Bursell, M. ... 26
Butler, K. H. ... 221
Butler, M. A. ... 239, 357
Butler, S. R. ... 150, 151
Butler, W. O. ... 30

Cahen, G. L., Jr. ... 264, 285
Calkins, J. ... 280
Call, P. J. ... 83
Calvin, M. ... 272
Campbell, R. B. ... 196
Carlin, W. W. ... 261
Carlson, D. ... 97
Carlsson, L. ... 31
Carnell, D.W. ... 260
Carr, R. C. ... 230
Carver, G. P. ... 193
Cave, R. J. ... 342
Cerf, G. ... 388
Chambers, J. Q. ... 301
Chan, H. C. ... 53
Chang, C.-A. ... 120
Chang, C. K. ... 270
Chang, L. L. ... 120, 128
Chang, M. ... 155, 158, 209
Chang, M. R.-W. ... 367
Chang, S.-C. ... 92
Chapman, G. E. ... 110
Chatterjee, P. K. ... 140
Chau, N. ... 165
Chen, C. S. ... 100, 115
Cheng, L. J. ... 195
Chenot, C. F. ... 213
Chesney, D. J. ... 305
Chin, A. K. ... 179, 180, 181
Chin, D-T. ... 42, 249
Cho, A. Y. ... 121, 131
Chokshi, H. R. ... 308
Christie, W. H. ... 49
Chuan-sin, C. ... 23
Chung, M. S. C. ... 94
Cipris, D. ... 320
Clayton, R. K. ... 273
Cogan, S. F. ... 401
Colby, J. W. ... 210
Comas, J. ... 106
Contamin, O. ... 350
Conway, B. E. ... 337, 355, 356
Cornely, R. H. ... 145
Couturier, G. ... 379
Cuddihy, E. F. ... 74
Curran, M. J. ... 9, 10

Abstract No.

Damjanovic, A. ... 351, 376, 377
Danto, Y. ... 379
Darlington, W. B. ... 261
Das, P. ... 77, 113
Dautartas, M. F. ... 297
Davari, B. ... 77
Davies, G. J. ... 123
Davis, J. R. ... 65
Dawson, L. R. ... 78, 178
Deal, B. E. ... 95, 135
de Jonge, R. M. ... 250
de Kock, A. J. R. ... 202
Dentai, A. G. ... 180
DeRidder, D. ... 145
Despic, A. R. ... 335
Diaz, A. F. ... 201, 296, 360
Diegle, R. B. ... 46
Dillon, J. ... 279
Dingle, R. ... 122, 129, 130
Diodato, P. ... 145
Dixit, A. ... 100
Doblhofer, K. ... 298
Doerr, R. ... 37
Dryhurst, G. ... 317
Duke, C. B. ... 324
Dunlap, H. L. ... 106, 107
Duriez, R. ... 308
Durr, W. ... 298
Dutton, R. W. ... 132, 133, 137

Eagar, T. W. ... 401
Eatough, D. J. ... 229, 234
Eisenberger, P. ... 131
Elliott, J. F. ... 50
Engler, E. M. ... 301
Ensor, D. S. ... 230
Esaki, L. ... 120, 128
Escher, J. S. ... 184
Etcheberry, A. ... 81
Evans, J. F. ... 297, 305
Evans, J. W. ... 259, 291

Fabis, P. M. ... 39
Fajer, J. ... 270
Falcony-Guajardo, C. ... 150
Farlee, R. ... 227
Farrington, M. ... 246
Fawcett, W. R. ... 334
Feigl, F. J. ... 150, 151
Feinberg, B. A. ... 387
Feldberg, S. W. ... 271
Fey, M. G. ... 59
Fichtner, W. ... 138
Fihey, J. L. ... 400
Finn, P. A. ... 7
Fisher, G. L. ... 228, 229
Fitch, R. H. ... 284
Fitzgibbons, E. T. ... 154
Flagan, R. C. ... 231
Fleischmann, M. ... 327
Fletcher, S. ... 361
Flowers, D. L. ... 156
Flükiger, R. ... 402
Foley, R. T. ... 247
Foner, S. ... 398, 400
Fontenille, J. ... 147
Foos, J. S. ... 248
Forsyth, E. B. ... 396
Fortino, A. G. ... 111
Foulds, A. W. ... 331
Fowler, I. ... 310
Foxon, C. T. ... 117
Franceschetti, D. R. ... 328
Fryburg, G. C. ... 235
Fujihira, M. ... 294

Abstract No.

Fujii, T. 127
Fujishima, A. 359

Gabara, T. 145
Gabrielli, C. 327
Gallagher, B. D. 70
Gallagher, P. K. 175
Gardini, G. P. 201
Gaylord, J. W. 142
Geipel, H. J. 111
Gerischer, H. 329
Gestaut, L. J. 30
Gevers, G. 47, 91
Ghez, R. 177
Ghosh, A. K. 79
Gileadi, E. 341
Ginley, D. S. 78, 239, 244
Giorgi, A. L. 403, 404
Givens, C. 213
Goldberger, W. 258
Golecki, I. 110
Gonser, B. W. 258
Gordon, R. S. 365
Gossard, A. C. 129, 130
Gottesfeld, S. 40, 339
Gould, R. M. 290
Grayson, P. E. 69
Gregory, P. E. 184
Gross, E. L. 274
Grune, H. 24
Gruner, R. 37
Grusell, E. 148
Guerrero, E. 138
Guidici, D. 204
Guilbeau, E. 384
Guinard-Baticle, A. M. 358
Guivarc'h, A. 147
Gurtler, R. W. 68
Guyer, K. L. 342

Hagans, P. 352
Hale, R. W. 258
Hamilton, D. J. 176
Hammond, M. L. 98
Hanna, R. B. 313
Hansen, L. D. 229, 234
Harada, S. 101
Harris, A. L. 313
Harrison, J. A. 336
Hashimoto, H. 127, 206
Hashimoto, N. 87, 153
Hassan, M. S. 90
Hause, J. 187
Hayashi, H. 168
Hayashida, T. 153
Haynes, G. 86, 385
Heckingbottom, R. 123
Heidersbach, R. 38, 39
Heindl, R. 226
Henderson, D. L. 170
Henriksen, G. L. 374, 375
Heyrovská, R. 354, 380
Hibbert, D. B. 173, 251
Hilbertz, W. H. 253
Hillman, A. R. 331
Hine, F. 281
Hiraiwa, A. 101
Hiyamizu, S. 127
Ho, C. 143
Hoare, J. P. 348
Hochberg, A. K. 115, 169
Hoekje, H. 286, 287
Hohnke, D. K. 2
Holmes, D. S. 401
Homa, A. 352
Hooper, R. G. 230
Hopkins, R. H. 65
Horino, N. 114
Horowitz, H. H. 22

Abstract No.

Hostetler, G. 299
Hovestreydt, G. 17
Hseuh, K. L. 249
Hsu, L.-C. 292
Huggins, R. A. 143
Hughes, B. 108
Humbert, M. A. 25
Hunt, L. P. 58
Hunt, M. 115
Hyde, R. W. 256
Hyder, S. B. 184

Ichikawa, F. 200
Iles, P. A. 71, 75
Isaacs, H. S. 1, 4, 41
Ishikawa, H. 152
Ito, K. 183
Itoh, K. 114
Iwamatsu, S. 88

Jaeger, C. D. 303
James, S. D. 372
Janssen, L. J. J. 250
John, R. C. 11
Johnson, K. H. 346
Johnson, L. F. 94
Johnston, W. D., Jr. 182
Jorda, J. L. 402
Jorne, J. 266, 267, 374, 375, 378, 382
Joyce, B. A. 117

Kadija, I. V. 283
Kaesche, H. 35
Kakiuchi, T. 363
Kalmijn, Ad. J. 322
Kamiyama, T. 87
Kampas, F. J. 270
Kanazawa, K. K. 201, 360
Kanegae, M. 114
Kannan, V. C. 116
Kaplan, P. 186
Kapur, V. K. 60
Karlsson, G. 26
Kashiwada, Y. 215
Kashiwagi, M. 134
Katan, T. 245, 373
Katz, J. J. 268
Katz, L. E. 210
Kaufman, F. B. 301
Kaufman, I. 141, 386
Kaufmann, K. J. 269
Kawana, Y. 168
Keiser, J. 38
Kendig, M. W. 41
Kennedy, R. 158
Kermani, A. 378
Kerr, J. 299
Kerwin, W. J. 176
Keuning, W. 17
Khalily, E. 137
Khattak, C. P. 62, 63
Khemthong, S. 71
Khutornoi, A. 29
Kikuchi, M. 167
Kim, J. T. 382
Kimura, Y. 225
Kinoshita, K. 7, 8
Kirkpatrick, A. R. 71
Kissel, G. 18
Knaff, D. B. 275
Knolle, W. R. 166
Koch, V. R. 85
Kodali, S. 374, 375, 378
Kohl, F. 235
Koliwad, K. M. 66
Kopf, L. 130
Kordesch, K. V. 13, 18
Kosa, Y. 174
Kostka, A. G. 269

Abstract No.

Kovatch, W. A. 30
Kowalski, J. M. 346
Koyanagi, M. 87, 153
Kramer, S. R. 301
Kran, A. 64
Kranzer, D. 138
Kruest, J. R. 115, 169
Kruus, P. 246
Kucera, G. H. 7, 8
Kulesa, F. 18
Kumar, R. 115, 169
Kuo, K. 293
Kurata, K. 183
Kurkela, M. 36
Kurosawa, K. 134
Kurtz, B. E. 284

Labram, M. 327
Lachter, A. 47, 91
Lafferty, J. F. 310
LaPrade, J. E. 154
Lascaud, M. 91
Laser, D. 40
Latanision, R. M. 36
Lau, S. S. 110
Lau, Y. K. 387
Le Contellec, M. 147
Lecrosnier, D. 160
Lee, J. B. 45
Lee, J. Y. M. 102
Lee, L. C. 366
Lee, M. L. 234
Legge, R. N. 68
Leontis, T. E. 258
Lesk, I. A. 76
Leung, D. C. 195
Levart, E. 350
Levich, V. G. ..... See page 102C
Liang, A. Y. 208
Liau, Z. L. 109
Liaw, H. M. 161
Ligeon, E. 147
Lilley, P. 190
Lin, A. M. 133
Lin, R. Y. 50
Lindstrom, O. 19
Ling, G. N. 389
Linholm, L. W. 191
Lipari, N. O. 203
Logothetis, E. M. 171
Lookichev, A. V. 383
Loriers, J. 226
Louvar, J. F. 267
Love, J. 112
Lu, P.-Y. 282
Lust, M. L. 139
Luthra, K. L. 236

Macdonald, J. R. 328
Maekawa, S. 118
Magner, G. 349
Mahajan, S. 180, 181, 182
Makita, Y. 118
Malkin, I. 262
Man, M. C. M. 263
Mangelson, N. F. 234
Mar, K. 164
Marcus, R. A. 323
Markowski, G. 230
Marra, W. C. 131
Marsh, O. J. 162
Marston, J. M. 390
Marston, P. G. 395
Martin, J. E. 185
Martinsons, A. 286, 287
Massetti, D. O. 102
Masterson, I. 291
Matsue, T. 294
Matsumoto, S. 159

Abstract No.

Matsushita, T. 168
Maxwell, H. R. Jr. 166
Mayer, J. W. 109, 110
McBreen, J. 18, 249
McCleer, T. J. 258
McClure, J. C. 364
McColl, J. R. 216
McCormick, J. R. 65
McGill, T. C. 162
McGregor, K. G. 272
McHardy, J. 248, 390, 391
McIntyre, J. D. E. 339
McNiff, E. J., Jr. 400
McVeigh, J. B. 248
Meehan, R. R. 213
Meindl, J. D. 144, 146
Melnicki, L. S. 338
Mendel, E. 186, 187, 188
Merkh, C. W. 284
Merz, M. D. 46, 54
Meyer, T. N. 59
Miller, D. C. 181
Miller, G. R. 365
Miller, L. L. 299
Minato, T. 118
Minnucci, J. A. 71
Miyata, T. 222
Mlavsky, A. I. 67
Mogab, C. J. 175
Mohammadi, F. 144, 146
Mohilner, D. M. 363
Mollenkopf, H. C. 65
Molnar, B. 105, 106
Monet, J-D. 309
Montgomery, D. B. 394
Moran, D. 308
Moran, P. J. 264
Mori, M. 183
Moriuchi, T. 103
Morkoc, H. 121
Mott, S. D. 265
Moulton, C. W. 405
Mozota, J. 355
Mukai, K. 101
Murakami, K. 281
Muramatsu, S. 101
Murota, J. 159
Murphy, D. W. 94
Murphy, J. 217
Murray, R. M. 293

Nagy, Z. 381
Nahory, R. E. 182
Nakajima, K. 189
Nanbu, K. 127
Nanis, L. 60
Narayanan, G. H. 108
Narita, T. 12
Natesh, R. 66
Needes, C. R. 260
Nelson, L. N. 176
Neureuther, A. R. 93
Newlin, D. E. 233
Ng, H. K. 173
Ng, W. P. 185
Niazy, N. 393
Niimi, T. 159
Nikolic, B. Z. 344
Nilsson, T. 15
Nishimura, T. 225
Norris, J. R. 269
Norton, L. A. 307
Nowick, A. S. 3

Oggioni, R. 219
O'Grady, W. E. 347
Oh, K. H. 115, 169
Oh-uchi, N. 168
Öjefors, L. 31

Abstract No.

Oldham, W. G. 93, 165
Olmer, L. J. 4
Olson, J. M. 276
O'Mara, W. C. 204
Ono, Y. 183
Onuchukwu, A. I. 53
Ormond, D. W. 89
Osa, T. 294
Ostrom, K. M. 312
Oswald, W. J. 278
Ota, Y. 126
Otvos, J. W. 272
Owens, B. B. 368
Oyama, N. 300

Pack, S. 368
Pan, R. L. 274
Pantelides, S. T. 203
Pappalardo, R. G. 213
Park, S.-M. 319
Parry, J. M. 256
Parsons, J. D. 195
Parsons, R. 333
Patel, C. 55, 56
Patsis, A. 186
Pau, J. K. 185
Paugam, J. 160
Pawel, R. E. 48
Peck, W. F., Jr. 339
Peerce, P. J. 302
Pellin, M. J. 269
Pelous, G. 160
Pemsler, J. P. 257
Pesce, S. 219
Pettit, R. B. 84
Phillips, L. R. 234
Pierini, P. 141, 384, 386
Pilla, A. A. 306, 309, 310, 388
Pistré, J. 379
Pohlman, S. L. 82
Pollack, M. A. 182
Pollock, G. A. 66, 75
Porter, J. D. 361
Potemski, R. M. 177
Preston, C. M. 246
Pringle, J. P. S. 51, 52
Puffer, I. M. 401
Pyle, T. 55

Rabatin, J. 218, 220
Ragsdale, S. 139
Rai-Choudhury, P. 65, 207
Raistrick, I. D. 143
Rapp, R. A. 11
Rasiyah, P. 251
Rasmussen, J. R. 365
Rathman, D. D. 151
Rau, J. 115, 169
Rauh, R. D. 199, 241
Raush, F. 37
Raymond, L. S. 176
Ray Yeh, L.-S. 376, 377
Razouk, R. R. 135
Redey, L. 371
Redman, J. D. 49
Redon, A. M. 358
Reed, T. B. 277
Reed, W. H. 59
Reeves, R. M. 333
Reichman, J. 240, 243
Reichmanis, M. 315
Reif, R. 132
Richard, J. 147
Richou, F. 160
Riedhammer, T. M. 338
Rissmann, E. 254
Robbins, D. J. 212
Robblee, L. S. 390, 391
Roberge, R. 400

Abstract No.

Roberts, J. S. 117
Robichaud, R. 385
Roche, M. F. 370
Rodan, G. A. 307
Roedel, R. J. 179
Roesch, A. 155
Rohatgi, A. 65, 196, 207
Rolison, D. 293
Rollins, V. 55
Roper, G. 116
Rose, A. 57
Rose, R. M. 401
Rosner, D. E. 235
Roth, E. P. 84
Rovedo, N. 165
Rozgonyi, G. A. 104
Ruzzak, M. A. 240
Ryan, F. M. 217
Ryan, M. D. 321
Ryssel, H. 138
Ryuzan, O. 127

Sabacky, B. J. 291
Sai-Halasz, G. A. 128
Sakurai, T. 127, 206
Salagoity, M. 47
Salama, A. M. 194
Salardenne, J 47, 91, 379
Salvi, M. 160
Sammells, A. F. 242
Sampson, W. B. 399
Samuelson, G. M. 164
Sanjurjo, A. 60
Saraswat, K. C. 144, 146
Sato, S. 139
Sato, T. 206
Sattar, A. 327
Savy, M. 349, 350
Saxena, R. R. 184
Scarbeck, G. 349
Schmickler, W. 326
Schmid, F. 62, 63
Schnaper, G. H. 85
Scholberg, H. M. 362
Schroeder, A. H. 301
Schultze, J. W. 332
Schumm, B., Jr. 20
Schwartz, B. B. 398, 400
Sculfort, J. L. 81
Seager, C. H. 244
Selman, J.R. 364
Sera, T. 118
Serrano, C. M. 120
Seshadri, K. 235
Sexton, F. W. 72
Shabrang, M. 265
Shahi, K. 367, 369
Sharma, G. C. 169
Sharpe, C. D. 190
Shepard, V. R. 304
Shinoda, M. 152
Shirasu, T. 174
Shone, M. 224
Shteyer, A. 307
Sim, J. W. 7
Simpson, T. L. 312
Sirtl, E. 149
Sisken, B. F. 310
Small, M. B. 177
Smalley, J. F. 271
Smeltzer, W. W. 12, 383
Smith, R. D. 102
Smith, S. D. 311
Smyrl, W. H. 33
Soled, S. L. 351
Sopori, B. L. 76
Spacil, H. S. 236
Spadaro, J. A. 314
Spaepen, G. 14

Abstract No.

Spasojevic, M. ... 353
Spindler, W. C. ... 245
Spitler, M. T. ... 329
Spray, D. C. ... 313
Srinivasan, S. ... 18, 249, 347
Staebler, D. L. ... 198
Staehle, R. W. ... 45
Stafford, G. R. ... 285
Stanford, T. G. ... 288
Stankovich, M. T. ... 318
Stearns, C. ... 235
Stephens, D. E. ... 265
Stewart, G. R. ... 403
Stewart, G. W. ... 233
Stinespring, C. D. ... 233
Stoner, G. E. ... 264, 285
Störmer, H. L. ... 129, 130
Strasser, K. ... 16
Strauss, B. P. ... 397
Strauss, J. B. ... 254
Street, G. B. ... 201
Struck, C. W. ... 211
Suchow, L. ... 145
Suenaga, M. ... 399
Sugier, A. ... 25
Sunami, H. ... 87
Sung, C. ... 93
Suzuki, A ... 215
Suzuki, H. ... 103
Swaroop, R. B. ... 8
Swarup, P. B. ... 112
Swartz, D. J. ... 34
Sweet, J. N. ... 84
Sy, C. C. ... 370
Sylwan, C. ... 19
Szklarz, E. G. ... 403

Tai, K. L. ... 94
Takahashi, S. ... 101
Takahashi, T. ... 223
Takasu, A. ... 189
Takeda, T. ... 222
Tallman, D. E. ... 305
Taniguchi, K. ... 134
Tanimizu, S. ... 215
Tanimoto, K. ... 119
Tanner, D. ... 75
Tarui, Y. ... 88
Tatsuta, S. ... 206
Tavakoli-Attar, J. ... 364
Taylor, E. J. ... 18, 347
Taylor, G. W. ... 140
Temkin, H. ... 179, 180
Terashima, K. ... 225

Abstract No.

Thaller, L. H. ... 252
Thompson, T. ... 97
Tischner, H. ... 35
Todd, C. J. ... 123
Tokunaga, H. ... 152
Toland, D. E. ... 248
Tomczuk, Z. ... 370
Tomiki, T. ... 222
Tong, H. S. ... 34
Toyokura, N. ... 152
Trainham, J. A. ... 288, 289
Tryk, D. A. ... 319
Tsai, K. C. ... 373
Tsaur, B. Y. ... 109, 110
Tseung, A. C. C. ... 27, 53, 173, 251, 263
Tsuchimoto, T. ... 114
Tuller, H. L ... 346
Turner, M. ... 248

Uchiyama, Y. ... 192
Ueda, R. ... 119
Ullevig, D. M. ... 297
Ulrich, G. D. ... 232
Umaña, M. ... 293
Ushio, S. ... 200

Vaaler, L. E. ... 258
Vaidyanathan, K. V. ... 107
Van de Mark, M. R. ... 299
Vandenberg, M. ... 90, 99
van den Brink, F. T. B. J. ... 32
van den Broeck, H. ... 14, 17
van de Wijgert, W. M. ... 202
van Nice, H. L. ... 227
van Poucke, L ... 14
Varahramyan, K. ... 113
Varker, C. J. ... 208
Varma, R. ... 112
Venkatesh, S. ... 42
Vielstich, W. ... 340
Vigneron, J. ... 358
Vilche, J. R. ... 43
Villet, R. H. ... 279
Virkar, A. V. ... 365
Visscher, W. H. M. ... 32
Vissers, D. R. ... 371
Volk, C. E. ... 100

Wagner, J. B., Jr. ... 367, 368, 369
Wakayama, S. ... 167
Walker, G. W. ... 247
Walpole, J. N. ... 124
Walton, E. G. ... 295
Wang, D. Y. ... 3

Abstract No.

Wang, R. ... 54
Warde, C. J. ... 374
Wasielewski, M. R. ... 269
Watanabe, K. ... 167
Watanabe, M. ... 225
Weaver, M. J. ... 342
Weber, M-C. ... 309
Webster, R. T. ... 77, 113
Weinberg, N. L. ... 255
Weisbrod, K. R. ... 44
Welch, C. ... 286, 287
Werner, W. M. ... 172
White, W. B. ... 214
Wiegmann, W. ... 129, 130
Wiesner, J. ... 97
Wiles, D. M. ... 73
Willig, F. ... 329
Willis, P. ... 74
Winemiller, S. L ... 274
Wirtz, G. P. ... 4
Witzke, H. ... 240
Wolf, J. F. ... 351, 376, 377
Wolfson, R. G. ... 61
Wrighton, M. S. ... 295
Wrona, M. Z. ... 317
Wronski, C. R. ... 80
Wu, J. J. ... 289
Wu, S. ... 156

Yamada, O. ... 223
Yamaguchi, T. ... 139
Yamamoto, N. ... 153
Yamashita, K. ... 270
Yamoto, H. ... 168
Yang, C. Y. ... 1
Yaniv, M. ... 40
Yao, T. ... 118
Yeager, E. ... 28, 29, 344, 352
Yeo, R. S. ... 249
Yeung, K. L. K. ... 27
Yoo, H. ... 75
Young, D. J. ... 12
Young, R. C. ... 271
Young, R. W. ... 89
Young, W. C. ... 136, 170
Youngman, D. ... 274
Yu, H. ... 197
Yueh, A. ... 321
Yuen-hong, C. ... 23

Zagal, J. ... 344
Zakzouk, A.-K. M. ... 205
Zeto, R. J. ... 96
Zundelvich, Y. ... 259

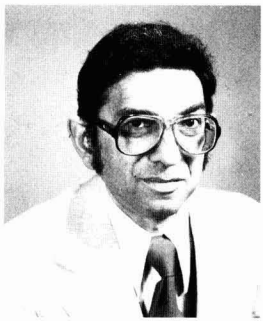
HIGHLIGHTS OF THE BOSTON MEETING

Morton B. Panish to Receive the Solid State Science and Technology Award

Morton B. Panish, head of the Material Science Research Department of the Solid State Electronics Laboratory at Bell Laboratories, has been selected as the fourth recipient of The Electrochemical Society Award in Solid State Science and Technology. The award will be presented at the Awards and Recognition Session on Tuesday, May 8, at 4:30 P.M. in the Grand Ballroom of the Sheraton Boston during the 155th Meeting of the Society in Boston, Massachusetts. Dr. Panish's address, entitled "III-V Heteroepitaxy and Heterostructure Lasers," will immediately follow the presentation.

The Solid State Science and Technology Award, which consists of a silver medal (and a bronze replica thereof) and a $1500 prize, was established by the Board of Directors of The Electrochemical Society to be bestowed every two years for "outstanding contributions to the field of Solid State Science and Technology."

Dr. Panish was born in 1929 in New York City. He attended the New York City schools and was an undergraduate student at Brooklyn College and Denver University. He received the B.S. degree from the latter in 1950. He attended graduate school at Michigan State University where he received his



M.S. and Ph.D. degrees in physical chemistry in 1952 and 1954. Dr. Panish's masters thesis concerned magnetic moments of some simple organic compounds, and his Ph.D. thesis was on thermodynamic and physical properties of several interhalogen compounds. From 1954 to 1957 he was a chemist at Oak Ridge National Laboratory where he investigated the thermodynamic properties of molten salts. From 1957 to 1964 he was at the Research and Advanced Development Division of AVCO Corporation where he was engaged primarily in thermodynamic studies of refractory materials at very high temperatures. In 1961 he was appointed chief of the Physical Chemistry Section and was responsible primarily for studies in very high temperature chemistry.

Dr. Panish was appointed a member of the technical staff of Bell Laboratories in 1964. He was initially concerned primarily with elucidating phase equilibria in III-V systems, particularly III-V dopant systems as a precondition for understanding dopant incorporation during crystal growth and diffusion of impurity elements into III-V compounds. In the late 1960's these efforts were expanded to include phase studies of crystalline solid solutions among III-V compounds, multilayer liquid phase epitaxy, and optoelectronic studies of III-V binary and ternary compounds. In 1969, Dr. Panish, with his collaborator Dr. Izuo Hayashi, demonstrated that the GaAs-$Al_xGa_{1-x}As$ heterojunction could be used to dramatically reduce the room temperature threshold current density of injection lasers, and in 1970 they presented the first experimental evidence for room temperature cw operation of an injection laser. In subsequent years, with a number of collaborators, Dr. Panish has continued studies

Continued on p. 162C

Philip Morrison To Give The Electrochemical Society Lecture

Philip Morrison has been selected to deliver the ECS Lecture at the Plenary Session of the 155th Society Meeting in Boston, Massachusetts. His lecture, entitled, "Microwatts to Supernovae—and Up—," is to be presented at 9:00 A.M. on Monday, May 6, in the Grand Ballroom of the Sheraton-Boston Hotel.

Dr. Morrison, Institute Professor and Professor of Physics at the Massachusetts Institute of Technology, is both a distinguished theoretical physicist and a respected scholar-philosopher whose ecumenical intellectual interests embrace the broad sweep of human and scientific history from the origins of the universe to the origins and definitions of life itself.

Professor Morrison is widely known for his own professional contributions to theoretical physics, in recent years mostly in astrophysics. He is the author of detailed theories aimed at explaining phenomena such as supernovae, cosmic x-rays, galaxies, quasars, and questions in cosmology.

He was one of the first scientists to predict that knowledge as to whether life exists on other planets may not be beyond our reach. He is a frequent contributor to literature having to do with the discovery of life elsewhere in the universe and was a principal participant in an international conference on the subject at Byurakan, U.S.S.R., in 1971, a widely reported symposium at



Boston University in 1973, and a NASA study completed in 1976. He took part in pre-Viking Symposium of July 1976.

Professor Morrison is equally well known as an interpreter of science and technology for the general public. He is the author of numerous popular-scientific articles which have appeared in "The New Yorker," "The Saturday Evening Post," "The New Republic," "Science," "Nation," "The Saturday Review," "Newsweek," "New York Times Book Review," and "Scientific American." He is coauthor of the physics text, "Introductory Nuclear Theory," and the author of a booklet based on a BBC TV series "Fabric of the Atom." He became associated with the Physical Science Study Committee (forerunner of Education Development Center, Incorporated) at its inception and is coauthor of its secondary school text, "Physics." He is also coeditor of "Charles Babbage and his Calculating Engines," a collection of writings by Babbage and others. In 1960 he received the AAAS-Westinghouse Science Writing Prize.

He was one of the 20 scholars who contributed the first "Courses by Newspaper" program. He has taken part in a number of television shows on educational and commercial networks and in the BBC.

Professor Morrison's own reading habits are voracious and almost legendary. He is, for example, the regular book editor of the magazine, "Scientific American," for which he writes a half dozen or more reviews monthly on all subjects ranging from theoretical physics to computerized baseball. Each December, he and his wife, Phylis, jointly review some 50 children's books in science for "Scientific American."

Professor Morrison was born in Somerville, New Jersey, in 1915. He attended Pittsburgh public schools and received his Bachelor of Science degree at the Carnegie Institute of Technology in 1936. He received the Ph.D. in theoretical physics at the University of California, Berkeley, in 1940, and for

Continued on p. 162C

NEW HONORARY MEMBERS



Ralph M. Hunter Elected Honorary Member

At the October 1978, meeting in Pittsburgh, Pennsylvania, the Honors and Awards Committee recommended to the Board of Directors that Ralph M. Hunter be designated an Honorary Member of the Society. The Board voted unanimously to approve the committee's recommendation and to present the Honorary membership scroll to Dr. Hunter at the Awards and Recognition Session on May 8, 1979, in Boston.

Dr. Hunter was born in Philadelphia in 1896. He received his B.S. degree in chemical engineering from Case Institute of Technology, which granted him an honorary doctorate in 1950. He joined The Dow Chemical Company in 1918, and remained with Dow until his retirement in 1961. He has developed many processes and designs in electrolytic production of magnesium, chlorine, caustic soda, liquefaction of chlorine, ammonia, and bromates. He has been granted 19 patents in the areas of electrolytic chlorine, magnesium cells, and brine treatment. He was the key man in the expansion of magnesium production and transfer of Dow magnesium technology during World War II. In 1945, he served as consultant for the Technical Industrial Intelligence Committee investigating and reporting on the German electrochemical industry. He is a chlorine and magnesium expert.

Dr. Hunter has participated in Society activities since the 1920's, attending many Society meetings. He was instrumental in forming the Industrial Electrolytic Division in 1943 and served as its vice-chairman and chairman. He also spear-headed the formation of the Midland Section of the Society. He presented the petition to the Board of Directors and was temporary chairman when the application was approved by the Board in 1944.

On the retirement of Colin Fink as secretary of the Society, Dr. Hunter was appointed to the "Committee on Survival" of the Society, along with Drs. Heise, Faust, Swann, and Lee, with Dr. Burns (as secretary). He has also served on numerous Society Committees, such as the Publication Commit-

Continued on p. 163C



Harry C. Gatos Elected Honorary Member

At the meeting in Pittsburgh, Pennsylvania in October 1978, Honorary Membership in the Society was conferred on Harry C. Gatos at the Awards and Recognition Session.

Professor Gatos was born in Amphissa, Greece in 1921. He received his undergraduate diploma in chemistry summa cum laude from the University of Athens. In the fall of 1946 he was awarded a one-year fellowship by the Institute of International Education, New York, New York, for graduate studies in the United States. He was awarded an M. A. degree in chemistry in 1948 from Indiana University and went on to attain a Ph.D. in inorganic chemistry from the Massachusetts Institute of Technology in 1950.

From 1950 to 1952 Professor Gatos was a research associate in M.I.T.'s Department of Metallurgy, carrying out research on self-diffusion in metals. In 1952 he joined the research staff of the Engineering Research Laboratory of E.I. du Pont de Nemours and Company, where he was involved until 1955 in research on the corrosion and corrosion inhibition of metals.

Becoming a United States citizen in 1955, in October of that year he accepted a position as leader of the chemistry section in the Solid State Group of M.I.T.'s Lincoln Laboratory. In that position he coordinated R&D work in electronic materials with the fundamental and applied physics research in the group. He was appointed the first Associate Head of the then newly established Solid State Division at Lincoln Laboratory, and he continued his research on structure-property relationships in semiconductors and superconductors. In 1962 he resigned as Associate Head of the Solid State Division to accept the joint appointment as Professor in the Departments of Metallurgy and of Electrical Engineering. Professor Gatos was Head of the Solid State Division of Lincoln Laboratory from the summer of 1964 until September 1965, and then he returned full time to teaching and research in his present position, Professor of Electronic Materials, Department of Materials Science and Engineering, and Professor of Molecular

Continued on p. 163C

DIVISION NEWS

Electronics Division

The Electronics Division announces the following slate of nominations for officers, with the election to be held at the Division luncheon at the Society's meeting in Boston.

Chairman: A. Reisman, IBM.

Vice-Chairman, General Materials and Processes: R. Enstrom, RCA.

Vice-Chairman, Luminescence: F. Ryan, Westinghouse.

Vice-Chairman, Semiconductors: D. W. Shaw, Texas Instruments.

Secretary: E. H. Nicollian, Bell Laboratories.

Treasurer: W. McAllister, Westinghouse.

Members at Large will be listed in the April 1979 issue of **This Journal.**

Organic and Biological Electrochemistry Division

Report of the Nominating Committee

The Nominating Committee of the Organic and Biological Electrochemistry Division has proposed the following slate of officers for the term 1979-1981:

Chairman—Larry Miller
Vice-Chairman—John Wagenknecht
Secretary-Treasurer—Martin Blank

Election of officers will take place at the Business Meeting of the Division to be held during the Spring 1979 Society Meeting in Boston, Massachusetts.

Allen J. Bard
Charles K. Mann
Stanley Wawzonek

Physical Electrochemistry Division

Report of the Nominating Committee

The following nominations for officers in the Physical Electrochemistry Division, 1979-1981, have been made by the Nominating Committee, consisting of J. D. E. McIntyre, Chairman, Fred Anson, and M. W. Breiter. All nominees have been notified of their nomination; all have accepted and have indicated their willingness to run and serve in their respective offices.

Chairman—Fritz G. Will
Vice-Chairman—Elton J. Cairns
Secretary-Treasurer—Robert A. Osteryoung

Members of the Executive Committee (two to be elected):
J. Braunstein
L. R. Faulkner

The election of officers will be held at the Division's Business Meeting and Luncheon during the 1979 Spring Meeting of the Society in Boston, Massachusetts.

Additional nominations for office may be made by petition signed by five members of the Division. These must be in the hands of the Chairman of the Nominating Committee at least ten days before election with written assurance of the nominee's willingness to

serve. Nominations in the form of a petition signed by five or more members may be made from the floor at the time of the annual meeting at which officers are elected, provided the willingness of the nominees to serve is expressed in writing prior to the election.

J. D. E. McIntyre, Chairman
Nominating Committee

PEOPLE



Jack Davis, Vice-President/R&D of Bright Star Industries, Clifton, New Jersey, is being retained as consultant to the company upon his retirement as vice-president, effective as of the first of 1979. In his new capacity, he will also be available for outside consultation practice.

Mr. Davis started as technical director of Bright Star in 1962, and later became manager of R&D, a period during which he led the company's development of its highly successful Battery-Pack systems for industrial flashlights currently being marketed.

Mr. Davis is widely identified with dry cell chemical technology both here and abroad. He holds battery patents connected with electrochemical systems and has published papers and articles on primary batteries, dry cells, mercury and nuclear batteries, wet cells, and reserve batteries. He is currently conducting seminars on electrochemical energy sources at various colleges including Cal Tech and Stevens Institute.

Schooled in England where he was born in 1913, Mr. Davis obtained a National Scholarship to King's College, University of London, from which he graduated with a BSC degree in special chemistry. He then completed work for his doctorate at London and New York Universities. He has taught and lectured at colleges both here and abroad.

Prior to joining Bright Star, Mr. Davis was employed as senior research chemist for Ever Ready Company, Limited, of Great Britain. He is an active member and past chairman of the Metropolitan New York Section of The Electrochemical Society; a fellow of the Royal Institute of Chemistry, as well as president of its American Section; fellow of the Chemical Society; member of the American Chemical Society and American Association for Advancement of Science. He is a committee member of American National Standards Institute, and of the National Electrical Manufacturers Association on Dry Cells and Batteries. In addition, he is national director of the American Institute of Chemists and is on the editorial board of "The Chemist" publication.

Aladar Tvarusko has joined Diamond Shamrock Electrosearch S.A. in Carouge/Geneva, Switzerland, as manager of the Exploratory Research Department. He was formerly associated with LSRH in Neuchâtel, Switzerland, with Western Electric Company, and ESB, Incorporated. Dr. Tvarusko has been a member of the Society for 13 years, and has served it in several functions.

NEW MEMBERS

It is a pleasure to announce the following new members of The Electrochemical Society as recommended by the Admissions Committee and approved by the Board of Directors in January 1979.

Active Members

Abramovich, M., Campinas, Brazil
Ashikawa, M., Mountain View, Ca.
Bartholomew, R. F., Poughkeepsie, N.Y.
Batchelder, G., Manitou Springs, Co.
Brookman, M. J., Clarence, N.Y.
Buchman, R. C., Alexandria, Va.
Chang, V. A., Rolling Meadows, Il.
Constant, G., Toulouse Cedex, France
Daforno, J. J., Cedar Knolls, N.J.
De Castro, M. A. C., Rio De Janeiro, Brazil
Demizu, K., Kikuchi-Gun Kumamoto-Pref., Japan
Downey, D. F., Gloucester, Ma.
Elliott, R. W., Missisauga, Ont., Canada
Emons, H. H., Leipziger Strabe, Germany
Evans, J. W., Berkeley, Ca.
Fisher, G. L., Mahwah, N.J.
Frankenthaler, J., Newton, Ma.
Gillis, H. P., Culver City, Ca.
Gottesfeld, S., Murray Hill, N.J.
Hadjicostantis, D. C., Xanthi, Greece
Hedgcoth, V. L., Azusa, Ca.
Heyrovska, R., Praha, Czechoslovakia
Jacobs, D. F., Houston, Tx.
Laudise, R. A., Berkeley Hts., N.J.
Malone, F. D., Richardson, Tx.
Middaugh, R. L., Rocky River, Oh.
Muschinske, J. E., Sunnyvale, Ca.
Pan, K.-C., Webster, N.Y.
Perini, C. A., Hauppauge, N.Y.
Queirolo, G., Milano, Italy
Racette, J. H. Katonah, N.Y.
Slattery, J. A., Utica, N. Y.
Spratt, D., Plano, Tx.
Streit, C. A., Clarence, N.Y.
Sumner, B. G., Washington, D.C.
Tunder, R., Scotia, N.Y.
Vilche, J. R., La Plata, Argentina
Wierschem, G. L., Milwaukee, Wi.
Wittmer, M., Baden, Switzerland

Student Members

Abderrassoul, R. A., Dallas, Tx.
Bennewitz, C. D., Hamilton, Ont., Canada
Grinolds, H., Minneapolis, Mn.
Hebert, K. R., Urbana, Il.
Khalily, E., Stanford, Ca.
Ma, D., Stony Brook, N.Y.
O'Malley, R. J., Cambridge, Ma.
Parthasarathy, L., Stony Brook, N.Y.
Perko, C. J., Golden, Co.
Roston, D. A., Cincinnati, Oh.
Wong, W. C., Los Angeles, Ca.

Member Representatives

Clauss, R. J., Allen Park, Mi.
Kelly, S. L., Houston, Tx.
Shannahan, C. E., Englewood Cliffs, N.J.

NEWS ITEMS

Symposium on Applied Surface Analysis

A Symposium on Applied Surface Analysis will be held June 13-15, 1979, at the University of Dayton, Dayton, Ohio. Topics will include, but are not limited to, corrosion, adhesion, semiconductors, energy conversion, thin films, thermionic emitters, and catalysts. The symposium will be preceded by a short course on "Techniques for Surface Analysis."

For further information, please contact: Dr. J. T. Grant, University of Dayton, Research Institute, Dayton, Ohio 45469, or Dr. T. W. Haas, AFML/MBM, Wright-Patterson Air Force Base, Dayton, Ohio 45433.

Société de Chimie Physique International Meeting

The next international meeting of the Société de Chimie Physique will be held September 24-28, 1979, in Villeurbanne-Lyon, France, on the topic, "Growth and Properties of Metal Clusters Applications to Catalysis and the Photographic Process." Titles and abstracts of papers must be submitted to Dr. Jean Bourdon, Chairman of the Organizing Committee, Société de Chimie Physique, 10, rue Vauquelin F 75231, Paris, Cedex 05, France.

Engineering Summer Conferences

The University of Michigan is again holding Engineering Summer Conferences on various topics on its campus in Ann Arbor, Michigan. Conferences of interest and their dates are as follows: Corrosion Engineering, June 25-27, 1979; Electrochemical Engineering, July 30-August 3, 1979; Solar Energy Measurements and Instrumentation, July 9-10, 1979; and Advanced Infrared Technology, June 25-29, 1979.

For further information, and to register, please write to: Engineering Summer Conferences, 800 Chrysler Center, North Campus, the University of Michigan, Ann Arbor, Mich. 48109; telephone 313-764-8490.

Glass Conference

Rensselaer Polytechnic Institute is hosting the next Glass Conference August 22-24, 1979, at RPI, Troy, New York. This Glass Conference is one of a series of university conferences, and the topic is to be electrical, magnetic, and optical properties of glasses.

A conference proceedings will be published, and a brochure of the conference will be circulated shortly. For further information, please contact R. H. Doremus, School of Engineering, Materials Engineering Dept., Rensselaer Polytechnic Institute, Troy, N.Y. 12181; telephone 518-270-6371.

Morton B. Panish continued

of III-V thermodynamics, crystal growth, and III-V optoelectronic material and device properties.

In 1969 Dr. Panish was appointed to head the Materials Science Research Department of the Solid State Electronics Laboratory at Bell Laboratories. This department has primarily been concerned with the study of the physics and chemistry of III-V compounds and of III-V epitaxy for fundamental studies of heterojunctions and periodic structures and for optoelectronic and microwave devices.

Dr. Panish has been accorded about a dozen U.S. patents. He is also coauthor with H. C. Casey, of the book, "Heterostructure Lasers." He is a fellow of the American Physical Society and a member of The Electrochemical Society. He has served on the Board of the Electronics Division of the Society and has been a member of the Board of Editors of the "Journal of Applied Physics" and "Applied Physics Letters." In 1972 Dr. Panish received The Electrochemical Society's Electronics Division Award.

Philip Morrison continued

the next two years taught physics first at San Francisco State College and then at the University of Illinois, before joining the Manhattan Project in 1943.

From 1943 to 1946, Professor Morrison was associated with the Manhattan Project, which was responsible for the development of the first atomic bomb. He rode in the back seat of an automobile with the plutonium core from Los Alamos to the New Mexico desert site for the first test of the bomb in 1945, and later witnessed the aftermath in Hiroshima, which he visited immediately after the war. In later years Professor Morrison opposed the development of the hydrogen bomb, and refused to participate in arms development.

In 1946 Professor Morrison joined the physics faculty at Cornell University, where he remained until he went to M.I.T. in 1964 as Francis L. Friedman Lecturer and Visiting Professor of Physics. He accepted a permanent faculty appointment at M.I.T. in 1965.

In 1973, he was appointed to the distinguished rank of Institute Professor at M.I.T., a rank M.I.T. reserves only for its most outstanding scholars.

He has given a course of lectures, among other places, at the Imperial College of Science in London, the Tata Institute for Fundamental Research in Bombay, the University of Kyoto, Japan, the University of Ife, Nigeria, at a series of Canadian Universities, and in the U.S. at UCLA and the University of Arizona.

A member of the National Academy of Sciences and a Fellow of the American Physical Society, Professor Morrison is also a member of the Federation of American Scientists (its chairman in 1973-1976), the American Association of Physics Teachers (which awarded him its 1965 Oersted Medal), the American Astronomical Society, and the International Astronomical Union. He gave an invited discourse at the IAU Grenoble, 1976.

In 1955 he received the Pregel Prize of the New York Academy of Science, and in 1957, the Babson Prize of the Gravity Foundation. In 1968-1969 he presented the 139th series of Christmas Lectures in science for children at the Royal Institution of London, which were broadcast by BBC-TV; and in 1975 he gave a similar lecture at Northwestern University. He was Danz Lecturer at the University of Washington, 1973.

Book Reviewers Needed

The Electrochemical Society needs competent individuals to review books for the Journal.

Any Society member who wishes to volunteer his services should send his name, address, and field of competence to the attention of the Book Review Editor, Dr. Julius Klerer, c/o The Electrochemical Society, P.O. Box 2071, Princeton, N.J. 08540

CALL FOR RECENT NEWS PAPERS AND EXTENDED RECENT NEWS PAPERS

Boston, Massachusetts, Meeting May 6-11, 1979

Triplicate copies of a 75-word abstract of a Recent News Paper, for a 10 minute presentation, must be received by the Symposium Chairman not later than March 20, 1979.
Triplicate copies of a 75-word abstract and, also, a 200-300 word abstract of an Extended Recent News Paper, for a 20 minute presentation, must be received by the Symposium Chairman not later than March 9, 1979.

ELECTRONICS DIVISION

Recent News Papers and Extended Recent News Papers are invited for the sessions sponsored by the Electronics Division for the 1979 Spring Meeting in Boston, Massachusetts. The time allotted for the 75-word Recent News Paper will be 10 minutes, including 2 minutes for discussion. The time allotted for the Extended Recent News Paper will be 20 minutes, including the question/answer period.

The Extended Recent News Paper requires, in addition to the 75-word abstract, a 200-300 word abstract in triplicate and should be received significantly earlier than the normal deadline date because these papers will be reviewed for technical content, appropriateness of the paper, time limitations, duplication of material, etc. Topics for Recent News Papers and Extended Recent News Papers include:

1. Low temperature processing
2. Ion implantation
3. Molecular beam epitaxy
4. Process and device modelling
5. Materials preparation, characterization, and device fabrication
6. Phosphor efficiency and saturation
7. X-ray phosphors and radiography
8. Packaging of electronic devices

Copies of all abstracts, as outlined above, should be sent to the Recent News Papers Symposium Chairman: W. A. Pliskin, IBM Corp., Dept. 175, Internal Zip 462, Route 52, Hopewell Junction, N.Y. 12533. Please note the deadlines above.

RESEARCH SCIENTIST/ENGINEER

Opportunity exists in the Research Laboratories of General Motors Corporation for a qualified individual interested in research and development work in the areas of electrodeposited surface coatings and associated processes.

Requirements include a Ph.D. in physical sciences or engineering with emphasis on physical chemistry or hydrometallurgy. Some knowledge of electrochemistry desirable but not necessary.

Applicants must have a Citizenship of Visa Status which permits them legally to accept permanent employment under U.S. Immigration Laws.

Send resume to:
Dr. J. L. Hartman, Head
Electrochemistry Department

GM
GENERAL MOTORS RESEARCH LABORATORIES
WARREN, MICHIGAN 48090
We Are An Equal Opportunity Employer

SENIOR RESEARCH CHEMIST

Due to expansion, Energetics Science requires a Senior Chemist for research and development of electrochemical air pollution instrumentation. Candidate must have a Ph.D. in electro or physical chemistry. This position can be filled by a recent graduate. Individual must be a self-starter and work with minimal amount of supervision.

Position offers excellent career opportunity with young growth company. Interested candidates should send complete resume/C.V. along with salary requirements to Supervisor Employment, Becton Dickinson and Company, Paramus, New Jersey 07652.

Energetics Science
"The Ecolyzer People"
division of
Becton Dickinson and Co.

Ralph M. Hunter continued

tee in 1943; the Acheson and Perkin Medal Committees; the Ways and Means Committee, being chairman in 1949; the Financial Advisory Committee, and others. He was vice-chairman in 1944 and chairman in 1946 of the Industrial Electrolytic Division. He was elected as vice-president of the Society in 1948 and president in 1951. He participated in Society activities until the 1970's, as a member of the Investment Advisory Panel and in other committee assignments.

Harry C. Gatos continued

Engineering, Department of Electrical Engineering, at M.I.T.

Awarded the NASA Medal for exceptional Scientific Achievement in 1974 for his work on crystal growth and segregation in space, Professor Gatos has served as a consultant to government agencies and many industrial organizations.

Professor Gatos has been very active in The Electrochemical Society. He served as Vice-Chairman (1961-1962) and Chairman (1962-1963) of the Corrosion Division. He was Secretary (1961-1962) and Chairman (1962-1963) of the Council of Local Sections. During 1958-1959 he served as Vice-Chairman of the Boston Local Section and as Chairman from 1959-1960. He was a Divisional Editor of **This Journal** of corrosion-semiconductors. He was elected as Vice-President of the Society in 1964 and President in 1967. He was selected as the second recipient of the Society's Solid State Science and Technology Award and received the award at the Toronto, Canada, Meeting of the Society in May 1975.

Boston, Massachusetts, Meeting Program 92C-158C
Highlights of the Boston, Massachusetts, Meeting 159C-162C
New Honorary Members 160C-163C
Division News 160C
People 161C
New Members 161C
News Items 161C
Call for Recent News Papers—Boston, Massachusetts, Meeting 162C
Wanted to Buy 164C
Position Wanted 164C
Notice to Members 164C
Call for Papers—Los Angeles, California, Meeting 169C-174C

ADVERTISERS' INDEX

Becton Dickinson and Co. 163C
GM Corp. 163C
IC MnO_2 Sample Office 166C
NCR Corp. 164C
Princeton Applied Research Corp. 165C

WANTED TO BUY

Wanted to Buy—rejected electrochemical instruments and equipment. Please quote to Box A-1.

POSITION WANTED

Please address replies to the box number shown, c/o The Electrochemical Society, Inc., P.O. Box 2071, Princeton, N. J. 08540.

Electrochemist/Battery Engineer—Ph.D. level. 22 years of experience in battery systems for commercial and aerospace applications both with battery vendors and aerospace companies. Innovative self-starter with many patents, papers, and publications. Research and development work in Ni-Cd, Ni-H_2, Ag-Cd, Ag-Zn, Al-Cl_2, metal-air, and fuel cell batteries. Seeks senior position with government, battery company, or aerospace firm. Reply Box C-211.

Positions Wanted

Society members of any class may, at no cost and for the purposes of professional employment, place not more than three identical insertions per calendar year, not to exceed 8 lines each. Count 43 characters per line, including box number, which the Society will assign.

Notice to Members

April 1 is Cut-Off Date

Your attention is called to Article III, Section 8 of the Society Constitution which states: "Any member delinquent in dues after April 1 of each year shall no longer receive the Society's publications, and will not be allowed to vote in any Society election until such dues are paid. All members in arrears for one year after the first of April shall lose their membership status and can be reinstated only by action of the Board of Directors." Members who have not sent in 1979 payments were mailed a second notice in February and are urged to make payment promptly in order to avoid delay in receipt of the JOURNAL.

Semiconductor Engineers & Scientists

NCR Microelectronics offers you a direct entry to VLSI.

We are a MOS/LSI design leader that's rapidly accelerating. We pigeon-hole nobody. Our pioneering work in non-volatile semiconductor memories (utilizing two-layer polysilicon N-channel silicon gate processing) will lead straight to next generation VLSI processes. We're shaping the whole future of NCR microprocessors and, unlike other LSI organizations, we're seeking Engineers and Scientists who are generalists rather than narrow specialists.

Right now, we're looking for **Advanced Process Development Engineers** who can be major contributors in developing VLSI. We require 3-5 years of industrial experience in MOS and CMOS or CMOS/SOS process and device development, and an MS or PhD in EE, Physics or Materials Science. And we're looking for **Device Physics Engineers** who are knowledgeable in MOS physics, have BS/MS in EE or Physics, and are capable of devising and analyzing VLSI structures.

Moreover, we offer an award-winning laboratory with the very latest design/manufacturing equipment, and generous relocation assistance to one of the most attractive and affordable communities in the Midwest.

Investigate a professionally stimulating future with NCR by sending your resume in strict confidence to: Mr. Thomas F. Wade, Manager, Personnel Resources, Dept.C-113, NCR Microelectronics Division, 8181 Byers Road, Miamisburg, Ohio 45342.

NCR
Complete Computer Systems

An equal opportunity employer

CHANGES OF ADDRESS SHOULD BE PROMPTLY REPORTED.

ATTACH LABEL HERE

Change of Address

To change your address, place address label here for proper identification. Print your NEW address below.

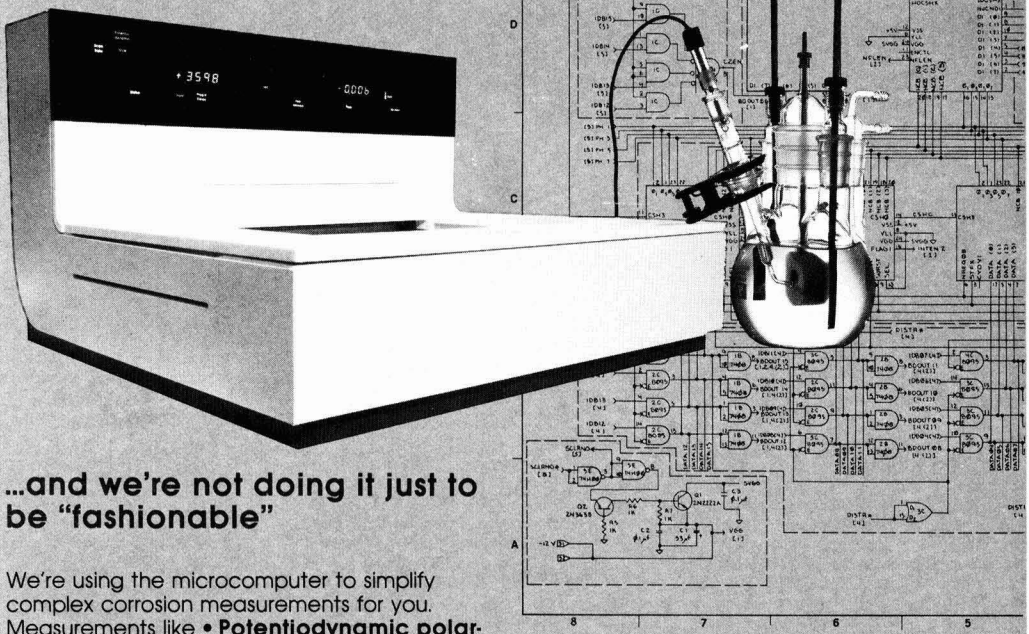
Mail to the Circulation Department, The Electrochemical Society, Inc., P. O. Box 2071, Princeton, N.J. 08540.

name

address

city state zip code

Not everybody's putting microcomputers into their corrosion measurement systems ... JUST US!

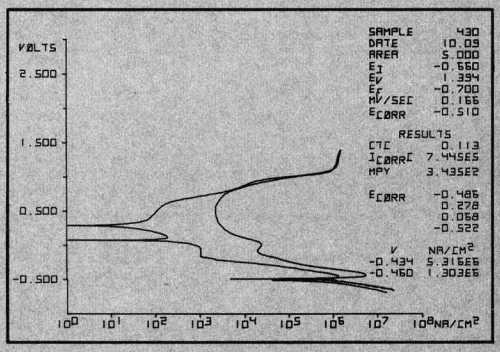


...and we're not doing it just to be "fashionable"

We're using the microcomputer to simplify complex corrosion measurements for you. Measurements like • **Potentiodynamic polarization** scans for passivation tendencies, • **Tafel** and **Polarization plots** for corrosion rates, • **Cyclic polarization scans** for pitting and crevice corrosion studies, • **Corrosion Behavior Diagrams** for rapid scans, • **Sensitization tests** for studying grain boundary attack, • **Galvanic corrosion,** • **Corrosion potentials,** and • **Current integrals.**

The microcomputer will assist you in defining the measurement and obtaining the data. It will replay the scan for you, properly scaled, on the built-in recorder. Calculations such as current density, Tafel constants, corrosion rates and current integrals are performed automatically.

If that weren't enough, the microcomputer also symbolizes the chart paper with the necessary information so you get a permanently labeled record of the experiment.



Cyclic polarization scan of 430 stainless steel in 1 N H_2SO_4. Note detailed legend printed out by Model 350.

Get the full story on the Model 350 Corrosion Measurement System. Write or phone for our Corrosion Measurement Catalog.

EG&G PRINCETON APPLIED RESEARCH

P. O. BOX 2565 • PRINCETON, NJ 08540 • 609/452-2111

487

(1) The 2nd International Symposium on MnO_2 in Japan

The 1st symposium was held in Cleveland (USA) in Oct. 1975. The 2nd symposium is scheduled as follows. The MnO_2 symposium will be held every 5 years. The 2nd symposium will be sponsored by The Electrochemical Society of Japan.

(1) Oct. 28-30, 1980 in Tokyo, Japan at Sasagawa Hall.
(2) Deadline for 75-word abstract: Aug. 31, 1979 **Sasagawa Hall**
(3) Deadline for the full paper: Feb. 28, 1980
(4) Deadline for the registration to attend: July 31, 1980
(5) Please write for information* and registration forms to The I.C. MnO_2 Sample Office below, or call 216-433-8600 Ext. 268.

*The information includes Hotels ($20-60 per night) in Tokyo and charter flight (about $730 for round trip from Chicago to Tokyo). A group trip to MnO_2 plants and historical places in Japan is planned.



Nature of Papers Solicited

(1) Basic properties of MnO_2 for dry cells and other applications, (2) Scientific significance of various measurements of pH value, water contents, particle size distribution, pore size distribution, X-ray pattern, absorption value, etc., (3) Discharge performance, shelf life, leakage, etc. relating to MnO_2 dry cells and alkaline MnO_2-Zn cells and lithium-MnO_2 cells, (4) Production of EMD, CMD and activated natural ore, (5) MnO_2 for lithium cells and capacitors. (See the book below, p. 236-263 in **Progress in Batteries and Solor Cells, Vol. 1, 1978.**) Number of papers to be scheduled is limited to 32.

(2) Battery Active MnO_2 Samples and Their Data Book

A reagent grade MnO_2 (the most pure 100% MnO_2) is quite inactive for dry cells. Some natural MnO_2 ores having MnO_2 content of only 70-80% produce electricity in dry cells far more (4 to 5 times) than the reagent grade pure MnO_2, EMD (electrolytic MnO_2) produces electricity in dry cell 2 to 5 times more than the natural MnO_2 ore. The behavior is not well understood and we call it "battery activity" of MnO_2. We believe this electrochemical activity of MnO_2 is deeply related to its crystal structure, pore size, pore structure, surface area etc. The BET surface area of the active MnO_2 is usually to 60 m_2/g. The BET surface area is mostly the pore walls. Because of the complex nature of MnO_2, we cannot reproduce exactly the same material. Therefore, it is convenient to study MnO_2 using international common (I.C.) MnO_2 samples listed below. For these samples, most properties (chemical and physical, electrochemical and optical properties are studied and published in the databook "Manganese Dioxide, Vol. 1." Therefore, people can measure their own special measurement to make contribution to our knowledge.

I.C. No. 1	**Electrolytic MnO_2 made by Ti anode**	**Japanese producer**
I.C. No. 2	**Electrolytic MnO_2 made by Pb anode**	**Japanese producer**
I.C. No. 3	**Electrolytic MnO_2 made by C anode**	**Japanese producer**
I.C. No. 4	**Electrolytic MnO_2**	**LaPile Leclanche, France**
I.C. No. 5	**Chemically prepared MnO_2**	**Japan Metals & Chemicals Co.**
I.C. No. 6	**Beta MnO_2**	**A reagent grade chemical**
I.C. No. 7	**Natural MnO_2 ore**	**Ghana Ore**
I.C. No. 8	**Chemically prepared MnO_2**	**Sedema, Belgium**
I.C. No. 9	**Electrolytic MnO_2 (coarse grade)**	**Kerr-McGee Corp., U.S.A.**
I.C. No. 10	**Electrolytic MnO_2**	**Kerr-McGee Corp., U.S.A.**
I.C. No. 11	**Chemically MnO_2 made by chlorate process**	**Kerr-McGee Corp., U.S.A.**
I.C. No. 12	**Chemical MnO_2**	**Sedema, Belgium**



Price: No. 1 to 12 is $10 each bottle except No. 11 ($4). Each bottle contain 1 Kg except No. 6 (500g) and No. 11 (100g). Shipping charge is extra. Send your order to The I.C. MnO_2 Office (see the address at the bottom of this page).

Data Book: "Manganese Dioxide Symposium **Vol. 1, Cleveland,** 1975" (538 pages, $35) Compiled by A. Kozawa and R. J. Brodd. This book contains all the papers in the 1st symposium and the data on I.C. MnO_2 samples so far collected. The contents are as follows.

1. Electrochemistry of MnO_2 by P. Ruetschi (Summary of all the previous work on the discharge mechanism of MnO_2) 2. Structural or Bound Water in MnO_2). by K. Miyazaki. 3. Pore characteristics of MnO_2 by Lee and Tye. 4. Discharge Data of These 10 MnO_2 Samples in Practical Cells (Leelanche Type and Alkaline Electrolyte Cells), by Matushita Electric, Toshiba Ray-O-Vac, Hitachi Maxell, Fuji Electrochemical Companies and Ray-O-Vac, Division of ESB, Inc. 5. Crystal Structure of MnO_2 by Prof Burns (M.I.T.). 6 Production Figures of Battery Operated Equipment (radio, tape recorder, flashlights, cameras, etc.) in Japan, 1953-1977, by K. Takahashi. 7. Data: density, MnO_2 content, BET surface area, DTA, TGA data, water content, zinc ion adsorption, data, discharge characteristics, electrode potential values measured in NH_4Cl or in KOH, infrared adsorption curves of MnO_2, x-ray diffraction curves, particle size distribution data, etc., compiled by A. Kozawa.

(3) Research Area on MnO_2 for Dry Batteries

The I.C. MnO_2 Sample Office inquired MnO_2 producers and dry battery manufacturers and collected various scientific and technical problems to be solved. These research areas are summarized in p.241-245 of **"Progress in Batteries and Solar Cells" (400 pages, $36)** edited by A. Kozawa, K. V. Kordesch, E. Voss, J. P. Gabano, etc. The book is available at **JEC Press Inc., Box 42041, Cleveland, Ohio 44142, USA.** The book contains: (1) **View from The Top** (opinions and suggestions on future battery research and business) by **E. B. Yeager, G. Launder, J. P. Brenet, F. L. Tye, M. Yamano, S. Hattori, M. Jacquier, J. Watanabe, T. Takagaki (2) Primary Batteries:** Li-Cells by Sanyo Electric, SAFT, Matsushita Electric, **Silver Oxide Cells: by Varta, Hitachi Maxell etc. Pollution Control** in Battery Production, zinc chloride cells, etc. (3) **Lead-acid Batteries: Overview** by M. J. Caserio General Motors Co., minimizing the grid weight by L. Horn, maintenance-free automobile batteries by K. A.Audo et al., new plastic material by U. Janeau et al., new generation of truck batteries by **J. H. Golz,** emergency power supplies by K. Eberts, stationary batteries with fine grain low antimony lead alloy by **D. Berndt et al.** (4) **Electric Vehicles and Batteries.**



The I.C. MnO_2 Sample Office: Box 6116 (UCC, Room D-19) Cleveland, Ohio 44101 USA

APPLICATION FOR ADMISSION

TO

The Electrochemical Society, Inc.

Return completed application to:

Secretary
The Electrochemical Society, Inc.
Post Office Box 2071, Princeton, New Jersey 08540
609-924-1902

For office use only

Notice of Ackn. _____

recap _____ $ _____

Checked: _____

Approved: _____

To the Board of Directors of The Electrochemical Society, Inc:

Please print complete name and address as it should appear on mailings.

Name: _____

Address: _____

_____

_____

_____

_____

Business Telephone: _____

I hereby make application for admission to The Electrochemical Society, Inc., as a _____ member, and enclose the amount of $ _____ covering the first year's dues. (Please see reverse side for proper class of membership and dues applying thereto, noting the options with regard to the date of election and active life membership and the credit available for nonmember meeting registration.)

1. Date of Birth: _____

2. Please check LOCAL SECTION with which you wish to affiliate:

— Boston (05)	— Detroit (25)	— Natl. Capital Area (45)	— Pacific Northwest (65)	— San Francisco (85)
— Chicago (10)	— Indianapolis (30)	— Niagara Falls (50)	— Philadelphia (70)	— So. Calif.-Nevada (90)
— Cleveland (15)	— Metropolitan N.Y. (35)	— North Texas (55)	— Pittsburgh (75)	— None (99)
— Columbus (20)	— Midland (Mich.) (40)	— Ontario-Quebec (60)	— Rocky Mountain (80)	

3. Please indicate your DIVISIONAL and GROUP interests, noting your primary interest(s) with the number 1 and secondary interest(s) with the number 2.

— Battery (AO)
— Corrosion (BO)
— Dielectrics and Insulation (CO)
— Electrodeposition (DO)
— Electronics (EO)
check specific interest(s) below
☐ General Materials and Processes (E1)
☐ Luminescence (E2)
☐ Semiconductors (E3)
— Electrothermics and Metallurgy (HO)
— Energy Technology Group (GO)
— Industrial Electrolytic (IO)
— Organic and Biological Electrochemistry (FO)
— Physical Electrochemistry (JO)

4. Education:

Institution	Dates Attended	Major Subject	Degree Earned

5. Work Experience:

Name of Employer (current, followed by previous)	Dates	Position

6. The Society's Constitution provides that two Active Members of the Society (who can substantiate the above record) must recommend you for admission to membership. It will facilitate the handling of your application if you are able to have your references sign this application form; if this is not convenient, please list their names and addresses. On a student application, only a single faculty member recommendation with signature (including title and and institution) is required.

Name (please print)	Signature	Address
Name (please print)	Signature	Address

The undersigned certifies that the above statements are correct and agrees, if elected to the Society, to be governed by its Constitution and Bylaws and to promote the objects of the Society as stated in its Constitution.

Date _____ 19 __

_____
(Signature)

Rev. 10/78

EXTRACTS FROM THE CONSTITUTION AND BYLAWS

CONSTITUTION—Article II

Membership

Section 1. The individual membership shall consist of Active, Honorary and Emeritus Members. The Board of Directors may from time to time authorize other classifications of membership as defined in the Bylaws of the Society.

(*Active Member—Annual Dues $30.00*)

Active Member

Section 2. An Active Member shall be interested in electrochemistry or allied subjects and possess a Bachelor's degree, or its equivalent, in engineering or natural science. In lieu of a Bachelor's degree, or its equivalent, any combination of years of undergraduate study and years of relevant work experience in electrochemistry or allied subjects adding to at least seven years shall be required. Election to Active Membership shall require the recommendation of two Active Members in good standing.

BYLAWS—Article II

Non-Voting Membership
(*Student Member—Annual Dues $3.00*)

Student Member

Section 1. Student Member. A Student Member shall be a full-time undergraduate or graduate student registered for a degree in natural science or engineering. The applicant for Student Membership shall be recommended by a member of the faculty of the school. Upon graduation with a Bachelor's degree or equivalent in natural science or engineering, the Student Member may apply for Active Membership. The application shall be approved by two Active Members of the Society in good standing. If the Student Member enters graduate school as a full-time student, the person may choose to apply for Active Membership or remain a Student Member.

BYLAWS—Article XXI

Dues and Fees

Dues

Section 1. The annual dues for Active Members shall be thirty dollars. The annual dues for Student Members shall be three dollars. Each member shall receive the JOURNAL OF THE ELECTROCHEMICAL SOCIETY.

Date of Election

Section 2. When individuals are elected to membership, they must elect to initiate their membership as of January 1 or July 1 of the year of election; or, if elected during the last quarter, January 1 of the year following election. In the case of a July 1 election for starting membership, dues will be prorated.

Active Life Membership

Section 3. Any Active Member who shall pay in one lump sum the amount equivalent to two-thirds of the remaining dues to age sixty-five at the time of payment, but not less than an amount of 5 years of full dues, shall be exempt from payment of any further dues and shall be considered an Active Member during the remainder of his or her life.

Nonmember Meeting Registration Credit

BOARD OF DIRECTORS ACTION OF OCTOBER 9, 1960

If application for new membership is received within four months of the payment of nonmember registration at a Society Meeting by the applicant, the difference between the nonmember and member registration fees shall be credited toward the first year's dues.

CONSTITUTION—Article III

Admission and Dismissal of Members

Section 1. Application for individual membership shall be in writing on a form adopted by the Board of Directors.

Section 2. The Admissions Committee shall be a rotating committee consisting of three members. One member shall be appointed each year by the President with the approval of the Board of Directors for a term of three years to replace the outgoing member. This Committee shall receive from the Secretary all properly executed and properly recommended applications for admission which he has received from persons desirous of becoming members of the Society. It shall be the duty of this Committee, after examining the credentials of applicants, to make appropriate recommendation to the Board as to approval or rejection of the applications. Unanimous approval of an applicant by this Committee shall be required before the candidate's name may be submitted to the Board of Directors for election. The election to membership shall be by a mail vote of the Board of Directors. The candidate shall be considered elected two weeks after the date the proposed membership list is mailed to the Board if no negative votes have been received by the Secretary. If a candidate receives one negative vote, his application shall then be considered and voted upon at the next meeting of the Board of Directors. Two negative votes cast at this meeting shall exclude a candidate. The Board of Directors may refuse to elect a candidate who, in its opinion, is not qualified for membership. The names of those elected shall be announced to the Society. Duly elected candidates shall have all the rights and privileges of membership as soon as their entrance fee, if any, and dues for the current year have been paid.

Section 3. A member desiring to resign shall send a written resignation to the Office of the Society.

Section 4. Upon the written request of ten or more Active Members that, for cause stated therein, a member be dismissed, the Board of Directors shall consider the matter and, if there appears to be sufficient reason, shall advise the accused of the charges against him. He shall then have the right to present a written defense, and to appear in person before a meeting of the Board of Directors, of which meeting he shall receive notice at least twenty days in advance. Not less than two months after such meeting the Board of Directors shall finally consider the case and, if in the opinion of the majority of the Board of Directors a satisfactory defense has not been made and the accused member has not in the meantime tendered his resignation he shall be dismissed from the Society.

Section 7. The entrance fee, if any, annual dues and any other payments to be made by the members of the Society shall be paid in accordance with regulations set forth in the Bylaws.

Section 8. Any member delinquent in dues after April 1 shall not receive the Society's publications and will not be allowed to vote in any Society election until such dues are paid. All members in arrears for one year after April 1 shall lose their membership status and can be reinstated only by action of the Board of Directors.

Call for Papers

156th Meeting, Los Angeles, California, October 14-19, 1979

Divisions which have scheduled sessions are listed on the overleaf, along with symposium topics.

1. Symposium Papers.

Authors desiring to contribute papers to a symposium listed on the overleaf should check first with the symposium chairman to ascertain appropriateness of the topic.

2. General Session Papers.

Each of the Society Divisions or Group which will meet in Los Angeles, California, can plan a general session. If your paper does not fit readily into a planned symposium, you should specify "General Session."

3. To Submit a Meeting Paper.

Each author who submits a paper for presentation at a Society Meeting must do three things:

A—Submit one original 75-word abstract of the paper on the attached form or a facsimile thereof. **Deadline for receipt of 75-word abstract is May 1, 1979.**

B—Submit original and one copy of an Extended Abstract of the paper. **Deadline for receipt of Extended Abstract is June 1, 1979.** See (5) below for details.

C—Determine whether the meeting paper is to be submitted to the Society Journal for publication. **See (6) below for details.**

Send all material to The Electrochemical Society, Inc., P.O. Box 2071, Princeton, N.J. 08540.

Unless the 75-word and required Extended Abstracts are received at Society Headquarters by stated deadlines, the papers will not be considered for inclusion in the program.

4. Meeting Paper Acceptance.

Notification of acceptance for meeting presentation, along with scheduled time, will be mailed to authors with general instructions no earlier than two months before the meeting. Those authors who require more prompt notification are requested to submit with their abstracts a self-addressed postal card with full author-title listing on the reverse.

5. Extended Abstract Volume Publication.

All scheduled papers will be published in the EXTENDED ABSTRACTS volume of the meeting. The volume is published by photo-offset directly from typewritten copy submitted by the author. Therefore, special care should be given to the following instructions to insure legibility.

A—Abstracts are to be from 500 to 1000 words in length and should not exceed two pages, single spaced. The abstract should contain to whatever extent practical all significant experimental data to be presented during oral delivery.

B—Abstracts should be typed single spaced on the typing guide forms which are sent to each author after the submission of a short abstract. If it is necessary to use white bond paper, it should be 8½ x 11 inches with 1¼ inch margins on all sides. Submit all copy in black ink. Do not use handwritten corrections.

C—Title of paper should be in capital letters. Author(s) name and affiliation and address should be typed immediately below in capital and lower case letters. Please include zip code in address. It is not necessary to designate paper as "Extended Abstract" or to quote the divisional symposium involved.

D—If figures, tables, or drawings are used, they should follow the body of the text and should not exceed one page. Submit only the important illustrations and avoid use of halftones. Lettering and symbols should be no smaller than ⅛ inch in size. Figure captions should be typed beneath the figure and be no wider than the figure. Table titles should be typed above, and the same width as, the table.

E—Mail original and one copy of the abstract to: The Electrochemical Society, Inc., P.O. Box 2071, Princeton, N.J. 08540, unfolded.

Abstracts exceeding the stipulated length will be returned to author for condensation and retyping.

6. Manuscript Publication in Society Journal.

All meeting papers upon presentation become the property of The Electrochemical Society, Inc. However, presentation incurs no obligation to publish. If publication in **Journal** is desired. papers should be submitted as promptly as possible in full manuscript form in order to be considered. If publication elsewhere after presentation is desired, written permission from Society Headquarters is required.

Los Angeles, California, Meeting Symposia Plans—Fall 1979
October 14-19, 1979

a.) For receipt no later than May 1, 1979, submit a 75-word abstract of the paper to be delivered on the attached form.
b.) For receipt no later than June 1, 1979, submit two copies of an extended abstract, 500-1000 words.
c.) Send all abstracts to The Electrochemical Society, Inc., P.O. Box 2071, Princeton, N.J. 08540. See details on preceding page.

BATTERY

Ambient Temperature Lithium Batteries

This symposium will be devoted to lithium battery technology pertinent to ambient temperature cells and batteries. Emphasis will be placed on studies leading to new or improved systems. Papers are solicited in the areas of primary and secondary cells utilizing either liquid or solid electrolytes. Subjects of interest are, for example: 1. electrodes' reactions, kinetics, and mechanisms of reaction; 2. electrolytes and their role in cell performance; 3. systems' performance at various temperatures before and after storage; 4. chemical and electrochemical intracell interactions including hardware; 5. safety in cell fabrication, use and disposal; 6. materials of choice for cell fabrication, including alloys, adsorbers, barriers, binders, conductors, hardware, and parts fabrication; and 7. design principles and techniques for cell fabrications including materials processing and sealing.

Suggestions and inquiries should be sent to the Symposium Chairman: N. Margalit, ESB Technology Co., 19 W. College Ave., Yardley, Pa. 19067.

Lead Acid—New Developments

This symposium will focus on recent advances in lead-acid battery technology that may lead to improvements in energy density, power density, or life, or that may result in simpler maintenance or less costly construction. Of special interest would be those improvements which could expand the role of lead-acid batteries in electric vehicles or bulk energy storage systems. Discussions of new developments in small sealed lead-acids are also encouraged. Suitable topics would include: 1. new grid alloys and grid designs; 2. advanced separators; 3. new approaches to cell corrosion and other failure mechanisms; 4. advances in electrolyte distribution and control; 5. unconventional electrodes or cells; 6. single-point watering techniques; and 7. sealed cell technology.

Suggestions and inquiries should be sent to the Symposium Chairman: A. J. Salkind, ESB Technology Co., 19 W. College Ave., Yardley, Pa. 19067.

Power Sources for Biomedical Implantable Applications

This symposium will include papers dealing with both the experimental and theoretical aspects of electrochemical batteries that have been developed or show promise for biomedical implantable applications. The papers may deal with both lithium and alkaline cell systems. Primary and secondary batteries may both be included in the discussions. Invited papers will review the development of the implantable medical devices from both the clinical and engineering perspectives, and will also cover the subsequent evolution in alkaline batteries and the more recent activity in the use of lithium batteries. Appropriate papers will not only deal with the chemistry of the various systems which have been implanted, but may also report on field experience with the variety of systems which have been implanted and relate the observed performance to longevity projections which have been made for the various batteries. Suitable topics include the following: 1. lithium implantable power sources; 2. primary alkaline cells; 3. rechargeable alkaline cells; 4. safety aspects of implanted batteries; 5. battery reliability and quality control; 6. microcalorimetry—a useful tool for battery analysis; 7. pacemaker battery specifications; 8. sealing technology in the pacemaker cell industry; 9. hermeticity—its maintenance and verification; and 10. battery evaluation—test methods and projections.

Suggestions and inquiries should be sent to the Symposium Chairman: B. B. Owens, Medtronic, Inc., 3055 Old Highway Eight, P.O. Box 1453, Minneapolis, Minn. 55440.

General Session

A portion of this session is aimed at stimulating dialogue between battery developers and manufacturers and research investigators. Papers are solicited which deal with practical considerations for the optimization of electrode and battery designs, and approaches to cell and battery modeling. More basic papers are sought from researchers dealing with theoretical and practical aspects of electrode modeling, electrode morphology changes as a function of discharge history, and porous electrode theory. Papers covering nondestructive cell testing methods, developments in test data collections, interpretation of test results, and advances in determination of state of charge will also be included.

Suggestions and inquiries should be sent to the Session Chairman: E. L. Littauer, Lockheed Palo Alto Research Lab, Dept. 52-35, Bldg. 204, 3251 Hanover St., Palo Alto, Calif. 94304.

BATTERY/ELECTROTHERMICS AND METALLURGY/PHYSICAL ELECTROCHEMISTRY/ENERGY TECHNOLOGY GROUP

Electrochemical Processes in High Temperature Batteries and Fuel Cells

This symposium will emphasize fundamental electrochemical processes which are common in many high temperature systems. Major objectives include summarizing the current understanding of these processes and identifying common problems. Several invited review papers will be presented. Contributed papers dealing with thermodynamic analyses, structure aspects, and kinetic and transport problems in high temperature systems are solicited. Appropriate systems include: 1. high temperature batteries such as the sodium-sulfur and the lithium-sulfur systems; and 2. high temperature fuel cells, such as the molten carbonate and solid-electrolyte cells.

Suggestions and inquiries should be sent to the Symposium Co-Chairman; W. L. Worrell, University of Pennsylvania, Dept. of Materials Science K1, Philadelphia, Pa. 19104; or J. J. Kelley, ESB Technology Co., 19 W. College Ave., Yardley, Pa. 19067.

BATTERY/ENERGY TECHNOLOGY GROUP

Electrochemical and Thermal Modeling of Batteries

This symposium will try to advance the theory required for the development of aqueous (acidic and basic), and nonaqueous (organic, solid, and molten salts), secondary battery systems. The objectives are two-fold: 1. to develop theoretical methods for electrochemical and thermal modeling of battery systems from a kinetic or thermodynamic viewpoint; and 2. to develop methods for predicting the behavior of batteries from small scale experiments. Papers that report experimental results that verify new theoretical consideration are appropriate. Papers on battery systems including such topics as: a priori requirements; resistivity of ionic phases; concentration profiles; effects of electrostatic charge on ionic transfers; solubility of charged species; morphological changes; optimization of electrodes and electrode distances; transfer numbers; solvent effects reasons for declining performance on cycling; kinetics; thermal effects; etc., are appropriate.

Suggestions and inquiries should be sent to the Symposium Co-Chairmen: A. R. Landgrebe or S. Ruby, Dept. of Energy, 600 E St., NW, Rm. 421, Washington, D.C. 20545; or H. F. Gibbard, Gould Labs, 40 Gould Ctr., Rolling Meadows, Ill. 60008.

BATTERY/ENERGY TECHNOLOGY GROUP/PHYSICAL ELECTROCHEMISTRY

Catalyst Structure and Catalyst Support Interactions in Energy Conversion and Storage Devices

The objectives of this symposium are to summarize methods for determining the structure of microcrystal catalyst particles and the effects of the support on both the structure and catalytic activity of these particles. Topics of particular interest to this symposium are: 1. preparation of microcatalyst particles including metals, alloys, oxides, and organometallic compounds; 2. methods for electrochemically characterizing the activity of microcatalyst particles; 3. methods for characterizing the structure of microcatalyst particles including x-ray diffraction, electromicroscopy, Mössbauer spectroscopy, and ESR, etc.; and 4. studies of supported catalysts and especially the effects of the support on the catalyst.

Suggestions and inquiries should be sent to the Symposium Co-Chairmen: W. E. O'Grady, Brookhaven National Lab, Bldg. 815, Upton, N.Y. 11973; or P. N. Ross, University of California, Lawrence Berkeley Lab. Bldg. 62, Berkeley, Calif. 94720.

CORROSION

Electrochemistry of Hot Corrosion

This symposium will include theoretical and experimental electrochemical studies of the accelerated oxidation of metals and alloys coated by fused electrolyte (salt) films at elevated temperatures. Particular topics of interest include: identity of cathodic reduction step; solubilities of protective oxides; hot corrosion models and mechanisms; new experimental techniques; laboratory prediction of service life; electrochemical polarization studies; correlations of corrosion morphologies to mechanism; and electrochemical determination of hot corrosion kinetics.

Suggestions and inquiries should be sent to the Symposium Chairman: R. A. Rapp, Ohio State University, Dept. of Metallurgical Engineering, Columbus, Ohio 43210.

General Session

Papers on all aspects of low and high temperature corrosion will be considered. Experimental techniques for the study of corrosion phenomena are also of interest.

Suggestions and inquiries should be sent to the Session Chairman: K. Nobe, University of California, Boelter Hall 5405, Los Angeles, Calif. 90024.

CORROSION/ELECTRONICS

Contact Metallurgy and Contact Resistance

This symposium will be concerned with various aspects of contact metallurgy and contact resistance such as: 1. preparation of materials; 2. characterization of materials; 3. materials stability with respect to corrosion electromigration and interievei diffusion; 4. device considerations such as electrical properties of structures, and, in particular, MOS structure and contact area effects; and 5. processing compatibility in device structures.

Suggestions and inquiries should be sent to the Symposium Co-Chairmen: D. B. Frazer, Bell Labs, Room 2C-334, Murray Hill, N.J. 07974; or P. B. Ghate, Texas Instruments, Inc., P.O. Box 225012, M/S 82, Dallas, Texas 75265.

CORROSION/ELECTROTHERMICS AND METALLURGY/NEW TECHNOLOGY SUBCOMMITTEE

Joint with Metallurgical Society of AIME

Amorphous Metals and Films

This symposium is divided into two parts: Part A—Role Played by Noncrystalline Films and Substrates in Corrosion Processes; and Part B—Amorphous Metals.

Part A will consider the influence of the amorphous state on all aspects of corrosion phenomena, including kinetics, morphology of attack, and effects of alloy composition. Part B is primarily tutorial and will consist of reviews of the formation and the structural, thermal, mechanical, electronic, and magnetic properties of metallic glasses. Papers addressing the role of the amorphous state as it pertains to the alloy substrate and/or the resulting corrosion product film are appropriate for Part A. Presentation of submitted papers is not planned for Part B.

Suggestions and inquiries for Part A should be sent to the Symposium Co-Chairmen: R. B. Diegle, Battelle Memorial Inst., Columbus Labs, 505 King Ave., Columbus, Ohio 43201; or R. M. Latanision, MIT, Dept. of Materials Science and Engineering, Cambridge, Mass. 02139.

Suggestions and inquiries for Part B should be sent to the Symposium Co-Chairman: B. C. Giessen, Northeastern University, Inst. of Chemical Analysis, Materials Science Div., Boston, Mass. 02115.

CORROSION/ENERGY TECHNOLOGY GROUP

Geothermal Energy Systems

This symposium will be concerned with those technical aspects of geothermal fluids utilization that lie within the interest areas of several Divisions of the Society. Corrosion and scaling and their amelioration will be featured, in addition to other topics of interest in electrochemistry, electronics, and materials technology. Contributed papers are particularly solicited in the following areas: 1. corrosion phenomena encountered in geothermal systems (general, pitting, crevice, embrittlement, stress, etc.); 2. corrosion-resistant materials and corrosion prevention in geothermal applications; 3. origin and circumvention of scaling in geothermal systems; 4. sampling and chemical analysis of geothermal fluids and effluents; 5. downhole probes for physicochemical measurements, e.g., pH, salinity, specific ions, dissolved gases; 6. electronics and materials for sensors operating in geothermal environments; 7. thermodynamics and chemistry of geothermal fluids, including experimental techniques and correlations of actual data; and 8. by-product recovery, including minerals from spent brines and "noncondensible" gases.

Suggestions and inquiries should be sent to the Symposium Co-Chairman: (corrosion and scaling) D. van Rooyan, Brookhaven National Lab, Dept. of Nuclear Energy, Upton, N.Y. 11973; or (other topics) W. W. Harvey, EIC Corp., 55 Chapel St., Newton, Mass. 02158.

DIELECTRICS AND INSULATION

General Session

Papers for this session are solicited on all aspects of dielectric materials, especially their preparation and characterization in both bulk and thin film forms.

Suggestions and inquiries should be sent to the Session Co-Chairmen: G. Schwartz or R. G. Frieser, IBM Corp., Semiconductors Products Div., Hopewell Junction, N.Y. 12603.

DIELECTRICS AND INSULATION/ ELECTRONICS

Applications of Glasses in Device Technology

Papers are solicited from all areas relating to the use of nonmetallic, inorganic glasses and ceramics in device technology and packaging. Emphasis will be placed on the chemical and physical properties necessary for the effective utilization of these materials. This includes composition, formulation, and techniques of application on devices and in packaging. Of particular interest are fritted glass compositions, used, for example, in passivation and isolation of devices as well as conventionally formulated solder glasses and ceramics now extensively employed in the electronics industry as sealing, dielectric, capacitor, and substrate materials.

Suggested topics include: the effect of composition on physical properties such as sealing temperature, coefficient of expansion, hardness, ductility, and chemical stability in wafer processing as well as electronic properties such as dielectric breakdown, polarization, apparent charge character under device bias, conductivity and surface leakage. Topics also included are, for example: methods of producing crystal- and bubble-free films of reflowed glasses; characterization of evaporated glass and ceramic films used in conventional semiconductor techniques; protection of memory devices in a hostile environment with chemically durable glasses; ways of sintering ceramic packages to protect highly conductive metallurgies; and fabrication of thin and thick films of metallized ceramics.

Suggestions and inquiries should be sent to the Symposium Co-Chairmen: J. L. Powell, IBM Corp., SPD, Dept. 300/414, East Fishkill Facility, Hopewell Junction, N.Y. 12533; or D. L. Flowers, Motorola, Inc., B136, 5005 East McDowell Rd., Phoenix, Ariz. 85008.

Degradation Mechanisms in Electronic Devices

This symposium will consist of invited and contributed papers on physical, chemical, electrochemical, metallurgical, electronic, or structural factors which result in parametric degradation or in catastrophic failure of electronic devices. Contributed papers are solicited in the following areas: 1. effects of technology trends such as smaller IC geometry on device reliability; 2. influence of in-process radiation effects on susceptability of devices to subsequent degradation during operating life; 3. effects of new materials used in device fabrication, such as plasma deposited silicon nitride or new plastics, on device reliability; 4. effects of multilevel metallization on device reliability; 5. effects of device surface topology, or of localized defects, on device reliability; 6. effects of moisture or other contaminants on degradation of hermetically sealed or plastic-encapsulated devices; 7. new materials or processes to avoid or reduce the effects of degradation mechanisms; 8. susceptability of newer IC technologies such as I^2L, VMOS, and CMOS/SOS to particular degradation mechanisms; 9. improved understanding of failure mechanisms or of the effects of processes such as gettering to avoid device degradation; and 10. methods for studying device degradation mechanisms.

Suggestions and inquiries should be sent to the Symposium Co-Chairmen: J. M. Eldridge, IBM Corp., Research Labs, San Jose, Calif. 95193; or G. L. Schnable, RCA Labs, Princeton, N.J. 08540.

Second Symposium on Display Technology

The main objective of this symposium is the active interchange of information between participants working in different display technologies. Papers are solicited in the following fields: 1. liquid crystals; 2. electroluminescence and cathode luminescence; 3. plasma display technology; and 4. electrochromic, electrophoretic, and electroluminescent devices. Papers containing new and unpublished information on materials aspects, devices, addressing schemes, etc., will be considered. In addition, invited papers summarizing the state-of-the-art in each field are planned.

Suggestions and inquiries should be sent to the Symposium Co-Chairmen: G. J. Sprokel, IBM Corp., Research Labs, 5600 Cottle Rd., San Jose, Calif. 95193; or P. N. Yocom, RCA Labs, Princeton, N.J. 08540.

Heteroepitaxial Silicon on Sapphire and Competing Technologies

Papers are solicited on all materials aspects of the silicon on sapphire and competing technologies. Emphasis will be placed on: 1. preparative parameters: identification of key preparative parameters such as substrate surface preparation, deposition conditions, and postdeposition treatments; 2. microstructure: development of an understanding of the relationship between materials microstructure and semiconducting properties; 3. new preparative methods: the characteristics realized by use of new preparative methods such as solid-state epitaxy and laser annealing; 4. characterization: the physical/chemical/electrical characterization and qualification of the heteroepitaxial deposits prior to final device processing; 5. capabilities of SOS in comparison with other technologies: the advantages and disadvantages of silicon on sapphire and other technologies directed toward achieving high speed, low power, radiation hardness, and ease of preparation and processing.

Suggestions and inquiries should be sent to the Symposium Co-Chairmen: (heteroepitaxial silicon) G. W. Cullen, RCA Labs, Princeton, N.J. 08540; P. Rai-Choudhury, Westinghouse R&D Ctr., Beulah Road, Pittsburgh, Pa. 15235; or (competing technologies) D. McGreivy, Hughes Aircraft Co., 500 Superior Ave., Newport Beach, Calif. 92663.

Thin Film Interfaces and Interactions

This symposium will deal with the processes by which thin films may interact with each other, with substrates, or with ambient atmospheres. The role of interface processes will receive special attention. Topics may include: 1. ion-beam interface mixing; 2. interactions peculiar to laser annealing or electron-beam annealing; 3. physics and chemistry of laser-solid interactions at interfaces; 4. new or metastable compound phases and solid solutions; 5. metal-metal and metal-alloy diffusion; 6. epitaxy, orientation, texture in reacting layers; 7. metal silicides and silicon-silicide reactions; 8. multilayer solar absorbers; and 9. dielectric films: SiO_2 growth mechanisms and film characteristics; Si_3N_4.

Suggestions and inquiries should be sent to the Symposium Co-Chairmen: J. E. E. Baglin, IBM Corp., T. J. Watson Research Ctr., P.O. Box 218, Yorktown Heights, N.Y. 10598; or J. M. Poate, Bell Labs, Murray Hill, N.J. 07974. Other Co-Chairmen are: W. L. Brown, S. S. Lau, and J. W. Mayer.

DIELECTRICS AND INSULATION/ ELECTRONICS/ELECTROTHERMICS AND METALLURGY

Seventh International Conference on Chemical Vapor Deposition

This conference will provide a forum for those interested in CVD to exchange recent results. The scope of the conference is broad and will include papers on: 1. fundamentals, kinetics, and gas flow dynamics; 2. diagnostics, in situ probes, process monitors; 3. process engineering, low pressure CVD, plasma-enhanced CVD, novel reactors; 4. materials/properties, semiconductors, metals, refractories, glasses, interfaces, wear and corrosion resistance, adhesions; and 5. applications, electronics, optics, mechanics, protective coatings, solar cells. A proceedings volume will be published, and deadlines are described in detail in the special Call for Papers which appeared in the October 1978 issue of the **Journal**.

Suggestions and inquiries should be sent to the Conference Co-Chairmen: T. Sedg-

(continued over)

wick, IBM Corp., T. J. Watson Research Ctr., P.O. Box 218, Yorktown Heights, N.Y. 10598; or H. Lydtin, Philips Gmbh, Forschunglaboratorium Aachen, Postfach 1980, Weishausstrasse, West Germany.

ELECTRODEPOSITION

General Session

Papers covering all theoretical and/or applied areas not included in the joint symposium are invited to this session. Suggestions and inquiries should be sent to the Session Chairman: N. Feldstein, Surface Technology, Inc., P.O. Box 2027, Princeton, N.J. 08540.

ELECTRODEPOSITION/ELECTRONICS

Metal Patterning by Selective Deposition

This symposium will emphasize selective plating techniques for electronics applications. Included will be metal patterning for: 1. conductors for semiconductor circuits; 2. thin film circuits (bubble memories, thin film heads and sensors, x-ray masks, and other devices); 3. printed circuits; 4. device assembly and packaging (interconnections, lead-frames, DIP's, etc.); and 5. electrical contacts and connectors. Emphasis will be on additive patterning techniques involving electroless and electroplating processes as well as vapor deposition. Included will be appropriate plating electrolytes, selective activation-sensitization techniques, selective catalysis and nucleation methods, associated photolithographic and other masking procedures, spot plating methods and cell design for selectivity. Substractive methods such as patterning by wet or dry etching will not be included, although lift-off or parting layer techniques are appropriate.

Suggestions and inquiries should be sent to the Symposium Co-Chairmen: E. D. Winters, Bell Labs, Allentown, Pa. 18103; A. H. Graham, E. I. Du Pont de Nemours, Experimental Station, Wilmington, Del. 19800; or L. T. Romakiw, IBM Corp., T. J. Watson Research Ctr., P.O. Box 218, Yorktown Heights, N.Y. 10598.

ELECTRONICS

Semiconductors

Business Trends in the Electronics Industry

This symposium is a new venture to introduce a nontechnical subject matter of broad interest and concern. The electronics industry focuses on product innovation and cost reduction to promote wider use but is also subject to a wide variety of external influences. This symposium will feature several invited papers to provide background for current economic trends and encourages presentations in areas such as: 1. the economics of silicon wafer size; 2. the influence of the introduction of new equipment on costs; 3. the economics of VLSI vs. LSI; 4. the present status of tariff laws between the U.S. and its major trading partners; 5. the role of currency fluctuations; 6. worldwide labor rates, capital and development costs, and productivity; 7. venture capital needs in the electronics industry; 8. product liability; 9. technology transfer within the U.S. and to other countries; 10. future prospects for the electronics industry; 11. patents and business; and 12. role of government in influencing the electronics business.

Suggestions and inquiries should be sent to the Symposium Co-Chairmen: R. E. Enstrom, RCA Labs, Princeton, N.J. 08540; or B. E. Deal, Fairchild Research and Development, 4001 Miranda Ave., Palo Alto, Calif. 94304.

International Symposium on Gettering in Semiconductors

The purpose of this symposium is to cover all aspects of gettering in semiconductors. The physics and chemistry of gettering phenomena will be highlighted, but authors are encouraged to relate process history and device performance insofar as is possible. Initial plans are for one-third of the papers to be comprehensive reviews, and the other two-thirds of the papers are to be contributed papers which may fit into the following categories: 1. capture mechanisms—diffused layers, ion-damaged layers, dislocation and defect arrays, polysilicon layers, disorder induced by laser damage etc. Frontside and backside localized capture; 2. diffusion mechanisms—vacancy and interstitial control, diffusion of impurities and defect motion; 3. release mechanisms—modification of precipitates, stacking fault contraction and expansion, fault and grain boundary decoration, etc.; and 4. device performance and applications—bipolar and MOS technologies, techniques for VLSI, thermal reversibility, thermal history, pregettering, and postprocess gettering. A symposium volume may be published if sufficient interest develops.

Suggestions and inquiries should be sent to the Symposium Co-Chairmen: T. Seidel, Bell Labs, Murray Hill, N.J. 07974; or H. Geipel, IBM Corp., GTD, Essex Junction, Vt. 05452.

Laser and Electron Beam Processing of Electronic Materials

This symposium will be devoted to processing technologies which use localized heating to modify the properties of electronic materials. The source of energy may be a laser, electron beam, or an intense incoherent light source. Abstracts are solicited in the following areas: 1. annealing of ion implantation damage; 2. epitaxial regrowth of amorphous and polycrystalline deposits; 3. metallurgical aspects of mixed compound formation; 4. electrical properties of materials or devices subjected to localized heating; 5. topological changes and machining induced by localized heating; 6. unique techniques and apparatus for introducing and controlling localized heating processes; and 7. laser—solid and electron beams—solid interaction fundamentals. In addition to invited speakers on the above topics, each session will combine oral 10 minute contributed papers with a one hour open poster session. An attempt will be made to accommodate authors who do not wish to participate in either the poster or the oral presentation format. A symposium volume will be published if sufficient interest develops. Interested authors should consult the special Call for Papers to be published in the January 1979 issue of the **Journal** before submitting abstracts.

Suggestions and inquiries should be sent to the Symposium Co-Chairmen: C. L. Anderson, Hughes Research Labs, Malibu, Calif. 90265; G. K. Celler, Western Electric ERC, Princeton, N.J. 08540; or G. A. Rozgonyi, Bell Labs, Murray Hill, N.J. 07974.

Magneto-Optical Materials

This symposium will include invited and contributed presentations. Topics to be discussed include the preparation and magneto-optical evaluation of bulk single crystals and thin films. Papers which describe magneto-optical materials of various categories will be acceptable, such as oxides, halides, fluorides, silicates, sulfides, and metals. Presentations which cover magneto-optical device applications and test procedures are solicited also.

Suggestions and inquiries should be sent to the Symposium Chairman: M. Kestigian, Sperry Research Ctr., Sudbury, Mass. 01776.

Semiconductors and Other Electronic Materials

General Session

Original papers are invited dealing with the following areas: 1. semiconductor materials preparation and characterization; 2. the formation of contacts to semiconductors including questions related to semiconductor-contact interfacial resistivity; 3. process-induced defect and gettering; 4. the formation and properties of thin films deposited by physical, chemical, and plasma-assisted techniques; 5. special techniques for the formation of extremely thin (<1000A) semiconductor films; 6. heterojunction interfacial characteristics; 7. the etching of thin films and bulk materials by solution, vapor phase, and plasma techniques; 8. patterning of small structures of light optical, x-ray, E-beam, and ion-beam techniques; 9. novel techniques for device fabrication; 10. materials aspects of novel devices; 11. high conductivity, high temperature interconnections, e.g., silicides; 12. formation of insulating films on compound semiconductors; and 13. process modeling.

Suggestions and inquiries should be sent to the Session Co-Chairmen: N. A. Masnari, University of Michigan, 3505 East Engineering Bldg., Ann Arbor, Mich. 48109; or A. Reisman, IBM Corp., T. J. Watson Research Ctr., P.O. Box 218, Yorktown Heights, N.Y. 10598.

ELECTRONICS/ENERGY TECHNOLOGY GROUP

Photoelectrochemistry at Semiconductor Electrodes

This symposium will emphasize the factors that influence chemical reactions on the surface of photoexcited semiconductor electrodes. Corrosion, suppression, photocatalytic reactions, photoelectrochemical synthesis, and water splitting pathways will be of particular interest. Modifications of electrode surface to mediate charge transfer and/or additions to the electrolyte that influence reaction paths are appropriate subjects.

Suggestions and inquiries should be sent to the Symposium Co-Chairmen: R. H. Wilson, General Electric Co., Corporate R & D, P.O. Box 8, Schenectady, N.Y. 12301; or A. J. Nozik, Allied Chemical Corp., P.O. Box 1021R, Morristown, N.J. 07960.

ENERGY TECHNOLOGY GROUP

General Session

A number of keynote lectures in energy-related science and technology will be presented. Contributed papers are solicited. Specific topics of interest are: 1. energy conversion; 2. energy storage; 3. energy conservation, distribution, and management; 4. primary energy sources (natural gas, petroleum, coal, nuclear, solar, geothermal, fusion) and their applications; 5. electricity and heat generation; 6. power sources for transportation; and 7. hydrogen energy systems.

Suggestions and inquiries should be sent to the Session Co-Chairmen: S. Srinivasan, Brookhaven National Lab, Dept. of Energy and Environment, Upton, N.Y. 11973; or H. Brandhorst, NASA—Lewis Research Ctr., M/S 302-1, 21000 Brookpark Rd., Cleveland, Ohio 44135.

NEW TECHNOLOGY SUBCOMMITTEE

Ion-Selective Electrodes

Ion-selective electrodes are classical electrochemical devices. The last decade has seen a very large growth in the variety of electrodes which have become commercially available, and their uses have ranged from the determination of activity coefficients in pure solutions to electrolyte concentration measurements in whole blood. This symposium will try to cover both theoretical and practical aspects. Appropriate topics include: 1. mechanism of electrode operation; 2. approaches to new electrodes; 3. thermodynamic measurements using electrodes; and 4. new practical applications of electrodes.

Suggestions and inquiries should be sent to the Symposium Chairman: M. S. Frant, Foxboro Analytical, P.O. Box 435, 78 Blanchard Rd., Burlington, Mass. 01803.

75-Word Abstract Form

(Deadline for receipt—May 1, 1979)

LOS ANGELES, CALIFORNIA, MEETING—OCTOBER 14-19, 1979

Submit to: **The Electrochemical Society, Inc.**
P.O. Box 2071, Princeton, N.J. 08540

Schedule for ..... of .....
Symposium ECS Division

Abstract No. .....
(do not write in this space)

(Title of paper) .....

.....

(Authors) (Underline name of author presenting paper) .....

.....

(Business Affiliation and Address) .....

.....

.....
(ZIP Code) (Tel. No.)

(Type abstract in this area—double spaced.)

Do you require any audiovisual equipment?
☐ 35 mm (2 x 2 in.) slide projector
☐ vugraph
☐ other (specify)
Is a full length paper on this work to be submitted for Society Journal publication?
☐ Yes ☐ No

Papers presented before a Society technical meeting become the property of the Society and may not be published elsewhere without written permission of the Society. Papers presented at Society technical meetings must be authored by a member or sponsored by an active member.

.....
Insert name of Society member author or sponsor

For use in submitting your abstract for
The 1979 Fall Meeting
of
The Electrochemical Society, Inc.
to be held at
The Los Angeles Bonaventure Hotel
Los Angeles, California
October 14-19, 1979

THE ELECTROCHEMICAL SOCIETY PATRON MEMBERS

Bell Laboratories
Murray Hill, N.J.

Dow Chemical Co.
Inorganic Chemicals Dept., Midland, Mich.

E. I. du Pont de Nemours and Co.
Plastic Products and Resins Department
Wilmington, Del.

Exxon Research and Engineering Company
Corporate Research Laboratories
Advanced Energy Systems Laboratory,
Solid State and Catalytic Sciences Laboratory,
Linden, New Jersey
Engineering Technology Division
Florham Park, New Jersey

General Electric Co.
Battery Business Department, Gainesville, Fla.
Chemical Laboratory, Knolls Atomic Power Laboratory,
Schenectady, N.Y.
Electronic Capacitor Products Section, Irmo, S.C.
Lamp Div., Cleveland, Ohio
Materials & Process Laboratory, Large Steam
Turbine-Generator Dept., Schenectady, N.Y.

General Electric Co. (continued)
Research and Development Center,
Physical Chemistry Laboratory & Power
Systems Laboratory,
Signal Processing & Communication Laboratory,
Schenectady, N.Y.
Semiconductor Products Dept.,
Syracuse, N.Y.

International Business Machines Corp.
New York, N.Y.

The International Nickel Co., Inc.
New York, N.Y.

Olin Corporation
Chemicals Division
Charleston Technology Center
Charleston, Tennessee

Philips Research Laboratories
Eindhoven, Holland

Westinghouse Electric Corp.
Electronic Tube Div., Elmira, N.Y.
Lamp Div., Bloomfield, N.J.
Semiconductor Div., Youngwood, Pa.
Research Laboratories, Pittsburgh, Pa.
K. W. Battery Co., Westinghouse Subsidiary,
Skokie, Ill.

THE ELECTROCHEMICAL SOCIETY SUSTAINING MEMBERS

The Aerospace Corporation
Los Angeles, Calif.

Airco Industrial Gases
Murray Hill, N.J.

Airco Speer Carbon-Graphite
St. Marys, Pa.

Allied Chemical Corp.
Industrial Chemicals Division
Solvay, N.Y.

Aluminum Co. of America
New Kensington, Pa.

Aluminum Co. of Canada, Ltd.
Montreal, P.Q., Canada

AMAX Inc.
New York, N.Y.

AMP Incorporated
Harrisburg, Pa.

Analog Devices, Inc.
Norwood, Mass.

Applied Materials, Inc.
Santa Clara, Calif.

Asahi Chemical Industry Canada, Ltd.
Toronto, Ontario, Canada

ASARCO Incorporated
South Plainfield, N.J.

BASF Wyandotte Corporation
Wyandotte, Mich.

Battelle Memorial Institute
Columbus, Ohio

Bell-Northern Research
Ottawa, Ont., Canada

Bethlehem Steel Corp.
Bethlehem, Pa.

Boeing Co.
Seattle, Wash.

The Borg-Warner Corp.
Roy C. Ingersoll Research Center
Des Plaines, Ill.

Brown, Boveri & Co., Ltd.
Research Center
Baden, Switzerland

Canadian Industries Ltd.
Montreal, P.Q., Canada

Carborundum Co.
Niagara Falls, N.Y.

Chrysler Corporation
Detroit, Michigan

Cominco Ltd.
Trail, B.C., Canada

The Continental Group, Inc.
Technical Office at LMSC
Palo Alto, Calif.

Corning Glass Works
Corning, N.Y.

Crawford & Russell Inc.
Stamford, Conn.

Diamond Shamrock Corp.
Painesville, Ohio

Dow Corning Corporation
Hemlock, Mich.

Duro-Test Corp.
North Bergen, N.J.

Eagle-Picher Industries, Inc.
Electronics Division
Joplin, Missouri

Eastman Kodak Co.
Rochester, N. Y.

Electric Power Research Institute
Palo Alto, California

Electrochemical Technology Corp.
Seattle, Wash.

Electrode Corporation
Chardon, Ohio

Eltra Corp.
Prestolite Div., Toledo, Ohio
C&D Batteries, Conshohocken, Pa.

Energy Development Associates,
A Gulf and Western Company
Madison Heights, Michigan

ESB Incorporated
Ray-O-Vac Div., Madison, Wisc.
Technology Center, Yardley, Pa.

SUSTAINING MEMBERS (CONTINUED)

Ever Ready Co. (Holdings) Ltd.
Whetstone, London, England

Exmet Corporation
Bridgeport, Conn.

Fairchild Camera & Instrument Corp.
Research and Development Laboratory
Palo Alto, Calif.

FMC Corp.
Inorganic Chemicals Div.
Buffalo, N.Y.

Ford Motor Co.
Dearborn, Mich.

General Motors Corporation
Delco Electronics Div., Kokomo, Ind.
Delco-Remy Div., Anderson, Ind.
Research Laboratories Div., Warren, Mich.

Globe-Union, Inc.
Milwaukee, Wisc.

B. F. Goodrich Chemical Co.
Cleveland, Ohio

Gould Inc.
Gould Laboratories—
Electrical & Electronics Research
Energy Research
Rolling Meadows, Ill.
Gould Laboratories
Cleveland, Ohio

Great Lakes Carbon Corp.
New York, N.Y.

GTE Laboratories
Waltham, Mass.

GTE Sylvania Incorporated
Chemical & Metallurgical Division
Towanda, Pa.

The Harshaw Chemical Co.
Cleveland, Ohio

Hewlett Packard Company
Loveland, Colo.

Hill Cross Co., Inc.
West New York, N.J.

Hoechst-Uhde Corporation
Englewood Cliffs, New Jersey

Honeywell, Inc.
Power Sources Center
Horsham, Pa.

Hooker Chemical Corp.
Niagara Falls, N.Y. (2 memberships)

HP Associates
Palo Alto, Calif.

Hughes Research Laboratories
Div. of Hughes Aircraft Co.
Malibu, Calif.

Industrial Innovation Center
Tehran, Iran

International Lead Zinc Research Organization, Inc.
New York, New York

International Minerals and Chemical Corporation
Electrochemical Division
Orrington, Maine

Kaiser Aluminum & Chemical Corp.
Pleasanton, Ca.

Kawecki Berylco Industries, Inc.
Boyertown, Pa.

Arthur D. Little, Inc.
Cambridge, Mass.

Lockheed Missiles & Space Co., Inc.
Research Laboratory
Palo Alto, Calif.

Mallory Battery Company
Tarrytown, N.Y. (2 memberships)

Marathon Battery Co.
Waco, Texas

Marston Bermuda
Hamilton, Bermuda

Matsushita Electric Industrial Co., Ltd.
Osaka, Japan

Microwave Associates, Inc.
Burlington, Mass.

Molycorp, Inc.
New York, N.Y.

Monsanto Company
St. Louis, Mo.

Motorola Inc.
Phoenix, Ariz.

M&T Chemicals Inc.
Detroit, Mich.

NL Industries, Inc.
New York, N.Y.

Noranda Research Centre
Pointe Claire, Quebec, Canada

Occidental Research Corporation
La Verne, California

Olin Corporation
Metals Research Laboratories
New Haven, Conn.

Owens-Illinois Inc.
Toledo, Ohio

Oxy Metal Industries Corp.
Warren, Mich.

Perkin-Elmer Corp.
Norwalk, Conn.

Phelps Dodge Refining Corp.
Maspeth, N.Y.

Philips Laboratories. Inc.
Briarcliff Manor, N.Y.

Poco Graphite, Inc.
Decatur, Texas

PPG Industries, Inc.
Chemical Div.
Pittsburgh, Pa.

Prototech Company
Newton Highlands, Mass.

RCA Corporation
Color Picture Tube Division
Lancaster, Pa.

Reynolds Metals Co.
Reduction Research Div.
Sheffield, Ala.

Rockwell International
El Segundo, Calif.

Sandia Laboratories
Albuquerque, N. M.

J. C. Schumacher Co.
Oceanside, Calif.

Shipley Company, Inc.
Newton, Massachusetts

Siemens Aktiengesellschaft
Munich, Germany

Signetics Corp.
Sunnyvale, Ca.

Siltec Corporation
Menlo Park, California

Sperry Research Center
Sudbury, Mass.

Sprague Electric Co.
North Adams, Mass.

Stackpole Carbon Co.
St. Mary's, Pa.

Standard Telecommunication Laboratories Ltd.
Essex, England

Stauffer Chemical Co.
Dobbs Ferry, N.Y.

St. Joe Minerals Corp.
Monaca, Pa.

Teletype Corp.
Skokie, Ill.

Texas Instruments Inc.
Attleboro, Mass.
Dallas, Texas

Tokyo Shibaura Electric Co., Ltd.
Toshiba Research and Development Center
Kawasaki, Japan

Union Carbide Corp.
Battery Products Div.,
Corporate Research Dept.
New York, N.Y.

United States Steel Corp.
Research Laboratory
Monroeville, Pa.

Varian Associates
Palo Alto, Calif.

Wacker Chemitronic
Burghausen, Germany

Western Electric
Princeton, N.J.

Xerox Corporation
Rochester, N.Y.

Yardney Electric Corporation
Pawcatuck, Conn.